RADIOLOGY AND ONCOLOGY

vol.56 no.4
december 2022

RADIOLOGY AND ONCOLOGY

December 2022
Vol. 56 No. 4
Pages 409-553
ISSN 1318-2099
UDC 616-006
CODEN: RONCEM

Publisher
Association of Radiology and Oncology

Aims and Scope
Radiology and Oncology is a multidisciplinary journal devoted to the publishing original and high-quality scientific papers and review articles, pertinent to oncologic imaging, interventional radiology, nuclear medicine, radiotherapy, clinical and experimental oncology, radiobiology, medical physics, and radiation protection. Papers on more general aspects of interest to the radiologists and oncologists are also published (no case reports).

Editorial office

Radiology and Oncology
Zaloška cesta 2
P. O. Box 2217
SI-1000 Ljubljana
Slovenia
Phone: +386 1 5879 369
Phone/Fax: +386 1 5879 434
E-mail: gsersa@onko-i.si

Reader for English
Vida Kološa

Secretary
Mira Klemenčič
Zvezdana Vukmirović

Design
Monika Fink-Serša, Samo Rovan, Ivana Ljubanović

Layout
Matjaž Lužar

Printed by
Tiskarna Ozimek, Slovenia

Published quarterly in 400 copies

Beneficiary name: DRUŠTVO RADIOLOGIJE IN ONKOLOGIJE
Zaloška cesta 2
1000 Ljubljana
Slovenia

Beneficiary bank account number: SI56 02010-0090006751
IBAN: SI56 0201 0009 0006 751
Our bank name: Nova Ljubljanska banka, d.d.,
Ljubljana, Trg republike 2,
1520 Ljubljana; Slovenia

SWIFT: LJBASI2X

Subscription fee for institutions EUR 100, individuals EUR 50

The publication of this journal is subsidized by the Slovenian Research Agency.

Indexed and abstracted by:

- *Baidu Scholar*
- *Case*
- *Chemical Abstracts Service (CAS) - CAplus*
- *Chemical Abstracts Service (CAS) - SciFinder*
- *CNKI Scholar (China National Knowledge Infrastructure)*
- *CNPIEC - cnpLINKer*
- *Dimensions*
- *DOAJ (Directory of Open Access Journals)*
- *EBSCO (relevant databases)*
- *EBSCO Discovery Service*
- *Embase*
- *Genamics JournalSeek*
- *Google Scholar*
- *Japan Science and Technology Agency (JST)*
- *J-Gate*
- *Journal Citation Reports/Science Edition*
- *JournalGuide*
- *JournalTOCs*
- *KESLI-NDSL (Korean National Discovery for Science Leaders)*
- *Medline*
- *Meta*
- *Microsoft Academic*
- *Naviga (Softweco)*
- *Primo Central (ExLibris)*
- *ProQuest (relevant databases)*
- *Publons*
- *PubMed*
- *PubMed Central*
- *PubsHub*
- *QOAM (Quality Open Access Market)*
- *ReadCube*
- *Reaxys*
- *SCImago (SJR)*
- *SCOPUS*
- *Sherpa/RoMEO*
- *Summon (Serials Solutions/ProQuest)*
- *TDNet*
- *Ulrich's Periodicals Directory/ulrichsweb*
- *WanFang Data*
- *Web of Science - Current Contents/Clinical Medicine*
- *Web of Science - Science Citation Index Expanded*
- *WorldCat (OCLC)*

This journal is printed on acid- free paper

On the web: ISSN 1581-3207
https://content.sciendo.com/raon
http://www.radioloncol.com

contents

review

nuclear medicine

radiology

clinical oncology

medical physics

review

Cancer immunotherapy with CAR T cells: well-trodden paths and journey along lesser-known routes

Anze Smole

Immunology and Cellular Immunotherapy (ICI) Group, Department of Genetic Toxicology and Cancer Biology, National Institute of Biology, Ljubljana, Slovenia

Radiol Oncol 2022; 56(4): 409-419.

Received 19 October 2022
Accepted 27 October 2022

Correspondence to: Anže Smole, Ph.D., Immunology and Cellular Immunotherapy (ICI) Group, Department of Genetic Toxicology and Cancer Biology, National Institute of Biology, SI-1000 Ljubljana, Slovenia. E-mail: anze.smole@nib.si

Disclosure: A.S. is a co-inventor on PCT International Patent Applications by The Trustees of the University of Pennsylvania, which include discoveries and inventions related to cellular immunotherapies using CAR and TCR T cells.

Background. Chimeric antigen receptor (CAR) T cell therapy is a clinically approved cancer immunotherapy approach using genetically engineered T cells. The success of CAR T cells has been met with challenges regarding efficacy and safety. Although a broad spectrum of CAR T cell variants and applications is emerging, this review focuses on CAR T cells for the treatment of cancer. In the first part, the general principles of adoptive cell transfer, the architecture of the CAR molecule, and the effects of design on function are presented. The second part describes five conceptual challenges that hinder the success of CAR T cells; immunosuppressive tumour microenvironment, T cell intrinsic properties, tumour targeting, manufacturing cellular product, and immune-related adverse events. Throughout the review, selected current approaches to address these issues are presented.

Conclusions. Cancer immunotherapy with CAR T cells represents a paradigm shift in the treatment of certain blood cancers that do not respond to other available treatment options. Well-trodden paths taken by pioneers led to the first clinical approval, and now the journey continues down lesser-known paths to treat a variety of cancers and other serious diseases with CAR T cells.

Key words: chimeric antigen receptor; adoptive cell therapy; cancer; cellular immunotherapy; gene-engineered immune cells

Introduction

It took a series of ground-breaking ideas and clever experiments to establish the role of the immune system in controlling cancer (reviewed in[1]). Current understanding of cancer immunosurveillence also considers the notion that the immune system not only controls tumour formation and growth, but also influences the immunogenicity of the tumour and potential outgrowth. This hypothesis is referred to as cancer immunoediting, in which the three phases of elimination, equilibrium, and escape can be distinguished (reviewed in[2]). These foundations are important for understanding the concepts of cancer immunotherapy, which aims to enhance the immune system's responses to tumour cells.

In the landmark study in 1988[3], *ex vivo* expanded autologous tumour-infiltrating lymphocytes (TILs) in combination with human interleukin-2 (rhIL-2) were developed and demonstrated objective responses in patients with metastatic malignant melanoma. In addition, this work provided the unequivocal evidence of tumour-specific T cell mediated immunity leading to cancer recognition and elimination in humans.[3] The next milestone was the development of a T cell-based cancer immunotherapy using genetically engineered T cells,

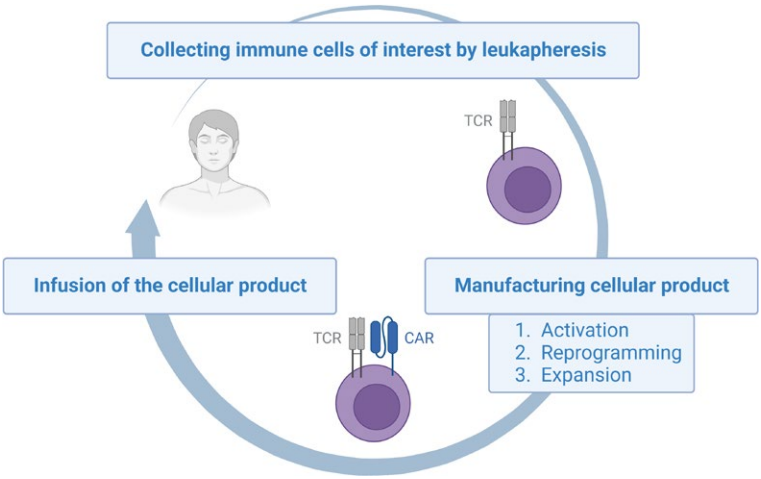

FIGURE 1. The principle of adoptive cellular immunotherapy.

CAR = chimeric antigen receptor; TCR = T-cell receptor

made possible by a better understanding of basic T cell biology and genetic engineering approaches.[4]

Currently, the two most widely used immune receptors that confer tumour specificity and functionality to genetically engineered T cells are a tumour-reactive synthetic chimeric antigen receptor (CAR) and an identified (e.g., from TILs) or further engineered T-cell receptor (TCR). To date, CD19-targeting CAR T cells emerged as the most successful cellular immunotherapy approach. Clinical trials in relapsed or refractory paediatric acute lymphoblastic leukaemia (ALL)[5–7] and high-grade B-cell lymphoma in adults[8–16] have demonstrated that CAR T cell immunotherapy can produce effective, long-lasting, and overall unprecedented clinical responses. CD19-targeting CAR T cells received the U.S. Food and Drug Administration and European Medicines Agency approval in 2017 and 2018, respectively. To date, genetically engineered T cell immunotherapies have mediated unprecedented clinical responses in hematologic malignancies[5–16] but the efficacy of these therapies is limited in solid tumours and also in certain blood cancers due to several factors, some of which are discussed in this review. In addition, adoptive cellular immunotherapies can cause potentially life-threatening complications such as cytokine release syndrome (CRS) and neurological toxicities.[17,18]

Nowadays, cellular immunotherapies include exciting research and clinical successes with TILs and T cells genetically modified with TCRs and CARs. In addition, alternative immune cells are being engineered with CARs[19,20] and CAR T cells are now being used outside of cancer treatment.[21–27] This review article focuses on CAR T cells to treat cancer. First, the concepts of adoptive cellular immunotherapy with CAR T cells are introduced. Then, the architecture of the CAR molecule is described and how design affects function. Current challenges and limitations regarding efficacy and safety are then presented, focusing on the immunosuppressive tumour microenvironment (TME), T cell intrinsic properties, tumour targeting, cellular product manufacturing and immune-related adverse events. Throughout, this paper presents selected recent next-generation approaches to the development of CAR T cells that have the potential to overcome some of these challenges.

Principles of cellular immunotherapy

Adoptive cell transfer

In its broadest sense, adoptive T cell transfer (ACT) involves the isolation of T lymphocytes from blood and their reinfusion into patients for the treatment of disease. Advances in the understanding of basic mechanisms in T cell biology, including target recognition, T cell activation, signal transduction, role of soluble factors, and co-stimulation signals, have led to a better understanding of T cell function, expansion, and persistence.[28] This knowledge has been critical for establishing optimized protocols for *ex vivo* culturing conditions, activation, and expansion. To redirect the specificity of T cells, genetic engineering approaches had to be developed to introduce the genetic cassette encoding TCR or CAR into primary T cells.[4] These significant advances enabled the development of sophisticated T cell-based therapies such as CAR T cells that transformed oncology.

Current clinical adoptive transfer of CAR T cells involves three steps (Figure 1). (1) Collection of T cells: The patient's own T cells (in the autologous ACT setting), which are the body's primary component for fighting infection and cancer, are first isolated from the blood in a procedure called leukapheresis. These cells express endogenous TCR. (2) *Ex vivo* reprogramming and manufacturing of the cellular product: Primary T cells are first activated using activation beads and then a genetic cassette encoding the CAR molecule is introduced into the primary T cells by viral transduction, which transforms donor T cells into CAR T cells. Introduction of these molecules reprograms T

cells to specifically recognize, target and eliminate cancer cells, while *ex vivo* expansion allows manufacturing of sufficient numbers of CAR T cells. (3) Infusion: Patients are treated with a preparatory chemotherapy and then reinfused with the modified T cells. After *ex-vivo* expansion, the reprogrammed cells are infused back to the patient where they find and eliminate the disease.[29]

Design of a CAR molecule

The Chimera is a creature of Greek mythology that consists of parts of various animals. Based on this analogy, CAR is a molecule that combines the properties of a monoclonal antibody that enables antigen recognition with the components of the TCR that drive T cell signalling and activation. CAR is a molecule composed of different domains, each of which contributes to a specific functionality, and together they effectively redirect T cells to the target of interest and elicit T cell responses (Figure 2).

Design of CAR molecule continues to evolve as we gain more knowledge from basic immunology and clinical trials. First-generation CARs consisted of an extracellular antigen-binding domain, usually in the form of an antibody-derived single-chain variable fragment (scFv) linked to intracellular signalling domains, most often derived from the components of the TCR complex, for example the CD3 zeta chain (CD3ζ).[30,31] This molecule was capable of recognizing antigens independent of HLA (human leukocyte antigens) presentation. First-generation CARs provided proof of principle but did not enable long-term T cell persistence and effector responses due to their limited signalling capacity.[32] This section describes CAR molecule architecture and its individual domains.

Antigen recognition domain

The specificity of the CAR molecule is defined by the antigen-targeting ectodomain. In most current designs, this is scFv, which is a fusion between variable heavy and variable light chains of an antibody connected by a flexible linker. The affinity of CAR has been shown to have important effects on the functions of CAR T cells. In a clinical study, enhanced CAR T cell expansion and prolonged persistence were observed with a low affinity CD19 CAR compared to CAR T cells with FMC63, a scFv in clinically approved CD19 targeting CAR T cells.[33] Interestingly, in a different study, linker length has also been shown to influence CAR clustering, antigen-independent signalling and function of CAR T cells.[34] ScFv have now been designed to target several cell surface molecules associated with cancer, most often proteins, but also glycans such as the aberrant cancer-associated Tn glycoform of MUC1, which is expressed in a variety of cancers.[35] Although the mechanism by which binding of CAR to its cognate antigen leads to T cell activation shares key similarities, it also differs substantially from the mechanism by which TCR binding leads to T cell activation. While CARs generally exhibit higher affinity that can also be tuned, the sensitivity is higher in TCRs.[36] Currently, CAR T cells that target CD19 (tisagenlecleucel, axicabtagene ciloleucel, lisocabtagene maraleucel and brexucabtagene autoleucel) and B-cell maturation antigen (BCMA also known as TNFRSF17) (idecabtagene vicleucel, ciltacabtagene autoleucel) are being FDA-approved and marketed[37,38] while several others are in clinical trials, including CD20, CD22, CD33, CD5, and CD7 (reviewed in[39]). Some of widely explored targets in solid tumours include alpha folate receptor (FOLR1), human epidermal growth factor receptor 2 (HER2), carcinoembryonic antigen (CEA), ganglioside G2 (GD2), mesothelin, epidermal growth factor receptor variant III (EGFRvIII), mucin1 (MUC1), interleukin-13 receptor subunit alpha-2 (IL13Ra2), prostate specific membrane antigen (PSMA), B7 homolog 3 (B7-H3), epidermal growth factor receptor (EGFR), and fibroblast activation protein (FAP) (reviewed in[39,40]).

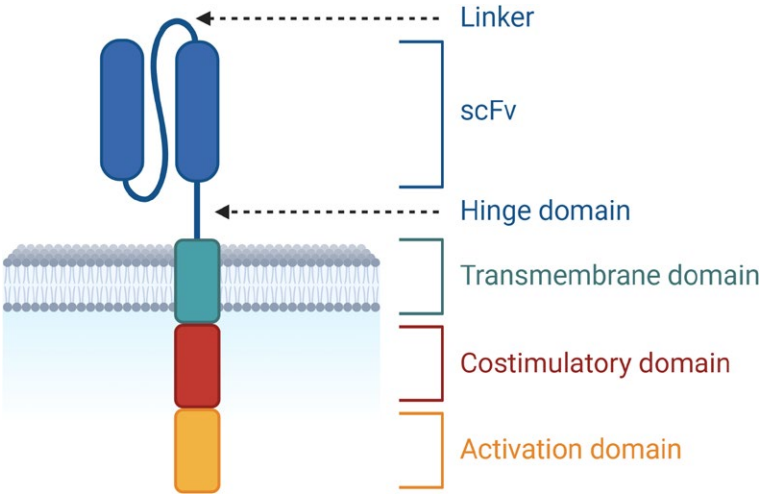

FIGURE 2. Schematics of the basic CAR architecture.

CAR = chimeric antigen receptor; scFv = single-chain variable fragment

Hinge and transmembrane domain

The scFv domain is connected via a hinge region to the transmembrane (TM) domain. The TM domain is often derived from CD8 or CD28 molecules and functions to anchor CAR in the membrane and facilitate signal transduction. The choice or engineering of TM domain may affect the interactions between CAR molecules themselves[41], or with other endogenous molecules such as CD28.[42] Innovative designs in hinge and TM domains may provide opportunities to tune CAR signalling.

Co-stimulatory domain

In the clinically approved CARs, the membrane proximal intracellular domain is the co-stimulatory domain. The need for costimulatory domain arose when limited clinical efficacy of the first generation CAR T cells was observed.[43] The authors concluded that genetically engineered tumour-reactive T cells are safe but do not persist and that strategies to prolong T cell persistence are needed. The first domain included in the CAR design was the CD28 costimulatory domain, initially alone[44] and then in combination with CD3ζ.[45,46] The CD28 domain provides robust response with an effector phenotype and high levels of secreted IL-2 and tumour lysis activity.[47] The other widely used co-stimulatory domain introduced into CAR design is CD137 (4-1BB). Compared to CD28, 4-1BB provides improved persistence, shift towards central memory phenotype differentiation, a lower propensity to exhaustion and reduced toxicity.[15,47,48] A recent comparison between the two marketed products, axicabtagene ciloleucel and tisagenlecleucel examined the differences between CD28 and 41BB in relapsed or refractory diffuse large B cell lymphoma and concluded that axicabtagene ciloleucel provides higher efficacy and also a higher toxicity.[48] Other co-stimulatory domains are also being studied including CD27[49], ICOS[50], and OX-40[51], each of which has certain favourable properties. Finally, third generation CARs comprise a combination of two costimulatory domains and some of these have already been tested in clinical trials.[52] However, excessive stimulation can lead to dysfunctional CAR T cells.[53]

The design of the second-generation CARs, which includes additional co-stimulatory domains that enhance the expansion, persistence, and effector functions of CAR T cells, has been key to the success of clinical trials. A recent study revealed that CAR T cells persisted for more than ten years after infusion, with sustained remission in a patient treated with CD19 targeting 4-1BB CAR T in 2010.[54] Selection of the co-stimulatory domain influences important parameters of CAR T cell therapy including effector function, response kinetics, expansion, differentiation, metabolism and toxicity.[47] Innovative studies are attempting to address the complexities and unknowns by characterizing multiple intracellular signalling domains in a high throughput manner to identify to the CAR designs that have improved functions compared to clinically used CAR T cells.[55]

Activation domain

The distal intracellular domain is CD3ζ, a signal transduction component of the TCR complex that has been repurposed to drive CAR signalling after recognition of its cognate target. Immunoreceptor tyrosine-based activation motifs (ITAMs) are key motifs in the CD3ζ domain. When the TCR recognises its target, ITAMs are phosphorylated through a series of molecular interactions mediated by Lck kinase (lymphocyte-specific protein tyrosine kinase). This leads to the recruitment and activation of ZAP-70 (Zeta-chain-associated protein kinase 70), which orchestrates a series of downstream phosphorylation events that result in the complex and highly regulated signal transduction required for T cell activation and effector functions.[56] CAR signalling resamples key features of TCR signalling but also differs in important ways. Analogous to the "two-step" T cell activation model, CD3ζ provides signal 1 whereas the co-stimulatory domain provides signal 2. CAR signalling is active area of research in basic T cell biology and has direct importance for the therapeutic implementations. As an alternative to the CD3ζ, other domains are investigated for CAR T cell therapy including the CD3ε.[57] An example of rational tuning and calibration of CAR activation and signalling demonstrated that combinatorial mutation of ITAM motifs directs differentiation towards memory T cell states, which translated in improved persistence and therapeutic potency in preclinical mouse models.[58] Moreover, using the genome editing approach, the TRAC locus was modified in primary human T cells to target cell-surface molecules via their TCR complex, which was reconfigured to use the same targeting component as a corresponding CAR. These HLA-independent TCRs, referred to by the authors as HIT receptors, have been shown to be particularly sensitive compared to CD28-based CARs.[59]

Challenges and opportunities of cellular immunotherapy

The success of CAR T cells is countered by challenges in efficacy in solid tumours[40] and immune-related adverse events. Underlying causes of limited efficacy include immunosuppressive TME and T cell and tumour intrinsic properties. In addition, the manufacturing of the cellular product and lack of tumour specific targets represent a major challenge. Here, some of these aspects are outlined and selected recent publications are presented that attempt to meet these challenges (Figure 3).

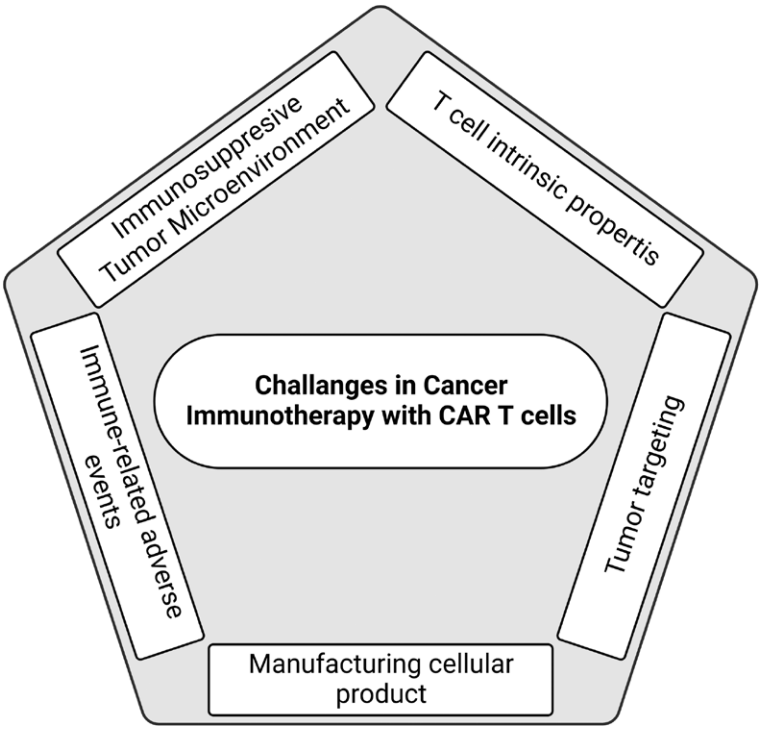

FIGURE 3. Challenges of cellular immunotherapy with chimeric antigen receptor (CAR) T cells.

Immunosuppressive tumour microenvironment

Immunosuppressive TME limits the efficacy of CAR T cells by interfering with their function. Various approaches have been developed to address these challenges, including upgrading engineered T cells with the expression of accessory molecules. Pioneering work has been done with tumour infiltrating-lymphocytes (TILs) engineered with inducible expression of the potent immune-enhancing molecule IL-12.[60] This approach was tested in human clinical trials and clinical activity but also toxicity were observed. Similarly, CAR T cells have been equipped with accessory molecules to counteract various aspects of the hostile immunosuppressive TME. These molecules include IL-18[61–64], PD-1[65], CTLA-4, or TIM3[66] blocking scFvs and minibodies, CD40L[67], dominant-negative Fas[68] or Fas-41BB switch[69] receptors, pro-inflammatory neutrophil-activating protein (NAP) from *Helicobacter pylori*[70] and dominant-negative TGFβ Receptor.[71] Recently, a pooled knock-in platform has been developed to screen for genetic constructs that can improve T cell functions for effective cell therapies when constitutively overexpressed.[72] Additional genetic approach coupling expression of effector molecule with specific antigen recognition was developed using a synNotch platform.[73] These approaches improve the efficacy of T cell therapy and highlight the need to develop robust and efficient gene expression systems suitable for clinical translation.

Depleting of cells that limit the efficacy of CAR T cells is a viable approach to increase CAR T cell activity in TME. One approach is the depletion of immunosuppressive M2 tumour-associated macrophages (TAMs) by CAR-mediated targeting of a folate receptor β (FRβ) positive subset of TAMs that exhibit an immunosuppressive M2-like profile. CAR T cells eliminated these FRβ+ TAMs, resulting in recruitment of endogenous tumour-specific CD8+ T cells, improved tumour control, and prolonged survival.[74]

Therefore, overcoming immunosuppressive TME with innovative approaches is an important pillar in improving the activity of CAR T cells.

T cell intrinsic properties

It is becoming increasingly clear that intrinsic T cell dysfunctions, such as T cell exhaustion limit the success of CAR T cells in solid tumours but also in hematologic malignancies that induce dysfunctional T cell states. A recent correlative study examined the determinants of response at genomic, phenotypic and functional levels and demonstrated that clinical efficacy in patients with chronic lymphocytic leukaemia (CLL) treated with CAR T cells is affected by complex intrinsic immune cell functions and dysfunctions.[75] Chronic stimulation of T cells with an antigen, as occurs also with CAR T cells targeting solid tumours, is an important reason for the dysfunction.[76] One approach to overcome this problem is a temporary resting period in which the functionality of the CAR T cells is restored.[77] Innovative approaches

have been developed to maintain functionality of CAR T cells, including overexpression of c-Jun[78] or a combination of BATF and IRF4.[79] Recent studies linked the heterogeneity of autologous CAR T cells in terms of cellular and molecular characteristics of the infusion products to differences in efficacy and toxicity following CD19 CAR T therapy.[80] In a distinct approach, CAR T cells were designed to express interleukin IL-7 and CCL19 to mimic a favourable milieu that forms and maintains T cell zones in lymphoid organs.[81] These upgraded CAR T cells demonstrated enhanced recruitment of T cells and dendritic cells into tumour and augmented therapeutic effects against solid tumours. Favourable effect on differentiation and persistence of CAR T cells has been demonstrated with the constitutive IL-7 receptor[82], IL-15[83], and synthetic receptors combining orthogonal extracellular IL-2 and intracellular IL-9 domains.[84] In a recent study, overexpression of more than 10,000 barcoded human open reading frames (ORFs) identified positive regulators of T cell function, with the aim of developing improved cellular immunotherapies including CAR T cells.[85]

The intrinsic properties of T cells in the context of CAR T cell therapy require careful study from the perspective of basic immunology. This knowledge is important to overcome the dysfunction that limits the activity of CAR T cells.

Tumour targeting

CD19 is an example of a target that is also expressed on normal cells (B cells), but humans can live with B cell aplasia and appropriate treatment, namely intravenous immunoglobulin (IVIG) treatment, which overcomes antibody deficiencies. However, a major challenge in the development of CAR T cells is to identify targets that are homogeneously expressed at sufficient levels on the surface of tumour cells and are not present on healthy tissues at levels that would cause damage. A tragic example is described in a case report where CAR T cells based on the humanized monoclonal antibody trastuzumab (Herceptin), which recognizes ERBB2, led to the patient's death.[86] The authors hypothesize that the large number of CAR T cells infiltrated in the lungs and triggered cytokine release after recognizing low levels of ERBB2 on lung epithelial cells.

Acute myeloid leukemia (AML) is a candidate disease for cellular immunotherapy. However, targeting the myeloid marker CD33 in (AML) leads to toxicity from destroying normal myeloid cells. The authors demonstrated the artificial generation of a leukaemia-specific antigen by deleting CD33 from normal hematopoietic stem and progenitor cells (HSPCs), generating a hematopoietic system resistant to CD33-targeted therapy and enabling specific targeting of AML with CAR T cells.[87] In this approach, the host was genetically engineered to avoid on-target and off-tumour toxicity.

Heterogeneity[88] and loss of antigen expression on cancer cells under selective pressure of targeted immunotherapy can lead to evasion strategies by cancer cells.[89] This has sparked the development of CARs with multiple specificities. Examples for hematologic malignancies include a dual CD19 and CD22 CAR T cells expressing two CAR receptors[90] or CAR T cells with a tandem scFv CAR molecule with dual targeting of CD19 and CD22.[91,92]

Another approach that allows on demand multiple antigen targeting to mitigate a potential antigen escape in CAR T cell therapy is adapter CAR platform. One example is the universal immune receptor based on SpyCatcher-SpyTag chemistry. The SpyCatcher immune receptor redirects primary human T cells upon adding SpyTag-labeled targeting ligands.[93] Another example is the so-called SUPRA CAR, a split-CAR design that allows the development of CAR T cells with multiple features and provides the ability to switch targets without re-engineering the T cells.[94]

TCRs have been shown to enable targeting of neoantigens[95–98] and recently CARs have also been developed that specifically target peptides derived from intracellular proteins presented by HLAs.[99] These results demonstrate that CAR T cells are not limited to recognizing molecules expressed on the surface, but can now be engineered to recognize intracellular targets presented by the HLAs, which mimics recognition by TCRs. This significantly increases the potential pool of CAR T targets.

Tumour targeting represents a challenge and an opportunity for innovative approaches and advances will be necessary to develop CAR T cell therapies for new disease indications, particularly in solid tumours.

Manufacturing cellular product

The manufacturing process, which involves the collection of autologous T cells and the generation of CAR T cells for each individual patient, is expensive and complex from an infrastructural and logistical perspective. In addition, unexpected challenges can emerge with some of the existing pipelines. One such example is the discovery that

the lentivirally delivered CAR gene was inadvertently introduced into a single leukemic B cell during T cell manufacturing. This anti-CD19 CAR molecule then bound the CD19 epitope on the surface of the same leukemic cells, which masked it from being recognized by the CD19-targeting CAR T cells, resulting in relapse.[100] Therefore, there is great interest in optimizing the manufacturing of the cellular product to make it safer, more effective and broadly available.

Recent study presented the shortened process of manufacturing of non-activated CAR T cells with improved functionality.[101] Another study investigated the approach where CAR T cells have been manufactured from the defined CD4+ and CD8+ T cell subsets and infused in a defined CD4+: CD8+ composition.[102] Recent study investigated the efficacy and safety of CAR T cells generated from preselected naïve/stem memory T cells, observing a superior safety and efficacy profile compared to unselected bulk T cells.[103] In addition, alternative sources of donor T cells are being explored, including allogeneic off-the-shelf approaches.[104,105] Recently, the first human clinical trials were reported with CRISPR/Cas9-engineered T cells that edited PD-1[106] or even demonstrated multiplex CRISPR/Cas9 editing of the endogenous T cell receptor and PD-1.[107]

Currently CAR T cells are produced via lentiviral or retroviral transduction, where integration of a gene encoding CAR is semi random and poses certain risks and challenges. Recent studies have demonstrated that genome editing technologies can be used for CRISPR/Cas9-mediated targeted integration of a CAR into an endogenous locus via homology-directed repair (HDR) and an adeno-associated virus (AAV) vector as a HDR donor template.[108,109] Further, a non-viral strategy using a double stranded DNA as a HDR donor template for CRISPR/Cas9-mediated targeted integration has been demonstrated.[110] CAR T cells generated with non-viral targeted integration have even been tested in a clinical trial.[111] Finally, approaches to generate CAR T cells *in vivo* are also being explored.[112]

Bringing the manufacture of cellular products to a level that enabled clinical approval required extensive efforts by pioneers and now continues to represent an area of opportunity to make CAR T cells safer, more effective, and broadly available.

Immune-related adverse events

Unfortunately, adoptive cancer immunotherapy carries safety risks such as cytokine release syndrome (CRS) and neurologic toxicities[113], that have led to life-threatening complications.[17] Current management strategies include systemic use of the antibody tocilizumab, which blocks IL-6 receptor.[114] CRS and neurotoxicity are the two main toxicities associated with clinically used CD19-targeting therapies. B-cell aplasia is on-target, off-tumour adverse effect of CARs that target B-cell differentiation antigens such as CD19[17] and can be effectively managed by IVIG, as mentioned earlier in the paper. Further, on-target off-tumour toxicity can have devastating effects[86] as described in previous sections.

A recent study illuminated a contributor to severe neurotoxicity observed in a subset of patients treated with CD19-targeting therapies. The authors show that brain mural cells, which surround the endothelium and are critical for the integrity of the blood-brain-barrier, express CD19, implying that on-target off-tumour toxicities may occur.[115]

Several approaches are being developed to mitigate toxicities, including platforms in which the activity of CAR T cells can be regulated by genetically encoded transient functions in a combination with the small molecules[116–118] or targeting ligands.[93,94] Suicide switches based on inducible caspase-9[119] or on expression of surface molecules, such as a truncated version of epidermal growth factor receptor (EGFRt) are being developed. In the latter case, EGFRt is expressed together with CAR on the surface of T cells, so that CAR T cells can be eliminated by addition of an antibody targeting EGFRt.[120]

SynNotch enabled AND-gate combinatorial targeting, in which the synNotch receptor first recognized one tumour antigen, which led to the release of a transcriptional activator domain to drive expression of a CAR targeting another tumour antigen.[121]

New insights into the biology of CAR T cells, experience from clinical trials, and advances in engineering approaches now provide the basis for making CAR T cells safer while maintaining their efficacy.

Conclusions

This review article focuses on CAR T cells for cancer immunotherapy. However, it is important to note that cellular immunotherapy using TILs[122,123] or T cells with engineered TCRs has achieved remarkable success in clinical studies in solid tumours and established approaches to target intra-

cellular antigens presented in the context of major histocompatibility complex (MHC) molecules including neoantigens.[95–97] The success of CAR T cells in treating cancer has led to their use outside of cancer treatment, including autoimmunity[21–23], infections[24,25], senescence-associated pathologies[26], and cardiac fibrosis.[27,112] Several cell types including Natural Killer (NK)[19] cells and macrophages[20] are being explored as alternatives to T cells that have certain advantages and provide new features. Cancer immunotherapy with CAR T cells represents a paradigm shift in the treatment of certain blood cancers that do not respond to other available treatment options. Well-trodden paths blazed by pioneers led to the first FDA and EMA approval, and the journey now continues on lesser-known paths to treat a variety of cancers and other serious diseases with CAR T cells.

Acknowledgments

A.S. thanks J. Pohar and K. Butina Ogorelec for reviewing and providing valuable feedback on the manuscript. A.S. received funding from Slovenian Research Agency (ARRS) for Project J3-3084 and Program P1-0245 and from Research fund of the National Institute of Biology for Project 10ICIGEN (ICI). Figures created with BioRender.com

References

1. Vesely MD, Kershaw MH, Schreiber RD, Smyth MJ. Natural innate and adaptive immunity to cancer. *Annu Rev Immunol* 2011; **29:** 235-71. doi: 10.1146/annurev-immunol-031210-101324

2. Schreiber RD, Old LJ, Smyth MJ. Cancer immunoediting: integrating immunity's roles in cancer suppression and promotion. *Science* 2011; **331:** 1565-70. doi: 10.1126/science.1203486

3. Rosenberg SA, Packard BS, Aebersold PM, Solomon D, Topalian SL, Toy ST, et al. Use of tumor-infiltrating lymphocytes and interleukin-2 in the immunotherapy of patients with metastatic melanoma. *N Engl J Med* 1988; **319:** 1676-80. doi: 10.1056/nejm198812223192527

4. Sadelain M, Rivière I, Riddell S. Therapeutic T cell engineering. *Nature* 2017; **545:** 423-31. doi: 10.1038/nature22395

5. Grupp SA, Kalos M, Barrett D, Aplenc R, Porter DL, Rheingold SR, et al. Chimeric antigen receptor-modified T cells for acute lymphoid leukemia. *N Engl J Med* 2013; **368:** 1509-18. doi: 10.1056/NEJMoa1215134

6. Maude SL, Laetsch TW, Buechner J, Rives S, Boyer M, Bittencourt H, et al. Tisagenlecleucel in children and young adults with B-cell lymphoblastic leukemia. *N Engl J Med* 2018; **378:** 439-48. doi: 10.1056/nejmoa1709866

7. Lee DW, Kochenderfer JN, Stetler-Stevenson M, Cui YK, Delbrook C, Feldman SA, et al. T cells expressing CD19 chimeric antigen receptors for acute lymphoblastic leukaemia in children and young adults: a phase 1 dose-escalation trial. *Lancet* 2015; **385:** 517-28. doi: 10.1016/S0140-6736(14)61403-3

8. Schuster SJ, Svoboda J, Chong EA, Nasta SD, Mato AR, Anak Ö, et al. Chimeric antigen receptor T cells in refractory B-cell lymphomas. *N Engl J Med* 2017; **28:** 2545-54. doi: 10.1056/NEJMoa1708566

9. Sommermeyer D, Hudecek M, Kosasih PL, Gogishvili T, Maloney DG, Turtle CJ, et al. Chimeric antigen receptor-modified T cells derived from defined CD8+ and CD4+ subsets confer superior antitumor reactivity in vivo. *Leukemia* 2016; **30:** 492-500. doi: 10.1038/leu.2015.247

10. Brentjens RJ, Rivière I, Park JH, Davila ML, Wang X, Stefanski J, et al. Safety and persistence of adoptively transferred autologous CD19-targeted T cells in patients with relapsed or chemotherapy refractory B-cell leukemias. *Blood* 2011; **118:** 4817-28. doi: 10.1182/blood-2011-04-348540

11. Porter DL, Levine BL, Kalos M, Bagg A, June CH, Levine BL, et al. Chimeric antigen receptor–modified T cells in chronic lymphoid leukemia. *N Engl J Med* 2011; **365:** 725-33. doi: 10.1056/nejmoa1103849

12. Neelapu SS, Locke FL, Bartlett NL, Lekakis LJ, Miklos DB, Jacobson CA, et al. Axicabtagene ciloleucel CAR T-cell therapy in refractory large B-cell lymphoma. *N Engl J Med* 2017; **377:** 2531-44. doi: 10.1056/nejmoa1707447

13. Schuster SJ, Bishop MR, Tam CS, Waller EK, Borchmann P, McGuirk JP, et al. Tisagenlecleucel in adult relapsed or refractory diffuse large B-cell lymphoma. *N Engl J Med* 2019; **380:** 45-56. doi: 10.1056/nejmoa1804980

14. Abramson JS, McGree B, Sarah Noyes N, Sean Plummer B, Curtis Wong B, Chen YB, et al. Anti-CD19 CAR T cells in CNS diffuse large-B-cell lymphoma. *N Engl J Med* 2017; **377:** 783-4. doi: 10.1056/NEJMc1704610

15. Kalos M, Levine BL, Porter DL, Katz S, Grupp SA, Bagg A, et al. T cells with chimeric antigen receptors have potent antitumor effects and can establish memory in patients with advanced leukemia. *Sci Transl Med* 2011; **3:** 95ra73. doi: 10.1126/scitranslmed.3002842

16. Kochenderfer JN, Wilson WH, Janik JE, Dudley ME, Stetler-Stevenson M, Feldman SA, et al. Eradication of B-lineage cells and regression of lymphoma in a patient treated with autologous T cells genetically engineered to recognize CD19. *Blood* 2010; **116:** 4099-102. doi: 10.1182/blood-2010-04-281931

17. Neelapu SS, Tummala S, Kebriaei P, Wierda W, Gutierrez C, Locke FL, et al. Chimeric antigen receptor T-cell therapy – assessment and management of toxicities. *Nat Rev Clin Oncol* 2017; **15:** 47-62. doi: 10.1038/nrclinonc.2017.148

18. Brudno JN, Kochenderfer JN. Recent advances in CAR T-cell toxicity: mechanisms, manifestations and management. *Blood Rev* 2019; **34:** 45-55. doi: 10.1016/j.blre.2018.11.002

19. Liu E, Marin D, Banerjee P, MacApinlac HA, Thompson P, Basar R, et al. Use of CAR-transduced natural killer cells in CD19-positive lymphoid tumors. *N Engl J Med* 2020; **382:** 545-53. doi: 10.1056/nejmoa1910607

20. Klichinsky M, Ruella M, Shestova O, Lu XM, Best A, Zeeman M, et al. Human chimeric antigen receptor macrophages for cancer immunotherapy. *Nat Biotechnol* 2020; **38:** 947-53. doi: 10.1038/s41587-020-0462-y

21. Ellebrecht CT, Bhoj VG, Nace A, Choi EJ, Mao X, Cho MJ, et al. Reengineering chimeric antigen receptor T cells for targeted therapy of autoimmune disease. *Science* 2016; **353:** 179-84. doi: 10.1126/science.aaf6756

22. Mackensen A, Müller F, Mougiakakos D, Böltz S, Wilhelm A, Aigner M, et al. Anti-CD19 CAR T cell therapy for refractory systemic lupus erythematosus. *Nat Med* 2022; **28:** 2124-32. doi: 10.1038/s41591-022-02017-5

23. Mougiakakos D, Krönke G, Völkl S, Kretschmann S, Aigner M, Kharboutli S, et al. CD19-Targeted CAR T cells in refractory systemic lupus erythematosus. *N Engl J Med* 2021; **385:** 567-9. doi: 10.1056/nejmc2107725

24. Maldini CR, Gayout K, Leibman RS, Dopkin DL, Mills JP, Shan X, et al. HIV-resistant and HIV-specific CAR-modified CD4+ T cells mitigate HIV disease progression and confer CD4+ T cell help in vivo. *Mol Ther* 2020; **28:** 1-15. doi: 10.1016/j.ymthe.2020.05.012

25. Maldini CR, Claiborne DT, Okawa K, Chen T, Dopkin DL, Shan X, et al. Dual CD4-based CAR T cells with distinct costimulatory domains mitigate HIV pathogenesis in vivo. *Nat Med* 2020; **26:** 1776-87. doi: 10.1038/s41591-020-1039-5

26. Amor C, Feucht J, Leibold J, Ho YJ, Zhu C, Alonso-Curbelo D, et al. Senolytic CAR T cells reverse senescence-associated pathologies. *Nature* 2020; **583:** 127-32. doi: 10.1038/s41586-020-2403-9

27. Aghajanian H, Kimura T, Rurik JG, Hancock AS, Leibowitz MS, Li L, et al. Targeting cardiac fibrosis with engineered T cells. *Nature* 2019; **573:** 430-3. doi: 10.1038/s41586-019-1546-z

28. Kalos M, June CH. Adoptive T Cell Transfer for cancer immunotherapy in the era of synthetic biology. *Immunity* 2013; **39:** 49-60. doi: 10.1016/j.immuni.2013.07.002

29. June CH, O 'connor RS, Kawalekar OU, Ghassemi S, Milone MC, O'Connor RS, et al. CAR T cell immunotherapy for human cancer. *Science* 2018; **1365:** 1361-5. doi: 10.1126/science.aar6711

30. Kuwana Y, Asakura Y, Utsunomiya N, Nakanishi M, Arata Y, Itoh S, et al. Expression of chimeric receptor composed of immunoglobulin-derived V resions and T-cell receptor-derived C regions. *Biochem Biophys Res Commun* 1987; **149:** 960-8. doi: 10.1016/0006-291X(87)90502-X

31. Eshhar Z, Waks T, Gross G, Schindler DG. Specific activation and targeting of cytotoxic lymphocytes through chimeric single chains consisting of antibody-binding domains and the γ or ζ subunits of the immunoglobulin and T-cell receptors. *Proc Natl Acad Sci U S A* 1993; **90:** 720-4. doi: 10.1073/pnas.90.2.720

32. Brocker T, Karjalainen K. Signals through T cell receptor-ζ chain alone are insufficient to prime resting T lymphocytes. *J Exp Med* 1995; **181:** 1653-9. doi: 10.1084/jem.181.5.1653

33. Ghorashian S, Kramer AM, Onuoha S, Wright G, Bartram J, Richardson R, et al. Enhanced CAR T cell expansion and prolonged persistence in pediatric patients with ALL treated with a low-affinity CD19 CAR. *Nat Med* 2019; **25:** 1408-14. doi: 10.1038/s41591-019-0549-5

34. Singh N, Frey N V., Engels B, Barrett DM, Shestova O, Ravikumar P, et al. Antigen-independent activation enhances the efficacy of 4-1BB-costimulated CD22 CAR T cells. *Nat Med* 2021; **27:** 842-50. doi: 10.1038/s41591-021-01326-5

35. Posey AD, Schwab RD, Boesteanu AC, Steentoft C, Mandel U, Engels B, et al. Engineered CAR T cells targeting the cancer-associated Tn-glycoform of the membrane mucin MUC1 control adenocarcinoma. *Immunity 2016*; **44:** 1444-54. doi: 10.1016/j.immuni.2016.05.014

36. Harris DT, Kranz DM. Adoptive T Cell therapies: a comparison of T cell receptors and chimeric antigen receptors. *Trends Pharmacol Sci* 2015; **37:** 220-30. doi: 10.1016/j.tips.2015.11.004

37. Bashor CJ, Hilton IB, Bandukwala H, Smith DM, Veiseh O. Engineering the next generation of cell-based therapeutics. *Nat Rev Drug Discov* 2022; **21:** 655-75. doi: 10.1038/s41573-022-00476-6

38. Mullard A. FDA approves second BCMA-targeted CAR-T cell therapy. *Nat Rev Drug Discov* 2022; **21:** 249. doi: 10.1038/d41573-022-00048-8

39. MacKay M, Afshinnekoo E, Rub J, Hassan C, Khunte M, Baskaran N, et al. The therapeutic landscape for cells engineered with chimeric antigen receptors. *Nat Biotechnol* 2020; **38:** 233-44. doi: 10.1038/s41587-019-0329-2

40. Johnson LA, June CH. Driving gene-engineered T cell immunotherapy of cancer. *Cell Res* 2016; **27:** 38-58. doi: 10.1038/cr.2016.154

41. Elazar A, Chandler NJ, Davey AS, Weinstein JY, Nguyen J V., Trenker R, et al. De novo-designed transmembrane domains tune engineered receptor functions. *Elife* 2022; **11:** 1-29. doi: 10.7554/eLife.75660

42. Muller YD, Nguyen DP, Ferreira LMR, Ho P, Raffin C, Valencia RVB, et al. The CD28-transmembrane domain mediates chimeric antigen receptor heterodimerization with CD28. *Front Immunol* 2021; **12:** 639818. doi: 10.3389/fimmu.2021.639818

43. Kershaw MH, Westwood J a, Parker LL, Wang G, Eshhar Z, Mavroukakis S a, et al. A phase I study on adoptive immunotherapy using gene-modified T cells for ovarian cancer. *Clin Cancer Res* 2006; **12:** 6106-15. doi: 10.1158/1078-0432.CCR-06-1183

44. Krause A, Guo HF, Latouche JB, Tan C, Cheung NK V., Sadelain M. Antigen-dependent CD28 signaling selectively enhances survival and proliferation in genetically modified activated human primary T lymphocytes. *J Exp Med* 1998; **188:** 619-26. doi: 10.1084/jem.188.4.619

45. Maher J, Brentjens RJ, Gunset G, Rivière I, Sadelain M. Human T-lymphocyte cytotoxicity and proliferation directed by a single chimeric TCRζ/CD28 receptor. *Nat Biotechnol* 2002; **20:** 70-5. doi: 10.1038/nbt0102-70

46. Hombach A, Wieczarkowiecz A, Marquardt T, Heuser C, Usai L, Pohl C, et al. Tumor-specific T cell activation by recombinant immunoreceptors: CD3ζ signaling and CD28 costimulation are simultaneously required for efficient IL-2 secretion and can be integrated into one combined CD28/CD3ζ signaling receptor molecule. *J Immunol* 2001; **167:** 6123-31. doi: 10.4049/jimmunol.167.11.6123

47. Kawalekar OU, O'Connor RS, Fraietta JA, Guo L, McGettigan SE, Posey AD, et al. Distinct signaling of coreceptors regulates specific metabolism pathways and impacts memory development in CAR T Cells. *Immunity* 2016; **44:** 380-90. doi: 10.1016/j.immuni.2016.01.021

48. Bachy E, Le Gouill S, Di Blasi R, Sesques P, Manson G, Cartron G, et al. A real-world comparison of tisagenlecleucel and axicabtagene ciloleucel CAR T cells in relapsed or refractory diffuse large B cell lymphoma. *Nat Med* 2022; **28:** 2145-54. doi: 10.1038/s41591-022-01969-y

49. Song DG, Ye Q, Poussin M, Harms GM, Figini M, Powell DJ. CD27 costimulation augments the survival and antitumor activity of redirected human T cells in vivo. *Blood* 2012; **119:** 696-706. doi: 10.1182/blood-2011-03-344275

50. Guedan S, Chen X, Madar A, Carpenito C, McGettigan SE, Frigault MJ, et al. ICOS-based chimeric antigen receptors program bipolar TH17/ TH1 cells. *Blood* 2014; **124:** 1070-80. doi: 10.1182/blood-2013-10-535245

51. Hombach AA, Heiders J, Foppe M, Chmielewski M, Abken H. OX40 costimulation by a chimeric antigen receptor abrogates CD28 and IL-2 induced IL-10 secretion by redirected CD4+ T cells. *Oncoimmunology* 2012; **1:** 458-66. doi: 10.4161/onci.19855

52. Ramos CA, Rouce R, Robertson CS, Reyna A, Narala N, Vyas G, et al. In vivo fate and activity of second- versus third-generation CD19-specific CAR-T cells in B cell Non-Hodgkin's lymphomas. *Mol Ther* 2018; **26:** 2727-37. doi: 10.1016/j.ymthe.2018.09.009

53. Wijewarnasuriya D, Bebernitz C, Lopez AV, Rafiq S, Brentjens RJ. Excessive costimulation leads to dysfunction of adoptively transferred T cells. *Cancer Immunol Res* 2020; **18:** 732-42. doi: 10.1158/2326-6066.CIR-19-0908

54. Melenhorst JJ, Chen GM, Wang M, Porter DL, Chen C, Collins MKA, et al. Decade-long leukaemia remissions with persistence of CD4+ CAR T cells. *Nature* 2022; **602:** 503-9. doi: 10.1038/s41586-021-04390-6

55. Gordon KS, Kyung T, Perez CR, Holec P V., Ramos A, Zhang AQ, et al. Screening for CD19-specific chimaeric antigen receptors with enhanced signalling via a barcoded library of intracellular domains. *Nat Biomed Eng* 2022; **6:** 855-66. doi: 10.1038/s41551-022-00896-0

56. Love PE, Hayes SM. ITAM-mediated signaling by the T-cell antigen receptor. *Cold Spring Harb Perspect Biol* 2010; **2:** 1-11. doi: 10.1101/cshperspect.a002485

57. Wu W, Zhou Q, Masubuchi T, Shi X, Li H, Xu X, et al. Multiple signaling roles of CD3ε and its application in CAR-T cell therapy. *Cell* 2020; **182:** 855-871. e23. doi: 10.1016/j.cell.2020.07.018

58. Feucht J, Sun J, Eyquem J, Ho YJ, Zhao Z, Leibold J, et al. Calibration of CAR activation potential directs alternative T cell fates and therapeutic potency. *Nat Med* 2019; **25:** 82-8. doi: 10.1038/s41591-018-0290-5

59. Mansilla-Soto J, Eyquem J, Haubner S, Hamieh M, Feucht J, Paillon N, et al. HLA-independent T cell receptors for targeting tumors with low antigen density. *Nat Med* 2022; **28:** 345-52. doi: 10.1038/s41591-021-01621-1

60. Zhang L, Morgan RA, Beane JD, Zheng Z, Dudley ME, Kassim SH, et al. Tumor-infiltrating lymphocytes genetically engineered with an inducible gene encoding interleukin-12 for the immunotherapy of metastatic melanoma. *Clin Cancer Res* 2015; **21:** 2278-88. doi: 10.1158/1078-0432.CCR-14-2085

61. Hu B, Ren J, Luo Y, Scholler J, Zhao Y, June CH, *et al.* CAR T cells secreting IL18 augment antitumor immunity and increase T cell proliferation and costimulation. *Cell Rep* 2017; **20:** 3025-33. doi: 10.1016/j.celrep.2017.09.002

62. Kunert A, Chmielewski M, Wijers R, Berrevoets C, Abken H, Debets R. Intratumoral production of IL18, but not IL12, by TCR-engineered T cells is non-toxic and counteracts immune evasion of solid tumors. *Oncoimmunology* 2017; **7:** 1-12. doi: 10.1080/2162402X.2017.1378842

63. Chmielewski M, Abken H. CAR T cells releasing IL-18 convert to T-Bet high FoxO1 low effectors that exhibit augmented activity against advanced solid tumors. *Cell Rep* 2017; **21:** 3205-19. doi: 10.1016/j.celrep.2017.11.063

64. Zimmermann K, Kuehle J, Dragon AC, Galla M, Kloth C, Rudek LS, et al. Design and characterization of an "all-in-one" lentiviral vector system combining constitutive anti-gd2 car expression and inducible cytokines. *Cancers* 2020; **12:** 1-22. doi: 10.3390/cancers12020375

65. Rafiq S, Yeku OO, Jackson HJ, Purdon TJ, van Leeuwen DG, Drakes DJ, et al. Targeted delivery of a PD-1-blocking scFv by CAR-T cells enhances anti-tumor efficacy in vivo. *Nat Biotechnol* 2018; **36:** 847-56. doi: 10.1038/nbt.4195

66. Yin Y, Boesteanu AC, Binder ZA, Xu C, Reid RA, Rodriguez JL, et al. Checkpoint blockade reverses anergy in IL-13Rα2 humanized scFv-based CAR T cells to treat murine and canine gliomas. *Mol Ther Oncolytics* 2018; **11:** 20-38. doi: 10.1016/j.omto.2018.08.002

67. Kuhn NF, Purdon TJ, van Leeuwen DG, Lopez A V., Curran KJ, Daniyan AF, et al. CD40 ligand-modified chimeric antigen receptor T cells enhance antitumor function by eliciting an endogenous antitumor response. *Cancer Cell* 2019; **35:** 473-88. doi: 10.1016/j.ccell.2019.02.006

68. Yamamoto TN, Lee P-HH, Vodnala SK, Gurusamy D, Kishton RJ, Yu Z, et al. T cells genetically engineered to overcome death signaling enhance adoptive cancer immunotherapy. *J Clin Invest* 2019; **129:** 1551-65. doi: 10.1172/JCI121491

69. Oda SK, Anderson KG, Ravikumar P, Bonson P, Garcia NM, Jenkins CM, et al. A Fas-4-1BB fusion protein converts a death to a pro-survival signal and enhances T cell therapy. *J Exp Med* 2020; **217:** 1-16. doi: 10.1084/jem.20191166

70. Jin C, Ma J, Ramachandran M, Yu D, Essand M. CAR T cells expressing a bacterial virulence factor trigger potent bystander antitumour responses in solid cancers. *Nat Biomed Eng* 2022; **6:** 830-41. doi: 10.1038/s41551-022-00875-5

71. Narayan V, Barber-Rotenberg JS, Jung IY, Lacey SF, Rech AJ, Davis MM, et al. PSMA-targeting TGFβ-insensitive armored CAR T cells in metastatic castration-resistant prostate cancer: a phase 1 trial. *Nat Med* 2022; **28:** 724-34. doi: 10.1038/s41591-022-01726-1

72. Roth TL, Li PJ, Blaeschke F, Nies JF, Apathy R, Mowery C, et al. Pooled knockin targeting for genome engineering of cellular immunotherapies. *Cell* 2020; **181:** 728-744.e21. doi: 10.1016/j.cell.2020.03.039

73. Roybal KT, Williams JZ, Morsut L, Walker WJ, Mcnally KA, Lim WA. Engineering T cells with customized therapeutic article engineering T cells with customized therapeutic response programs using synthetic notch receptors. *Cell* 2016; **167:** 419-32. doi: 10.1016/j.cell.2016.09.011

74. Rodriguez-garcia A, Lynn RC, Poussin M, Eiva MA, Shaw LC, Connor RSO, et al. CAR-T cell-mediated depletion of immunosuppressive tumor-associated macrophages promotes endogenous antitumor immunity and augments adoptive immunotherapy. *Nat Commun* 2021; **12:** 877. doi: 10.1038/s41467-021-20893-2

75. Fraietta JA, Lacey SF, Orlando EJ, Pruteanu-Malinici I, Gohil M, Lundh S, et al. Determinants of response and resistance to CD19 chimeric antigen receptor (CAR) T cell therapy of chronic lymphocytic leukemia. *Nat Med* 2018; **24:** 563-71. doi: 10.1038/s41591-018-0010-1

76. Good CR, Aznar MA, Kuramitsu S, Samareh P, Agarwal S, Donahue G, et al. An NK-like CAR T cell transition in CAR T cell dysfunction. *Cell* 2021; **184:** 6081-6100.e26. doi: 10.1016/j.cell.2021.11.016

77. Weber EW, Parker KR, Sotillo E, Lynn RC, Anbunathan H, Lattin J, et al. Transient rest restores functionality in exhausted CAR-T cells through epigenetic remodeling. *Science* 2021; **372:** eaba1786. doi: 10.1126/science.aba1786

78. Lynn RC, Weber EW, Sotillo E, Gennert D, Xu P, Good Z, et al. c-Jun overexpression in CAR T cells induces exhaustion resistance. *Nature* 2019; **576:** 293-300. doi: 10.1038/s41586-019-1805-z

79. Seo H, González-Avalos E, Zhang W, Ramchandani P, Yang C, Lio CWJ, et al. BATF and IRF4 cooperate to counter exhaustion in tumor-infiltrating CAR T cells. *Nat Immunol* 2021; **22:** 983-95. doi: 10.1038/s41590-021-00964-8

80. Deng Q, Han G, Puebla-Osorio N, Ma MCJ, Strati P, Chasen B, et al. Characteristics of anti-CD19 CAR T cell infusion products associated with efficacy and toxicity in patients with large B cell lymphomas. *Nat Med* 2020; **26:** 1878-87. doi: 10.1038/s41591-020-1061-7

81. Adachi K, Kano Y, Nagai T, Okuyama N, Sakoda Y, Tamada K. IL-7 and CCL19 expression in CAR-T cells improves immune cell infiltration and CAR-T cell survival in the tumor. *Nat Biotechnol* 2018; **36:** 346-51. doi: 10.1038/nbt.4086

82. Shum T, Omer B, Tashiro H, Kruse RL, Wagner DL, Parikh K, et al. Constitutive signaling from an engineered IL7 receptor promotes durable tumor elimination by tumor-redirected T cells. *Cancer Discov* 2017; **7:** 1238-47. doi: 10.1158/2159-8290.CD-17-0538

83. Alizadeh D, Wong RA, Yang X, Wang D, Pecoraro JR, Kuo CF, et al. IL15 enhances CAR-T cell antitumor activity by reducing mTORC1 activity and preserving their stem cell memory phenotype. *Cancer Immunol Res* 2019; **7:** 759-72. doi: 10.1158/2326-6066.CIR-18-0466

84. Kalbasi A, Siurala M, Su LL, Tariveranmoshabad M, Picton LK, Ravikumar P, et al. Potentiating adoptive cell therapy using synthetic IL-9 receptors. *Nature* 2022; **607:** 360-5. doi: 10.1038/s41586-022-04801-2

85. Legut M, Gajic Z, Guarino M, Daniloski Z, Rahman JA, Xue X, et al. A genome-scale screen for synthetic drivers of T cell proliferation. *Nature* 2022; **603:** 728-35. doi: 10.1038/s41586-022-04494-7

86. Morgan RA, Yang JC, Kitano M, Dudley ME, Laurencot CM, Rosenberg SA. Case report of a serious adverse event following the administration of t cells transduced with a chimeric antigen receptor recognizing ERBB2. *Mol Ther* 2010; **18:** 843-51. doi: 10.1038/mt.2010.24

87. Kim MY, Yu KR, Kenderian SS, Ruella M, Chen S, Shin TH, et al. Genetic inactivation of CD33 in hematopoietic stem cells to enable CAR T cell immunotherapy for acute myeloid leukemia. *Cell* 2018; **173:** 1439-1453.e19. doi: 10.1016/j.cell.2018.05.013

88. Qazi MA, Vora P, Venugopal C, Sidhu SS, Moffat J, Swanton C, et al. Intratumoral heterogeneity: pathways to treatment resistance and relapse in human glioblastoma. *Ann Oncol* 2017; **28:** 1448-56. doi: 10.1093/annonc/mdx169

89. Ruella M, Maus M V. Catch me if you can: leukemia escape after CD19-directed T cell immunotherapies. *Comput Struct Biotechnol J* 2016; **14:** 357-62. doi: 10.1016/j.csbj.2016.09.003

90. Cordoba S, Onuoha S, Thomas S, Pignataro DS, Hough R, Ghorashian S, et al. CAR T cells with dual targeting of CD19 and CD22 in pediatric and young adult patients with relapsed or refractory B cell acute lymphoblastic leukemia: a phase 1 trial. *Nat Med* 2021; **27:** 1797-805. doi: 10.1038/s41591-021-01497-1

91. Fry TJ, Shah NN, Orentas RJ, Stetler-Stevenson M, Yuan CM, Ramakrishna S, et al. CD22-targeted CAR T cells induce remission in B-ALL that is naive or resistant to CD19-targeted CAR immunotherapy. *Nat Med* 2018; **24:** 20-8. doi: 10.1038/nm.4441

92. Spiegel JY, Patel S, Muffly L, Hossain NM, Oak J, Baird JH, et al. CAR T cells with dual targeting of CD19 and CD22 in adult patients with recurrent or refractory B cell malignancies: a phase 1 trial. *Nat Med* 2021; **27:** 1419-31. doi: 10.1038/s41591-021-01436-0

93. Minutolo NG, Sharma P, Poussin M, Shaw LC, Brown DP, Hollander EE, et al. Quantitative control of gene-engineered T-cell activity through the covalent attachment of targeting ligands to a universal immune receptor. *J Am Chem Soc* 2020; **142:** 6554-68. doi: 10.1021/jacs.9b11622

94. Cho JH, Collins JJ, Wong WW. Universal chimeric antigen receptors for multiplexed and logical control of T cell responses. *Cell* 2018; **173:** 1426-1438.e11. doi: 10.1016/j.cell.2018.03.038

95. Tran E, Robbins PF, Lu Y-C, Prickett TD, Gartner JJ, Jia L, et al. T-cell transfer therapy targeting mutant KRAS in cancer. *N Engl J Med* 2016; **375:** 2255-62. doi: 10.1056/NEJMoa1609279

96. Chheda ZS, Kohanbash G, Okada K, Jahan N, Sidney J, Pecoraro M, et al. Novel and shared neoantigen derived from histone 3 variant H3.3K27M mutation for glioma T cell therapy. *J Exp Med* 2018; **215:** 141-57. doi: 10.1084/jem.20171046

97. Leidner R, Sanjuan Silva N, Huang H, Sprott D, Zheng C, Shih Y-P, et al. Neoantigen T-cell receptor gene therapy in pancreatic cancer. *N Engl J Med* 2022; **386:** 2112-9. doi: 10.1056/nejmoa2119662

98. Bear AS, Blanchard T, Cesare J, Ford MJ, Richman LP, Xu C, et al. Biochemical and functional characterization of mutant KRAS epitopes validates this oncoprotein for immunological targeting. *Nat Commun* 2021; **12:** 1-16. doi: 10.1038/s41467-021-24562-2

99. Yarmarkovich M, Marshall QF, Warrington JM, Premaratne R, Farrel A, Groff D, et al. Cross-HLA targeting of intracellular oncoproteins with peptide-centric CARs. *Nature* 2021; **599:** 477-84. doi: 10.1038/s41586-021-04061-6

100. Ruella M, Xu J, Barrett DM, Fraietta JA, Reich TJ, Ambrose DE, *et al.* Induction of resistance to chimeric antigen receptor T cell therapy by transduction of a single leukemic B cell. *Nat Med* 2018; **24:** 1499-503. doi: 10.1038/s41591-018-0201-9

101. Ghassemi S, Durgin JS, Nunez-Cruz S, Patel J, Leferovich J, Pinzone M, et al. Rapid manufacturing of non-activated potent CAR T cells. *Nat Biomed Eng* 2022; **6:** 118-28. doi: 10.1038/s41551-021-00842-6

102. Turtle CJ, Hanafi LA, Berger C, Gooley TA, Cherian S, Hudecek M, et al. CD19 CAR-T cells of defined CD4+:CD8+ composition in adult B cell ALL patients. *J Clin Invest* 2016; **126:** 2123-38. doi: 10.1172/JCI85309

103. Arcangeli S, Bove C, Mezzanotte C, Camisa B, Falcone L, Manfredi F, et al. CAR T cell manufacturing from naive/stem memory T lymphocytes enhances antitumor responses while curtailing cytokine release syndrome. *J Clin Invest* 2022; **132:** e150807. doi: 10.1172/JCI150807

104. Depil S, Duchateau P, Grupp SA, Mufti G, Poirot L. 'Off-the-shelf' allogeneic CAR T cells: development and challenges. *Nat Rev Drug Discov* 2020; **19:** 185-99. doi: 10.1038/s41573-019-0051-2

105. Qasim W, Zhan H, Samarasinghe S, Adams S, Amrolia P, Stafford S, et al. Molecular remission of infant B-ALL after infusion of universal TALEN gene-edited CAR T cells. *Sci Transl Med* 2017; **9:** 1-9. doi: 10.1126/scitranslmed.aaj2013

106. Lu Y, Xue J, Deng T, Zhou X, Yu K, Deng L, et al. Safety and feasibility of CRISPR-edited T cells in patients with refractory non-small-cell lung cancer. *Nat Med* 2020; **26:** 732-40. doi: 10.1038/s41591-020-0840-5

107. Stadtmauer EA, Fraietta JA, Davis MM, Cohen AD, Weber KL, Lancaster E, et al. CRISPR-engineered T cells in patients with refractory cancer. *Science* 2020; **367:** 1-12. doi: 10.1126/science.aba7365

108. Eyquem J, Mansilla-Soto J, Giavridis T, Van Der Stegen SJC, Hamieh M, Cunanan KM, et al. Targeting a CAR to the TRAC locus with CRISPR/Cas9 enhances tumour rejection. *Nature* 2017; **543:** 113-7. doi: 10.1038/nature21405

109. Dai X, Park JJ, Du Y, Kim HR, Wang G, Errami Y, et al. One-step generation of modular CAR-T cells with AAV-Cpf1. *Nat Methods* 2019; **16:** 247-54. doi: 10.1038/s41592-019-0329-7

110. Roth TL, Puig-Saus C, Yu R, Shifrut E, Carnevale J, Li PJ, et al. Reprogramming human T cell function and specificity with non-viral genome targeting. *Nature* 2018; **559:** 405-9. doi: 10.1038/s41586-018-0326-5

111. Zhang J, Hu Y, Yang J, Li W, Zhang M, Wang Q, et al. Non-viral, specifically targeted CAR-T cells achieve high safety and efficacy in B-NHL. *Nature* 2022; **609:** 369-74. doi: 10.1038/s41586-022-05140-y

112. Rurik JG, Tombácz I, Yadegari A, Fernández POM, Shewale S V, Li L, et al. CAR T cells produced in vivo to treat cardiac injury. *Science* 2022; **96:** 91-6. doi: 10.1126/science.abm0594

113. June CH, Warshauer JT, Bluestone JA. Is autoimmunity the Achilles' heel of cancer immunotherapy? *Nat Med* 2017; **23:** 540-7. doi: 10.1038/nm.4321

114. Singh N, Hofmann TJ, Gershenson Z, Levine BL, Grupp SA, Teachey DT, et al. Monocyte lineage-derived IL-6 does not affect chimeric antigen receptor T-cell function. *Cytotherapy* 2017; **19:** 867-80. doi: 10.1016/j.jcyt.2017.04.001

115. Parker KR, Migliorini D, Perkey E, Yost KE, Bhaduri A, Bagga P, et al. Single-cell analyses identify brain mural cells expressing CD19 as potential off-tumor targets for CAR-T immunotherapies. *Cell* 2020; **183:** 126-142.e17. doi: 10.1016/j.cell.2020.08.022

116. Wu C-Y, Roybal KT, Puchner EM, Onuffer J, Lim WA. Remote control of therapeutic T cells through a small molecule-gated chimeric receptor. *Science* 2015; **350:** aab4077. doi: 10.1126/science.aab4077

117. Juillerat A, Marechal A, Filhol JM, Valton J, Duclert A, Poirot L, et al. Design of chimeric antigen receptors with integrated controllable transient functions. *Sci Rep* 2016; **6:** 1-7. doi: 10.1038/srep18950

118. Giordano-Attianese G, Gainza P, Gray-Gaillard E, Cribioli E, Shui S, Kim S, et al. A computationally designed chimeric antigen receptor provides a small-molecule safety switch for T-cell therapy. *Nat Biotechnol* 2020; **38:** 426-32. doi: 10.1038/s41587-019-0403-9

119. Hoyos V, Savoldo B, Quintarelli C, Mahendravada A, Zhang M, Vera J, et al. Engineering CD19-specific T lymphocytes with interleukin-15 and a suicide gene to enhance their anti-lymphoma/leukemia effects and safety. *Leukemia* 2010; **24:** 1160-70. doi: 10.1038/leu.2010.75

120. Paszkiewicz PJ, Fräßle SP, Srivastava S, Sommermeyer D, Hudecek M, Drexler I, et al. Targeted antibody-mediated depletion of murine CD19 CAR T cells permanently reverses B cell aplasia. *J Clin Invest* 2016; **126:** 4262-72. doi: 10.1172/JCI84813

121. Roybal KT, Rupp LJ, Morsut L, Walker WJ, McNally KA, Park JS, et al. Precision tumor recognition by T cells with combinatorial antigen-sensing circuits. *Cell* 2016; **164:** 1-10. doi: 10.1016/j.cell.2016.01.011

122. Tran E, Ahmadzadeh M, Lu YC, Gros A, Turcotte S, Robbins PF, et al. Immunogenicity of somatic mutations in human gastrointestinal cancers. *Science* 2015; **350:** 1387-90. doi: 10.1126/science.aad1253

123. Zacharakis N, Chinnasamy H, Black M, Xu H, Lu YC, Zheng Z, et al. Immune recognition of somatic mutations leading to complete durable regression in metastatic breast cancer. *Nat Med* 2018; **1:** 724-30. doi: 10.1038/s41591-018-0040-8

review

Imaging perfusion changes in oncological clinical applications by hyperspectral imaging: a literature review

Rok Hren[1,2], Gregor Sersa[3], Urban Simoncic[1,4], Matija Milanic[1,4]

[1] Faculty of Mathematics and Physics, University of Ljubljana, Ljubljana, Slovenia
[2] Institute of Mathematics, Physics, and Mechanics, Ljubljana, Slovenia
[3] Institute of Oncology Ljubljana, Ljubljana, Slovenia
[4] Jozef Stefan Institute, Ljubljana, Slovenia

Radiol Oncol 2022; 56(4): 420-429.

Received 27 October 2022
Accepted 2 November 2022

Correspondence to: Matija Milanic, Ph.D., Faculty of Mathematics and Physics, University of Ljubljana, Jadranska ulica 19, SI-1000 Ljubljana, Slovenia. E-mail matija.milanic@fmf.uni-lj.si

Disclosure: No potential conflicts of interest were disclosed.

Background. Hyperspectral imaging (HSI) is a promising imaging modality that uses visible light to obtain information about blood flow. It has the distinct advantage of being noncontact, nonionizing, and noninvasive without the need for a contrast agent. Among the many applications of HSI in the medical field are the detection of various types of tumors and the evaluation of their blood flow, as well as the healing processes of grafts and wounds. Since tumor perfusion is one of the critical factors in oncology, we assessed the value of HSI in quantifying perfusion changes during interventions in clinical oncology through a systematic review of the literature.

Materials and methods. The PubMed and Web of Science electronic databases were searched using the terms "hyperspectral imaging perfusion cancer" and "hyperspectral imaging resection cancer". The inclusion criterion was the use of HSI in clinical oncology, meaning that all animal, phantom, *ex vivo*, experimental, research and development, and purely methodological studies were excluded.

Results. Twenty articles met the inclusion criteria. The anatomic locations of the neoplasms in the selected articles were as follows: kidneys (1 article), breasts (2 articles), eye (1 article), brain (4 articles), entire gastrointestinal (GI) tract (1 article), upper GI tract (5 articles), and lower GI tract (6 articles).

Conclusions. HSI is a potentially attractive imaging modality for clinical application in oncology, with assessment of mastectomy skin flap perfusion after reconstructive breast surgery and anastomotic perfusion during reconstruction of gastrointenstinal conduit as the most promising at present.

Key words: hyperspectral imaging; oncology; resection; perfusion; cancer

Introduction

Cancer is the leading health problem in the world. Only in the EU-27 each year are 2.7 million people diagnosed with cancer, while 1.3 million die from the disease.[1] To deal with cancer, knowledge of cancer physiology is essential, where tissue perfusion is one of the most important physiological parameters. Perfusion of tumors is critical in their development and growth. Early studies have shown that tumor growth is dependent on the development of vasculature that has the capacity to supply oxygen and nutrients to dividing tumor cells.[2] However, the vasculature is important not only for the supply of oxygen to tumors but also for the delivery of drugs into tumors.[3] Finally, vasculature is also important for the response of tumors to surgery and other ablative techniques, such as ra-

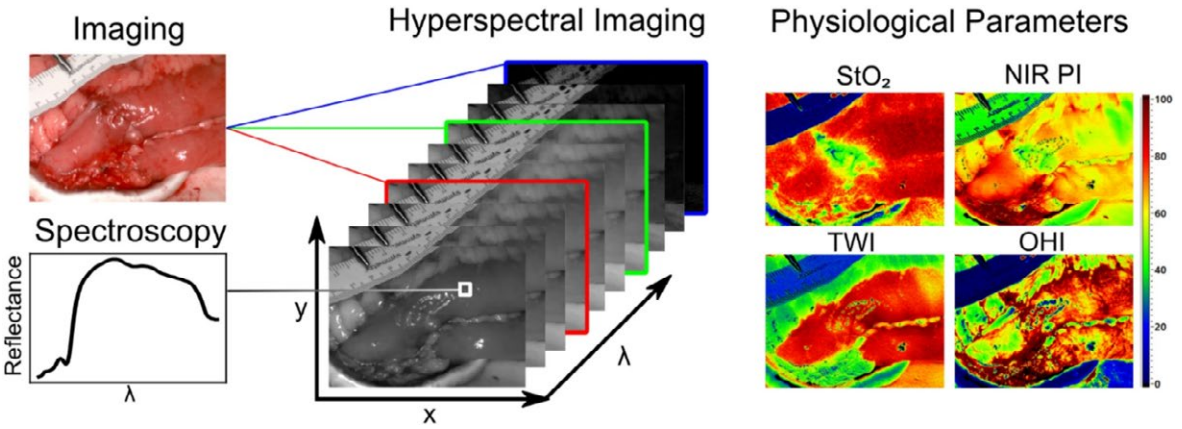

FIGURE 1. Structure and composition of hyperspectral images and physiological parameters derived from the images, which are typically displayed in false color.

NIR PI = near-infrared perfusion index; OHI = organ hemoglobin index; StO_2 = oxygen saturation of tissue; TWI = tissue water index

Taken from Pfahl *et al.*[15] and reprinted with permission from the publisher.

diotherapy and thermal and nonthermal ablative techniques.[4,5]

It was demonstrated that information about the tumor and healthy tissue perfusion can improve therapy outcome either by guiding tumor resection[6,7] or monitoring the reperfusion of the resected tissues (e.g., anastomosis or tissue flaps).[4,5] Conventional techniques for perfusion imaging in oncology are CT and MR imaging.[10] CT perfusion imaging provides information on tissue hemodynamics by analyzing the first passage of an intravenous contrast bolus through the vessels. On the other hand, MR perfusion imaging utilizes either endogenous or exogenous tracers. In the latter case, it is based on following an injected bolus of contrast agent over time, which is then used to determine the perfusion characteristics of tissues. While both imaging techniques are promising, radiation exposure (CT), potential adverse events due to contrast (CT/MRI), limited access (MRI), high cost (MRI), and inability to scan at the bedside or in operating theater are disadvantages of the conventional techniques.[10] To address these shortcomings, various imaging techniques, including optical imaging, have been explored for tissue perfusion imaging.[11,12] In optical imaging, the optical contrast of tissues is intrinsically sensitive to tissue abnormalities, such as changes in oxygenation, blood concentration or scattering.[13,14] These changes are characteristic of many tumors, since they include angiogenesis, hypervascularization, hypermetabolism, and hypoxia, making optical imaging techniques promising candidates for perfusion imaging in oncology.

Hyperspectral imaging (HSI) is an emerging optical imaging technique that uses light to obtain information about perfusion, or more specifically about oxygenation, water content or hemoglobin content of the tissue. The distinct advantage of HSI is that it is a noncontact, nonionizing, and noninvasive modality and does not require a contrast agent. HSI integrates conventional imaging and spectroscopy techniques by creating a set of images called a hypercube, which contains the spectral signature of the underlying tissue and in turn points to clinically relevant changes, such as angiogenesis or hypermetabolism. Figure 1 illustrates the structure and composition of hyperspectral images and physiological parameters derived from these images.

HSI was originally employed in remote sensing applications[16,17] and then expanded into other fields, such as vegetation type and water source detection[18,19], wood product control[20], drug analysis[21], food quality control[22-25], artwork authenticity and restoration[26,27], and security[28]. HSI is also an attractive modality in the medical field and has been successfully applied for the detection of various types of tumors, particularly in conjunction with histopathologic diagnosis.[29-31] HSI has, *inter alia*, already proven value in plastic and vascular surgery, where assessing perfusion predicted the outcome of healing processes in transplants and wounds.[32,33]

How valuable HSI could be in quantifying perfusion changes during interventions in clinical oncology remains unclear, and to that end, we decided to systematically review the literature with

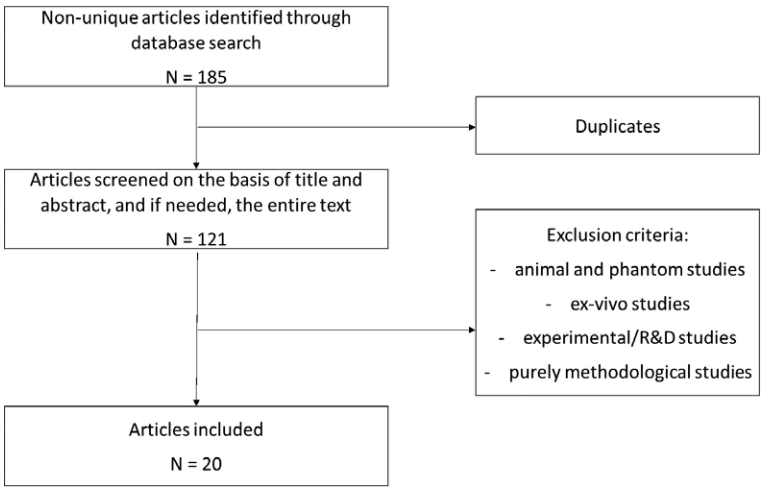

FIGURE 2. Flow diagram of the selection strategy.

the intention of exclusively focusing only on studies in which HSI was performed on patients in the clinical oncology setting.

Materials and methods

Two authors (R.H. and M.M.) conducted jointly – to preclude potential bias – a comprehensive literature search on October 3, 2022 through PubMed and Web of Science electronic databases using the following search terms: »hyperspectral imaging perfusion cancer« and »hyperspectral imaging resection cancer«. No restrictions in publication date or language were imposed. The inclusion criterion was the application of the hyperspectral imaging modality in the oncological clinical setting, meaning that all animal and phantom, *ex vivo*, experimental, research and development, and purely methodological studies were excluded. Special care was taken that duplications were removed, both across databases and across studies; for example, if the study was first published in proceedings and later in the journal, then proceedings article was considered a nonprimary publication and therefore excluded. Studies were categorized with respect to the anatomical location of the tumors.

Results

A flow diagram of the selection strategy is shown in Figure 2; in total, 101 and 84 articles were found to be of interest in the PubMed and Web of Science databases, respectively. After excluding duplicates and applying the exclusion criteria, first considering the title and abstract, and next, if necessary, reading the entire article, 20 articles were identified for further analysis. The anatomical locations of tumors in the selected articles were as follows: kidneys (1 article), breasts (2 articles), eye (1 article), brain (4 articles), entire gastrointestinal (GI) tract (1 article), upper GI tract (5 articles) and lower GI tract (6 articles).

Kidneys

Pioneering effort in assessing perfusion by means of HSI in clinical oncology was the work of Best *et al.*[34] They applied modality to monitor renal oxygenation during partial nephrectomy using the parameter called the percentage of oxyhemoglobin (HbO_2) and categorized 26 patients into the preoperative groups of high (>75% HbO_2) and low (<75% HbO_2) oxygenation. Parameter HbO_2 has proven useful before, during and after the application of a clamp, with an example of the image presented in Figure 3. The study demonstrated that patients with low oxygenation had a statistically significant postoperative decline in estimated glomerular filtration rate. While further research is needed, HSI indicates potential for assessing susceptibility to renal ischemic injury in patients undergoing partial nephrectomy.

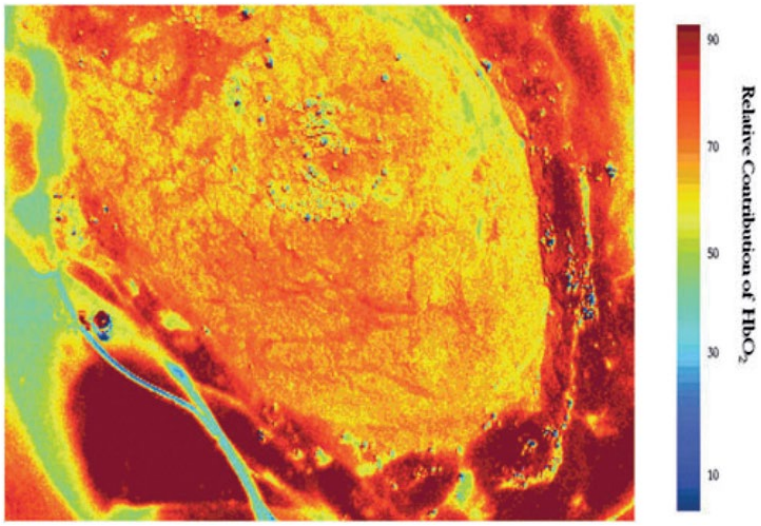

FIGURE 3. Images of the kidney depicting the percentage of HbO_2 as a function of color. A dark red represents high values while the yellows and greens indicate lower values.

Taken from Best *et al.*[34] and reprinted with permission from the publisher.

TABLE 1. Included articles reporting the use of hyperspectral imaging (HSI) to quantify perfusion changes in clinical applications in oncology

Reference	Year of publication	Number of patients	Oncologic intervention	System	Algorithm
Kidneys					
Best[34]	2013	26	Partial nephrectomy	DLP HSI, 520–645 nm	Supervised multivariate least squares regression
Eye					
Rose[35]	2018	8	Radiation retinopathy	Tunable laser, 520–620 nm with 5 nm steps	PHYSPEC software (Photon etc., Montreal, QC, Canada)
Breasts					
Chin[36]	2017	43	Skin response to radiation	OxyVu-2™ (Hypermed, Inc., Waltham, MA), 500–600 nm	The OxyVu-2™ software (Hypermed, Inc., Waltham, MA)
Pruimboom[8]	2022	10	Mastectomy skin flap necrosis	TIVITA™ (Diaspective Vision GmbH, Am Salzhaff, Germany), 500–1000 nm with 5 nm step	TIVITA™ (Diaspective Vision GmbH, Am Salzhaff, Germany)
Brain					
Fabelo[37]	2018	22	Craniotomy for resection of intraaxial brain tumor	Hyperspec VNIR A-Series (HeadWall Photonics, Massachusetts, USA), 400–1000 nm	Spectral angle mapper
Fabelo[38]	2018	5	Craniotomy for resection of intraaxial brain tumor; all 5 patients with grade IV glioblastoma	As in Fabelo[37]	As in Fabelo[37]
Fabelo[39]	2019	6	Craniotomy for resection of intra-axial brain tumor; all 6 patients with grade IV glioblastoma	As in Fabelo[37]	As in Fabelo[37]
Fabelo[40]	2019	22	Craniotomy for resection of intraaxial brain tumor	As in Fabelo[37]	As in Fabelo[37]
Entire GI tract					
Jansen-Winkeln[41] [Article in German]	2018	47	Gastrointestinal surgery with esophageal, gastric, pancreatic, small bowel or colorectal anastomoses	As in Pruimboom[8]	As in Pruimboom[8]
Upper GI tract					
Kohler[9]	2019	22	Hybrid or open esophagectomy followed by reconstruction of gastric conduit	As in Pruimboom[8]	As in Pruimboom[8]
Moulla[42] [Article in German]	2020		Video presentation of hybrid esophagectomy	As in Pruimboom[8]	As in Pruimboom[8]
Schwandner[43]	2020	4	Hybrid esophagectomy followed by reconstructing gastric conduit	As in Pruimboom[8]	As in Pruimboom[8]
Hennig[44]	2021	13	Hybrid esophagectomy followed by reconstructing gastric conduit	As in Pruimboom[8]	As in Pruimboom[8]
Moulla[45]	2021	20	Pancreatoduodenectomy	As in Pruimboom[8]	As in Pruimboom[8]
Lower GI tract					
Jansen-Winkeln[46]	2019	24	Colorectal resection	As in Pruimboom[8]	As in Pruimboom[8]
Jansen-Winkeln[47]	2020	32	Colorectal resection	As in Pruimboom[8]	As in Pruimboom[8]
Pfahl[48]	2022	128	Colorectal resection	As in Pruimboom[8]	As in Pruimboom[8]
Jansen-Winkeln[49]	2021	54	Colorectal resection	As in Pruimboom[8]	As in Pruimboom[8]
Jansen-Winkeln[50]	2022	115	Colorectal resection	As in Pruimboom[8]	As in Pruimboom[8]
Barberio[51]	2022	52	Colorectal resection	As in Pruimboom[8]	As in Pruimboom[8]

GI = gastrointestinal

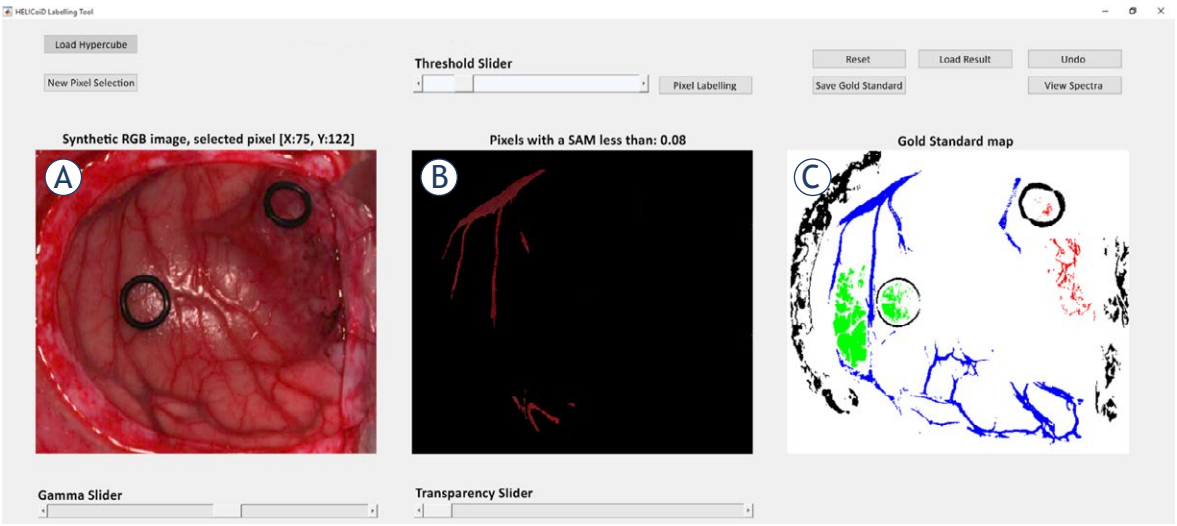

FIGURE 4. (A) Red-Green-Blue (RGB) representation of the imaged brain, including normal and tumor tissue. **(B)** Extraction of blood vessels from hyperspectral images using the spectral angle mapper algorithm (SAM). **(C)** Tissue classification map generated from hyperspectral images: tumor tissue is red, normal tissue is green, blood vessels are blue, and background is black.

Taken from Fabelo *et al.*[38] and reprinted with permission from the publisher.

Eye

In the study of Rose *et al.*[35], clinicians used Doppler spectral domain optical coherence tomography (SD-OCT) in 8 patients diagnosed with radiation retinopathy to measure total retinal blood flow, while retinal blood oxygen saturation was quantified by a specially designed HSI retinal camera. They found that blood flow in the retinopathy eye was significantly lower than that in the fellow eye, while arteriolar oxygen saturation and venular oxygen saturation were higher in the retinopathy eye than in the fellow eye. Unfortunately, researchers conducted no follow-up studies, in which they would further evaluate microvascular changes due to radiation-induced retinopathy.

Breasts

Chin *et al.*[36] studied a dose–response relationship between radiation exposure and oxygenated hemoglobin in 43 women undergoing breast-conserving therapy radiation. The authors concluded that HSI may prove useful as an objective measure of patients' skin response to radiation dose. However, they also noted that interpatient variability remains a challenge, as approximately 40% of the variability in change in oxygenated hemoglobin is accounted for by dose, 25% by individual woman, and 35% by causes that they could not identify.

Pruimboom *et al.*[8] used HSI in a prospective clinical pilot study enrolling women with breast reconstruction and detected mastectomy skin flap necrosis in 3 out of 10 patients. Somewhat analogously to the study of Best *et al.*[34], they found that tissue oxygenation was statistically significantly lower in the group of patients who developed flap necrosis than in the group of patients who did not. It appears that HSI is specifically suited for the early detection of flap necrosis, which could in turn aid in the timely and accurate debridement of necrotic tissue. Future work should confirm the modality's potential also in identifying partial deep inferior epigastric artery perforator (DIEP) flap necrosis.

Brain

Fabelo *et al.*[37-40] developed an intraoperative HSI acquisition system and were able to assemble an *in vivo* hyperspectral human brain image database with the overall goal of accurately delineating tumor tissue from normal brain tissue. As the brain tumor typically infiltrates the surrounding tissue, it is extremely difficult to identify the border; in addition, both overresection of adjacent normal brain tissue and leaving tumor tissue behind have detrimental impacts on the results of the surgery and patient outcomes, either adversely affecting the patient's quality of life or causing tumor progression.

The work of Fabelo *et al.* was performed as a part of the European Future and Emerging Technologies (FET) project HELICoiD (HypErspectraL Imaging Cancer Detection).

In their first methodological paper, they designed a special cancer detection algorithm utilizing spatial and spectral features of hyperspectral images from 5 patients with grade IV glioblastoma.[38] They demonstrated that it was possible to accurately discriminate between normal tissue, tumor tissue, blood vessels and background by generating classification and segmentation maps in surgical time during neurosurgical operations, as shown in Figure 4.

In their second methodological paper[39], they used data from 6 patients with grade IV glioblastoma and applied improved algorithms to create maps, in which the parenchymal area of the brain could be delineated; an overall average accuracy of 80% was achieved.

Their HSI system was systematically assessed at two clinical institutions enrolling 22 patients, and researchers found that results relevant for surgeons were obtained within 15 to 70 seconds.[40] They also made available to the public this first *in vivo* hyperspectral human brain image database specifically designed for cancer detection. While authors were hopeful in their conclusion that HSI could facilitate brain tumor surgeries, no further studies beyond 2019 were published.

HSI files from the studies by Fabelo and coworkers are available from http://hsibraindatabase.iuma.ulpgc.es database.

Entire gastrointestinal tract

During the past 3 years, the main focus of applying HSI in clinical oncology has been in the domain of the gastrointestinal tract, or more specifically, addressing anastomotic insufficiency, which is one of the most serious postsurgery complications of reconstructing the gastrointestinal conduit. As anastomotic healing fundamentally depends on adequate perfusion, HSI could be a suitable modality in assessing anastomotic perfusion in clinical practice. In a pilot study, Jansen-Winkeln *et al.*[41] collected hyperspectral images in 47 patients who underwent gastrointestinal oncologic resection followed by esophageal, gastric, pancreatic, small bowel or colorectal anastomoses. The recorded hyperspectral images were analyzed to extract the following specific physiological tissue parameters, which were deemed characteristic for perfusion changes at the sites of anastomoses: oxygen saturation of the tissue (StO_2), organ hemoglobin index (*OHI*), near-infrared perfusion index (*NIR-PI*), and tissue water index (*TWI*); the most clinically relevant appeared to be StO_2. They concluded that intraoperative HSI provided a noncontact, noninvasive modality, which enabled real-time analysis of potential anastomotic leakage without the use of a contrast medium. Their group followed their initial work with several studies focusing on the upper and lower gastrointestinal tract, respectively, described in more detail below.

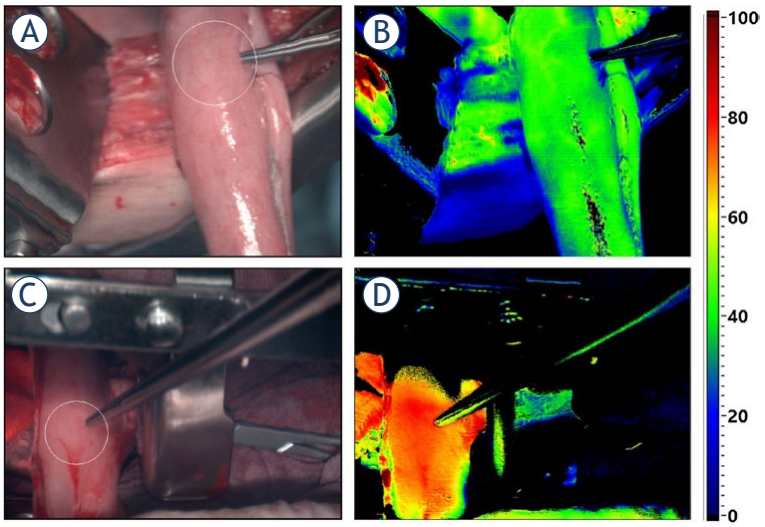

FIGURE 5. Comparison of Red-Green-Blue (RGB) images and near-infrared perfusion index (NIR PI) images recorded in a patient with **(A, B)** and without postoperative anastomotic insufficiency **(C, D)**.

Taken from Köhler *et al.*[9] and reprinted with permission from the publisher.

Upper gastrointestinal tract

Köhler *et al.*[9] applied intraoperative HSI in 22 patients during esophagectomy to the tip of the gastric tube, which later became esophagogastric anastomosis; they compared physiological HSI parameters (StO_2, *OHI*, *NIR PI* and *TWI*) in 14 patients who underwent laparoscopic gastrolysis and ischemic conditioning of the stomach with those in 8 patients without pretreatment. They noted that the values of physiological HSI parameters were higher in patients with ischemic preconditioning than in patients without ischemic preconditioning; however, only StO_2 exhibited weak statistical significance. In a single patient who developed anastomotic insufficiency of the intrathoracic esophagogastric anastomosis, all physiological HSI parameters were substantially lower than those in

FIGURE 6. Hyperspectral imaging (HSI) acquisition system in the operating room. Hyperspectral images were acquired within a few seconds with physiologic HSI parameters displayed in false colors.

Taken from Moulla *et al.*[45] and reprinted with permission from the publisher.

other patients. Figure 5 compares the *NIR PI* image recorded in this patient with the corresponding image taken in the patient without postoperative anastomotic leakage. Hybrid esophagectomy along with intraoperative HSI used in the paper of Köhler *et al.*[9] was presented as a video article by Moulla *et al.*[42], while another clinical group[43] corroborated the findings of Köhler *et al.*[9] by reporting a case study including four patients.

Hennig *et al.*[44] continued the systematic evaluation of the capabilities of intraoperative HSI in 13 consecutive patients who underwent hybrid esophagectomy and reconstruction of the gastric conduit. Researchers also decided to use both intraoperative HSI and fluorescence imaging with indocyanine green (FI-ICG) to define the optimal position of anastomosis. While there are no threshold values yet established to define adequately and insufficiently perfused tissues, they decided that HSI physiological parameter StO_2 at >75% determined the well-perfused area. It was noteworthy that imaging modalities recorded simultaneously in 10 out of 13 patients identified the perfusion border zone more peripherally than the one designated subjectively by the surgeon. While HSI and FI-ICG may complement each other as intraoperative modalities, Hennig *et al.*[44] were of the opinion that HSI may be advantageous due to "the lower costs, noninvasiveness, and lack of contraindications".

Moulla *et al.*[45] expanded oncological clinical applications in the domain of pancreatic surgery. Hyperspectral images were recorded during pancreatoduodenectomy in 20 consecutive patients before and after gastroduodenal artery clamping. In this pilot study, they were able to detect by the means of physiologic HSI parameter StO_2 improvement in liver perfusion after median acute ligament division in one patient with celiac artery stenosis. The HSI acquisition system in the operating room is shown in Figure 6.

Lower gastrointestinal tract

Jansen-Winkeln *et al.*[9] applied intraoperative HSI in 24 patients to define the transection line during colorectal surgery. They found that the transection line subjectively delineated by the surgeon

deviated from the border line determined by HSI; in 13 patients subjectively, planned resection was up to 13 mm too distal in the poorly perfused area, while in 11 patients, it was too far in the well-perfused area. Similar to esophagectomy[44], intraoperative HSI has shown potential in determining the optimal anastomotic area during colorectal surgery.

Jansen-Winkeln *et al.*[47] applied further intraoperative HSI along with FI-ICG in 32 consecutive patients undergoing colorectal resection and concluded that both modalities provided similar information in specifying the perfusion border zone and could complement each other. To optimize the performance of both modalities, Pfahl *et al.*[48] constructed the combined FI-ICG and HSI system, which was tested in 128 patients.

In another study[49], Jansen-Winkeln *et al.* imaged colorectal tumors in 54 consecutive patients during colorectal resections and found that HSI used in combination with a neural-network algorithm was able to classify cancer or adenomatous margins around the central tumor with a sensitivity of 86% and a specificity of 95%. Recently, they published a large study[50] enrolling 115 patients who underwent colorectal resection to systematically assess the feasibility of HSI in quantifying tissue perfusion, and in accordance with a smaller patient series, they found that "well-perfused areas were clearly distinguishable from the less perfused ones only after one minute".[46,47] Similar conclusions were reached in a group of 52 patients undergoing colorectal surgery by Barberio *et al.*[51], who also found that the physiological HSI parameter StO_2 was significantly lower in patients receiving neoadjuvant radio/chemotherapy than in other oncological patients. Figure 7 illustrates the usefulness of HSI in establishing the transection line during colorectal surgery.

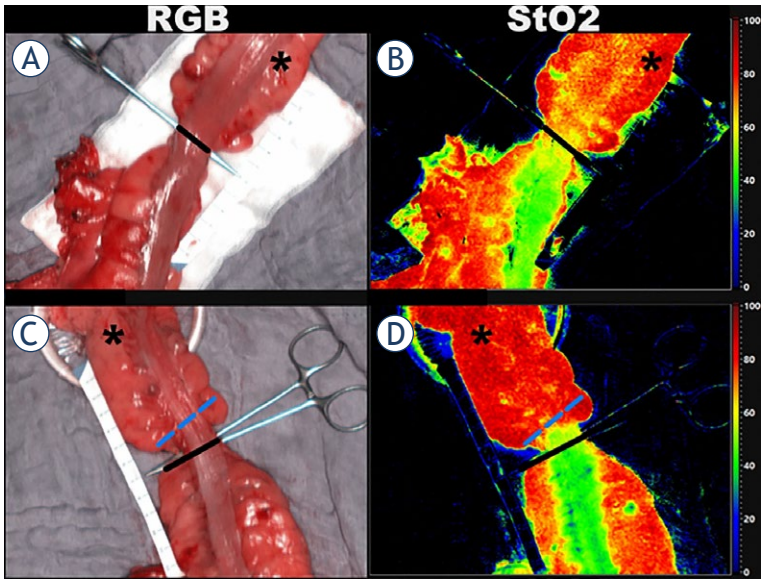

FIGURE 7. Usefulness of hyperspectral imaging (HSI) in establishing transection line during colorectal surgery. The Red-Green-Blue (RGB) image **(A)** and StO_2 map **(B)** show a patient in whom the clinical transection line (continuous line in black) and HSI transection line (dotted line in blue) were aligned; **(C)** and **(D)** show the RGB image and StO_2 map, respectively, of a patient in whom the clinical transection line deviated from the HSI transection line.

Taken from Barberio *et al.*[51] and reprinted with permission from the publisher.

Discussion

Based on this literature review, the following inferences could be made: HSI is still finding its place in oncological clinical applications with the assessment of (i) mastectomy skin flap perfusion after breast reconstructive surgery[8] and (ii) anastomotic perfusion during reconstruction of gastrointenstinal conduit[9,44,45,48-50] as the most promising. However, caution needs to be advised because recently much research has been done in the arena of using HSI during brain surgery for glioblastoma, yet this clinical effort has not been sustained.

In addition, the need for an obvious expansion of the study of Pruimboom *et al.*[8] to a larger patient group, which would also include cases of DIEP flap necrosis, a meaningful and robust establishment of cutoff values for physiological HSI parameters is mandatory if HSI is to retain its clinical appeal. In their study, oxygen saturation of tissue StO_2 appeared to be the most useful HSI index, and the cut-off value of 36.3% predicting tissue necrosis was found; this value was close to that defined by a pilot study[52] enrolling mostly nononcological patients (19 out of 22), in which the values of both StO_2 and *NIR PI* above 40% indicated regular healing without any revision surgery; furthermore, operators in that study noted that HSI was superior to assessments based on clinical and Doppler ultrasound monitoring both in accuracy and speed. It is worthwhile to emphasize that HSI parameters are in general easy to follow by the operator as they are visualized as false-colour images (Figure 1).

When evaluating applications of HSI in assessing anastomotic perfusion during reconstructing gastrointestinal conduits, two main challenges become apparent: (i) the first challenge is, as in the case of breast reconstructive surgery, related to the establishment of a clear cutoff value indicating

adequate tissue perfusion so that the operator can convincingly identify the optimal anastomosis area; (ii) the second challenge is related to HSI being limited to open surgery due to the large size of the HSI camera. The first challenge will need to be approached by enrolling progressively larger patient groups undergoing various oncological surgical interventions. It appears that the group of Jansen-Winkeln *et al*.[48,50] is already moving in this direction by conducting progressively larger clinical studies. However, with the application of neural networks, requirements for cohort sizes become far higher but could also be partially satisfied with the data augmentation. The second challenge has been recently addressed by the same group[15], with *ex vivo* testing of laparoscopic HSI camera and a highlight that the clinical trial with minimally invasive HSI has commenced already.

Comparison of HSI and FI-ICG[44,47,48] revealed similar results in defining the perfusion border of anastomosis, while both modalities were documented to be reliable, fast, and intuitive. Even if HSI is completely noninvasive, injection of ICG rarely provokes allergic reactions. Since there is a potential for each of the two modalities to contribute complementary information, it is not surprising that Pfahl *et al*.[48] constructed a combined HSI and FI-ICG recording system.

In conclusion, HSI is at this stage emerging as an attractive imaging modality to quantify perfusion in oncological patients. Hopefully, a larger number of clinical sites will initiate clinical trials to address the challenges, which still preclude the final acceptance of this promising imaging technique in the oncological clinical setting.

Acknowledgment

This work was financially supported by the state budget by the Slovenian Research Agency, research grant no. J3-3083 and research program no. P3-0003, P3-0307, and P1-0389.

We would like to thank Dr. Ivan Stajduhar from University of Rijeka, Faculty of Engineering for his technical support in preparing Figures for publishing.

References

1. European Commission. ECIS - European cancer information system [Internet]. 2022. [cited 2022 Oct 15]. Available from: https://ecis.jrc.ec.europa.eu/
2. Folkman J. Role of angiogenesis in tumor growth and metastasis. *Semin Oncol* 2002; **29:** 15-8. doi: 10.1053/sonc.2002.37263
3. Stylianopoulos T, Munn LL, Jain RK. Reengineering the tumor vasculature: improving drug delivery and efficacy. *Trends Cancer* 2018; **4:** 258-9. doi: 10.1016/j.trecan.2018.02.010
4. Sersa G, Ursic K, Cemazar M, Heller R, Bosnjak M, Campana LG. Biological factors of the tumour response to electrochemotherapy: review of the evidence and a research roadmap. *Eur J Surg Oncol* 2021; **47:** 1836-46. doi: 10.1016/j.ejso.2021.03.229
5. Kanthou C, Tozer G. Targeting the vasculature of tumours: combining VEGF pathway inhibitors with radiotherapy. *Brit J Radiol* 2019; **92:** 20180405. doi: 10.1259/bjr.20180405
6. Popiel B, Gupta D, Misra S. Value of an intraoperative real time tissue perfusion assessment system following a nipple-sparing radical mastectomy for advanced breast cancer. *Int J Surg Case Rep* 2014; **5:** 30-3. doi: 10.1016/j.ijscr.2013.11.007
7. Crawford T, Moshnikova A, Roles S, Weerakkody D, DuPont M, Carter LM, et al. pHLIP ICG for delineation of tumors and blood flow during fluorescence-guided surgery. *Sci Rep* 2022; **10:** 18356. doi: 10.1038/s41598-020-75443-5
8. Pruimboom T, Lindelauf AAMA, Felli E, Sawor JH, Deliaert AEK, van der Hulst RRWJ, et al. Perioperative hyperspectral imaging to assess mastectomy skin flap and DIEP flap perfusion in immediate autologous breast reconstruction: a pilot study. *Diagnostics* 2022; **12:** 184. doi: 10.3390/diagnostics12010184
9. Köhler H, Jansen-Winkeln B, Maktabi M, Barberio M, Takoh J, Holfert N, et al. Evaluation of hyperspectral imaging (HSI) for the measurement of ischemic conditioning effects of the gastric conduit during esophagectomy. *Surg Endosc* 2019; **33:** 3775-82. doi: 10.1007/s00464-019-06675-4
10. Trinh A, Wintermark M, Iv M. Clinical review of computed tomography and MR perfusion imaging in neuro-oncology. *Radiol Clin North Am* 2021; **59:** 323-34. doi: 10.1016/j.rcl.2021.01.002
11. van Manen L, Handgraaf HJM, Diana M, Dijkstra J, Ishizawa T, Vahrmeijer AL, et al. A practical guide for the use of indocyanine green and methylene blue in fluorescence-guided abdominal surgery. *J Surg Oncol* 2018; **118:** 283-300. doi: 10.1002/jso.25105
12. Wiesinger I, Jung F, Jung EM. Contrast-enhanced ultrasound (CEUS) and perfusion imaging using VueBox®. *Clin Hemorheol Microcirc* 2021; **78:** 29-40. doi: 10.3233/CH-201040
13. Jacques SL. Optical properties of biological tissues: a review. *Phys Med Biol* 2013; **58:** R37-61. doi: 10.1088/0031-9155/58/11/R37
14. Bashkatov AN, Genina EA, Tuchin VV. Optical properties of skin, subcutaneous, and muscle tissues: a review. *J Innov Opt Health Sci* 2011; **04:** 9-38. doi: 10.1142/S1793545811001319
15. Pfahl A, Köhler H, Thomaßen MT, Maktabi M, Bloße AM, Mehdorn M, et al. Clinical evaluation of a laparoscopic hyperspectral imaging system. *Surg Endosc* 2022; **36:** 7794-9. doi: 10.1007/s00464-022-09282-y
16. Goetz AFH, Vane G, Solomon JE, Rock BN. Imaging spectrometry for earth remote sensing. *Science* 1985; **228:** 1147-53. doi: 10.1126/science.228.4704.1147
17. Selci S. The future of hyperspectral imaging. *J Imaging* 2019; **5:** 84. doi: 10.3390/jimaging5110084
18. Govender M, Chetty K, Bulcock H. A review of hyperspectral remote sensing and its application in vegetation and water resource studies. *Water SA* [Internet]. 2007; **33:** 145-51. [cited 2022 Oct 8]. Available from: http://www.ajol.info/index.php/wsa/article/view/49049
19. Castro-Esau K. Discrimination of lianas and trees with leaf-level hyperspectral data. *Remote Sens Environ* 2004; **90:** 353-72. doi: 10.1016/j.rse.2004.01.013
20. Schimleck L, Ma T, Inagaki T, Tsuchikawa S. Review of near infrared hyperspectral imaging applications related to wood and wood products. *Appl Spectrosc Rev* 2022; 1-25. doi: 10.1080/05704928.2022.2098759
21. Puchert T, Lochmann D, Menezes JC, Reich G. Near-infrared chemical imaging (NIR-CI) for counterfeit drug identification—A four-stage concept with a novel approach of data processing (Linear Image Signature). *J Pharm Biomed Anal* 2010; **51:** 138-45. doi: 10.1016/j.jpba.2009.08.0221
22. Feng YZ, Sun DW. Application of hyperspectral imaging in food safety inspection and control: a review. *Crit Rev Food Sci Nutr* 2012; **52:** 1039-58. doi: 10.1080/10408398.2011.651542

23. Huang H, Liu L, Ngadi M. Recent developments in hyperspectral imaging for assessment of food quality and safety. *Sensors* 2014; **14:** 7248-76. doi: 10.3390/s140407248

24. Gowen A, Odonnell C, Cullen P, Downey G, Frias J. Hyperspectral imaging – an emerging process analytical tool for food quality and safety control. *Trends Food Sci Technol* 2007; **18:** 590-8. doi: 10.1016/j.tifs.2007.06.001

25. Soni A, Dixit Y, Reis MM, Brightwell G. Hyperspectral imaging and machine learning in food microbiology: Developments and challenges in detection of bacterial, fungal, and viral contaminants. *Comp Rev Food Sc Food Safe* 2022; **21:** 3717-45. doi: 10.1111/1541-4337.12983

26. Balas C, Epitropou G, Tsapras A, Hadjinicolaou N. Hyperspectral imaging and spectral classification for pigment identification and mapping in paintings by El Greco and his workshop. *Multimed Tools Appl* 2018; **77:** 9737-51. doi: 10.1007/s11042-017-5564-2

27. Sandak J, Sandak A, Legan L, Retko K, Kavčič M, Kosel J, et al. Nondestructive evaluation of heritage object coatings with four hyperspectral imaging systems. *Coatings* 2021; **11:** 244. doi: 10.3390/coatings11020244

28. Yuen PW, Richardson M. An introduction to hyperspectral imaging and its application for security, surveillance and target acquisition. *Imaging Sci J* 2010; **58:** 241-53. doi: 10.1179/174313110X12771950995716

29. Ortega S, Fabelo H, Camacho R, de la Luz Plaza M, Callicó GM, Sarmiento R. Detecting brain tumor in pathological slides using hyperspectral imaging. *Biomed Opt Express* 2018; **9:** 818. doi: 10.1364/BOE.9.000818

30. Ortega S, Fabelo H, Iakovidis D, Koulaouzidis A, Callico G. Use of hyperspectral/multispectral imaging in gastroenterology. Shedding some – different – light into the dark. *J Clin Med* 2019; **8:** 36. doi: 10.3390/jcm8010036

31. Ma L, Halicek M, Zhou X, Dormer JD, Fei B. Hyperspectral microscopic imaging for automatic detection of head and neck squamous cell carcinoma using histologic image and machine learning. In: Tomaszewski JE, Ward AD, editors. *Medical Imaging 2020: Digital Pathology* [Internet]. Houston, United States: SPIE; 2020. p. 31. [cited 2022 Oct 8]. Available from: https://www.spiedigitallibrary.org/conference-proceedings-of-spie/11320/2549369/Hyperspectral-microscopic-imaging-for-automatic-detection-of-head-and-neck/10.1117/12.2549369.full

32. Keller A. A new diagnostic algorithm for early prediction of vascular compromise in 208 microsurgical flaps using tissue oxygen saturation measurements. *Ann Plast Surg* 2009; **62:** 538-43. doi: 10.1097/SAP.0b013e3181a47ce8

33. Jafari-Saraf L, Wilson SE, Gordon IL. Hyperspectral image measurements of skin hemoglobin compared with transcutaneous PO2 measurements. *Ann Vasc Surg* 2012; **26:** 537-48. doi: 10.1016/j.avsg.2011.12.002

34. Best SL, Thapa A, Jackson N, Olweny E, Holzer M, Park S, et al. Renal oxygenation measurement during partial nephrectomy using hyperspectral imaging may predict acute postoperative renal function. *J Endourol* 2013; **27:** 1037-40. doi: 10.1089/end.2012.0683

35. Rose K, Krema H, Durairaj P, Dangboon W, Chavez Y, Kulasekara SI, et al. Retinal perfusion changes in radiation retinopathy. *Acta Ophthalmol* 2018; **96:** e727-31. doi: 10.1111/aos.13797

36. Chin MS, Siegel-Reamer L, FitzGerald GA, Wyman A, Connor NM, Lo YC, et al. Association between cumulative radiation dose, adverse skin reactions, and changes in surface hemoglobin among women undergoing breast conserving therapy. *Clin Transl Radiat Oncol* 2017; **4:** 15-23. doi: 10.1016/j.ctro.2017.03.003

37. Fabelo H, Ortega S, Lazcano R, Madroñal D, M. Callicó G, Juárez E, et al. An intraoperative visualization system using hyperspectral imaging to aid in brain tumor delineation. *Sensors* 2018; **18:** 430. doi: 10.3390/s18020430

38. Fabelo H, Ortega S, Ravi D, Kiran BR, Sosa C, Bulters D, et al. Spatio-spectral classification of hyperspectral images for brain cancer detection during surgical operations. Fred AL, editor. *PLoS ONE* 2018; **13:** e0193721.

39. Fabelo H, Halicek M, Ortega S, Shahedi M, Szolna A, Piñeiro J, et al. Deep learning-based framework for in vivo identification of glioblastoma tumor using hyperspectral images of human brain. *Sensors* 2019; **19:** 920. doi: 10.3390/s19040920

40. Fabelo H, Ortega S, Szolna A, Bulters D, Pineiro JF, Kabwama S, et al. *In-vivo* hyperspectral human brain image database for brain cancer detection. *IEEE Access* 2019; **7:** 39098-116. doi: 10.1109/ACCESS.2019.2904788

41. Jansen-Winkeln B, Maktabi M, Takoh JP, Rabe SM, Barberio M, Köhler H, et al. [Hyperspectral imaging in gastrointestinal anastomoses]. [German]. *Chirurg* 2018; **89:** 717-25.

42. Moulla Y, Reifenrath M, Rehmet K, Niebisch S, Jansen-Winkeln B, Sucher R, et al. [Hybrid esophagectomy with intraoperative hyperspectral imaging: video contribution]. [German]. *Chirurg* 2020; **91(S1):** 1-12.

43. Schwandner F, Hinz S, Witte M, Philipp M, Schafmayer C, Grambow E. Intraoperative assessment of gastric sleeve oxygenation using hyperspectral imaging in esophageal resection: a feasibility study. *Visc Med* 2021; **37:** 165-70. doi: 10.1159/000509304

44. Hennig S, Jansen-Winkeln B, Köhler H, Knospe L, Chalopin C, Maktabi M, et al. Novel intraoperative imaging of gastric tube perfusion during oncologic esophagectomy – a pilot study comparing hyperspectral imaging (HSI) and fluorescence imaging (FI) with indocyanine green (ICG). *Cancers* 2021; **14:** 97. doi: 10.3390/cancers14010097

45. Moulla Y, Buchloh DC, Köhler H, Rademacher S, Denecke T, Meyer HJ, et al. Hyperspectral Imaging (HSI) – A new tool to estimate the perfusion of upper abdominal organs during pancreatoduodenectomy. *Cancers* 2021; **13:** 2846. doi: 10.3390/cancers13112846

46. Jansen-Winkeln B, Holfert N, Köhler H, Moulla Y, Takoh JP, Rabe SM, et al. Determination of the transection margin during colorectal resection with hyperspectral imaging (HSI). *Int J Colorectal Dis* 2019; **34:** 731-9. doi: 10.1007/s00384-019-03250-0

47. Jansen-Winkeln B, Germann I, Köhler H, Mehdorn M, Maktabi M, Sucher R, et al. Comparison of hyperspectral imaging and fluorescence angiography for the determination of the transection margin in colorectal resections – a comparative study. *Int J Colorectal Dis* 2021; **36:** 283-91. doi: 10.1007/s00384-020-03755-z

48. Pfahl A, Radmacher GK, Köhler H, Maktabi M, Neumuth T, Melzer A, et al. Combined indocyanine green and quantitative perfusion assessment with hyperspectral imaging during colorectal resections. *Biomed Opt Express* 2022; **13:** 3145. doi: 10.1364/BOE.452076

49. Jansen-Winkeln B, Barberio M, Chalopin C, Schierle K, Diana M, Köhler H, et al. Feedforward artificial neural network-based colorectal cancer detection using hyperspectral imaging: a step towards automatic optical biopsy. *Cancers* 2021; **13:** 967. doi: 10.3390/cancers13050967

50. Jansen-Winkeln B, Dvorak M, Köhler H, Maktabi M, Mehdorn M, Chalopin C, et al. Border line definition using hyperspectral imaging in colorectal resections. *Cancers* 2022; **14:** 1188. doi: 10.3390/cancers14051188

51. Barberio M, Lapergola A, Benedicenti S, Mita M, Barbieri V, Rubichi F, et al. Intraoperative bowel perfusion quantification with hyperspectral imaging: a guidance tool for precision colorectal surgery. *Surg Endosc* [Internet]. 14 July 2022. [cited 2022 Oct 8]. Available from: https://link.springer.com/10.1007/s00464-022-09407-3

52. Kohler LH, Köhler H, Kohler S, Langer S, Nuwayhid R, Gockel I, et al. Hyperspectral imaging (HSI) as a new diagnostic tool in free flap monitoring for soft tissue reconstruction: a proof of concept study. *BMC Surg* 2021; **21:** 222. doi: 10.1186/s12893-021-01232-0

review article

Advances in diagnostics and management of gestational trophoblastic disease

Nusa Lukinovic[1], Eva Pavla Malovrh[1], Iztok Takac[1,2], Monika Sobocan[1,2], Jure Knez[1,2]

[1] Faculty of Medicine, University of Maribor, Maribor, Slovenia
[2] Divison of Gynecology and Perinatology, University Medical Centre Maribor, Maribor, Slovenia

Radiol Oncol 2022; 56(4): 430-439.

Received 13 May 2022
Accepted 30 August 2022

Correspondence to: Assist. Monika Sobočan, M.D., Division for Gynecology and Perinatology, University Medical Centre Maribor, Ljubljanska ulica 5, SI-2000 Maribor, Slovenia. E-mail: monika.sobocan@gmail.com

Disclosure: No potential conflicts of interest were disclosed.

Background. Gestational trophoblastic disease (GTD) is a heterogeneous group of rare tumours characterised by abnormal proliferation of trophoblastic tissue. It consists of benign or premalignant conditions, such as complete and partial molar pregnancy and variants of malignant diseases. The malignant tumours specifically are commonly referred to as gestational trophoblastic neoplasia (GTN). They consist of invasive mole, choriocarcinoma, placental-site trophoblastic tumour (PSTT) and epithelioid trophoblastic tumour (ETT).

Conclusions. Patients with GTD are often asymptomatic, although vaginal bleeding is a common presenting symptom. With the advances in ultrasound imaging in early pregnancy, the diagnosis of molar pregnancy is most commonly made in the first trimester of pregnancy. Sometimes, additional imaging such as chest X-ray, CT or MRI can help detect metastatic disease. Most women can be cured, and their reproductive function can be preserved. In this review, we focus on the advances in management strategies for gestational trophoblastic disease as well as possible future research directions.

Key words: gestational trophoblastic disease; hydatidiform mole; molar pregnancy; gestational trophoblastic neoplasia; human chorionic gonadotropin; invasive mole; choriocarcinoma

Introduction

Gestational trophoblastic disease (GTD) is a heterogeneous group of rare tumours characterised by abnormal proliferation of trophoblastic tissue. Complete and partial molar pregnancy are the most common GTDs. They are generally considered to be benign disorders, but they can develop into gestational trophoblastic neoplasia and can be considered as premalignant conditions. The malignant tumours specifically are commonly referred to as gestational trophoblastic neoplasia (GTN). They consist of invasive mole, choriocarcinoma, placental-site trophoblastic tumour (PSTT) and epithelioid trophoblastic tumour (ETT).[1] The malignant trophoblastic disorders are collectively known as gestational trophoblastic neoplasia.[2] GTD and GTN may both arise after normal pregnancies, miscarriage, ectopic pregnancies, or abortion, but most GTNs will develop from complete molar pregnancies.[3] Hydatidiform mole (HM) is the most common type of GTD. In most parts of the world, the incidence of hydatidiform mole is 1 per 1000 pregnancies, although higher frequencies have been reported.[1,4] A classification of GTD with incidences is presented in Figure 1. The aim of this review is to provide up-to-date information on current evaluation and management strategies for gestational trophoblastic disease.

Hydatidiform mole

Our understanding of HM has changed considerably over the last decades. It wasn't until the late 1970s that a partial mole was distinguished from

a complete mole.[6] Clinical presentation of HM also changed dramatically over the years. In the 1960–1970s, the mean gestational age at diagnosis was 16 weeks and classic clinical signs were vaginal bleeding, uterine enlargement greater than expected for gestational age, theca-lutein cysts due to ovarian hyperstimulation by high serum hCG values, hyperemesis, preeclampsia, hyperthyroidism, and respiratory insufficiency.[1,6,7] Nowadays, many patients are asymptomatic at diagnosis due to wide use of ultrasound scans in early pregnancy.[1] At present, mean gestational age at diagnosis is 10–12 weeks. A HM is therefore detected before the onset of classic clinical signs. However, vaginal bleeding continues to be the most common presenting symptom and it can occasionally present with passage of hydropic villi.[1,7] Because bleeding may be prolonged and occult, patients may be anaemic at presentation.[6] Symptoms can be vague and resemble complaints often present in normal pregnancy.[1]

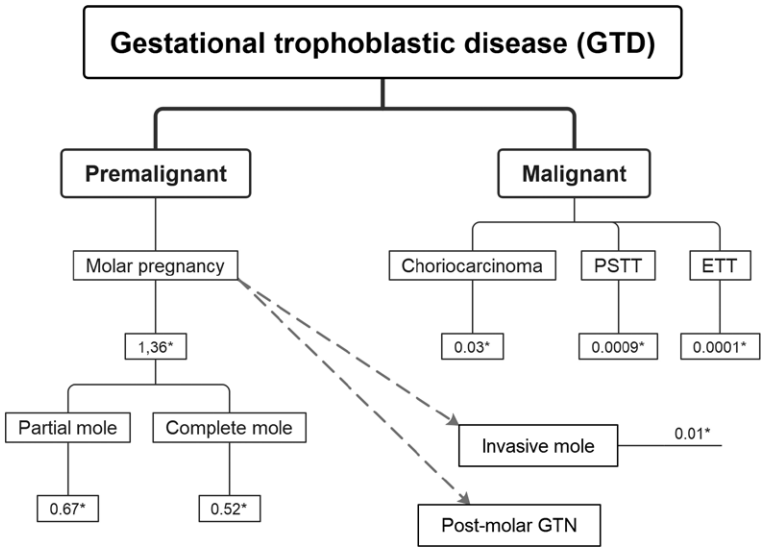

* Incidence rates per 1000 deliveries per year in Netherlands between 1994–2013[5]; ETT = epithelioid type trophoblastic tumour; PSTT = placental-site trophoblastic tumour

FIGURE 1. Classification of GTD with incidence rates.

Classification of hydatidiform moles

HM can be classified as a complete hydatidiform mole (CHM) or partial hydatidiform mole (PHM) based on histopathological exam and genetics.[8] The common pathology of these lesions is excessive proliferation of trophoblast.[6] In both conditions, the placental villi become oedematous, forming hydatidiform structures.[7] In CHM hydrops is fully developed and most villi are involved. In PHM however, the hydrops remains characteristically focal.[6] In CHM foetal parts are absent.[9] In PHM evidence of foetal development, such as amnion vessels with foetal red blood cells, is a prominent pathologic feature.[7] HMs are genetically characterised with two copies of the paternal genome. Typical CHMs are diploid and androgenetic with both sets of chromosomes derived from the paternal genome and no contribution to the nuclear genome from the mother.[8] The monospermic 46, XX karyotype is most common, resulting from fertilisation of an ovum by a single sperm that then duplicates its DNA.[8,10] About 10% of CHMs are 46, XY, arising by dispermy. 46, YY embryos are presumed to be non-viable.[8] PHMs are almost always triploid, having an additional set of chromosomes from the father of the embryo. Most have a 69, XXX or 69, XXY karyotype usually resulting from fertilisation of an ovum by two sperms, or less frequently a diploid sperm.[7,8] Trisomy with XYY karyotype is rarely seen and YYY karyotype has not been observed.[7] Most molar pregnancies are sporadic. A small subset of women has an inherited predisposition to recurrent molar pregnancies, referred to as familiar recurrent hydatidiform mole (FRHM).[8,9]

Diagnosis of hydatidiform mole

The diagnosis of HM is usually suspected on ultrasound imaging. Clinical signs, symptoms, and human chorionic gonadotropin (hCG) levels can be helpful in the diagnostic process.[11] Diagnosis should always be confirmed by histology with or without ancillary techniques such as genotyping and p57kip2 staining.[12]

Ultrasound

Ultrasound (US) is the imaging modality of choice for an initial diagnostic suspicion of GTD.[13] The advances of ultrasound imaging in the last decades and the wide availability of high-resolution transvaginal ultrasound (TVUS) in early pregnancy have shifted the diagnosis of HMs from the second to the first trimester of pregnancy.[14,15] This allows the detection of HM before the onset of systemic manifestations such as anaemia, hyperemesis, preeclampsia, hyperthyroidism or even signs of metastatic disease.[16]

In the first trimester, accurate US diagnosis of a CHM is more frequent than that of a PHM, because the latter has subtler US changes.[13] In a cohort study of 295 women[14] US imaging diagnosed

TABLE 1. Ultrasound characteristics of partial hydatidiform mole (PHM) versus complete hydatidiform mole (CHM)[13,16,18]

Feature	CHM	PHM
US characteristics	Enlarged uterus filled with a heterogeneous predominantly echogenic mass with several hypoechoic foci (snowstorm appearance), multiple small anechoic cystic spaces varying in size from 1 to 30 mm (cluster of grapes). Theca lutein cysts presenting as multiple large, bilateral, functional ovarian cysts can be present.	Subtler US changes. Hydropic changes of some villi are often not visible before 10 weeks of gestation. Enlarged placenta relative to the size of the uterine cavity with internal cystic changes producing a "Swiss cheese pattern" is often seen. Theca lutein cysts are infrequent.
Foetal parts	Absent, except in the rare event of a CHM with a coexisting diploid twin.	Present as amorphous echoes. If a foetus is formed, it carries a typical spectrum of severe abnormalities. Growth retardation is common.
Colour-power Doppler of the uterus	Variable	Variable

a significantly ($p < 0.001$) higher number of CHM (74.2%) than PHM (40.7%). These data show that for PHM the diagnosis is more difficult. Hydropic villi in PHM are only focal and difficult to differentiate from the hydropic changes associated with prolonged retention after foetal demise often seen in missed abortions.[18]

Ultrasound feature suggestive of a complete molar pregnancy is thick, cystic tissue within the uterine cavity without a visible gestational sac. Partial hydatidiform mole is often suspected in women with intact gestational sac with cystic placental changes. The accuracy of ultrasound to diagnose molar pregnancy is difficult to assess in modern practice as the majority of miscarriages are managed conservatively and histological confirmation of diagnosis is available only in a minority of women.[19] The available data show that ultrasound diagnosis of complete molar pregnancy is very sensitive with the reported detection rates between 80% and 95%.[16,17] The diagnosis of partial molar pregnancy is less accurate with the detection rates between 20% and 30%. The accuracy of US diagnosis is also operator dependent, therefore a broader awareness of the early US signs of HM should improve the detection rate of molar pregnancy in women presenting with early pregnancy complications.[15]

Doppler US does not seem to differentiate between CHM and PHM. However, it is a useful tool in the diagnosis of GTN because abnormal myometrial vascularisation and lower uterine artery Doppler indices seem to be correlated with invasive disease.[20]

Human chorionic gonadotropin (hCG)

Most GTDs secrete hCG which is therefore a sensitive tumour marker.[1] HCG is a glycoprotein hormone produced by trophoblastic tissue. It comprises an α and a β subunit. The α subunit is shared with other members of the glycoprotein hormones, including thyroid-stimulating hormone (TSH), luteinizing hormone (LH) and follicle-stimulating hormone (FSH). In hCG, the α subunit can mimic the α subunit of the other glycoprotein hormones and therefore cause symptoms seen in hyperthyroidism.[1,10] The β subunit is a unique part of the hCG structure that allows the production of highly specific antibodies and the utilisation of highly specific immunologic assays.[21] In a healthy pregnancy, intact hCG is the predominant protein, whereas in cancer patients various hCG isoforms can be present. These include intact hCG (α & β), the partially degraded or nicked forms of hCG (hCGn) and hCGβ (hCGβn) and the β-core fragment (hCG βcf)).[22] The combination of US findings with elevation of hCG above expected for gestational age is highly suggestive of molar pregnancy[7] and is crucial in diagnosis of GTD or GTN.[1] Due to hyperplastic trophoblastic cells in CHM, patients will have marked elevations in hCG, sometimes greater than 100.000 IU/L. However, such elevations are seen in fewer than 10% of patients with PHM.[11]

Histological confirmation of diagnosis

HM is sometimes diagnosed only by pathology after suction dilation and curettage (D&C) is performed for a suspected early embryonic demise. When HM is suspected beforehand, it should be evacuated as soon as possible.[7] Histological confirmation of GTD after evacuation is mandatory.[12]

Treatment of hydatidiform mole

The initial treatment of HM in women who wish to preserve fertility is D&C.[23] Pre-treatment evaluation consists of measurement of serum quantitative beta-hCG, complete blood count, clotting stud-

ies (PT, PTT), renal and liver functions, blood type and screen, pelvic ultrasound examination, chest X-ray and thyroid function test if hyperthyroidism is suspected.[7] Where available, D&C is performed under ultrasound guidance which helps to remove all molar tissue and avoid uterine perforation.[11,24] Usually, it is performed under general anaesthesia.[7] Intravenous oxytocin infusion may be started at the onset of suction D&C and may be continued for several hours after operation. Oxytocin enhances uterine contractility and decreases blood loss.[24] There is theoretical concern over the routine use of oxytocic agents, because of the potential to embolise and disseminate trophoblastic tissue through the venous system.[25] However, the authors recommend the use of oxytocin in management of molar pregnancy.[2,7,24] The risk of bleeding after suction D&C increases with uterine size. When the uterus is greater than 16 weeks in gestational size, blood transfusion should be available.[24] Because RhD factor is expressed on trophoblastic tissue, RhD immunoglobulin should be administered at the time of uterine evacuation in Rh negative women. If HM is diagnosed at early gestational age, complications during or after evacuation are uncommon.[26] Most common complications are excessive bleeding, uterine perforation, and respiratory distress syndrome.[27] Respiratory distress syndrome may be caused by trophoblastic embolization, high-output congestive heart failure caused by anaemia, hyperthyroidism, preeclampsia, or iatrogenic fluid overload.[7] At the end of suction D&C, the evacuated tissues should be inspected and sent for histological examination.[27] Uterine evacuation by medication only method is not recommended due to high failure rates, risk of haemorrhage, increased risk of post-molar GTN and increased maternal morbidity.[7,23]

Hysterectomy with salpingectomy is an alternative method to suction D&C if molar pregnancy is presumed and childbearing is complete.[24,28] Hysterectomy is especially used in women older than 40 years, because these patients have a higher risk of post molar GTN. Hysterectomy eliminates the possibility of local myometrial invasion as a source of persistent disease and hence reduces the need for subsequent chemotherapy.[7,27,28] Usually the adnexa may be preserved, even if theca lutein cysts are present. Theca lutein cysts usually regress over few months after uterine evacuation as hCG levels decrease.[7,27] Hysterectomy, compared to uterine evacuation, has a significant advantage in preventing post-molar GTN with an approximately 80% reduction in risk.[26,28] Because hysterectomy does not eliminate the possibility of post molar gestational trophoblastic neoplasia these patients should also be monitored postoperatively with serial hCG measurements.[7]

Prophylactic administration of either methotrexate or actinomycin D chemotherapy at the time of or immediately following molar evacuation is associated with a reduction in the incidence of post molar GTN to 3%-8%. However, it should be limited to special situations where adequate hCG follow-up is not possible and the risk of post molar GTN is much greater than normal.[24]

Surveillance after molar evacuation

The gold standard for clinical management of women diagnosed with a HM is to monitor the hCG levels in urine or serum.[22] Following evacuation of molar pregnancy, monitoring of hCG levels postoperatively is mandatory to identify and manage post-molar GTN.[27] HCG is used as a marker in post molar monitoring because of the correlation between hCG levels and trophoblastic tumour burden, allowing early diagnosis and treatment of GTN.[29] The mean time to hCG normalization in case of partial HM is 6 weeks and in case of complete HM 7 weeks. For both complete and partial HM, 95% of patients reached normal serum hCG concentrations within 14 weeks after evacuation.[30] FIGO recommends hCG monitoring every 1-2 weeks until hCG is normalised, and then on monthly intervals. For PHM, one additional confirmatory normal hCG measurement 1 month after first hCG normalisation is recommended. For CHM, monthly hCG measurements are required for 6 months after hCG normalisation.[27,31] After evacuation of a HM effective contraception is crucial because a new pregnancy may confound the interpretation of hCG levels.[29]

Gestational trophoblastic neoplasia (GTN)

GTN includes invasive mole, choriocarcinoma, placental site trophoblastic tumour (PSTT), and epithelioid trophoblastic tumour (ETT). Recently, atypical placental site nodule (APSN) has been added to the GTD spectrum.[24]

The reported incidence of GTN after molar pregnancy is 18% to 29%. This rate appears to be stable despite the progressively earlier diagnosis of HM.[11] Choriocarcinoma affects approximately 1 in 40.000 pregnancies and 1 in 40 HMs. It is 1000 times more

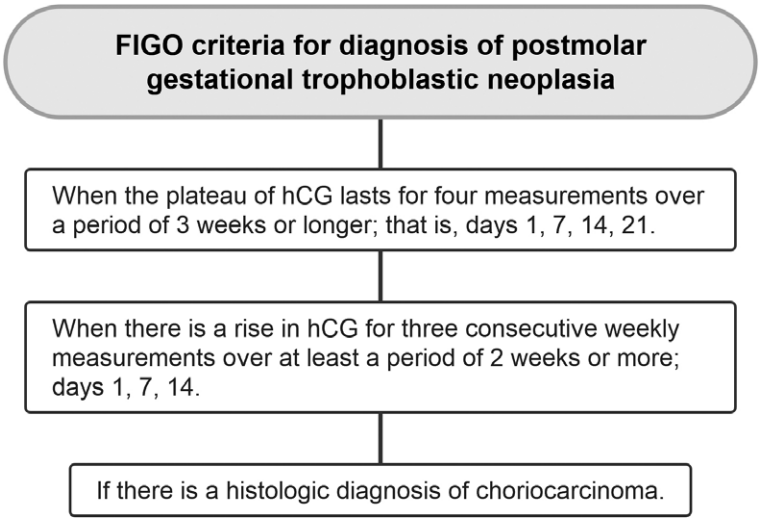

FIGURE 2. FIGO criteria for diagnosis of postmolar gestational trophoblastic neoplasia (GTN).[24]

likely after a CHM than another pregnancy event. 50% of choriocarcinoma cases arise from HMs, 25% follow abortion or tubal pregnancy and 25% are associated with other gestational events.[11,32] PSTT and ETT are rare subtypes of GTN with an incidence of 1 in 100.000 pregnancies. They represent approximately 1% of all GTN cases.[11]

Post-molar GTN

Most GTN will arise after the evacuation of a HM.[1] GTN following a HM is referred to as post-molar GTN.[24] Post-molar GTN includes invasive mole and choriocarcinoma.[11] In contrast, PSTT and ETT can develop after any type of antecedent pregnancy, including normal pregnancy, non-molar abortion, or ectopic pregnancy.[7] Risk factors for post molar GTN include age 40 years, hCG levels more than 100.000 IU/L, excessive uterine enlargement, and/or theca lutein cysts larger than 6 cm.[11] In most patients, HMs regress spontaneously after evacuation of the molar tissue, but in approximately 15% - 20% of CHMs and 0.5% - 1% PHMs, trophoblastic tissue remains active. Consequently, hCG levels have a sustained rise or plateau, which indicates the need for evaluation and treatment.[7] At the FIGO Gynaecology Oncology Committee meeting in 2000, the definition of postmolar GTN based on hCG level changes were agreed (Figure 2).[2,24,33]

Invasive mole

Invasive mole arises from invasion of CHM or PHM into the myometrium and/or uterine blood vessels.[9,11] The tendency of invasive mole to invade myometrium can result in uterine perforation and extension to adjacent organs. However, some degree of myometrial invasion of the trophoblast is probably present in most moles.[9] The diagnosis of invasive mole can only be histologically confirmed after hysterectomy.[1] As hysterectomy is nowadays rarely performed, chemotherapy is usually started without histologic confirmation of the diagnosis. Chemotherapy is essential to prevent further complications, although invasive moles rarely metastasize and are usually self-limited.[7,9]

Choriocarcinoma

Choriocarcinoma is the most common malignant GTN. It is characterised by abnormal trophoblastic hyperplasia and anaplasia, absence of chorionic villi with varying degrees of haemorrhage and necrosis.[9,34] The tumour is mainly uterine but extrauterine sites such as fallopian tubes and ovaries can also be involved. Patients with gestational choriocarcinomas tend to develop early systemic metastasis.[7] Metastases have been reported in the lung, liver, spleen, kidney, bowel, or brain.[9,24] In contrast to ectopic tubal or ovarian choriocarcinoma, primary choriocarcinoma in other organs is likely to represent non-gestational carcinoma with trophoblastic differentiation.[9]

Placental-site trophoblastic tumour (PSTT) and epithelioid trophoblastic tumour (ETT)

PSTT and ETT are the rarest subtypes of GTN. PSTT originates from the intermediate trophoblast on the maternal side of the placental bed with half of the cases invading deep into the myometrium. Chorionic villi are absent.[1,24] In contrast to choriocarcinoma, PSTT forms uterine lesions with less haemorrhage. Tumour necrosis is often extensive.[35] ETT is even rarer, and it develops from the chorionic type of intermediate trophoblast.[1] Nearly half arise in the cervix or lower segment of the uterus and some in the fundus or broad ligament. The characteristic nodular and expansive growth mimics cervical carcinoma.[24,25] PSTT and ETT share several overlapping features. They are both slow growing

tumours and can occur months to years after any type of antecedent pregnancy.[35] They both produce less hCG and metastasize in later stages. Typically, both tumours have limited chemosensitivity.[1,7]

Clinical signs and symptoms

GTN has a varying presentation depending on the antecedent pregnancy event, disease type and extent. Post molar GTN can be associated with irregular bleeding after initial treatment for molar pregnancy, an enlarged and irregular uterus, and bilateral ovarian enlargement. However, these signs may be absent.[11] Patients often present with symptoms of metastatic disease. The most common metastatic sites are the lungs, but metastatic lesions can also be found in vagina, liver, brain, spleen, kidneys, and bowel. Characteristically, gestational choriocarcinoma forms a rapidly growing tumour with the ability to metastasize to virtually every body site and present with widespread dissemination. Metastatic lesions often produce abnormal bleeding because trophoblastic tumours have fragile vessels.[9,11] Embolization of trophoblastic tissue is also possible, and it can cause dyspnoea, coughing, chest pain, tachypnoea, and haemoptysis. Vaginal metastases can present with bleeding, which cannot be distinguished from the uterine blood loss. A gynaecological examination upon presentation is therefore important.[1] Liver metastases are rare and often have a poor prognosis, especially if they present with intra-abdominal bleeding, which is life-threatening. Central nervous system lesions may be asymptomatic or produce subtle neurologic symptoms such as headache. Symptoms from brain metastases can also be very severe, even fatal if they cause intracranial haemorrhage.[1,7] PSTT and ETT often present with irregular bleeding after some time has passed from a previous pregnancy and there may also be signs of metastatic disease.[11] Other rare symptoms such as virilisation and nephrotic syndrome have also been described.[34]

Diagnosis of GTN

GTN is most frequently diagnosed based on hCG values as discussed above, most often without histologic verification.[7] It is essential to measure hCG in any woman of childbearing age who has unexplained metastatic disease.[36] A serum hCG determination and exclusion of normal pregnancy is essential to diagnose GTN in these circumstances, which can spare the patient an unnecessary surgery to establish the diagnosis.[7]

When a GTN diagnosis is made or suspected, immediate evaluation for metastases is needed. Along with the history and physical examination, the following evaluation should be performed: complete blood count, clotting function studies, renal and liver function studies, blood type and determination of pre-treatment hCG concentration.[7,37] A gynaecological examination should be done to exclude vaginal or pelvic metastases. Biopsy of metastatic lesions without the ability to control bleeding is highly risky due to abundant vascularisation of this type of tumours and is not essential before starting chemotherapy.[11,36] However, where complete excision is possible, histologic confirmation of the diagnosis is also valuable.[36]

Extensive radiographic evaluation should be performed. Chest X-ray is appropriate to diagnose lung metastases and can be used for counting the number of lung metastases to evaluate the risk score. Lung CT may not be used in the risk score. Liver metastases may be diagnosed by US or CT. Brain metastases may be diagnosed by MRI or CT.[11,24]

Classification and staging of GTN

To categorise patients with GTN, two different systems can be used. They both correlate with clinical outcomes and identify patients at risk for failure of treatment.[7] Currently, the 2000 FIGO staging system is the standard classification (Table 2).

Patients are also assigned a modified World Health Organisation (WHO) prognostic index score based on prognostic factors modified as FIGO score (Table 3). It comprises age, antecedent pregnancy, interval from index pregnancy (in months), pre-treatment hCG (in mIU/mL), largest tumour size including uterus (in cm), site of metastases including uterus, number of metastases identified and previous failed chemotherapy.[24] A WHO risk score of 6 or lower is classified as low-risk and scores higher than 6 are classified as high-risk.[7,24] Staging notation uses a Roman numeral indicating FIGO anatomical staging followed by an Arabic numeral that represents WHO prognostic scoring.[37] FIGO risk scoring is not recommended in PSTT and ETT, although it may be of value in guiding management.[35]

Treatment of low-risk GTN

Low-risk GTN (FIGO/WHO score 0–6) is primarily treated with one of two single-agent drugs,

TABLE 2. FIGO staging and classification for gestational trophoblastic neoplasia[24]

FIGO stage	Description
I	Gestational trophoblastic tumours strictly confined to the uterine corpus
II	Gestational trophoblastic tumours extending to the adnexa or to the vagina but limited to the genital structures
III	Gestational trophoblastic tumour extending to the lungs and may or may not involve the genital tract.
IV	Gestational trophoblastic tumours extending to all other metastatic sites

methotrexate (MTX) or actinomycin-D (Act-D). A variety of doses and infusion schedules for these drugs have been utilized.[24,26] To date, there is not a clearly superior regimen between these two drugs. Treatment therefore is often determined by institutional preference.[26] In Europe and North America, the methotrexate with folinic acid (MTX-FA) 8-day and MTX 5-day regimens are favoured over Act-D as first-line treatment.[38] Single-agent chemotherapy induces complete remission in 83.5% patients with stage I GTN, 80% patients with low risk stage II GTN and 81.8% patients with low risk stage III GTN.[39] Chemotherapy response is monitored by hCG measurements at least every 1 or 2 weeks. Chemotherapy resistance is indicated by plateau in hCG over 3 consecutive cycles or a rise in hCG over 2 consecutive cycles.[11] Approximately 25–30% of low-risk patients develop resistance or excessive toxicity to initial single-agent chemotherapy.[38] Resistance to initial single-agent chemotherapy is up to 70–80% in patients with FIGO/WHO score 5 or 6. Current challenge is whether these patients should be still considered low risk and initially treated with single-agent chemotherapy or treated with more intensive therapy from the onset.[38,40] Low-risk patients experiencing treatment failure with one single agent are treated with other.[41] Patients with low-risk GTN resistant to either single-agent chemotherapy or relapsed disease following complete response to initial single-agent chemotherapy, are treated with multi-agent chemotherapy. Most commonly with EMA-CO regimen (etoposide, methotrexate, actinomycin D, cyclophosphamide, vincristine).[38,41] Multi-agent chemotherapy is associated with increased short- and longer-term toxicities. For this reason, promising new strategies are being investigated. For example, the use of carboplatin and immunotherapy agents (programmed death protein 1 (PD-1) inhibitors and programmed death ligand 1 (PD-L1) inhibitors).[38,42-44] In women who no longer wish to retain their fertility, first-line hysterectomy can be considered as an alternative to chemotherapy for treatment of low-risk non-metastatic GTN.[27] Once hCG has normalised treatment is continued for a minimum of four weeks, which represents at least two consolidation cycles.[12,38]

Treatment of high-risk GTN

High-risk GTN (FIGO/WHO score > 6) is treated with multi-agent chemotherapy, with or without adjuvant surgery or radiotherapy. The most used chemotherapy protocol is EMA-CO.[24] In EMA-CO failures, the most employed regimen is EMA-EP (substituting etoposide and cisplatin for cyclophosphamide and vincristine in the EMA-CO regimen).[26] In high-risk GTN patients EMA-CO regimen induces complete response at rates of 71-78% and long-term survival rates of 85-94%.[45] Unlike for patients with low-risk GTN, primary hysterectomy is not effective in reducing requirement for chemotherapy or improving cure rates in patients with high-risk GTN.[27] As with low-risk disease, chemotherapy for high-risk disease is continued for at least 2 to 3 consolidation courses after the

TABLE 3. World Health Organization scoring system based on prognostic factors modified as FIGO score[24]

FIGO score	0	1	2	4
Age	<40	>40	-	-
Antecedent pregnancy	Mole	Abortion	Term	
Interval from index pregnancy, months	<4	4–6	7–12	>12
Pretreatment hCG IU/L	$<10^3$	$>10^3$–10^4	$>10^4$–10^5	$>10^5$
Largest tumour size including uterus, cm	-	3–4	≥5	-
Site of metastases including uterus	Lung	Spleen, kidney	Gastrointestinal tract	Brain, liver
Number of metastases identified	-	1–4	5–8	>8
Previous failed chemotherapy	-	-	Single drug	Two or more drugs

TABLE 4. Ongoing clinical trials involving treatment of gestational trophoblastic disease

	Trial Drug Design	Reg. Nr.	Recruitment status
Immunotherapy	Camrelizumab combined with apatinib for recurrent resistant GTN	NCT04047017	Completed
	Pebrolizumab for resistant GTN	NCT04303884	Not yet recruiting
	Camrelizumab combined with apatinib in patients with high-risk GTN	NCT05139095	Not yet recruiting
	Avelumab combined with methotrexate for low-risk GTN	NCT04396223	Recruiting
	Avelumab in chemo-resistant GTN	NCT03135769	Completed
	Camrelizumab combined with bevacizumab in high-risk GTN after combined chemotherapy	NCT04812002	Recruiting
	TRC105 and/or bevacizumab in refractory GTN	NCT02664961	Terminated
Chemotherapy	Paclitaxel plus cisplatin vs EMA-CO in high-risk GTN	NCT02639650	Unknown
	Rescue regimen with MTX vs high-dose MTX protocol in persistent GTN	NCT03280979	Unknown
	Pemetrexed disodium as salvage therapy for failed low-risk GTN	NCT00096187	Terminated
	Dactinomycin in patients with persistent or recurrent low-risk GTN	NCT00003688	Completed
	Single dose MTX vs MTX and Actinomycin-D single dose vs MTX multiple courses	NCT01823315	Unknow
	Biweekly actinomycin-D treatment vs multi-day methotrexate in low-risk GTN	NCT04562558	Recruiting
	Methotrexate vs dactinomycin in low-risk GTN	NCT00003702	Completed
	Methotrexate for prevention of postmolar GTN	NCT01984099	Completed
	Dactinomycin vs methotrexate in low-risk GTN	NCT01535053	Completed
	Chemotherapy vs follow up in hydatidiform mole with lung nodule	NCT03785574	Recruiting
	Pemetrexed in recurrent or persistent low-risk GTN	NCT00190918	Completed
	Methotrexate vs methotrexate plus actinomycin in low-risk GTN patients with score 5-6	NCT03885388	Recruiting
Surgical treatment	Hysteroscopic repeat curettage vs methotrexate in low-risk GTN	NCT03703271	Recruiting
	Total abdominal hysterectomy and methotrexate vs methotrexate plus folinic acid	NCT02606539	Unknown
	Second uterine evacuation vs chemotherapy in low-risk GTN	NCT04756713	Recruiting
	Second curettage in low-risk, non-metastatic GTN	NCT00521118	Completed
	Single evacuation vs double evacuation of mole	NCT01630954	Unknown

* accurate date as of 22th January 2022; EMA-CO = etoposide, methotrexate, actinomycin D, vincristine, cyclophosphamide; GTN = gestatinal trophoblastic neoplasia; hCG = human chorionic gonadotropin; MTX = methotrexate

first hCG normalization.[11,41] A separate category of ultra-high-risk GTN, defined as WHO score 13 or more, identifies women at high risk of early death and poor outcome.[26,41] These patients are treated with low dose induction chemotherapy before initiating multi-agent chemotherapy. Induction chemotherapy reduces the risk of life-threatening complications, predominantly haemorrhage from metastatic implants.[26] For induction chemotherapy combination of low dose etoposide (100 mg/m^2) and cisplatin (20 mg/m^2) (EP on days 1 and 2 every 7 day, one to three cycles) is used.[26,40] Active areas of investigation include the utilization of high-dose chemotherapy with stem cell support, use of immunotherapy and other chemotherapy regimens.[11,26]

Treatment of PSTT and ETT

Treatment of PSTT and ETT is determined by two independent poor prognostic factors: an interval of ≥48 months from the causative pregnancy and stage IV disease. Stage I tumours (confined to the uterus) arising <48 months since the antecedent pregnancy are treated with a total abdominal hysterectomy including removal of any suspicious pelvic and retroperitoneal lymph nodes. Adjuvant systemic therapy is not required. In contrast, if the PSTT/ETT originated from a pregnancy > 48 months previously, then such stage I patients and stage II–IV patients should be offered aggressive platinum-based chemotherapy including the option for experimental treatments such as high-

dose chemotherapy or immunotherapy.[41] Residual masses after treatment should be excised wherever possible to confirm no active cancer remains.[35,41] The survival rate is approximately 100% for non-metastatic disease and 50-60% for metastatic disease.[45]

The future in GTN management

Research in GTD is mainly focused on the development of new treatment strategies (Table 4). Especially, finding alternatives to multi-agent chemotherapy and associated short- and longer-term toxicities.[38] The use of immunotherapy is an important development in the management of GTN, particularly in drug-resistant disease.[44] The programmed cell death ligand 1 (PD-L1) is expressed in all pre-malignant and malignant GTD and anti-PD-1 monoclonal antibodies, such as pembrolizumab, are becoming important part of the management of relapsed chemo-resistant GTB.[38,41,44] The use of immunotherapy must be further evaluated, particularly because of the high cost and lack of longer-term safety data.[38]

Surveillance after GTN

Remission of GTN is defined as three consecutives normal hCG (hCG normalisation).[26] Posttreatment surveillance for low and high-risk GTN consists of weekly hCG measurements for 6 weeks after normalisation, then monthly for at least 12 months.[24,41,42] Surveillance for ultra-high-risk GTN is longer and consists of monthly hCG measurements for 24 months after completion of consolidation chemotherapy.[26] A minimum of 5-year-follow-up is advised.[12] Rising serum hCG in not sensitive for identifying recurrence of PSTT and ETT. Therefore, in cases of PSTT and ETT surveillance with 6 monthly MRIs is recommended.[26] Throughout surveillance period, patients must use reliable contraception because a new pregnancy may confound the interpretation of hCG levels [24]. Because of the 1–2% risk for a second mole in subsequent pregnancy, early ultrasound examination is recommended during all future pregnancies in addition to histologic evaluation of the placenta, and postdelivery hCG.[7]

Roots for further investigation

There is a need for possible future investigations to identify factors, predicting which molar pregnancies will resolve spontaneously, persist as GTN or transform into choriocarcinoma, PSTT or ETT.[25]

It has become evident, a redefinition of the FIGO/WHO scoring system to predict resistance to single-agent chemotherapy, is needed. With an "intermediate" risk group patients scoring WHO 5 and 6 can be identified for more intensive multi-agent chemotherapy from the outset.[25,38]

Although medical outcomes of GTD have been widely explored, limited data are available regarding the related psychological, sexual and fertility issues.[46] Improved understanding of the impact of GTD on women and their families, and how they may suffer is warranted.[25]

Conclusions

GTD is a rare disease and was historically associated with significant morbidity and mortality. Nowadays, many patients are asymptomatic at diagnosis due to wide use of ultrasound in early pregnancy. Initial detection of suspected HM is usually made based on ultrasound imaging, clinical signs, symptoms and hCG levels, which are above expected for gestational age. In a smaller proportion of patients, GTD leads to post molar GTN. This requires further systemic or surgical management. Posttreatment surveillance for GTN consists of regular hCG measurements. Most women with GTD can be successfully managed. One of the main future challenges in this regard is the optimization of treatment for patients with resistant GTN.

References

1. Lok C, Frijstein M, van Trommel N. Clinical presentation and diagnosis of gestational trophoblastic disease. *Best Pract Res Clin Obstet Gynaecol* 2020; **74:** 42-52. doi: 10.1016/j.bpobgyn.2020.12.001

2. Ngan HYS, Seckl MJ, Berkowitz RS, Xiang Y, Golfier F, Sekharan PK, et al. Update on the diagnosis and management of gestational trophoblastic disease. *Int J Gynaecol Obstet* 2018; **143(Suppl 2):** 79-85. doi: 10.1002/ijgo.12615

3. Fehlmann A, Benkortbi K, Rosseel G, Meyer-Hamme U, Tille JC, Sloan-Bena F, et al. Gestational trophoblastic disease in Switzerland: retrospective study of the impact of a regional reference centre. *Swiss Med Wkly* 2021; **151:** w20406. doi: 10.4414/smw.2021.20406

4. Capobianco G, Tinacci E, Saderi L, Dessole F, Petrillo M, Madonia M, et al. High incidence of gestational trophoblastic disease in a third-level university-hospital, Italy: a retrospective cohort study. *Front Oncol* 2021; **11:** 684700. doi: 10.3389/fonc.2021.684700

5. Eysbouts YK, Bulten J, Ottevanger PB, Thomas CMG, ten Kate-Booij MJ, van Herwaarden AE, et al. Trends in incidence for gestational trophoblastic disease over the last 20 years in a population-based study. *Gynecol Oncol* 2016; **140:** 70-5. doi: 10.1016/j.ygyno.2015.11.014

6. Hancock BW, Seckl MJ, Berkowitz RS. *Gestational trophoblastic disease.* London: Hodder Education Publishers; 2022.
7. Soper JT. Gestational trophoblastic disease: current evaluation and management. *Obstet Gynecol* 2021; **137:** 355-70. doi: 10.1097/AOG.0000000000004240
8. Fisher RA, Maher GJ. Genetics of gestational trophoblastic disease. *Best Pract Res Clin Obstet Gynaecol* 2021; **74:** 29-41. doi: 10.1016/j.bpobgyn.2021.01.004
9. Kaur B. Pathology of gestational trophoblastic disease (GTD). *Best Pract Res Clin Obstet Gynaecol* 2021; **74:** 3-28. doi: 10.1016/j.bpobgyn.2021.02.005
10. Seckl MJ, Sebire NJ, Berkowitz RS. Gestational trophoblastic disease. *Lancet* 2010; **376:** 717-29. doi: 10.1016/S0140-6736(10)60280-2
11. Abu-Rustum NR, Yashar CM, Bean S, Bradley K, Campos SM, Sook Chon H, et al. Gestational trophoblastic neoplasia, version 2.2019. *J Natl Compr Canc Netw* 2019; **17:** 1374-91. doi: 10.6004/jnccn.2019.0053
12. Lok C, van Trommel N, Massuger L, Golfier F, Seckl M. Practical clinical guidelines of the EOTTD for treatment and referral of gestational trophoblastic disease. *Eur J Cancer* 2020; **130:** 228-40. doi: 10.1016/j.ejca.2020.02.011
13. Cavoretto P, Cioffi R, Mangili G, Petrone M, Bergamini A, Rabaiotti E, et al. A pictorial ultrasound essay of gestational trophoblastic disease. *J Ultrasound Med* 2020; **39:** 597-613. doi: 10.1002/jum.15119
14. Memtsa M, Johns J, Jurkovic D, Ross JA, Sebire NJ, Jauniaux E. Diagnosis and outcome of hydatidiform moles in missed-miscarriage: a cohort-study, systematic review and meta-analysis. *Eur J Obstet Gynecol Reprod Biol* 2020; **253:** 206-12. doi: 10.1016/j.ejogrb.2020.07.030
15. Jauniaux E, Memtsa M, Johns J, Ross JA, Sebire NJ, Jurkovic D. Ultrasound diagnosis of complete and partial hydatidiform moles in early pregnancy failure: an inter-observer study. *Placenta* 2020; **97:** 65-7. doi: 10.1016/j.placenta.2020.06.013
16. Kirk E, Papageorghiou AT, Condous G, Bottomley C, Bourne T. The accuracy of first trimester ultrasound in the diagnosis of hydatidiform mole. *Ultrasound Obstet Gynecol* 2007; **29:** 70-5. doi: 10.1002/uog.3875
17. Shaaban AM, Rezvani M, Haroun RR, Kennedy AM, Elsayes KM, Olpin JD, et al. Gestational trophoblastic disease: clinical and imaging features. *Radiographics* 2017; **37:** 681-700. doi: 10.1148/rg.2017160140
18. Jauniaux E, Memtsa M, Johns J, Ross JA, Jurkovic D. New insights in the pathophysiology of complete hydatidiform mole. *Placenta* 2018; **62:** 28-33. doi: 10.1016/j.placenta.2017.12.008
19. Knez J, Day A, Jurkovic D. Ultrasound imaging in the management of bleeding and pain in early pregnancy. *Best Pract Res Clin Obstet Gynaecol* 2014; **28:** 621-36. doi: 10.1016/j.bpobgyn.2014.04.003
20. Lin LH, Bernardes LS, Hase EA, Fushida K, Francisco RPV. Is Doppler ultrasound useful for evaluating gestational trophoblastic disease? *Clinics* 2015; **70:** 810. doi: 10.6061/clinics/2015(12)08
21. Taylor HS, Pal L, Seli E. *Speroff's clinical gynecologic endocrinology and infertility*. Philadelphia: Wolters Kluwer; 2020.
22. McMahon LM, Stewart WW, Cuthill L. Human chorionic gonadotrophin assays to monitor GTD. *Best Pract Res Clin Obstet Gynaecol* 2021; **74:** 109-21. doi: 10.1016/j.bpobgyn.2021.05.001
23. Sato A, Usui H, Shozu M. Comparison between vacuum aspiration and forceps plus blunt curettage for the evacuation of complete hydatidiform moles. *Taiwan J Obstet Gynecol* 2019; **58:** 650-5. doi: 10.1016/j.tjog.2019.07.012
24. Ngan HYS, Seckl MJ, Berkowitz RS, Xiang Y, Golfier F, Sekharan PK, et al. Diagnosis and management of gestational trophoblastic disease: 2021 update. *Int J Gynaecol Obstet* 2021; **155:** 86-93. doi: 10.1002/ijgo.13877
25. Tidy J, Seckl M, Hancock BW, on behalf of the Royal College of Obstetricians and Gynaecologists. Management of gestational trophoblastic disease. *BJOG* 2021; **128:** e1-27. doi: 10.1111/1471-0528.16266
26. Horowitz NS, Eskander RN, Adelman MR, Burke W. Epidemiology, diagnosis, and treatment of gestational trophoblastic disease: a society of gynecologic oncology evidenced-based review and recommendation. *Gynecol Oncol* 2021; **163:** 605-13. doi: 10.1016/j.ygyno.2021.10.003
27. Ngu SF, Ngan HYS. Surgery including fertility-sparing treatment of GTD. *Best Pract Res Clin Obstet Gynaecol* 2021; **74:** 97-108. doi: 10.1016/j.bpobgyn.2020.10.005
28. Zhao P, Lu Y, Huang W, Tong B, Lu W. Total hysterectomy versus uterine evacuation for preventing post-molar gestational trophoblastic neoplasia in patients who are at least 40 years old: a systematic review and meta-analysis. *BMC Cancer* 2019; **19:** 13. doi: 10.1186/s12885-018-5168
29. Gockley AA, Lin LH, Davis M, Melamed A, Rizzo A, Sun SY, et al. Impact of clinical characteristics on human chorionic gonadotropin regression after molar pregnancy. *Clinics* 2021; **76:** e2830. doi: 10.6061/clinics/2021/e2830
30. Eysbouts Y, Brouwer R, Ottevanger P, Massuger L, Sweep F, Thomas C, et al. Serum human chorionic gonadotropin normogram for the detection of gestational trophoblastic neoplasia. *Int J Gynecol Cancer* 2017; **27:** 1035-41. doi: 10.1097/IGC.0000000000000966
31. Snyman LC. Gestational trophoblastic disease: an overview. *S Afr J Gynaecol Oncol* 2009; **1:** 32-7. doi: 10.1080/20742835.2009.11441132
32. Lurain JR. Gestational trophoblastic tumors. *Semin Surg Oncol* 1990; **6:** 347-53. doi: 10.1002/SSU.2980060610
33. FIGO Oncology Committee. FIGO staging for gestational trophoblastic neoplasia 2000. FIGO Oncology Committee. *Int J Gynaecol Obstet* 2002; **77:** 285-7. doi: 10.1016/S0020-7292(02)00063-2
34. Lurain JR. Gestational trophoblastic disease I: epidemiology, pathology, clinical presentation and diagnosis of gestational trophoblastic disease, and management of hydatidiform mole. *Am J Obstet Gynecol* 2010; **203:** 531-9. doi: 10.1016/j.ajog.2010.06.073
35. Hancock BW, Tidy J. Placental site trophoblastic tumour and epithelioid trophoblastic tumour. *Best Pract Res Clin Obstet Gynaecol* 2021; **74:** 131-48. doi: 10.1016/j.bpobgyn.2020.10.004
36. Seckl MJ, Sebire NJ, Fisher RA, Golfier F, Massuger L, Sessa C. Gestational trophoblastic disease: ESMO clinical practice guidelines for diagnosis, treatment and follow-up. *Ann Oncol* 2013; **24(Suppl 6):** 39-50. doi: 10.1093/annonc/mdt345
37. Biscaro A, Braga A, Berkowitz RS. Diagnosis, classification and treatment of gestational trophoblastic neoplasia. *Rev Bras Ginecol Obstet* 2015; **37:** 42-51. doi: 10.1590/SO100-720320140005198
38. Winter MC. Treatment of low-risk gestational trophoblastic neoplasia. *Best Pract Res Clin Obstet Gynaecol* 2021; **74:** 67-80. doi: 10.1016/j.bpobgyn.2021.01.006
39. Berkowitz RS, Goldstein DP. Current management of gestational trophoblastic diseases. *Gynecol Oncol* 2009; **112:** 654-62. doi: 10.1016/j.ygyno.2008.09.005
40. Braga A, Mora P, Melo AC de, Nogueira-Rodrigues A, Amim-Junior J, Rezende-Filho J, et al. Challenges in the diagnosis and treatment of gestational trophoblastic neoplasia worldwide. *World J Clin Oncol* 2019; **10:** 28-37. doi: 10.5306/wjco.v10.i2.28
41. Clark JJ, Slater S, Seckl MJ. Treatment of gestational trophoblastic disease in the 2020s. *Curr Opin Obstet Gynecol* 2021; **33:** 7-12. doi: 10.1097/GCO.0000000000000674
42. Clair KH, Gallegos N, Bristow RE. Successful treatment of metastatic refractory gestational choriocarcinoma with pembrolizumab: a case for immune checkpoint salvage therapy in trophoblastic tumors. *Gynecol Oncol Rep* 2020; **34:** 100625. doi: 10.1016/j.gore.2020.100625
43. Choi MC, Oh J, Lee C. Effective anti-programmed cell death 1 treatment for chemoresistant gestational trophoblastic neoplasia. *Eur J Cancer* 2019; **121:** 94-7. doi: 10.1016/j.ejca.2019.08.024
44. Ghorani E, Kaur B, Fisher RA, Short D, Joneborg U, Carlson JW, et al. Pembrolizumab is effective for drug-resistant gestational trophoblastic neoplasia. *Lancet* 2017; **390:** 2343-5. doi: 10.1016/S0140-6736(17)32894-5
45. Lurain JR. Gestational trophoblastic disease II: classification and management of gestational trophoblastic neoplasia. *Am J Obstet Gynecol* 2011; **204:** 11-8. doi: 10.1016/j.ajog.2010.06.072
46. di Mattei V, Mazzetti M, Perego G, Rottoli S, Mangili G, Bergamini A, et al. Psychological aspects and fertility issues of GTD. *Best Pract Res Clin Obstet Gynaecol* 2021; **74:** 53-66. doi: 10.1016/j.bpobgyn.2020.10.007

research article

Detection and localization of hyperfunctioning parathyroid glands on [^{18}F]fluorocholine PET/CT using deep learning – model performance and comparison to human experts

Leon Jarabek[1], Jan Jamsek[2], Anka Cuderman[2], Sebastijan Rep[2,3], Marko Hocevar[4,5], Tomaz Kocjan[5,6], Mojca Jensterle[5,6], Ziga Spiclin[7], Ziga Macek Lezaic[8], Filip Cvetko[5], Luka Lezaic[2,5]

[1] Department of Radiology, General Hospital Novo Mesto, Slovenia
[2] Department for Nuclear Medicine, University Medical Centre Ljubljana, Slovenia
[3] Faculty of Health Sciences, University of Ljubljana, Ljubljana, Slovenia
[4] Department of Surgical Oncology, Institute of Oncology, Ljubljana
[5] Faculty of Medicine, University of Ljubljana, Ljubljana, Slovenia
[6] Department for Endocrinology, Diabetes and Metabolic Diseases, University Medical Centre Ljubljana, Slovenia
[7] Faculty of Electrical Engineering, University of Ljubljana, Slovenia
[8] Rožna dolina, c. VI/8, Ljubljana, Slovenia

Radiol Oncol 2022; 56(4): 440-452.

Received 21 April 2022
Accepted 22 August 2022

Correspondence to: Assist. Prof. Luka Ležaić, M.D., Ph.D., Department for Nuclear Medicine, University Medical Centre Ljubljana, Slovenia.
E-mail: luka.lezaic@kclj.si

Disclosure: No potential conflicts of interest were disclosed.

Background. In the setting of primary hyperparathyroidism (PHPT), [^{18}F]fluorocholine PET/CT (FCH-PET) has excellent diagnostic performance, with experienced practitioners achieving 97.7% accuracy in localising hyperfunctioning parathyroid tissue (HPTT). Due to the relative triviality of the task for human readers, we explored the performance of deep learning (DL) methods for HPTT detection and localisation on FCH-PET images in the setting of PHPT.

Patients and methods. We used a dataset of 93 subjects with PHPT imaged using FCH-PET, of which 74 subjects had visible HPTT while 19 controls had no visible HPTT on FCH-PET. A conventional Resnet10 as well as a novel mPETResnet10 DL model were trained and tested to detect (present, not present) and localise (upper left, lower left, upper right or lower right) HPTT. Our mPETResnet10 architecture also contained a region-of-interest masking algorithm that we evaluated qualitatively in order to try to explain the model's decision process.

Results. The models detected the presence of HPTT with an accuracy of 83% and determined the quadrant of HPTT with an accuracy of 74%. The DL methods performed statistically worse ($p < 0.001$) in both tasks compared to human readers, who localise HPTT with the accuracy of 97.7%. The produced region-of-interest mask, while not showing a consistent added value in the qualitative evaluation of model's decision process, had correctly identified the foreground PET signal.

Conclusions. Our experiment is the first reported use of DL analysis of FCH-PET in PHPT. We have shown that it is possible to utilize DL methods with FCH-PET to detect and localize HPTT. Given our small dataset of 93 subjects, results are nevertheless promising for further research.

Key words: primary hyperparathyroidism, deep learning, nuclear medicine, fluorocholine, PET/CT

Introduction

Primary hyperparathyroidism (PHPT) is the third most common endocrine disorder with a reported prevalence ranging from 1 to 21 per 1,000 among the general population.[1] PHPT is the result of hyperfunctioning parathyroid tissue (HPTT), which becomes insensitive to the inhibitory effect of hy-

percalcemia. Histologically HPTT can be either an adenoma (in approximately 80% of cases), multiple adenomas, hyperplasia or rarely a carcinoma (in approximately 1% of cases).[2] The treatment of PHPT typically requires surgical removal of HPTT. Modern, minimally invasive surgical techniques require precise preoperative localization of HPTT. For this task, [18F]fluorocholine PET/CT (FCH-PET) is one of the most promising imaging modalities, with reported sensitivities of 94–100% and specificities of 88–100%.[3-13] Performance of FCH-PET was repeatedly shown to be superior to other HPTT localization methods, while at the same time having lower radiation exposure compared to other nuclear medicine modalities.[14]

Deep learning (DL) techniques with convolutional neural networks (CNN) have proven to be useful in various computer vision tasks, such as super-resolution, image synthesis, denoising, classification, segmentation and object detection.[15-22] In medical imaging, CNNs have shown promising performance, even exceeding experts in some specific cases, such as grading diabetic retinopathy from fundus images, detecting skin cancer from photographs and detecting abnormalities on chest X-ray images.[23-25] Research of CNNs in nuclear medicine showed its potential in reducing the PET radiation dose, improving image quality, lesion detection and segmentation as well as prediction of prognosis.[21-36]

Given the excellent human performance of analysing FCH-PET for the presence and localisation of HPTT, an interesting opportunity to challenge DL techniques is presented. An automated analysis pipeline of FCH-PET that would classify HPTT presence and location would allow for efficient surgical planning and could serve to double check the experts' reports. Such analysis would also allow for more accurate and objective comparison of potential follow-up studies; these are not often required, but unavoidable in cases of persistent or recurrent hyperparathyroidism. Furthermore, if the model could visualise the pathological uptake in the study, it would provide more visual feedback to the surgeon in axial images to allow for better visualisation of HPTT and would allow faster interpretation of interplay of surrounding anatomical structures. Our aim was to explore the performance of DL analysis of FCH-PET in the setting of PHPT, since the use of DL for FCH-PET analysis in PHPT has not yet been thoroughly investigated.

To this end, we developed a classification model which classifies whether HPTT is present in the study and its location. We also attempt to model in a novel unsupervised manner the regions-of-interest fed to the model. Furthermore, we aimed to provide a preliminary comparison of the diagnostic accuracy of the DL models to human experts to determine clinical applicability, as the model should be as accurate as an expert in evaluating FCH-PET studies to be clinically applicable.

Patients and methods

This was a retrospective analysis of prospective clinical trial data (NCT03203668) performed at the University Medical Centre Ljubljana and Institute of Oncology Ljubljana. The clinical trial was approved by the Medical Ethics Committee of the Republic of Slovenia (approval number 77/11/12). The trial only included patients with biochemically confirmed primary hyperparathyroidism; hypercalcemic patients had elevated or inappropriately normal parathormone (PTH) levels, whereas normocalcemic patients had inappropriately elevated PTH levels. All included patients were older than 18 years and had no clinical history of oncological, inflammatory, or infectious disease of the head and neck. No pregnant women were included in the trial. The retrospective use of the data was approved by the Medical Ethics Committee of the Republic od Slovenia (approval number 0120-582/2021/4) and the patient consent was waived due to the retrospective nature of the analysis.

The study only included images of patients with biochemically confirmed PHPT at time of FCH-PET imaging. Since the trial did not include healthy controls, data of patients with the following criteria were chosen as "controls": no visible HPTT in FCH-PET at time of imaging; have not undergone surgery in thyroid region; were biochemically normocalcemic at 6 months' follow-up.

Dataset description and PET-CT image acquisition

We used the data of 79 participants (22 male, 57 female) with visible HPTT lesions on FCH-PET (referred below as *patients*) and 19 participants (7 male, 12 female) without visible HPTT lesions on FCH-PET (referred below as *controls*). Average age (± SD) of *patients* was 58.7 ± 12.7 years and average age of *controls* was 60.1 ± 11.8 years. Both *patients* and *control* groups were comparable in terms of age ($p = 0.659$) as well as male to female ratio ($p = 0.852$), as determined by Student *t*-test and normalised Chi-square test, respectively.[37,38]

FCH-PET imaging was performed at the Department for Nuclear Medicine of the University Medical Centre Ljubljana. The acquisition details were the same as in Cuderman *et al*.[3] The patients fasted 6 hours prior to the examination, were well hydrated and injected with 100 MBq of [18F] Fluorocholine (FCH). Acquisition was performed on a Siemens Biograph mCT® PET/CT (Siemens Healthineers AG, München, DE) 5 minutes and 60 minutes after the FCH application. The imaging region extended from the angle of mandible to the aortic arch. The imaging consisted of a low-dose CT (120 kVp, 25 mAs, CARE Dose 4D, FBP reconstruction), followed by PET imaging (one bed position of 4 minutes). PET images were reconstructed using Siemens HD PET software with iterative TrueX + TOF OSEM method (2 iterations, 21 subsets) with 400 × 400 matrix, zoom 1 and Gaussian filter with FWHM of 4 mm. To train and evaluate DL models, we used only images acquired 60 minutes after FCH application, where the balance of image quality and target-to-backround ratio is typically highest.

All *patients* with HPTT present on FCH-PET were surgically treated at Institute of Oncology Ljubljana. Ground truth HPTT presence and location for training the CNNs was based on the post-surgical histopathological results. Furthermore, our dataset included formatted information from FCH-PET reports as used by Cuderman *et al*. that we used to compare the performance of DL models with human experts.[3] These reports were used to guide the subsequent surgical removal of the HPTT.

For simplicity, we only used *patients* who had single gland disease and had HPTT in the typical anatomic location of parathyroid glands. HPTT was thus in one of 4 possible locations: upper left (UL, 21 *patients*), lower left (LL, 27 *patients*), upper right (UR, 5 *patients*) and lower right (LR, 26 *patients*). Since the UR location in our dataset contained only 5 patients, it was removed from the final analysis due to under-representation. For the final model development and evaluation, we used 19 *controls* and 74 *patients*, among them 21 with UL HPTT, 27 with LL HPTT and 26 with LR HPTT.

Image pre-processing

We used the same pre-processing pipeline for all analyzed images. First, we resampled the CT image using bivariate spline interpolation from *scipy* library to match the PET image matrix of 200 × 200 × 56.[39] 3D interpolation was not needed as CT was reconstructed at same slices as PET. Both images were concatenated to produce a 200 × 200 × 56 × 2 matrix representing the PET/CT. Next, we cropped the desired region of interest containing the hyperfunctioning parathyroid tissue to the matrix of size 64 × 64 × 32. For all patients, the region was cropped at same PET/CT coordinates, which were chosen empirically, such that it contained HPTT in all studies. In this way, there are lower memory requirements to run deep learning models.

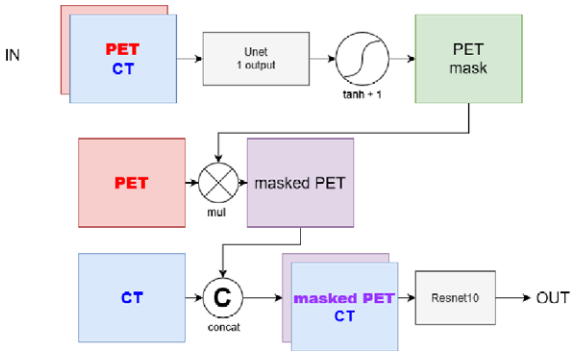

FIGURE 1. mPETResnet10 architecture. First, PET-CT images are fed into UNet with a single channel output and tanh+1 activation function. This output is the PET mask. This mask is elementwise multiplied with PET image to produce a masked PET image. Masked PET is concatenated with the original CT and the masked PET-CT is fed into the ResNet10 classifier. Gray boxes represent deep-learning models, coloured boxes represent data, and circles represent operations of *tanh+1*, *multiplication* (mul) by element and *concatenation* (concat).

The labels for an image were represented by a one-hot encoded vector of length 4, representing locations UL, LL, LR and a dummy variable representing "healthy" *controls*.

Modelling

For modelling, we defined 2 tasks: (i) a task of classifying whether the HPTT is present in the image or not (CPr, classification of presence) and (ii) a task of classifying in which quadrant the HPTT was present in the image (CLoc, classification of location). CPr is a simple binary classification task where *p(HPTT) = 1 – p(healthy)*. CLoc is a multi-class classification task where each output of the model is analogous to the probability of HPTT being present at one of three considered locations UL, LL and LR.

With normalized PET-CT images represented by a matrix of shape 200 × 200 × 56 × 2 as input, the output of the model was a vector of length 4, activated by *SoftMax* activation function, corresponding to *p(UL)*, *p(LL)*, *p(LR)* and *p(healthy)* (Figure 1).

The model was therefore trained for both CPr and CLoc simultaneously. Furthermore, the dataset was well balanced, containing a similar number of cases for each of the 4 classes, and thus ensured stable training using cross entropy as a loss function.[40] For training, batch size of 5 was used with stochastic gradient descent optimizer with momentum of 0.9 and weight decay of 0.005. The initial learning rate was determined by a grid search in log space and learning rate decay on plateau scheduling was used. Identical procedure was used for all models. All models were trained from scratch.

For both CPr and CLoc classification tasks, we performed baseline experiments using the 3D version of *Resnet10* (RN10) architecture and using our novel architecture as described below.[41,42] Our choice of architecture of Resnet10 was based on extensive experiments which included other state-of-the-art, and larger architectures, namely using 3D versions of *Densenet121*[43], *wideResNet101*[44], *PreActResnet101*[45], *Resnet101*[41] and *Resnet50.* For all architectures except our novel architecture, implementations from Kensho *et al*. were used.[42]

We provide comprehensive comparison between the performance of RN10 and proposed architecture "*masked-PET Resnet10*" (mRN10), as well as the comparison of mRN10 to experts' performance.

Masked-PET Resnet10

We developed a novel architecture designed to mask PET signals from unimportant (i.e., physiological uptake) regions with high signal (eg. muscle tissue, salivary glands) before entering the RN10 classifier. This is important as the FCH-PET images are heteroscedastic, with some regions - like muscle - having high variance between subjects and other regions - like air - having low variance. To mitigate this, and to improve conditioning of the data and therefore the stability of the classifier,[46] we decided to allow the model itself to optimize for differentiable masking of these potentially problematic regions. We named the proposed architecture "*masked-PET Resnet10*" (mRN10).

The mRN10 consisted of 2 parts. First, a *Unet* architecture was used to mask the PET-CT.[47] Next, *Resnet10* was used to classify the masked PET-CT. We decided on *Unet* architecture since it is commonly used in segmentation tasks[21] and we deemed the task of masking to be similar to segmentation of the region-of-interest. Masking was achieved by first activating per-voxel output of *Unet* with activation function $f(x) = tanh(x)+1$. These output values were in interval (0,2), such that regions where *Unet* output was negative were closer to 0, while regions where *Unet* output was positive were closer to 2. This matrix, representing the mask, was then multiplied elementwise by the PET matrix, to produce a masked PET image.

The architecture of mRN10 is depicted on Figure 1. Regions in PET image where *Unet* output was negative were multiplied by values close to 0 and were therefore effectively "masked" from the PET image. This masked PET was then concatenated with CT and the masked PET-CT was used as input for the *Resnet10* classifier. The entire mRN10 was trained end-to-end, therefore the masking was optimized for the lowest loss in the classification task of the downstream *Resnet10* classifier.

The models were written in *python 3.8.0* using *Pytorch 1.10* framework and trained on a single *GTX 1080Ti* graphics card (*Nvidia Corporation, Santa Clara, US*).[48,49] The code is freely available online at: https://github.com/ljarabek/AI_FCH

Training and evaluation

For training, we used 12-fold cross-validation with data split into a test set of 10 random subjects, with the remaining subjects being randomly split into a training set (90% of the remaining subjects) and validation set (10% of the remaining subjects). Data was normalised using z-score normalization upon splitting accordingly, such that the mean and standard deviation were computed only using the training set. Sets were sampled such that each set contained at least 1 subject from each class (UL, LL, LR and *control*). For testing, the model with the lowest validation loss was used. The confusion matrix for CPr evaluation was computed by summing the confusion matrices for the test set across the 12 data splits, providing 120 total samples. The confusion matrix for CLoc was obtained by summing the 3 confusion matrices for evaluated locations UL, LL, LR across the best performing 12 data splits, providing 360 "samples". Similarly, the area under the receiver operating characteristic curve (AUCROC) was computed.

We used *epiR* package for *R* to determine the diagnostic performance metrics and *McNemar* test from *DTComPair* package for determining statistically significant ($p < 0.05$) differences.[50-53] Only binary diagnostic performance metrics were used for evaluation, even though CLoc is theoretically a multi-class classification task. In this way, the results comparable to studies evaluating the performance of FCH-PET, since they also mostly used binary classification metrics.[3-13]

TABLE 1. Confusion matrices for CPr **(A)** and CLoc **(B)** for both RN10 and mRN10 models. Note that the confusion matrices for CLoc have more samples (360 in total), as they were computed by summing the confusion matrices for each of the three included locations (UL, LL, LR)

Ⓐ

	CPr task with RN10				CPr task with mRN10		
	HPTT present	HPTT not present	**sum**		HPTT present	HPTT not present	**sum**
Model output HPTT present	79	8	**87**	Model output HPTT present	90	11	**101**
Model output HPTT not present	20	13	**33**	Model output HPTT not present	9	10	**19**
sum	**99**	**21**	**120**	**sum**	**99**	**21**	**120**

Ⓑ

	CLoc task with RN10				CLoc task with mRN10		
	HPTT at GTLoc	HPTT not at GTLoc	**sum**		HPTT at GTLoc	HPTT not at GTLoc	**sum**
Predicted GTLoc	35	51	**86**	Predicted GTLoc	53	50	**103**
Not predicted GTLoc	61	213	**274**	Not predicted GTLoc	43	214	**257**
sum	**96**	**264**	**360**	**sum**	**96**	**264**	**360**

CPr = classification of presence; CLoc = classification of location; GTLoc = ground truth location based on postsurgical histopathological reports; HPTT = hyperactive parathyroid tissue; mRN10 = novel *masked-PET Resnet10* model; RN10 = baseline *Resnet10* model

Results

We determined the best performing models for both RN10 and mRN10 were trained using the initial learning rate of 0.013. The confusion matrices for RN10 and mRN10 are presented in Tables 1A and 1B, while the diagnostic performances for both tasks using the RN10 and mRN10 models are presented in Table 2. Both models had comparable performance in the CPr task. The mRN10 had a significantly higher accuracy for the CLoc task than the RN10 and was therefore used for comparison with human performance.

We performed a comprehensive comparison with human expert evaluation only for the CLoc task. Healthy controls had, by definition, no HPTT visible on FCH-PET (as reported by human experts), so the comparison could not be made for the CPr task, as human performance for CPr was 100%. Comparison of performance metrics for the CLoc task between the mRN10 model and human performance (based on the same subset of 83 patients used for the DL model development) is shown in Table 3.

Studies with different architectures

Studies across multiple models were performed to determine the use of RN10 as the base architecture. The results of other models are stated below, as well as the number of trainable parameters and optimal initial learning rate. Mean CPr AUCROC and 95% confidence intervals were computed as population statistics of 50 models obtained from 5 runs of 10-fold cross-validation at optimal learning rate. The highest performance among the models tested was achieved with RN10 and mRN10. The performance of other models is noted in the table below.

PET masking qualitative results

Qualitative results were evaluated across all subjects and using an iteration of the model trained from a single data split. The qualitative results did not change in a significant manner with repeated training. In qualitative analysis of PET masking results, the region-of-interest mask correctly identified the foreground, while we have found that in

TABLE 2. Diagnostic performance metrics of RN10 and mRN10 as well as *p*-values as determined by McNemar test comparing both models for each task (except AUCROC)

	CPr ***RN10***	**CPr** ***mRN10***	*CPr p-value*	**CLoc** ***RN10***	**CLoc** ***mRN10***	*CLoc p-value*
Sensitivity [95% CI]	0.800 [0.719; 0.877]	**0.909** [0.852; 0.965]	**0.028**	0.365 [0.268; 0.460]	**0.552** [0.453; 0.652]	**0.018**
Specificity [95% CI]	**0.619** [0.411; 0.827]	0.476 [0.263; 0.690]	0.257	0.807 [0.759; 0.854]	**0.811** [0.763; 0.858]	0.910
Positive predictive value [95% CI]	**0.908** [0.847; 0.969]	0.891 [0.830; 0.951]	0.507	0.407 [0.303; 0.511]	**0.515** [0.418; 0.611]	0.089
Negative predictive value [95% CI]	0.394 [0.227; 0.560]	**0.526** [0.302; 0.751]	0.205	0.777 [0.728; 0.827]	**0.833** [0.787; 0.878]	**0.021**
Accuracy [95% CI]	0.767 [0.681; 0.839]	**0.833** [0.756; 0.895]	**0.050**	0.689 [0.638; 0.736]	**0.742** [0.693 0.786]	**0.031**
AUCROC	0.815	**0.849**	/	0.702	**0.770**	/

AUCROC = area under the receiver operating characteristic curve; CPr = classification of presence; CLoc = classification of location; mRN10 = novel *masked-PET Resnet10* model; RN10 = baseline *Resnet10* model

all but 3 subjects, 1 with LL HPTT and 2 LR HPTT, that the mask completely obscured (masked) the original location of HPTT on masked PET. In the 3 subjects with visible HPTT in the masked PET in the original location, the mask still partially obscured the HPTT, as seen in Figure 3, rows d), f) and g).

Figure 2 shows a typical example of mRN10 masking, where HPTT was masked and cannot be distinguished in masked PET image. The network correctly classified the subject in Figure 2 as having lower right HPTT. The region of air outside the patient is masked to approximately 25% of the original PET signal, with mask having a value of approximately 0.25. The high signal from the salivary glands is masked in all cases, whereas signal from the thyroid gland is only partially masked in all cases, as seen in Figure 3.

Discussion

The aim of the study was to evaluate the potential of DL models in classifying HPTT presence and location in FCH-PET studies in the setting of PHPT. For our experiments to be representative of results of such a model in practice, we used data of representative cohort of subjects with PHPT. Classification of FCH-PET studies was performed using multiple common DL models and we found that the simplest among the models tested, RN10, achieved the highest performance. Furthermore, we improve the model's performance by modifying the architecture to include a region-of-interest masking step, which produced a region-of-interest mask, which successfully identified the foreground of PET. The mRN10 achieved superior performance to models of similar size. Overall, given the size of our dataset and achieved performance, we found that the use of deep learning is highly promising in potential evaluation of FCH-PET in PHPT.

Dataset and patient characteristics

Both our *patients* and the *controls* had representative demographic characteristics of patients with PHPT, with male-to-female ratio in literature being 1:3 to 1:4 and the peak incidence of 62 ± 13 years.[54-57] Therefore, the models were more likely to have learned the correct features to classify HPTT presence and were trained on a relatively representative dataset that would be encountered in real-life

TABLE 3. Comparison of mRN10 and human performance for the CLoc task. *p*-values were determined by using the McNemar test

	CLoc *mRN10*	**CLoc** *human*	*p-value*
Sensitivity [95% CI]	0.552 [0.453; 0.652]	**0.917** [0.857; 0.958]	**< 0.001**
Specificity [95% CI]	0.811 [0.763; 0.858]	**0.997** [0.986; 0.999]	**< 0.001**
Positive predictive value [95% CI]	0.515 [0.418; 0.611]	**0.992** [0.945; 0.999]	**< 0.001**
Negative predictive value [95% CI]	0.833 [0.787; 0.878]	**0.972** [0.952; 0.984]	**< 0.001**
Accuracy [95% CI]	0.742 [0.693; 0.786]	**0.977** [0.960; 0.988]	**< 0.001**

CLoc = classification of location; mRN10 = novel *masked-PET Resnet10* model; RN10 = baseline *Resnet10* model

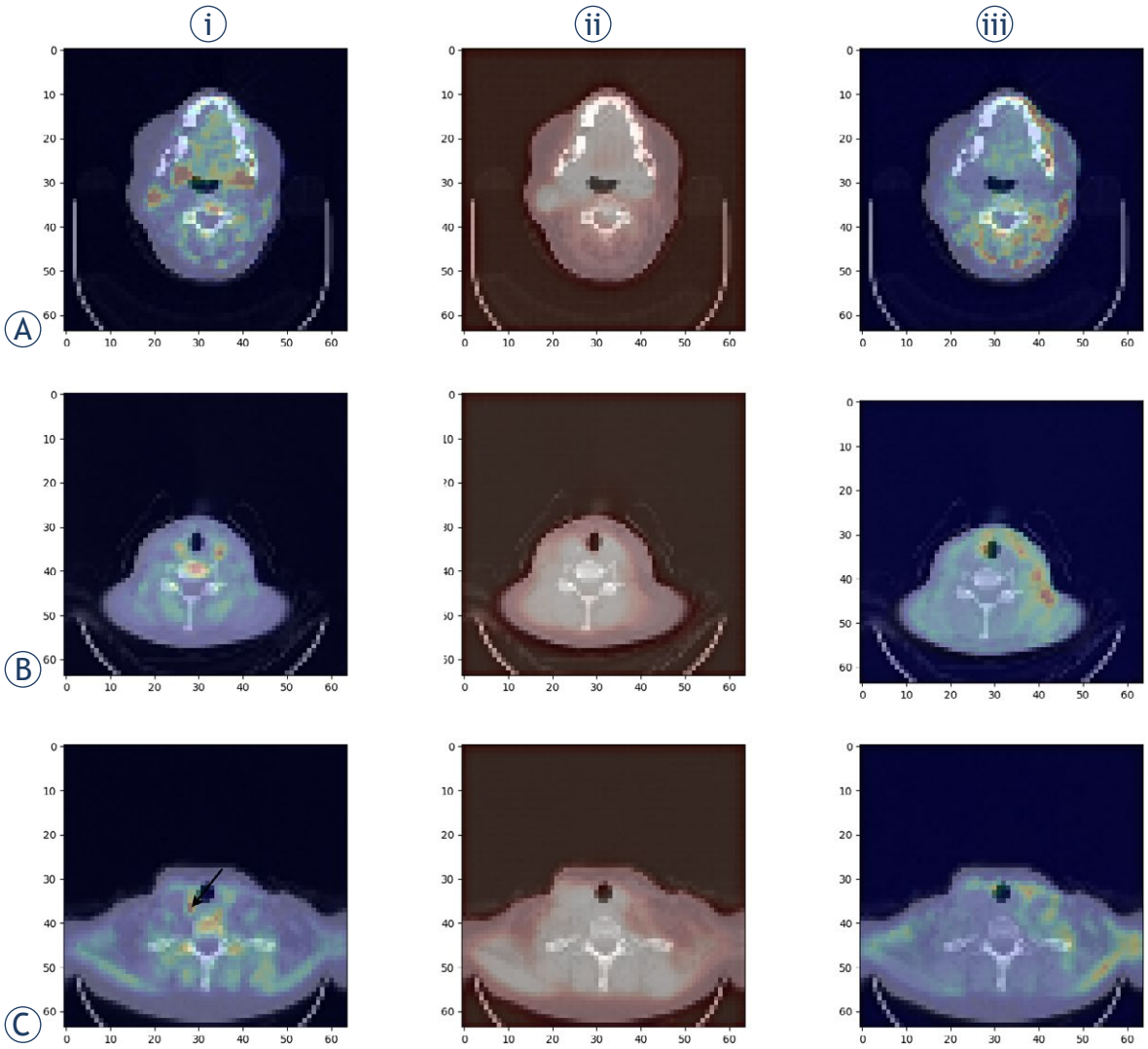

FIGURE 2. Example of novel masked-PET Resnet10 model (mRN10) masking of PET signal in a subject with parathyroid adenoma in the region of lower right parathyroid gland (black arrow in row c). Each row represents a different slice through the pre-processed [18F]fluorocholine PET/CT (FCH-PET) images (**(A)** – mandibular region, **(B)** – upper neck region **(C)** – lower neck region containing parathyroid adenoma). The first column shows a pre-processed PET/CT image (64 × 64 × 32 matrix), where colours toward the "warm" (red) part of the spectrum indicate higher PET signal and colours toward the "cool" (blue) part of the spectrum indicate lower PET signal. The second column shows the mask, where regions coloured toward the red part of the spectrum have higher weights (non-masked) and regions toward the yellow part of the spectrum have lower weights (masked). The third column represents the final masked PET/CT images computed by multiplying the mask with the original PET/CT. The image was correctly classified as containing the adenoma in the lower right region.

application. Representation per quadrant of HPTT in our cohort was also congruous to numbers reported in the literature. Marzouki *et al*. provide 95% confidence intervals of HPTT ratio per site as follows: lower left 32–51%, lower right 25–42%, upper left 10–23% and upper right 4–15%.[58-60]

Unfortunately, the dataset was imbalanced with respect to patients vs "controls". However, obtaining negative FCH-PET studies is difficult due to high positivity rate of finding HPTT in FCH-PET, since only patients with biochemically confirmed PHPT are imaged. Such patients are highly likely to have visible HPTT, as reported in studies exploring the effectiveness of FCH-PET.[3-13] Since healthy subjects are generally not referred to undergo FCH-PET imaging, the best attempt was made to select the criteria for choosing "controls" among patients with negative visual assessment of FCH-PET. Our controls therefore had negative imaging findings and biochemical criteria for PHPT

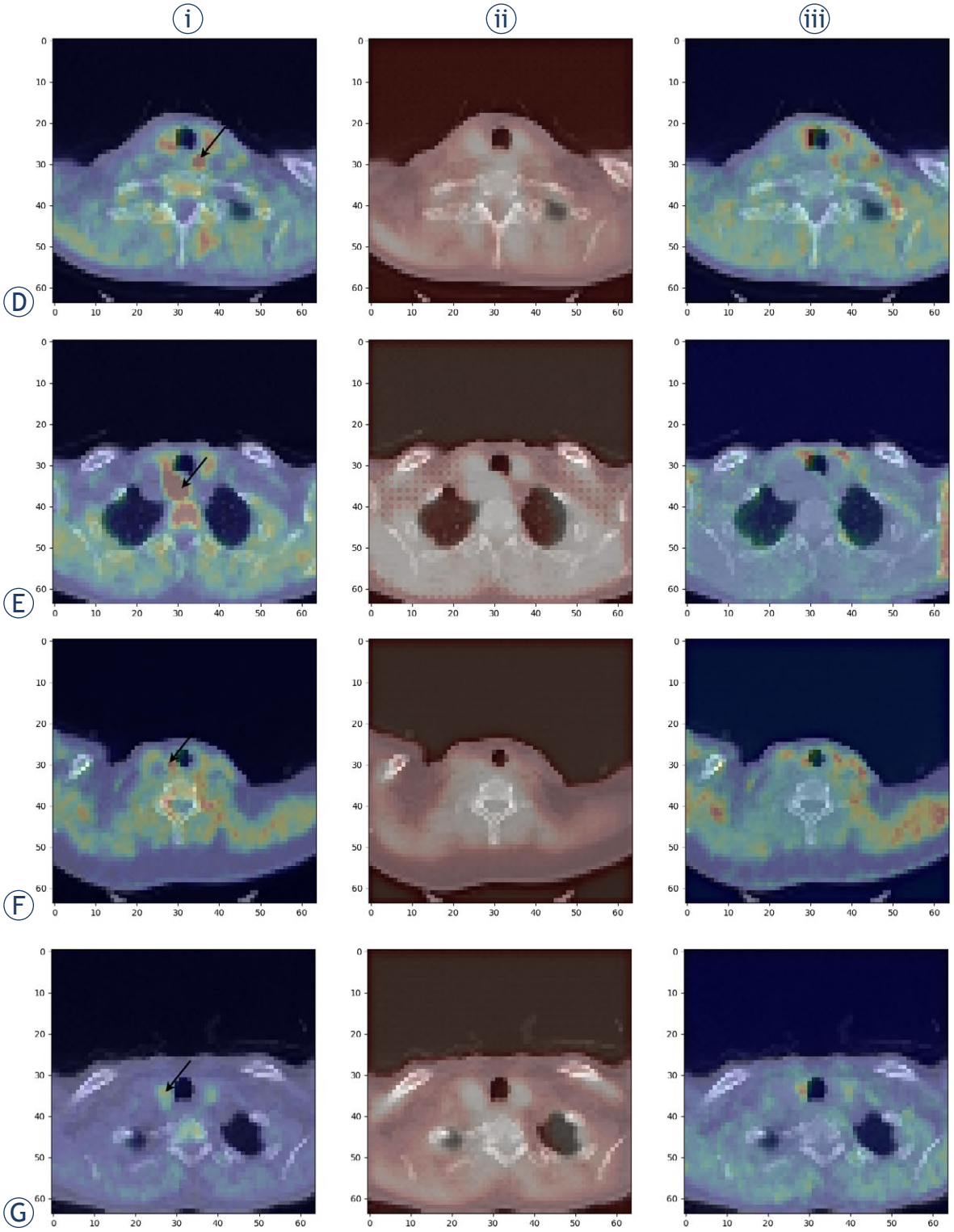

FIGURE 3. Some examples of masking of hyperactive parathyroid tissue (HPTT), which is indicated by an arrow in column **(I)**. The images are shown in the same format as in Figure 2. Rows **(D)**, **(F)** and **(G)** represent the only 3 cases where HPTT was not completely masked.

TABLE 4. Performance of several models on CPr task

Model name	mRN10	RN10	*Resnet50*	*Resnet101*	*Densenet101*	*PreActResnet101*	*WideResnet101*
# Trainable parameters (millions)	33.5	14.3	46.2	85.2	112.9	85.2	85.2
Optimal initial learning rate	0.0136	0.0136	$2.15*10^{-3}$	$1.47*10^{-4}$	0.316	$1.47*10^{-4}$	$2.15*10^{-3}$
Mean CPr AUCROC [95% CI]	**0.850 [0.734; 0.998]**	**0.812 [0.716; 0.994]**	0.754 [0.624; 0.980]	0.527 [0.410; 0.639]	0.703 [0.606; 0.905]	0.739 [0.486; 0.998]	0.752 [0.653; 0.966]

AUCROC = area under the receiver operating characteristic curve; CPr = classification of presence; mRN10 = novel *masked-PET Resnet10* model; RN10 = baseline *Resnet10* model

resolved at follow-up after 6 months without surgical treatment.

For ground truth location, histopathological results were used as opposed to expert visual assessment of FCH-PET, in order to simulate real-world use of the models in guiding surgical removal of HPTT.

Deep-learning model architecture

We have chosen the 3D *Resnet10* as our baseline model since multiple research groups have shown it provides promising results in classification tasks on both medical and non-medical images and is the basis of modern architectures.[41,61-63] *Resnet10* also achieved the highest performance among the models tested. The other tested models with more parameters performed worse, as they seemed overparameterized and likely learned aberrant features, thus overfitting to the training data. Not many studies explore this phenomenon in detail, but a similar phenomenon was noted in the results of a recent study of Bailly *et al.*[64] studying the effects of dataset size, dataset complexity, and model complexity on performance.

The main motivation behind the design of mRN10 and implementation of masking is the way experts interpret FCH-PET. Experienced nuclear medicine physicians know that HPTT usually appears around the thyroid region, and we wanted to allow for the model to learn to mask regions that were deemed unimportant for classification. Furthermore, these unimportant regions (e.g., muscle) commonly produced high intensity PET signal that might affect the classifier. Using end-to-end training with only cross-entropy classification loss, we allowed the network to learn to mask these unimportant regions in an unsupervised manner by carefully tailoring the architecture. Given how experts interpret FCH-PET, mRN10 was an attempt to integrate expert knowledge into the model to improve the *Resnet10* classifier.

The *Unet* was chosen as the masking architecture as we deem our masking to be a task that is comparable to segmentation. For the activation function, we used *tanh* (hyperbolic tangent), since it was shown to be more stable in backpropagation compared to sigmoid function.[65] Since our initial goal was to mask unimportant parts of the image, and *tanh* is a function bound between –1 and 1, we used *tanh* + 1, such that regions where the *Unet* output was very negative were close to 0 and subsequently masked when multiplied by the PET signal intensity. The use of batch normalisation layers in the downstream *Resnet10* in mRN10 ensures stable training even when masked PET is the input, which is not explicitly normalized apriori. The masking *Unet* was trained end-to-end along with *Resnet10* in the mRN10 architecture for optimal performance of the classification task. This was an attempt to explain the classification decision of the classifier by allowing it to optimize for masking of unimportant parts of the image as well as increase the performance by improving the conditioning of the input data to the classifier.[46]

Classification results

One of the goals of the study was to compare the model's performance to nuclear medicine experts. The task of detecting and localizing HPTT on FCH-PET is relatively "trivial" for human experts, with reported accuracies of up to 98%.[3-13] We therefore feel that a small dataset is sufficient for training a model to similar performance. However, the results differed from our expectations, as the achieved performance was significantly below the one of humans for both of our tasks. It is most likely that by increasing the dataset to several hundred subjects, the performance gap would be closed.

Given the size of our dataset, our results are comparable to other published studies on other medical imaging related tasks. The study with a similarly sized dataset (85 subjects) in the classification of cardiac sarcoidosis by Togo *et al*. achieved sensitivity and specificity of 84% and 87%.[66] In line with the established best practice, Lu *et al*. explored the diagnosis of Alzheimer disease from PET and MRI images using a multimodal approach on a dataset of 397 subjects and achieved 93% accuracy at detecting Alzheimer disease; Ma *et al*. used a DL method to classify thyroid diseases from SPECT with a dataset of more than 2000 subjects and achieved accuracy of up to 100% for some tasks.[67,68] Because the aforementioned tasks are different and generally have different difficulty compared to ours, these comparisons and potential conclusions are hypothetical, but they give us a rough estimate of the number of subjects needed to substantially improve the performance of our model.

We feel that by increasing the size of our dataset to several hundred patients, similar levels of performance metrics to human performance could most likely be achieved. One supporting data point for this assumption is that the upper-bound of the 95% CI of AUC in the population statistics of 50 model iterations used in experiments was 0.998. Given the right data split, the model could perfectly classify the test set.

PET mask discussion

Qualitatively, we observed interesting properties of the mask created using the *UNet*, with examples depicted in Figures 2 and 3. In Figure 2 row a), we can see that the physiological signal from the salivary glands was masked, and the weak signal of the paravertebral musculature is amplified. In row b), the physiological signal from the red marrow in the vertebral body was masked and signal from the neck musculature on the left was enhanced. In row c), the physiological signal from the thyroid gland and paravertebral musculature were masked, contradicting findings in row a). The model likely learns to amplify the weak signal from the musculature with low uptake of FCH and to suppress strong signal from salivary glands and certain muscle groups with high uptake.

The physiologically high PET activity in salivary glands and the thyroid were correctly masked. This is likely because there is usually high PET activity in these regions. The masking of the thyroid region is especially problematic since the signal from HPTT can also be masked along with the thyroid. This resulted in HPTT being masked in all but 3 cases, as shown in Figure 3. Still, this did not always result in a false classification of the HPTT location. The parathyroid adenoma in row c) is crucial to the task for experts and yet it was masked in this case by the network. Even though the model masked the adenoma, the mRN10 model output in this case was still correct (lower right adenoma location). It is likely that *UNet* learns to encode the information of adenoma into the mask that is passed to the *Resnet10*.

Regions near the skin and the skin itself were always enhanced – we assumed that this was an important signal to the model, as skin-air interface exhibits high contrast on PET and CT and acts as a rough anatomical landmark. It is also much higher in contrast than soft tissue interfaces of the structures in the parathyroid region and produces stronger gradients in training. The region outside the patient (air) was not masked to 0, but to approximately 25% of the signal (value of mask was 0.25), since it is irrelevant to the classification and likely does not produce a gradient in training, so the *Unet* output for this region is closer to the initialization state.

We find the obtained masks to be interpretable in terms of optimizing downstream *Resnet10*, yet they did not enhance HPTT signal on masked PET as could be expected. Highly active PET regions were therefore always masked (thyroid, salivary glands). The regions which produced high PET activity only in some subjects (musculature) were masked only if they produced high PET activity (Figure 2, row c), if not, these regions were enhanced (Figure 2 row a), introducing noise to masked PET. This further makes the masked PET uninterpretable as the intensity of the introduced noise is higher than the masked signal from the parathyroid adenoma, which can itself be masked. However, in terms of optimizing the *Resnet10* classification performance, these findings make sense, since the mechanism acts to adaptively scale the inputs to stabilize *Resnet10* classifier.

While the proposed mRN10 model, using *Unet* and *Resnet* sequentially for region-of-interest identification and classification tasks, respectively, somewhat resembles the state-of-the-art region proposal algorithms, we have not found such a model presented in existing literature. Firstly, it is unlikely that such architecture would achieve superior performance on other tasks as *Resnet* is a good classifier on its own if it is trained on a large enough database.[20,41] Secondly, the masking results we achieved did not appear to consistently add

value to FCH-PET interpretation when explored by humans, however, according to our results, the mask can be clearly interpreted in terms of optimizing downstream *Resnet10* performance.

Namely, we found the mRN10 to be superior in performance to the RN10 in CLoc task. This is probably due to the improved conditioning of the masked input to *Resnet10* in mRN10, leading to increased stability, which in turn increases the performance of the trained model.[46]

Limitations of the study

In the model selection, we found that the model with lowest number of parameters performed the best. This is one limitation of our study since experiments with even simpler models were not carried out. Another potential performance improvement could be using transfer learning, but we have not found suitable pretrained models for the FCH-PET images.

Our PET masking was an attempt to make the model more interpretable. Most notable similar mechanisms that exist within literature are the attention mechanisms.[69] The main problem with most attention mechanisms is that they rely on weighing of the image features, which are obtained by embedding a small image patch into a vector. Because of this, the spatial resolution of the attention map is limited by the size of the image patch, which is commonly 16 × 16 in visual transformers.[70] In analogy, if we used 16 × 16 × 16 for our theoretical attention, the feature map of our entire image would be of spatial dimensions 4 × 4 × 2, which is too low detailed enough interpretation. Another method of explaining the model output is the class activation mapping (CAM), which also relies on feature embeddings before fully connected layers and therefore entails a loss of spatial resolution;[71] in case of the RN10, the CAM resolution would be 4 × 4 × 2. Gradient-based attribution methods, which do provide pixel-level (or in our case voxel-level) input attribution to the model output, have received criticism due to their inconsistency and poor theoretical foundations.[72]

Conclusions

We provide extensive experiments in deep learning analysis of FCH-PET using standard classification model RN10 and a novel architecture tailored to the task. As deep learning for FCH-PET analysis in PHPT has to our knowledge not yet been described in literature, our experiments provide a baseline for future work. Even though inferior performance to human experts was achieved, the results seem very promising considering the small dataset and the achieved accuracy of 83% for detecting HPTT and 74% accuracy for localizing the quadrant of HPTT.

References

1. Fraser WD. Hyperparathyroidism. *Lancet* 2009; **374:** 145-58. doi: 10.1016/s0140-6736(09)60507-9
2. Grimelius L, Akerström G, Johansson H, Bergström R. Anatomy and histopathology of human parathyroid glands. *Pathol Annu* 1981; **16(Pt 2)**: 1-24. PMID: 7036057
3. Cuderman A, Senica K, Rep S, Hocevar M, Kocjan T, Sever, et al. 18F-Fluorocholine PET/CT in primary hyperparathyroidism: superior diagnostic performance to conventional scintigraphic imaging for localization of hyperfunctioning parathyroid glands. *J Nucl Med* 2019; **61:** 577-83. doi: 10.2967/jnumed.119.229914
4. Lezaic L, Rep S, Sever MJ, Kocjan T, Hocevar M, Fettich J. 18F-Fluorocholine PET/CT for localization of hyperfunctioning parathyroid tissue in primary hyperparathyroidism: a pilot study. *Eur J Nucl Med Mol Imaging* 2014; **41:** 2083-9. doi: 10.1007/s00259-014-2837-0
5. Graves CE, Hope TA, Kim J, Pampaloni MH, Kluijfhout W, Seib CD, et al. Superior sensitivity of 18F-fluorocholine: PET localization in primary hyperparathyroidism. *Surgery* 2022; **171:** 47-54. doi: 10.1016/j.surg.2021.05.056
6. Michaud L, Balogova S, Burgess A, Ohnona J, Huchet V, Kerrou K, et al. A pilot comparison of 18F-fluorocholine PET/CT, ultrasonography and 123I/99mTc-sestaMIBI dual-phase dual-isotope scintigraphy in the preoperative localization of hyperfunctioning parathyroid glands in primary or secondary hyperparathyroidism. *Medicine* 2015; **94:** e1701. doi: 10.1097/md.0000000000001701
7. Kluijfhout WP, Vorselaars WM, van den Berk SA, Vriens MR, Borel Rinkes IH, Valk GD, et al. Fluorine-18 fluorocholine PET-CT localizes hyperparathyroidism in patients with inconclusive conventional imaging. *Nucl Med Commun* 2016; **37:** 1246-52. doi: 10.1097/mnm.0000000000000595
8. Kluijfhout WP, Pasternak JD, Drake FT, Beninato T, Gosnell JE, Shen WT, et al. Use of PET tracers for parathyroid localization: a systematic review and meta-analysis. *Langenbecks Arch Surg* 2016; **401:** 925-35. doi: 10.1007/s00423-016-1425-0
9. Thanseer N, Bhadada SK, Sood A, Mittal BR, Behera A, Gorla A K R, et al. Comparative effectiveness of ultrasonography, 99mTc-sestamibi, and 18F-fluorocholine PET/CT in detecting parathyroid adenomas in patients with primary hyperparathyroidism. *Clin Nucl Med* 2017; **42:** e491-7. doi: 10.1097/rlu.0000000000001845
10. Whitman J, Allen IE, Bergsland EK, Suh I, Hope TA. Assessment and comparison of 18F-Fluorocholine PET and 99mTc-sestamibi scans in identifying parathyroid adenomas: a metaanalysis. *J Nucl Med* 2021; **62:** 1285-91. doi: 10.2967/jnumed.120.257303
11. Beheshti M, Hehenwarter L, Paymani Z, Rendl G, Imamovic L, Rettenbacher R, et al. 18F-Fluorocholine PET/CT in the assessment of primary hyperparathyroidism compared with 99mTc-MIBI or 99mTc-tetrofosmin SPECT/CT: a prospective dual-centre study in 100 patients. *Eur J Nucl Med Mol Imaging* 2018; **45:** 1762-71. doi: 10.1007/s00259-018-3980-9
12. Broos WAM, Wondergem M, Knol RJJ, Van der Zant FM. Parathyroid imaging with 18F-fluorocholine PET/CT as a first-line imaging modality in primary hyperparathyroidism: a retrospective cohort study. *EJNMMI Res* 2019; **9:** 72. doi: 10.1186/s13550-019-0544-3
13. Hope TA, Graves CE, Calais J, Ehman EC, Johnson GB, Thompson D, et al. Accuracy of 18 F-fluorocholine PET for the detection of parathyroid adenomas: prospective single-center study. *J Nucl Med* 2021; **62:** 1511-6. doi: /10.2967/jnumed.120.256735

14. Rep S, Hocevar M, Vaupotic J, Zdesar U, Zaletel K, Lezaic L. ^{18}F-choline PET/CT for parathyroid scintigraphy: significantly lower radiation exposure of patients in comparison to conventional nuclear medicine imaging approaches. *J Radiol Prot* 2018; **38:** 343-56. doi: 10.1088/1361-6498/aaa86f

15. Li Y, Sixou B, Peyrin F. A review of the deep learning methods for medical images super resolution problems. *IRBM* 2021; **42:** 120-33. doi: 10.1016/j.irbm.2020.08.004

16. Yang W, Zhang X, Tian Y, Wang W, Xue J-H, Liao Q. Deep learning for single image super-resolution: a brief review. *IEEE Trans Multimedia* 2019; **21:** 3106-21. doi: 10.1109/tmm.2019.2919431

17. Wang L, Chen W, Yang W, Bi F, Yu FR. A state-of-the-art review on image synthesis with generative adversarial networks. *IEEE Access* 2020; **8:** 63514-37. doi: 10.1109/access.2020.2982224

18. Liu B, Liu J. Overview of image denoising based on deep learning. *J Phys Conf Ser* 2019; **1176:** 022010. doi: 10.1088/1742-6596/1176/2/022010

19. Chartrand G, Cheng PM, Vorontsov E, Drozdzal M, Turcotte S, Pal CJ, et al. Deep learning: a primer for radiologists. *RadioGraphics* 2017; **37:** 2113-31. doi: 10.1148/rg.2017170077

20. Al-Saffar AAM, Tao H, Talab MA. Review of deep convolution neural network in image classification. In: *2017 International Conference on Radar, Antenna, Microwave, Electronics, and Telecommunication.* IEEE 2017. p. 26-31. doi: 10.1109/icramet.2017.8253139

21. Minaee S, Boykov Y, Porikli F, Plaza A, Kehtarnavaz N, Terzopoulos D. Image segmentation using deep learning: a survey. [Internet]. *arXiv:* 2001.05566 2020. Available from: https://doi.org/10.48550/arXiv.2001.05566

22. Jiao L, Zhang F, Liu F, Yang S, Li L, Feng Z, et al. A survey of deep learning-based object detection. [Internet]. *arXiv:* 2019. Available from: http://arxiv.org/abs/1907.09408

23. Sahlsten J, Jaskari J, Kivinen J, Turunen L, Jaanio E, Hietala K, et al. Deep learning fundus image analysis for diabetic retinopathy and macular edema grading. *Sci Rep* 2019; **9:** 10750. doi: 10.1038/s41598-019-47181-w

24. Esteva A, Kuprel B, Novoa RA, Ko J, Swetter SM, Blau HM, et al. S. Dermatologist-level classification of skin cancer with deep neural networks. *Nature* 2017; **542:** 115-8. doi: 10.1038/nature21056

25. Irvin J, Rajpurkar P, Ko M, Yu Y, Ciurea-Ilcus S, Chute C, et al. CheXpert: a large chest radiograph dataset with uncertainty labels and expert comparison. *Proc Conf AAAI Artif Intell* 2019; **33:** 590-7. doi: 10.1609/aaai.v33i01.3301590

26. Nie D, Cao X, Gao Y, Wang L, Shen D. Estimating CT image from MRI data using 3D fully convolutional networks. *Deep Learn Data Label Med Appl* 2016; **2016:** 170-8. doi: 10.1007/978-3-319-46976-8_18

27. Torrado-Carvajal A, Vera-Olmos J, Izquierdo-Garcia D, Catalano OA, Morales MA, Margolin J, et al. Dixon-VIBE Deep Learning (DIVIDE) pseudo-CT synthesis for pelvis PET/MR attenuation correction. *J Nucl Med* 2019; **60:** 429-35. doi: 10.2967/jnumed.118.209288

28. Guo R, Hu X, Song H, Xu P, Xu H, Rominger A, et al. Weakly supervised deep learning for determining the prognostic value of 18F-FDG PET/CT in extranodal natural killer/T cell lymphoma, nasal type. *Eur J Nucl Med Mol Imaging* 2021; **48:** 3151-61. doi: 10.1007/s00259-021-05232-3

29. Hwang D, Kang SK, Kim KY, Seo S, Paeng JC, Lee DS, et al. Generation of PET attenuation map for whole-body time-of-flight ^{18}F-FDG PET/MRI using a deep neural network trained with simultaneously reconstructed activity and attenuation maps. *J Nucl Med* 2019; **60:** 1183-9. doi: 10.2967/jnumed.118.219493

30. Liu F, Jang H, Kijowski R, Bradshaw T, McMillan AB. Deep learning MR imaging-based attenuation correction for PET/MR imaging. *Radiology* 2018; **286:** 676-84. doi: 10.1148/radiol.2017170700

31. Leynes AP, Yang J, Wiesinger F, Kaushik SS, Shanbhag DD, Seo Y, et al. Zero-Echo-Time and Dixon Deep Pseudo-CT (ZeDD CT): direct generation of pseudo-CT images for pelvic PET/MRI attenuation correction using deep convolutional neural networks with multiparametric MRI. *J Nucl Med* 2018; **59:** 852-8. doi: 10.2967/jnumed.117.198051

32. Blanc-Durand P, Van Der Gucht A, Schaefer N, Itti E, Prior JO. Automatic lesion detection and segmentation of 18F-FET PET in gliomas: a full 3D U-Net convolutional neural network study. *PLoS One* 2018; **13:** e0195798 doi: 10.1371/journal.pone.0195798

33. Zhao X, Li L, Lu W, Tan S. Tumor co-segmentation in PET/CT using multi-modality fully convolutional neural network. *Phys Med Biol* 2018; **64:** 015011 doi: 10.1088/1361-6560/aaf44b

34. Zhong Z, Kim Y, Plichta K, Allen BG, Zhou L, Buatti J, et al. Simultaneous cosegmentation of tumors in PET-CT images using deep fully convolutional networks. *Med Phys* 2019; **46(2):** 619-33. doi: 10.1002/mp.13331

35. Schwyzer M, Ferraro DA, Muehlematter UJ, Curioni-Fontecedro A, Huellner MW, von Schulthess GK, et al. Automated detection of lung cancer at ultralow dose PET/CT by deep neural networks – initial results. *Lung Cancer* 2018; **126:** 170-3. doi: 10.1016/j.lungcan.2018.11.001

36. Hatt M, Laurent B, Ouahabi A, Fayad H, Tan S, Li L, et al. The first MICCAI challenge on PET tumor segmentation. *Med Image Anal* 2018; **44:** 177-95. doi: 10.1016/j.media.2017.12.007

37. Student. The probable error of a mean. *Biometrika* 1908; **6:** 1. doi: 10.2307/2331554

38. Pearson K. X. On the criterion that a given system of deviations from the probable in the case of a correlated system of variables is such that it can be reasonably supposed to have arisen from random sampling. *Lond Edinb Dublin Philos Mag J Sci* 1900; **50:** 157-75. doi: 10.1080/14786440009463897

39. Jones E, Oliphant T, Peterson P, Others. SciPy.org. *SciPy Open source Sci. tools Python2*. 2001.

40. Good IJ. Rational decisions. *J R Stat Soc Ser B* 1952; **14:** 107-14. doi: 10.1111/j.2517-6161.1952.tb00104.x

41. He K, Zhang X, Ren S, Sun J. Deep residual learning for image recognition. *2016 IEEE Conference on Computer Vision and Pattern Recognition (CVPR)* 2016. doi: 10.1109/cvpr.2016.90

42. Hara K, Kataoka H, Satoh Y. Learning spatio-temporal features with 3D residual networks for action recognition. *2017 IEEE International Conference on Computer Vision Workshops (ICCVW)* 2017. doi: 10.1109/iccvw.2017.373

43. Huang G, Liu Z, Van Der Maaten L, Weinberger KQ. Densely connected convolutional networks. *2017 IEEE Conference on Computer Vision and Pattern Recognition (CVPR)* 2017. doi: 10.1109/cvpr.2017.243

44. Zagoruyko S, Komodakis N. Wide residual networks. *Procedings of the British Machine Vision Conference 2016;* 2016. doi: 10.5244/c.30.87

45. He K, Zhang X, Ren S, Sun J. Identity mappings in deep residual networks. *Computer Vision – ECCV 2016.* **2016:** 630-45. doi: 10.1007/978-3-319-46493-0_38

46. Full stack deep learning. Lecture 1: DL fundamentals [Internet]. Fullstackdeeplearning.com. [cited 2022 Aug 28]. Available from: https://fullstackdeeplearning.com/spring2021/lecture-1/

47. Ronneberger O, Fischer P, Brox T. U-Net: convolutional networks for biomedical image segmentation. In: Navab N, Hornegger J, Wells W, Frangi A. editors. *Medical Image Computing and Computer-Assisted Intervention – MICCAI 2015. MICCAI 2015. Lecture Notes in Computer Science* 2015; **9351:** 234-41. Cham: Springer.doi: 10.1007/978-3-319-24574-4_28

48. Rossum G Van, Drake FL. Python Tutorial, Technical Report CS-R9526. *Cent voor Wiskd en Inform* 1995.

49. Paszke A, Gross S, Chintala S, Chanan G, Yang E, DeVito Z, et al.. Automatic differentiation in PyTorch. *31st Conf Neural Inf Process Syst* 2017.

50. Stevenson M, Sergeant E, Nunes T, Heuer C, Marshall J, Sanchez J, et al. *epiR: Tools for the analysis of epidemiological data.* v1.0-15. 2020. [cited 2022 Mar 15]. Available at: https://CRAN.R-project.org/package=epiR

51. R Development Core Team. *R: a language and environment for statistical computing*. Vienna; R Foundation for Statistical Computing. Available at: . http://www.R-project.org

52. McNemar Q. Note on the sampling error of the difference between correlated proportions or percentages. *Psychometrika* 1947; **12:** 153-7. doi: 10.1007/bf02295996

53. Stock C, Hielscher T. DTComPair: comparison of binary diagnostic tests in a paired study design. R package version 1.0.3. [Internet]. 2014. Available from: http://cran.r-project.org/package=DTComPair

54. Rao SD. Epidemiology of parathyroid disorders. *Best Pract Res Clin Endocrinol Metab* 2018; **32:** 773-80. doi: 10.1016/j.beem.2018.12.003

55. Somnay YR, Craven M, McCoy KL, Carty SE, Wang TS, Greenberg CC, et al. Improving diagnostic recognition of primary hyperparathyroidism with machine learning. *Surgery* 2017;**161:** 1113-21. doi: 10.1016/j.surg.2016.09.044

56. Press DM, Siperstein AE, Berber E, Shin JJ, Metzger R, Monteiro R, et al. The prevalence of undiagnosed and unrecognized primary hyperparathyroidism: a population-based analysis from the electronic medical record. *Surgery* 2013; **154:** 1232-8. doi: 10.1016/j.surg.2013.06.051

57. Bilezikian JP, Marcus R, Levine MA, Marcocci C, Silverberg SJ, Potts JT, editors. *Parathyroids: basic and clinical concepts*. 3rd edition. 2014. Elsevier, Academic Press.

58. Marzouki HZ, Chavannes M, Tamilia M, Hier MP, Black MJ, Levental M, et al. Location of parathyroid adenomas: 7-year experience. *J Otolaryngol Head Neck Surg* 2010; **39:** 551-4. PMID: 20828518

59. Filser B, Uslar V, Weyhe D, Tabriz N. Predictors of adenoma size and location in primary hyperparathyroidism. *Langenbeck's Arch Surg* 2021; **406:** 1607. doi: 10.1007/s00423-021-02179-9

60. Shah VN, Bhadada SK, Bhansali A, Behera A, Mittal BR. Changes in clinical & biochemical presentations of primary hyperparathyroidism in India over a period of 20 years. *Indian J Med Res* 2014; **139:** 694-9. PMID: 25027078

61. Xie S, Girshick R, Dollár P, Tu Z, He K. Aggregated residual transformations for deep neural networks. *Proc - 30th IEEE Conf Comput Vis Pattern Recognition, CVPR 2017* 2017. doi: 10.1109/cvpr.2017.634

62. Gao S, Cheng MM, Zhao K, Zhang XY, Yang MH, Torr PHS. Res2Net: a new multi-scale backbone architecture. *IEEE Trans Pattern Anal Mach Intell* 2019. doi: 10.1109/TPAMI.2019.2938758

63. Chen S, Tan X, Wang B, Hu X. Reverse attention for salient object detection. *Computer Vision – ECCV 2018* 2018; 236-52. doi: 10.1007/978-3-030-01240-3_15

64. Bailly A, Blanc C, Francis É, Guillotin T, Jamal F, Wakim B, et al. Effects of dataset size and interactions on the prediction performance of logistic regression and deep learning models. *Comput Methods Programs Biomed* 2022; **213:** 106504 doi: 10.1016/j.cmpb.2021.106504

65. Hochreiter S, Schmidhuber J. Long Short-Term Memory. *Neural Comput* 1997; **9:** 1735-80. doi: 10.1162/neco.1997.9.8.1735

66. Togo R, Hirata K, Manabe O, Ohira H, Tsujino I, Magota K, et al. Cardiac sarcoidosis classification with deep convolutional neural network-based features using polar maps. *Comput Biol Med* 2019; **104:** 81-6. doi: 10.1016/j.compbiomed.2018.11.008

67. Lu D, Popuri K, Ding GW, Balachandar R, Beg MF. Multiscale deep neural network based analysis of FDG-PET images for the early diagnosis of Alzheimer's disease. *Med Image Anal* 2018; **46:** 26-34. doi: 10.1016/j.media.2018.02.002

68. Ma L, Ma C, Liu Y, Wang X. Thyroid diagnosis from SPECT images using convolutional neural network with optimization. *Comput Intell Neurosci* 2019; **2019:** 6212759. doi: 10.1155/2019/6212759

69. Niu Z, Zhong G, Yu H. A review on the attention mechanism of deep learning. *Neurocomputing* 2021; **452:** 48-62. doi: 10.1016/j.neucom.2021.03.091

70. Liu Y, Zhang Y, Wang Y, Hou F, Yuan J, Tian J, et al. A survey of visual transformers. *arXiv* [csCV] [Internet]. 2021 [cited 2022 Aug 28]; Available from: http://arxiv.org/abs/2111.06091

71. Zhou B, Khosla A, Lapedriza A, Oliva A, Torralba A. Learning deep features for discriminative localization. *arXiv* [csCV] [Internet]. 2015 [cited 2022 Aug 28]; Available from: http://arxiv.org/abs/1512.04150

72. Ancona M, Ceolini E, Öztireli C, Gross M. Towards better understanding of gradient-based attribution methods for deep neural networks. *arXiv* [csLG] [Internet]. 2017 [cited 2022 Aug 28]; Available from: http://arxiv.org/abs/1711.06104

research article

FDG PET-CT as an important diagnostic tool and prognostic marker in suspected recurrent cervical carcinoma after radiotherapy: comparison with MRI

Milica Stojiljkovic[1,2], Dragana Sobic Saranovic[1,2], Strahinja Odalovic[1,2], Marina Popovic[3], Jelena Petrovic[1,2], Nevena Rankovic[1], Milos Veljkovic[1], Vera Artiko[1,2]

[1] Center for Nuclear Medicine with PET, University Clinical Center of Serbia, Belgrade, Serbia
[2] Faculty of Medicine, University of Belgrade, Belgrade, Serbia
[3] Institute of Oncology and Radiology of Serbia, Belgrade, Serbia

Radiol Oncol 2022; 56(4): 453-460.

Received 18 April 2022
Accepted 15 September 2022

Correspondence to: Milica Stojiljkovic, M.D., Ph.D., Center for Nuclear Medicine with PET, University Clinical Center of Serbia, Bul. Arsenija Čarnojevića 124/III/5, 11000 Beograd, Serbia. E-mail: milica_stoji@yahoo.com

Disclosure: No potential conflicts of interest were disclosed.

Background. Recurrent disease in post-irradiation patients with cervical cancer is often difficult to delineate on magnetic resonance imaging (MRI), because posttreatment changes can have a similar appearance, and further evaluation is often required. The aims of the study were to evaluate positron emission tomography/computed tomography with 18F-fluorodeoxyglucose (FDG PET-CT) diagnostic role in suspected recurrent cervical cancer after radiotherapy, compare it to MRI, and assess their prognostic impact in these patients.

Patients and methods. This cohort retrospective study included patients previously treated with radiotherapy for carcinoma of uterine cervix with suspected recurrence, who had undergone MRI of abdomen and pelvis, and were subsequently evaluated on FDG PET-CT, with minimum follow-up period of 12 months.

Results. In the total of 84 patients included in analysis, MRI *vs.* FDG PET-CT showed sensitivity, specificity and accuracy of 80.1%, 52.4% and 66.7%, *vs.* 97.6%, 61.9% and 79.8%, respectively. Patients with positive findings on MRI (Log Rank, $p = 0.003$) and PET-CT (Log Rank, $p < 0.001$) had shorter progression-free survival (PFS) than those with negative results. In univariate Cox regression models, MRI and FDG PET-CT results were found to be related to PFS ($p = 0.005$ and $p < 0.001$, respectively). However, multivariate analysis proved only FDG PET-CT to be independent prognostic factor, where patients with positive FDG PET-CT results had almost nine times higher risk of progression ($p < 0.001$).

Conclusion. FDG PET-CT represents useful diagnostic tool in suspected recurrent cervical cancer after radiotherapy, showing high sensitivity in its detection. In addition, it is an independent factor in predicting progression-free survival in these patients.

Key words: uterine cervical neoplasms; recurrence; PET-CT; MRI; progression-free survival; sensitivity and specificity

Introduction

Cervical cancer is the fourth most frequently diagnosed cancer and the fourth leading cause of cancer-related death in women.[1] In low-and middle-income countries, it is even more common, being the second most common cancer among women and the third most common in terms of mortality.[2]

Recurrent disease is defined as tumor re-appearance or development of metastatic disease more than six months after the end of treatment. The recurrence rates of International Federation of Gynecology and Obstetrics (FIGO) stage IB–IIA and IIB–IVA cervical cancer are 11% to 22% and 28% to 64%.[3] Treatment options in recurrent cervical cancer are limited. Patients with local

recurrence may be candidates for radical retreatment, with disease free survival rates reaching up to 40%.[4] However, more widespread disease can only be subjected to systemic chemotherapy with minimal chances of success or supportive care. Therefore, improved survival and outcomes require early detection of recurrence and precise localization of the disease spread.[5]

Magnetic resonance imaging (MRI) plays a significant role not only in guiding the primary treatment in women diagnosed with cervical cancer, but also in treatment response assessment and surveillance. However, recurrent disease in post-irradiation patients is often difficult to delineate, because posttreatment changes can have a similar appearance, and further evaluation is often required.[6]

Positron emission tomography/computed tomography with ^{18}F-fluorodeoxyglucose (FDG PET-CT) provides functional data about the glucose metabolism of the tumor, nodes, and metastases, in addition to morphological data from CT which are used for topographical localization and attenuation correction. One of the most important advantages of FDG PET-CT is its whole-body evaluation, *i.e.* the ability to detect disseminated disease along with locoregional status, compared to standard MRI. FDG PET-CT has an important role in cases of suspected recurrence where MRI or CT are equivocal, as suggested by the Royal College of Radiologists guidelines and in cases of local vaginal recurrence seen on CT or MRI as per the Cancer Care Ontario guidelines.[5] However, Updated National Comprehensive Cancer Network (NCCN) guidelines Version 1.2021, state FDG PET-CT as the preferred modality for surveillance imaging in stage II–IV disease and in suspected recurrence or metastasis.

The prognosis of cervical cancer is influenced by the disease stage, tumor grade and histological subtype, patient age, intratumoral oxygenation, tumor vascularity, DNA ploidy, and the presence of HPV infection.[7] Patients with higher FIGO stage, over 50 years old, with adenocarcinoma compared to those with epidermoid carcinoma, as well as with high, compared to low and intermediate-grade tumors, tend to have worse prognosis.[8,9] Pretreatment MRI and FDG PET-CT were also shown to have prognostic role in cervical cancer patients. Maximal standardized uptake value (SUVmax), lymph node status and volume-based FDG PET-CT parameters such as metabolic tumor volume (MTV) and total lesion glycolysis (TLG), as well as the mean apparent diffusion coefficient (ADC) on MRI have been shown to be of prognostic value in a number of studies.[10-15]

With increasing data available on imaging in various malignancies, there is no doubt that the information provided by FDG PET-CT is invaluable in guiding patient' management. However, data on FDG PET-CT imaging in gynecological malignancies are limited and more studies are needed to establish its utility especially in cancer of uterine cervix.[7] Therefore, the aims of this research were to evaluate diagnostic performances of FDG PET-CT in suspected recurrent cervical cancer after radiation therapy, and its prognostic impact in these patients, with comparison to MRI, clinical and histopathological factors.

Patients and methods

Study population

This retrospective cohort study included all consecutive patients previously treated with radiation for carcinoma of the uterine cervix (with or without surgery and chemotherapy), who underwent PET-CT examination for suspected recurrent disease from January 2014 until December 2019, and who fulfilled certain criteria. Indications for FDG PET-CT were: symptoms suspecting recurrence, new lesions on surveillance imaging studies, or abnormal results on physical or cytologic examination on routine surveillance. Inclusion criteria were: (1) histopathological confirmation of cervical cancer; (2) previous treatment by the standard therapeutic option which included radiation treatment, and was completed at least six months prior to PET-CT examination; (3) available data regarding initial disease stage and tumor histopathology; (4) MRI of the pelvis and abdomen within three months of FDG PET-CT examination; (5) follow-up for at least one year after FDG PET-CT. Exclusion criteria were previous histopathological confirmation of another malignant tumor, and unavailability of obtaining all necessary clinical and follow-up data. Data regarding initial disease stage and tumor histological type and grade were acquired from patients' medical documentation. Initial clinical staging was performed according to the FIGO 2009 classification system for cancer of uterine cervix. WHO criteria from 2004 were used in defining histopathological type, and tumor grade was determined according to the modified Broder's system or architectural and cytological criteria.[16,17] The study was approved by the Institutional Ethics Committee (approval No.

668/6) and written consent was obtained from all patients.

FDG PET-CT imaging

PET-CT examination was performed on hybrid PET-CT scanner Biograph True64 (Siemens Medical Solutions USA Inc, Malvern, PA, USA). Patients were given an average dose of 5.5 MBq/kg body weight ^{18}F-FDG intravenously, after starving period of at least 6 hours, and with blood glucose level below 11 mmol/l. After resting period (60–90 minutes following FDG administration), patients underwent low-dose CT (120 kV, 40 mAs, slice thickness 5 mm, pitch 1.5, rotation time 0.5 sec) without contrast, for topographic localization and attenuation correction. That was followed by PET acquisition (standard whole-body procedure) of region from the base of scull to the mid-thighs (3 minutes per bed, 6–7 beds per examinee) in three-dimensional mode. Obtained PET-CT data were interpreted on Syngo Multimodality Workplace VE31A (Syngo 2008B, Siemens, Medical systems, Erlangen, Germany). Any lesion with high ^{18}F-FDG uptake on PET-CT was defined as positive for recurrent disease if any abnormal ^{18}F-FDG uptake was observed after exclusion of benign and physiological lesions, with or without clearly visible corresponding CT malformation. Lesions were analyzed qualitatively and semi-quantitatively. For assessment of glucose metabolism level in active disease sites, SUVmax was used, that is singular voxel within volume of interest with maximal standard uptake value, calculated as follows: activity in tissue (count/pixel/s) multiplied by calibration factor and divided by dose applied (MBq/kg of body weight). Tumor lesions were defined by volume of interest (VOI) placed around every suspected focus of increased FDG uptake, with 50% threshold. The measurements of SUVmax were done on reconstructed images, after using ordered subsets expectation maximization as statistical reconstruction method, but no absolute cut-off value of SUVmax was used for

TABLE 1. Patients' characteristics

Characteristic	Value
Age *(years)*	
Mean ± sd	53 ± 11
Initial FIGO disease stage, *n (%)*	
IB	9 (11%)
IIA	2 (2%)
IIB	38 (45%)
III	26 (31%)
IV	9 (11%)
Tumor histological type, *n (%)*	
Squamous cell	70 (83%)
Adenocarcinoma	11 (14%)
Adenosquamous	2 (2%)
Small cell	1 (1%)
Tumor grade, *n (%)*	
Low grade	6 (7%)
Intermediate grade	50 (60%)
High grade	10 (12%)
Unknown	18 (21%)
Previous treatment, *n (%)*	
Surgery with (chemo)radiotherapy	11 (13%)
Radiotherapy only	10 (12%)
Radiotherapy with concurrent chemotherapy	49 (58%)
Primary (chemo)radiation with salvage hysterectomy	14 (17%)
MRI findings, *n (%)*	
Positive	54 (64%)
Negative	30 (36%)
PET-CT findings, *n (%)*	
Positive	57 (68%)
Negative	27 (32%)

MRI = magnetic resonance imaging; PET-CT = positron emission tomography/computed tomography

TABLE 2. Diagnostic performance of MRI and PET-CT

	TP(n)	TN(n)	FP(n)	FN(n)	Sensitivity (%)	Specificity (%)	Accuracy (%)
MRI	34	22	20	8	80.1%	52.4%	66.7%
PET-CT	41	26	16	1	97.6%	61.9%	79.8%

FN = false negative; FP = false positive; MRI = magnetic resonance imaging; PET-CT = positron emission tomography/computed tomography; TN = true negative; TP = true positive

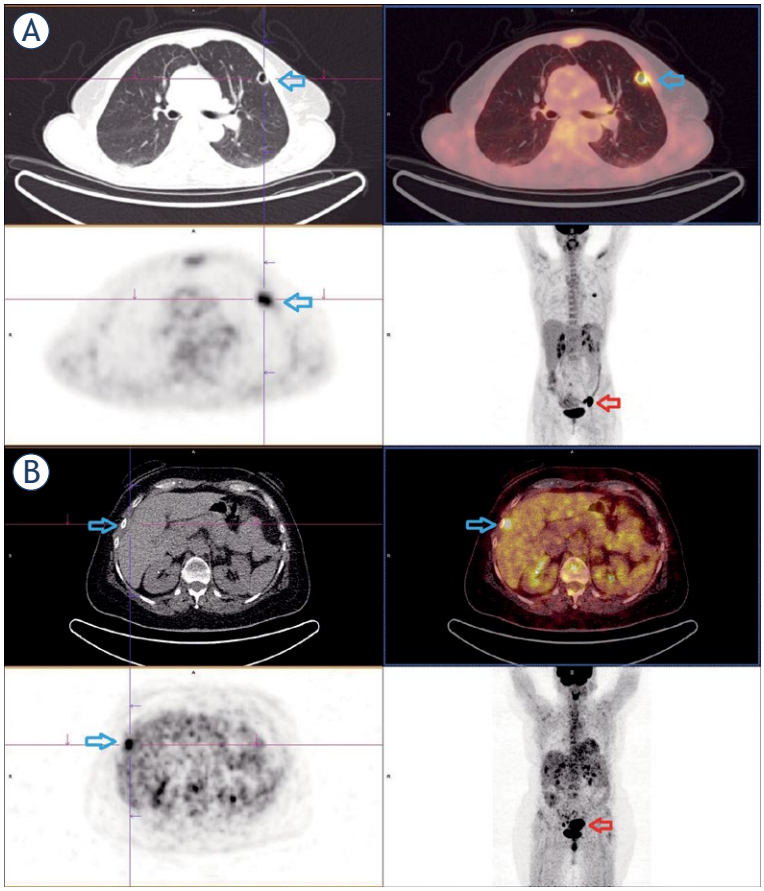

FIGURE 1. (A) A 51-year-old patient, with squamocellular carcinoma, presenting on FDG PET/CT with metastasis in left upper lung (blue arrow), and left iliac lymphadenopathy (red arrow). On MRI only left iliac disease was detected. **(B)** A 59-year-old patient, with adenocarcinoma, presenting on FDG PET/CT with active locoregional disease in pelvis (red arrow) also seen on MRI, and peritoneal deposit in front of the right liver lobe (blue arrow) which was missed by MRI.

the diagnosis. Images were interpreted separately by two nuclear medicine physicians, unaware of results of other imaging modalities. In cases of discrepancy, images were presented to multidisciplinary team and experts' opinion was adopted. Findings were classified as positive or negative for recurrent disease, and positive findings were further categorized as locoregional recurrence only, or distant spread of disease (with or without locoregional disease).

MR imaging

FDG PET-CT findings were compared to written reports of MR imaging. T1 weighted, T2 weighted, diffusion-weighted images (DWI), as well as contrast enhanced images of abdomen and pelvis were acquired in all patients. All findings were classified as positive or negative, based on standard evaluation criteria by visual characteristics.

Final diagnosis of recurrent disease, which was used as a gold standard in calculating diagnostic accuracy parameters for MRI and PET-CT, was made by either histopathological examination or clinical and imaging follow-up within the first six months after PET-CT.

Follow-up

Follow-up data were obtained from medical records, surveillance was done clinically, with imaging (CT and/or MRI and/or FDG PET-CT) performed once a year, with maximum follow-up period up to 5 years. Progression was defined as occurrence of cancer related death, new lesions seen on follow-up imaging, or progression in size and/or metabolic activity of existing lesions. Progression-free survival (PFS) was calculated from the day of FDG PET-CT examination until detected disease progression, or the end of follow-up period if no progression was detected. Median follow-up duration time was 18 months.

Statistical analysis

All statistical analyses were performed with IBM SPSS Statistics for Windows, Version 25.0. (IBM Corp, Armonk, NY, USA). Kaplan-Meier survival curves and Log Rank tests were used to analyze the survival data in patients with positive/negative MRI, positive/negative PET-CT findings, and with negative/only locoregional disease/distant disease present on FDG PET-CT. Univariate and multivariate Cox regression analyses were fitted to estimate the impact of patients' age, initial tumor stage (stages IB and IIA *vs.* stages IIB, III and IV), histological type (squamocellular *vs.* other), tumor grade (grades 1 and 2 *vs.* grade 3), MRI results (positive *vs.* negative) and FDG PET-CT results (positive *vs.* negative). Calculated p value < 0.05 was considered statistically significant. Sensitivity, specificity and accuracy for MRI and PET-CT were calculated on a patient-based level.

Results

A total of 84 patients were included in the analysis, with mean age 53 ± 11 years. The majority of patients were presented with locally advanced disease on initial diagnosis, where stage IIB or higher was diagnosed in 73 patients (87%), while the minority was diagnosed with early disease (*i.e.* stage IB or IIA). Most common histological tumor type

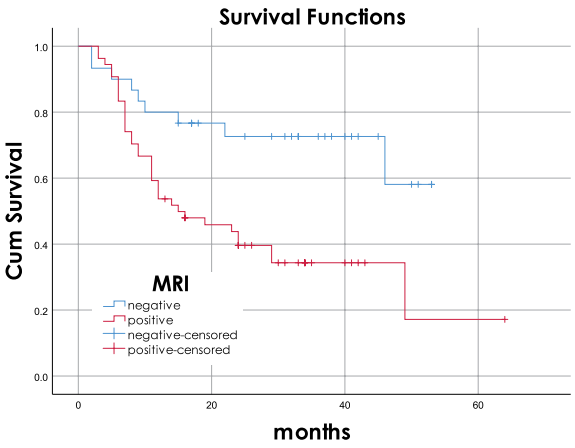

FIGURE 2. Kaplan-Meier survival curves showing progression free survival for patients with positive and negative magnetic resonance imaging; Log Rank, p = 0.003.

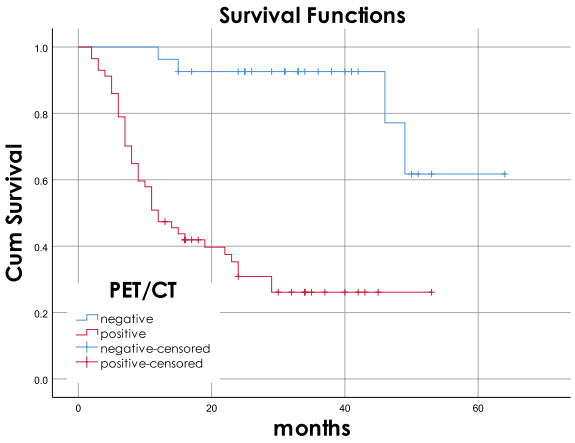

FIGURE 3. Kaplan-Meier survival curves showing progression free survival for patients with positive and negative fluorodeoxyglucose positron emission tomography/computed tomography; Log Rank, p < 0.001.

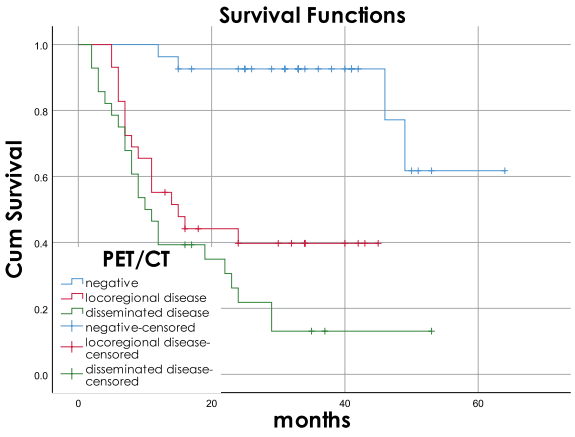

FIGURE 4. Kaplan-Meier survival curves showing progression free survival for patients with normal findings on fluorodeoxyglucose positron emission tomography/computed tomography, locoregional recurrence, and presence of disseminated disease (with or without locoregional disease); Log Rank, p < 0.001.

TABLE 3. Univariate Cox regression analysis of possible progression-free survival predictors in suspected recurrent cervical cancer (n = 84)

Predictor	HR (95% confidence interval)	p value
Age	1.013 (0.987–1.040)	0.336
Initial stage (IB/IIA vs. IIB/III/IV)	2.024 (0.753–5.962)	0.155
Histological type (squamocellular vs. other)	1.245 (0.597–2.598)	0.558
Histological grade (1/2 vs. 3)*	0.831 (0.448–1.905)	0.831
MRI (positive vs. negative)	2.873 (1.370–6.027)	0.005†
PET-CT (positive vs. negative)	9.491 (3.302–27.274)	< 0.001†

HR = hazard ratio; MRI = magnetic resonance imaging; PET-CT = positron emission tomography/computed tomography; * = analysis was conducted on n = 66 patients with known tumor grade; † = statistical significance (p < 0.05)

TABLE 4. Multivariate Cox regression analysis of possible progression-free survival predictors in suspected recurrent cervical cancer (n = 84)

Predictor	HR (95% confidence interval)	p value
Age	0.995 (0.966–1.024)	0.727
Initial stage (IB/IIA vs. IIB/III/IV)	1.605 (0.520–4.957)	0.411
Histological type (squamocellular vs. other)	0.892 (0.419–1.898)	0.766
MRI (positive vs. negative)	1.959 (0.888–4.323)	0.096
PET-CT (positive vs. negative)	8.787 (2.877–26.834)	< 0.001*

HR = hazard ratio; MRI = magnetic resonance imaging; PET-CT = positron emission tomography/computed tomography; *statistical significance (p < 0.05)

was squamocellular carcinoma, which was proven in 70 patients, and other types were adenocarcinoma in 11 patients, 2 adenosquamous cancers and one small cell carcinoma. Histological tumor grade was known in 66 patients, whereas in remaining 18 patients data regarding tumor grade were not available. All clinical, histopathological and imaging data are presented in Table 1.

Magnetic resonance imaging results were positive for recurrent tumor in 54 patients (64%), while 30 patients (36%) had normal MRI findings. Sensitivity of MRI in detecting recurrent disease was 80.1%, with 52.4% specificity. Positive predictive value of MRI was 63% and negative predictive value was 73.3%. Overall accuracy of MRI in suspected recurrent cervical cancer was 66.7%.

Twenty-seven patients (32%) had negative FDG PET-CT findings, with no recurrent disease. Out of the remaining 57 patients that were positive, 29 (35%) had only locoregional hypermetabolic lesions, six (7%) were diagnosed with distant metastasis, while 22 women (26%) had both locoregional

and distant spread of the disease (Figure 1). FDG PET-CT showed better diagnostic performance compared to MRI, with sensitivity 97.6%, specificity 61.9%, PPV 71.9%, NPV 96.3% and overall accuracy of 79.8% (Table 2).

Disease progression was detected in 44 patients during follow-up. In two patients, disease progression was confirmed by histopathology, 16 women had progressive disease on follow-up PET scan, and in remaining 26 women, progression was diagnosed based on clinical signs/examination and conventional imaging (CT/MRI). Patients with positive MRI had mean PFS time of 27.2 ± 3.6 months, whereas in those with normal findings, PFS was 40 ± 3.6 months ($p = 0.003$) (Figure 2). With regard to FDG PET-CT, PFS in patients with detected recurrence was 22.3 ± 2.6 months, and for those with negative PET scan results was 55.2 ± 3.7 months ($p < 0.001$) (Figure 3). In addition, patients with only locoregional disease on FDG PET-CT had longer PFS (24 ± 3.3 months) than women with distant metastases on PET scan (17.6 ± 3.1 months) ($p < 0.001$) (Figure 4). In univariate Cox regression models, MRI findings and FDG PET-CT results were found to be related to PFS ($p = 0.005$ and $p < 0.001$, respectively), whereas age, initial disease stage, histological type and tumor grade were not proven to be predictors of progression (Table 3). However, in multivariate analysis only FDG PET-CT remained statistically significant predictor of progression with HR 8.787 (95% CI = 2.877-26.834) (Table 4).

Discussion

This study evaluated diagnostic performances of FDG PET-CT and MRI in women with suspected recurrent carcinoma of uterine cervix previously treated with radiation therapy, and their impact as prognostic factors, together with age, disease stage, and histopathological tumor type and grade, in predicting progression free survival in these patients. The results suggest that FDG PET-CT is more sensitive and accurate in detection of recurrence and metastases of carcinoma of uterine cervix after radiation than MRI. Moreover, positive FDG PET-CT findings are associated with the disease progression.

MRI showed good sensitivity and low specificity. That is only partially in concordance with literature data, where the reported sensitivity and specificity of MRI in pelvic recurrence is higher, and varies between 82 and 100% and between 78 and 100%, respectively, in the systematic review and meta-analysis by Meads *et al*.[18] However, our sample included only patients previously treated with radiation, and it is known that capabilities of MRI could be subpar in these settings. With regard to FDG PET-CT, the same authors found pooled sensitivity of 94.8% and specificity of 86.9% by analyzing nine studies with mostly symptomatic patients, which is comparable with our study in terms of sensitivity, whereas we had lower specificity. However, the sensitivities and specificities of the detection of local and distant recurrence with FDG PET-CT in all researched papers ranged between 83 and 100% and between 50 and 100%, thus being in concordance with our results. In another meta-analysis, by Chu *et al*.[19], which included eight PET-CT papers, the pooled sensitivity and specificity were 94% and 84%, respectively. Overall low specificity in our research, of both MRI and FDG PET-CT, could be explained by high number of false positive findings, caused mostly by nonspecific inflammatory changes and in two cases by occurrence of another malignancy (renal cell carcinoma and low-grade malignant mesenchymal tumor).

To the best of our knowledge, this is the first study to directly compare FDG PET-CT with MRI on a patient level in suspected recurrent uterine cervix cancer, in terms of diagnostic accuracy. In our research, FDG PET-CT had better diagnostic performance than MRI in detecting recurrent disease, with regard to both sensitivity (97.6% *vs*. 80.1%) and specificity (61.9% *vs*. 52.4 %). Pallardy *et al*.[20] evaluated PET-CT in 40 patients with suspected recurrence, and compared it to CT or MRI, with a sensitivity of 94% for PET-CT compared to 42.5% for conventional imaging. Bjurberg *et al*.[21] also analysed PET-CT in 36 suspected recurrent patients, and comparison was done with conventional imaging (CT or MRI). They achieved 100% sensitivity and specificity for PET-CT, and 92% sensitivity and 78% specificity for CT/MRI. A prospective study of 40 patients with recurrent cervical carcinoma that underwent restaging on PET identified significant superiority of PET imaging compared to CT/MRI in detection of metastatic lesions (sensitivity 92% *vs*. 60%).[22] In another study, by Yen *et al*.[23] CT/MRI falsely downstaged 38.4% of the 125 patients and falsely upstaged 17.6%, with 85.4% of the falsely downstaged patients having extra-pelvic recurrence. In contrast, FDG PET falsely downstaged only 15.2% and falsely upstaged 16% of patients. The authors concluded that, for recurrent cervical cancer, the benefits of FDG PET exceeded those of

CT/MRI owing to the ability of FDG PET to identify extra-pelvic metastases and its higher sensitivity and specificity.

In our research, MRI and PET-CT findings in patients with suspected recurrence following radiotherapy were found to be linked with progression-free survival in both, Kaplan Meier analysis and univariate Cox analysis. However, only FDG PET-CT was proven to be an independent prognostic factor by multivariate analysis, and patients with positive PET scan have almost nine times more chance of disease progression. In addition, women with only locoregional disease tend to have better chances of disease-free survival than patients with distant metastasis detected on FDG PET-CT. Patient age, initial disease stage, histological type and grade did not have effect on PFS in our study cohort. With regard to PET-CT detection of recurrence and its impact in prognosis, it is important to mention that the disease evaluation is not only based on tumor visibility but also on tumor metabolic activity, and tumors with high metabolic activity generally have a poor prognosis. In the literature, there are mostly studies that evaluated FDG PET in therapy response assessment and its impact on prognosis, i.e., Grigsby *et al*.[24] showed in their research on 152 patients with mean time of 3 months between end of the standard treatment and PET scan, that patients with new, residual, or no disease demonstrate 5-years survival rates of 0%, 46%, and 92%, respectively. Schwarz *et al*.[25] reported that visual analysis of the PET data in therapy response assessment with three categories (complete metabolic response (CMR), partial metabolic response (PMR), and progressive disease (PD)) predicts survival. The 3-year PFS rate was 78% for CMR, 33% for PMR, and 0% for PD. Kim *et al*.[26] found in their systemic report and meta-analysis, based on 11 studies, that response results of a 18F-FDG PET after definitive radiotherapy with or without chemotherapy were significant prognostic factors in patients with uterine cervical cancer. With regard to patients with CMR after definitive chemoradiotherapy, TLG and MTV are predictive of both overall survival and PFS.[27] On the other hand, Chung *et al*.[28], conducted a research that included 276 patients evaluated on PET-CT for suspected recurrent disease. It was shown that the 5-year PFS and OS rates of patients with a negative PET-CT scan for recurrence were significantly better than those with a positive PET-CT (98.62% *vs*. 17.8 3%, $p < 0.0001$ for PFS, 99.31% *vs*. 85.38%, $p = 0.0015$ for OS), which agrees with our results, however there is some difference in study population, as we only included patients previously treated with radiotherapy.

There are some limitations of our study. It is mostly retrospective study design, which could lead to bias in the choice of patients. However, all patients fulfilled the inclusion criteria with suspicion of recurrence. Furthermore, not all of the progression was proven by histopathology. However, clinical follow-up justifies presence or absence of the disease progression. There is also an issue of heterogeneity in imaging follow-up of patients, which was done by different imaging modalities (CT, MRI, PET-CT), which could influence the time of detected disease progression since not all modalities have the same sensitivity.

Conclusions

Our results suggest that FDG PET-CT is an important tool in clinical practice in the detection of suspected recurrent cervical cancer in post-irradiation patients, with high sensitivity. In addition, it is proved to be an independent factor in predicting progression-free survival in these patients.

References

1. Sung H, Ferlay J, Siegel RL, Laversanne M, Soerjomataram I, Jemal A, et al. Global cancer statistics 2020: GLOBOCAN estimates of incidence and mortality worldwide for 36 cancers in 185 Countries. *CA Cancer J Clin* 2021; **71:** 209-49. doi: 10.3322/caac.21669
2. Bhatla N, Aoki D, Sharma DN, Sankaranarayanan R. Cancer of the cervix uteri. *Int J Gynaecol Obstet* 2018; **143(Suppl 2):** S22-36. doi: 10.1002/ijgo.13865
3. Quinn MA, Benedet JL, Odicino F, Maisonneuve P, Beller U, Creasman WT, et al. Carcinoma of the cervix uteri. FIGO 26th annual report on the results of treatment in gynecological cancer. *Int J Gynaecol Obstet* 2006; **95(Suppl 1):** S43-103. doi: 10.1016/S0020-7292(06)60030-1
4. Thomas GM, Dembo AJ, Myhr T, Black B, Pringle JF, Rawlings G. Long-term results of concurrent radiation and chemotherapy for carcinoma of the cervix recurrent after surgery. *Int J Gynecol Cancer* 1993; **3:** 193-8. doi: 10.1046/j.1525-1438.1993.03040193.x
5. Gandy N, Arshad MA, Park WE, Rockall AG, Barwick TD. FDG-PET Imaging in cervical cancer. *Semin Nucl Med* 2019; **49:** 461-70. doi: 10.1053/j.semnuclmed.2019.06.007.
6. Patel-Lippmann K, Robbins JB, Barroilhet L, Anderson B, Sadowski EA, Boyum J. MR imaging of cervical cancer. *Magn Reson Imaging Clin N Am* 2017; **25:** 635-49. doi: 10.1016/j.mric.2017.03.007
7. Palaniswamy SS, Borde CR, Subramanyam P. 18F-FDG PET/CT in the evaluation of cancer cervix: where do we stand today? *Nucl Med Commun* 2018; **39:** 583-92. doi: 10.1097/MNM.0000000000000851
8. Vinh-Hung V, Bourgain C, Vlastos G, Cserni G, De Ridder M, Storme G et al. Prognostic value of histopathology and trends in cervical cancer: a SEER population study. *BMC Cancer* 2007; **7:** 164. doi:10.1186/1471-2407-7-164
9. Cancer.Net. Cervical Cancer: Statistics. [Internet]. American Society of Clinical Oncology (ASCO); c2005-21. [cited 2021 Aug 17]. Available from: https://www.cancer.net/cancer-types/cervical-cancer/statistics

10. Kidd EA, Siegel BA, Dehdashti F, Grigsby PW. The standardized uptake value for F-18 fluorodeoxyglucose is a sensitive predictive biomarker for cervical cancer treatment response and survival. *Cancer* 2007; **110:** 1738-44. doi: 10.1002/cncr.22974

11. Kidd EA, Siegel BA, Dehdashti F, Rader JS, Mutch DG, Powell MA, et al. Lymph node staging by positron emission tomography in cervical cancer: relationship to prognosis. *J Clin Oncol* 2010; **28:** 2108-13. doi: 10.1200/JCO.2009.25.4151

12. Yen TC, See LC, Lai CH, Tsai CS, Chao A, Hsueh S, et al. Standardized uptake value in para-aortic lymph nodes is a significant prognostic factor in patients with primary advanced squamous cervical cancer. *Eur J Nucl Med Mol Imaging* 2008; **35:** 493-501. doi: 10.1007/s00259-007-0612-1

13. Han S, Kim H, Kim YJ, Suh CH, Woo S. Prognostic value of volume-based metabolic parameters of 18F-FDG PET/CT in uterine cervical cancer: a systematic review and meta-analysis. *AJR Am J Roentgenol* 2018; **211:** 1112-21. doi: 10.2214/AJR.18.19734

14. Miccò M, Vargas HA, Burger IA, Kollmeier MA, Goldman DA, Park KJ, et al. Combined pre-treatment MRI and 18F-FDG PET/CT parameters as prognostic biomarkers in patients with cervical cancer. *Eur J Radiol* 2014; **83:** 1169-76. doi: 10.1016/j.ejrad.2014.03.024

15. Ho JC, Allen PK, Bhosale PR, Rauch GM, Fuller CD, Mohamed AS, et al. Diffusion-weighted magnetic resonance imaging as a predictor of outcome in cervical cancer after chemoradiation. *Int J Radiat Oncol Biol Phys* 2017; **97:** 546-53. doi: 10.1016/j.ijrobp.2016.11.015

16. Tavassoéli FA, Devilee P. *IARC WHO classification of tumours, pathology and genetics tumours of the breast and female genital organs*. Vol 4. 3rd edition. Lyon: IARC publications; 2003.

17. Kurman RJ, Hedrick-Ellenson L, Ronnett BM. *Blaustein's pathology of the female genital tract*. 6th edition. New York: Springer; 2011.

18. Meads C, Davenport C, Małysiak S, Kowalska M, Zapalska A, Guest P, et al. Evaluating PET-CT in the detection and management of recurrent cervical cancer: systematic reviews of diagnostic accuracy and subjective elicitation. *BJOG* 2014; **121:** 398-407. doi: 10.1111/1471-0528.12460

19. Chu Y, Zheng A, Wang F, Lin W, Yang X, Han L, et al. Diagnostic value of 18F-FDG-PET or PET-CT in recurrent cervical cancer: a systematic review and meta-analysis. *Nucl Med Commun* 2014; **35:** 144-50. doi: 10.1097/MNM.0000000000000026

20. Pallardy A, Bodet-Milin C, Oudoux A, Campion L, Bourbouloux E, Sagan C, et al. Clinical and survival impact of FDG PET in patients with suspicion of recurrent cervical carcinoma. *Eur J Nucl Med Mol Imaging* 2010; **37:** 1270-8. doi: 10.1007/s00259-010-1417-1

21. Bjurberg M, Brun E. Clinical impact of 2-deoxy-2-[18F] fluoro-D-glucose (FDG)-positron emission tomography (PET) on treatment choice in recurrent cancer of the cervix uteri. *Int J Gynecol Cancer* 2013; **23:** 1642-6. doi: 10.1097/IGC.0b013e3182a50537

22. Lai CH, Huang KG, See LC, Yen TC, Tsai CS, Chang TC, et al. Restaging of recurrent cervical carcinoma with dual-phase [18F] fluoro-2-deoxy-D-glucose positron emission tomography. *Cancer* 2004; **100:** 544-52. doi: 10.1002/cncr.11928

23. Yen TC, Lai CH, Ma SY, Huang KG, Huang HJ, Hong JH, et al. Comparative benefits and limitations of 18F-FDG PET and CT-MRI in documented or suspected recurrent cervical cancer. *Eur J Nucl Med Mol Imaging* 2006; **33:** 1399-407. doi: 10.1007/s00259-006-0090-x

24. Grigsby PW, Siegel BA, Dehdashti F, Rader J, Zoberi I. Posttherapy [18F] fluorodeoxyglucose positron emission tomography in carcinoma of the cervix: response and outcome. *J Clin Oncol* 2004; **22:** 2167-71. doi: 10.1200/JCO.2004.09.035

25. Schwarz JK, Siegel BA, Dehdashti F, Grigsby PW. Association of posttherapy positron emission tomography with tumor response and survival in cervical carcinoma. *JAMA* 2007; **298:** 2289-95. doi: 10.1001/jama.298.19.2289

26. Kim YJ, Han S, Kim YS, Nam JH. Prognostic value of post-treatment 18F-fluorodeoxyglucose positron emission tomography in uterine cervical cancer patients treated with radiotherapy: a systematic review and meta-analysis. *J Gynecol Oncol* 2019; **30:** e66. doi: 10.3802/jgo.2019.30.e66.

27. Onal C, Guler OC, Reyhan M, Yapar AF. Long-term outcomes of cervical cancer patients with complete metabolic response after definitive chemoradiotherapy. *J Gynecol Oncol* 2021; **32:** e74. doi: 10.1016/j.clon.2021.03.022

28. Chung HH, Kim JW, Kang KW, Park NH, Song YS, Chung JK, et al. Predictive role of post-treatment [18F] FDG PET/CT in patients with uterine cervical cancer. *Eur J Radiol* 2012; **81:** e817-e822. doi: 10.1016/j.ejrad.2012.02.015

research article

Diagnostic performance of tomosynthesis, digital mammography and a dedicated digital specimen radiography system versus pathological assessment of excised breast lesions

Sa'ed Almasarweh[1,2,3], Mazen Sudah[1,2], Hidemi Okuma[1], Sarianna Joukainen[4], Vesa Kärjä[5], Ritva Vanninen[1,2], Amro Masarwah[1,2]

[1] Department of Clinical Radiology, Diagnostic Imaging Center, Kuopio University Hospital, Kuopio, Finland
[2] Clinical Radiology, Institute of Clinical Medicine, School of Medicine, University of Eastern Finland, Kuopio, Finland
[3] Department of Gynecology and Obstetrics, Essen University Hospital, Essen, Germany
[4] Department of Plastic Surgery, Division of Surgery, Kuopio University Hospital, Kuopio, Finland
[5] Department of Clinical pathology, Diagnostic Imaging Center, Kuopio University Hospital, Kuopio, Finland

Radiol Oncol 2022; 56(4): 461-470.

Received 23 May 2022
Accepted 6 July 2022

Correspondence to: Sa'ed Almasarweh, M.D., Department of Obstetrics and Gynaecology, Essen University Hospital, Hufelandstraße 55, D-45147 Essen, Germany. E-mail: saed.almasarweh@uk-essen.de; Phone: +49 (201) 723 2241

Disclosure: No potential conflicts of interest were disclosed.

Background. The aim of the study was to compare the performance of full-field digital mammography (FFDM), digital breast tomosynthesis and a dedicated digital specimen radiography system (SRS) in consecutive patients, and to compare the margin status of resected lesions versus pathological assessment.

Patients and methods. Resected tissue specimens from consecutive patients who underwent intraoperative breast specimen assessment following wide local excision or oncoplastic breast conservative surgery were examined by FFDM, tomosynthesis and SRS. Two independent observers retrospectively evaluated the visibility of lesions, size, margins, spiculations, calcifications and diagnostic certainty, and chose the best performing method in a blinded manner.

Results. We evaluated 216 specimens from 204 patients. All target malignant lesions were removed with no tumour-on-ink. One papilloma had positive microscopic margins and one patient underwent reoperation owing to extensive *in situ* components. There were no significant differences in measured lesion size among the three methods. However, tomosynthesis was the most accurate modality when compared with the final pathological report. Both observers reported that tomosynthesis had significantly better lesion visibility than SRS and FFDM, which translated into a significantly greater diagnostic certainty. Tomosynthesis was superior to the other two methods in identifying spiculations and calcifications. Both observers reported that tomosynthesis was the best performing method in 76.9% of cases. The interobserver reproducibilities of lesion visibility and diagnostic certainty were high for all three methods.

Conclusions. Tomosynthesis was superior to SRS and FFDM for detecting and evaluating the target lesions, spiculations and calcifications, and was therefore more reliable for assessing complete excision of breast lesions.

Key words: breast cancer; radiography; digital breast tomosynthesis; surgery; mammography

Introduction

Breast conserving surgery (BCS) is an established treatment modality for early breast cancer, offering better aesthetic results and less morbidity, without compromising survival, compared with radical mastectomy.[1,2]

A clear resection margin after surgical excision is associated with a reduced risk of local recurrence. Positive margins are associated with a 2-fold increased risk of ipsilateral recurrence.[3] This risk is not eliminated by radiotherapy, systemic chemotherapy or endocrine therapy. Therefore, to achieve the best local disease-free survival, a negative margin must be achieved during surgery and confirmed by the final microscopic assessment of the excised tissue.

The published reoperation rates for patients with early stage breast cancer vary considerably, between 10% and 60%, depending on the treating centre and the surgeon's practice, with an average rate of ~20%.[4] To reduce the rate of reoperation in patients with non-palpable lesions, intraoperative assessment is performed to confirm adequate removal of the detected lesions and margin. The resected sample is imaged, most commonly by digital mammography, while the patient is under general anaesthesia. The images are analysed and information about the resection margins is given to the surgeon. Proper assessment of the margins reduces the need for reoperation, the cost of hospital stay and the subsequent psychological or cosmetic impact on the patient. Failure to achieve negative margins usually results in re-excision or mastectomy.[5]

Digital breast tomosynthesis eliminates tissue superimposition and provides a clearer view of dense breasts because it provides three-dimensional (3D) images unlike mammography, which provides two-dimensional (2D) images.[6] Specimen tomosynthesis was previously shown to be superior to digital mammography for depicting excised lesions and evaluation of resection margins.[7-13] Mobile, dedicated digital specimen radiography is a rapid method for intraoperative specimen assessment that can image the excised specimen in the operating room, thus avoiding the need to send the specimen to the radiology department. This shortens the duration of anaesthesia, reducing morbidity and mortality, and decreases operating room occupancy, thus reducing costs, while still providing comparable results to digital mammography.[14-16]

The aim of this study was to directly compare the diagnostic performance of full-field digital mammography (FFDM), digital breast tomosynthesis and a dedicated digital specimen radiography system (SRS) for the evaluation of resected breast lesions in consecutive patients, and to compare the margin status of resected lesions versus the final pathological report.

Patients and methods

This study was undertaken as part of the continuous improvement, quality control and internal validation of modern surgical specimen imaging technologies at the Breast Unit at Kuopio University Hospital (Kuopio, Finland). During the study period, clinical decisions concerning lesion removal and margin status were made by experienced breast radiologists and surgeons and based on all available images.

The detailed analyses and intertechique comparisons described here were performed retrospectively and did not affect patient management. The Chair of the hospital district waived the need to obtain written informed consent from the patients owing to the retrospective nature of the analyses (Approval: FinMargins 5063573; 508/2021). All clinical investigations were conducted according to the relevant guidelines and the principles expressed in the Declaration of Helsinki.

Study population

The study population comprised all consecutive patients who required radiological intraoperative breast specimen assessment at our tertiary university hospital between April 2018 and December 2019. Patients were included in this study if they were diagnosed with invasive breast cancer, ductal carcinoma *in situ* (DCIS) or high-risk and atypical lesions and had been referred to our tertiary university hospital for further evaluation and breast surgery.

All patients were evaluated preoperatively with a minimum of a two-view mammogram and ultrasound. Any suspicious lesions were evaluated using additional lateral and spot-compression views. All mammograms were re-evaluated upon referral by an experienced, specialist senior breast radiologist, and further workup was performed if deemed necessary. Breast magnetic resonance imaging is not routinely performed preoperatively in all patients at our centre; instead, it is performed according to national guidelines that are in concordance with the European Society of Breast Cancer Specialists' recommendations.[17] Patients underwent ultrasound-guided core biopsy or stereotactic vacuum-assisted biopsy and were histologically diagnosed with breast cancer and high-risk or atypical lesions before surgery. If lesions were found in both breasts, each specimen was evaluated separately. Patients who underwent neoadjuvant chemotherapy were excluded from this

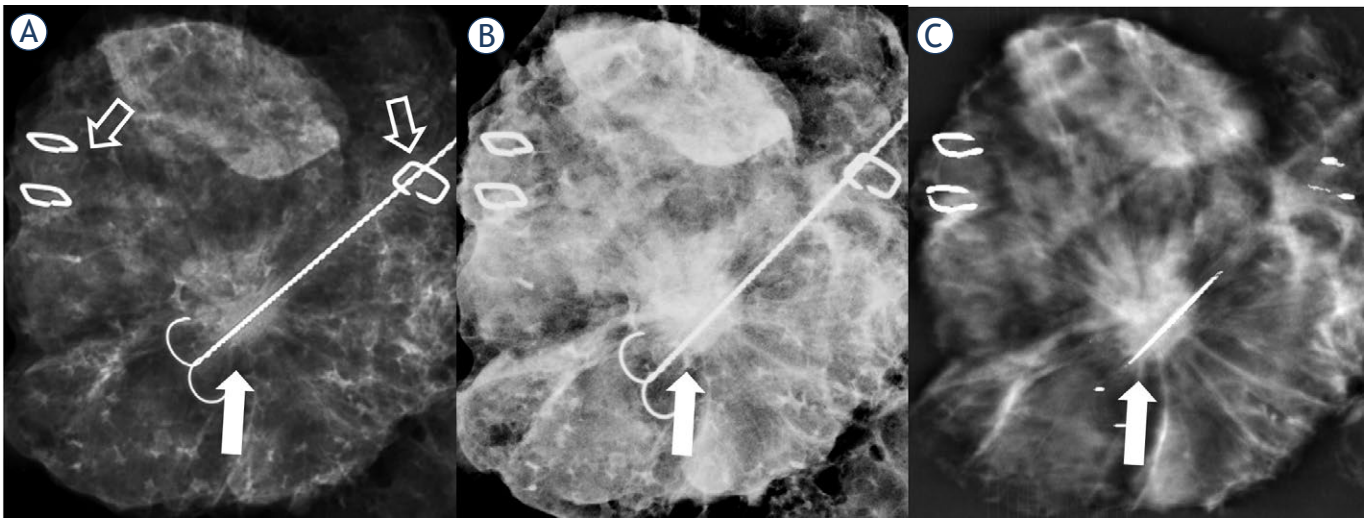

FIGURE 1. Specimen radiographs of a spiculated invasive ductal carcinoma excised after ultrasound guidewire localisation. The tumour and spicules are clearly visible in all three imaging modalities (closed arrows). **(A)** Specimen radiography system, **(B)** full-field digital mammography and **(C)** tomosynthesis (1 mm reconstructed image at the level of the tumour). Metal clips indicate the anatomical position (open arrows; 1 clip-lateral and 2 clips-medial). The position of the specimen is constant in all three imaging modalities.

study. The final analyses comprised 216 specimens from 204 women (mean age 62.5 ± 10.6 years, range 33–95 years).

Lesion localisation and surgery

The surgical procedure was planned individually according to the patient's preference, tumour size, tumour location, clinical findings, breast shape and breast size. All patients were evaluated at multidisciplinary meetings, at least twice, pre- and postoperatively.

Non-palpable tumours were localised preoperatively using at least one guidewire (breast localization needle Duo, SOMATEX® Medical Technologies GmbH) under ultrasound or stereotactic guidance. Two-view mammography (CC and lateromedial) was routinely performed to confirm the position of each lesion relative to the guidewire, and the location of the lesion was ink-marked on the skin, including supine MRI-guided localisation projections.[18] Tumours were excised en bloc from the subcutaneous area to the muscle, and the overlying skin was removed in patients with superficial lesions to achieve a healthy macroscopic surgical margin of ≥1 cm, in accordance with national guidelines, and hence achieve microscopically negative margins (defined as no "tumour-on-ink"). In ductal carcinoma in-situ (DCIS), the need for reoperation is evaluated in a multidisciplinary meeting whenever DCIS margins are less than 2 mm. Intraoperatively, the specimens were placed on a Styrofoam slab, fixed with wooden sticks, and the location of the excision was anatomically marked. Metallic clips were placed directly on the specimen to indicate the orientation. The fascia posterior to the tumour was removed and fixed aside if removed separately (Figure 1, 2). The specimen was then placed in a plastic container and immediately transported to the Breast Radiology Unit.

Imaging protocol

Each specimen was first imaged by 2D FFDM in craniocaudal and lateral projections (Selenia Dimensions® breast tomosynthesis system, Hologic Inc., Bedford) followed immediately by tomosynthesis (images reconstructed into a series of 1-mm-thick slices at 1-mm intervals) and radiography using a dedicated digital SRS (Xpert 40; Kubtec Medical Imaging, Stratford, CT). The specimen was imaged bare, without tissue compression, in all three modalities.

Retrospective image analysis

All images were stored in the regional picture archiving and communication system and were evaluated retrospectively by two radiologists, with 12 and 2 years of experience, in a blind, independent manner. In order to minimise possible bias, the observers analysed the images obtained by each modality separately, presented in a random order,

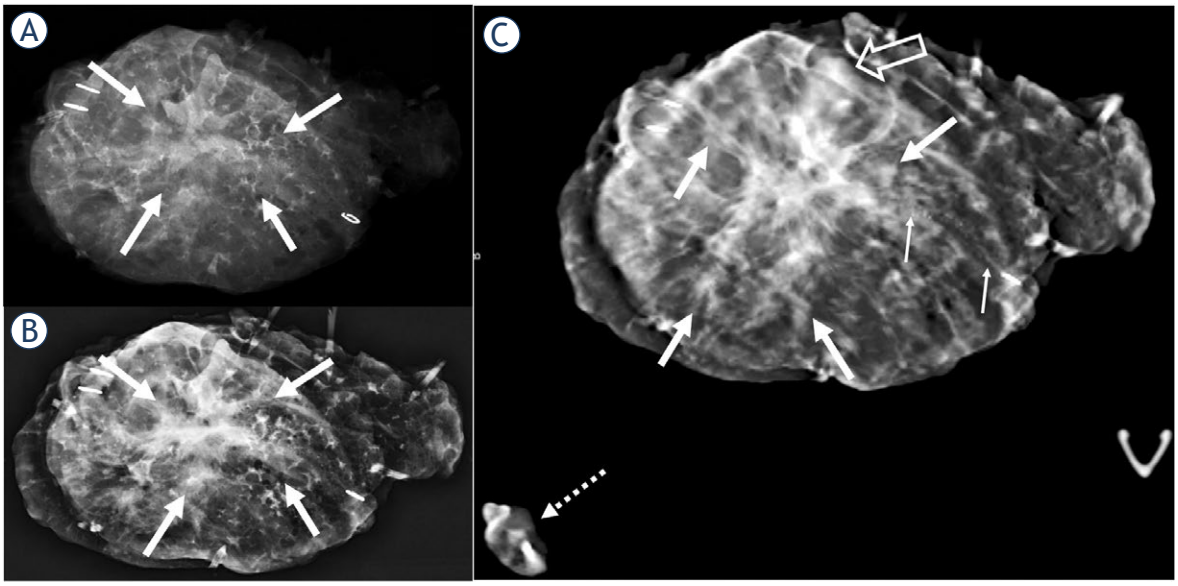

FIGURE 2. A 44-year-old female presented with a 5 × 4.5 cm multifocal invasive lobular carcinoma and underwent supine magnetic resonance imaging-guided oncoplastic conservative resection. Although the irregular area of the tumour (thick arrows) is visible on the specimen radiography system **(A)** and full-field digital mammography **(B)** images, the tumour margins are best delineated by tomosynthesis **(C)** (1 mm reconstructed image at the level of the tumour). The pleomorphic lobular carcinoma *in situ* is clearly depicted by tomosynthesis as an area of linear calcifications (thin arrows). The shortest margins at imaging were 4 mm (open arrow; superior) and 5 mm at final pathology. The fascia at the level of tumour was removed separately (dotted arrow).

with a short interval before analysing the images obtained from the next modality, which was also presented in a random order. Both observers were blinded to the clinical and pathological features of the lesions and were only allowed to refer to the preoperative images when assessing each image. The detectability and visibility of the main lesions, margins, spiculations and calcifications, measured lesion size and diagnostic certainty were recorded using 5-point scales for each modality. In a final session, the observers independently evaluated all images simultaneously and decided which method performed best in their subjective opinion. Specimen radiography was not routinely performed for additional intraoperative resections, and margin analysis was evaluated and compared with the pathological assessment of the primary resected specimen.

Mammographic features were described according to the 5th edition of the Breast Imaging Reporting and Data System (BI-RADS) by the senior radiologist as masses, calcifications, asymmetry, and architectural distortion. Masses were further classified by their shape and margins, and calcifications were further classified by their morphology and distribution. The amount of peritumoral fibroglandular tissue was documented in quartile percentages.

Histopathological evaluation

The specimens were measured, photographed, margins ink-marked and sliced upon arrival at 5-mm intervals. All macroscopically detected and/or guidewire localised areas were examined meticulously under a microscope and the size and characteristics of each tumour were reported separately. The extent of involvement between the invasive and/or *in situ* cancer in each margin was reported in all six directions. The histopathological data, including the margin status, tumour size, histological grade, estrogen receptor status, progesterone receptor status, human epidermal growth factor receptor 2 status and Ki-67 index, were obtained from the structured histopathological reports.

Statistical analysis

All statistical analyses were performed with SPSS for Windows version 27 (IBM Corporation, Armonk, NY, USA). P values of < 0.05 were considered to be statistically significant. The interclass correlation analysis (ICC) was used to evaluate the agreement between lesion visibility and diagnostic certainty recorded by both observers. Pearson's correlation coefficient was used to assess the linear association between the diameters measured

TABLE 1. Characteristics of the patients, surgical procedures and tumours

Mean age years (range)	62.5 (33–95)
Mammography negative	20 (9.3%)
Surgery	
Wide local excision	158 (73.1%)
Oncoplastic	58 (26.9%)
Specimen diameter (mm)	
Mean	97.65
Median	89.0
Range	25–285
Histology n (%)	
Invasive ductal	120 (55.6%)
Invasive lobular	27 (12.5%)
Mixed malignant	7 (3.2%)
Pure DCIS	26 (12.0%)
Other malignant	11 (5.1%)
Benign	25 (11.6%)
Size of tumour mean mm (range)	15.69 (0–70)
Presence of DCIS	114 (52.8%)
Grade	
1	62 (28.7%)
2	94 (43.5%)
3	35 (16.2%)
T-stage	
Tis	27 (14.1%)
T1	122 (63.9%)
T2	40 (20.9%)
T3	2 (1.0%)
N-Stage	
N0	145 (75.9%)
N1	39 (20.4%)
N2	6 (3.1%)
N3	1 (0.5%)
ER-Status	
Positive	152 (92.2%)
Negative	13 (7.8%)
PR-Status	
Positive	147 (89.2%)
Negative	18 (10.8%)
HER2-Status	
Positive	12 (7.3%)
Negative	153 (92.7)

DCIS = ductal carcinoma *in situ*; ER = estrogen rec eptor; HER2 = human epidermal growth factor receptor 2; N = node; PR = progesterone receptor; T = tumour;

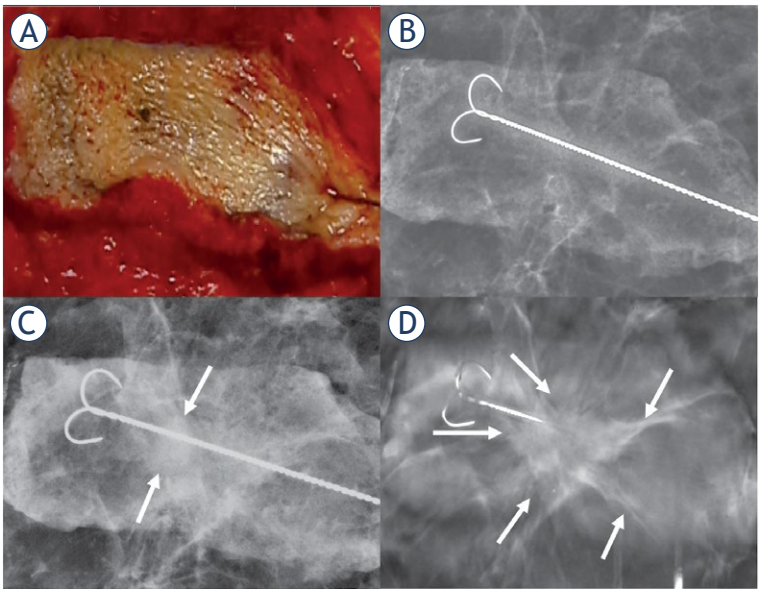

FIGURE 3. A 68-year-old female presented with invasive ductal carcinoma, papillary ductal carcinoma *in situ*, and papillomatosis, and underwent oncoplastic conservative breast resection. **(A)** Shows the excised skin area above the tumour that was deemed not visible by both observers on the specimen radiography system image **(B)**. **(C)** Full-field digital mammography shows a small oval lesion (arrow). **(D)** Tomosynthesis (1 mm reconstructed image) shows the full extension of the large spiculated area (arrows).

using the imaging modalities and histopathology. Bland–Altman analysis and plots were used to assess the differences between mean diameters, as measured by the observers and histopathology, among the two observers.

Results

The final analyses included 204 patients with a mean age of 62.5 years (range 33–95 years). The patient characteristics, histological diagnosis and surgical procedures are presented in Table 1. The majority of lesions were treated by wide local excision (158/216, 73.1%), and oncoplastic conservative breast resection was performed for more than a quarter of lesions (58/216, 26.9%). The mammographic features of the lesions are presented in Table 2.

Regarding interobserver agreement, the ICC was high for lesion visibility (0.787) and diagnostic certainty (0.684) with tomosynthesis. Similar results were observed for SRS and FFDM, with ICCs of 0.742 and 0.804 for lesion visibility and 0.671 and 0.683 for diagnostic certainty, respectively.

As shown in Table 3, both observers felt that tomosynthesis was the best performing imaging

TABLE 2. Mammographic features and lesion descriptors according to the Breast Imaging Reporting and Data System, 5th Edition

Breast density							
A	57	**B**	121	**C**	34	**D**	4
Peritumoral density %							
< 25%	90	**25%–50%**	20	**50%–75%**	24	**75%–100%**	60
Mass Shape							
Oval	17	Round	70	Irregular	58		
Mass Margin							
Circumscribed	4	Obscured	7	Microlobulated	36		
Indistinct	27	Spiculated	71				
Calcifications							
Amorphous		2		Fine Pleomorphic		42	
Coarse Heterogenous		2		Fine linear or branching		7	
Calcification distribution							
Regional		9		Linear		6	
Grouped		33		Segmental		5	
Architectural Distortion							
Yes		15		No		201	

modality in 76.9% of cases (Figure 2, 3). SRS was the least favoured method, chosen only once (0.5%) by observer 1 and six times by observer 2 (2.8%).

Table 4 presents the results reported by both observers. For both observers, tomosynthesis provided significantly better lesion visibility than SRS and FFDM, which translated into a significantly greater diagnostic certainty. Moreover, tomosynthesis was superior to the other two methods for identifying spiculations and calcifications. The high performance of tomosynthesis was not affected by peritumoral density (p = 0.851).

All three methods showed comparable results for estimating the diameters of the excised lesions (Table 5). Observer 1, who was more experienced, estimated the lesion sizes with greater accuracy relative to the final pathological report than observer 2, who was less experienced and tended to overestimate the lesion sizes using all three methods. The Pearson's correlation coefficient for tomosynthesis relative to the final pathology was greater than those for SRS and FFDM. The Bland-Altman plots constructed using the lesion diameters measured by the three imaging methods relative to the final pathological report are shown in Figure 4 for both observers. The plots illustrate the greater accuracy of observer 1 compared with the less-experienced observer 2, as well as the superior agreement of tomosynthesis to the final pathological report. The plots also indicate that the differences in measurements increase with increasing lesion diameter for each imaging modality.

TABLE 3. The preferred imaging modalities for individual lesions selected by the two observers

	Observer 1	Observer 2
Tomosynthesis	166 (76.9%)	166 (76.9%)
SRS	1 (0.5%)	6 (2.8%)
FFDM	21 (9.7%)	14 (6.5%)
All equal	5 (2.3%)	12 (5.6%)
None	23 (10.6%)	18 (8.3%)

FFDM = full-field digital mammography; SRS = specimen radiography system

Of 204 patients included in this study, only one underwent reoperation owing to inadequate margins. Small invasive ductal carcinoma foci were associated with a 6.5 × 5.5 cm DCIS close to three margins. Upon re-resection, a 2.5 cm residual grade 3 DCIS was found. Intraoperative findings revealed multicentric disease in one patient that was confirmed by pathological assessment of frozen section, and mastectomy was performed. The margins of that specimen were found to be macroscopically and microscopically adequate. One patient with papilloma had a small, microscopic extension to the edge of the specimen. In addition, nine cancers (one DCIS, one invasive lobular and seven invasive ductal cancers) that were not vis-

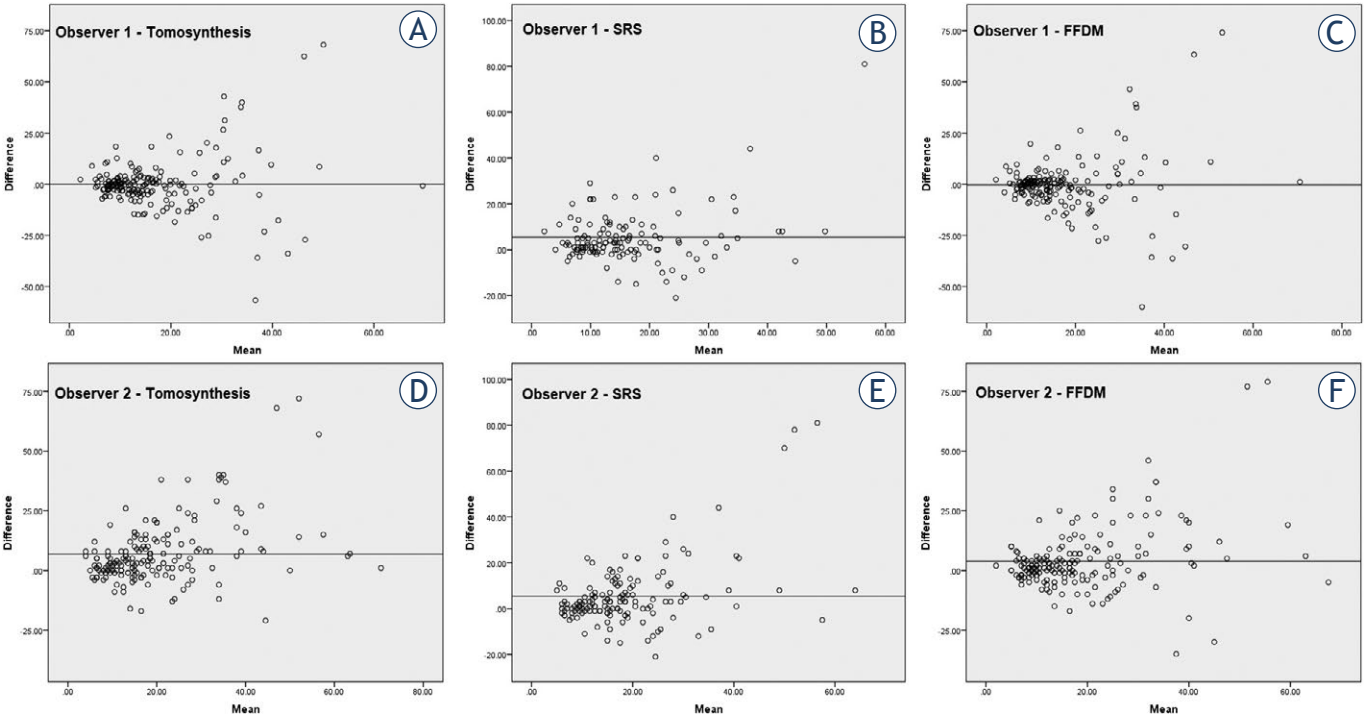

FIGURE 4. Bland-Altman plots of tumour diameters compared with the pathological report, as measured by observer 1 **(A-C)** and observer 2 **(D-F)** using tomosynthesis **(A,D)**, specimen radiography system **(B,E)**, and full-field digital mammography **(C,F)**.

FFDM = full-field digital mammography; SRS = specimen radiography system

ible on preoperative imaging were found on the marginal resection specimens removed by the surgeons for cosmetic or additional marginal purposes; all nine had negative margins.

Discussion

Intraoperative assessment of resected specimens is particularly important for successful BCS. To the best of our knowledge, this study is the first to compare the performance of three imaging modalities performed simultaneously in the same patients. Of the three modalities, digital tomosynthesis was superior for visualising lesions, calcifications and spiculations in the majority of specimens, and therefore provided the best confirmation of complete removal of the target lesion. Moreover, both observers, with different levels of experience, felt that tomosynthesis was the superior imaging modality for the majority of cases and reported greater certainty of diagnosis compared with the use of FFDM and SRS.

The cross-sectional capability of tomosynthesis reduces the effect of breast tissue superimposition and therefore helps to delineate the tumour margins. In this study, tomosynthesis was superior to the other imaging modalities, regardless of the fact that the majority of our patients had fatty breasts (BI-RADS density A or B) and approximately two-thirds of the lesions had low peritumoral tissue densities. This may reflect the better image quality of tomosynthesis compared with 2D techniques. Our results are in concordance with those of prior studies.[12,13,19]

The underperformance of SRS is noticeable because it did not visualise one in five lesions. Prior studies showed that using mobile SRS in an operating theatre reduced the duration and cost of surgery significantly[9,14-16], at the expense of inferior image quality.[14] However, a mobile SRS equipped with tomosynthesis exhibited greater accuracy than standard mammography and reduced the rate of re-excision.[11]

The reoperation rate after BCS varied markedly in earlier studies. Tumour-related factors that may influence decisions regarding reoperation include focality, presence of DCIS and tumour size[4], and non-tumour-related factors include inadequate assessment of the extent of macroscopic disease at diagnosis, inaccurate impalpable disease localisation and limited use of intraoperative specimen radi-

TABLE 4. Evaluated parameters of the specimen with three different imaging modalities by both observers

Margins	**> 10mm**		**6–10**		**≤ 5mm**					
Observer	**1**	**2**	**1**	**2**	**1**	**2**				
Tomosynthesis	156	114	20	37	19	49				
SRS	132	126	15	15	8	23				
FFDM	158	135	14	38	13	28				
Diagnostic Certainty	**Not at all**		**Somehow Certain**		**Average**		**Almost Certain**		**Completely Certain**	
Observer	**1**	**2**	**1**	**2**	**1**	**2**	**1**	**2**	**1**	**2**
Tomosynthesis	21	19	12	6	15	22	40	46	128	123
SRS	61	53	21	12	22	26	59	40	53	85
FFDM	32	23	13	19	18	34	61	53	92	87
Lesion Visibility	**0%**		**0□10%**		**10□50%**		**50□90%**		**90□100%**	
Observer	**1**	**2**	**1**	**2**	**1**	**2**	**1**	**2**	**1**	**2**
Tomosynthesis	22	16	15	18	13	24	34	40	132	118
SRS	60	50	20	51	26	50	65	35	45	30
FFDM	32	21	15	27	18	40	57	60	94	68
Spiculation visibility	**Not visible**		**Partially visible**		**Completely visible**		**No spiculations**			
Observer	**1**	**2**	**1**	**2**	**1**	**2**	**1**	**2**		
Tomosynthesis	1	8	23	30	45	103	147	75		
SRS	11	32	43	68	3	5	159	111		
FFDM	5	31	54	67	9	42	148	76		
Calcifications	**Present**		**Less visible**		**Equally visible**		**More visible**			
Observer	**1**	**2**	**1**	**2**	**1**	**2**	**1**	**2**		
Tomosynthesis	48	53	4	13	25	30	19	10		
SRS	47	41	40	30	7	9	0	2		
FFDM	49	53	18	28	28	21	3	4		

FFDM = full-field digital mammography; SRS = specimen radiography system

ography.[4,5] BCS is not specifically limited based on cut-off values for tumour size; instead, surgeons should balance their decision between the assessed tumour size and the total breast volume. More intraoperative tissue sampling – such as shaving the resection margins after lumpectomy in certain situations or oncoplastic BCS techniques – may help reduce the rate of reoperation.[5,20] In this study, the reoperation rate was low, which is presumably multifactorial. All preoperative imaging findings were re-evaluated by specialist breast radiologists and multidisciplinary specialists. Every effort was made to evaluate the tumour extent preoperatively and to transfer these findings to the surgical position by ink-marking the skin. Furthermore, all procedures were standardised, including tumour localisation, macroscopic resection margins of ≥1 cm, en bloc resection for anterior and posterior margins, structured specimen orientation, specimen fixation, imaging and structured histopathological reporting. All of these factors might help to reduce positive margins.[4]

The efficacy of specimen mammography for margin assessment is not yet well established. Laws *et al*. reported that the use of any margin assessment technique did not improve margin status compared with guidewire localisation alone.[21] According to a meta-analysis, specimen radiography to assess the surgical margin had lower sensitivity than frozen sections (53% *vs*. 86%, respectively).[22] However, frozen section is a resource-demanding procedure, is not always readily available and it might prolong the duration and cost of surgery. By contrast, intraoperative imaging is simple, rapid and readily available. In our opinion, its lower accuracy is due mainly to the inability to comprehensively evaluate the microscopic tumour extension from the target lesion. Mammography

TABLE 5. Diameters of the excised lesions evaluated by the two observers using three imaging modalities and in the final pathology report

Lesion diameter	Mean (mm)	Median (mm)	Minimum (mm)	Maximum (mm)	Pearson's coefficient (r)
Observer 1					
Tomosynthesis	16.82	12.70	2.90	84.10	0.471
SRS	17.45	13.90	2.10	96.90	0.421
FFDM	16.96	12.60	2.00	90.10	0.452
Observer 2					
Tomosynthesis	23.04	19.00	4.00	88.00	0.614
SRS	21.31	17.00	5.00	97.00	0.457
FFDM	20.21	15.00	3.00	95.00	0.550
Final Pathology					
	15.69	14.00	0	70	

FFDM = full-field digital mammography; SRS = specimen radiography system

tends to underestimate the size of DCIS and, although the sensitivity of specimen imaging is higher for invasive cancers, it is lower for DCIS.[23] A greater resection margin threshold may reduce the risk of missing a positive margin but increases unnecessary resection of healthy tissue.[23] Mazouni *et al.* determined the sensitivity and specificity of different radiological threshold values (1, 5 and 10 mm), and found that the 10 mm threshold value had the highest sensitivity (75%).[24] Britton *et al.* reported that a maximum distance of ≥11 mm from the lesion to the specimen edge was associated with a 77% likelihood of having a clear final histological margin.[25] Leung *et al.* reported that a 15 mm radiological margin showed the highest combination of sensitivity and specificity for predicting a positive margin.[26] DCIS is often associated with invasive cancer and, in this study, half of the specimens included DCIS components. Therefore, the consistent wide macroscopic resection margins in this study presumably contributed to the microscopically clear margins.

It is difficult to directly compare the results of studies assessing the clinical value of specimen radiography because of marked heterogeneity in the study designs and inclusion criteria, as well as the methodology and terminology used, thus making comparisons inconclusive.[27] Inconsistencies may be due to different imaging protocols, specimen compression, selective inclusion of patients with different stages of cancer, inclusion of mainly invasive or DCIS patients and the definitions of the outcome measures.[27,28] In this study, we sought to include all consecutive patients treated at our institution. We excluded only those patients who underwent BCS after neoadjuvant therapy because some of these patients only have residual microscopic disease or marking clips. Therefore, the patient population in this study closely represents clinical practice at a specialist tertiary hospital.

This study has limitations to consider. This was a single-centre study and the analysis was performed retrospectively. The observers had varying years of experience, which may contribute to the interobserver variability and is consistent with a previous report.[29] Furthermore, we could not perform more extensive analysis of the diagnostic accuracy of each method in the evaluation of margins owing to complete primary resection of the lesions without positive margins for malignant lesions. Regardless of these limitations, we analysed a cohort of consecutive patients, which is consistent with and representative of actual clinical practice. Moreover, we included 216 specimens from 204 patients, a considerably larger cohort than most of the related studies reported to date. We also performed three different imaging modalities for each specimen, which allowed us to directly compare radiographs obtained in the same orientation for all imaging methods and thus remove some potential sources of error.

In conclusion, tomosynthesis was superior to SRS and FFDM for the detection and evaluation of target breast lesions, and detected spiculations and calcifications. Therefore, tomosynthesis was more reliable than other intraoperative imaging modalities for evaluating complete excision of breast lesions.

Acknowledgement

This work was supported in part by a grant (to AM and MS) from Kuopio University Hospital (VTR grant 5063573). The authors declare no relationships with any companies, whose products or services may be related to the subject matter of the article. The funding sources were not involved in study design, data collection or analysis, preparation of the manuscript or the decision to submit the manuscript.

References

1. Fisher B, Anderson S, Bryant J, Margolese RG, Deutsch M,Fisher ER, et al. Twenty-year follow-up of a randomized trial comparing total mastectomy, lumpectomy, and lumpectomy plus irradiation for the treatment of invasive breast cancer. *N Engl J Med* 2002; **347:** 1233-41. doi: 10.1056/NEJMoa022152
2. Veronesi U, Cascinelli N, Mariani L, Greco M, Saccozzi R, Luini A, et al. Twenty-year follow up of a randomized study comparing breast-conserving surgery with radical mastectomy for early breast cancer. *N Engl J Med* 2002; **347:** 1227-32. doi: 10.1056/NEJMoa020989
3. Houssami N, Macaskill P, Marinovich ML, Morrow M. The association of surgical margins and local recurrence in women with early-stage invasive breast cancer treated with breast-conserving therapy: a meta-analysis. *Ann Surg Oncol* 2014; **21:** 717-30. doi: 10.1245/s10434-014-3480-5
4. Landercasper J, Borgert AJ, Fayanju OM, Cody H 3rd, Feldman S, Greenberg C, et al. Factors associated with reoperation in breast-conserving surgery for cancer: a prospective study of American Society of Breast Surgeon Members. *Ann Surg Oncol* 2019; **26:** 3321-36. doi: 10.1245/s10434-019-07547-w
5. McEvoy MP, Landercasper J, Naik HR, Feldman S. Update of the American Society of Breast Surgeons Toolbox to address the lumpectomy reoperation epidemic. *Gland Surg* 2018; **7:** 536-53. doi: 10.21037/gs.2018.11.03
6. Mall S, Lewis S, Brennan P, Noakes J, Mello-Thoms C. The role of digital breast tomosynthesis in the breast assessment clinic: a review. *J Med Radiat Sci* 2017; **64:** 203-211. doi: 10.1002/jmrs.230
7. Polat YD, Taşkın F, Çildağ MB, Tanyeri A, Soyder A, Ergin F. The role of tomosynthesis in intraoperative specimen evaluation. *Breast J* 2018; **24:** 992-6. doi: 10.1111/tbj.13070
8. Urano M, Shiraki N, Kawai T, Goto T, Endo Y, Yoshimoto N, et al. Digital mammography versus digital breast tomosynthesis for detection of breast cancer in the intraoperative specimen during breast-conserving surgery. *Breast Cancer* 2016; **23:** 706-11. doi: 10.1007/s12282-015-0628-5
9. Romanucci G, Mercogliano S, Carucci E, Cina A, Zantedeschi E, Caneva A, et al. Diagnostic accuracy of resection margin in specimen radiography: digital breast tomosynthesis versus full-field digital mammography. *Radiol Med* 2021; **126:** 768-773. doi: 10.1007/s11547-021-01337-9
10. Schulz-Wendtland R, Dilbat G, Bani M, Fasching PA, Lux MP, Wenkel E, et al. Full field digital mammography (FFDM) versus CMOS technology versus tomosynthesis (DBT) – which system increases the quality of intraoperative imaging? *Geburtshilfe Frauenheilkd* 2012; **72:** 532-8. doi: 10.1055/s-0032-1314942
11. Garlaschi A, Fregatti P, Oddone C, Friedman D, Houssami N, Calabrese M, et al. Intraoperative digital breast tomosynthesis using a dedicated device is more accurate than standard intraoperative mammography for identifying positive margins. *Clin Radiol* 2019; **74:** 974.e1-e6. doi: 10.1016/j.crad.2019.08.004
12. Partain N, Calvo C, Mokdad A, Colton A, Pouns K, Clifford E, et al. Differences in re-excision rates for breast-conserving surgery using intraoperative 2D versus 3D tomosynthesis specimen radiograph. *Ann Surg Oncol* 2020; **27:** 4767-76. doi: 10.1245/s10434-020-08877-w
13. Park KU, Kuerer HM, Rauch GM, Leung JWT, Sahin AA, Wei W, et al. Digital breast tomosynthesis for intraoperative margin assessment during breast-conserving surgery. *Ann Surg Oncol* 2019; **26:** 1720-8. doi: 10.1245/s10434-019-07226-w
14. Wang Y, Ebuoma L, Saksena M, Liu B, Specht M, Rafferty E. Clinical evaluation of a mobile digital specimen radiography system for intraoperative specimen verification. *AJR Am J Roentgenol* 2014; **203:** 457-62. doi: 10.2214/AJR.13.11408
15. Miller CL, Coopey SB, Rafferty E, Gadd M, Smith BL, Specht MC. Comparison of intra-operative specimen mammography to standard specimen mammography for excision of non-palpable breast lesions: a randomized trial. *Breast Cancer Res Treat* 2016; **155:** 513-9. doi: 10.1007/s10549-016-3700-8
16. Mariscotti G, Durando M, Pavan LJ, Tagliafico A, Campanino PP, Castellano I, et al. Intraoperative breast specimen assessment in breast conserving surgery: comparison between standard mammography imaging and a remote radiological system. *Br J Radiol* 2020; **93:** 20190785. doi: 10.1259/bjr.20190785
17. Sardanelli F, Boetes C, Borisch B, Decker T, Federico M, Gilbert FJ, et al. Magnetic resonance imaging of the breast: recommendations from the EUSOMA working group. *Eur J Cancer* 2010; **46:** 1296-316. doi: 10.1016/j.ejca.2010.02.015
18. Joukainen S, Okuma H, Kaarela O, Laaksonen E, Kärjä V, Vanninen R, et al. Can supine breast magnetic resonance imaging help hit the target in extreme oncoplastic surgery? *Eur J Surg Oncol* 2021; **47:** 2788-96. doi: 10.1016/j.ejso.2021.07.027
19. Amer HA, Schmitzberger F, Ingold-Heppner B, Kussmaul J, El Tohamy MF, Tantawy HI, et al. Digital breast tomosynthesis versus full-field digital mammography – which modality provides more accurate prediction of margin status in specimen radiography? *Eur J Radiol* 2017; **93:** 258-64. doi: 10.1016/j.ejrad.2017.05.041
20. Chen JY, Huang YJ, Zhang LL, Yang CQ, Wang K. Comparison of oncoplastic breast-conserving surgery and breast-conserving surgery alone: a meta-analysis. *J Breast Cancer* 2018; **21:** 321-29. doi: 10.4048/jbc.2018.21.e36
21. Laws A, Brar MS, Bouchard-Fortier A, Leong B, Quan ML. Intraoperative margin assessment in wire-localized breast-conserving surgery for invasive cancer: a population-level comparison of techniques. *Ann Surg Oncol* 2016; **23:** 3290-6. doi: 10.1245/s10434-016-5401-2
22. St John ER, Al-Khudairi R, Ashrafian H, Athanasiou T, Takats Z, Hadjiminas DJ, et al. Diagnostic accuracy of intraoperative techniques for margin assessment in breast cancer surgery: a meta-analysis. *Ann Surg* 2017; **265:** 300-10. doi: 10.1097/SLA.0000000000001897
23. Versteegden DPA, Keizer LGG, Schlooz-Vries MS, Duijm LEM, Wauters CAP, Strobbe LJA. Performance characteristics of specimen radiography for margin assessment for ductal carcinoma in situ: a systematic review. *Breast Cancer Res Treat* 2017; **166:** 669-79. doi: 10.1007/s10549-017-4475-2
24. Mazouni C, Rouzier R, Balleyguier C, Sideris L, Rochard F, Delaloge S, et al. Specimen radiography as predictor of resection margin status in non-palpable breast lesions. *Clin Radiol* 2006; **61:** 789-96. doi: 10.1016/j.crad.2006.04.017
25. Britton PD, Sonoda LI, Yamamoto AK, Koo B, Soh E, Goud A. Breast surgical specimen radiographs: how reliable are they? *Eur J Radiol* 2011; **79:** 245-9. doi: 10.1016/j.ejrad.2010.02.012
26. Leung BST, Wan AYH, Au AKY, Lo SSW, Wong WWC, Khoo JLS. Can intraoperative specimen radiograph predict resection margin status for radioguided occult lesion localisation lumpectomy for ductal carcinoma in situ presenting with microcalcifications? *Hong Kong J Radiol* 2015; **18:** 11-21. doi: 10.12809/hkjr1414265
27. Williams D, McCormack S. Intraoperative mammography for breast cancer surgery: a review of clinical effectiveness, cost-effectiveness, and guidelines [Internet]. Ottawa (ON): Canadian Agency for Drugs and Technologies in Health; 2019. [cited 2022 Apr 15]. PMID: 31411841. Avilable at: https://pubmed.ncbi.nlm.nih.gov/31411841/
28. Butler-Henderson K, Lee AH, Price RI, Waring K. Intraoperative assessment of margins in breast conserving therapy: a systematic review. *Breast* 2014; **23:** 112-9. doi: 10.1016/j.breast.2014.01.002
29. Mario J, Venkataraman S, Fein-Zachary V, Knox M, Brook A, Slanetz P. Lumpectomy specimen radiography: does orientation or 3-dimensional tomosynthesis improve margin assessment? *Can Assoc Radiol J* 2019; **70:** 282-91. doi: 10.1016/j.carj.2019.03.005

research article

Reliability of haemophilia early arthropathy detection with ultrasound (HEAD-US) in children: a comparative magnetic resonance imaging (MRI) study

Domen Plut[1,2], Barbara Faganel Kotnik[3], Luka Pusnik[2], Peter Slak[1,2], Ziga Snoj[1,2], Vladka Salapura[1,2]

[1] Clinical Radiology Institute, University Medical Centre Ljubljana, Ljubljana, Slovenia
[2] Faculty of Medicine, University of Ljubljana, Ljubljana, Slovenia
[3] Department of Haematology and Oncology, Children's Hospital, University Medical Centre Ljubljana, Slovenia

Radiol Oncol 2022; 56(4): 471-478.

Received 23 August 2022
Accepted 4 September 2022

Correspondence to: Assist. Prof. Domen Plut, M.D., Ph.D., Clinical Radiology Institute, University Medical Centre Ljubljana, Zaloška cesta 7, SI-1000 Ljubljana, Slovenia. E-mail: plut.domen@gmail.com

Disclosure: No conflicts of interest were disclosed.

Background. Ultrasound (US) has been proven to be reliable in the assessment of early haemophilic arthropathy in the adult haemophilic population, however few studies so far focused on the reliability of US specifically in the paediatric haemophilic population. We were interested if the changing appearance of the growing bone hinders the ultrasonographic evaluation of the pathologic processes caused by haemophilic arthropathy. The aim of the study was to assess the reliability of US for evaluation of haemophilic arthropathy in children in comparison to magnetic resonance imaging (MRI).

Patients and methods. The study included all children aged 6 years or more with severe haemophilia in the country (n = 10). We assessed their elbows, knees, and ankles bilaterally by US and compared the results to the MRI as the reference standard. Pearson correlation coefficient (r) was used to analyse correlation.

Results. The correlation with MRI for the US for the total score was excellent for all joints (r = 0.849 for the elbows, r = 1 for knees, r = 0.842 for ankles). The correlation of scores for specific joint components showed fair, moderate, or excellent correlation for all joint components in all joints. The correlation was the lowest for the evaluation of cartilage and bone in the ankles (r = 0.546 and r = 0.478) and bone in the elbows (r = 0.499).

Conclusions. Our study proved that US using the HEAD-US method performed by paediatric radiologists is a reliable tool for detection and quantification of haemophilic arthropathy in children in comparison to MRI.

Key words: haemophilia; children; haemophilic arthropathy; HEAD-US; ultrasound; magnetic resonance imaging

Introduction

Haemophilic arthropathy (HA) is caused by recurrent bleeding into joints and is characterized by synovial hypertrophy with hemosiderin deposition, cartilage destruction, and structural changes of subchondral bone. Long-term repeated hemarthroses lead to joint destruction and severe functional impairment.[1] As the development of HA ordinarily begins during childhood, albeit with minimal changes, early detection is indispensable. Early recognition of subclinical arthropathy based on the imaging modalities is fundamental as it enables appropriate prophylactic treatment modification and prevents further disease progression.[2,3] Among the imaging tools, magnetic resonance

imaging (MRI) with its high spatial and contrast resolution is superior to the other modalities and enables the most precise assessment of early arthropathic changes.[4] As MRI is a time-consuming modality with limited availability, a high cost, and requires sedation in young children, routine assessment of multiple joints with it is not feasible. Ultrasound (US) has been proven to be highly reliable in the assessment of early inflammatory and destructive joint changes in the adult haemophilic population[5-7], however very few studies so far focused on the reliability of US in the paediatric haemophilic population. The US has even more advantages in the paediatric population: it is a safe technique without radiation, it enables a quick assessment of multiple joints, and sedation is not required even in young children. Thus, with possible detection of joint effusions, synovial hypertrophy, cartilage changes, and subchondral bone erosions it may be an invaluable tool for recognition of subclinical HA in children.[8,9]

We were interested if the changing appearance of the growing bone hinders the ultrasonographic evaluation of the pathologic processes caused by HA. Hitherto, a paucity of data has been published regarding US measurements of hyaline cartilage thickness in healthy children in comparison to MRI measurements. Consequently, published values are not standardised and require further research to distinguish unaffected growing bone from the pathologic processes caused by HA.[10–14] The aim of our study was to assess the reliability of the US for evaluation of haemophilic arthropathy in children in comparison to the MRI.

Patients and methods

Board approval

The study was approved by the National Medical Ethics Committee (reference number 0120-523/2015-8). The participants in this study were children, therefore informed consent for the participants was signed by their parents. The participants, however, gave their informed assent to the study. Research was conducted following the Helsinki Declaration.

Patients

The study included all children with severe haemophilia A in the country. The patients were recruited at the Slovenian National Haemophilia Comprehensive Care Centre at the University Medical Centre Ljubljana. The inclusion criteria were: diagnosis of severe haemophilia A, prophylactic treatment with factor concentrates, and age between 6 and 18 years. The age of 6 years as the low cut-off was chosen to avoid the need for anaesthesia for the MRI. The exclusion criteria were non-cooperation and contraindications for the MRI. Patient history (history of joint bleeds, haemophilia joint health score (HJHS), prophylaxis information) was retrieved from their medical records.

Ultrasonography

A ProSound F75 US scanner with a 13–5 MHz electronic linear-array transducer (Hitachi Aloka Medical, Ltd. Tokyo, Japan) was used to perform the US examinations. US was performed by an experienced paediatric radiologist (7 years of subspecialty experience). The assessment of each joint was made using the HEAD-US protocol and scoring method. This standardised method includes bilateral systematic evaluation of the elbows, knees, and ankles in defined positions for the detection of hypertrophied synovium and osteochondral damage. The results for each joint are expressed on a 9-point scale (0–8; 0 corresponds to the best joint condition, while 8 corresponds to the worst joint condition).[8] The total scanning time per patient for all joints combined was approximately 20 minutes. A series of images and clips from all examinations for each patient were additionally independently reviewed and scored by another paediatric radiologist (2 years of subspecialty experience) to determine the inter-rater reliability. Both US reviewers were blinded to the results of MRI examinations.

Magnetic resonance imaging

MRI was performed on a 3T Achieva unit (Philips Healthcare, Eindhoven, The Netherlands). Phased array coils were used for the imaging of each joint. The protocol included 3D T2*-weighted water selective gradient echo sequence (FOV, 160×160×108mm; voxel size, 0.58×0.58×0.50mm; flip angle: 15°; TE 9.2/6.1ms; TR 26ms), and 3D proton density (PD) weighted turbo spin echo sequence (FOV, 160×160×161mm; voxel size: 0.52×0.52×0.52mm; TE 33ms; TR 1000ms). The total scanning time for each joint was approximately 15 minutes. In each patient, all joints were scanned in a single session for a total examination time around 1.5 hours. The MRI examinations were scored according to the International Prophylaxis Study Group (IPSG)

TABLE 1. Characteristics of subjects included in the study

Age: mean; range (years)	11.5; 6–17			
Age at the start of prophylaxis: mean; range (years) Primary prophylaxis – 5 patients: Secondary prophylaxis – 5 patients:	3; 0.8–6.6 2.2; 0.8–3.8 3.8; 2.5–6.6			
Duration of prophylaxis: mean; range (years)	9.1; 3.2–14.7			
Haemophilia Joint Health Score (HJHS): mean; range	0.9; 0–7			
Number of previous joint bleeds per patient: mean; range	16.2; 0–83			
Number of previous joint bleeds per joint: mean; range	2.5; 0–71			
Number of previous joint bleeds:	Elbows	Knees	Ankles	Overall
0 (number of joints)	14	7	9	30
1–4 (number of joints)	5	12	8	25
> 5 (number of joints)	1	1	3	5

MRI scale. The IPSG score includes evaluation of joint effusion, hypertrophied synovium with hemosiderin deposition, and osteochondral damage. The IPSG score uses an 18-point scale (0–17; 0 corresponds to the best joint condition with no disease present, while 17 corresponds to the worst joint condition with progressive arthropathy).[15] The presence of HA was defined as IPSG score > 0. The scoring was performed independently by two experienced musculoskeletal radiologists (19 and 4 years of subspecialty experience) who were blinded regarding the results of the US examinations.

Statistical analysis

Descriptive statistics were obtained to describe the characteristics of the study group. Pearson correlation coefficient (r) was used to analyse the correlation between US and MRI examinations. Correlation was considered poor if r was < 0.3, fair if r was < 0.6, substantial if r was < 0.8, and excellent if r was > 0.8.[16] The correlation results were graphically illustrated. The inter-rater reliability of HEAD-US and IPSG MRI scoring system for the total scores was made with Lin's concordance correlation coefficient (CCC) and for all the sub-scores using Cohen's kappa statistics (with quadratic weights). The results of US were referenced to the results of MRI in order to obtain measures of diagnostic accuracy (specificity, sensitivity, positive predictive value, and negative predictive value). Statistical analysis was performed using IBM SPSS Statistics for Windows software, version 25 (IBM Corp.). A two-tailed P value < 0.05 was considered to indicate statistical significance.

Results

Patient and joint characteristics

The study group included a total of 10 patients (age range 6 to 17 years, mean age 11.5 years). In each patient, six joints (elbows, knees, and ankles bilaterally) were systematically examined first using the US, followed by MRI, according to the protocols. Altogether in the study we assessed 60 joints: 20 elbows, 20 knees, and 20 ankles.

All the patients included in the study have been receiving prophylactic treatment with clotting factor concentrates. The type of prophylaxis for the patients was primary or secondary. The patients were on three times per weekly regimen. A proportion of patients were on individual prophylactic regimens according to population-based pharmacokinetic tools. Two patients developed inhibitors to prophylactic treatment. In one patient the inhibitors were successfully eradicated by immune tolerance induction. Details on treatment and joint-bleeds history are shown in Table 1 along with other study group baseline characteristics.

Results of US and MRI

Descriptive statistics for US and MRI results are gathered in Table 2.

MRI results were used as a reference standard for joint status. The results of the correlation between US and MRI for detection and evaluation of HA in children are summarized in Table 3. The correlation with MRI for each joint type is graphically depicted in Figure 1. The correlation with MRI for US for the total score was excellent for all

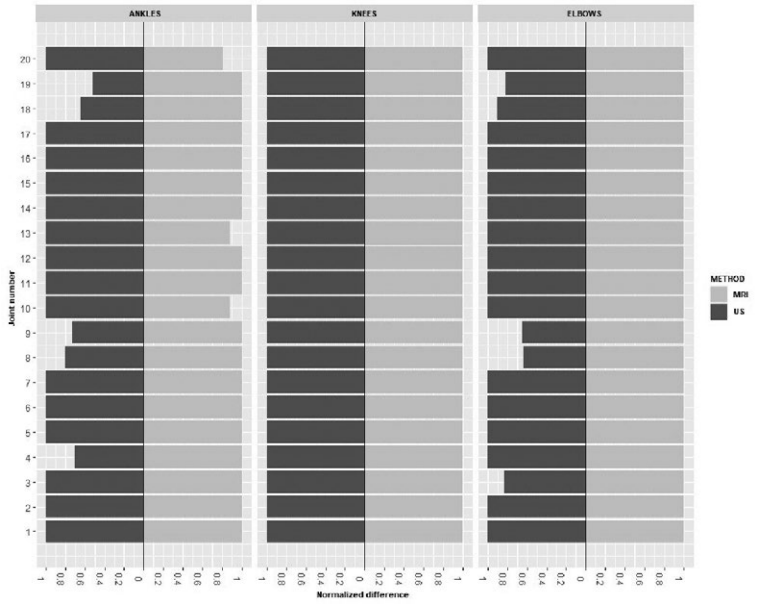

FIGURE 1. Concordance plot for depicting agreement between US and MRI scores for all three joints. Equal size of the fields denotes perfect agreement. The plots demonstrate overall an excellent agreement between the methods. It can also be observed, that in most cases of discordance, US slightly undervalued the progression of the joint disease.

joints (r = 0.849 for the elbows, r = 1 for knees, r = 0.842 for ankles). The correlation of scores for specific joint components showed fair, moderate, or excellent correlation for all joint components in all joints. The correlation was the lowest for the evaluation of cartilage and bone in the ankles (r = 0.546 and r = 0.478) and bone in the elbows (r = 0.499). Figures 2-5 show images from the study.

The inter-rater reliability of interpretation was excellent for the US examinations of all joints. The Lin's CCC values for the total scores ranged from 0.986 to 1.000. The inter-rater reliability for the MRI was also excellent for all joints with the CCC values for the total scores ranging from 0.957 to 0.993.

Measures of diagnostic accuracy

Our study included 49 joints (15 elbows, 20 knees, and 14 ankles) with no signs of HA on MRI (IPSG scores were 0) and 11 joints with HA (5 elbows and 6 ankles). The IPSG MRI score of joints with HA ranged from 1 to 8, mean was 4.8. Two joints that showed signs of HA on MRI (two elbows in the same patient with IPSG MRI scores 4 and 1) were scored 0 on the US. There was one false positive on the US, an ankle with a score of 1. The calculated measures of diagnostic accuracy for HEAD-US are presented in Table 4.

TABLE 2. Descriptive statistics for US and MRI assessment scores

Joints	Statistic	US	MRI
Elbows	% of zeros	85	75
	Median	0	0
	Mean	0.35	1.05
	SD	0.93	2.82
Knees	% of zeros	100	100
	Median	0	0
	Mean	0	0
	SD	0	0
Ankles	% of zeros	65	70
	Median	0	0
	Mean	0.8	1.6
	SD	1.2	2.2
Overall	% of zeros	83.3	81.7
	Median	0	0
	Mean	0.38	0.88
	SD	0.92	2.16

TABLE 3. The results of the correlation analysis

US vs MRI	Pearson's correlation coefficient (r)		
	Elbows	Knees	Ankles
Total score	0.849	1	0.842
Synovium	0.841	1	0.722
Cartilage	0.829	1	0.546
Bone	0.499	1	0.478

Note: all the reported correlations are statistically significant ($p < 0.05$).

Discussion

Our study aimed to evaluate the reliability of US (HEAD-US scanning protocol and scoring method) for the detection and evaluation of haemophilic arthropathy in children in comparison to MRI (ISPG MRI scoring scale). We evaluated the three most commonly affected joints (ankles, knees, and elbows) in all children with severe haemophilia A in our country (n = 10). Overall, we evaluated 60 joints. The results of the correlation analysis showed a very high correlation for the evaluation of haemophilic arthropathy between the US and

TABLE 4. Measures of diagnostic accuracy for detection of haemophilic arthropathy by US (HEAD-US) in comparison to MRI (IPSG MRI score) as the reference standard

Specificity	81.8%
Sensitivity	98%
Positive predictive value	90%
Negative predictive value	96%

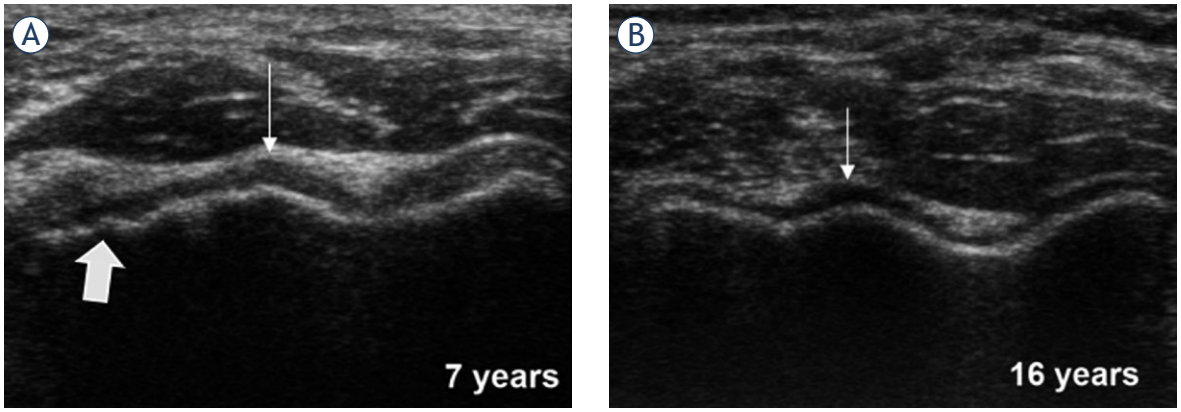

FIGURE 2. Anterior transverse US images over the distal humeral epiphysis in a 7-years and 16-years old healthy boys. A wavy osteochondral surface consisting of the convex capitellum and the concave trochlea is shown. Note the age-dependent anatomic differences: subchondral bony surface in the younger child **(A)** shows physiological irregularities (thick arrow); the articular cartilage, which appears as a uniform hypoechoic band overlying the subchondral bone (thin arrows), is thinner in the older child **(B)**.

MRI for all the joints (r = 0.849 for elbows; r = 1 for knees; r = 0.842 for ankles). Excellent inter-rater reliability for both the US and MRI in our study further supports the validity of both methods for haemophilia imaging in children.

These results show that the HEAD-US method is reliable in comparison to MRI for the detection and quantification of HA in children. High specificity and sensitivity (81.8% and 98%) confirm the method as a dependable tool for the recognition of the presence of HA, whereas high correlation proves the method is also reliable in the quantification of the disease progression. Our results indicate that US is reliably applicable for all evaluated joints (elbows, knees, and ankles), however the detailed analysis of the joint components (synovium, cartilage, bone) showed some important differences. The correlation between the methods was the lowest for the evaluation of the cartilage and bone changes of the ankles (r = 0.546 and 0.478) and bone changes of the elbows (r = 0.499) in comparison to other joint components (r > 0.7). The

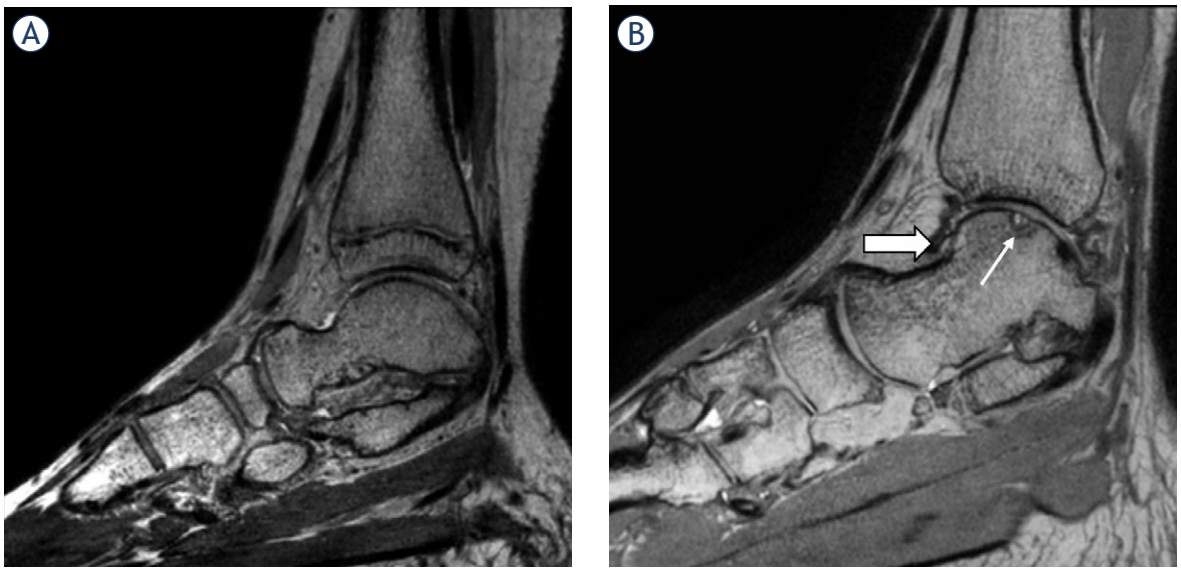

FIGURE 3. PD weighted MRI of ankles in sagittal plane. Image **(A)** shows an ankle with no signs of haemophilic arthropathy in an 11-years old boy, while image **(B)** shows a severely affected ankle in a 17-years old boy. The thin arrow marks a talar osteochondral defect, while the thick arrow marks synovial hypertrophy with hemosiderin deposition.

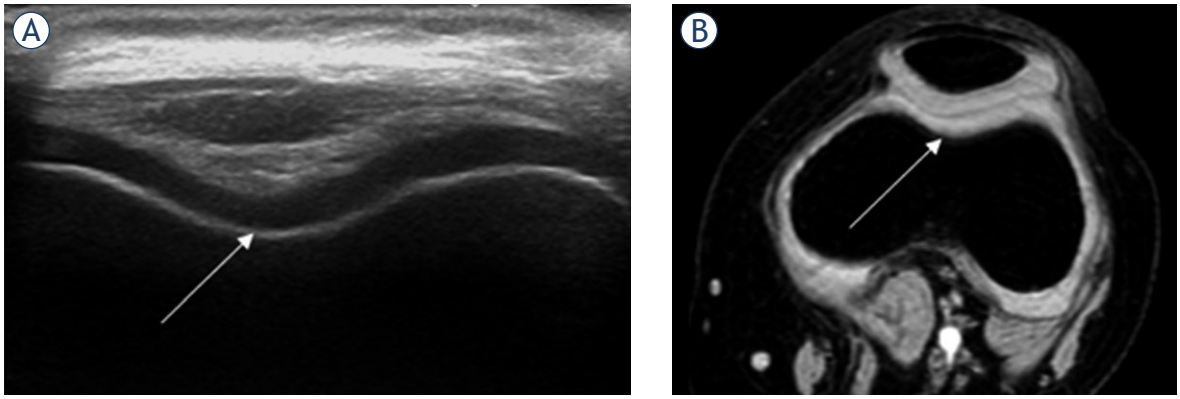

FIGURE 4. An example of good concordance between HEAD-US and MRI in a 7-years old child. US image of the femoral trochlea in the transverse plane is shown **(A)**. T2* weighted MR image in the transverse plane **(B)** of the same knee is shown for comparison of the corresponding structures. The smooth bone surface and normal thickness trochlear joint cartilage with homogenous structure are shown (white arrow); the corresponding intact structures are shown on MR image. On MRI, there were also no additional arthropathic changes in the parts of the joint not visualized by the US. The images show a perfect concordance between US and MRI findings in this knee with no signs of haemophilic arthropathy.

lower correlation for the evaluation of osteochondral changes in the ankles was due to the limited visualization of the central weight-bearing part of the osteochondral surface of the ankle joint by US, which is a more commonly affected area of the joint. Comparable results were observed in our previously performed study in the adult population.[17] Similarly, the lower correlation for the bone changes in the elbows was due to inability of the US to detect centrally located subchondral cysts. Nevertheless, as noted above, the overall correlation between both methods for all the joint components for all the joints was still substantial. In our study in the adult population, we observed a lower correlation between the US and MRI for the detection and evaluation of synovial hypertrophy in the ankles (r = 0.561). In this study in the paediatric population however, this was not the case (r = 0.722). We believe this can be attributed to a generally better ability of US to differentiate soft tissues in children due to a higher tissue water content. As synovial hypertrophy is the earliest sign of HA, high reliability to evaluate this finding in all joints in children is important for the clinical application of the method.

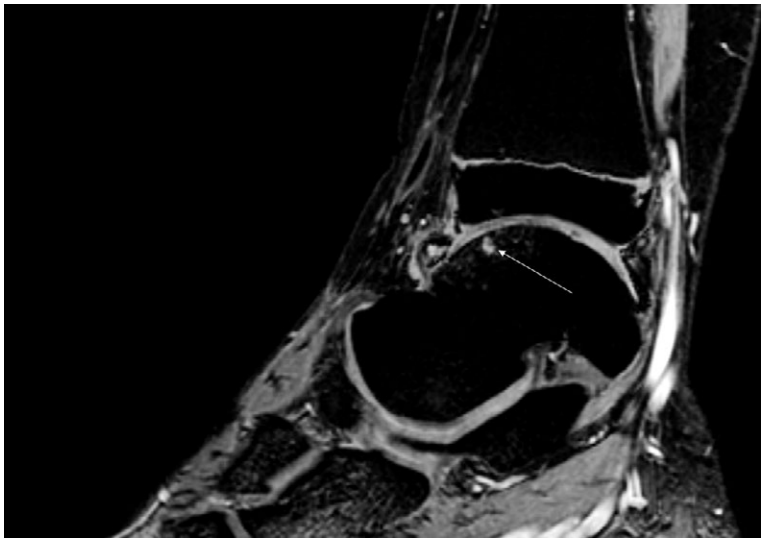

FIGURE 5. An example of a lesion causing a discordance between the US and MRI. A T2* weighted MR image of an ankle of a 16-years old boy in the sagittal plane is shown. A small subchondral cyst covered with intact cortical bone and articular cartilage (white arrow) is shown. MRI demonstrates a defect which cannot be visualized by US.

In the published literature, the comparisons of the joint assessment between the US and MRI within the paediatric haemophilic population are scant. Only three studies included exclusively children within their study group. Doria *et al.* evaluated ankles and knees in children with haemophilia and von Willebrand disease and reported that if performed by experienced radiologists US is highly reliable for assessing soft-tissue abnormalities and substantially to highly reliable for assessing osteochondral changes in these joints. These results are concordant with the findings of our study. However, it is worthy to note that in their study the US interpreters were unblinded to the MRI results.[6] Prasetyo *et al.* evaluated knees in 27 children with haemophilia, employing a complex US examination including Doppler evaluation and evaluation of hemosiderin deposits, and reported moderate correlation between the US and MRI scores.[18] In another study that evaluated ankles in

11 boys with haemophilia, Prasetyo *et al.* evaluated only the ability of US to detect hemosiderin deposits within the joint and determined that the association between the US and MRI for detection of hemosiderin deposits was weak.[19] Additional two studies included children as a part of their study group. Sierra Aisa *et al.* included patients with HA between the age of 4-82 years and reported sensitivity, specificity, positive predictive value, and negative predictive value for diagnosing HA within the same interval as presented in our study.[5] Acharya *et al.* evaluated the use of US with Power Doppler in comparison to contrast-enhanced MRI to detect haemophilic synovitis in subjects between the ages of 6-60 years and concluded that the correlation between the methods is good.[20] All of the aforementioned studies already showed great potential for the use of US in the diagnostics of HA in children, however, each study had some limitations, such as different and complex US protocols or evaluation limited to specific joints or joint components. Therefore, in our study we used a simplified standardized US protocol (HEAD-US) for the joint evaluation, which allows quick examination with great repeatability, we systematically evaluated all three most commonly involved joints in haemophilia, and made sure the US evaluators were blinded to the results of the MRI examination.

The findings of the currently presented study and our previously published study in the adult population[17] made us reconsider our clinical practice. Due to the good availability of US machines and reliability of the US to detect even early HA in clinically asymptomatic joints, we incorporated the US into our regular clinical yearly follow-up of paediatric patients with haemophilia. All the children with severe haemophilia in our country have been included in the screening program, even children younger than 6 years old. During this time, we found early HA in clinically asymptomatic joints with no previously recorded bleeds in two children and consequently modified their prophylactic treatment regimen.

The study had some research design limitations. Although our study group included all children with severe haemophilia A in the country, due to the rarity of the disease, the overall number of patients was relatively low (n = 10). Furthermore, we couldn't include the youngest children with haemophilia aged under 6 years due to the requirement of general anaesthesia to perform MRI in this group of children. Most joints we evaluated in our study were either healthy or had only early HA. This is because HA is a progressive chronic disease and all of the included patients had prophylactic treatment since the early youth, therefore more progressive disease forms were prevented. However, extensive studies evaluating the value of US in comparison with MRI in patients with progressive HA have been already performed in the adult population and, moreover, diagnosing early HA remains the challenge for today's medicine.

Conclusions

Our study proved that US using the HEAD-US method performed by paediatric radiologists is a reliable tool for detection and quantification of haemophilic arthropathy in children in comparison to MRI. Due to its simplicity, availability, and reliability, HEAD-US is an invaluable tool in diagnostics and regular follow-up of children with haemophilia and can be safely included into the regular screening protocols of children with severe haemophilia where possible. Further studies are needed to answer some important questions regarding the use of HEAD-US in children with haemophilia: what is the ideal start age for the screening? How often should the screening be performed during the childhood, and who should perform the scanning (radiologist, clinician, physiotherapist)?

Acknowledgments

This study was funded by Pfizer Inc., USA. The authors have no competing interests. We would like to thank Anja Silič, Marko Gabrijelčič, Damjana Ključevšek, and Lidija Kitanovski for their contribution to the study.

References

1. Gualtierotti R, Solimeno LP, Peyvandi F. Hemophilic arthropathy: current knowledge and future perspectives. *J Thromb Haemost* 2021; **19:** 2112-21. doi: 10.1111/jth.15444
2. Plut D, Faganel Kotnik B, Preložnik Zupan I, Ključevšek D, Vidmar G, Snoj Ž, et al. Detection and evaluation of haemophilic arthropathy: which tools may be considered more reliable. *Haemophilia* 2021; **27:** 156-63. doi: 10.1111/hae.14153
3. Pergantou H, Platokouki H, Matsinos G, Papakonstantinou O, Papadopoulos A, Xafaki P, et al. Assessment of the progression of haemophilic arthropathy in children. *Haemophilia* 2010; **16:** 124-9. doi: 10.1111/j.1365-2516.2009.02109.x
4. Kilcoyne RF, Nuss R. Radiological assessment of haemophilic arthropathy with emphasis on MRI findings. *Haemophilia* 2003; **9:** 57-64. doi: 10.1046/j.1365-2516.9.s1.11.x

5. Sierra Aisa C, Lucía Cuesta JF, Rubio Martínez A, Fernández Mosteirín N, Iborra Muñoz A, Abío Calvete M, et al. Comparison of ultrasound and magnetic resonance imaging for diagnosis and follow-up of joint lesions in patients with haemophilia. *Haemophilia* 2014; **20:** e51-7. doi: 10.1111/hae.12268

6. Doria AS, Keshava SN, Mohanta A, Jarrin J, Blanchette V, Srivastava A, et al. Diagnostic accuracy of ultrasound for assessment of hemophilic arthropathy: MRI correlation. *Am J Roentgenol* 2015; **204:** W336-47. doi: 10.2214/AJR.14.12501

7. De la Corte-Rodriguez H, Rodriguez-Merchan EC, Jimenez-Yuste V. Point-of-care ultrasonography in orthopedic management of hemophilia: multiple uses of an effective tool. *HSS J* 2018; **14:** 307-13. doi: 10.1007/s11420-018-9604-x

8. Martinoli C, Casa Alberighi O Della, Di Minno G, Graziano E, Claudio Molinari A, Pasta G, et al. Development and definition of a simplified scanning procedure and scoring method for haemophilia early arthropathy detection with ultrasound (HEAD-US). *Thromb Haemost* 2013; **109:** 1170-9. doi: 10.1160/TH12-11-0874

9. Di Minno MND, Iervolino S, Soscia E, Tosetto A, Coppola A, Schiavulli M, et al. Magnetic resonance imaging and ultrasound evaluation of "healthy" joints in young subjects with severe haemophilia A. *Haemophilia* 2013; **19:** e167-73. doi: 10.1111/hae.12107

10. Keshava SN, Gibikote SV, Mohanta A, Poonnoose P, Rayner T, Hilliard P, et al. Ultrasound and magnetic resonance imaging of healthy paediatric ankles and knees: a baseline for comparison with haemophilic joints. *Haemophilia* 2015; **21:** e210-22. doi: 10.1111/hae.12614

11. Soliman M, Daruge P, Dertkigil SSJ, De Avila Fernandes E, Negrao JR, de Aguiar Vilela Mitraud S, et al. Imaging of haemophilic arthropathy in growing joints: pitfalls in ultrasound and MRI. *Haemophilia* 2017; **23:** 660-72. doi: 10.1111/hae.13249

12. Samanta M, Mitra S, Samui PP, Mondal RK, Hazra A, Sabui TK. Evaluation of joint cartilage thickness in healthy children by ultrasound: an experience from a developing nation. *Int J Rheum Dis* 2018; **21:** 2089-94. doi: 10.1111/1756-185X.13374

13. Spannow A, Stenboeg E, Pfeiffer-Jensen M, Fiirgaard B, Haislund M, Ostergaard M, et al. Ultrasound and MRI measurements of joint cartilage in healthy children: a validation study. *Ultraschall Med* 2010; **32(Suppl 1):** S110-6. doi: 10.1055/s-0029-1245374

14. Sidharthan S, Yau A, Almeida BA, Shea KG, Greditzer HG, Jones KJ, et al. Patterns of articular cartilage thickness in pediatric and adolescent knees: a magnetic resonance imaging–based study. *Arthrosc Sport Med Rehabil* 2021; **3:** e381-90. doi: 10.1016/j.asmr.2020.09.029

15. Lundin B, Manco-Johnson ML, Ignas DM, Moineddin R, Blanchette VS, Dunn AL, et al. An MRI scale for assessment of haemophilic arthropathy from the International Prophylaxis Study Group. *Haemophilia* 2012; **18:** 962-70. doi: 10.1111/j.1365-2516.2012.02883.x

16. Chan YH. Biostatistics 104: correlational analysis. *Singapore Med J* 2005; **46:** 153-60.

17. Plut D, Kotnik BF, Zupan IP, Kljucevsek D, Vidmar G, Snoj Z, et al. Diagnostic accuracy of haemophilia early arthropathy detection with ultrasound (HEAD-US): a comparative magnetic resonance imaging (MRI) study. *Radiol Oncol* 2019; **53:** 178-86. doi: 10.2478/raon-2019-0027

18. Prasetyo M, Gatot D, Tulaar A, Pandelaki J, Bardosono S, Sukrisman L, et al. Association between US and MRI scores and correlations with urinary C-terminal telopeptide Type II collagen levels for early detection of hemophilic arthropathy of the knee. *J Phys Conf Ser* 2018; **1073:** 042022. doi: 10.1088/1742-6596/1073/4/042022

19. Prasetyo M, Mongan AE, Chozie NA, Prihartono J, Setiawan SI. Hemosiderin deposition evaluation in hemophilic ankle joints: association between US finding and gradient-recalled echo MR imaging sequence. *Insights Imaging* 2021; **12:** 1-7. doi: 10.1186/s13244-021-01050-1

20. Acharya SS, Schloss R, Dyke JP, Mintz DN, Christos P, Dimichele DM, et al. Power Doppler sonography in the diagnosis of hemophilic synovitis - a promising tool. *J Thromb Haemost* 2008; **6:** 2055-61. doi: 10.1111/j.1538-7836.2008.03160.x

research article

MRI-identified multidimensional nodal features predict survival and concurrent chemotherapy benefit for stage II nasopharyngeal carcinoma

Yang Liu[1], Jianghu Zhang[1], Jingbo Wang[1], Runye Wu[1], Xiaodong Huang[1], Kai Wang[1], Yuan Qu[1], Xuesong Chen[1], Yexiong Li[1], Ye Zhang[1], Junlin Yi[1,2]

[1] Department of Radiation Oncology, National Cancer Center/National Clinical Research Center for Cancer/Cancer Hospital, Chinese Academy of Medical Sciences and Peking Union Medical College, China

[2] Department of Radiation Oncology, National Cancer Center/National Clinical Research Center for Cancer/Hebei Cancer Hospital, Chinese Academy of Medical Sciences (CAMS), China

Radiol Oncol 2022; 56(4): 479-487.

Received 10 September 2022
Accepted 11 October 2022

Correspondence to: Junlin Yi, M.D., Ph.D., 17 Panjiayuan Nanli, Chaoyang District, Beijing, 100021, P.R. China and Tongxi Road, Guangyang District, Langfang, Hebei Province, 065001, P.R. China. E-mail: yijunlin1969@163.com and Ye Zhang, MD, PhD, 17 Panjiayuan Nanli, Chaoyang District, Beijing, 100021, P.R. China. E-mail: dr_zye1983@163.com

Dr. Yang Liu and Dr. Jianghu Zhang contributed equal to the work.

Disclosure: No potential conflicts of interest were disclosed.

Background. Reliable predictors are urgently needed to identify stage II nasopharyngeal carcinoma (NPC) patients who could benefit from concurrent chemoradiotherapy (CCRT). We aimed to develop a nomogram integrating MRI-identified multidimensional features of lymph nodes to predict survival and assist the decision-making of CCRT for stage II NPC.

Patients and methods. This retrospective study enrolled 242 stage II NPC patients treated from January 2007 to December 2017. Overall survival (OS) was the primary endpoint. Performance of nomogram was evaluated using calibration curves, Harrell Concordance Index (C-index), area under the curve (AUC) and decision curves analysis (DCA) and was compared with TNM staging. According to the individualized nomogram score, patients were classified into two risk cohorts and therapeutic efficacy of CCRT were evaluated in each cohort.

Results. Three independent prognostic factors for OS: age, number and location of positive lymph nodes were included into the final nomogram. T stage was also incorporated due to its importance in clinical decision-making. Calibration plots demonstrated a good match between the predicted and our observed OS rates. C-index for nomogram was 0.726 compared with 0.537 for TNM staging ($p < 0.001$). DCAs confirmed the superior clinical utility of nomograms compared with TNM staging. CCRT compared to intensity-modulated radiotherapy (IMRT) delivered OS benefit to patients in the high-risk group (5-year: 89.9% *vs.* 72.1%; 10-year: 72.5% *vs.* 34.2%, $p = 0.011$), but not in the low-risk group.

Conclusions. This lymph node features-based nomogram demonstrated excellent discrimination and predictive accuracy for stage II patients and could identify patients who can benefit from CCRT.

Key words: nasopharyngeal carcinoma; stage II; concurrent chemotherapy; nomogram; nodal features

Introduction

Nasopharyngeal carcinoma (NPC) is a disease in head and neck that is especially prevalent in Southeast Asia, with an age-standardized incidence rate of five per 100,000 population.[1] Given its complex anatomical location and high radiosensitivity, radiotherapy (RT) has been the mainstay of treatment. The predominant failure pattern of distant metastases highlights the importance of chemotherapy to improve survival outcomes in NPC patients.[2,3] Currently, the National Comprehensive

Cancer Network (NCCN) guidelines recommend that concurrent chemoradiotherapy (CCRT) be the primary treatment for T1–2N1M0 patients and T2N0M0 patients with high-risk features.[4] This is based on a prospective phase III study that showed that CCRT provided survival benefits over two-dimensional (2D) conventional RT alone for stage II NPC.[5]

With rapid technological advances, intensity-modulated radiotherapy (IMRT) has yielded excellent treatment outcomes for patients with stage II NPC, with 5-year overall survival (OS) and local control rates exceeding 90%.[6] A recent phase II randomized clinical trial demonstrated that CCRT might be unnecessary for stage II patients treated with IMRT, as it failed to improve treatment efficacy while increasing the incidence of toxicity.[7] A similar recommendation can be found in the latest European Society for Medical Oncology (ESMO) guidelines.[8] Nonetheless, the survival outcomes remain poor for certain populations screened using adverse prognostic determinants (*e.g.*, high plasma Epstein–Barr virus [EBV] DNA levels).[9,10] The latest American Society of Clinical Oncology/Chinese Society of Clinical Oncology (ASCO/CSCO) guideline also highlights that CCRT can be offered when a bulky tumor burden is present.[11] Therefore, the application of CCRT should consider risk assessment, and more effective prognostic factors are urgently needed to identify stage II NPC patients who may benefit from CCRT.

American Joint Committee on Cancer (AJCC) N staging is consistently recognized as one of the most important determinants for prognosis prediction and treatment decision-making in stage II NPC. However, N1 disease represents a heterogeneous setting in which the size of the lymph node ranges from 1 to a 6-cm mass. Furthermore, the unresolved issue is the accuracy and consistency of N staging, which merely considers nodal size, laterality and location. With advances in imaging modalities, MRI imaging-based analyses have extracted diverse nodal features containing essential information closely related to NPC staging, treatment, and prognosis.[12-16] As morphological lymph node features, high-level extranodal extension and central nodal necrosis have consistently been proven to be predictors of distant metastases.[17-19] Furthermore, the burden-related lymph node features, such as volume and number of positive lymph nodes (PLNs), and number of positive lymph node regions, are proved prognostic factors for NPC progression.[20-23] However, to the best of our knowledge, no comprehensive lymph node feature-based prognosis stratification and concurrent chemotherapy decision-making protocol has been reported for patients with stage II NPC.

In this study, we explored the prognostic value of multidimensional lymph node features in stage II NPC patients and established a lymph node feature-based nomogram. Furthermore, we examined the clinical validity of this model in guiding CCRT utility for patients with stage II NPC.

Patients and methods

This study was approved by the Ethics Committee of our institute, and the requirement for informed consent was waived due to its observational nature. The present study was conducted in accordance with the guidelines from the Declaration of Helsinki.

Patients

Between January 2007 and December 2017, 242 stage II NPC patients were consecutively included (restaged according to the 8th AJCC staging system,). The eligibility criteria were as follows (Supplementary Figure 1): (1) histologically confirmed World Health Organization (WHO) type II–III NPC; (2) no evidence of distant metastases; (3) complete pretreatment evaluation and having complete baseline MRI scans of the nasopharynx and neck; and (4) treatment with IMRT or CCRT (cisplatin, cumulative dose ≥ 200 mg/m^2).

MRI image acquisition

Head and neck T1- and T2-weighted MRI images (T1WI, T2WI) were obtained with a 1.5 or 3T scanner (GE Healthcare, Discovery MR, United States) axially, coronally, and sagittally. The axial slice thickness was 3 mm from the suprasellar cistern to the inferior margin of the sternal end of the clavicle.

Nodal characteristics identified on MRI images

The gross volumes of the primary tumor and nodes were identified as GTVnx and GTVnd, respectively. The diagnostic criteria of positive lymph nodes included: (1) any cervical lymph node with the shortest diameter > 10 mm, any retropharyngeal lymph node (RPLN) in the lateral group with the minimum diameter > 5 mm, and any visible RPLN in the me-

dian group; (2) central nodal necrosis or a contrast-enhanced rim; (3) extranodal extension; and (4) ≥ 3 contiguous converging lymph nodes, each with an minimum diameter > 8 mm.[24] When more than two lymph nodes could not be distinguished from each other, they were counted as one. The maximal axial diameter of lymph nodes was measured on the largest plane of cross-sectional images. Extranodal extension was assessed on T1-weighted fat-suppressed contrast images and classified as follows (Figure 1): Grade 0, without extranodal extension; Grade 1, infiltrating the surrounding fat; Grade 2, matted nodes; and Grade 3, infiltrating the adjacent muscle, parotid gland, vessels and skin.[13] Central nodal necrosis was identified as a focal area of high signal intensity on T2WI.[19]

Treatment

All 242 patients completed whole-course simultaneous-integrated boost (SIB) IMRT. Doses of 69.96 Gray (Gy)/33 fractions were prescribed for GTVnx and GTVnd. High- and low-risk regions of the clinical target volume (CTV) received a prophylactic dose of 60.06 Gy/33 fractions and 50.96 Gy/28 fractions, respectively. The concurrent chemotherapy plan included a weekly (40 mg/m²) or three-weekly (80–100 mg/m²) cisplatin regimen.

Clinical outcomes and follow-up

The primary endpoint was OS (date of treatment start, to date of documented death from any cause or last follow-up). The secondary endpoints were disease-specific survival (DSS, date of treatment start to date of documented death from NPC-related cause or last follow-up), regional recurrence-free survival (RRFS, date of treatment start to date of the first observation of regional recurrence) and distant metastasis-free survival (DMFS, date of treatment start to date of the first observation of distant metastases).

Patients were followed up at least every three months for the first two years, every six months for the third to fifth years, and then yearly. Evaluations included complete physical examination, fiberoptic nasopharyngoscopy, MRI of the nasopharynx and neck, chest X-ray/CT, and abdomen sonography/CT with or without bone scans. Other additional investigations (*e.g.*, FDG PET/CT) would also be scheduled if clinically necessary. Late toxicities were assessed according to the Common Terminology Criteria for Adverse Events (CTCAE) version 4.0.

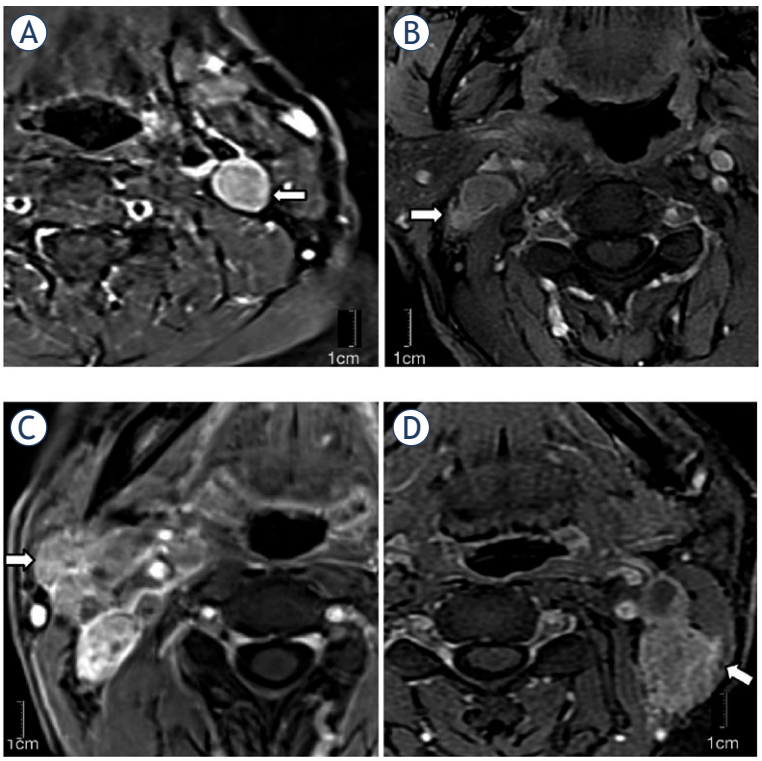

FIGURE 1. Axial T1-weighted fat-suppressed contrast MRI images of grade 0–2 extranodal extension (ENE) in four stage II nasopharyngeal carcinoma patients. **(A)** Grade 0: without ENE; **(B)** Grade 1: lymph node (LN) infiltrating surrounding fat; **(C)** Grade 2: matted LNs; and **(D)** Grade 3: LN infiltrating sternocleidomastoid muscle (wight arrows).

Statistical analysis

The Kaplan–Meier method was performed to estimate survival rates, and log-rank test was used to examine the significance of differences. Youden indexes derived from the time-dependent receiver operating characteristic (ROC) analysis were utilized to dichotomize continuous variables into categorical variables and determine the optimal cutoffs. Cox proportional hazards regression with backward selection was performed in multivariable analysis (MVA) and to calculate hazard ratios (HRs). To assess the effect of the continuous variables on OS, an additive Cox model was used to generate pointwise estimates of HR curves by using the "smoothHR" package.[25] Based on the risk factors identified by MVA, a nomogram was developed. The calibration curves, Harrell concordance index (C-index), area under the curve (AUC) and decision curve analysis (DCA) were used to evaluate the performance of nomogram. Each patient was stratified into low- or high-risk groups based on the final sum of the nomogram scores. R (ver-

TABLE 1. Characteristics of 242 patients with stage II nasopharyngeal carcinoma

Characteristics	No. (%)
Age, median (range)	50 (18–76)
< 50	120 (49.6)
≥ 50	122 (50.4)
Sex	
Male	173 (71.5)
Female	69 (28.5)
AJCC 8th T stage	
T1	104 (43.0)
T2	138 (57.0)
AJCC 8th N stage	
N0	30 (12.4)
N1	212 (87.6)
AJCC 8th subgroup	
T1N1M0	104 (43.0)
T2N0M0	31 (12.8)
T2N1M0	107 (44.2)
GTVnx volume (cm^3), median (range)	19.1 (2.1–74.0)
< 13.7	70 (28.9)
≥ 13.7	172 (71.1)
GTVnd volume (cm^3), median (range)	8.7 (0–71.0)
< 29.1	212 (87.6)
≥ 29.1	30 (12.4)
Lateral of RPLNs	
None	90 (37.2)
Unilateral	113 (46.7)
Bilateral	39 (16.1)
LN located in level III	
Yes	195 (80.6)
No	47 (19.4)
LN size (cm)	1.7 (0–6.0)
MAD < 2.2	152 (62.8)
MAD ≥ 2.2	90 (37.2)
Number of positive LN	2 (0–9)
0	30 (12.4)
1	69 (28.5)
2	60 (24.8)
3	51 (21.1)
4	19 (7.9)
≥ 5	13 (5.4)
†ENE grade	
Grade 0	153 (63.2)
Grade 1,2	52 (21.5)
Grade 3	37 (15.3)
CNN	
No	179 (74.0)
Yes	63 (26.0)
Treatment	
IMRT	158 (65.3)
CCRT	84 (34.7)

† ENE Grade 0 = none; Grade 1 = LN Infiltrating surrounding fat; Grade 2 = matted nodes; and Grade 3 = LN infiltrating adjacent muscle and (or) vessels and(or) skin

AJCC = American Joint Committee on Cancer staging system; CCRT = concurrent chemoradiotherapy; CNN = central nodal necrosis; ENE = extranodal extension; GTVnx/GTVnd = gross target volume of nasopharyngeal tumor/lymph nodes; IMRT = intensity-modulated radiotherapy; LN = lymph node; MAD = maximum diameter; RPLN = retropharyngeal lymph node

sion 4.1.0) and SPSS (version 26.0) were adopted for the statistical analysis. All the tests were two-sided, and significance was defined as $p < 0.05$.

Results

Patient characteristics

The general characteristics of the 242 stage II patients are summarized in Table 1 (median age 50-years old, range 18–76; 173 men, male-to-female ratio 2.5:1). Overall, 158 (65.3%) patients received IMRT, and 84 (34.7%) received CCRT.

Survival and toxicities after treatment

With a median follow-up of 10.3 years (range: 0.6–17.5 years), the 5-year and 10-year OS, DSS, RRFS and DMFS rates of the entire cohort were 91.9% and 79.1%, 93.6% and 86.7%, 96.5% and 93.6%, and 92.3% and 89.1%, respectively. At the last follow-up, 42 (17.4%) patients had died, and 45 (18.6%) experienced treatment failure. The patterns of treatment failure and causes of death are shown in Supplementary Table 1.

Compared with IMRT, patients receiving CCRT had significantly higher rates of Grade 1–2 gastrointestinal reactions, ear toxicities and severe (Grade 3–4) leukopenia. No significant differences were observed in terms of the incidence or severity of late toxicities between the two groups (Supplementary Table 2).

Risk score model and risk stratification

The ROC-determined optimal cutoffs for GTVnx volume, GTVnd volume and lymph node size to predict OS were 13.7 cm^3, 29.1 cm^3 and 2.2 cm, respectively. Smooth HR trend showed that the log HR of overall death increased linearly with an increasing number of PLNs from 1 to 4 and reached a plateau from 5 and above (Supplementary Figure 2). Therefore, the number of PLNs was categorized into 6 groups (*i.e.*, from 0 to 4 and ≥ 5).

Univariate analysis showed that age ≥ 50 years, GTVnd ≥ 29.1 cm^3, lymph nodes located in level III (Figure 2A), lymph node size ≥ 2.2 cm (Figure 2B), PLN number (Figure 2C), and positive central nodal necrosis (Figure 2D) were associated with poor OS. MVA demonstrated that age, location and number of PLNs were independent determinants for OS (Supplementary Table 3). T stage was also included in the nomogram for its importance in clinical decision-making (Figure 3A). The cali-

bration curves manifested excellent consistency in terms of the 5- and 10-year OS (Figure 3B–C).

The C-index of the nomogram in predicting OS was 0.726 (95% CI: 0.638–0.813) in comparison with 0.537 (95% CI: 0.498–0.608) for TNM stage ($p < 0.001$). Analysis of AUCs revealed that the total nomogram score for predicting OS was also significantly superior to TNM staging (Figure 4A). Likewise, DCAs indicated that the risk model had a higher net benefit for predicting 5- and 10-year OS than TNM staging for almost all threshold probabilities (Figure 4B–C).

The linear correlation between the nomogram score and the hazard of overall death is shown in Supplementary Figure 3. Based on cutoffs for the total score, patients were stratified into low-risk (score: 0–134) and high-risk groups (score: >134). There were no significant differences in any endpoint among the T1N1M0, T2N0M0, and T2N1M0 subgroups (Figure 5A–D). The high-risk group had significantly worse OS, DSS, RRFS or DMFS rates than low-risk group (Figure 5E–H).

Nomogram-based adaptive utilization of CCRT

Based on the stratified groups derived from the nomogram, we further analyzed the clinical efficacy of CCRT in two cohorts with different prognoses. Although a trend that CCRT improves OS was observed in the whole population, it did not reach a significant difference (Figure 6A). Nevertheless, high-risk patients could benefit from CCRT compared to IMRT (5-year OS 89.9% *vs.* 72.1% and 10-year OS: 72.5% *vs.* 34.2%, $p = 0.011$), while low-risk patients failed to benefit from CCRT (Figure 6B–C, Figure 7). CCRT did not improve the OS rates among the T1N1M0, T2N0M0, and T2N1 M0 subgroups (Figure 7).

Discussion

In this study, we comprehensively evaluated the prognostic value of multidimensional nodal features in patients with stage II NPC and further established a lymph node feature-based nomogram. The nomogram demonstrated superior predictive performance for OS and outperformed the current AJCC TNM staging. In addition, the nomogram-derived prognostic stratification contributes to identifying high-risk patients who are more likely to benefit from CCRT. To the best of our knowledge, this current study is the first to incorporate

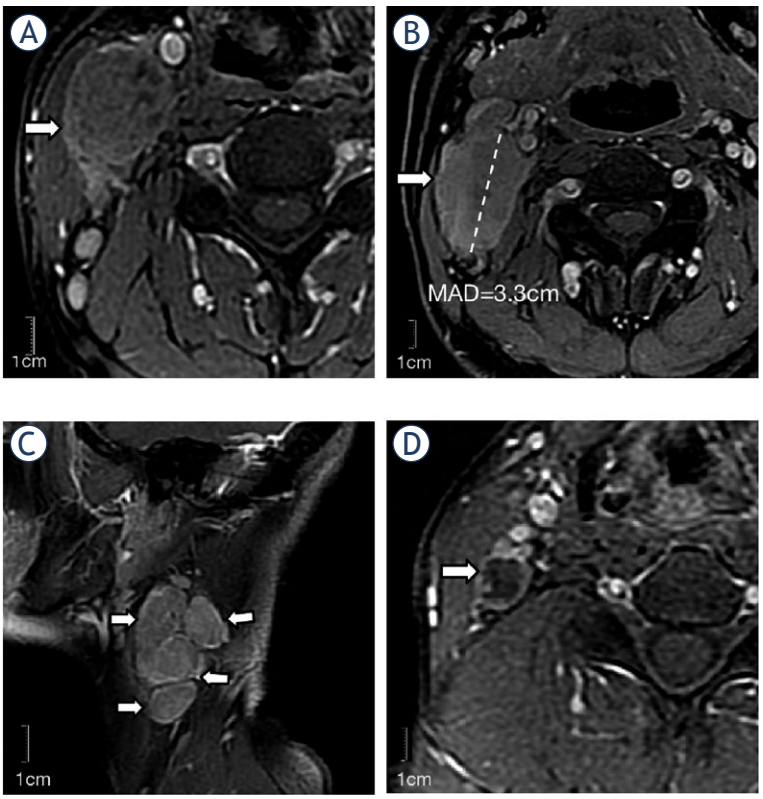

FIGURE 2. Multidimensional nodal features of stage II nasopharyngeal carcinoma significantly associated with survival outcomes in univariate or multivariate analysis. Axial T2-weighted fat-suppressed image of **(A)** a 24-year-old man with one lymph nodes (LN) in level III; **(B)** a 56-year-old man with maximum diameter of lymph node 3.3cm; **(C)** a 50-year-old woman with four metastatic LNs; and (D) Sagittal T1-weighted fat-suppressed contrast images of a 45-year-old woman showing central nodal necrosis (CNN) (wight arrows).

MAD = maximal axial diameter

various nodal features into a nomogram to predict the prognosis of stage II NPC and to further guide the management of concurrent chemotherapy.

The latest NCCN guidelines recommend CCRT for stage II NPC, which is based on a phase III study from the conventional 2D-RT era that showed significant improvements in 5-year OS and progression-free survival (PFS) with CCRT over RT alone.[4] The survival benefit of CCRT might be due to its radiosensitizing effect and the fact that it compensated for the dosimetric deficiencies of the conventional RT technique. In the IMRT era, the role of CCRT in stage II NPC has not been absolutely defined given the paucity of data from phase III trials. The majority of studies revealed that the addition of concurrent chemotherapy did not significantly improve survival but increased the prevalence of acute toxic reactions in patients with stage II NPC.[7,26] Nonetheless, Luo *et al.* reported that

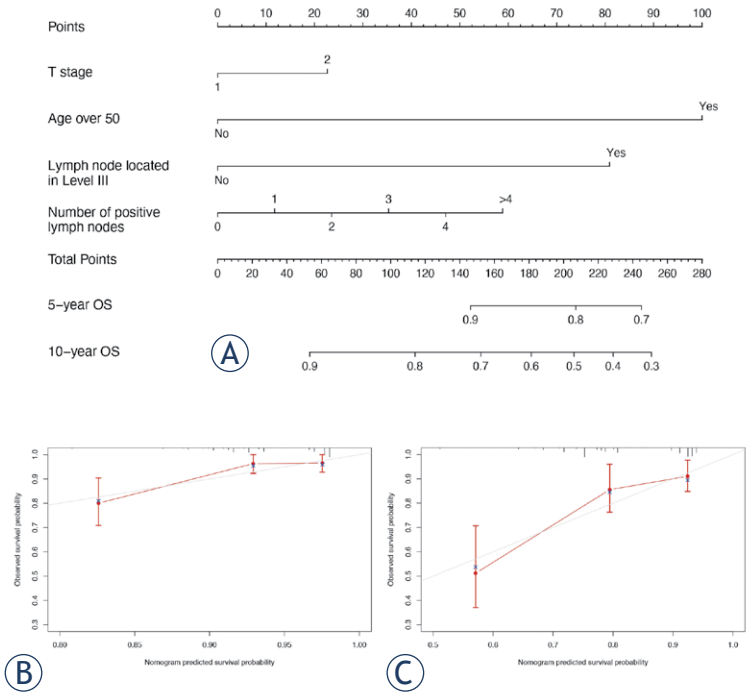

FIGURE 3. Nomogram and calibration plots of 5- and 10-year overall survival (OS). Number of positive lymph nodes was as continuous variable.

T2N1M0 patients receiving CCRT had better 3-year OS, LRFS, and DMFS than those receiving IMRT.[27] Similarly, Kang *et al.* found that CCRT contributed to improving the 5-year locoregional relapse-free survival and PFS for stage II patients.[28] It should be noted that the limitation of the above studies was that all patients were from nonendemic areas, and WHO I/II was the most common histological type. In our study, although a trend that CCRT could improve OS was observed in the whole population, it did not reach a significant difference. Collectively, this evidence supports the utilization of concurrent chemotherapy in a specific portion rather than the stage II disease population. Therefore, it is critical to identify high-risk patients with stage II NPC who are more likely to benefit from CCRT.

Lymph node status is one of the most important determinants associated with prognosis and treatment decisions.[15,16] The determination of AJCC N1 classification depends primarily on the location and size of the ipsilateral cervical lymph nodes. Nonetheless, in recent years, alternative nodal parameters, such as the number of PLNs, extranodal extension and central nodal necrosis status, have been increasingly reported to better assess the profile of nodal burden.[12-16] The number of MRI-positive lymph nodes has been reported to be a predominant independent prognostic factor for survival in NPC patients and is a better proxy for the cumulative effect of lymph nodes than AJCC N staging.[22] Additionally, quantitative metastatic lymph node regions were shown to be superior to N classification in terms of prognosis in NPC.[23] In addition, high-grade extranodal extension was reported as an evaluable predictor that could assist in the selection of stage II patients with a high risk of distant metastases.[13,17,18] Another critical lymph node feature was central nodal necrosis, which was proven to be an independent negative prognostic factor in patients with NPC.[12,16] In the current study, by applying an additive Cox model based on P-penalized, we observed the impact of consecutive PLN on survival: the hazard of overall death increased linearly with increasing PLNs from 1 to 4, eventually reaching a plateau at PLNs of 5 and above. Based on this tendency, PLN surpassed the traditional AJCC N stage and emerged as an independent variable in the MVA model. Likewise, lymph node located in level III was found to be an important prognostic factor that outperformed N stage, which could be explained by the fact that lymph node often metastasizes in an orderly fash-

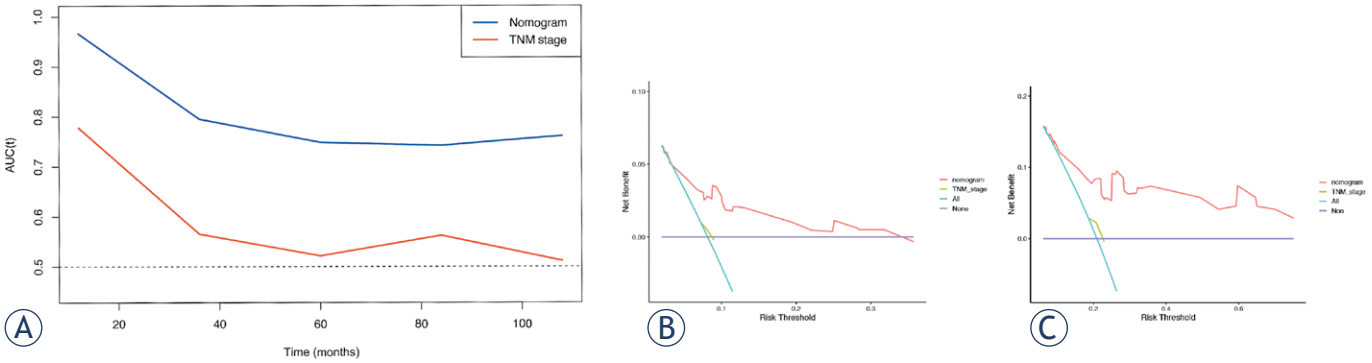

FIGURE 4. Comparison of **(A)** area under the curve (AUC) plots, decision curves of **(B)** 5-year overall survival (OS) and **(C)** 10-year OS between the nomogram and TNM stage.

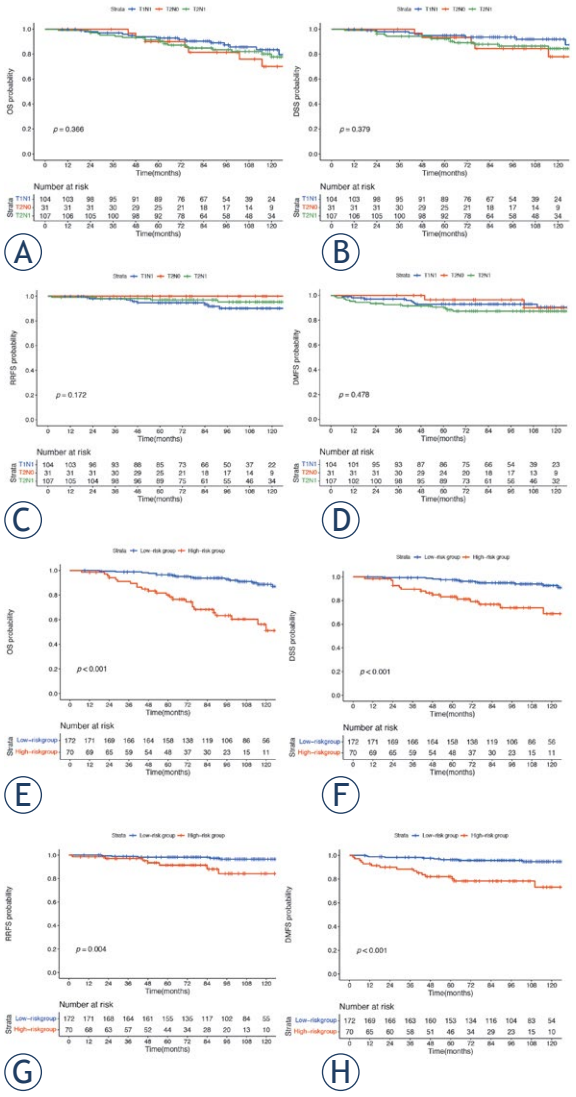

FIGURE 5. Survival curves of the **(A-D)** three subgroups in American Joint Committee on Cancer staging system (AJCC), TNM staging and **(E-H)** the low- and high-risk groups stratified by the nomogram-derived score.

ion from upper to lower level lymph nodes, and patients with level III lymph node involvement tend to have an increased number of positive lymph nodes. Lymph node size, GTVnd volume, extranodal extension and central nodal necrosis were no longer independent prognostic factors for OS, probably because they were surrogates for the number of PLNs or LNs located in level III and were included when all served as positive lymph node criteria in multivariable Cox analysis.

As per the results of the multivariate analysis, we finally included age, T stage, number of PLNs and location (lymph node located in level III) in

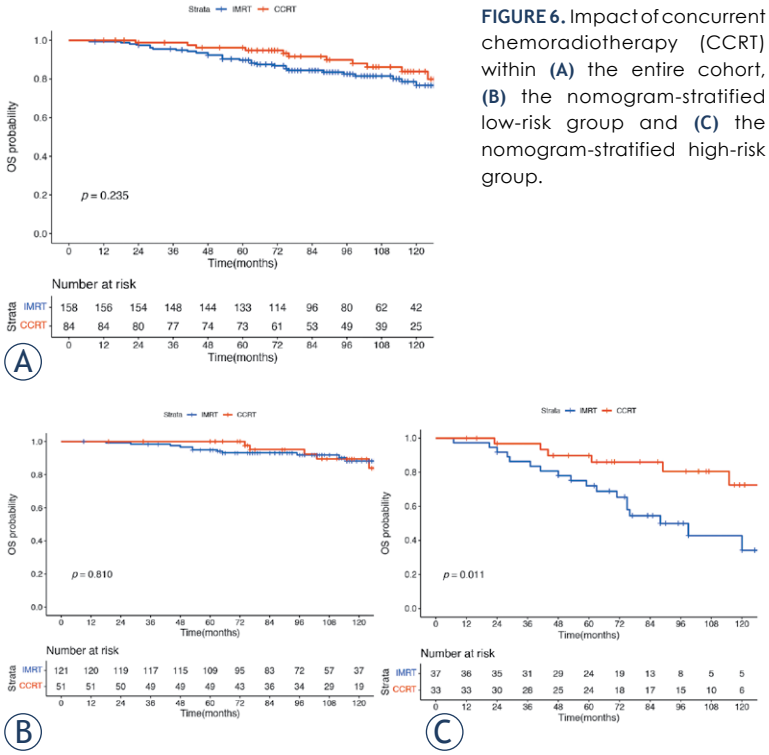

FIGURE 6. Impact of concurrent chemoradiotherapy (CCRT) within **(A)** the entire cohort, **(B)** the nomogram-stratified low-risk group and **(C)** the nomogram-stratified high-risk group.

the nomogram for OS. Although nomograms have been established in various manners in stage II NPC[20-23], the notable hallmark of our nomogram is that it is the first to incorporate lymph node status, while in the previous nomogram, the effect of lymph node burden was merely assessed by N staging and lacked more detailed categorization.[19] In terms of the discriminative performance of this nomogram, its C-index, AUC and DCA are

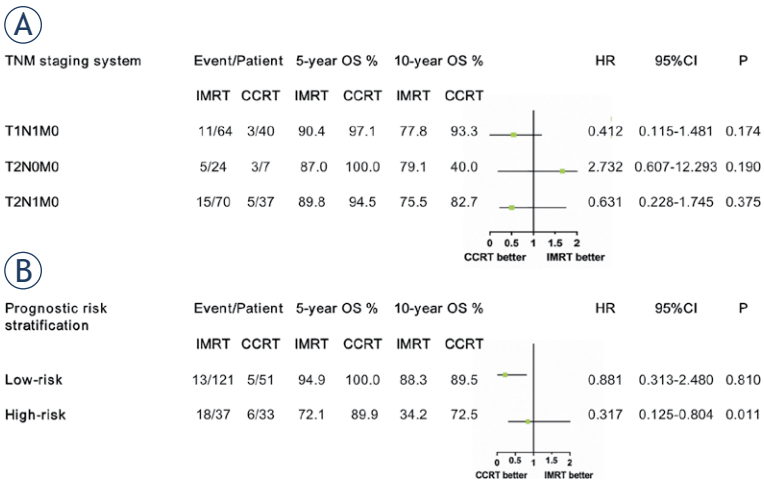

FIGURE 7. The 5-year and 10-year overall survival (OS) rates and hazard ratio (HR) between intensity-modulated radiotherapy (IMRT) group and concurrent chemoradiotherapy (CCRT) group according to **(A)** TNM staging system and **(B)** prognostic risk model.

significantly better than AJCC TNM staging and are comparable to previous nomograms for stage II NPC.[20-23]

Despite the growing evidence supporting the prognostic value of lymph node features in NPC, very little stratification based on lymph node features has been incorporated into treatment decisions from a clinical management perspective. To our knowledge, only one previously published study of nomograms in NPC analyzed the ability of the lymph node features-based nomogram model to guide personalized induction chemotherapy combined with CCRT management in stage II–IVA patients.[16] In the current study, we implemented the time-dependent ROC method to identify two subgroups according to the nomogram scores, which was more reasonable and discriminatory than arbitrary groupings based on medians or quartiles. We then found that CCRT was associated with improved survival outcomes in the high-risk group, with reductions in the overall death hazards of approximately 70%. These results underline that this nomogram may be valid enough to be used as a practical tool for clinicians to select stage II patients for concurrent chemotherapy.

This study has several limitations. First, the plasma EBV-DNA levels were not included in the survival analysis. Only five patients in this cohort had EBV-DNA over 500 copies/ml, which is consistent with previous studies reporting relatively low EBV-DNA copies in stage II patients[29,30], suggesting that their prognostic value may not be as critical as in stage III/IV patients. Another possible reason for the relatively low EBV-DNA in this cohort is the continued lack of standardized EBV-DNA testing[31,32]; therefore, we sought to re-examine the prognostic value of pretreatment EBV-DNA for stage II NPC after standardization of testing methods. Second, although the sample size of the present study was the largest reported for nodal feature prognostication in stage II NPC to date, our data were obtained from a single cancer center. A larger sample size cohort for external independent validation is warranted to further assess the prognostic and predictive value of this lymph node feature-based nomogram.

Conclusions

In summary, this study established a nodal features-based nomogram with excellent performance, which provided statistically significantly superior discrimination to TNM staging in predicting the OS in patients with stage II NPC. Furthermore, the nomogram-based stratification effectively identified patients who were more likely to gain survival benefit from CCRT. It offers a useful tool for providing patient counseling and clinical assessments. To generalize the clinical utility of this nomogram, external validation should be considered.

Acknowledgments

This work was supported by National Natural Science Foundation of China grant (grant numbers 81172125) and Beijing hope run fund (LC2021L06).

References

1. Chen YP, Chan ATC, Le QT, Blanchard P, Sun Y, Ma J. Nasopharyngeal carcinoma. *Lancet* 2019; **394:** 64-80. doi: 10.1016/s0140-6736(19)30956-0
2. Sun X, Su S, Chen C, Han F, Zhao C, Xiao W, et al. Long-term outcomes of intensity-modulated radiotherapy for 868 patients with nasopharyngeal carcinoma: an analysis of survival and treatment toxicities. *Radiother Oncol* 2014; **110:** 398-403. doi: 10.1016/j.radonc.2013.10.020
3. Tian YM, Liu MZ, Zeng L, Bai L, Lin CG, Huang SM, et al. Long-term outcome and pattern of failure for patients with nasopharyngeal carcinoma treated with intensity-modulated radiotherapy. *Head Neck* 2019; **41:** 1246-52. doi: 10.1002/hed.25545
4. National Comprehensive Cancer Network. *NCCN Guidelines in Oncology*. Head and Neck Cancers. Version 2.2022. [Internet]. [cited 2022 Apr 26]. Available at https: //www.nccn.org/guidelines/guidelines-detail?category=1&id=1437
5. Chen QY, Wen YF, Guo L, Liu H, Huang PY, Mo HY, et al. Concurrent chemoradiotherapy *vs* radiotherapy alone in stage II nasopharyngeal carcinoma: phase III randomized trial. *J Natl Cancer Inst* 2011; **103:** 1761-70. doi: 10.1093/jnci/djr432
6. Su SF, Han F, Zhao C, Chen CY, Xiao WW, Li JX, et al. Long-term outcomes of early-stage nasopharyngeal carcinoma patients treated with intensity-modulated radiotherapy alone. *Int J Radiat Oncol Biol Phys* 2012; **82:** 327-33. doi: 10.1016/j.ijrobp.2010.09.011
7. Huang X, Chen X, Zhao C, Wang J, Wang K, Wang L, et al. Adding concurrent chemotherapy to intensity-modulated radiotherapy does not improve treatment outcomes for stage II nasopharyngeal carcinoma: a phase 2 multicenter clinical trial. *Front Oncol* 2020; **10:** 1314. doi: 10.3389/fonc.2020.01314
8. Bossi P, Chan AT, Licitra L, Trama A, Orlandi E, Hui EP, et al. Nasopharyngeal carcinoma: ESMO-EURACAN clinical practice guidelines for diagnosis, treatment and follow-up(dagger). *Ann Oncol* 2021; **32:** 452-65. doi: 10.1016/j.annonc.2020.12.007
9. Sun XS, Li XY, Xiao BB, Liu SL, Chen QY, Tang LQ, et al. Establishment and validation of a nomogram for predicting the benefit of concurrent chemotherapy in stage II nasopharyngeal carcinoma: a study based on a phase III randomized clinical trial with 10-year follow-up. *Oral Oncol* 2020; **100:** 104490. doi: 10.1016/j.oraloncology.2019.104490
10. He SS, Wang CT, Peng ZW, Ren YF, Lu LX, Chen RW, et al. Development and external validation of a nomogram for predicting the overall survival of patients with stage II nasopharyngeal carcinoma after curative treatment. *Cancer Manag Res* 2019; **11:** 4403-12. doi: 10.2147/CMAR.S202151
11. Chen YP, Ismaila N, Chua MLK, Colevas AD, Haddad R, Huang SH, et al. Chemotherapy in combination with radiotherapy for definitive-intent treatment of stage II-IVA nasopharyngeal carcinoma: CSCO and ASCO guideline. *J Clin Oncol* 2021; **39:** 840-59. doi: 10.1200/jco.20.03237

12. Du YY, Luo DH, Sun XS, Tang LQ, Mai HQ, Chen QY, et al. Combining pretreatment plasma Epstein-Barr virus DNA level and cervical node necrosis improves prognostic stratification in patients with nasopharyngeal carcinoma: a cohort study. *Cancer Med* 2019; **8:** 6841-52. doi: 10.1002/cam4.2481

13. Hu Y, Lu T, Huang SH, Lin S, Chen Y, Fang Y, et al. High-grade radiologic extra-nodal extension predicts distant metastasis in stage II nasopharyngeal carcinoma. *Head Neck* 2019; **41:** 3317-27. doi: 10.1002/hed.25842

14. Liu Y, Chen S, Dong A, Ai F, Quan T, Cui C, et al. Nodal grouping in nasopharyngeal carcinoma: prognostic significance, N classification, and a marker for the identification of candidates for induction chemotherapy. *Eur Radiol* 2020; **30:** 2115-24. doi: 10.1007/s00330-019-06537-6

15. Lin TY, Lan MY, Tsou HH, Ho CY, Twu CW, Liu YC, et al. Survival impacts of different nodal characteristics and T-classification in N3 nasopharyngeal carcinoma patients. *Oral Oncol* 2020; **108:** 104820. doi: 10.1016/j.oraloncology.2020.104820

16. Chen X, Cao X, Jing B, Xia W, Ke L, Xiang Y, et al. Prognostic and treatment guiding significance of MRI-based tumor burden features and nodal necrosis in nasopharyngeal carcinoma. *Front Oncol* 2020; **10:** 537318. doi: 10.3389/fonc.2020.537318

17. Ai QY, King AD, Poon DMC, Mo FKF, Hui EP, Tong M, et al. Extranodal extension is a criterion for poor outcome in patients with metastatic nodes from cancer of the nasopharynx. *Oral Oncol* 2019; **88:** 124-30. doi: 10.1016/j.oraloncology.2018.11.007

18. Lu T, Hu Y, Xiao Y, Guo Q, Huang SH, O'Sullivan B, et al. Prognostic value of radiologic extranodal extension and its potential role in future N classification for nasopharyngeal carcinoma. *Oral Oncol* 2019; **99:** 104438. doi: 10.1016/j.oraloncology.2019.09.030

19. Lan M, Huang Y, Chen CY, Han F, Wu SX, Tian L, et al. Prognostic value of cervical nodal necrosis in nasopharyngeal carcinoma: analysis of 1800 patients with positive cervical nodal metastasis at MR imaging. *Radiology* 2015; **276:** 619. doi: 10.1148/radiol.15141251

20. Li JY, Huang CL, Luo WJ, Zhang Y, Tang LL, Peng H, et al. An integrated model of the gross tumor volume of cervical lymph nodes and pretreatment plasma Epstein-Barr virus DNA predicts survival of nasopharyngeal carcinoma in the intensity-modulated radiotherapy era: a big-data intelligence platform-based analysis. *Ther Adv Med Oncol* 2019; **11:** 1758835919877729. doi: 10.1177/1758835919877729

21. Huang CL, Chen Y, Guo R, Mao YP, Xu C, Tian L, et al. Prognostic value of MRI-determined cervical lymph node size in nasopharyngeal carcinoma. *Cancer Med* 2020; **9:** 7100-6. doi: 10.1002/cam4.3392

22. Ma H, Liang S, Cui C, Zhang Y, Xie F, Zhou J, et al. Prognostic significance of quantitative metastatic lymph node burden on magnetic resonance imaging in nasopharyngeal carcinoma: a retrospective study of 1224 patients from two centers. *Radiother Oncol* 2020; **51:** 40-6. doi: 10.1016/j.radonc.2020.07.023

23. Zhou X, Ou X, Yang Y, Xu T, Shen C, Ding J, et al. Quantitative metastatic lymph node regions on magnetic resonance imaging are superior to AJCC N classification for the prognosis of nasopharyngeal carcinoma. *J Oncol* 2018; **2018:** 9172585. doi: 10.1155/2018/9172585

24. van den Brekel MW, Stel HV, Castelijns JA, Nauta JJ, van der Waal I, Valk J, et al. Cervical lymph node metastasis: assessment of radiologic criteria. *Radiology* 1990; **177:** 379-84. doi: 10.1148/radiology.177.2.2217772

25. Meira-Machado L, Cadarso-Suarez C, Gude F, Araujo A. smoothHR: an R package for pointwise nonparametric estimation of hazard ratio curves of continuous predictors. *Comput Math Methods Med* 2013; **2013:** 745742. doi: 10.1155/2013/745742

26. Liu DH, Zhou XY, Pan YG, Chen S, Ye ZH, Chen GD. Survival of stage II nasopharyngeal carcinoma patients with or without concurrent chemotherapy: a propensity score matching study. *Cancer Med* 2020; **9:** 1287-97. doi: 10.1002/cam4.2785

27. Luo S, Zhao L, Wang J, Xu M, Li J, Zhou B, et al. Clinical outcomes for early-stage nasopharyngeal carcinoma with predominantly WHO II histology treated by intensity-modulated radiation therapy with or without chemotherapy in nonendemic region of China. *Head Neck* 2014; **36:** 841-7. doi: 10.1002/hed.23386

28. Kang MK, Oh D, Cho KH, Moon SH, Wu HG, Heo D, et al. Role of chemotherapy in stage II nasopharyngeal carcinoma treated with curative radiotherapy. *Cancer Res Treat* 2015; **47:** 871-8. doi: 10.4143/crt.2014.141

29. Lee VH, Kwong DL, Leung TW, Choi CW, O'Sullivan B, Lam KO, et al. The addition of pretreatment plasma Epstein-Barr virus DNA into the eighth edition of nasopharyngeal cancer TNM stage classification. *Int J Cancer* 2019; **144:** 1713-22. doi: 10.1002/ijc.31856

30. Guo R, Tang LL, Mao YP, Du XJ, Chen L, Zhang ZC, et al. Proposed modifications and incorporation of plasma Epstein-Barr virus DNA improve the TNM staging system for Epstein-Barr virus-related nasopharyngeal carcinoma. *Cancer* 2019; **125:** 79-89. doi: 10.1002/cncr.31741

31. Leung SF, Zee B, Ma BB, Hui EP, Mo F, Lai M, et al. Plasma Epstein-Barr viral deoxyribonucleic acid quantitation complements tumor-node-metastasis staging prognostication in nasopharyngeal carcinoma. *J Clin Oncol* 2006; **24:** 5414-18. doi: 10.1200/JCO.2006.07.7982

32. Sun XS, Chen WH, Liu SL, Liang YJ, Chen QY, Guo SS, et al. Individualized concurrent chemotherapy by pretreatment plasma Epstein-Barr viral DNA in II-III stage nasopharyngeal carcinoma: a propensity score matching analysis using a large cohort. *Cancer Med* 2019; **8:** 4214-25. doi: 10.1002/cam4.2343

research article

Impact of the COVID-19 epidemic on cancer burden and cancer care in Slovenia: a follow-up study

Tina Zagar[1], Sonja Tomsic[1], Vesna Zadnik[1], Nika Bric[1], Mojca Birk[1], Blaz Vurzer[2], Ana Mihor[1], Katarina Lokar[1], Irena Oblak[3]

[1] Epidemiology and Cancer Registry, Institute of Oncology Ljubljana, Ljubljana, Slovenia
[2] National Institute of Public Health, Regional unit Murska Sobota, Murska Sobota, Slovenia
[3] Department of Radiation Oncology, Institute of Oncology Ljubljana, Ljubljana, Slovenia

Radiol Oncol 2022; 56(4): 488-500.

Received 11 October 2022
Accepted 30 October 2022

Correspondence to: Tina Žagar, Ph.D., Epidemiology and Cancer Registry, Institute of Oncology Ljubljana, Zaloška cesta 5, SI-1000 Ljubljana, Slovenia. E-mail: tzagar@onko-i.si

Disclosure: No potential conflicts of interest were disclosed.

Background. In Slovenia, cancer care services were exempt from government decrees for COVID-19 containment. Nevertheless, cancer control can be impacted also by access to other health services and changes in health-seeking behaviour. In this follow up study, we explored changes in cancer burden and cancer care beyond the first months after the onset of the COVID-19 epidemic.

Materials and methods. We analysed routinely collected data for the period January 2019 through July 2022 from three sources: (1) pathohistological and clinical practice cancer notifications from two major cancer centres in Ljubljana and Maribor (source: Slovenian Cancer Registry); (2) referrals issued for oncological services (source: e-referral system); and (3) outpatient appointments and diagnostic imaging performed (source: administrative data of the Institute of Oncology Ljubljana – IOL). Additionally, changes in certain clinical and demographic characteristics in patients diagnosed and treated during the epidemic were analysed using the Hospital-Based Cancer Registry of the IOL (period 2015–2021).

Results. After a drop in referrals to follow-up cancer appointments in April 2020, in June-August 2020, there was an increase in referrals, but it did not make-up for the drop in the first wave; the numbers in 2021 and 2022 were even lower than 2020. Referrals to first cancer care appointments and genetic testing and counselling increased in 2021 compared to 2019 and in 2022 increased further by more than a quarter. First and follow-up outpatient appointments and cancer diagnostic imaging at the IOL dropped after the onset of the epidemic in March 2020 but were as high as expected according to 2019 baseline already in 2021. Some deficits remain for follow-up outpatients' appointments in surgical and radiotherapy departments. There were more CT, MRI and PET scans performed during the COVID-19 period than before. New cancer diagnoses dropped in all observed years 2020, 2021 and until July 2022 by 6%, 3% and 8%, respectively, varying substantially by cancer type. The largest drop was seen in the 50−64 age group (almost 14% in 2020 and 16% in 2021), while for patients older than 80 years, the numbers were above expected according to the 2015–2019 average (4% in 2020, 8% in 2021).

Conclusions. Our results show a varying effect of COVID-19 epidemic in Slovenia for different types of cancers and at different stages on the patient care pathway – it is probably a mixture of changes in health-seeking behaviour and systemic changes due to modifications in healthcare organisation on account of COVID-19. A general drop in new cancer cases reflects disruptions in the pre-diagnostic phase and could have profound long-term consequences on cancer burden indicators.

Key words: cancer; COVID-19; delay in diagnosis; referral

Introduction

The COVID-19 pandemic and the non-pharmacological measures adopted by governments for containment of its spread have substantially influenced the provision and use of health care system services for health problems unrelated to COVID-19 in different countries.[1-5] Although healthcare services for serious conditions, such as cancer, were mostly exempt from restriction measures, nevertheless, they were affected by the COVID-19 pandemic.[6-16]

As previously reported for Slovenia[17], a middle European country with a universal health care system, in the first wave of COVID-19 containment measures (from March 2020 until May 2020) there was a decrease of over 30% in the number of new cancer diagnoses, 30% in referrals to cancer care (33% for first appointments, 46% for follow-up appointments and 85% for genetic testing and counselling), 20% in the number of outpatients appointments at the Institute of Oncology Ljubljana (IOL) and 40% in the number of diagnostic imaging performed, despite the fact that provision of oncology services was included among exemptions to healthcare-related restriction measures and was thus not directly scaled-down.

An overview of the COVID-19 epidemic in Slovenia

The first wave of the COVID-19 epidemic in Slovenia, starting in March 2020, has been previously described in detail.[17] After the declaration of the epidemic on 12th March 2020, strict control measures were implemented. All non-essential ambulatory visits, elective surgery appointments and even preventive care activities, including all three national screening programmes (for cervical, breast and colorectal cancer), were temporarily stopped. On 9th May, all restrictions concerning the provision of healthcare services were lifted and on 31th May 2020, the end of the epidemic was declared. Throughout the whole period, oncological healthcare was exempt from these mandates. The cancer screening programmes began operating normally in June 2020. They provided extra services during the summer months of 2020 and by the end of 2020 eliminated the deficits in services caused by their mandatory suspension.[18] In the following epidemic waves, the cancer screening programmes were not stopped again.

Following a rise in cases, on 19th October 2020 the epidemic was declared for a second time and restriction measures were re-introduced. In addition to various measures concerning movement of people and public gatherings, all non-emergency health services with the exception of oncology services were once again suspended, strict triage measures were introduced at the primary health care level, COVID-19 hospitals/departments were set-up and staff were temporarily reallocated. The highest number of COVID-19 cases needing hospital treatment was between November 2020 and February 2021. By the end of year 2020, Slovenia introduced rapid antigen testing and commenced vaccinations in December 2020. Vaccination uptake was at first limited to priority groups such as the elderly and healthcare workers and was thus relatively slow. After April 2021, it started improving and has reached around 60% by the end of 2021 but has plateaued since.[19] Cases among healthcare staff were highest during observed peaks[20,21], increasing the COVID-19 strain on healthcare through staff shortages[22,23] and limiting provision of services. Furthermore, by the end of 2020 pandemic fatigue had already started to appear among Slovenian residents.[24,25] In January and April 2021, new surges of COVID-19 cases appeared, while afterwards cases started to decrease. The 15th June 2021 was the last day of the epidemic being officially declared, though most of the restrictive measures and process adaptations concerning the health care system remained.[20,21]

On 15th September 2021, due to the growing number of infections with the Delta variant of the novel coronavirus 2 (SARS-CoV-2), the recovered/vaccinated/tested (RVT) rule was implemented for most services. Emergency visits were exceptions. Alongside the RVT implementation, demand for vaccination among the general population grew. The Delta wave caused a new surge in COVID-19 hospitalizations and admissions to intensive care units (most notably during November and December 2021 and between September and November 2021, Slovenia had one of the highest rates among EU countries with a large number of excess deaths[26]). Healthcare shortages were also very pronounced. During the Omicron wave in January and February 2022 the largest number of COVID-19 confirmed cases were recorded. However, proportionally less infected people needed hospital or intensive care treatment. Since 18th February 2022, COVID-19 in Slovenia is no longer considered a quarantine disease, meaning close contacts are no longer required by law to self-isolate. From this point on, COVID-19 cases decreased until the beginning of June 2022.

From February 2022, restrictions imposed due to COVID-19 begun to be lifted, with the final regulation annulling all COVID-19 restrictions, including limitations imposed on access and provision of health care services, implemented on 30th May 2022.[21,27,28]

Monitoring of cancer burden and cancer care in Slovenia

Cancer is a non-communicable chronic disease and rapid changes in incidence are not expected in normal circumstances. On rare occasions we have an opportunity to observe rapid changes in cancer burden indicators during crisis situations, for example due to catastrophes resulting in an increased exposure to certain cancer risk factors or major and/or prolonged disruptions of a country's health system, such as occur during wars or widespread epidemics.[29]

Population-based cancer registries, such as the Slovenian Cancer Registry (SCR), are public health entities that are established on a national or regional level for continuous systematic collection of data on the occurrence, characteristics, and outcome of reportable cancers, and are thus able to record such events.[30] Even though many registries across the world reported disruptions in cancer registration during COVID-19[4,5], in Slovenia active registration was uninterrupted and allowed for up-to date national trend estimates.[31] The Hospital-Based Cancer Registry of the IOL collects data on all new first-time patients seen at the IOL for cancer diagnostics and treatment. These data are the source of valuable information for medical work and research at the IOL; at the same time, the data are promptly forwarded also to the population-based SCR, thus upgrading the central database. Cancer treatment in Slovenia is highly centralised. The IOL provides more than 80% of all systemic treatments, over 60% of all cancer surgeries and almost all radiotherapy treatments in Slovenia. The University Medical Centre (UMC) Maribor is Slovenia's second oncological centre. Both provide up-to-date information to the SCR on newly diagnosed cancer patients through an online-based registration process.[31] The IOL provided care almost exclusively for cancer patients, establishing its first department for COVID-19 patients as late as the first half of 2022, whereas UMC Maribor had been a COVID-19 hospital during the whole time, but its oncology department was running normally, if we disregard disruptions caused by staff shortages at both centres.

Slovenia has a gate-keeping system in place, where specialised health care is only possible with referrals from general practitioners. Thus, the number of referrals is an accurate reflection of demand for specialist cancer care. The e-referral system was introduced in 2017 and is maintained by the National Institute of Public Health (NIPH).[32]

Shortly after the start of the COVID-19 pandemic, we carried out a preliminary analysis of its impact on cancer diagnosis and care in Slovenia[17] using the preliminary data from the SCR and other available heath databases. After receiving widespread interest following publication of the preliminary results, to provide healthcare experts, policy-makers and the general public with up-to date continuous monitoring of the effect of COVID-19 epidemic on oncology services and cancer burden, in 2021 we set up a web page named onKOvid (available at http://www.slora.si/en/onkovid) where up-to-date indicators on cancer burden and management are available to the professional and lay public.[33]

Aim of the study

In order to provide an update on the situation and expand the scope of the preliminary study of the COVID-19 epidemic impact on cancer burden in Slovenia during the first 2020 wave, we aimed to analyse the impact of the COVID-19 epidemic on cancer diagnosis and management in Slovenia in over two years since the onset of the epidemic in more detail. Primarily, we focused on fluctuations in cancer diagnoses from the two main cancer centres during this period, while also examining whether there were declines in demand for specialized oncological care at the national level. Furthermore, we provide an overview of certain diagnostic and treatment procedures carried out at the IOL during the epidemic.

Materials and methods

Our study was based on routinely collected data for the period March 2020 – July 2022. For the analysis of the impact of COVID-19 epidemic on cancer burden and care indicators in Slovenia, four routine data sources were used:

The SCR data on new cancer diagnoses collected via active registration (direct access to electronic patient files) from the two major cancer centres in Ljubljana and Maribor for the evaluation of possible delays in cancer diagnoses.

The Hospital-Based Cancer Registry of the IOL for the evaluation of changes in the distribution of prognostic factors in patients diagnosed and treated during the epidemic.

The national e-referral system for the evaluation of changes in demand for specialized cancer care.

The administrative hospital data of the IOL for analysing the level of realization of services during the epidemic.

From the SCR, we extracted the most up-to-date data on online cancer notifications for the two major oncological centres in Slovenia, the IOL and the UMC Maribor. Active notifications from other hospitals were not available yet in 2019, the start of the study period, therefore we were unable to include them. Notifications were extensively computer processed to extract only one (most relevant) cancer diagnosis per person and as such serve as a good approximation to cancer incidence, i.e. the number of new cases diagnosed in these two hospitals. The analyses were carried out for all new cancer diagnoses and for selected cancer types: colorectal cancer (ICD-10 codes C18–C20), breast (C50), lung (C33–C34), prostate (C61), skin, non-melanoma (C44), skin melanoma (C43) and lymphoma (C81–C85).

For patients seen for the first time at the IOL for diagnostics and/or treatment of a particular disease up to the end of 2021, in addition to the location of cancer, data was available also on the stage at diagnosis and the reason for the first outpatient appointment or hospitalisation (hereafter first visit) at the IOL. Thus, for the cohort of patients first seen at the IOL in 2020 and 2021, stratification was possible by gender (males; females), age groups according to the age at first visit to the IOL (20–49; 50–64; 65–79; 80+), stage at diagnosis (local; regional; distant; unknown; not applicable – for haematological cancers) and the reason for the first visit to the IOL (primary cancer diagnostics; primary cancer treatment; diagnostics or treatment for disease relapse; other or unknown).

The data source for the analysis of referrals to cancer care services was the national e-referral system, operated by NIPH. From the NIPH, we retrieved the absolute number of all monthly referrals issued in Slovenia for selected types of cancer care services as coded in the Codebook of Healthcare Services, namely the first cancer appointment, control cancer appointment and oncological genetic testing and counselling.

We also examined the administrative data of the IOL on monthly outpatient visits, stratified according to first and follow-up visits by divisions (medical oncology, surgery, radiotherapy), and data on cancer diagnostic imaging, namely the monthly number of X-rays, mammograms, ultrasounds, CT, MRI and PET scans performed.

In all the analyses the monthly (or yearly) absolute numbers of new diagnoses, referrals, appointments and imaging tests performed for the epidemic years 2020, 2021 and up-to July 2022 were compared with the expected absolute numbers, where the baseline was the monthly (or yearly) numbers observed in 2019. The exception was the analysis performed for the cohort of patients first seen at the IOL in 2020 and 2021, where the baseline represents the average for the period 2015–2019 and where the data for 2022 were not yet available for the analysis.

We calculated the relative difference, expressed in percent change, between epidemic and pre-epidemic numbers. To evaluate statistically significant differences, we calculated confidence intervals (CI) using Fisher's exact test where observed cases in years 2020 to 2022 were compared to expected cases (2019 data). An alpha level of 0.05 was set for statistical significance. Data management and analysis was performed in R software version 4.1.2 and some additional calculations and graphical presentations in Microsoft Excel 2019.

Results

Cancer incidence

Based on cancer notifications received by the SCR from the two major oncological centres in Slovenia, we can observe a drop in newly diagnosed cancers in all three epidemic years (2020–2022) for most cancer types except lung cancer (Figure 1).

The overall number of notifications for new cancer diagnoses in the years 2020, 2021 and until July 2022 was lower than in 2019, that is 6%, 3% and 8%, respectively, largely varying by cancer type. The most prominent drops in cancer notifications were for prostate (around 20% in all years) and breast cancer (up to 25%), while notifications for lung cancer increased by over 10%.

In general, drops in the monthly number of new cancer diagnoses were more coincidental with imposed restrictions, which were more pronounced at the beginning of the observed period, than with observed surges in COVID-19 cases (Figure 2). The largest drop in new diagnoses was observed in April 2020 (around 30%). The results show, that the second and third wave of COVID-19 (autumn 2020, winter and spring 2021) had a smaller nega-

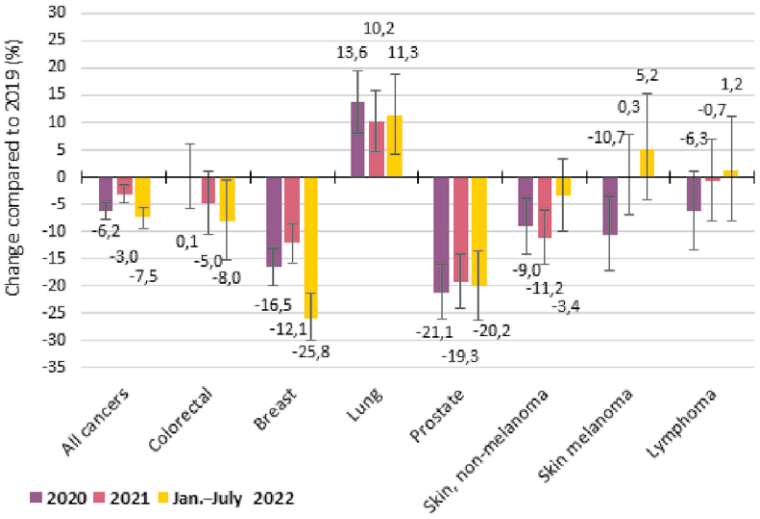

FIGURE 1. Change in the number of newly diagnosed cases of different types of cancers in years 2020, 2021, 2022 compared to the pre-COVID-19 year 2019. Data were collected from the two major cancer centres (Institute of Oncology Ljubljana and University Medical Centre Maribor). For 2022, only data from January to July are included and compared to corresponding months in 2019.

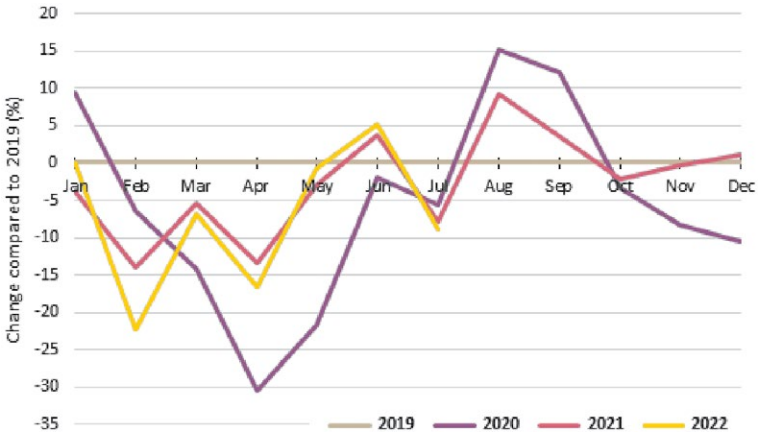

FIGURE 2. Monthly change in the number of newly diagnosed cancer cases (%) in years 2020, 2021 and up-to July 2022 compared to corresponding months in 2019. Data were collected from the two major cancer centres (Institute of Oncology Ljubljana and University Medical Centre Maribor).

tive effect on the number of new cancer diagnoses, around 10%. In the second half of 2021, the number of new cancer diagnoses was roughly the same as in 2019. Looking at the whole period, no compensatory surges in new cancer diagnoses are visible that would make up for the significant drops in the first, second or third wave. At the beginning of 2022 (the Omicron wave), there was another drop in the number of new cancer cases (around 15%) compared to 2019.

Monthly fluctuations in new cancer diagnoses for specific cancer types are available in the supplementary material (Supplementary Figure 1). In the first wave of the epidemic, the largest drop was for prostate cancer (54% in April 2020), non-melanoma skin cancer (45% in March and April 2020), skin melanoma (41% in March 2020), breast cancer (between 37% and 41% in March–June 2020) and lymphoma (33% in May 2020). Most peaks above expected numbers were during summer months.

Characteristics of patients and their disease

There was a 6% decrease in the number of patients first seen at the IOL in 2020 and over 8% in 2021 compared to the average in the 2015–2019 pre-COVID-19 period (Table 1). The decrease was similar in males and females. The largest decrease was seen in the 50–64 age group (almost 14% in 2020 and 16% in 2021), while for patients older than 80 years, the numbers were above expected (4% in 2020, 8% in 2021 (Figure 3).

Compared to the 2015–2019 average, in 2020 we observed 11% less first visits due to diagnostics and treatment of progression and relapse of cancer, while drops in first visits for primary cancer diagnostics (not significant) and primary cancer treatment (6%) were smaller. Regarding drops in first visits by stage of cancer at diagnosis, of those who were first seen at the IOL for primary diagnostic work-up or primary cancer treatment, fewer than expected were diagnosed in regional (9%) and distant (8%) stage (Table 1), whereas the decrease for localized stage was not statistically significant. The situation was somewhat reversed in 2021, when drops were more pronounced for primary cancer diagnostics (14%) and primary cancer treatment (9%) than for diagnostics and treatment of progression or relapse (not significant) and the drops were larger for localized (9%) and regional (16%) stage, while the drop for distant stage (8%) was similar as in 2020.

Demand for and realization of specialist oncological care

In 2020 there was a drop in referrals in Slovenia to first and follow-up cancer appointments as well as to oncological genetic testing and counselling (Table 2). Monthly fluctuations in investigated measures are presented in the supplementary material (Supplementary Figures 2–5). Decreases were first observed during the first wave (March

TABLE 1. Number of cancer patients, who first visited the Institute of Oncology Ljubljana (outpatient appointments and hospitalisations together) for a particular disease in years 2021 and 2022 with percentage change compared to the 2015–2019 average by year of first visit, gender, age group at first visit, reason for the first visit and stage at diagnosis (only for those admitted for primary cancer diagnostics or primary cancer treatment). The 2015–2019 average is accompanied with 95% confidence interval, which the numbers for years 2020 and 2021 are compared to (statistically significant lower/higher number are coloured)

	Average 2015–2019 (95% CI)		N for 2020	Change (%) in 2020 against average (95% CI)	N for 2021	Change (%) in 2021 against average (95% CI)
Total	6635.4	(6458.9 ; 6811.9)	6217	-6.3 (-8.6 ; -3.9)	6064	-8.6 (-10.9 ; -6.3)
Gender						
Males	3334.0	(3219.4 ; 3448.6)	3157	-5.3 (-8.6 ; -1.9)	2978	-10.7 (-13.9 ; -7.4)
Females	3301.4	(3218.9 ; 3383.9)	3060	-7.3 (-10.6 ; -4.0)	3086	-6.5 (-9.8 ; -3.2)
Age group						
20-49	939.6	(911.9 ; 967.3)	935	-0.5 (-6.8 ; 6.1)	901	-4.1 (-10.3 ; 2.4)
50-64	2287.6	(2189.2 ; 2386.0)	1958	-14.4 (-18.2 ; -10.5)	1912	-16.4 (-20.1 ; -12.6)
65-79	2651.6	(2534.0 ; 2769.2)	2546	-4.0 (-7.7 ; -0.2)	2493	-6.0 (-9.6 ; -2.2)
80+	695.4	(676.2 ; 714.6)	721	3.7 (-3.7 ; 11.5)	750	7.9 (0.3 ; 15.9)
Reason for the first visit to Institute of Oncology Ljubljana						
Primary diagnostics	904.4	(858.9 ; 949.9)	884	-2.3 (-8.6 ; 4.4)	777	-14.1 (-20 ; -7.8)
Primary treatment	4791.2	(4664.9 ; 4917.5)	4493	-6.2 (-8.9 ; -3.4)	4358	-9.0 (-11.7 ; -6.3)
Diagnostics or treatment for relapse	874.8	(824.9 ; 924.7)	779	-11.0 (-17.1 ; -4.5)	838	-4.2 (-10.6 ; 2.5)
Other or unknown	65.0	(43.5 ; 86.5)	61	-6.2 (-28.2 ; 20.5)	91	40.0 (12.7 ; 71.9)
Stage at diagnosis (for primary diagnosis and primary treatment only)						
Localized	2029.2	(1956.8 ; 2101.6)	1943	-4.2 (-8.5 ; 0.1)	1843	-9.2 (-13.3 ; -4.9)
Regional	2061.0	(2026.1 ; 2095.9)	1879	-8.8 (-12.9 ; -4.6)	1723	-16.4 (-20.3 ; -12.4)
Distant	1093.4	(1018.3 ; 1168.5)	1010	-7.6 (-13.2 ; -1.8)	1009	-7.7 (-13.3 ; -1.8)
Unknown	41.6	(36.4 ; 46.8)	56	34.6 (1.7 ; 74.8)	92	121.2 (78.3 ; 171.2)
Not applicable	470.4	(430.7 ; 510.1)	489	4.0 (-5.1 ; 13.6)	468	-0.5 (-9.3 ; 8.9)

CI = confidence interval

Red numbers are below and green above the 95% confidence interval for the 2015–2019 average.

and April 2020). In months from June to August 2020, there was an increase in the number of referrals to follow-up cancer appointments, but the increase did not make-up for the drop in the previous months. In 2021, there was a 5.4% increase in the number of referrals to first appointments, while the number of referrals to follow-up appointments was still significantly lower than in 2019 (-14.3%). Demands for first cancer appointments and genetic testing and counselling increased by more than a quarter in 2022 compared to 2019 (27.0%), while referrals to follow-up cancer appointments were even fewer than in 2021 (-28.5%; Table 2).

In general, first and follow-up outpatient appointments and cancer diagnostic imaging performed at the IOL dropped after the onset of the COVID-19 epidemic in March 2020 but had returned to expected levels by 2021, according to the 2019 baseline. Some deficits remain for follow-up outpatients visits in surgical (-2.1%) and radiotherapy departments (-8.1%) (Table 2). There were more CT, MRI and PET scans performed during the COVID-19 period than before (Table 2, Supplementary Figures 2–5).

Discussion

Significant decreases, especially at the begging of the epidemic, in referrals to first cancer appoint-

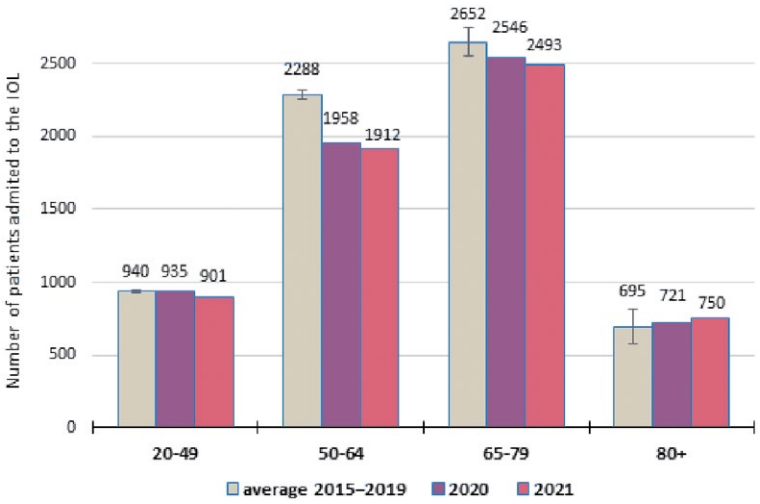

FIGURE 3. Number of cancer patients who first visited the Institute of Oncology Ljubljana (IOL) (outpatient appointments and hospitalisations together) for a particular disease in years 2015–2021 by year of first visit and by age group at first visit with percentage change against 2015–2021 average (an asterisk indicates statistically significant change). For average values for the years 2015–2019, 95% confidence intervals are also presented.

ments, as well as drops in first cancer appointments, X-rays, mammograms and ultrasounds performed at the IOL along with drops in new cancer diagnoses from the two major cancer centres point to a delay in diagnosis and treatment for some cancer patients during the COVID-19 epidemic in Slovenia. Similar findings were reported in many other countries worldwide.[8,9,12,14] The reasons that led to this decline cannot be assessed in our study but are presumed to be a combination of changes in health-seeking behaviour of patients, day-to-day work of doctors as well as the organization of the health care system and its management during the COVID-19 peaks. Pandemic fatigue also likely played a role in service provision and uptake in 2021 and 2022, especially during summer months when both healthcare staff as well as patients were eager for a return to normal holidaying after a period of travel restrictions. Cancer registries themselves experienced disruptions with their regular operations due to changes in the work modalities for the personnel, as well as difficulties in accessing sources and/or receiving the notifications on cancer registration and cancer care.[4,5]

We did not incorporate the number of COVID-19 cases into the analyses, since governmental control measures did not always follow changes in the number of COVID-19 cases and, furthermore, the severity of restrictions was not proportional to the number of cases (for example, in spring 2020 the restrictions were much more severe compared to autumn 2021 despite the fact that the number of cases was 120-times higher).[21] Monthly fluctuations of analysed data were more in line with the severity of restrictions than the absolute number of COVID-19 cases, the former being the mildest during summer months.[21]

Overall, fewer new cancer cases were reported from the two major centres during COVID-19. It is important to emphasize that the average growth of new cancer cases (crude incidence rate on the population level) was 2% per year before the epidemic in 2010–2019.[31] Regarding specific cancer types, there was a drop in the number of newly diagnosed cancers in all of the observed epidemic years for breast, prostate and non-melanoma skin cancer. For these cancers, it is also important to note that from the pre-epidemic trends an increase in incidence would have been otherwise expected, since the annual percentage change in incidence during 10 years before the epidemic was 2.6% for female breast, 0.7% for prostate and 5.4% for non-melanoma skin cancers.[31] The drop in new diagnoses of non-melanoma skin cancer during the epidemic in Slovenia could be explained by changes in health-seeking behaviour on the part of patients, since most non-melanoma skin changes occur over a longer period and would thus not be considered urgent by many people[34]. Results from a national survey among adults regarding the impact of the COVID-19 pandemic on people's lives (SI-PANDA) have shown that in 2020 and beginning of 2021, more than 35% of respondents avoided seeing a doctor for reasons other than COVID-19; by the end of 2021, over 26% of respondents still reported they avoided seeing a doctor.[24,25] Another contributing factor is that probably, access to doctor appointments was limited due to epidemic adaptations in healthcare services organization. The access was likely limited both at primary as well as secondary levels, most notably when strict mandates on provision of non-urgent care were in place which limited investigations for non-specific, early cancer symptoms The primary level was reorganized in such a way, that a dual-track approach was implemented, meaning primary health care providers had to perform COVID-19 response services and at the same time maintain essential health services.[35] This put an unprecedented strain on the primary level, especially during COVID-19 peaks. Throughout most of the period, people had to contact their doctor

TABLE 2. Change (%) with 95% confidence interval in the referrals to cancer care services, and patient care provided at the Institute of Oncology Ljubljana in years 2020, 2021, 2022 compared to pre-COVID-19 year 2019. For 2022, only data from January to July are included and compared to corresponding months in 2019

	2020	2021	Jan.–July 2022
Referrals			
First cancer appointment	-1.8 (-4.4; 0.9)	5.4 (2.6; 8.2)	29.0 (25.0; 33.1)
Follow-up cancer appointment	-2.8 (-3.8; -1.9)	-14.3 (-15.2; -13.3)	-28.5 (-29.6; -27.4)
Oncological genetic testing and counselling	-11.9 (-16.3; -7.3)	15.3 (10.2; 20.5)	27.0 (20.1; 34.3)
First outpatient appointments at the Institute of Oncology Ljubljana			
Radiotherapy	5.7 (2.7; 8.8)	12.6 (9.4; 15.8)	13.8 (9.7; 18.1)
Surgery	-10.9 (-13.5; -8.3)	5.8 (3.0; 8.7)	15.7 (11.8; 19.6)
Medical oncology	-2.0 (-5.7; 1.8)	2.4 (-1.4; 6.3)	10.9 (5.7; 16.4)
All	-3.1 (-4.8; -1.3)	8.7 (6.9; 10.6)	15.3 (12.8; 17.8)
Follow-up outpatient appointments at the Institute of Oncology Ljubljana			
Radiotherapy	-13.6 (-14.6; -12.6)	-2.6 (-3.7; -1.6)	-2.1 (-3.5; -0.8)
Surgery	-13.2 (-14.3; -12.1)	-4.7 (-5.9; -3.5)	-8.1 (-9.6; -6.6)
Medical oncology	2.3 (1.3; 3.3)	12.8 (11.8; 13.9)	18.4 (17.0; 19.9)
All	-6.9 (-7.5; -6.3)	7.0 (6.3; 7.6)	8.1 (7.3; 9.0)
Cancer diagnostic imaging at the Institute of Oncology Ljubljana			
X-ray	-8.4 (-10.3; -6.4)	-0.5 (-2.5; 1.5)	-2.2 (-4.8; 0.5)
Mammography	2.8 (0.8; 4.8)	7.7 (5.7; 9.7)	8.2 (5.5; 10.8)
Ultrasound scans	-4.5 (-6.2; -2.8)	9.6 (7.8; 11.4)	19.6 (17.1; 22.1)
CT imaging	22.8 (20.8; 24.9)	45.7 (43.6; 47.9)	70.1 (67.0; 73.3)
MRI	14.8 (11.5; 18.1)	35.9 (32.4; 39.6)	38.5 (33.8; 43.3)
PET	4.6 (0.5; 8.8)	8.9 (4.8; 13.2)	11.7 (6.2; 17.4)

Change (in %) are coloured red when their 95% confidence interval is below zero; they are coloured green when their 95% confidence interval is above zero.

over the telephone or via e-mail to get an appointment, and they were also triaged over the telephone to determine whether an in-person visit was deemed necessary or not as well as then having to undergo a triage at entry points before seeing their doctor. Getting through on the telephone was relatively hard, since demand was great on account of COVID-19-related calls, while doctors at the primary level had also been reallocated to COVID-19 primary ambulatory clinics and to vaccination centres, which further limited their availability. Since most of the population with non-melanoma skin cancer are elderly (more than 69% of cases occur in people older than 65 years)[31], contact by e-mail was not a suitable alternative for a major part of this population. Access to dermatological appointments was lower during the epidemic, since there were periods when non-urgent appointments were banned by a governmental decree and all health care workers were asked to participate in the management of COVID-19.[28] Even in pre-pandemic times, getting a dermatological appointment was relatively hard, since waiting times for dermatological appointments within the public health care network in Slovenia are lengthy – in February 2020, the average waiting time for a first dermatological visit via a regular referral was almost 190 days and over 70 days for a very fast referral.[32] Thus, already in the pre-epidemic period a significant number of patients likely paid out of pocket for services at privately owned dermatological practices.[36]

Annual percentage growth of new skin melanoma diagnoses in Slovenia before the epidemic was among the highest, 2.6%.[31] Because they share similar risk factors as well as pathways through the health care system, a similar trend in incidence as for non-melanoma is expected for skin

melanoma. Our results show that shortly after the epidemic started, the number of new skin melanoma diagnoses decreased significantly, however in 2021 the incidence was at the 2019 level and rose by 5% in 2022 compared to 2019 – as expected if we consider pre-epidemic trends. The increase in melanoma cases could also result from a public health campaign that was launched in Slovenia to raise awareness about cancer and featured widely in Slovenian media[37]. The campaign aimed to raise public awareness on the pandemic's staggering disruption of cancer care by an overarching message: "Don't let COVID-19 stop you from tackling cancer".

Further, the up-to-date reports at onKOvid internet web page on delays in cancer diagnosis, which were also presented to the media, informed patients and decision-makers on the detrimental influence of COVID-19 epidemic restriction measures on oncology care, regardless of the fact that oncology services were exempt from measures and should have in theory remained undisturbed. We hypothesise that the intense public health interventions to raise general public awareness on the need to seek care when experiencing cancer related symptoms reflected also in the reversal of trends in new lymphoma cases during the epidemic – the number of diagnoses dropped in the beginning of the epidemic, but returned to expected numbers shortly afterwards, but we will only be able to evaluate this claim properly once standard registration procedures for the pandemic incidence years have been completed with more precise data on stage distribution and other characteristics. Furthermore, the heightened awareness perhaps also influenced doctors to be more alert to non-specific symptoms in patients that might be due to cancer.

If women in Slovenia are experiencing breast cancer symptoms, the first step in the care pathway is either their family doctor or primary level gynaecologist. During most pronounced restrictions, only urgent gynaecological services were performed, which limited their availability, while changes in health-seeking behaviour also likely played a role. The national screening programme for breast cancer, DORA programme, was stopped for two and a half months in total (since the middle of March until the beginning of June 2020). The programme managed to provide additional services during the summer months in 2020 and ended the year with only slightly lower numbers of performed mammographies (close to 8%), and discovering only 4% less breast cancers than in 2019.[38] In 2021, the programme performed 5% more mammographies and discovered 1% more cancers than in 2019.[39]

Likewise, the cervical and colorectal cancer screening programmes also resolved backlogs by the end of 2020 and did not report any backlogs in 2021, therefore, a negative outcome on population health in terms of a surge in cancers that would otherwise have been detected through screening programmes is not expected.[18,40,41] For colorectal cancer, there was no difference in the number of newly diagnosed cases in 2020 (after the initial drop in March through May, the numbers increased and were comparable to 2019 at the end of 2020), while yearly numbers decreased in 2021 (by 5%) and 2022 (by 8%), which is in line with the pre-epidemic downward incidence trend observed since 2010.[31]

There is no organised screening programme for prostate cancer in place in Slovenia, however many cases are diagnosed by opportunistic PSA testing. PSA testing is usually performed by a physician at the primary level or at higher levels following a referral issued by primary physicians. As already described, their accessibility was limited and thus fewer men had an opportunity to be offered PSA testing during a doctor visit, resulting in the observed drop of newly diagnosed prostate cancer cases.

Lung cancer was the only cancer with persistently higher diagnostic rates in the three epidemic years 2020, 2021 and 2022 compared to 2019. We theorize that this could be due to changed hospitalization patterns due to establishment of COVID-19 hospitals. In normal conditions, approximately one quarter of all lung cancer cases are treated at the University Clinical Hospital Golnik[31,42], which is a specialized hospital for lung diseases. During the epidemic, this hospital was converted into one of three referral hospitals for COVID-19 patients in Slovenia, which would mean that patients who under normal circumstances would be treated at University Clinical Hospital Golnik would have instead been referred to other hospitals. Since IOL is in relative proximity to the University Clinical Hospital Golnik and usually provides radiation therapy for all lung cancer cases, a significant number of lung cancer patients that would otherwise have been referred to the University Clinical Hospital Golnik were instead referred to the IOL due to changes in patient pathways. Since data from the University Clinical Hospital Golnik were not included in this analysis, the rise in lung cancer cases observed might not reflect the true pop-

ulation trend. However, the rise in detected lung cancer cases could also be the result of more intense imaging diagnostics for COVID-19 patients, the disease that effects the same organ, the lung. More reliable and detailed analyses are needed once standard incidence procedures for this period are completed.

The overall decline in the number of new cancer cases may be a real decline in incidence (eg. due to competing causes such as death from COVID-19) or it may simply reflect delays in diagnosis that the health system in Slovenia has not yet caught up with. Delays in diagnosis can lead to a higher proportion of cancers being detected at higher stages, which could result in worse outcomes (worse prognosis, poorer quality of life and, in some cases, earlier death) as shown in an Italian study of lung cancer patients[43] or the Swiss study on malignant melanoma.[6] Our results show, that at least at the IOL, the stage distribution of patients first seen for diagnostics or treatment has not significantly changed in comparison to the pre-epidemic period 2015–2019. However, there were significantly fewer patients first seen at the IOL in 2020 and 2021 at almost all ages except the oldest group (80+), but most pronounced for ages 50–64 years, and in 2020 fewer were seen for cancer progression or relapse. This age group might stand out because they were under a lot of stress with respect to employment during COVID-19 as well as perhaps having school-aged children who they had to take care of, with high levels of pandemic fatigue contributing to changed health-seeking behaviors. The impact of COVID-19 epidemic on the long-term indicators of cancer burden, such as survival, will only be possible to evaluate correctly in the longer term.

In general, outpatient appointments and cancer diagnostic imaging at the IOL dropped after the onset of COVID-19 epidemic. The exception was the CT imaging where the numbers were higher also immediately after the onset of COVID-19 epidemic. CT imaging was preferred to ultrasounds and x-rays as distance preventive measures were easier to implement and furthermore the relocation of personnel from other imaging diagnostic procedures was needed to make up for the CT scan delays from before the epidemic, which was considered urgent. This is also reflected in the significant drop of other cancer diagnostic imaging in March and April 2020, followed by a rise by the end of 2020 compared to 2019 to make up for the back-logs. In total, there were more cancer diagnostic imaging tests performed in 2020 compared to 2019 (with the exception of ultrasound scans) with numbers rising even more in 2021 and 2022. This rise was probably caused by cancer patients from other hospitals who were referred to IOL for imaging since other hospitals were overburdened with COVID-19 patients.

After a drop in 2020, the number of referrals to first cancer appointments and oncological genetic testing and counselling increased by more than a quarter in 2022 compared to 2019 figures. In particular, the staggering 77% drop in April 2020 (compared to April 2019) in oncological genetic testing and counselling was followed by intensive catch up in the following months (figures are available in the supplementary material). The Department of Oncological Clinical Genetics at the IOL reorganized its daily practice in line with official requirements, shifting appointments to additional hours in months with a lower COVID-19-burden, introducing telegenetic consultations that can also be performed when working from home, and introducing other new clinical pathways for genetic counselling and treatment. They carried out more first consultations, which helped them catch up on cancelled genetic consultations. With a good reorganization of the work, personnel reinforcement and the acquisition of premises for outpatient activities, they managed to catch up on the backlog of the first wave.[44]

In contrast to the first appointments, non-urgent care was largely postponed at the IOL. First outpatient appointments were not affected but the number of follow-up outpatient appointments dropped by more than 13% for both radiotherapy and surgery in 2020 compared to 2019, which persisted in 2021 and 2022. These could be due to changed clinical practice pathways.[45]

Cancer registries have a legal background for accessing many different data sources and they can and should convey their point of view on the COVID-19 epidemic. The SCR has a rich history of data collection, operating uninterrupted since 1950, and is considered one of the highest quality cancer registries that is leading the way in modern registration practices. Traditionally, hospitals report cases to the cancer registry via a customized paper-based Cancer Notification Form. In 2018, the gradual transition from passive (paper) to active (web) registration allowed for up-to-date online access to cancer records in health institutions. Active registration is an important advantage of the SCR and has enabled carrying out a real-time analysis of the impact of COVID-19 epidemic on delays in cancer diagnosis, based on the fact that delays in cancer diagnosis can be detected as tem-

porary drops in incidence over time. Under regular cancer registration procedures, delays in registration would have meant changes in trends could have been evaluated only after two to three years and would not have been as informative for decision makers who need up-to-date knowledge during crisis responses. Additionally, unlike the national cancer registry, the Hospital-Based Cancer Registry of the IOL has shorter delays in cancer registration, which allowed for more detailed real-time analyses including more patient characteristics. However, coverage in active registration and the IOL Hospital Registry is not national and including only the two major cancer centres is a disadvantage of our study as unknown biases might prevent extrapolations to the whole of Slovenia. We think the coverage is sufficient to minimise the potential for this type of bias in normal circumstances, but we cannot assess the scale of redirecting patients across health institutions due to measures for controlling the COVID-19 epidemic, which could have influenced observed trends. The IOL and the UMC Maribor are two out of three largest oncological centres in Slovenia and as such good representatives of all diagnosed cancer cases. For additional clarification we should emphasize that data on cancer cases cannot be interpreted as true incidence (number of all newly diagnosed cases of a disease that develop in a defined population in defined time period) but are simply comparisons of received cancer notification forms. At the time of conducting the present analysis, the SCR completed registration procedures up to the incidence year 2019. Additional reasoning not to conduct analyses on (estimated) incidence for years from 2020 on was that procedures on death certificates and notifications from Slovenian screening programmes were not yet processed. Based on CRS's previous analyses, this data sources could contribute to incidence up to 10%.[46]

Furthermore, to determine changes in cancer burden and cancer care we used a variety of sources, some with national coverage (referrals) and all pointing to a possibility of delay in cancer diagnosis, which makes our results more reliable. One of the disadvantages is that we were not able to evaluate and identify the causes behind results and were only able to hypothesise on causes. Off course, routinely collected data on a population level, which were used in our study, cannot convey the problems experienced on a patient's level – we recommend further studies based on individual-level retrospective investigation of cancer patients and how measures for controlling epidemic or having COVID-19 influenced their cancer diagnostics and treatment.

Conclusions

Our results show that the effects of the COVID-19 epidemic on cancer management in Slovenia vary for different cancers as well as by the level of the patient-care pathway – it is probably a mixture of changes in health-seeking behaviour and systemic changes due to modifications in healthcare organisation on account of COVID-19.

During the COVID-19 pandemic, management of cancer, which often starts with non-specific symptoms not deemed urgent but which need to be addressed quickly, was significantly affected. In Slovenia, the delay in cancer services from the first wave of the epidemic from March through May 2020 has been eliminated by 2022, but we still see fewer than expected new cancer cases in 2022, which reflects disruptions in the pre-diagnostic phase and could have profound long-term consequences on cancer burden indicators. To make incidence figures fully comparable with previous years on the population level, it is necessary to review all the notifications obtained by the SCR for the study period. Due to different disease trajectories of different cancer types we expect different medium- and long-term effects, such as the population-based survival of cancer patients, which serves as a complex indicator reflecting the characteristics of patients as well as the organization, accessibility, quality and efficiency of healthcare system, and which could be examined in a few years' time.

Acknowledgments

The authors of this article would like to express thanks to Associate Professor Mateja Krajc, Ph.D., head of the Cancer Genetics Clinic at Institute of Oncology Ljubljana, for useful insights into the actual workflow and management of patients at the Institute, and to Ms. Metka Zaletel, the head of the Health Data Centre at the National Institute of Public Health, for all the support in accessing and analysing data from the national e-referral system.

This work was funded by the Slovenian Research Agency and the Ministry of Health through a targeted research project entitled "The Impact of the COVID-19 Epidemic on Cancer Control in Slovenia" (grant number V3-2032). The

funding sources had no role in study design, the collection, analysis or interpretation of data, the writing of the report, or the decision to submit the article for publication.

References

1. OECD/European Union. How resilient have European health systems been to the COVID-19 crisis? In: *Health at a glance: Europe 2020: state of health in the EU cycle*. Paris: OECD Publishing; 2020.
2. Lazzerini M, Barbi E, Apicella A, Marchetti F, Cardinale F, Trobia G. Delayed access or provision of care in Italy resulting from fear of COVID-19. *Lancet Child Adolesc Health* 2020; **4:** e10-1. doi: 10.1016/S2352-4642(20)30108-5
3. Tangcharoensathien V, Bassett MT, Meng Q, Mills A. Are overwhelmed health systems an inevitable consequence of covid-19? Experiences from China, Thailand, and New York State. *BMJ* 2021; **372:** n83. doi: 10.1136/bmj.n83
4. Neamtiu L, Martos C, Giusti F, Negrao Carvalho R, Randi G, Dimitrova N, et al. Impact of the first wave of the COVID-19 pandemic on cancer registration and cancer care: a European survey. *Eur J Public Health* 2021; **32:** 311-5. doi: 10.1093/eurpub/ckab214
5. Soerjomataram I, Bardot A, Aitken J, Piñeros M, Znaor A, Steliarova-Foucher E, et al. Impact of the COVID-19 pandemic on population-based cancer registry. *Int J Cancer* 2022; **150:** 273-8. doi: 10.1002/ijc.33792
6. Kostner L, Cerminara SE, Pamplona GSP, Maul JT, Dummer R, Ramelyte E, et al. Effects of COVID-19 lockdown on melanoma diagnosis in Switzerland: increased tumor thickness in elderly females and shift towards stage IV melanoma during lockdown. *Cancers* 2022; **14:** 2360. doi: 10.3390/cancers14102360
7. Ribes J, Pareja L, Sanz X, Mosteiro S, Escribà JM, Esteban L, et al. Cancer diagnosis in Catalonia (Spain) after two years of COVID-19 pandemic: an incomplete recovery. *ESMO Open* 2022; **7:** 100486. doi: 10.1016/j.esmoop.2022.100486
8. Dinmohamed AG, Visser O, Verhoeven RHA, Louwman MWJ, Nederveen FH, Willems SM, et al. Fewer cancer diagnoses during the COVID-19 epidemic in the Netherlands. *Lancet Oncol* 2020; **21:** 750-1. doi: 10.1016/S1470-2045(20)30265-5
9. Peacock HM, Tambuyzer T, Verdoodt F, Calay F, Poirel HA, Schutter H, et al. Decline and incomplete recovery in cancer diagnoses during the COVID-19 pandemic in Belgium: a year-long, population-level analysis. *ESMO Open* 2021; **6:** 100197. doi: 10.1016/j.esmoop.2021.100197
10. Hamilton AC, Donnelly DW, Loughrey MB, Turkington RC, Fox C, Fitzpatrick D, et al. Inequalities in the decline and recovery of pathological cancer diagnoses during the first six months of the COVID-19 pandemic: a population-based study. *Br J Cancer* 2021; **125:** 798-805. doi: 10.1038/s41416-021-01472-0
11. Skovlund CW, Friis S, Dehlendorff C, Nilbert MC, Mørch LS. Hidden morbidities: drop in cancer diagnoses during the COVID-19 pandemic in Denmark. *Acta Oncol* 2021; **60:** 20-3. doi: 10.1080/0284186X.2020.1858235
12. Skovlund CW, Friis S, Christensen J, Nilbert MC, Mørch LS. Drop in cancer diagnosis during the COVID-19 pandemic in Denmark: assessment of impact during 2020. *Acta Oncol* 2022; **61:** 658-61. doi: 10.1080/0284186X.2021.2024879
13. Griewing S, Wagner U, Lingenfelder M, Fischer R, Kalder M. Chronological development of in-patient oncology in times of COVID-19: a retrospective analysis of hospitalized oncology and COVID-19 patients of a German University Hospital. *J Cancer Res Clin Oncol* 2022; online ahead of print. doi: 10.1007/s00432-022-04044-8
14. Blay JY, Boucher S, Le Vu B, Cropet C, Chabaud S, Perol D, et al. Delayed care for patients with newly diagnosed cancer due to COVID-19 and estimated impact on cancer mortality in France. *ESMO Open* 2021; **6:** 100134. doi: 10.1016/j.esmoop.2021.100134
15. Lai AG, Pasea L, Banerjee A, Hall G, Denaxas S, Chang WH, et al. Estimated impact of the COVID-19 pandemic on cancer services and excess 1-year mortality in people with cancer and multimorbidity: near real-time data on cancer care, cancer deaths and a population-based cohort study. *BMJ Open* 2020; **10:** e043828. doi: 10.1136/bmjopen-2020-043828
16. Onyeaka H, Anumudu CK, Al-Sharify ZT, Egele-Godswill E, Mbaegbu P. COVID-19 pandemic: A review of the global lockdown and its far-reaching effects. *Sci Prog* 2021; **104:** 368504211019854. doi: 10.1177/00368504211019854
17. Zadnik V, Mihor A, Tomšič S, Žagar T, Bric N, Lokar K, Oblak I. Impact of COVID-19 on cancer diagnosis and management in Slovenia – preliminary results. *Radiol Oncol* 2020; **54:** 329-34. doi: 10.2478/raon-2020-0048
18. Ivanuš U, Jerman T, Gašper Oblak U, Meglič L, Florjančič M, Strojan Fležar M, et al. The impact of the COVID-19 pandemic on organised cervical cancer screening: The first results of the Slovenian cervical screening programme and registry. *Lancet Reg Health Eur* 2021; **5:** 100101. doi: 10.1016/j.lanepe.2021.100101
19. National Institute of Public Health. [Vaccination against covid-19 in Slovenia]. [Slovenian]. [cited 2022 Oct 26]. Available from: https://app.powerbi.com/view?r=eyJrIjoiYWQ3NGE1NTMtZWJkMi00NzZmLWFiNDItZDc5YjU5MGRkOGMyIiwidCI6ImFkMjQ1ZGFlLTQ0YTAtNGQ5NC04OTY3LTVjNjk5MGFmYTQ2MyIsImMiOjl9
20. Leban E, Grašek M, Mozetič M, Učakar V. The COVID-19 epidemic in Slovenia. In: Vračko P, Kolar U, editors. *Public Health Achivements in Slovenia*. Ljubljana: National Institute of Public Health; 2021. p. 104.
21. Sledilnik.org. *COVID-19 situation in Slovenia*. Project COVID-19 Tracker Slovenia. [cited 2022 Sept 15]. Available from: https://covid-19.sledilnik.org/en/stats
22. National Institute of Public Health. [Daily monitoring of SARS-CoV-2 (COVID-19) infections]. [Slovenian]. [cited 2022 Oct 26]. Available from: https://www.nijz.si/sl/dnevno-spremljanje-okuzb-s-sars-cov-2-covid-19
23. STA. *Hospitals prepare for expected rise in hospitalisations amid staff shortage.s* [cited 2022 Oct 26]. Available from: https://www.total-slovenia-news.com/lifestyle/7626-hospitals-prepare-for-expected-rise-in-hospitalisations-amid-staff-shortages
24. Hočevar Grom A, Belščak Čolaković A, Rehberger M, Lavtar D. SI-PANDA – survey on the impact of the COVID-19 pandemic on people's lives. In: Vračko P, Kolar U, editors. *Public health achivements in Slovenia*. Ljubljana: National Institute of Public Health; 2021. p. 17.
25. National Institute of Public Health. [*Survey on the impact of the COVID-19 pandemic on people's lives = SI-PANDA*.] [Slovenian]. [cited 2022 Sept 15]. Available from: https://www.nijz.si/sl/izsledki-panelne-spletne-raziskave-si-panda
26. COVID-19 Excess Mortality Collaborators. Estimating excess mortality due to the COVID-19 pandemic: a systematic analysis of COVID-19-related mortality, 2020–21. *Lancet* 2022; **399:** 1513-36. doi: 10.1016/ S0140-6736(21)02796-3
27. National Laboratory of Health, Environment and Food. [Monitoring of SARS-CoV-2 Variants]. [Slovenian]. [cited 2022 Sept 15]. Available from: https://www.nlzoh.si/objave/sledenje-razlicicam-sars-cov-2-62/; https://www.ius-info.si/medijsko-sredisce/v-srediscu/295761
28. IUS-INFO. [Monitoring of legislative concerning COVID]. [Slovenian]. [cited 2022 Sept 15]. Available from: https://www.iusinfo.si/medijsko-sredisce/v-srediscu/259417
29. Jawad M, Millett C, Sullivan R, Alturki F, Roberts B, Vamos EP. The impact of armed conflict on cancer among civilian populations in low- and middle-income countries: a systematic review. *Ecancermedicalscience* 2020; **14:** 1039. doi: 10.3332/ecancer.2020.1039
30. Zadnik V, Primic Žakelj M, Lokar K, Jarm K, Ivanuš U, Žagar T. Cancer burden in Slovenia with the time trends analysis. *Radiol Oncol* 2017; **51:** 47-55. doi: 10.1515/raon-2017-0008
31. *Cancer in Slovenia 2019*. Zadnik V, Gašljević G, Hočevar M, Jarm K, Pompe-Kirn V, Strojan P, et al, editors. Ljubljana: Institute of Oncology Ljubljana, Epidemiology and Cancer Registry, Slovenian Cancer Registry; 2022.
32. Breznikar D. [National monitoring of waiting times, Monthly report on status on 01. 02. 2020]. [Slovenian]. Ljubljana: National Institute of Public Health. Available from: https://www.nijz.si/sites/www.nijz.si/files/publikacije-datoteke/porocilo_enarocanje_1._2._2020_0.pdf
33. Zadnik V, Žagar T, Bric N, Tomšič S, Mihor A, Lokar K, Jarm K. *onKOvid*. Epidemiology and Cancer Registry, Institute of Oncology Ljubljana. [cited 2022 Sep 15]. Available from: http://www.slora.si/en/onkovid
34. Walter FM, Humphrys E, Tso S, Johnson M, Cohn S. Patient understanding of moles and skin cancer, and factors influencing presentation in primary care: a qualitative study. *BMC Family Practice* 2010; **11:** 62.

35. Vračko P, Petrič VK, Borgermans B. *Community health centres with multidisciplinary teams provide an effective dual-track approach to COVID-19*. World Health Organization, Regional office for Europe; 2021.

36. Hrovatin B. [Analysis of the causes of waiting times in the field of dermatology] [Slovenian]. Master thesis. Ljubljana: University of Ljubljana, School of Economics and Business; 2016.

37. Time To Act. *Don't let COVID-19 stop you from tackling cancer.* [cited 2022 Oct 25]. Available from: https://www.sip-platform.eu/campaign/time-to-act-campaign/time-to-act-don-t-let-covid-19-stop-you-from-tackling-cancer

38. National Breast Cancer Screening Programme DORA. [Yearly report for 2020]. [Slovenian]. [cited 2022 Aug 15]. Ljubljana: Institute of Oncology Ljubljana; 2021. Available from: https://dora.onko-i.si/fileadmin/user_upload/Dokumenti/DORA_Letno_porocilo_2020_splet.pdf

39. National Breast Cancer Screening Programme DORA. [Yearly report for 2021]. [Slovenian]. [cited 2022 Aug 15]. Ljubljana: Institute of Oncology Ljubljana; 2022. Available from: https://dora.onko-i.si/fileadmin/user_upload/Dokumenti/DORA_Letno_porocilo_2021_WEB_apr_2022.pdf

40. Novak Mlakar D, Kofol Bric T, Šinkovec A, Fistrič Š. [The impact of the COVID-19 epidemic on programme Svit]. [Slovenian]. In: Gabrovec B, Eržen I, Trop Skaza A, Fafangel M, Vrdelja M, Selak Š, editors. Public Health and COVID-19. Scientific and Professional Conference: Ljubljana, 29th September, 2021: a compendium of abstracts and peer-reviewed papers. Ljubljana: National Institute of Public Health; 2021. p. 102–107. Available from: https://www.nijz.si/sl/publikacije/zbornik-povzetkov-in-recenziranih-prispevkov-javno-zdravje-in-covid-19

41. Jarm K, Kurir Borovčić M, Hertl K, Vrhovec M, Škrbec V, Kutnar V. [Slovenian breast cancer screening programme and COVID-19]. [Slovenian]. In: Gabrovec B, Eržen I, Trop Skaza A, Fafangel M, Vrdelja M, Selak Š, editors. In: Public Health and COVID-19. Scientific and Professional Conference: Ljubljana, 29th September, 2021: a compendium of abstracts and peer-reviewed papers. Ljubljana: National Institute of Public Health; 2021. p. 102–107. Available from: https://www.nijz.si/sl/publikacije/zbornik-povzetkov-in-recenziranih-prispevkov-javno-zdravje-in-covid-19

42. [Report of hospital registry of University Clinic Golnik of tumours of the chest 2010–2018]. [Slovenian]. [cited 2022 Sep 15]. Available from: https://www.klinika-golnik.si/storage/_sites/golnik/app/media/Onkolo%C5%A1ka%20dejavnost%20-%20klini%C4%8Dni%20register%20bolnikov/Register%20raka%20plju%C4%8D%202010%20-%202017%20PDF%20za%20internet.pdf

43. Bertolaccini L, Sedda G, Spaggiari L. Paying another tribute to the COVID-19 pandemic: the decrease of early lung cancers. *Ann Thorac Surg* 2021; **111**: 745-6. doi: 10.1016/j.athoracsur.2020.11.013

44. Klopčič N, Hotujec S, Kerševan T, Blatnik A, Strojnik K, Krajc M. [Impact of the covid-19 epidemic on the oncogenetic assessment at the Cancer Genetics Clinic of the Institute of Oncology Ljubljana]. [Slovenian]. *Onkologija* 2021; **25:** 24-33. doi:10.25670/oi2021-014on

45. Osterrieder A, Cuman G, Pan-Ngum W, Kin Cheah P, Cheah PK, Peerawaranun P, et al. Economic and social impacts of COVID-19 and public health measures: results from an anonymous online survey in Thailand, Malaysia, the UK, Italy and Slovenia. *BMJ Open* 2021; **11:** e046863. doi:10.1136/bmjopen-2020-046863

46. Primic-Žakelj M, Žagar T, Zadnik V, Škrlec F. *Linkage of the Slovenian Cancer Registry data to other state databases and to screening registries*. In: Rosso S, et al, editors. Towards a harmonised cancer information system in Europe. ENCR Scientific Meeting and General Assembly, 12-14 November 2014. Ispra, Italy: ENCR-JRC; 2014. p. 71.

research article

Plasma sICAM-1 correlates with tumor volume before primary radiochemotherapy of head and neck squamous cell carcinoma patients

Kerstin Clasen[1], Stefan Welz[2], Heidrun Faltin[3], Daniel Zips[1,4], Franziska Eckert[1,3,4,5]

[1] Department of Radiation Oncology, Medical Faculty and University Hospital, Eberhard Karls University, Tuebingen, Germany
[2] Department of Radiation Oncology, Marienhospital Stuttgart, Stuttgart, Germany
[3] Section for Experimental Radiation Oncology, Department of Radiation Oncology, Medical Faculty and University Hospital, Eberhard Karls University, Tuebingen, Germany
[4] German Cancer Consortium (DKTK), German Cancer Research Center (DKFZ) partner site Tuebingen, Tuebingen, Germany
[5] Department of Radiation Oncology, Medical University Vienna, AKH, Comprehensive Cancer Center, Vienna, Austria

Radiol Oncol 2022; 56(4): 501-507.

Received 31 August 2022
Accepted 29 September 2022

Correspondence to: Franziska Eckert, M.D., Department of Radiation Oncology, Medical University Vienna, AKH, Comprehensive Cancer Center, Waehringer Guertel 18-20, A-1090 Vienna, Austria. E-mail: franziska.eckert@meduniwien.ac.at

Disclosure: K. Clasen, S. Welz, F. Eckert have research and educational grants from Elekta, Philips, Siemens, Sennewald. D. Zips has research and educational grants from Elekta, Philips, Siemens, Sennewald, Kaikuu, Therapanacea. H. Faltin declares that she has no conflict of interest.

Background. Biomarkers are of major interest to optimize diagnosis, prognosis and to guide treatment in head and neck cancer patients. Especially blood-based biomarkers appear promising as they can be easily collected and repeatedly analyzed during the course of radiochemotherapy.

Patients and methods. At first, for a broad overview, multiple immune markers were evaluated in six plasma samples of three head and neck squamous cell carcinoma (HNSCC) patients at the beginning and the end of radiochemotherapy. In this pre-selection, the soluble Intercellular Adhesion Molecule 1 (sICAM-1) appeared most promising. Thus, this marker was measured in multiple samples (n = 86) during treatment and follow-up in a cohort of eleven patients and correlated with tumor features and clinical data.

Results. We found a strong correlation between the initial levels of sICAM-1 in the plasma and the gross tumor volumes of the primary tumor and the involved lymph nodes. However, during the course of treatment no systematic dynamics could be identified. Toxicity or infections did not seem to influence sICAM-1 concentrations.

Conclusions. sICAM-1 appears to reflect the pre-treatment total tumor burden (primary tumor and involved lymph nodes) in head and neck tumor patients. However, it does not seem to be a dynamic marker reflecting response during radiochemotherapy. Thus, if our findings are confirmed in future, sICAM-1 could be used as a staging marker: if high sICAM-1 levels but low tumor burden are found it might be reasonable to intensify staging investigations to rule out further, yet undetected, tumor sites.

Key words: head and neck cancer; biomarker; radiotherapy; tumor volume; gross tumor volume, sICAM-1

Introduction

Biomarkers are a promising feature to personalize radiotherapy treatment of head and neck squamous cell carcinoma (HNSCC). To some extent the focus has already shifted from sole anatomical tumor stage to biological features[1] with HPV being integrated in the 8th edition of the AJCC staging manual.[2] The superior discrimination of patient outcomes by combined anatomical and biological factors have been validated in the US national cancer database.[3] HPV / p16 positive HNSCC might be

treated differently than HPV / p16 negative cancers in the near future.[4] Due to the superior prognosis treatment de-escalation has been proposed in this subgroup of patients.[5] Blood-based biomarkers have not been developed this far yet, however, there is major interest, as blood samples can be easily obtained not only at time of diagnosis, but also throughout treatment and follow-up. Different classes of blood biomarkers have been described in HNSCC such as circulating tumor cells and nucleic acids (e.g. circulating cell-free DNA (cfDNA), circulating cell-free tumor DNA (ctDNA), exosomal RNA).[6] In addition, microRNAs, long non-coding RNAs and DNA methylation patterns have been described as potential biomarkers in blood and saliva of HNSCC patients.[7] Proteomics approaches have been used to identify protein biomarkers in HNSCC tumors and body fluids of patients.[8] For radiation oncology, different clinical settings and treatment modifications based on circulating biomarkers have been hypothesized.[9,10] Possible approaches are patient stratification for more or less intense treatment based on prognostic markers or adaptive approaches tailoring treatment to biomarker responses e.g. during fractionated radio(chemo)therapy.[9,10]

Cytokines and chemokines play a crucial role in the intercellular communication of cancer and immune cells and can be measured in serum / plasma of patients with different tumor entities. Different cytokine profiles have been reported to be altered in cancer patients compared to healthy volunteers (e.g. in breast cancer[11], nasopharyngeal carcinoma[12] and HNSCC[13]). Clinical response to systemic therapy has been linked to cytokine profiles for metastatic renal cell carcinoma[14], non-small cell lung cancer treated with tyrosine kinase inhibitor[15] and nasopharyngeal carcinoma.[12,16] For HNSCC, several reports focusing on different cytokines have been published. Osteopontin has been linked to initial tumor burden and response to radiochemotherapy.[17] CXCL12 (SDF-1) but not its receptor CXCR4 was elevated in the serum of HNSCC patients compared to healthy volunteers.[18] Radiochemotherapy for HNSCC significantly decreased TGFβ levels[19], whereas high plasma C-reactive protein (CRP) and TNFα levels were found in patients and was associated with worse prognosis.[20]

In this prospective pilot study, at first, diverse plasma cytokine levels were evaluated in HNSCC patients undergoing definitive radiochemotherapy. Subsequently, focusing on the soluble Intercellular Adhesion Molecule 1 (sICAM-1), dynamics during and after radiochemotherapy as well as associations with clinical patient and tumor characteristics and patient outcome were evaluated.

Patients and methods

In this prospective pilot biomarker study, patients with newly diagnosed, locally advanced HNSCC were included. All patients declared their informed written consent and the study was approved by the local ethics committee (reference number 064/2016BO2). The study was performed in accordance with the ethical standards as laid down in the 1964 Declaration of Helsinki and its later amendments.

As described previously[21], eleven patients were included in this study, who underwent primary radiochemotherapy. Radiotherapy to 54 / 60 / 70 Gy to elective nodal regions / high risk regions / macroscopic primary tumor and lymph node metastases was combined with cisplatin in eight cases or 5-fluorouracil and mitomycin C in three patients, respectively. For every patient initial tumor volumes, as contoured for radiotherapy including the primary tumor and involved lymph nodes were recorded, as well as disease free survival (DFS, local or distant recurrence or death of any cause). Clinically manifest infections and toxicity graded according to the Radiation Therapy Oncology Group (RTOG) were recorded and correlated with sICAM-1 levels in the plasma.

Blood sampling was planned weekly on Mondays before the application of the radiotherapy fraction during radiochemotherapy as well as at every available follow-up time point. For one patient, the initial sample was taken on day 2 of radiochemotherapy. In total, 86 samples were analyzed, 62 during treatment, 24 during follow-up, respectively. A median of six samples (range: 4–7) were analyzed per patient during treatment. Blood was collected in EDTA tubes (Sarstedt, Nümbrecht, Germany), plasma isolation was performed by centrifugation. Plasma samples were stored in -80°C in aliquots until further use.

For three patients, plasma samples before radiochemotherapy and at end of treatment were analyzed by the human cytokine array Proteome ProfilerTM Array, Human Cytokine Array Panel A (R&D Systems Europe, Abingdon, UK) analyzing CCL1, CCL2, CCL3, CCL5, CD40L, C5/C5a, CXCL1, CXCL10, CXCL11, CXCL12 (SDF1), G-CSF, GM-CSF, sICAM-1, IFNγ, IL-1F1, IL-1F2, IL-1F3, IL2, IL4, IL5, IL6, IL8, IL10, IL12, IL13, IL16, IL17A,

IL17E, IL18, IL21, IL27, IL32α, MIF, SerpinE1, TNFα and sTREM-0. Plasma samples were incubated on the membranes and washing and staining steps were performed according to manufacturer's instructions. After development of films, semi-quantitative analysis was performed by densitometric assessment of the films with ImageJ normalized to control regions adjacent to analyzed areas. Arbitrary densitometry units were analyzed for all six samples, mean of technical duplicates were used for further analyses.

For further analysis of sICAM-1, all available samples of all time points were analyzed with Enzyme-linked Immunosorbent Assay (ELISA) according to manufacturer's instruction (Human ICAM1 ELISA Kit (CD54) (ab174445), Abcam, Cambridge, UK). Standard curves were measured with the following concentrations of ICAM-1: 0 pg/ml, 19.53 pg/ml, 39.06 pg/ml, 78.13 pg/ml, 156 pg/ml, 312 pg/ml, 625 pg/ml, 1250 pg/ml, 2500 pg/ml, 5000 pg/ml ($R^2 = 0.99$). Every sample was measured in technical duplicates, means were used for further analyses. For every patient, absolute sICAM-1 concentrations at each time point as well as relative sICAM-1 concentrations normalized to the baseline value of the respective patient were recorded. Patients stratified by median initial sICAM-1 values were analyzed for DFS. Pooled values of all patients were used for the analysis of time points with and without manifest infection (53 available time points) as well as RTOG graded toxicity (58 available time points). Plasma sICAM-1 concentrations at the beginning of radiochemotherapy were correlated with gross tumor volumes (GTVs) for the primary tumor, lymph node metastases and hull of both.

Statistical analysis included Kaplan Meier method of DFS and comparison by log-rank-test. Means were compared by t-test or Mann-Whitney test depending on whether values passed normality test. In case of multiple testing Bonferroni correction was performed. Pearson correlation coefficients were used to characterize correlations of continuous variables (moderate correlation defined as 0.4–0.7; strong correlation defined as > 0.7). Level of significance was defined with $p < 0.05$. Analyses were done with IBM SPSS Version 26 and GraphPad Version 8.

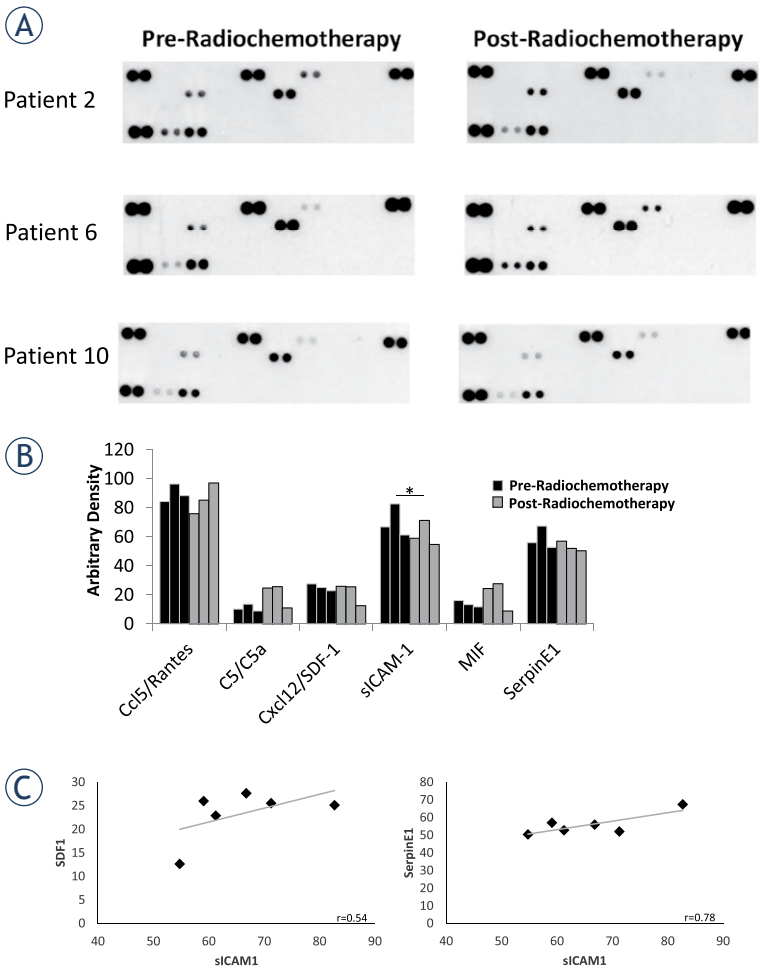

FIGURE 1. Plasma of three patients before and at end of radiochemotherapy for head and neck squamous cell carcinoma were analyzed with a human cytokine array. Of the tested cytokines, only six were present in detectable concentrations (Ccl5, Complement Component, SDF1, sICAM-1, MIF and SerpinE1). sICAM-1 was the only cytokine with a significant difference between the tested time points decreasing after treatment. sICAM-1 abundance showed moderate and strong correlations with SDF1 and SerpinE1, respectively.

Results

The patient cohort has been described previously in Clasen *et al.*[21] Patients exhibited typical features for primary radiochemotherapy of HNSCC. Three female and eight male patients were included and the tumors were located in the oropharynx (n = 5), hypopharynx (n = 5) and larynx (n = 1). With three of eleven patients (27%) developing recurrences or metastases (range of follow-up: 2.5 to 4.0 years (mean 3.7)), oncologic outcomes seem in the range of published data. At the time point of the analysis, all patients were alive.

Cytokine abundances

Six of the 36 cytokines measured by the human cytokine array (CCL5/ Rantes, C5/C5a, CXCL12 / SDF-1, sICAM-1, MIF, SerpinE1) showed measur-

A

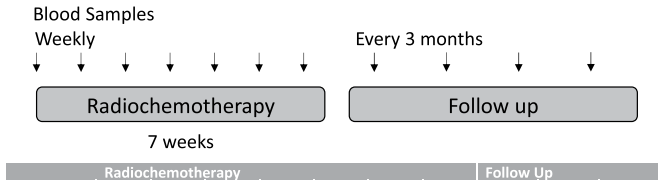

	Radiochemotherapy							Follow Up		
	Week 1	Week 2	Week 3	Week 4	Week 5	Week 6	Week 7	Follow Up 1	Follow Up 2	Follow Up 3
Patient 1	x		x	x	x	x		x	x	x
Patient 2	x	x	x	x	x	X			x	x
Patient 3	x	x	x	x	x		x	x	x	
Patient 4	x	x	x	x	x	X	x	x	x	x
Patient 5	x	x	x	x	x	x	x		x	x
Patient 6	x	x	x	x	x		x			
Patient 7	x	x	x		x	x		x	x	x
Patient 8	x	x	x		x			x	x	x
Patient 9	x	x	x	x	x			x	x	x
Patient 10	x	x	x	x		x			x	x
Patient 11	x	x	x	x	x	x			x	

B

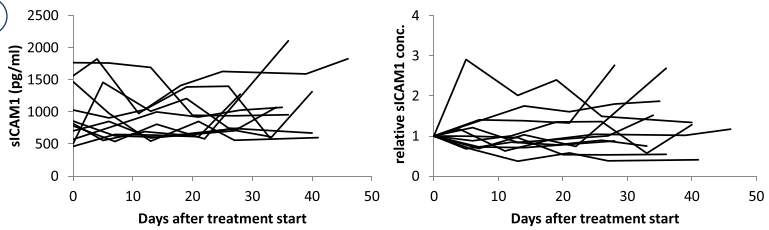

C

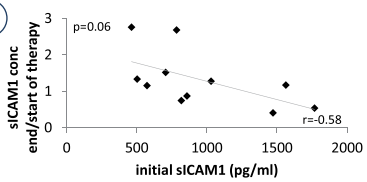

FIGURE 2. Blood samples were taken weekly during radiochemotherapy and at every follow-up visit of the patients. In total, 86 samples were evaluated at the different time points as shown in the table for every single patient included in the study **(A)**. sICAM-1 concentrations measured by ELISA in plasma samples of 11 patients differed significantly between patients. Over the course of treatment and compared intraindividually before and after treatment sICAM-1 concentrations did not show significant changes **(B)**. Initial sICAM-1 concentrations showed a moderate negative correlation with relative sICAM-1 levels at the end of treatment **(C)**.

able abundances in the plasma of three HNSCC patients before and at the end of radiochemotherapy (Figure 1A, B). The only cytokine with a significant difference over the course of radiotherapy was sICAM-1 (Figure 1B). sICAM-1 abundances decreased significantly at the end of radiochemotherapy. sICAM-1 levels in all six samples showed a moderate and strong correlation with SDF1 and SerpinE1, respectively (Figure 1C). SDF-1 was not associated with GTV volumes, whereas SerpinE1 showed a strong positive correlation (r = 0.92, data not shown).

sICAM-1 levels during radiochemotherapy

sICAM-1 concentrations at 86 time points (Figure 2A) during and after radiochemotherapy of eleven patients measured by ELISA differed significantly at baseline with a median of 818.4 pg/ml (range: 462.0–1767.5 pg/ml). Over the course of treatment, no systematic changes were observed (Figure 2B). Relative sICAM-1 levels also did not change significantly during radiochemotherapy (Figure 2B). Patients with high initial sICAM1 concentrations tended to have decreasing levels over the course of therapy as demonstrated by a moderate negative correlation between initial sICAM-1 concentrations and relative sICAM-1 levels at end of radiochemotherapy (Figure 2C).

Disease free survival

Mean disease-free survival for the whole cohort was 3.3 ± 0.4 years. All patients experiencing a recurrence had N2 disease before radiochemotherapy ($p = 0.23$, data not shown). Median initial sICAM-1 concentration was used to stratify the patient cohort in two groups. The two patients experiencing early recurrences in the first year were in the group of high initial sICAM-1 concentrations. The patient experiencing a late recurrence had low initial sICAM-1 values. Overall, no statistical significance was observed (Figure 3).

sICAM-1 levels and infection and toxicity

A pooled analysis of relative sICAM-1 concentrations normalized to baseline values at all time points of all patients was performed. sICAM-1 levels were slightly higher at time points of clinically manifest infections, although without statistical significance (Figure 4A). No difference was observed for sICAM-1 levels at time points with toxicity graded according to RTOG (Figure 4B).

Tumor volumes (GTV) and initial sICAM-1 concentrations

For the analysis of tumor volumes contoured for radiotherapy planning, one patient with an exceptionally large lymph node metastasis was excluded (GTV LN of 150.2 cm^3, compared to 3.3–23.9 cm^3 for the other patients). Primary tumor volume (GTV PT) as well as volume of lymph node metastases (GTV LN) showed a moderate correlation with sICAM-1 concentrations measured at the start of radiochemotherapy (Figure 5A, B). GTV PT

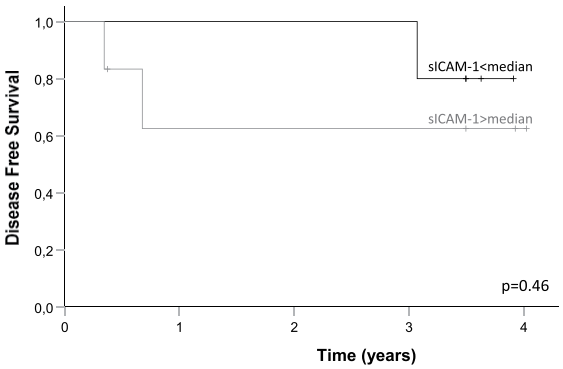

FIGURE 3. Kaplan Meier analysis of disease-free survival stratified by median initial sICAM-1 concentration showed that the two patients with early recurrence in the first year after treatment were in the group with high sICAM-1 levels. Disease-free survival in the small patient cohort did not differ significantly for high and low sICAM-1 concentrations.

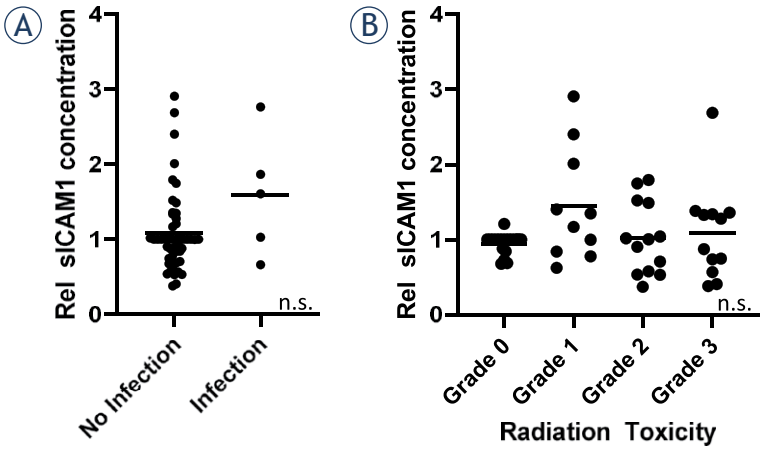

FIGURE 4. sICAM-1 levels at time points with manifest infections showed a tendency to higher concentrations compared to all other time points, however, without statistical significance **(A)**. No difference in sICAM-1 concentrations was observed comparing time points with different documented Radiation Therapy Oncology Group (RTOG) toxicity grades **(B)**.

and GTV LN were not correlated with each other (r = -0.17, data not shown). The hull of GTV PT and GTV LN reflecting the total tumor burden of the patient before the start of radiochemotherapy showed a strong correlation with initial sICAM-1 concentrations (Figure 5C). With a cut-off of 50 cm^3, sCIAM1 levels were significantly higher for larger tumors with 1600.8 ± 87.5 pg/ml vs 718.2 ± 79.3 pg/ml ($p < 0.01$).

Discussion

In this study, sICAM-1 was identified as a plasma cytokine that significantly decreased during definitive radiochemotherapy of three head and neck cancer patients in a cytokine array of 36 cytokines. In a larger patient cohort of eight additional patients (eleven in total) and additional time points during therapy and during follow-up these findings could not be confirmed. No conclusions can be drawn concerning sICAM-1 and oncological outcomes. The fact that both patients developing early recurrences presented with high initial sICAM-1 levels might be of notice. No correlation of sICAM-1 levels with infection and toxicity were observed (in contrast to recent findings for HMGB1 in the same patient cohort).[21] The most prominent finding is a strong correlation of initial sICAM-1 concentrations with the tumor burden of the patients at the start of radiochemotherapy as contoured for radiotherapy planning. This finding is in line with a report on hepatocellular carcinoma, which also found a correlation of sICAM-1 levels with tumor volume and tumor stage.[22] In colorectal cancer, sICAM1 levels correlated with tumor diameter.[23]

ICAM-1 (CD54) on endothelial cells is a crucial mediator of leukocyte adhesion to blood vessel walls.[24] In its soluble form, sICAM-1 is involved in autoimmune and inflammatory diseases, as well as infections and cancer.[25] Elevated sICAM-1 levels have been described in various cancer entities and have been linked to tumor stage and prognosis in HCC[22], gastric cancer[26,27] and cervical cancer.[28] The largest body of evidence was found for breast cancer with an association with tumor stage but no effect on immune function[29,30,31], colorectal cancer with an association with tumor stage and prognosis[32,33,34] and meta-analyses for lung cancer.[35,36] In HNSCC, elevated levels of sICAM-1 were found in comparison to healthy controls, without significant changes after radiochemotherapy[37], which is in line with our findings. The positive correlation of sICAM-1 with SerpinE1 might be explained by the link of both parameters to total tumor burden. SerpinE1 has been established as a prognostic marker in breast cancer and seems to be associated with cancer spread and metastasis.[38] The association with SDF1 is not that easily explainable as SDF1 was not associated with tumor size.

sICAM-1 might be a soluble plasma marker for initial tumor burden. In contrast to cfDNA[39] and HMGB1[21], sICAM-1 levels were not significantly influenced by infection or toxicity. As these con-

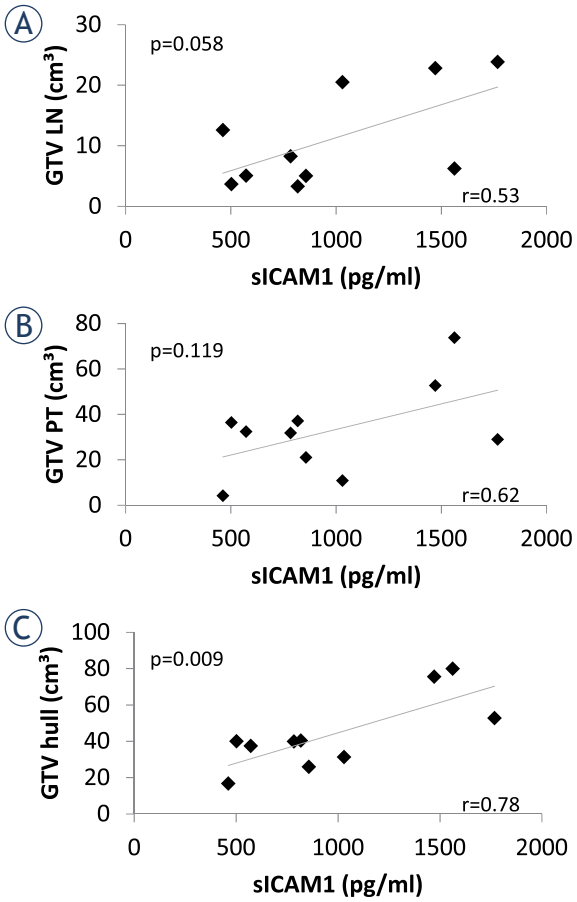

FIGURE 5. After exclusion of one patient with a large, mostly necrotic lymph node metastasis, initial pretherapeutic sICAM-1 levels showed moderate positive correlations with primary tumor volumes **(A)** and volumes of lymph node metastases **(B)** contoured for radiotherapy planning and a strong correlation with the sum of these volumes (gross tumor volume [GTV] hull, **(C)**) indicating the total tumor burden of the patient at the time point of initiation of radiotherapy.

founders do not seem to play a major role in measuring sICAM-1, sICAM-1 levels might be evaluated at any time point during radiochemotherapy. However, we did not find conclusive changes of s-ICAM-1 concentrations during therapy. Thus, further investigation is needed to confirm and explain the missing decline during treatment as some tumor shrinkage is usually already observed during the course of radiochemotherapy. Maybe our cohort was too small for significant findings or confounders other than inflammation and infection might play a role in measuring sICAM-1 during cancer treatment. However, if our results can be confirmed in larger patient cohorts, sICAM-1 might become a tumor marker for patients with HNSCC at initial diagnosis with exceedingly high values and low clinical tumor burden prompting further staging imaging due to suspicion of further undetected tumor manifestations. This might also be in line with the two patients developing early recurrences with high initial sICAM-1 levels as large tumor mass or micrometastases might limit curative treatment options.

Therefore, sICAM-1 seems to be a biomarker for total tumor burden (primary tumor and lymph node metastases) in head and neck cancer patients prior to definitive radiochemotherapy. No systematic changes were observed during radiochemotherapy and with toxicity or infections. High sICAM-1 concentrations initially or during follow-up might hint at higher tumor burden than clinically suspected and might prompt further investigations after validation in larger cohorts.

Acknowledgments

This work was supported by the "Wilhelm Schuler-Stiftung" in Tuebingen, Germany (material expenses). Besides, K. Clasen was supported by the intramural Fortüne / PATE Program of the Medical Faculty, Eberhard Karls Univer-sity of Tuebingen under Grant 2447-0-0. F. Eckert was partly supported by the Gesellschaft für KinderKrebsForschung (GKKF) and by the Deutsche Krebshilfe under grant 70114187. We acknowledge support by Open Access Publishing Fund of University of Tübingen.

References

1. Bose P, Brockton NT, Dort JC. Head and neck cancer: from anatomy to biology. *Int J Cancer* 2013; **133:** 2013-23. doi: 10.1002/ijc.28112
2. Amin MB, Greene FL, Edge SB, Compton CC, Gershenwald JE, Brookland RK, et al. The Eighth Edition AJCC Cancer Staging Manual: continuing to build a bridge from a population-based to a more "personalized" approach to cancer staging. *CA Cancer J Clin* 2017; **67:** 93-9. doi: 10.3322/caac.21388
3. Cramer JD, Hicks KE, Rademaker AW, Patel UA, Samant S. Validation of the eighth edition American Joint Committee on Cancer staging system for human papillomavirus-associated oropharyngeal cancer. *Head Neck* 2018; **40:** 457-66. doi: 10.1002/hed.24974
4. Nevens D, Nuyts S. HPV-positive head and neck tumours, a distinct clinical entity. *B-ENT* 2015; **11:** 81-7. PMID: 26563006
5. Rosenberg AJ, Vokes EE. Optimizing treatment de-escalation in head and neck cancer: current and future perspectives. *Oncologist* 2021; **26:** 40-48. doi: 10.1634/theoncologist.2020-0303
6. Nonaka T, Wong DTW. Liquid biopsy in head and neck cancer: promises and challenges. *J Dent Res* 2018; **97:** 701-8. doi: 10.1177/0022034518762071
7. Arantes L, De Carvalho AC, Melendez ME, Lopes Carvalho A. Serum, plasma and saliva biomarkers for head and neck cancer. *Expert Rev Mol Diagn* 2018; **18:** 85-112. doi: 10.1080/14737159.2017.1404906

8. Schaaij-Visser TB, Brakenhoff RH, Leemans CR, Heck AJ, Slijper M. Protein biomarker discovery for head and neck cancer. *J Proteomics* 2010; **73:** 1790-803. doi: 10.1016/j.jprot.2010.01.013

9. Rostami A, Bratman SV. Utilizing circulating tumour DNA in radiation oncology. *Radiother Oncol* 2017; **124:** 357-64. doi: 10.1016/j.radonc.2017.07.004

10. De Michino S, Aparnathi M, Rostami A, Lok BH, Bratman SV. The utility of liquid biopsies in radiation oncology. *Int J Radiat Oncol Biol Phys* 2020; **107:** 873-86. doi: 10.1016/j.ijrobp.2020.05.008

11. Kawaguchi K, Sakurai M, Yamamoto Y, Suzuki E, Tsuda M, Kataoka TR, et al. Alteration of specific cytokine expression patterns in patients with breast cancer. *Sci Rep* 2019; **9:** 2924. doi: 10.1038/s41598-019-39476-9

12. Chang KP, Chang YT, Wu CC, Liu YL, Chen MC, Tsang NM, et al. Multiplexed immunobead-based profiling of cytokine markers for detection of nasopharyngeal carcinoma and prognosis of patient survival. *Head Neck* 2011; **33:** 886-97. doi: 10.1002/hed.21557

13. Mojtahedi Z, Khademi B, Yehya A, Talebi A, Fattahi MJ, Ghaderi A. Serum levels of interleukins 4 and 10 in head and neck squamous cell carcinoma. *J Laryngol Otol* 2012; **126:** 175-9. doi: 10.1017/s0022215111002349

14. Chehrazi-Raffle A, Meza L, Alcantara M, Dizman N, Bergerot P, Salgia N, et al. Circulating cytokines associated with clinical response to systemic therapy in metastatic renal cell carcinoma. *J Immunother Cancer* 2021; **9**. doi: 10.1136/jitc-2020-002009

15. Nikolinakos PG, Altorki N, Yankelevitz D, Tran HT, Yan S, Rajagopalan D. et al. Plasma cytokine and angiogenic factor profiling identifies markers associated with tumor shrinkage in early-stage non-small cell lung cancer patients treated with pazopanib. *Cancer Res* 2010; **70:** 2171-9. doi: 10.1158/0008-5472.Can-09-2533

16. Jin YB, Zhang GY, Lin KR, Chen XP, Cui JH, Wang YJ, et al. Changes of plasma cytokines and chemokines expression level in nasopharyngeal carcinoma patients after treatment with definitive intensity-modulated radiotherapy (IMRT). *PLoS One* 2017; **12:** e0172264. doi: 10.1371/journal.pone.0172264

17. Snitcovsky I, Leitão GM, Pasini FS, Brunialti KC, Mangone FR, Maistro S, et al. Plasma osteopontin levels in patients with head and neck cancer undergoing chemoradiotherapy. *Arch Otolaryngol Head Neck Surg* 2009; **135:** 807-11. doi: 10.1001/archoto.2009.103

18. Lavaee F, Zare S, Mojtahedi Z, Malekzadeh M, Khademi B, Ghaderi A. Serum CXCL12, but not CXCR4, is associated with head and neck squamous cell carcinomas. *Asian Pac J Cancer Prev* 2018; **19:** 901-4. doi: 10.22034/apjcp.2018.19.4.901

19. Feltl D, Zavadova E, Pala M, Hozak P. The dynamics of plasma transforming growth factor beta 1 (TGF-beta1) level during radiotherapy with or without simultaneous chemotherapy in advanced head and neck cancer. *Oral Oncol* 2005; **41:** 208-13. doi: 10.1016/j.oraloncology.2004.09.005

20. Andersson B, Lewin F, Lundgren J, Nilsson M, Rutqvist LE, Löfgren S, et al. Plasma tumor necrosis factor-α and C-reactive protein as biomarker for survival in head and neck squamous cell carcinoma. *J Cancer Res Clin Oncol* 2014; **140:** 515-9. doi: 10.1007/s00432-014-1592-8

21. Clasen K, Welz S, Faltin H, Zips D, Eckert F. Dynamics of HMBG1 (High Mobility Group Box 1) during radiochemotherapy correlate with outcome of HNSCC patients. *Strahlenther Onkol* 2021; **98:** 194-200. doi: 10.1007/s00066-021-01860-8

22. Shimizu Y, Minemura M, Tsukishiro T, Kashii Y, Miyamoto M, Nishimori H, et al. Serum concentration of intercellular adhesion molecule-1 in patients with hepatocellular carcinoma is a marker of the disease progression and prognosis. *Hepatology* 1995; **22:** 525-31. PMID: 7543436

23. Araki T, Miki C, Kusunoki M. Biological implications of circulating soluble intercellular adhesion molecule-1 in colorectal cancer patients. *Scand J Gastroenterol* 2001; **36:** 399-404. doi: 10.1080/003655201300051234

24. Long EO. ICAM-1: getting a grip on leukocyte adhesion. *J Immunol* 2011; **186:** 5021-3. doi: 10.4049/jimmunol.1100646

25. Witkowska AM, Borawska MH. Soluble intercellular adhesion molecule-1 (sICAM-1): an overview. *Eur Cytokine Netw* 2004; **15:** 91-8. PMID: 15319166

26. Maruo Y, Gochi A, Kaihara A, Shimamura H, Yamada T, Tanaka N, et al. ICAM-1 expression and the soluble ICAM-1 level for evaluating the metastatic potential of gastric cancer. *Int J Cancer* 2002; **100:** 486-90. doi: 10.1002/ijc.10514

27. Yoo NC, Chung HC, Chung HC, Park JO, Rha SY, Kim JH, et al. Synchronous elevation of soluble intercellular adhesion molecule-1 (ICAM-1) and vascular cell adhesion molecule-1 (VCAM-1) correlates with gastric cancer progression. *Yonsei Med J* 1998; **39:** 27-36. doi: 10.3349/ymj.1998.39.1.27

28. Okamoto Y, Tsurunaga T, Ueki M. Serum soluble ICAM-1 levels in the patients with cervical cancer. *Acta Obstet Gynecol Scand* 1999; **78:** 60-5. PMID: 9926894

29. Basoglu M, Atamanalp SS, Yildirgan MI, Aydinli B, Ozturk G, Akcay F, et al. Correlation between the serum values of soluble intercellular adhesion molecule-1 and total sialic acid levels in patients with breast cancer. *Eur Surg Res* 2007; **39:** 136-40. doi: 10.1159/000100110

30. Köstler WJ, Tomek S, Brodowicz T, Budinsky AC, Flamm M, Hejna M, et al. Soluble ICAM-1 in breast cancer: clinical significance and biological implications. *Cancer Immunol Immunother* 2001; **50:** 483-90. doi: 10.1007/s002620100223

31. Levin I, Klein T, Shapira Y, Lurie H, Kfir B, Narinsky R, et al. Serum intracellular adhesion molecule-1 (sicam-1) and soluble hla class-1 antigens in breast-cancer patients in relation to tumor burden. *Oncol Rep* 1994; **1:** 217-20. doi: 10.3892/or.1.1.217

32. Dymicka-Piekarska V, Guzinska-Ustymowicz K, Kuklinski A, Kemona H. Prognostic significance of adhesion molecules (sICAM-1, sVCAM-1) and VEGF in colorectal cancer patients. *Thromb Res* 2012; **129:** e47-50. doi: 10.1016/j.thromres.2011.12.004

33. Schellerer VS, Langheinrich MC, Zver V, Grützmann R, Stürzl M, Gefeller O, et al. Soluble intercellular adhesion molecule-1 is a prognostic marker in colorectal carcinoma. *Int J Colorectal Dis* 2019; **34:** 309-17. doi: 10.1007/s00384-018-3198-0

34. Toiyama Y, Miki C, Inoue Y, Okugawa Y, Koike Y, Yokoe T, et al. Soluble intercellular adhesion molecule-1 as a prognostic marker for stage II colorectal cancer patients. *Ann Surg Oncol* 2008; **15:** 1617-24. doi: 10.1245/s10434-008-9874-5

35. Gu X, Ma C, Yuan D, Song Y. Circulating soluble intercellular adhesion molecule-1 in lung cancer: a systematic review. *Transl Lung Cancer Res* 2012; **1:** 36-44. doi: 10.3978/j.issn.2218-6751.08.01

36. Wu M, Tong X, Wang D, Wang L, Fan H. Soluble intercellular cell adhesion molecule-1 in lung cancer: A meta-analysis. *Pathol Res Pract* 2020; **216:** 153029. doi: 10.1016/j.prp.2020.153029

37. Kawano T, Yanoma S, Nakamura Y, Shiono O, Kokatu T, Kubota A, et al. Evaluation of soluble adhesion molecules CD44 (CD44st, CD44v5, CD44v6), ICAM-1, and VCAM-1 as tumor markers in head and neck cancer. *Am J Otolaryngol* 2005; **26:** 308-13. doi: 10.1016/j.amjoto.2005.02.005

38. Kubala MH, DeClerck YA. The plasminogen activator inhibitor-1 paradox in cancer: a mechanistic understanding. *Cancer Metastasis Rev* 2019; **38:** 483-92. doi: 10.1007/s10555-019-09806-4

39. Zwirner K, Hilke FJ, Demidov G, Ossowski S, Gani C, Rieß O, et al. Circulating cell-free DNA: A potential biomarker to differentiate inflammation and infection during radiochemotherapy. *Radiother Oncol* 2018; **129:** 575-81. doi: 10.1016/j.radonc.2018.07.016

research article

Crystalloids vs. colloids for fluid optimization in patients undergoing brain tumour surgery

Jasmina Markovic-Bozic[1], Bozidar Visocnik[1], Polona Music[1], Iztok Potocnik[2], Alenka Spindler Vesel[1]

[1] Department of Anaesthesiology and Surgical Intensive Therapy, University Medical Centre Ljubljana, Ljubljana, Slovenia
[2] Department of Anaesthesiology and Intensive Care, Institute of Oncology Ljubljana, Ljubljana, Slovenia

Radiol Oncol 2022; 56(4): 508-514.

Received 22 February 2022
Accepted 5 July 2022

Correspondence to: Assist. Prof. Jasmina Markovic-Bozic, M.D., Ph.D., Department of Anaesthesiology and Surgical Intensive Therapy, University Medical Centre Ljubljana, Zaloška 2, SI-1000 Ljubljana, Slovenia; E-mail: jasmina.markovic1@kclj.si

Disclosure: No potential conflicts of interest were disclosed.

Background. This randomised, double-blinded, single-centre study prospectively investigated the impact of goal directed therapy and fluid optimization with crystalloids or colloids on perioperative complications in patients undergoing brain tumour surgery. Main aim of the study was to investigate the impact of fluid type on postoperative complications.

Patients and methods. 80 patients were allocated into two equal groups to be optimised with either crystalloids (n = 40) or colloids (n = 40). Invasive hemodynamic monitoring was used to adjust and maintain mean arterial pressure and cerebral oxygenation within the baseline values (± 20%) and stroke volume variation (SVV) ≤ 10%. Postoperative complications from different organ systems were monitored during the first 15 days after surgery. Hospital stay was also recorded.

Results. Crystalloid group received significantly more fluids (p = 0.003) and phenylephrine (p = 0.02) compared to colloid group. This did not have any significant impact on perioperative complications and hospital stay, since no differences between groups were observed.

Conclusions. Either crystalloids or colloids could be used for fluid optimization in brain tumour surgery. If protocolised perioperative haemodynamic management is used, the type of fluid does not have significant impact on the outcome.

Key words: brain tumour surgery; fluid optimization; haemodynamic management

Introduction

Proper intravenous fluid therapy has effect on perioperative care and long-term postoperative outcome. Perioperative fluid therapy, guided by flow based haemodynamic monitors, can improve outcome. Optimization of hemodynamic and oxygen delivery by using a goal-directed therapy (IV fluids and/or vasoactive infusions), guided by objective monitoring, could be more personalised approach.[1-3]

Recent studies showed that haemodynamic management should be tailored to the cardiovascular physiology and the clinical situation of each individual patient, the so called personalised haemodynamic management.[4] It improves outcome of the surgery (better wound healing, shorter hospital stay, less surgical site infections, cardiovascular and pulmonary complications).[5]

It is unclear whether crystalloid or colloid fluids or a combination should be used for goal directed therapy to optimise patient outcome and what is the clinical impact of this technique.[5-8]

Brain oedema prevention and optimization of cerebral perfusion and oxygenation are main goals of anaesthetic technique during brain surgery.[9,10]

Optimal neuroprotective strategies include appropriate patient positioning, management of systemic and cerebral haemodynamic, maintenance of fluid, electrolyte and coagulation balance, and postoperative prevention and treatment of pain, postoperative nausea and vomiting.[8,9]

The optimal volume status during brain surgery is not known. There are two main dilemmas regarding fluids, the use of liberal or restrictive protocol and the type of fluid used. Fluid therapy may augment both cardiac output and cerebral blood flow. Fluid overload may result in poor neurological outcome, but it is still uncertain if fluid restriction is favourable or damaging to post-craniotomy neurological outcome. There is also concern regarding possible negative impact of colloids on coagulation that can cause bleeding and worsen outcome perioperatively.[10-12]

Stroke volume variation (SVV) is one of the dynamic haemodynamic parameters that predicts intraoperative fluid responsiveness also in brain surgery.[13,14] The goal is to maintain systemic and cerebral haemodynamic variables (cardiac output, arterial blood pressure, cardiac rhythm, cerebral blood flow).[8,9] In our previous study we showed that type of anaesthesia for brain surgery does not have impact on haemodynamic stability and the occurrence of postoperative complications.[8] But the question arised if the type of fluid used for managing systemic and cerebral haemodynamic variables does have any impact on the postoperative outcome.

Thus, we hypothesized that for prevention of postcraniotomy complications haemodynamic optimization is more important than the type of fluid (crystalloid or colloid) used.

Main aim of the study was to investigate the impact of fluid type on perioperative complications.

The primary outcome measure was the impact of type and consumption of fluid on the incidence of perioperative complications.

The secondary outcome measure was the impact of perioperative complications on the length of hospital stay and mortality.

Patients and methods

Prospective, randomised, double-blind, single-centre study, with two parallel group, was conducted at the University Medical Centre Ljubljana, Department of Anaesthesiology and Surgical Intensive Care and Department of Neurosurgery in years 2016–2018 (trial registry on 15/08/2017; number NCT03249298 at www.clinicaltrials.gov). The study was approved by the National Medical Ethics Committee of the Republic of Slovenia. All the procedures were performed in accordance with the declaration of Helsinki. The CONSORT recommendations for reporting randomized trials were followed. Written informed consent was obtained from all subjects participating in the trial.

ASA (American Society of Anaesthesiologists) Class 1–3 high risk surgical patients from the Clinical department of neurosurgery were included in the study. Adult patients that underwent brain tumour surgery were included.

Exclusion criteria were (a) unwillingness to give a written informed consent, (b) cardiac arrhythmia (c) hemodynamic unstablity or shock, (d) coagulation disorder and (e) underage.

All patients were visited by a member of our team a day prior to surgery to seek an informed consent and to answer any question. Patients were able to freely withdraw from the trial.

Using a computer-generated list, the patients were randomised into two groups by the fourth author, not involved in patient care. The first author enrolled the patients and informed them about the participation in the study.

In the operating room standard monitoring was instituted. An arterial catheter was placed in the radial artery for continuous blood pressure monitoring. Advanced pulse contour cardiac output monitoring using the EVA 1000/FloTrac device (Edwards Lifescience, CA, USA) and near infrared spectroscopy oximetry (NIRS) monitoring (Medtronic, MN, USA) were applied.

Patients were premedicated (midazolam 7.5 mg po). Antibiotic prophylaxis with intravenous cefazolin 2 g in 100 ml of 0,9% NaCl was invariably used in all patients.

Anaesthesia was induced with propofol 1–2 $mgkg^{-1}$ (Propoven, Fresenius Kabi AG, Bad Homburg, Germany). Before intubation all patients received remifentanil 0.5–1 μgkg^{-1} (Ultiva, GlaxoSmithKline) and rocuronium 0.6 $mgkg^{-1}$ (Esmeron, MSD, NY, USA).

Patients were intubated and mechanically ventilated (oxygen-air mixtures, I/E ratio 1:2, tidal volume 8 $mlkg^{-1}$). The goal was to reach normal values of partial pressure of carbon dioxide in arterial blood ($paCO_2$) and normal values of partial pressure of oxygen in arterial blood. Anaesthesia was maintained by continuous infusion of propofol 4–6 $mgkg^{-1}h^{-1}$. Remifentanil was adjusted according to the degree of surgical manipulation (0.1–2 $\mu gkg^{-1}min^{-1}$) and was increased when mean arterial pressure and heart rate increased over 30% from base-

line. The depth of anaesthesia was measured with bispectral index (BIS) and maintained from 40 to 60. This is according to hospital policy, since total intravenous infusion was used in order to prevent intraoperative awareness.

Haemodynamic management was followed by study protocol. Intraoperative basal fluid replacement was realized with continuous infusion 2–4 $mlkg^{-1}h^{-1}$ of balanced crystalloid regimes (Sterofundin ISO, B. Braun Melsungen AG). Additional boluses of 250 ml fluid were given when stroke volume variation (SVV) measured by EVA 1000/FloTrac system rose above 10% (a sustained change during the previous 5 minutes) or in the case of a positive response to previous fluid challenge until normal SVV value. Colloid group (CO) received colloid solution (Voluven 130/0.4 6%; Fresenius Kabi AG, Bad Homburg, Germany) and crystalloid group (CR) balanced crystalloid (Sterofundin). If mean arterial pressure (MAP) or cerebral oxygenation (rSO2) after fluid boluses were still < 20% from the baseline values with normal SVV values, vasoactive drugs were given (ephedrine 5–10 mg (0.5% Ephedrine, UMC Ljubljana Pharmacy, Slovenia) or phenylephrine 50 μg (0.01%, UMC Ljubljana Pharmacy, Slovenia)) to maintain MAP and/or rSO2 ± 20% from the baseline values. Bradycardia (heart rate (HR) < $40min^{-1}$) was treated with atropine 0.5 mg. If MAP and/or HR increased over 30% from baseline, the infusion of remifentanil was increased by 0.1 μg $kg^{-1}min^{-1}$. Any adverse haemodynamic events (increase of MAP and/or HR over 30% from baseline) that did not respond to higher remifentanil infusion rate, were managed with urapidil or metoprolol, as appropriate**.** Blood loss was replaced with colloids (CO group) or crystalloids (CR group) until a reduced PRBC transfusion trigger (haemoglobin level < 90 gl^{-1}) was reached, which is desirable level for neurosurgical patients. Haemodynamic parameters were recorded continuously in 5-min intervals (from induction to discharge from the postanaesthesia care unit (PACU)).

Blood samples were collected before surgery, at the end of the surgery and on the first postoperative day to compare lactate values, to detect early coagulopathy with rotational tromboelastometry (ROTEM) and to predict blood transfusion requirements.[15]

During dura closing piritramide 0.1 $mgkg^{-1}$ (Dipidolor, Janssen-Cillag GmbH, Neuss, Germany), metamizole 2.5 g (Analgin, Stada AG, Bad Vilbel, Germany) and ondansetron 4 mg were given to the patients.

Propofol infusion was stopped at the last skin suture. Remifentanil infusion was stopped after the removal of the Mayfield head holder.

Postoperatively intravenous infusion of piritramide was started as patient-controlled analgesia (PCA). The definition of operation duration was the time from the application of the Mayfield head holder to its removal. Duration of anaesthesia was measured from induction to extubation. The time from anaesthetics cessation to tracheal extubation was also recorded. All the patients were extubated in the operating theatre and then transferred to the PACU, where they stayed for not more than 2 hours. Afterwards they were admitted to the Department of Neurosurgery intensive care unit (ICU).

Standard postoperative monitoring generally used in these procedures was implemented. Oxygen was administered via a Venturi mask and titrated to the lowest level needed to achieve arterial oxygen saturation greater than 96%. During the hospital stay the main investigator (JMB) visited the patients daily to check the postoperative complications and the fluid loading.

Measurements

The following data were collected: demographics, duration of surgery and anaesthesia, the consumption of intraoperative drugs, haemodynamic variables, fluid balance, and serum safety control markers (lactate, haemoglobin, coagulation status), the length of hospital stay and postoperative complications during 15 days after surgery.

Postoperative complications were defined as any unintended changes in body function or well-being, such as hypertension (systolic blood pressure 30% higher than the baseline level), infection, pulmonary, neurological events, reoperation and death.

Statistical analysis

The appropriate sample size was calculated from our previous pilot study of two independent groups (20 patients optimised with colloids and 20 patients treated with standard non-optimised approach) using a priori two-tailed t-test power analysis. The difference in the mean colloid consumption between the groups was used for the effect size calculation and the sample size determination. For a significance level of 5% ($\alpha = 0.05$) and a power of 90% ($\beta = 0.1$), the calculated minimum sample size was 36. To compensate for possible withdrawals, 40 patients were included in each group. Two pa-

tients from each group were excluded for further analysis because of technical reasons (Figure 1).

The two-tailed t-test with unequal variances or the Chi-square test were used to test the differences in demographic data, duration of the procedure and anaesthesia, drug consumption, fluid balance, haemodynamic parameters, postoperative complications and length of hospital stay.

The means of continuous variables are presented, and categorical data are summarized as counts. A p-value of less than 0.05 was considered statistically significant. Data were analysed by SPSS 13.0 software package (IBM Corp., Armonk, NY, USA).

Results

80 patients, aged 18–80 years, ASA (American Society of Anaesthesiologists) Class 1–3 and GCS (Glasgow coma score) of 15, scheduled for brain tumour surgery, were included in the study, 40 in the CO group and 40 in CR group (Figure 1). There were sixty-nine primary operations and 7 reoperations. No significant differences ($p > 0.05$) were found between the groups regarding their demographics, ASA class, position during surgery, type of surgery and duration of the procedure or anaesthesia (Table 1).

During the surgery CR group received statistically significant more fluids (1120 ml *vs* 653 ml; $p = 0.003$) and vasoactive drug phenylephrine (874 mcg *vs.* 210 mcg; $p = 0.02$) (Table 2). On the other hand, differences in fluid balance (total fluids, blood transfusion, fresh frozen plasma, blood loss, urine volume) and the levels of serum safety markers (lactate, haemoglobin) during and 24 hours after the surgery were not significant ($p > 0.05$) (Table 2). Rotational tromboelastometry was normal in all patients before and after the surgery, whereas 9 patients had pathological result during the surgery, with nonsignificant differences between the groups ($p = 0.57$) (Table 2).

15 days after the surgery no significant differences were recorded in the variables that could have influence on the outcome. 46 patients did not have any additional diseases or organ failure (including renal failure) in comparison with preoperative condition (23 in each group; $p = 0.41$). In CR group one patient died and one had wound infection. In CO group one patient had systemic inflammation and two pulmonary embolism. In both groups minor neurological complications were recorded (13 *vs.* 12). The length of hospital stay was 9 days in both groups ($p = 0.7$).

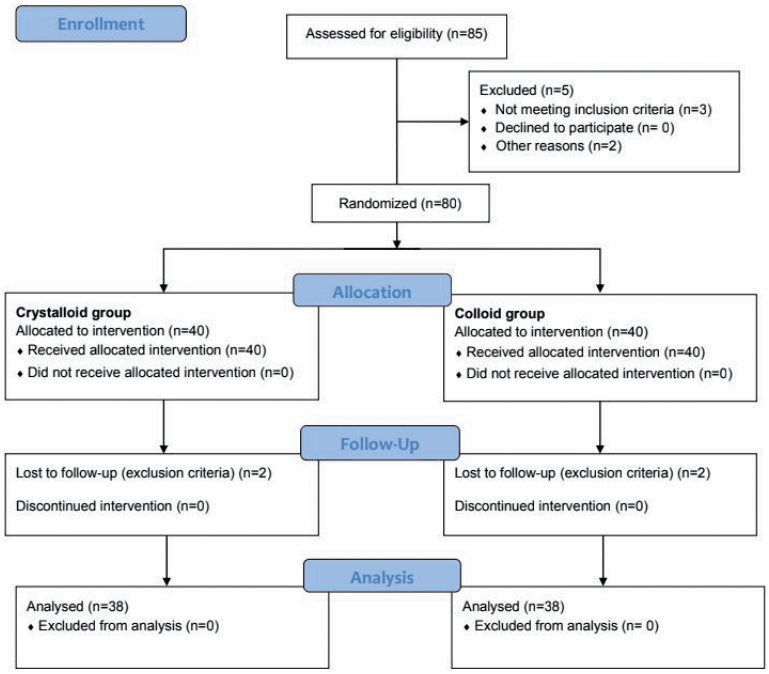

FIGURE 1. Flow diagram of the study.

TABLE 1. Baseline demographics and surgical procedure

Group	CR (N = 38)	CO (N = 38)	p value
Age (years)	54 ± 14	55 ± 16	0.69
Weight (kg)	79 ± 16	76 ± 15	0.45
Gender (M/F)	17/21	14/24	0.32
ASA (I/II/III)	8/19/11	7/24/7	0.46
First operation/reoperation	33/5	36/2	0.43
Patient position			
Supine	24	22	0.48
Lateral	13	12	
Sitting	1	2	
Prone	0	2	
Localization			
Supratentorial/infratentorial	33/5	33/5	0.63
Type of surgery			
Craniotomy/endoscopic	35/3	37/1	0.50
Duration of procedure (min)	195 ± 60	209 ± 101	0.49
Duration of anaesthesia (min)	242 ± 64	247 ± 105	0.82

The results are expressed as mean ± SD or number of patients.

The differences between groups were not significant ($p > 0.05$).

ASA = American Society of Anaesthesiologists; CO = colloid group; CR = crystalloid group; F = female; M = male

TABLE 2. Intraoperative and postoperative variables and outcome

Group *Intraoperative data*	CR	CO	P
Propofol (mg)	1355 ± 451	1307 ± 766	0.74
Remifentanil (mg)	15 ± 8	13 ± 8	0.25
Total loss of blood (ml)	311 ± 262	461 ± 486	0.09
Urine volume (ml)	996 ± 510	772 ± 655	0.99
Total fluids (ml)	2250 ± 1000	2122 ± 758	0.53
Blood transfusion (ml)	17 ± 107	73 ± 203	0.14
Fresh frozen plasma (ml)	13 ± 78	61 ± 185	0.14
Fluid optimization boluses (1/2/3/>3 times)	5/6/2/14	8/13/6/9	0.16
Consumption of optimization fluid (ml)	1120 ± 816	653 ± 365	0.003*
Intraoperative hypotension (1/2/3/>3 times)	9/7/6/8	6/7/3/6	0.88
Vasoactive drugs (1/2/3/>3 times/infusion)	6/4/4//3/11	6/5/1/5/5	0.41
Phenylephrine (mcg)	874 ± 1632	210 ± 530	0.02*
Ephedrine (mg)	8 ± 10	7 ± 13	0.64
Urapidil (mg)	3 ± 10	3 ± 8	0.88
Metoprolol (mg)	0.13 ± 0.8	0.13 ± 0.8	1
Atropine (mg)	0.07 ± 0.2	0.08 ± 0.2	0.7
Tromboelastometry (normal/ pathological)	33/5	33/4	0.57
Lactate (mmol/l)	1.1 ± 0.4	0.88 ± 0.5	0.1
Haemoglobin (g/l)	120±13	115 ± 12	0.1
Postoperative data (24 h)			
Arterial pressure (normal/low/high)	37/1/0	34/0/4	0.08
Postoperative CT of the head (good/ oedema/haematoma/other)	30/6/1/1	28/6/4/0	0.41
Total fluids (ml)	1693 ± 520	1772 ± 684	0.57
Urine volume (ml)	1382 ± 660	1297 ± 735	0.59
Lactate (mmol/l)	1.1 ± 0.4	0.95 ± 0.4	0.25
Haemoglobin (g/l)	123 ± 17	119 ± 13	0.29
Postoperative data (15 days)			
No difference (comparing to data before surgery)	23	23	0.41
Death	1	0	
Wound infection	1	0	
Inflammation	0	1	
Pulmonary (pneumonia/embolism)	0/0	0/2	
Neurological complications (minor/ major)	13/0	12/0	
Hospital stay (days)	9 ± 4	9 ± 5	0.70

The results are expressed as mean ± SD or number of patients;

The differences between groups that are significant are labelled with * ($p<0.05$)

CO = colloid group; CR = crystalloid group

Discussion

Historically anaesthesiologists observed patients and act according to clinical changes. If decision to give fluid bolus or vasoactive drugs is based only on low blood pressure, one could easily overlook the need for fluid and give just vasoactive drugs and vice versa. Namely, liberal fluid approach can prolong hospital stay and lead to oedema, on the other hand restrictive fluid regime is correlated with postoperative complications.[16-19] That is extremely important in neurosurgery, where infusing too much fluid can result in brain oedema and hypoperfusion. Invasive haemodynamic monitoring is therefore important to control brain perfusion. According to the results of Luo and co- workers goal directed fluid therapy significantly reduces the consumption of colloids and crystalloids compared to the group, where therapeutic decisions were left at the discretion of the attending anesthesiologist and intensivist.[20]

Feldheiser and colleagues showed that colloids have longer intravenous effect and enable better haemodynamic stability and flow measurement.[5] This can explain why in our study the crystalloid group received more phenylephrine.

Our first goal was to achieve the desired SVV with fluid optimisation. Vasoactive drugs were used only if hypotension persisted.[21] Hypotension occurred more often in crystalloid group, but non-significant. These patients needed more fluid, and even when optimised, they still needed fenilefrin to achieve desired perfusion pressure. This was the reason why crystalloid group needed more phenylephrine, even though number of fenilefrin interventions did not vary between the groups.

Lactate is a measurement of adequate tissue perfusion and was not significantly raised in our groups. Wu and co-workers showed that for supratentorial brain tumor resection, fluid boluses targeting lower SVV are more beneficial than a restrictive protocol, and result in lower lactate, brain biomarkers and postoperative neurological events.[22]

The incidence of intraoperative events that needed intervention (fluid and/or vasoactive drugs) did not differ between our groups. Intraoperative stabile patients did not need any intervention with fluid bolus or vasoactive drugs for haemodynamic optimisation.

Optimal brain perfusion prevents brain ischemia and oedema in patient undergoing neurosurgical procedure. Haemostasis is also essential to prevent worse outcome caused with haematoma. Colloids could have impact on coagulation. It was shown by Lindroos and colleagues that HES induced a slight disturbance in fibrin formation and clot strength.[23]

We used ROTEM to exclude possible side effects of colloids on haemostasis.

We also showed that fluid optimisation with crystalloids is safe. Even though their consump-

tion was larger compared to colloids. The amount of colloids needed for optimisation was 41% lower, which was less then described in the literature.[23,24] Obviously, good outcome with no postoperative neurological complications in both our groups showed that technique and haemodynamic management are more important than the type and volume of fluid. Namely, cognitive functions such as attention, concentration and memory can also be transient affected due to temporary brain swelling.[25] Xia and co-workers showed that goal-directed colloid therapy was not superior to goal-directed cristalloid therapy for brain relaxation, cerebral oxygenation or cerebral metabolism, although less fluid was needed to maintain the target SVV in the colloid group.[26] Fluids and vasoactive drugs should be applied according to haemodynamic measurements.[4] Every patient should receive as much fluid as needed at appropriate time.[27]

Conclusions

Our study showed that either crystalloids or colloids could be used for fluid optimization for brain tumour surgery. If protocolised perioperative haemodynamic management is used, the type of fluid does not have significant impact on outcome. Future studies in this area should focus on the development of broad goal directed strategies in perioperative fluid therapy rather than trying to find the best type of fluid.

Acknowledgments

We are thankful to Department of Anaesthesiology and Surgical Therapy, University Medical Centre Ljubljana, Slovenia which supported the research and to all colleagues, anaesthesiologists, surgeons and nurses at the Department of Anaesthesiology and Surgical Therapy and at the Department of Neurosurgery who in any way helped in this work. We are also thankful to all the patients who cooperated in the study.

References

1. Manning MW, Dunkman WJ, Miller TE. Perioperative fluid and hemodynamic management within an enhanced recovery pathway. *J Surg Oncol* 2017; **116:** 592-600. doi: 10.1002/jso.24828
2. Žličar M. Current concepts in fluid therapy and non-invasive haemodynamic monitoring. *Signa Vitae* 2017; **13:** 53-5. doi: 10.22514/SV131.032017.7
3. Saugel B, Cecconi M, Wagner JY, Reuter DA. Noninvasive continuous cardiac output monitoring in perioperative and intensive care medicine. *Br J Anaest* 2015; **114:** 562-75. doi: 10.1093/bja/aeu447
4. Saugel B, Vincent JL. Protocolised personalised peri-operative haemodynamic management. *Eur J Anaesthesiol* 2019; **36:** 551-4. doi: 10.1097/EJA.0000000000001015
5. Feldheiser A, Pavlova V, Bonomo T, Jones A, Fotopoulou C, Sehouli J, et al. Balanced crystalloid compared with balanced colloid solution using goal-directed haemodynamic algorithm. *Br J Anaesth* 2013; **110:** 231-40. doi: 10.1093/bja/aes377
6. Yates DRA, Davies SJ, Milner HE, Wilson RJT. Crystalloid or colloid for goal-directed fluid therapy in colorectal surgery. *Br J Anaesth* 2014; **112:** 281-9. doi: 10.1093/bja/aet307
7. Doherty M, Buggy DJ. Intraoperative fluids: how much is too much? *Br J Anaesth* 2012; **109:** 69-79. doi: 10.1093/bja/aes171
8. Markovič-Božič J, Karpe B, Potočnik I, Jerin A, Vranič A, Novak-Jankovič V. Effect of propofol and sevoflurane on the inflammatory response of patients undergoing craniotomy. *BMC Anesthesiol* 2016; **16:** 18. doi: 10.1186/s12871-016-0182-5
9. El Beheiry H. Protecting the brain during neurosurgical procedures: strategies that can work. *Curr Opin Anaesthesiol* 2012; **25:** 548-55. doi: 10.1097/ACO.0b013e3283579622
10. Wu CY, Lin YS, Tseng HM, Cheng HL, Lee TS, Lin PL, et al. Comparison of two stroke volume variation-based goal-directed fluid therapies for supratentorial brain tumour resection: randomized controlled trial. *Br J Anaesth* 2017; **119:** 934-42. doi: 10.1093/bja/aex189
11. Xia J, He Z, Cao X, Che X, Chen L, Zhang J, et al. The brain relaxation and cerebral metabolism in stroke volume variation-directed fluid therapy during supratentorial tumors resection: crystalloid solution versus colloid solution. *J Neurosurg Anesthesiol* 2014; **26:** 320-7. doi: 10.1097/ANA.0000000000000046
12. Tommasino C. Fluid management. In: Newfield P, Cottrell JE, editors. *Handbook of Neuroanaesthesia*. 4 th Edition. New York: Lippincott-Williams & Wilkins; 2007. 379-95.
13. Benes J, Haidingerova L, Pouska J, Stepanik J, Stenglova A, Zatloukal J, et al. Fluid management guided by a continuous non-invasive arterial pressure device is associated with decreased postoperative morbidity after total knee and hip replacement. *BMC Anesthesiol* 2015; **15:** 148. doi: 10.1186/s12871-015-0131-8
14. Saugel B, Reuter DA. Are we ready for the age of non-invasive haemodynamic monitoring? *Br J Anaesth* 2014; **113:** 340-3. doi: 10.1093/bja/aeu145
15. Ellenberger C, Garofano N, Barcelos G, Diaper J, Pavlovic G, Licker M. Assessment of haemostasis in patients undergoing emergent neurosurgery by rotational elastometry and standard coagulation tests: a prospective observational study. *BMC Anesthesiol* 2017; **17:** 146. doi: 10.1186/s12871-017-0440-1
16. Thacker JKM, Mountford WK, Ernst FR, Krukas MR, Mythen MMG. Perioperative fluid utilization variability and association with outcomes. Considerations for enhanced recovery efforts in sample US surgical populations. *Ann Surg* 2016; **263:** 502-10. doi: 10.1097/SLA.0000000000001402
17. Giglio MT, Marucci M, Testini M, Brienza N. Goal-directed haemodynamic therapy and gastrointestinal complications in major surgery: a meta-analysis of randomized controlled trials. *Br J Anaesth* 2009; **103:** 637-46. doi: 10.1093/bja/aep279
18. Grocott MPW. The Cochrane database of systematic reviews 2012–2014. John Wiley & Sons, Ltd.; 2006. doi: 10.1002/14651858.CD004082.pub2
19. Grocott MPW, Dushianthan A, Hamilton MA, Mythen MG, Harrison D, Rowan K. Perioperative increase in global blood flow to explicit defined goals and outcomes after surgery: a Cochrane systematic review. *Br J Anaesth* 2013; **111:** 535-48. doi: 10.1093/bja/aet155
20. Luo J, Xue J, Liu J, Liu B, Liu L, Chen G. Goal-directed fluid restriction during brain surgery: a prospective randomized controlled trial. *Ann Intensive Care* 2017; **7:** 16. doi: 10.1186/s13613-017-0239-8
21. Berkenstadt H, Margalit N, Hadani M, Z Friedman, E Segal, Y Villa, et al. Stroke volume variation as a predictor of fluid responsiveness in patients undergoing brain surgery. *Anesth Analg* 2001; **92:** 984-9. doi: 10.1097/00000539-200104000-00034

22. Wu CY, Lin YC, Tsend HM, Cheng HL, Lee TS, Lin PL, et al. Comparison of two stroke volume variation-based goal-directed fluid therapies for supratentorial brain tumour resection: a randomized controlled trial. *Br J Anaesth* 2017; **119:** 934-42. doi: 10.1093/bja/aex189

23. Lindroos AC, Niiya T, Randell T, Niemi TT. Stroke volume-directed administration of hydroxyethyl starch (HES 130/0.4) and Ringer's acetate in prone position during neurosurgery: a randomized controlled trial. *J Anesth* 2014; **28:** 189-97. doi: 10.1007/s00540-013-1711-8

24. Lindroos AC, Niiya T, Silvasti-Lundell M, Randell T, Hernesniemi J, Niemi TT. Stroke volume-directed administration of hydroxyethyl starch or Ringer's acetate in sitting position during craniotomy. *Acta Anaesthesiol Scand* 2013; **57:** 729-36. doi: 10.1111/aas.12105

25. Kos N, Kos B, Benedicic M. Early medical rehabilitation after neurosurgical treatment of malignant brain tumours in Slovenia. *Radiol Oncol* 2016; **50:** 139-44. doi: 10.1515/raon-2015-0004

26. Xia J, He Z, Cao X, Che X, Chen L, Zhang J, et al. The brain relaxation and cerebral metabolism in stroke volume variation – directed fluid therapy during supratentorial tumors resection: crystalloid solution versus colloid solution. *J Neurosurg Anesthesiol* 2014; **26:** 320-27. doi: 10.1097/ANA.0000000000000046

27. Kirov, MY, Kuzkov VV, Molnar Z. Perioperative haemodynamic therapy. *Curr Opin Crit Care* 2010; **16:** 384-92. doi: 10.1097/MCC.0b013e32833ab81e

research article

Dose-escalated radiotherapy with simultaneous integrated boost for bone metastases in selected patients with assumed favourable prognosis

Vlatko Potkrajcic[1], Arndt-Christian Mueller[1,2], Bettina Frey[1], Cihan Gani[1], Daniel Zips[1,3,8], Ruediger Hoffmann[4], Sandra Frantz[5], Verena Warm[6], Frank Paulsen[1], Franziska Eckert[1,3,7]

[1] Eberhard-Karls-University Tuebingen, Department of Radiation Oncology, Tuebingen, Germany
[2] RKH-Kliniken Ludwigsburg, Department of Radiation Oncology and Radiotherapy, Ludwigsburg, Germany
[3] German Cancer Consortium (DKTK) Partnersite Tuebingen, German Cancer Research Center (DKFZ) Heidelberg, Germany
[4] Eberhard-Karls-University Tuebingen, Department for Radiology, Tuebingen, Germany
[5] Eberhard-Karls-University Tuebingen, Department of Orthopaedic Surgery, Tuebingen, Germany
[6] Eberhard-Karls-University Tuebingen, Department of Pathology, Tuebingen, Germany
[7] Medical University Vienna, AKH, Comprehensive Cancer Center, Department of Radiation Oncology, Wien, Austria
[8] Charité University Hospital, Department of Radiation Oncology and Radiotherapy, Berlin, Germany

Radiol Oncol 2022; 56(4): 515-524.

Received 26 July 2022
Accepted 11 October 2022

Correspondence to: Vlatko Potkrajcic, M.D., and Frank Paulsen, M.D., Department of Radiation Oncology, Eberhard-Karls-University of Tuebingen, Hoppe-Seyler-Str. 3, D-72076 Tuebingen, Germany. E-mail: vlatko.potkrajcic@med.uni-tuebingen.de and frank.paulsev@med.uni-tuebingen

Disclosure: VP, BF, CG, DZ, FP, FE and ACM have research and educational grants from Elekta, Philips, Siemens, Sennewald. The other authors declare that they have no conflict of interest.

Background. Stereotactic body radiotherapy (SBRT) concepts for dose escalation are increasingly used for bone metastases in patients with oligometastatic or oligoprogressive disease. For metastases that are not suitable for SBRT-regimens, a treatment with 30/40 Gy with simultaneous integrated boost (SIB) in 10 fractions represents a possible regimen. The aim of this study was to investigate the feasibility of this concept and the acute and subacute toxicities.

Patients and methods. Clinical records for dose-escalated radiotherapy of all consecutive patients treated with this regimen were evaluated retrospectively (24 patients with 28 target volumes for oncologic outcomes and 25 patients with 29 target volumes for treatment feasibility and dose parameters analysis). Analysis of radiotherapy plans included size of target volumes and dosimetric parameter for target volumes and organs at risk (OAR). Acute and subacute toxicities were evaluated according to Common Terminology Criteria for Adverse Events (CTCAE) V4.0.

Results. The most common localization was the spine (71.4%). The most common histology was prostate cancer (45.8%). Oligometastatic or oligoprogressive disease was the indication for dose-escalated radiotherapy in 19/24 patients (79.2%). Treatment was feasible with all patients completing radiotherapy. Acute toxicity grade 1 was documented in 36.0% of the patients. During follow up, one patient underwent surgery due to bone instability. The 1-year local control and patient-related progression-free survival (PFS) were 90.0 ± 6.7% and 33.3 ± 11.6%, respectively.

Conclusions. Dose-escalated hypofractionated radiotherapy with simultaneous integrated boost for bone metastases resulted in good local control with limited acute toxicities. Only one patient required surgical intervention. The regimen represents an alternative to SBRT in selected patients.

Key words: radiotherapy; oligometastatic disease; oligoprogressive disease; bone metastases; hypofractionated radiotherapy; simultaneous integrated boost

Introduction

Bone metastases represent one of the most frequent metastatic sites in advanced malignant disease.[1-3] This site is associated with a wide range of symptoms including pain, hypercalcemia, increased risk of pathological fracture and neurological symptoms.[1,2,4,5] Due to their complications, bone metastases can decrease the quality of life in cancer patients.[6] A significant number of patients with advanced malignant disease present with symptomatic bone metastases.[7] The analgesic effect of radiotherapy for painful bone metastases has been established for years and therefore irradiation is the preferred treatment for localized bone pain in advanced malignant disease. Approximately 70–80% of patients will respond with pain relief, up to one-third will achieve complete pain response.[1]

Significant progress in systemic and supportive therapy has increased patients' life expectancy.[2] Furthermore, beginning with Hellman and Weichselbaum in 1995, the hypothesis of the existence of an oligometastatic state of cancer, as an intermediate stage of cancer spread, has been established[8] and is nowadays differentiated from widespread metastatic disease. With improvements in diagnostic modalities, oligometastatic malignant disease is being diagnosed more frequently than before[9], resulting in earlier detection of metastases.[10] However, various definitions and different cut-offs are discussed in the literature. In most studies, oligometastatic state was defined as limited number of metastases, with 1–3 or 1–5 metastatic lesions.[9,11,12] Accumulating clinical evidence suggests that metastasis-directed local therapy for these patients might result in improved clinical response, prevent additional metastatic spread and delay the initiation of systemic therapies.[13,14] Adequate radiotherapy regimens to achieve sufficient pain relief have been discussed in the literature and different regimens in the palliative situation have been reported and summarized in various studies.[2,7,15,16] However, the optimal fractionation and dose regimen for patients with oligometastatic disease is still an unresolved issue. Considering improved survival for patients with oligometastatic disease, the goal of an aggressive metastases-directed approach is not only to achieve an optimal pain relief, but also long-term local control (LC).

To deliver high doses to the target, maximize targeting capabilities and minimize damage to organ at risk (OAR) or healthy tissue, stereotactic body radiotherapy (SBRT) has been introduced.[17] In a systematic review published in 2019 by Spencer *et al.*, the role of stereotactic radiotherapy in 1-6 fractions in the management of bone metastases from solid-organ tumours was examined. Excellent local control rates, as well as superior rates for pain relief (compared to conventional radiotherapy) were reported in this analysis.[3] However, for some bone metastases, stereotactic radiotherapy in a few fractions might be unsuitable, due to their close proximity to OAR or size or limited definability of target volumes. For this reason, many study protocols exclude tumours within a distance of < 3 mm to the spinal cord, with the aim to respect its dose limitations.[18] Various studies examined intensity modulated radiotherapy (IMRT) regimes with simultaneous integrated boost (SIB) for radiotherapy of spine metastases.[18-20] Compared to conventional IMRT, this approach should offer dose reduction in the spinal cord and dose escalation in the target volume using SIB.[21] In our institution, a higher-dose fractionated regimen for bone metastases with 30 Gy and 40 Gy radiotherapy in 10 fractions with dose escalation by SIB ("30/40 Gy") to treat patients oligometastatic and oligoprogressive malignant disease was introduced. This regimen enables not only a dose escalation in the target as an alternative to SBRT, but also a coverage of tumour-affected compartment (according to clinical assessment).

The aim of this study was to assess the feasibility concerning completion of treatment, acute toxicity and to evaluate oncologic outcomes after fractionated radiotherapy using this concept for bone metastases in selected patients with assumed favourable prognosis. In addition, dose constraints for palliative radiotherapy of the spine have been adapted to higher-dose radiotherapy.

Patients and methods

The study protocol was submitted to the Ethics Committee of the Medical Faculty in our institution and approved in 2020 (990/2020B02). This study represents a single institution retrospective analysis of all consecutive patients treated with this regimen at our institution. Clinical records of all patients treated with radiotherapy of bone metastases with intensity modulated radiotherapy (IMRT) with 30/40 Gy SIB in 10 fractions between 2017 and 2020 in were evaluated. Patients treated with the evaluated regimen were not considered for SBRT, due to close proximity of the tumour to OAR, size or limited definability of target volumes.

In most cases, patients included in the study had malignant disease in oligometastatic or oligoprogressive state. However, the evaluated treatment was also offered to patients with diffuse metastatic disease, in case of radioresistant histology (such as pheochromocytoma or renal cell carcinoma) or vertebral-body metastasis with intraspinal component, where improved LC with higher-dose fractionated regimen was desired (due to favourable prognosis and expected efficient systemic treatment). The indication for radiotherapy was mainly not palliative symptom control but local treatment of all macroscopic or progressive tumour localizations. Various definitions of oligometastatic disease have been described in the literature. Foster *et al.* reports that a definition of ≤3 metastases was used in 12/25 retrospective studies.[11] Therefore, for the purpose of this study, we defined an oligometastatic disease as 3 or less extracranial metastases. If patients had locally untreated organ metastases, disease was classified as diffuse metastatic disease. Oligoprogression was defined as progression of 3 or less extracranial metastases under systemic therapy. To determine the number of metastases, the last radiological imaging before radiotherapy was used.

Data were collected retrospectively and abstracted by chart review. Feasibility was defined as conducting radiotherapy without interruption and no toxicity ≥ grade 3 (Common Terminology Criteria for Adverse Events [CTCAE] V 4.0). Due to the retrospective study design, pain response to radiotherapy was evaluated based on clinical records and therefore not graded. Overall survival (OS) and progression-free survival (PFS) were evaluated per patient based on the follow up scans and prostate-specific antigen (PSA) measures (for prostate cancer). OS was defined as the time from the date of the end of radiotherapy to the last contact or death. LC and PFS were defined as the time from the end of radiotherapy to last follow-up or to the diagnosis of local progression for LC and local progression or distant progression for PFS. LC was calculated for each irradiated metastasis. In patients with prostatic cancer, in case of no PSA-elevation and no progression of clinical symptoms (such as pain or neurological symptoms connected to irradiated localization), no radiological imaging was performed during follow-up. PSA-level was used as a measurement to assess LC and PFS in these patients.

IMRT was planned based on a three-dimensional planning CT using 3 mm slice thickness, 4-dimensional-CT (4D-CT) was used for metastases of the ribs. Similar to the regimen described by Guckenberger *et al.*[20], we generated multiple target volumes to receive different doses per fraction and maintain the same number of fractions. Gross tumour volume (GTV), *i.e.* the macroscopic metastasis, was contoured on the planning CT by the aid (and in most cases co-registration) of diagnostic imaging. Clinical target volume (CTV) included GTV and was delineated depending on the localization: the whole vertebral body for spine, or additional assumed subclinical expansion (*e.g.* along affected ribs). Planning target volume (PTV) for the spine (PTV30) for the 30 Gy-volume was CTV plus 5 mm margin. Planning target volume (PTV40) was generated with 0-2 mm margin around the GTV for the 40 Gy-volume, depending on the localization with 0 mm next to the spinal cord. For metastases in ribs, GTV was contoured as macroscopic tumour in 4D-CT. Internal target volume (ITV) was generated by the aid of 4D-CT to incorporate all potential locations of the tumour. CTV included GTV and 2–3 mm in craniocaudal extension, as well as the whole affected rib on the metastasis level in transverse plane. Additional 6 mm margins were used on CTV to generate PTV30 for metastases in ribs. For metastases in other non-vertebrae bones (sacral bone, sternum, femur), CTV was generated to involve the whole affected bone for sacral bone and sternum (due to large metastasis-size), as well as assumed subclinical expansion along affected long bone. PTV30 was generated with different margins (5–15 mm), dependant on the size of the metastasis and considering positioning inaccuracies. Dose prescription according to International Commission on Radiation Units and Measurements (ICRU)50 was aimed at for the GTV with prioritization of limited dose to the spinal cord. Maximal tolerated dose was 107%. The PTV30 should have been covered with ≥ 90% of the prescribed dose to 98% of the contoured volume (D98) and ≤ 107% of the prescribed dose to 2% of the contoured volume (D2). An example of a treatment plan for radiotherapy with SIB with 30/40 Gy in 10 fractions is demonstrated in Figure 1. Spinal cord was limited to 34 Gy total dose, *i.e.* 50 Gy equivalent dose (2 Gy) (EQD2), estimated by the linear quadratic model with an alpha/beta = 0.87 Gy for spinal cord, according to QUANTEC.[22] An EQD2 of 60 Gy (alpha/beta = 2 Gy) was allowed for metastases localized at the level of the cauda equina. Target volumes were delineated using Monaco planning system, version 5.11.03 or Oncentra Masterplan treatment planning system 4.3 (both Elekta AB, Stockholm,

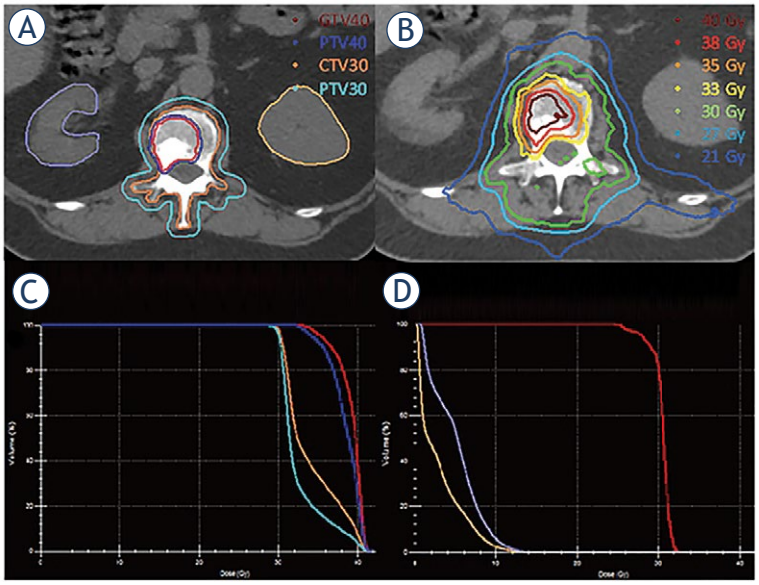

FIGURE 1. Example of a radiation plan for a bone metastasis in the first lumbar vertebra. Gross tumour volume (GTV)40 was contoured by coregistered diagnostic positron emission tomography-computed tomography (PET-CT). Clinical target volume (CTV)30 included GTV40 and the whole vertebral body. Planning target volume (PTV)40 and PTV30 were generated with 2 and 5 mm margins **(A)**. Panel **(B)** demonstrates isodose distribution. Dose-volume histograms (DVHs) PTV30, PTV40, CTV30 and GTV40 show dose coverage **(C)**. GTV40 coverage is compromised due to spinal cord sparing **(B, C)**. DVHs for both kidneys (purple and yellow), as well as spinal cord (red) are demonstrated as well **(D)**. Medical history: patient was diagnosed with high-risk prostate cancer in 2012. Initial treatment included the combination of radiotherapy (prostate and pelvic lymph node) and long-term androgen-deprivation therapy. A single metastasis in the first lumbar vertebra was diagnosed in 2018. Radiotherapy with 30/40 Gy in 10 fractions with integrated simultaneous integrated boost (SIB) was applied for better local control. By the last documented follow up in 2021, no progression was observed in the irradiated metastasis. However, the patient developed diffuse skeletal metastases (treated with secondary androgen-deprivation therapy with abiraterone and enzalutamide).

Sweden). Treatment planning (optimization) was performed by the above-mentioned version of Monaco or the inhouse product Hyperion 2.4.5, respectively. Treatment was delivered by 6 MV Elekta linear accelerators and image-guided radiotherapy (IGRT) with positioning controls using cone-beam CT and daily online corrections. No specific patient immobilisation was needed, due to daily IGRT controls and corrections.

Additionally, dose constraints for OAR and radiotherapy data were evaluated for all irradiated metastatic sites. Mean values for the volume, D2% (D2) and D98% (D98) for GTV40, CTV30, PTV40 and PTV30 were evaluated. Dose values for spinal cord were calculated for patients with metastases in the vertebral body. Mean value for the maximal point dose in the spinal cord (Dmax), D2 and D0.5ccm were reported. The mean dose (Dmean) values were analyzed for kidneys. Patients with Dmean for kidneys below 1 Gy were excluded from this part of the analysis (target volumes far away).

Statistical analysis was performed with IBM SPSS Version 26. Means were compared by two-sided Student's t-test. Survival times were examined using Kaplan-Meier estimator and compared using the log-rank test. Chi-square test was used to describe correlations between categorized variables. Significance was considered in case of $p < 0.05$ and $0.05 < p < 0.1$ was defined as a trend to statistical significance. Pearson´s correlations coefficient was used to measure the statistical relationship between two continuous variables. Pearson`s correlation coefficient $0.4 < r < 0.7$ was defined as moderate correlation, coefficient ≥0.7 was defined as a strong correlation.

Results

Patient population

A total of 25 patients with 29 irradiated metastases were included in our analysis. For oncological outcomes and patient characteristics, 24 patients with 28 irradiated localizations were evaluated. For the analyses of treatment feasibility and dosimetric parameters of all 25 patients (29 irradiated localizations) were included. One patient with non-seminomatous, extragonadal germ cell tumour with diffuse lung metastases and a single bone metastasis in a thoracic vertebral body was treated with curative therapy and therefore was excluded from the oncological outcomes-analysis (also excluded from patient characteristics table) due to specific diagnosis and curative treatment regardless of diffuse metastatic situation (high-dose chemotherapy with stem cell transplantation, resection of lung metastases and irradiation of a single bone metastasis with evaluated regimen). However, the radiation plan of this patient was included in the analyses of feasibility and radiotherapy parameter.

Median follow-up was 1.48 years (0.33–4.67 years). Follow-up data was missing for 3 patients with 4 target volumes. Median age was 67.5 years (range 28–81 years). Predominant sex was male (70.8%). Spine was the most common location (71.4%) followed by ribs (14.3%). According to histopathological reports, prostate cancer was the most frequent histology (45.8%), followed by renal cell carcinoma (12.6%), urothelial cancer (8.3%) and breast cancer (8.3%).

Staging was carried out with positron emission tomography-computed tomography (PET-CT) for 11/24 patients, but not necessarily as the last imaging before radiotherapy. In the subgroup of patients with prostate cancer (n = 11), PSMA-PET-CT was performed in 8 patients. Somatostatin-receptor-PET-CT was performed in 2 patients (pheochromocytoma and endocrine mucin-producing sweat gland carcinoma). FDG-PET-CT was performed for one patient with rectal cancer. In other patients, staging was performed depending on the histology and localization of primary disease, with whole-body CT-scan or with a combination of different imaging modalities (such as magnetic resonance imaging [MRI], skeletal scintigraphy or CT). Median time from last staging to the beginning of radiotherapy was 32 ± 20 days.

Most of the patients had oligometastatic disease in the last staging before radiotherapy (n = 16, 66.7%). In eight patients with diffuse metastases (33.3%), the indication for higher-dose radiotherapy regimen was based on oligoprogression under systemic therapy for 3 patients, radioresistent disease in 3 patients (1 pheochromocytoma and 2 renal cell carcinoma) and metastases with spinal localization and intraspinal component in 2 patients. Both patients with metastasis in the spine with intraspinal component had prostate cancer with efficient systemic therapy options and had favorable prognosis according to the prognostic score introduced by de Vin.[23]

All metastatic sites (or all progressive metastatic sites) were irradiated in 18/24 patients (75%). Two patients with prostate cancer had either synchronous oligometastatic disease at the time of primary tumour diagnosis (n = 1) or metachronous oligometastatic disease with local recurrence after initial treatment of the primary tumour (n = 1). All tumour sites were irradiated (local recurrence included) in these patients. In the group of patients with oligometastatic disease, all sites were irradiated in 15/16 patients. A very slow progression of one bone metastasis was not irradiated in 1 patient. One metastasis was irradiated with the described regimen in 20 patients, two metastases were irradiated in 4 patients. Most of the patients were treated with systemic therapy directly before, simultaneously or directly after radiotherapy (n = 20). An overview of the patient characteristics is provided in Table 1.

Pain was the main clinical symptom in the whole patient cohort (n = 13), although not the main indication for radiotherapy. Additionally, two patients had neurological symptoms, due to spinal metastasis-localization. Possible risk for pathological fracture before radiotherapy was documented in clinical records for eight patients.

TABLE 1. Patient, tumour and therapy characteristics (number of patients n = 24, number of irradiated metastases n = 28), one patient with germ cell tumour not included

Age (Years)		
Median and range	67.5 (28–81)	
Sex (n = 24)		
Female	7	29.2%
Male	17	70.8%
Histology (n = 24)		
Prostate cancer	11	45.8%
Renal cell carcinoma	3	12.6%
Urothelial cancer	2	8.3%
Other*	8	33.3%
Localization of irradiated metastasis (n = 28)		
Spine	20	71.4%
Rib	4	14.3%
Other (sternum, femur 2x, sacral bone)	4	14.3%
Oligometastatic *vs.* diffuse metastatic disease (n = 24)		
Oligometastatic disease	16	66.7%
Diffuse metastatic disease	8	33.3%
Indication for radiation therapy (n = 24)		
Oligometastatic disease	15	62.5%
Oligoprogression under systemic therapy	4	16.7%
Radiation resistant histology	3	12.5%
Intraspinal tumour component	2	8.3%
Systemic therapy (n = 24)		
No systemic therapy	4	16.7%
Chemotherapy or immunotherapy	10	41.7%
Hormonal therapy	10	41.7%

* Includes 2 patients with breast cancer, as well as one patient with rectal cancer, myxofibrosarcoma, metastatic chordoma, leiomyosarcoma, pheochromocytoma and endocrine mucin-producing sweat gland carcinoma, respectively

Feasibility

All patients (n = 25) finished all planned radiotherapy sessions. Acute toxicity grade 1 (CTCAE V4.0) was documented for 36.0% of the patients and included erythema (n = 4), gastrointestinal (n = 3), urinary (n = 2) or oesophageal toxicity (n = 2) and nausea (n = 1). No acute radiation toxicity > grade 1 was observed. One patient with metastasis in the distal femur was operated 4 months after the end of radiotherapy due to bone instability and result-

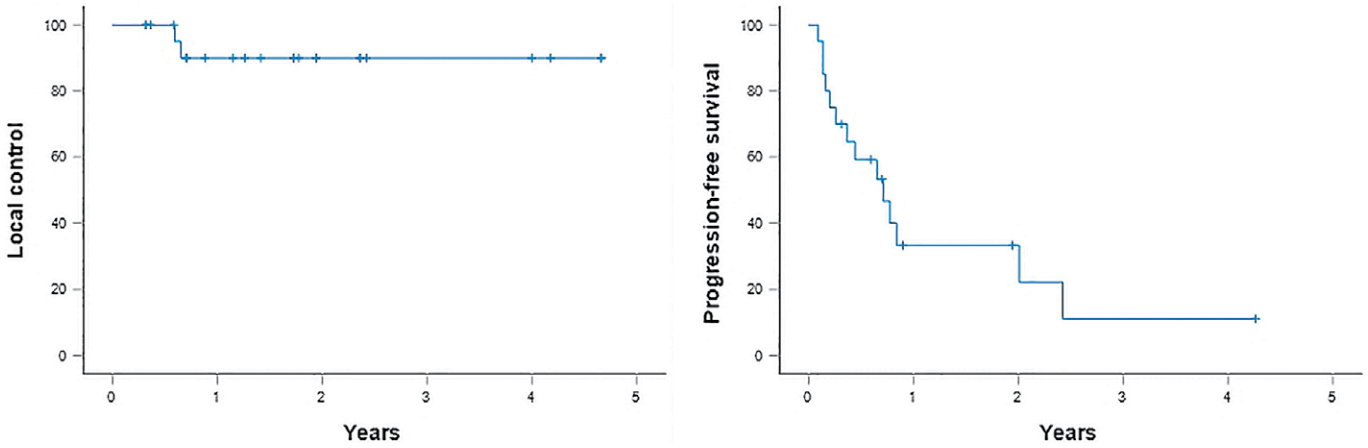

FIGURE 2. Kaplan-Maier survival curves demonstrating local control (LC) and PFS. LC-rates at 1 and 2 years (calculated per total number of irradiated metastases) was 90.0 ± 6.7% and 83.3 ± 15.2%. Estimated PFS-rates at 1 and 2 years (calculated per number of patients) were 33.3 ± 11.6% and 22.2 ± 11.9%.

ing pain during axial loading. Otherwise, no subacute toxicities were documented during follow up. No pathological fractures and no neurologic toxicity were observed with our limited follow-up. Pain relief was reported by 9/13 (69.2%) patients initially reporting pain. In one patient, no data on pain relief were available.

Oncologic outcomes

Oncologic outcomes are presented in Figure 2. During the follow-up, two local recurrences were observed (in both cases 7 months after the end of radiotherapy) in patients with spinal metastasis of clear cell renal cell carcinoma and urothelial carcinoma. In both patients, local progression was in-field. In patient with urothelial carcinoma metastasis localized in the spine (with paravertebral spread), no underdosage in target volume was observed. Tumour progression in this patient was detected in GTV area (both in the spine and in paravertebral component). In a patient treated for a renal cell carcinoma metastasis in the spine (with intraspinal and paravertebral spread), the D98 in the PTV40 was 32.31 Gy in order to respect the constraints for spinal cord. D98 of the PTV30 in this patient was 28.49 Gy. However, tumour progression in this patient seems to rather be limited to an area, where target volume coverage was sufficient.

Dependent on tumour histology and metastasis localization, LC was assessed using different imaging modalities (MRI, CT or PET-CT) or laboratory parameters (PSA). For 20/28 (71.4%) irradiated target volumes, LC was assessed using radiological imaging during follow-up. In 3 patients with 4 target volumes (14.2%), no radiological imaging was performed. However, all of these patients had prostate cancer and had no PSA-elevation nor progression of clinical symptoms during follow-up and therefore no imaging was performed. The patients were rated as locally controlled as without PSA-elevation and no symptom progression, tumour recurrence is unlikely. In 3 patients with 4 target volumes, no follow-up information was available.

Stratified by tumour histology, our analysis demonstrated significant differences in estimated 1-year PFS rates for patients with prostate cancer (66.7 ± 19.2%) vs. other malignancies (11.1 ± 10.1%), p = 0.003. However, 72.7% of patients with prostate cancer had oligometastatic disease, whereabout only 53.8% of patients with other malignancies had oligometastatic disease (not significant). No deaths were documented during follow up.

Dosimetric parameters

Dosimetric parameters and radiotherapy data were evaluated for all 25 patients (in total 29 metastatic localizations). Various parameters were evaluated for spinal cord and kidney constraints. Distribution of dose-volume histogram (DVH) derived parameters is demonstrated in Figure 3. According to ICRU prescription, good dose coverage was demonstrated for PTV30-volumes. GTV40 coverage was compromised in selected cases due to spinal cord sparing.

DVH parameters for spinal cord were calculated for 21 radiation plans for patients with metastases in the vertebral body. Respecting the dose

constraints for spinal cord had first priority, even if the GTV40 coverage was compromised. However, three patients had Dmax values above 34 Gy. To achieve improved CTV30 dose coverage, higher Dmax values were allowed in two patients due to its localization in fourth lumbar vertebra (Dmax = 34.25 Gy) and sacral bone (Dmax = 39.89 Gy), where dose constraints for cauda equina allowed higher doses than for spinal cord (max. EQD2 of 60 Gy with alpha/beta = 2 Gy). The third patient had slightly higher Dmax value (Dmax = 34.09 Gy) for spinal cord for irradiation of a metastasis in the first lumbar vertebra with intraspinal component. Mean kidney dose was limited to 12 Gy. Dose values for kidneys were calculated for 21 kidneys. Dose constraints were respected in all patients.

Radiotherapy data for the patient being operated due to painful bone instability of the distal femur were analyzed in detail. Maximal dose for GTV40 was 41.73 Gy (104% of the prescribed dose for GTV), mean dose on femoral bone was 24.7 Gy. 14.1% of delineated femoral bone received a dose of at least 40 Gy. Radiation therapy data for this patient did not exceed ICRU recommendations. Furthermore, more than 50% of the bone circumference was excluded from the PTV40. Due to the metastasis size, GTV40 (88.91 cm^3), CTV30 (534.69 cm^3) and PTV30 (1096.43 cm^3) volumes were larger than mean values in the whole cohort, also resulting in the largest PTV30 in the whole patient cohort. In multidisciplinary discussion, the bone instability was not rated as radiotherapy toxicity but rather possibly related to the size of the metastasis. Radiotherapy plan as well as follow-up MRIs for this metastasis are shown in Figure 4.

Discussion

Sufficient LC-rates were demonstrated with the evaluated regimen in our cohort, with LC at 1 and 2 years of 90.0 ± 6.7% and 83.3 ± 15.2%, respectively. SBRT regimen with SIB for patients with spinal bone metastases have been increasingly studied[18-21], and although inclusion criteria and dosing varied between studies, our 1-year LC-rate is in line with reported data.[19] In a prospective study published by Guckenberger *et al.*, spinal metastases were irradiated with SBRT regimen with SIB with either 48.5/30 Gy or 35/20 Gy in 10 fractions.[20] Lubgan *et al.* reports good LC-rates after irradiation of spinal metastases using various SBRT regimen with SIB (median dose of 42.0/ 32.39 Gy in 10–12 fractions.[19] Comparable to our data, both studies

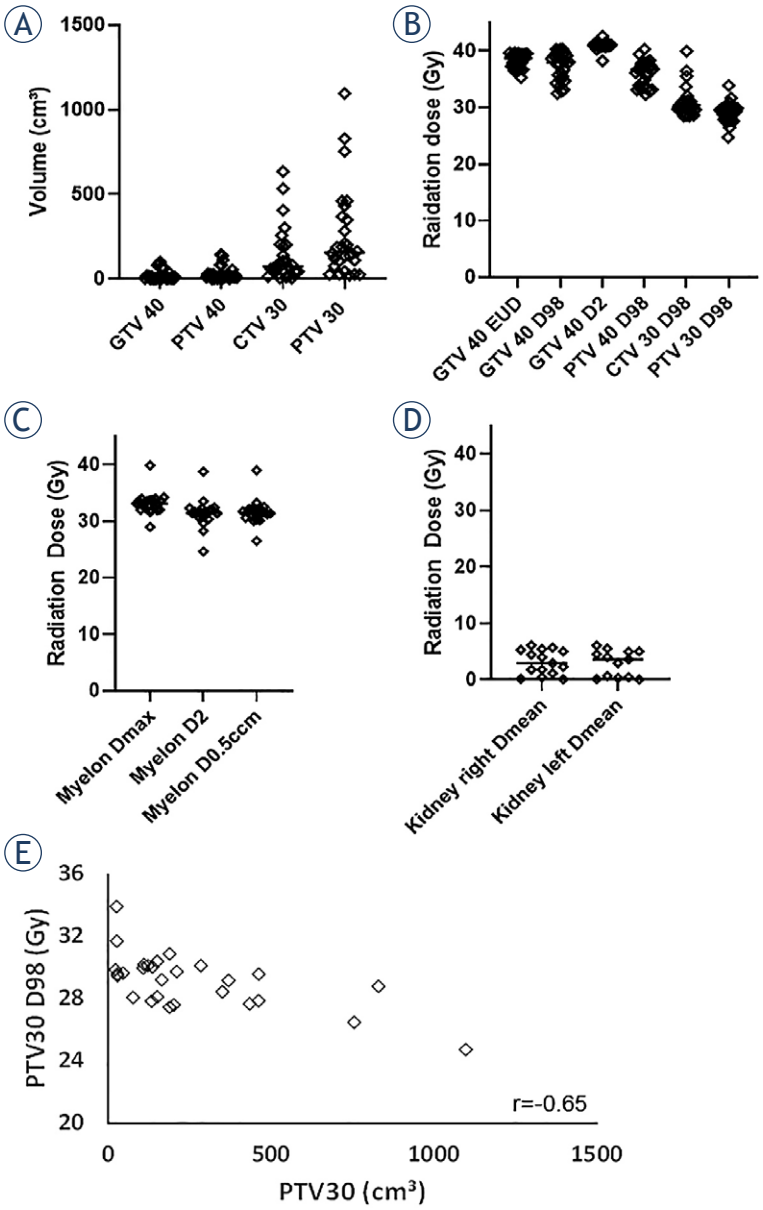

FIGURE 3. Distribution of radiation therapy parameter. Target volume size for gross tumour volume (GTV)40, clinical target volume (CTV)30, planning target volume (PTV)40 and PTV30 is shown in panel **(A)**. Mean values of the volume for GTV40, CTV30, PTV40 and PTV30 for the whole cohort were 25.90 cm^3 (range 0.11-100.74 cm^3), 140.04 cm^3 (range 5.33-635.19 cm^3), 40.43 cm^3 (range 0.11-185.43 cm^3) and 249.44 cm^3 (range 22.28-1096.43 cm^3). Panel **(B)** demonstrates target volume coverage for GTV40 minimal dose covering 98% of the target volume (D98), GTV40 maximal dose covering 2% of the target volume (D2), PTV40 D98, CTV30 D98 and PTV30 D98, as well as for GTV40 equivalent uniform dose (EUD). Mean value for D2 for GTV40 was 40.99 ± 0.65 Gy. Mean values for D98 for GTV40, CTV30, PTV40 and PTV30 were 37.26 ± 2.49 Gy, 30.94 ± 2.61 Gy, 35.75 ± 1.96 Gy and 29.10 ± 1.75 Gy. Mean value for GTV40 EUD was 38.21 ± 1.19 Gy. Panel **(C)** demonstrates radiation parameters for spinal cord (Dmax, D2 and D0.5cm). Mean values for spinal cord Dmax and D0.5ccm were 32.77 ± 1.18 Gy and 31.61 ± 2.07 Gy. Mean value for spinal cord D2 was 31.41 ± 2.36 Gy. Radiation parameter for kidneys (Dmean) are shown in panel **(D)**. Mean value for Dmean for the kidneys was 4.18 ± 1.49 Gy. Maximal kidney Dmean value was 6.14 Gy. Panel e demonstrates moderate negative correlation of the size of the target volume with PTV30 D98 coverage, showing worse target volume coverage for larger target volumes.

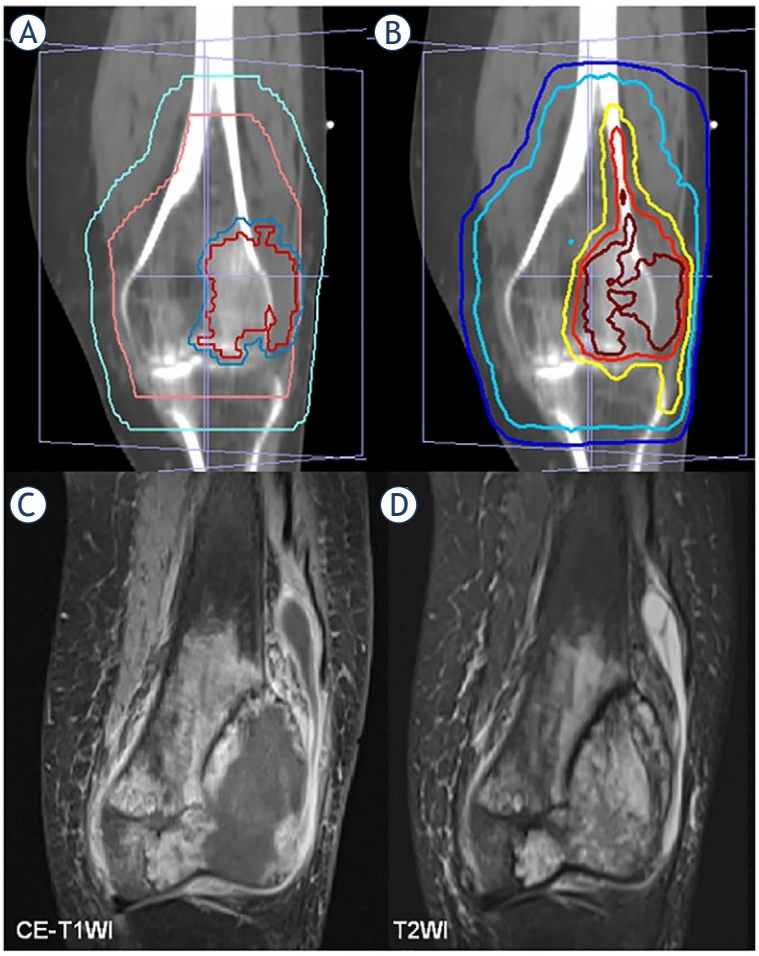

FIGURE 4. Example of the radiation plan for a metastasis in femoral bone requiring subsequent surgery. The patient was diagnosed with bladder urothelial cancer in 2007. After tumour resection in 2007, the patient was diagnosed with diffuse bone metastases in 2018. Femoral bone metastasis was the only progressive tumour localization and higher-dose radiation therapy with 30/40 Gy with simultaneous integrated boost (SIB) was applied in 2018. Four months after the end of radiation therapy, the patient developed pain during axial loading of the knee due to a bone instability. Therefore, distal femur was replaced by a prothesis. Histopathological report after surgery showed a mixture of tumour and bone necrosis without signs of progressive vital tumour. No further local tumour progression in remaining femoral bone was documented in the follow up. Panel **(A)** demonstrates target volume delineation (gross tumour volume [GTV]40 = red, planning target volume (PTV)40 = dark blue, clinical target volume [CTV]30 = orange, PTV30 = light blue). Isodose distribution is shown in panel **(B)** (dark red = 40 Gy, red = 38.3 Gy, yellow = 34.9 Gy, light blue = 29.8 Gy, dark blue = 21.0 Gy). Panel **(C)** and **(D)** present magnetic resonance imaging (MRI) 4 months after the end of radiation therapy, showing tumour metastasis and necrosis. T1-weighted contrast-enhanced MRI (CE-T1WI) sequence **(C)** demonstrates a small contrast enhanced ring with large hypointense core. T2-weighted MRI (T2WI) sequence **(D)** shows diffuse bone oedema.

reported good feasibility and no radiation-induced myelopathy as long-term side effect.[24]

Although radiotherapy for the treatment of painful bone metastases has been established[25], optimal fractionation and dose regimens for patients with oligometastatic disease seem to remain challenging and are still an unresolved issue. Various fractionation and dose schedules for palliative radiotherapy for bone metastases have been examined and can be divided broadly into two categories: short-course radiotherapy (delivered in up to five fractions) and long-course radiotherapy (delivered in 10 or more fractions).[26] Different studies found no difference in pain relief[26,27] or toxicity rates between short-course and long-course therapies.[26] However, conventional radiotherapy with 8 Gy single dose is associated with shorter pain relief (3–6 months) and can be insufficient for patients with longer life expectancy.[24] Furthermore, accumulating clinical data suggest better local control rates after irradiation of bone metastases with long-course radiotherapy. Improved 1-year local control rates for spinal metastases with spinal canal compression in patients with breast and prostate cancer were reported after long-course radiotherapy, compared to short-course palliative radiotherapy with 8 Gy in one fraction.[1] In addition, the incidence of repeated irradiation to the same metastatic site is lower in patients treated with longer fractionated schedules, compared to patients treated with 8 Gy in one fraction.[25,27]

With improved survival rates for patients with oligometastatic disease and predominant bone metastases[26], aggressive metastasis-directed therapy has been proposed to improve clinical response and eventually delay the initiation of systemic therapies.[13,14,28] In a study published in 2011 by Rades *et al*., improved local control, as well as survival benefit were demonstrated for patients with favourable survival prognoses after radiotherapy with total dose escalated beyond 30 Gy (40 Gy in 20 fractions or 37.5 Gy in 15 fractions).[29] A fractionated regimen with SIB (to escalate the dose in the target volume and reduce the dose for organs at risks) for radiotherapy of spine metastases was examined in various studies.[18,19] Various regimen for palliative radiotherapy in patients with spinal bone metastases are being evaluated in one ongoing prospective study (30 Gy in 10 fractions, 30/40 Gy in 10 fractions, 20 Gy in 5 fractions and 20/30 Gy in five fractions).[21] To increase the duration of pain relief, achieve better local control, deliver higher dose to the target volume with proper sparing of organs at risks, a higher-dose IMRT fractionated regime with 30/40 Gy with SIB was introduced in our institution. This regimen differs from stereotactic radiotherapy not only in its dose, but also in target volume delineation concept, as it integrates

two target volumes (macroscopic tumour and localized adjuvant region within the affected bone).

We included patients with favourable prognostic factors (*e.g.* number of metastases, systemic treatment options) and assumed longer life expectancy. Oligometastatic disease and oligoprogression under systemic therapy were the indication for this regimen for most of the patients (79.2%). Patients with diffuse metastatic disease were included in case of assumed radioresistant disease or vertebral metastasis with intraspinal component (if the patients had favourable prognosis and efficient systemic therapy options), where the higher-dose regime was applied to achieve better local control. This assumption was supported by a systematic literature review published in 2009 by Gerszten *et al.* They defined tumour histology as a prognostic factor in treatment response after conventional radiotherapy of spine metastases.[30]

Although the reported dataset is limited with number of patients and limited follow up, we observed sufficient LC rates using this regime. However, 83.4% of the patients received systemic therapy directly before, in parallel to or after radiation therapy, which might have influenced our LC-rates with its synergistic effect. In comparison to our results, a retrospective study published by Makita *et al.* reported a 1-year LC-rates of 60% for biological effective dose $(BED)_{10}$ < 39.0 Gy (= 1 x 8 Gy, 5 x 4 Gy, 4 x 5 Gy or 10 x 2.5 Gy) and 80% for BED_{10} = 39.0 Gy (= 10 x 3 Gy).[31] Two patients in our analysis developed local progression. In both cases, local progression seems to be limited to area with sufficient target volume coverage. These cases included radioresistant tumour histology (clear cell renal carcinoma and urothelial carcinoma) which indicates that this regimen should be evaluated in larger series for patients with radioresistant malignancies. Furthermore, feasibility of this regimen was good, with all patients completing the treatment and no patients developing acute toxicity beyond grade 1. Grade 1 acute toxicity was documented for 36.0% of the patients and included mild urinary or gastrointestinal toxicity, dysphagia and nausea. Assuming the extended life expectancy for most patients with oligometastatic disease, late side effects are much more clinically relevant than acute toxicity. Thus, one patient was operated due to painful bone instability 4 months after the end of radiation therapy. No pathological fractures and no neurologic toxicity were observed. However, these results might be limited with absence of imaging during follow-up in some patients with prostatic cancer, where no imaging was performed in case of no PSA-elevation and no progression of clinical symptoms connected to irradiated localization. We adjusted dose constraints for spinal cord using our institutional constraints for normofractionated radiotherapy for vertebral body. Respecting the dose limitation for spinal cord was priority, which led to underdosage in target volume coverage in selected cases. Thus, with this approach, clinically satisfying results were achieved regarding late neurologic toxicity as well as LC-rate.

One patient with urothelial carcinoma and metastasis in distal femur required surgery due to bone instability (rated by orthopaedic surgeons as instability due to the metastasis and not as radiotherapy-induced osteonecrosis). In our analysis, no exceed in ICRU recommendations in radiation plan for this patient was observed. This patient had the largest PTV30 in the whole patient cohort. However, this was the only metastasis in a long bone and is therefore hardly comparable to the spine and ribs volumes (where no osteonecrosis or pathological fractures were detected). This indicates that a further evaluation of this regimen for metastases therapy in long bones is needed, as there might be additional factors to be considered in radiation therapy planning for this localization (*e.g.* functional load). Pain as an initial symptom was reported in 13/25 patients. Pain relief was documented for 69.2% patients at some point during follow-up, which is comparable to another study that examined pain response after IMRT with 30 Gy in 10 fractions for spinal metastases.[32] However, due to the retrospective study design, no pain grading or accurate analyses of pain relief duration was possible.

Conclusions

In summary, higher-dose IMRT fractionated regimen with 30/40 Gy with SIB is a safe and feasible treatment regimen for selected patients with bone metastases, with all patients completing all therapy sessions with no acute radiation toxicity > grade 1. With limited number of patients and follow-up, as well as methodological limitations of a retrospective study, good LC-rates were demonstrated in our cohort. Using this treatment method, we managed to deliver a high radiation dose to the target volume and simultaneously achieve proper sparing of organs at risk. This intermediate-dose regimen represents a therapy in between clear palliative schedules and stereotactic body radiation

therapy (SBRT) in few fractions and might be the preferred option for patients with oligometastatic or oligoprogressive disease and long-life expectancy, if SBRT cannot be applied. Furthermore, this treatment can be convenient for bone metastases with intraspinal component, when improved LC-rate might be achieved using this higher-dose fractionated regime. However, late toxicity after this treatment concept and special combinations of metastasis localization and histology warrants further evaluation.

References

1. Agarawal JP, Swangsilpa T, van der Linden Y, Rades D, Jeremic B, Hoskin PJ. The role of external beam radiotherapy in the management of bone metastases. *Clin Oncol (R Coll Radiol)* 2006; **18:** 747-60. doi: 10.1016/j.clon.2006.09.007
2. De Felice F, Piccioli A, Musio D, Tombolini V. The role of radiation therapy in bone metastases management. *Oncotarget* 2017; **8:** 25691-9. doi: 10.18632/oncotarget.14823
3. Spencer KL, van der Velden JM, Wong E, Seravalli E, Sahgal A, Chow E, et al. Systematic review of the role of stereotactic radiotherapy for bone metastases. *J Natl Cancer Inst* 2019; **111:** 1023-32. doi: 10.1093/jnci/djz101
4. Fornetti J, Welm AL, Stewart SA. Understanding the bone in cancer metastasis. *J Bone Miner Res* 2018; **33:** 2099-113. doi: 10.1002/jbmr.3618
5. Pontoriero A, Lillo S, Caravatta L, Bellafiore F, Longo S, Lattanzi E, et al. Cumulative dose, toxicity, and outcomes of spinal metastases re-irradiation. *Strahlenther Onkol* 2021; **197:** 369-84. doi: 10.1007/s00066-021-01748-7
6. Turpin A, Duterque-Coquillaud M, Vieillard MH. Bone metastasis: current state of play. *Transl Oncol* 2020; **13:** 308-20. doi: 10.1016/j.tranon.2019.10.012
7. Tang X, Hu Q, Chen Y, Wang X, Li X, Cheng K, et al. Optimal dose-fractionation schedule of palliative radiotherapy for patients with bone metastases: a protocol for systematic review and network meta-analysis. *BMJ Open* 2020; **10:** e033120. doi: 10.1136/bmjopen-2019-033120
8. Hellman S, Weichselbaum RR. Oligometastases. *J Clin Oncol* 1995; **13:** 8-10. doi: 10.1200/JCO.1995.13.1.8
9. Tosoian JJ, Gorin MA, Ross AE, Pienta KJ, Tran PT, Schaeffer EM. Oligometastatic prostate cancer: definitions, clinical outcomes, and treatment considerations. *Nat Rev Urol* 2017; **14:** 15-25. doi: 10.1038/nrurol.2016.175
10. Hurmuz P, Onal C, Ozyigit G, Igdem S, Atalar B, Sayan H, et al. Treatment outcomes of metastasis-directed treatment using 68Ga-PSMA-PET/CT for oligometastatic or oligorecurrent prostate cancer: Turkish Society for Radiation Oncology group study (TROD 09-002). *Strahlenther Onkol* 2020; **196:** 1034-43. doi: 10.1007/s00066-020-01660-6
11. Foster CC, Weichselbaum RR, Pitroda SP. Oligometastatic prostate cancer: Reality or figment of imagination? *Cancer* 2019; **125:** 340-52. doi: 10.1002/cncr.31860
12. Palma DA, Salama JK, Lo SS, Senan S, Treasure T, Govindan R, et al. The oligometastatic state - separating truth from wishful thinking. *Nat Rev Clin Oncol* 2014; **11:** 549-57. doi: 10.1038/nrclinonc.2014.96
13. Fraser M, Koontz B, Emmenegger U, De Meerleer G, Khoo V, Feng F, et al. What is oligometastatic prostate cancer? *Eur Urol Focus* 2019; **5:** 159-61. doi: 10.1016/j.euf.2018.12.009
14. Ost P, Reynders D, Decaestecker K, Fonteyne V, Lumen N, De Bruycker A, et al. Surveillance or metastasis-directed therapy for oligometastatic prostate cancer recurrence: a prospective, randomized, multicenter phase II trial. *J Clin Oncol* 2018; **36:** 446-53. doi: 10.1200/JCO.2017.75.4853
15. Hoskin PJ, Yarnold JR, Roos DR, Bentzen S, Second Workshop on Palliative R, Symptom C. Radiotherapy for bone metastases. *Clin Oncol (R Coll Radiol)* 2001; **13:** 88-90. doi: 10.1053/clon.2001.9225
16. Rades D, Stalpers LJ, Veninga T, Schulte R, Hoskin PJ, Obralic N, et al. Evaluation of five radiation schedules and prognostic factors for metastatic spinal cord compression. *J Clin Oncol* 2005; **23:** 3366-75. doi: 10.1200/JCO.2005.04.754
17. Jaffray D, Kupelian P, Djemil T, Macklis RM. Review of image-guided radiation therapy. *Expert Rev Anticancer Ther* 2007; **7:** 89-103. doi: 10.1586/14737140.7.1.89
18. Lee YK, Bedford JL, McNair HA, Hawkins MA. Comparison of deliverable IMRT and VMAT for spine metastases using a simultaneous integrated boost. *Br J Radiol* 2013; **86:** 20120466. doi: 10.1259/bjr.20120466
19. Lubgan D, Ziegaus A, Semrau S, Lambrecht U, Lettmaier S, Fietkau R. Effective local control of vertebral metastases by simultaneous integrated boost radiotherapy: preliminary results. *Strahlenther Onkol* 2015; **191:** 264-71. doi: 10.1007/s00066-014-0780-4
20. Guckenberger M, Mantel F, Sweeney RA, Hawkins M, Belderbos J, Ahmed M, et al. Long-term results of dose-intensified fractionated stereotactic body radiation therapy (SBRT) for painful spinal metastases. *Int J Radiat Oncol Biol Phys* 2021; **110:** 348-57. doi: 10.1016/j.ijrobp.2020.12.045
21. Sprave T, Welte SE, Bruckner T, Förster R, Bostel T, Schlampp I, et al. Intensity-modulated radiotherapy with integrated-boost in patients with bone metastasis of the spine: study protocol for a randomized controlled trial. *Trials* 2018; **19:** 59. doi: 10.1186/s13063-018-2452-7
22. Kirkpatrick JP, van der Kogel AJ, Schultheiss TE. Radiation dose-volume effects in the spinal cord. *Int J Radiat Oncol Biol Phys* 2010; **76(3 Suppl):** S42-9. doi: 10.1016/j.ijrobp.2009.04.095
23. de Vin T, Engels B, Gevaert T, Storme G, De Ridder M. Stereotactic radiotherapy for oligometastatic cancer: a prognostic model for survival. *Ann Oncol* 2014; **25:** 467-71. doi: 10.1093/annonc/mdt537
24. Guckenberger M, Mantel F, Gerszten PC, Flickinger JC, Sahgal A, Letourneau D, et al. Safety and efficacy of stereotactic body radiotherapy as primary treatment for vertebral metastases: a multi-institutional analysis. *Radiat Oncol* 2014; **9:** 226. doi: 10.1186/s13014-014-0226-2
25. Lutz S, Balboni T, Jones J, Lo S, Petit J, Rich SE, et al. Palliative radiation therapy for bone metastases: update of an ASTRO Evidence-Based Guideline. *Pract Radiat Oncol* 2017; **7:** 4-12. doi: 10.1016/j.prro.2016.08.001
26. Fujino M, Suzuki K, Nishio M, Nishiyama N, Osaka Y. Strategy of radiation therapy for bone metastases and MSCC in breast cancer patients. *Breast Cancer* 2011; **18:** 238-43. doi: 10.1007/s12282-011-0288-z
27. Hartsell WF, Scott CB, Bruner DW, Scarantino CW, Ivker RA, Roach M, 3rd, et al. Randomized trial of short- versus long-course radiotherapy for palliation of painful bone metastases. *J Natl Cancer Inst* 2005; **97:** 798-804. doi: 10.1093/jnci/dji139
28. Hölscher T, Baumann M, Kotzerke J, Wirth M, Thomas C, Zips D, et al. OLI-P: Toxicity and efficacy of local ablative radiotherapy in PSMA-PET staged, oligometastatic prostate cancer – a phase II trial. [abstract]. *J Clin Oncol* 2021; **39(6 Suppl):** 115. doi: 10.1200/JCO.2021.39.6_suppl.115
29. Rades D, Panzner A, Rudat V, Karstens JH, Schild SE. Dose escalation of radiotherapy for metastatic spinal cord compression (MSCC) in patients with relatively favorable survival prognosis. *Strahlenther Onkol* 2011; **187:** 729-35. doi: 10.1007/s00066-011-2266-y
30. Gerszten PC, Mendel E, Yamada Y. Radiotherapy and radiosurgery for metastatic spine disease: what are the options, indications, and outcomes? *Spine* 2009; **34(22 Suppl):** S78-92. doi: 10.1097/BRS.0b013e3181b8b6f5
31. Makita K, Hamamoto Y, Kanzaki H, Kataoka M, Yamamoto S, Nagasaki K, et al. Local control of bone metastases treated with external beam radiotherapy in recent years: a multicenter retrospective study. *Radiat Oncol* 2021; **16:** 225. doi: 10.1186/s13014-021-01940-0
32. Sprave T, Verma V, Forster R, Schlampp I, Hees K, Bruckner T, et al. Bone density and pain response following intensity-modulated radiotherapy versus three-dimensional conformal radiotherapy for vertebral metastases – secondary results of a randomized trial. *Radiat Oncol* 2018; **13:** 212. doi: 10.1186/s13014-018-1161-4

research article

Quantifying the changes in the tumour vascular micro-environment in spinal metastases treated with stereotactic body radiotherapy - a single arm prospective study

Balamurugan Vellayappan[1], Dennis Cheong[2], Salil Singbal[3], Jeremy Tey[1], Yu Yang Soon[1], Cheng Nang Leong[1], Alvin Wong[4], Sein Lwin[5], Chau Hung Lee[6], Pravin Periasamy[7], Simon Lo[8], Naresh Kumar[9]

[1] Department of Radiation Oncology, National University Cancer Institute Singapore, National University Hospital, Singapore
[2] Clinical Imaging Research Centre, National University of Singapore
[3] Department of Diagnostic Imaging, National University Hospital, Singapore
[4] Department of Haematology-Oncology, National University Cancer Institute Singapore, National University Hospital, Singapore
[5] Division of Neurosurgery, Department of Surgery, National University Hospital, Singapore
[6] Department of Radiology, Tan Tock Seng Hospital, Singapore
[7] Centre for Life Sciences (CeLS), National University of Singapore
[8] Department of Radiation Oncology, University of Washington, Seattle, WA, USA
[9] Department of Orthopaedic Surgery, National University Hospital, Singapore

Radiol Oncol 2022; 56(4): 525-534.

Received 24 August 2022
Accepted 29 September 2022

Correspondence to: Assist. Prof. Balamurugan Vellayappan, M.D., Department of Radiation Oncology, National University Cancer Institute Singapore, National University Hospital, Singapore, Level 7 Tower Block, 1E Lower Kent Ridge Road, Singapore 119228.
E-mail: mdcbav@nus.edu.sg ; bala_vellayappan@nuhs.edu.sg

Disclosure: No conflicts of interest were disclosed.

Background. The primary objective was to quantify changes in vascular micro-environment in spinal metastases (SM) patients treated with stereotactic body radiotherapy (SBRT) with multi-parametric dynamic contrast enhanced (DCE) magnetic resonance imaging (MRI). The secondary objective was to study plasma biomarkers related to endothelial apoptosis.

Patients and methods. Patients were imaged with DCE-MRI at baseline/1-week/12-weeks post-SBRT. Metrics including normalised time-dependent leakage (Ktrans), permeability surface product (PS), fractional plasma volume (Vp), extracellular volume (Ve) and perfusion (F) were estimated using distributed parameter model. Serum acid sphingomyelinase (ASM) and sphingosine-1-phosphate (S1P) were quantified using ELISA. Clinical outcomes including physician-scored and patient-reported toxicity were collected.

Results. Twelve patients (with varying primary histology) were recruited, of whom 10 underwent SBRT. Nine patients (with 10 lesions) completed all 3 imaging assessment timepoints. One patient died due to pneumonia (unrelated) before follow-up scans were performed. Median SBRT dose was 27 Gy (range: 24–27) over 3 fractions (range: 2–3). Median follow-up for alive patients was 42-months (range: 22.3–54.3), with local control rate of 90% and one grade 2 or higher toxicity (vertebral compression fracture). In general, we found an overall trend of reduction at 12-weeks in all parameters (Ktrans/PS/Vp/Ve/F). Ktrans and PS showed a reduction as early as 1-week. Ve/Vp/F exhibited a slight rise 1-week post-SBRT before reducing below the baseline value. There were no significant changes, post-SBRT, in plasma biomarkers (ASM/S1P).

Conclusions. Tumour vascular micro-environment (measured by various metrics) showed a general trend towards downregulation post-SBRT. It is likely that vascular-mediated cell killing contributes to excellent local control rates seen with SBRT. Future studies should evaluate the effect of SBRT on primary-specific spinal metastases (e.g., renal cell carcinoma).

Key words: spine metastases; stereotactic body radiotherapy; DCE-MRI; endothelial apoptosis

Introduction

Approximately 40% of patients with cancer, will develop spinal metastases (SM) in their cancer journey.[1] Symptomatic SM is usually treated with a combination of analgesia, radiotherapy and/or surgery.[2] Stereotactic body radiotherapy (SBRT) is an emerging treatment technique which is indicated for patients with oligo-metastatic disease, symptomatic SM from radio-resistant histological subtypes (e.g., renal cell carcinoma, colon adenocarcinoma), or in selected patients with expected long survival where durable tumour control becomes a priority.

SMs from some primaries such as renal cell carcinoma are known to be vascular, as evidenced by large intra-operative blood losses, in patients undergoing surgical resection (e.g., decompression, separation surgery, corpectomy). Data from our research group has estimated the mean intra-operative blood loss to be 870 + 720 ml, with an average blood transfusion requirement of 1.5 + 1.9 units.[3] This has prompted surgeons to utilise pre-operative angio-embolisation prior to resection, however, the effectiveness of this is highly variable.[4]

SBRT uses highly focused ablative radiotherapy, with the key feature being large fraction sizes (ranging 6–24 Gy), given over 1–5 sessions. This contrasts with palliative conventional external beam radiotherapy, with smaller fraction sizes (2.5–4 Gy) given over 5 – 15 sessions. Large fraction sizes have been mechanistic linked to a novel way of vascular-mediated cell killing, through the ceramide pathway.[5] The key players in the ceramide pathway include ASM and S1P.[6] The use of large fraction sizes has been shown in pre-clinical studies to significantly reduce the vascular volume.[7] However, this is poorly understood in the clinical setting.

The effect of SBRT on tumour vasculature has been explored by other research groups, particularly with the use of Dynamic Contrast enhanced MRI imaging (DCE-MRI).[8-11] DCE-MRI is an advanced non-invasive modality which provides functional information on vascular micro-environment and hemo-dynamics, where quantitative assessment of vascular parameters can be obtained through a pharmacokinetic model of contrast uptake to determine the signal intensity changes over time.[12] There are multiple models available to obtain quantitative information, and our group prefers the use of the distributed parameter (DP) model, over compartment models (e.g. Toft's model), especially in the post-treatment setting.[13] In contrast to Toft's model, the DP model does not assume well-mixed compartments (between the plasma and extracellular, extravascular spaces) and accounts for concentration changes with both time and distance along the capillary length. A schematic representation of the DP model can be seen in Figure 1. The variables of the DP model include time-dependent leakage (Ktrans), perfusion (F), permeability surface area product (PS), fractional plasma volume (Vp) and fractional extracellular volume (Ve). As such, the DP model offers the possibility of estimating flow and permeability separately, as well as estimating fractional vascular and interstitial volumes.

DCE parameters such as Vp and Ktrans were found to be reduced post-SBRT, and Vp has been suggested to be an early response biomarker for tumour control. Notably, most of these studies were not done in a prospective manner, where the time points of assessment were highly variable between patients. Moreover, only two parameters have been reported (Vp and Ktrans) in these studies, and this may not provide a comprehensive assessment of tumour vascular compartment.

We hypothesize that SBRT to SM will reduce the vascular micro-environment and perfusion parameters, in keeping with previous studies. Our aim is to prospectively quantify the effects of SBRT on SM using DCE-MRI metrics, and to describe changes in correlative plasma biomarkers of the ceramide pathway.

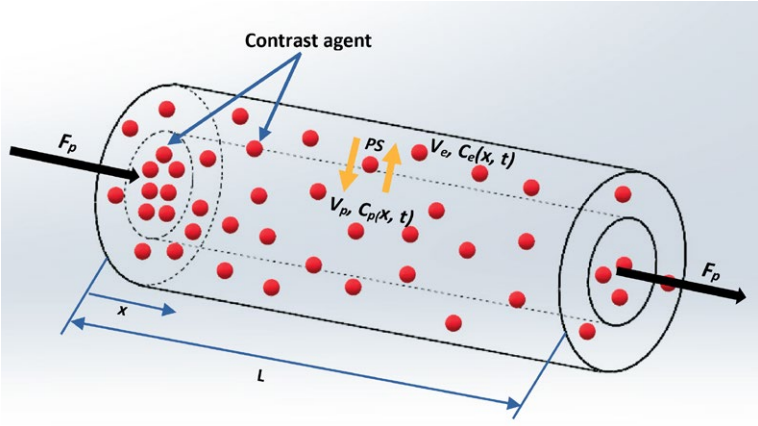

FIGURE 1. Schematic illustration of the DP model. Contrast agent (CA) concentration within the vessel decreases with position (x) along the vessel length (L), producing concentration gradients between the arterial (x = 0) and venous (x = L) capillary ends. During the CA passage, a portion of the CA molecules diffuses between the plasma and extracellular, extravascular space (EES) at a controlled permeability surface area product (PS) rate, so that the plasma, Cp(x, t), and EES, Ce(x, t), concentrations show both spatial and temporal dependence.

TABLE 1. Inclusion and exclusion criteria

Inclusion criteria	Exclusion criteria
1. Age ≥ 21 years	1. Metastatic haematological and germ cell neoplasms
2. Proven metastatic disease	2. Inability to undergo MRI or receive gadolinium contrast
3. Life expectancy > 3 months	3. Prior radiotherapy to region of interest
4. Eastern Cooperative Oncology group (ECOG) 0–2	4. Recent surgery to affected spinal levels, or patients requiring immediate surgical intervention
5. ≤ 3 contiguous vertebral body segments, including para-spinal disease	5. Spinal instability score (SINS) > 12
6. Able to lie supine for ≥ 60 minutes	6. Symptomatic cord compression (Bilksy grade 2 or 3), or worsening neurological deficits

Patients and methods

This prospective study was approved by Institutional Review Board (NHG, 2016/1179), and registered on clinicaltrials.gov (NCT03072979). This was designed as a single-arm cohort study, conducted from May 2017 to December 2018, and patients were recruited from National University Hospital, Singapore. Written consent was obtained from all patients prior to any study related procedures. This study was conducted in accordance with the declaration of Helsinki.

Participants

Only adult patients who in whom SBRT for SM was clinically indicated were eligible for recruitment. Inclusion and exclusion criteria are described in Table 1. Patients who were undergoing systemic chemotherapy at recruitment, had to observe a one-week wash-out period between their last chemotherapy and first SBRT treatment.

SBRT planning and treatment details

SBRT for SM were carried out as per our department protocol. In brief, patients with lesions at T3 and above were immobilized using a rigid 5-point thermoplastic mask, and patients with lesions below T3 were immobilized using a rigid body bag (Elekta AB, Stockholm, Sweden). CT simulation imaging was performed and reconstructed at 2 mm for RT planning. A dedicated MRI in the region of interest was obtained within a few days of CT simulation. Axial T1 and T2 volumetric MRI sequences were co-registered with CT simulation images to define the target volumes and organs-at-risk. The gross tumour volume (GTV) included bony metastatic disease within the vertebral level, including any para-vertebral extension. Clinical target volume (CTV) included the adjacent compartment, as per contouring guidelines.[14] A 2-5 mm margin was applied in patients with para-vertebral extension to form the final CTV. The CTV was expanded by 2 mm isotropically to create the planning target volume (PTV). The spinal cord was defined using the axial T2 imaging, and a 2 mm planning organ at risk volume (PRV) margin was applied. For lesions at L2 and below, the thecal sac was contoured and a PRV margin was not given. The portion of the PTV that overlapped with the PRV Cord was carved out. Recommended SBRT doses are 24 – 27 Gy in 3 fractions, or 24 Gy in 2 fractions (delivered on alternate days). SBRT treatment was planned using Monaco (Elekta AB, Stockholm, Sweden) using volumetric modulated arc therapy (1 or 2 arcs). We aimed for a CTV coverage of D90/90. Priority was given to the avoidance of critical organs at risk (such as spinal cord PRV, thecal sac, brachial and sacral plexuses), and published dose limits were adhered to.[15] Image guided radiotherapy was performed on Elekta Infinity, with cone-beam CT (CBCT) guidance pre- and post-treatment. For long treatment sessions lasting more than 20 minutes, a mid-treatment CBCT was performed.

Clinical follow-up protocol

Patients were assessed clinically at time of CT simulation, 1-week and 3-months post RT as part of the study. Patients were followed up 3–6 months thereafter (as part of shared care between medical oncology and radiation oncology). Patients were recommended to have a MR imaging every 3–6 months as part of follow-up. Information collected at baseline and 3 months include: primary histology, baseline pain score (VAS), analgesia requirement and spinal instability score (SINS). Pain score was assessed at time of CT simulation (approximately 2 weeks prior to SBRT) and 12-week post-SBRT, using VAS 0-10.

Local tumour response was evaluated according to the MD Anderson criteria[16] at 3 months

TABLE 2. Patient characteristics

Patient ID	Age	Gender	Primary histology	Level of spinal metastases	Extraspinal disease site	Baseline analgesia requirement: opioid/ non-opioid/nil	Prior chemotherapy	Prior anti-VEGF therapy	Prior immunotherapy	ECOG	Pre-treatment VAS	SINS	Indication	SBRT	
														Dose (Gy)	Fractions
1	69	M	RCC	C1	Lung	Non-opioid	No	No	Yes	1	8	6	Radioresistant histology, pain control	24	3
2	60	M	RCC	S1	Nil	Nil	No	No	No	0	3	3	Oligometatasis	27	3
3	60	M	NSCLC-EGFR -	T5	Brain, bone. lung	Nil	Yes	No	No	1	5	6	Oligometastasis	24	3
4	62	F	NSCLC-EGFR -	C5	Brain, nodal, bone	Opioid	No	No	No	1	8	7	Oligometastasis, pain control	24	2
5	75	M	Prostate adenocarcinoma	T1	Bone	Nil	No	No	No	1	6	5	Oligometastasis	24	3
6	62	M	Colon adenocarcinoma	L1	LN, lung	Nil	Yes	No	No	1	3	9	Oligometastasis	27	3
7a	52	M	RCC	L1	Bone	Opioid	No	No	Yes	1	7	7	Radioresistant histology, pain control	27*	3*
7b	52	M	RCC	L2	Bone	Opioid	No	No	Yes	1	7	7	Radioresistant histology, pain control	27*	3*
8a	69	F	NSCLC-EGFR +	T1	Brain, bone. lung	Non-Opioid	No	No	Yes	1	3	5	Oligometastasis	24	3
8b	69	F	NSCLC-EGFR +	T10	Brain, bone. lung	Non-Opioid	No	No	Yes	1	3	4	Oligometastasis	27*	3*
8c	69	F	NSCLC-EGFR +	T12	Brain, bone. lung	Non-Opioid	No	No	Yes	1	3	6	Oligometastasis	27	3
9	51	F	Breast Invasive ductal carcinoma	T4	Nil	Nil	Yes	No	No	1	0	2	Oligometastasis	27	3
10	72	M	Prostate adenocarcinoma	L3	Nil	Nil	No	No	No	2	3	2	Oligometastasis	24	2

ECOG = Eastern Cooperative Oncology Group; F = female; LN = lymph nodes; M = male; Nil = nihil; NSCLC-EGFR - = non-small cell lung cancer without epidermal growth factor receptor mutation; NSCLC-EGFR + = non-small cell lung cancer with epidermal growth factor receptor mutation; RCC = renal cell carcinoma; SINS = spinal instability neoplastic score; VAS = visual analogue score

*Patient only completed 2 out of 3 fractions

(complete response (CR), partial response (PR), progressive disease (PD), stable disease (SD)) by a MSK radiologist (15 years' experience) who was blinded to the treatment (SS). Local recurrence was assessed based on available clinical imaging at the last follow-up. Data was censored at the time of last follow-up. Acute toxicity was assessed at 1 week post RT and late toxicity was assessed at 3 months and during further clinical follow-up, using the Common Terminology Criteria for Adverse Events version 5.0.

Magnetic resonance imaging protocol

All MRI examinations were performed using a 3-T MRI scanner (Siemens Biograph mMR) located at clinical imaging research centre (CIRC), National University of Singapore. MRI was performed at baseline (during time of CT simulation, approximately 2 weeks prior to the start of SBRT), 1-week after completing SBRT (median 8 days, range 6 to 13 days) and at 12 weeks post SBRT (median 92 days, range 82 to 100 days). MRI was obtained in the region of interest (target vertebral level, with 2 levels superior and inferior). The following conventional MRI sequences were acquired prior to contrast administration: sagittal T2, axial T2 (2 mm slice thickness), axial T2 TIRM (3 mm slice thickness), pre-contrast axial T1 VIBE with fat-saturation (2 mm slice thickness).

DCE-MRI was performed using a T1-weighted three-dimensional fast field-echo sequence in the axial plane. Before contrast injection, the pre-contrast T1-weighted fast field echo sequences were acquired at 4 flip angles (5, 10, 15 and 20 degrees) according to the same geometry to calculate the baseline T1 maps. DCE-MRI was performed after an intravenous bolus injection Dotarem (gadoterate meglumine), at 3 ml/s and dose of 0.2 ml/kg. This was done using an automatic injector and was

TABLE 3. Clinical outcomes

Patient ID	Post-SBRT VAS (Change from pre-SBRT baseline)	Acute toxicity	Late toxicity	Response assessment at 3 months (MD Anderson criteria)	Follow-up duration (months)	Local recurrence at last follow-up	Status of patient at last follow-up
1	0 (-8)	G1 esophagitis	Nil	PR	39	No	Dead
2	0 (-3)	Nil	Nil	PR	54	Yes	Alive
3	0 (-5)	Nil	G1 compression fracture	PR	50	No	Alive
4	0 (-8)	G1 esophagitis	Nil	SD	15	No	Dead
5	3 (-3)	G1 esophagitis	Nil	PR	22	No	Dead
6	0 (-3)	Nil	Nil	SD	13	No	Dead
7a	2 (-5)	Nil	G1 compression fracture	PR	42	No	Alive
7b	2 (-5)	Nil	Nil	PR	42	No	Alive
8a	-	Nil	N/A	-	N/A	N/A	Dead
8b	-	Nil	N/A	-	N/A	N/A	Dead
8c	-	Nil	N/A	-	N/A	N/A	Dead
9	0	Nil	G3 compression fracture	SD	37	No	Alive
10	0 (-3)	Nil	Nil	PR	22	No	Alive

Nil = nihil; PR = Partial response; SD = Stable disease; VAS = Visual analog scale

followed by a 15 ml saline flush. Seventy phases were acquired over 5 minutes with a temporal resolution of 4.3 s (flip angle 15 degrees), using parallel imaging. Delayed post-contrast axial T1 VIBE sequences with fat-saturation (2 mm slice thickness) were then acquired after DCE imaging.

The same sequences were performed at 1-week and 12-weeks post SBRT. The length of the aorta or major artery was included in the scan where possible, to minimize inflow artefacts.

Assessment of correlative plasma biomarkers

Blood was collected, in EDTA tube, at baseline (within 2 weeks prior to SBRT) and immediately after the last fraction of SBRT. Samples were centrifuged for 15 minutes at 1000×g at 2 - 8°C within 30 minutes of collection, and plasma was removed to be stored at -80°C. Once plasma was collected from all patients, ASM (Human Acid Sphingomyelinase ELISA Kit, Elabscience) and S1P (Sphingosine 1-phosphase ELISA kit, Echelon Biosciences, UT, USA) was batch evaluated using a semi-quantitative method, using the Sandwich-ELISA method. The optical density (OD) is measured spectrophotometrically at a wavelength of 450 ± 2 nm. The OD value is proportional to the concentration of S1P or ASM. The concentration of S1P and ASM were calculated by comparing the OD of the samples to the standard curve.

Analysis for DCE MRI metrics

Tumour regions of interest (ROI) were drawn in consensus by spine radiation oncologist (BV 12 years' experience) and two musculoskeletal radiologists (SS 15 years' experience, LCH 12 years' experience) on the non-contrast T1 and T2-weighted sequences. The soft tissue component of the metastatic deposits was delineated. For tumours without a predominant soft tissue component, the area showing T1 signal change was delineated.

Control ROI were drawn in the red marrow outside of the radiation volume. The same process was repeated for post-treatment imaging taking into account tumour regression.

All ROIs were drawn taking care to avoid venous structures, hemangiomas, disc spaces, cortical bone and spondylotic changes. ROIs drawn on anatomic reference images were simultaneously and automatically transferred to the corresponding location on the DCE parameter maps.

Raw blood perfusion data, obtained from DCE-MRI was processed and analysed using an in-house programme written on Matlab (MathWorks, Natick, MA, USA). Pre-processing steps included background spatial & temporal smoothing, noise removal. AIF was individually calculated for each acquisition of every patient, using a 3 x 3 (voxel averaged) window placed over an adjacent large vessel (aorta, or large calibre artery). Linear assumption between change in signal intensity and

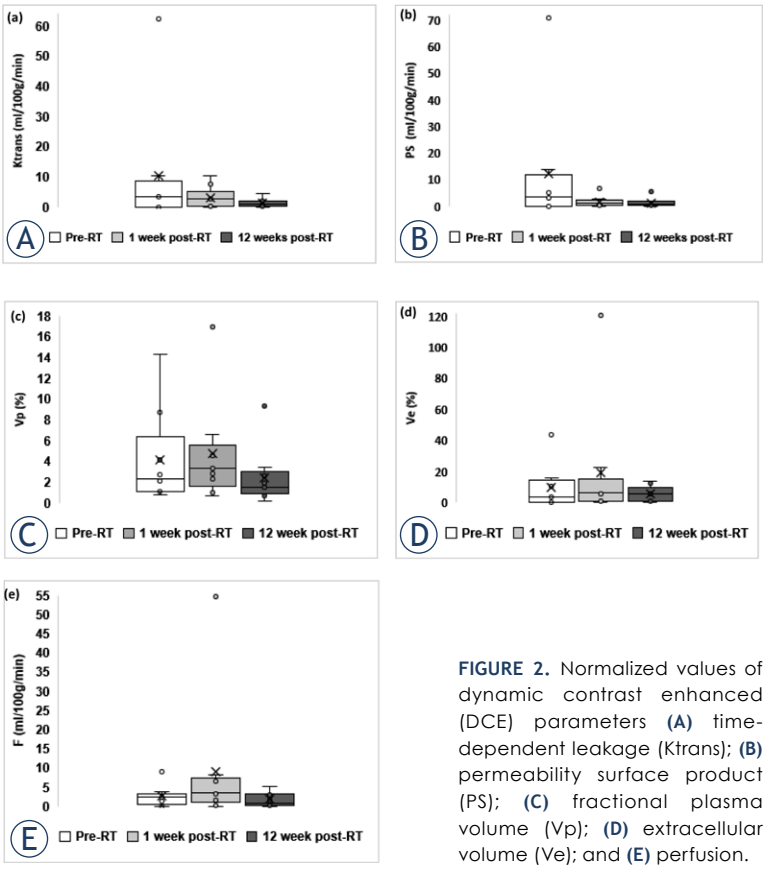

FIGURE 2. Normalized values of dynamic contrast enhanced (DCE) parameters **(A)** time-dependent leakage (Ktrans); **(B)** permeability surface product (PS); **(C)** fractional plasma volume (Vp); **(D)** extracellular volume (Ve); and **(E)** perfusion.

gadolinium concentration was made to convert the signal intensity curve to the concentration-time curve. The "Distributed Parameter" model was used for the calculation of quantitative perfusion parameters.

Both tumour and control ROIs were subjected to the same pre-processing, processing steps and analysis. Parameters were normalized using the readout from the control ROI on each scan. The median parameter value in the tumour, and control, ROIs were taken as the representative for each ROI. For quantitative parameters, including perfusion parameters and correlative plasma markers, mean, median, minimum, and maximum values were calculated. Quantitative perfusion parameters were also compared with the control cases.

Statistical analysis

We hypothesized a 30% reduction in DCE-parameters post SBRT. Working with a power of 80%, and alpha of 5%, we estimated a sample size of 8 - 10 patients. Differences between pre- and post-treatment values (of DCE-MRI metrics and plasma biomarkers) were compared using a paired T-test. Two-sided p-values of ≤ 0.05 were considered statistically significant. Statistical analysis performed using STATA v 14.

Results

Patient demographics and clinical presentation

Twelve participants were consented for the prospective study. Two patients withdrew consent before SBRT. Ten patients (with 13 lesions) were treated with SBRT. All 10 patients underwent blood sample collection. Nine of the ten patients underwent MRI assessment at 1 week and 3 months post SBRT. One patient died 1-month post SBRT secondary to pneumonia (unrelated to treatment). Overall, the median age was 62 years (range 51–75 years) and 70% were male. Majority of the patients (46%) had lesions in the thoracic spine, followed by 30% involving the lumbar spine. Kidney and lung were the most common primary tumour sites (30% each respectively). Median follow-up for alive patients was 42 months (range 22.3–54.3 months). Patient demographics and treatment related details are shown in Table 2. The most common indication for SBRT was oligometastasis (8/10). Median prescribed dose was 27 Gy (24–27 Gy) delivered in 3 fractions, with detailed breakdown of the dose and fractionation in Table 2. A majority of participants had prior systemic therapy (6/10). Three patients had prior immunotherapy, and none had prior anti-VEGF therapy.

DCE-MRI results

The normalised mean and median DCE-parameter values at baseline, 1 week and 12 weeks post SBRT are reported in Figure 2A-E. Representative images of Patient 7a are shown in Figure 3.

K trans (mL/100g/min): The normalised mean, median value at baseline was 12.08, 3.65 (range 0.03–62.49), at 1-week post SBRT, 3.10, 2.66 (range 0.01–10.55), and at 12-weeks post SBRT, 1.30, 0.92 (range 0.001–4.60) respectively. P-value comparing baseline & 1 week ($p = 0.14$), comparing baseline & 12 weeks ($p = 0.13$), and comparing 1 week & 12 weeks ($p = 0.08$) were obtained.

Permeability surface product PS (mL/100g/min): The normalised mean, median value at baseline was 13.89, 3.59 (range 0.02–70.83), at 1-week post SBRT, 1.66, 1.21 (range 0.01–6.56), and at 12-weeks post SBRT, 1.29, 0.66 (range 0.001–5.60) respectively. P-value comparing baseline and 1 week ($p = 0.12$),

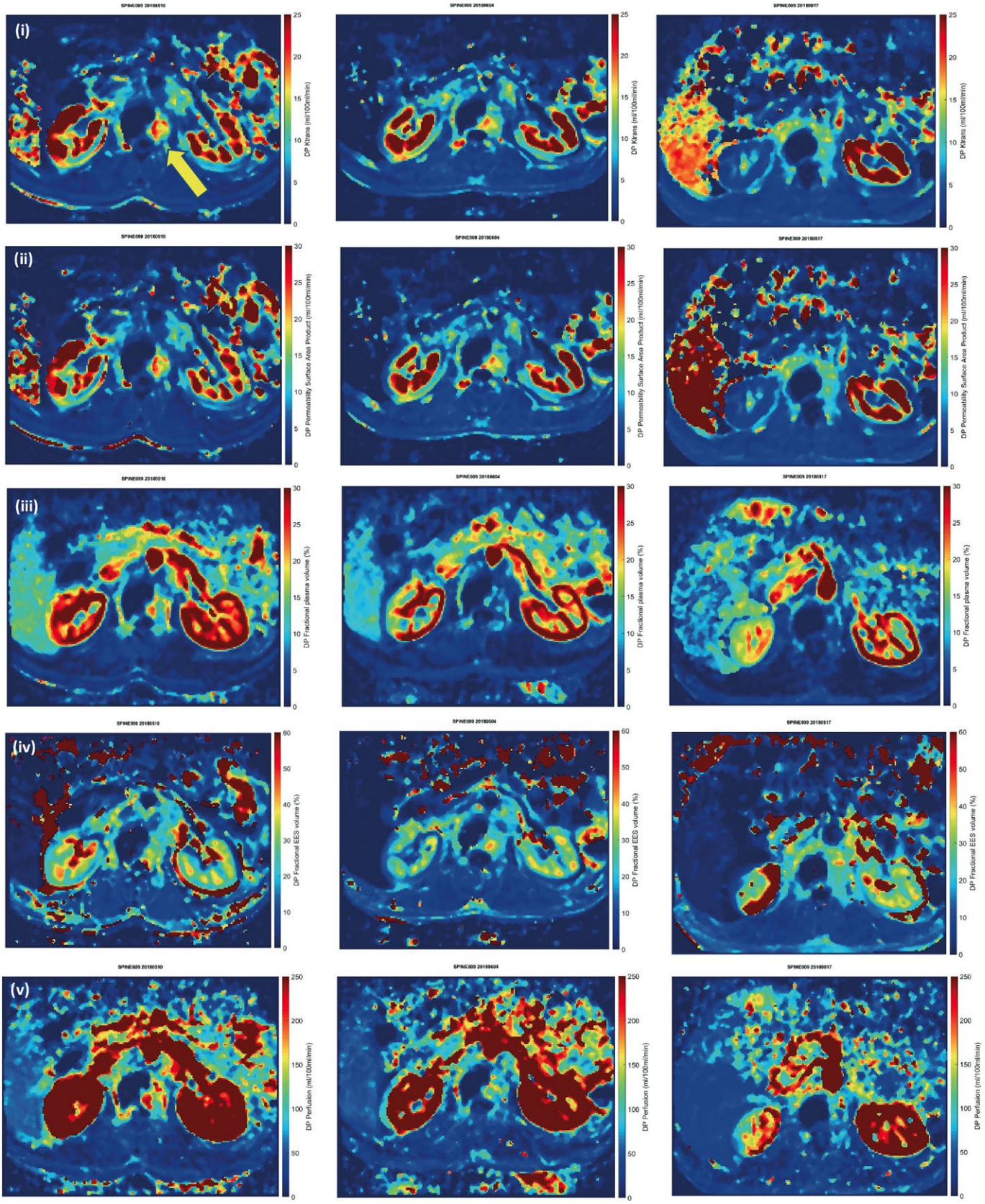

FIGURE 3. (A) Representative images for Patient 7a showing at L1 with reduction in dynamic contrast enhanced (DCE) parameters [i] time-dependent leakage (Ktrans); [ii] permeability surface product (PS); [iii] fractional plasma volume (Vp); [iv] extracellular volume (Ve); and [v] perfusion (F) across the 3 time points.

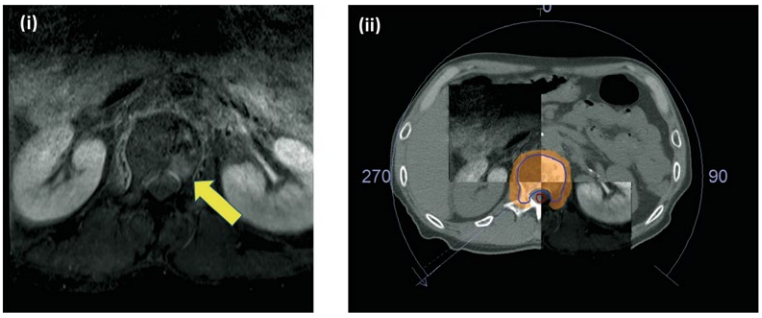

FIGURE 3. (B) [i] Metastatic deposit in L1 vertebral body (yellow arrow), as shown on T1 Axial MR (with gadolinium contrast); [ii] stereotactic body radiotherapy (SBRT) planning image (CT, MRI fused). SBRT 27 Gy in 3 fractions, delivered using volumetric modulated arc therapy. Clinical target volume (CTV) (blue outline), planning organ at risk volume (PRV)_cord (red outline), 95% isodose (orange colourwash).

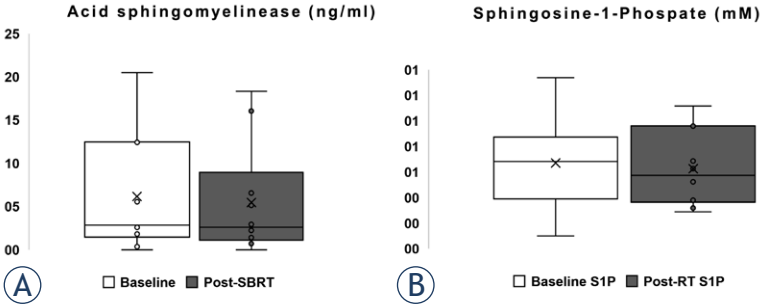

FIGURE 4. Correlative plasma markers **(A)** acid sphingomyelinase (ASM); and **(B)** sphingosine-1-phosphate (S1P).

comparing baseline and 12 weeks (p = 0.12), comparing 1 week and 12 weeks (p = 0.16).

Vp (%): The normalised mean, median value at baseline was 4.14, 2.21 (range 0.82–14.31), at 1-week post SBRT, 4.73, 3.27 (range 0.67–16.90) and at 12-weeks post SBRT, 2.40, 1.45 (range 0.20–9.30) respectively. P-value comparing baseline and 1 week (p = 0.41), comparing baseline and 12 weeks (p = 0.14), comparing 1 week and 12 weeks (p = 0.13).

Ve (%): The normalised mean, median value at baseline was 11.04, 4.03 (range 0.29–43.46), at 1-week post SBRT, 18.88, 5.92 (range 0.06–22.44) and at 12-weeks post SBRT, 6.01, 5.86 (range 0.65–13.51) respectively. P-value comparing baseline and 1 week (p = 0.11), comparing baseline and 12 weeks (p = 0.17), comparing 1 week and 12 weeks (p = 0.15).

Perfusion, F (mL/100g/min): The normalised mean, median value at baseline was 2.65, 2.37 (range 0.03–9.03), at 1-week post SBRT, 3.62, 3.54 (range 0.08–8.10) and at 12-weeks post SBRT, 1.77, 0.93 (range 0.07–5.23) respectively. P-value comparing baseline and 1 week (p = 0.25), comparing baseline and 12 weeks (p = 0.20), comparing 1 week and 12 weeks (p = 0.01).

Correlative plasma biomarker results

ASM levels did not show any significant change post SBRT (baseline mean 6.15 ng/ml *vs.* post SBRT mean 5.46 ng/ml, p = 0.71). Similarly, S1P levels did not show any significant change (baseline mean 0.67 μM *vs.* post-SBRT 0.63 μM, p = 0.52) (Figure 4)

Clinical outcomes

All patients tolerated SBRT well, with 3 patients experiencing mild acute toxicity (Grade 1 esophagitis). Three patients developed vertebral compression fractures (VCF) approximately 6 months post SBRT (23% on a per-lesion analysis). Of these, 2 were mild (Grade 1) and pre-existing, and did not require any intervention. One patient developed severe (Grade 3) symptomatic VCF and required stabilisation surgery. All patients had pain improvement 3 months post SBRT, with a median reduction of VAS of 5 (range 3 to 8). Response (MD Anderson criteria) at 3 months – with all patients, who were alive, demonstrating Partial Response (70%) or Stable disease (30%). There was one local recurrence (at 54 months) in the cohort, with data censored at last follow-up. These results are summarised in Table 3.

Discussion

To our knowledge, we are the first to prospectively quantify vascular changes, post SBRT (which uses large doses per fraction), in spine metastases. A controlled setting is important, as variabilities in baseline and follow-up assessment timepoints, and variability in scanner settings, may influence the interpretation of data.

We used a non-invasive method, using DCE-MRI, to quantify the vascular parameters at 1-week and 12-weeks post SBRT. We found an overall trend of reduction at 12 weeks in all the parameters (Ktrans, PS, Vp, Ve, F). Parameters such as Ktrans and PS showed a reduction as early as 1 week. Parameters (Ve, Vp, F) exhibited a slight rise 1-week post-SBRT before reducing below the baseline value – suggesting that there could be a short-term inflammatory response post RT. However, our findings can only be considered as hypothesis-generating, as majority of the P values were >0.05 (due to the small sample size). We did not find any

significant differences in DCE-MRI parameters between known vascular primaries (such as renal cell carcinoma versus other primary histologies)

Previous groups have utilised DCE-MRI to determine treatment response. Chu and colleagues, from Memorial Sloan Kettering Cancer Centre, performed DCE-MRI before and after radiotherapy for 15 patients.[8] They reported that changes in Vp were an early predictor of treatment response. In their study, both Vp and Ktrans were reduced post radiotherapy. However, the type of RT that the patients had undergone was not reported, and it remains unclear if patients were treated with conventionally fractionated RT or SBRT. The time point of assessment of the vascular parameters were also highly variable – baseline assessment ranged from 2 – 115 days, and post-treatment assessment ranged from 10 – 187 days. Another distinction from our study, is that they had utilised absolute parameter values, as there were limitations in drawing ROIs in normal marrow. To mitigate this variability, we normalised all our values, using an internal (patient level) control, by identifying non-irradiated marrow above or below the spine segment.

Another study from MSKCC, performed DCE-MRI, 1-hour post SBRT on 6 patients.[10] Similar to Chu *et al*., they only reported on Vp and Ktrans, which was derived using Toft's pharmacokinetic model.[8] The authors normalized the parameters using adjacent non-irradiated marrow. Authors observed a significant drop in Vp within 1-hour post SBRT, with a mean decrease of 65.2%. Ktrans was reduced as well, but to a lesser extent (pre-treatment mean 4.84, post-treatment mean 2.3). In contrast, we did not find a drastic drop in Vp at 1-week post RT. It remains unclear if these differences can be explained by the use of Toft's model (versus distributed parameter model). Although it is possible that these values are dynamic and may fluctuate with time, this is less likely to be the case as both Lis *et al.* and our study report a sustained and continuous reduction in Vp (baseline mean 4.14 *vs*. 2.4 at 12 weeks). We had planned to use the distributed parameter model a priori in view of the previous findings within our research group. The Toft's model was described in 1999, primarily based on intra-cranial conditions.[17] This is classified under the umbrella of "compartmental PK model", where the assumptions are that the compartments are homogenous at any given time, and the output of contrast agent is directly proportional to its concentration. The Toft's model has been more widely used due to its simplicity. In contrast, the distributed parameter model is classified as a "spatially distributed kinetic model". Unlike compartmental models, DP model accounts for both spatial and temporal variations in the administered contrast agent. These are believed to be closer to reality, taking into account underlying physiology. Interested readers can find more information about the various models in the referenced review article.[18]

These vascular changes seen post SBRT are suggested to be a result of endothelial cell apoptosis and mediated by the acid sphingomyelinase (ASMase) pathway. Radiation, particularly in doses above 8 Gy per fraction, induce translocation of the secretory ASMase from cytosol into glycosphingolipid contained in the plasma membrane, which in turn break downs sphingomyelin to ceramide.[5] Ceramide is a pro-apoptotic molecule. Endothelial cells have a high level of secretory ASMase, and therefore are susceptible to ceramide-mediated apoptosis with radiation. We had hypothesized for plasma ASM to increase, and S1P to decrease post SBRT. However, we did not find any significant changes. One possibility is that changes seen within the cellular micro-environment may not be reliably assessed in the serum, due to a lack of sensitive assays. To our knowledge, we are the first to report on the plasma ASM and S1P levels in patients undergoing SBRT. A previous study by Dubois *et al*., reported that the ceramide levels (and their sub-species), measured by LC–ESI-MS/MS, were elevated at 3- and 10-days post SBRT in responders.[19]

In our cohort, SBRT was well tolerated and provided a local control rate of 90%. Patients with baseline symptomatic SM, had a good pain response at 3 months (assessed using VAS). Patients are typically followed up every 3 – 6 months with MRI imaging for surveillance. The effectiveness of SBRT is in keeping with multiple other cohorts and randomized controlled trials.

The implications of our study support the preceding data that tumour vasculature is predominantly reduced with SBRT. We had initially conceptualised the idea of pre-operative spine SBRT, in order to reduce intra-operative blood loss. This can potentially be performed in lieu of embolization, and in addition this may reduce intra-operative tumour dissemination. However, from our study, not all vascular parameters were reduced at 1 week, and therefore it remains unclear if this will translate clinically. The concept of pre-operative SBRT is already being investigated for brain metastases in a randomized Phase III trial (NCT03741673).

The main strengths of our trial are as follows – prospective design, where assessment time points were pre-defined. In addition, the same scanner, and settings were used for repeated measurements, thereby reducing variability. SBRT was carried out following our department protocol by a specialized team (radiation oncologist, dosimetrist, radiation therapist), where the doses and prescription practices are uniform. In addition, we determined the arterial input function, on an individual basis, instead of using general population estimates. Lastly, we used the distributed parameter model to quantify the normalised vascular estimates. This is expected to be closer to reality compared to other similar studies.

We fully acknowledge our study's limitations. Firstly, we have a small sample size of patients with varying primary cancers – and thus our results may be under-powered and subject to inter-histology variations. Secondly, the serum assay that we had utilised to quantify ASM/S1P may not have been sensitive enough to pick up small changes. Thirdly, as only one patient developed local recurrence at 54 months, we could not investigate the difference in DCE-MRI parameters between responders and non-responders.

In conclusion, our study has shown that vascular changes post-SBRT can be quantified by DCE-MRI using the distributed parameter model. The tumour vascular micro-environment (measured by various metrics) shows a general trend towards downregulation post SBRT, and it is hypothesised that this is one of the reasons for improved local control.

Acknowledgments

We would like to acknowledge Keith Gerard Lopez, Sridharan Alathur Ramakrishnan and Corin Chen Jiali for preparation of this manuscript. This study was funded through National University Cancer Institute, Singapore (NCIS) seed grant and NCIS research fellowship to Dr Vellayappan.

References

1. Coleman RE. Clinical features of metastatic bone disease and risk of skeletal morbidity. *Clin Cancer Res* 2006; **12(20 Pt 2):** 6243s-9s. doi: 10.1158/1078-0432.CCR-06-0931
2. Kumar N, Malhotra R, Zaw AS, Maharajan K, Naresh N, Kumar A, et al. Evolution in treatment strategy for metastatic spine disease: presently evolving modalities. *Eur J Surg Oncol* 2017; **43:** 1784-801. doi: 10.1016/j.ejso.2017.05.006
3. Kumar N, Zaw AS, Khine HE, Maharajan K, Wai KL, Tan B, et al. Blood loss and transfusion requirements in metastatic spinal tumor surgery: evaluation of influencing factors. *Ann Surg Oncol* 2016; **23:** 2079-86. doi: 10.1245/s10434-016-5092-8
4. Clausen C, Dahl B, Frevert SC, Hansen LV, Nielsen MB, Lonn L. Preoperative embolization in surgical treatment of spinal metastases: single-blind, randomized controlled clinical trial of efficacy in decreasing intraoperative blood loss. *J Vasc Interv Radiol* 2015; **26:** 402-12.e1. doi: 10.1016/j.jvir.2014.11.014
5. Garcia-Barros M, Paris F, Cordon-Cardo C, Lyden D, Rafii S, Haimovitz-Friedman A, et al. Tumor response to radiotherapy regulated by endothelial cell apoptosis. *Science* 2003; **300:** 1155-9. doi: 10.1126/science.1082504
6. Sathishkumar S, Boyanovsky B, Karakashian AA, Rozenova K, Giltiay NV, Kudrimoti M, et al. Elevated sphingomyelinase activity and ceramide concentration in serum of patients undergoing high dose spatially fractionated radiation treatment: implications for endothelial apoptosis. *Cancer Biol Ther* 2005; **4:** 979-86. doi: 10.4161/cbt.4.9.1915
7. Song CW, Kim MS, Cho LC, Dusenbery K, Sperduto PW. Radiobiological basis of SBRT and SRS. *Int J Clin Oncol* 2014; **19:** 570-8. doi: 10.1007/s10147-014-0717-z
8. Chu S, Karimi S, Peck KK, Yamada Y, Lis E, Lyo J, et al. Measurement of blood perfusion in spinal metastases with dynamic contrast-enhanced magnetic resonance imaging: evaluation of tumor response to radiation therapy. *Spine* 2013; **38:** E1418-24 doi: 10.1097/BRS.0b013e3182a40838
9. Kumar KA, Peck KK, Karimi S, Lis E, Holodny AI, Bilsky MH, et al. A pilot study evaluating the use of dynamic contrast-enhanced perfusion MRI to predict local recurrence after radiosurgery on spinal metastases. *Technol Cancer Res Treat* 2017; **16:** 857-65. doi: 10.1177/1533034617705715
10. Lis E, Saha A, Peck KK, Zatcky J, Zelefsky MJ, Yamada Y, et al. Dynamic contrast-enhanced magnetic resonance imaging of osseous spine metastasis before and 1 hour after high-dose image-guided radiation therapy. *Neurosurg Focus* 2017; **42:** E9. doi: 10.3171/2016.9.FOCUS16378
11. Lee JH, Yoo GS, Yoon YC, Park HC, Kim HS. Diffusion-weighted and dynamic contrast-enhanced magnetic resonance imaging after radiation therapy for bone metastases in patients with hepatocellular carcinoma. *Sci Rep* 2021; **11:** 10459. doi: 10.1038/s41598-021-90065-1
12. Yankeelov TE, Gore JC. Dynamic contrast enhanced magnetic resonance imaging in oncology: Theory, data acquisition, analysis, and examples. *Curr Med Imaging Rev* 2009; **3:** 91-107. doi: 10.2174/157340507780619179
13. Koh TS, Bisdas S, Koh DM, Thng CH. Fundamentals of tracer kinetics for dynamic contrast-enhanced MRI. *J Magn Reson Imaging* 2011; **34:** 1262-76. doi: 10.1002/jmri.22795
14. Cox BW, Spratt DE, Lovelock M, Bilsky MH, Lis E, Ryu S, et al. International Spine Radiosurgery Consortium consensus guidelines for target volume definition in spinal stereotactic radiosurgery. *Int J Radiat Oncol Biol Phys* 2012; **83:** e597-605. doi: 10.1016/j.ijrobp.2012.03.009
15. Sahgal A, Weinberg V, Ma L, Chang E, Chao S, Muacevic A, et al. Probabilities of radiation myelopathy specific to stereotactic body radiation therapy to guide safe practice. *Int J Radiat Oncol Biol Phys* 2013; **85:** 341-7 doi: 10.1016/j.ijrobp.2012.05.007
16. Costelloe CM, Chuang HH, Madewell JE, Ueno NT. Cancer response criteria and bone metastases: RECIST 1.1, MDA and PERCIST. *J Cancer* 2010; **1:** 80-92. doi: 10.7150/jca.1.80.
17. Tofts PS, Brix G, Buckley DL, Evelhoch JL, Henderson E, Knopp MV, et al. Estimating kinetic parameters from dynamic contrast-enhanced T(1)-weighted MRI of a diffusable tracer: standardized quantities and symbols. *J Magn Reson Imaging* 1999; **10:** 223-32. doi: 10.1002/(sici)1522-2586(199909)10:3<223::aid-jmri2>3.0.co;2-s
18. Khalifa F, Soliman A, El-Baz A, Abou El-Ghar M, El-Diasty T, Gimel'farb G, et al. Models and methods for analyzing DCE-MRI: a review. *Med Phys* 2014; **41:** 124301 doi: 10.1118/1.4898202
19. Dubois N, Rio E, Ripoche N, Ferchaud-Roucher V, Gaugler MH, Campion L, et al. Plasma ceramide, a real-time predictive marker of pulmonary and hepatic metastases response to stereotactic body radiation therapy combined with irinotecan. *Radiother Oncol* 2016; **119:** 229-35. doi: 10.1016/j.radonc.2016.03.014

research article

Cardiac myxoma: single tertiary centre experience

Polona Kacar[1,2], Nejc Pavsic[1,2], Mojca Bervar[1,2], Zvezdana Dolenc Strazar[3], Vesna Zadnik[4], Matija Jelenc[5], Katja Prokselj[1,2]

[1] Department of Cardiology, University Medical Center Ljubljana, Ljubljana, Slovenia
[2] Faculty of Medicine, University of Ljubljana, Ljubljana, Slovenia
[3] Institute of Pathology, Faculty of Medicine, University of Ljubljana, Ljubljana, Slovenia
[4] Epidemiology and Cancer Registry, Institute of Oncology Ljubljana, Ljubljana, Slovenia
[5] Department of Cardiovascular Surgery, University Medical Center Ljubljana, Ljubljana, Slovenia

Radiol Oncol 2022; 56(4): 535-540.

Received 24 Jun 2022
Accepted 12 Sep 2022

Correspondence to: Assist. prof. Katja Prokšelj, M.D., Ph.D., Department of Cardiology, University Medical Center Ljubljana, Zaloška cesta 7, 1525 Ljubljana, Slovenia. E-mail: katja.prokselj@gmail.com

Disclosure: No potential conflicts of interest were disclosed.

Background. Although cardiac myxoma (CM) are rare and benign, they can cause life-threatening complications, such as hemodynamic disturbances or embolization. Surgical excision of the tumour is the treatment of choice. The aim of the study was to evaluate the epidemiological characteristics, clinical presentation, imaging findings, and outcomes of surgical treatment of patients with CM treated in the largest tertiary care centre in Slovenia.

Patients and methods. We retrospectively analysed the medical records of all patients referred to our institution between January 2005 and December 2020 and identified 39 consecutive adult patients with pathologically confirmed CM.

Results. The average annual incidence of CM in the study was 3 per 2 million population per year. Patients were more often female (n = 25, 64%). The mean age at diagnosis was 63.1 ± 13.6 years. Dyspnoea was the most common presenting symptom (31%). CM was an incidental finding in 11 patients (28%). Seven patients presented with thromboembolic event (18%). Transthoracic echocardiography (TTE) was performed in all patients, however additional imaging was required in 22 patients (56%). All patients in our series were successfully treated surgically without in-hospital mortality. During the follow-up period (6 months to 16 years) three patients (8%) died, and all deaths were unrelated to CM. There was no recurrence of CM during the follow-up.

Conclusions. Our single-centre study confirms that CM is rare cardiac tumour with diverse clinical presentation. Our data shows data that CM might be more prevalent than considered before. Surgical resection of the tumour is safe with excellent short- and long-term outcomes.

Key words: cardiac myxoma; cardiac tumours; echocardiography

Introduction

Cardiac tumours are rare and usually benign.[1-3] Cardiac myxoma (CM) is the most common benign cardiac tumour in adults and accounts for 50% of all primary cardiac tumors.[4] The estimated incidence is 0.5–1 cases per million population per year.[5] The average age of diagnosis is between the fourth and sixth decade of life, with female preponderance (the female-to-male ratio is approximately 2:1), but myxomas can be diagnosed at any age.[5,6] Nowadays, CM are detected more frequently due to the increasing availability of multimodality imaging.

Although CM is benign in nature, it can lead to life-threatening complications such as sys-

temic embolisms or hemodynamic disturbances. The clinical presentation of CM is highly variable and is determined by size, location, and mobility of the tumour. The classic triad of CM includes embolic, obstructive cardiac, and constitutional symptoms.[5-7] Systemic, cerebral, or pulmonary embolization may be the first symptom of CM.[7,8] Obstructive cardiac symptoms include dyspnoea, syncope, arrhythmias, heart failure, or sudden cardiac death and are caused by obstruction of the heart valve or heart chamber.[9] Constitutional symptoms are nonspecific and include fever, weight loss, malaise, myalgia, and muscle weakness. Up to 30% of patients are asymptomatic and CM is an incidental finding.[3,6,8] Prompt and correct diagnosis is essential because of the potentially life-threatening complications and the different treatment options for different cardiac masses.

Transthoracic echocardiography (TTE) is the diagnostic method of choice.[6,7] TTE is used to determine the size and location of a CM, its point of attachment, morphology, mobility, and relationship to neighbouring structures. CM are typically located in the left atrium, attached to the atrial septum in the region of the fossa ovalis.[5] Size and appearance vary considerably. They can reach a diameter of more than 10 cm and occupy the entire cardiac chamber.[9] Morphologically, they are classified as polypoid or papillary.[6,8] Multimodality imaging is considered when CM cannot be reliably assessed with TTE, usually due to poor acoustic window or atypical presentation.[10,11] A definite diagnosis can only be made by histopathological evaluation, which is the gold standard of CM diagnosis.[7]

Surgical excision of CM is the treatment of choice and is usually curative.[7,12,13] Because of potential serious complications of CM, surgery should be performed without delay. The short- and long-term prognosis is excellent.[12,14,15] Tumour recurrence is rare.[6,12]

As CM is rare, most data are based on small single centre studies. Furthermore, there are no data on cardiac myxomas in Slovenia. Therefore, the aim of the study was to evaluate epidemiological characteristics, clinical presentation, diagnostic findings, and outcomes of surgical treatment in patients with CM treated in the largest tertiary care centre in Slovenia.

Patients and methods

We retrospectively analysed the medical records of all adult patients (>18 years of age) referred to our Department of Cardiology between January 2005 and December 2020 due to suspected CM. Only patients with a pathologically confirmed CM were included in the final analysis and their demographic, clinical, imaging, and surgical characteristics were reviewed.

The study has been performed in accordance with the ethical standards laid down in the 1964 Declaration of Helsinki and its later amendments. The study, protocol number 0120-512/2020-3, has been approved by Slovenian National Ethics Committee on 15.12.2020. Participants gave their informed consent.

Statistical analysis

Continuous variables are presented as mean ± standard deviation and categorical variables as number and percentage. Continuous variables were tested for normality using Shapiro-Wilk test. Independent Student's t-test was used to compare continuous variables. Statistical analysis was performed by SPSS version 26.0. P value below 0.05 was considered as statistically significant.

TABLE 1. Demographic and clinical characteristics

Characteristic	n (%)
Sex	
Female	25 (64)
Rhythm	
Sinus rhythm	37 (95)
Clinical presentation*	
Dyspnea	12 (31)
Chest pain	6 (15)
Embolism	7 (18)
- Cerebrovascular	6
- Coronary artery	1
Palpitations	1 (3)
Constitutional signs	2 (5)
Asymptomatic	11 (28)

Values are presented as number (percentage). *Patients may report several symptoms

Results

During a 16-year period, 39 patients with pathologically confirmed CM were treated at our de-

TABLE 2. Surgical results and follow-up

Characteristic	n (%)
Location	
- Left atrium	33 (85)
- Right atrium	6 (15)
Post-operative complications	7 (18)
- Arrhythmia*	6 (86)
- Pleural effusion*	1
- Surgical site infection	1

* One patient suffered from both arrhythmia and pleural effusion. Values are presented as number (percentage).

partment. Of these, 25 were female (64%) and the mean age at diagnosis was 63.1 ± 13.6 years (Table 1). Most patients (n = 37, 95%) were in sinus rhythm on admission. We diagnosed an average of three CM per year, with an increase in recent years (Figure 1).

Clinical presentation

The majority of patients were symptomatic (72%). The most common presenting symptoms were dyspnoea (31%) and chest pain (15%) (Table 1). In 11 patients (28%), CM was an incidental finding on TTE or chest computed tomography (CT) performed for other indications. Seven patients (18%) presented with thromboembolic events (four with stroke, two with central retinal artery occlusion, and one with acute coronary syndrome due to coronary artery embolism). Two patients (5%) presented with constitutional signs and symptoms such as fever and fatigue, and one patient complained of palpitations.

Diagnostic methods

TTE was performed in all patients (Figure 2). Additional imaging was performed in 22 patients (56%), either due to suboptimal image quality of TTE or due to atypical location of the tumour. Cardiac magnetic resonance (CMR) was performed most frequently (n = 15, 68%) (Figure 3), followed by transoesophageal echocardiography (TEE) (n = 9, 41%) and computed tomography (CT) (n = 2, 9%).

The average size of CM was 31.9 ± 18.4 mm (range: 10–81 mm). They were most commonly located in LA attached either to the interatrial septum, atrial wall or to the mitral valve (n = 33,

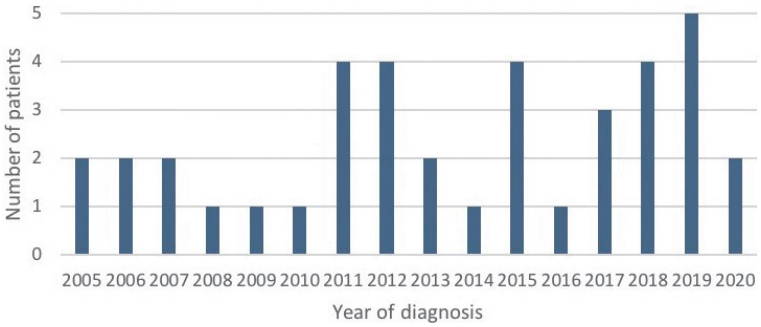

FIGURE 1. Distribution of patients diagnosed per year.

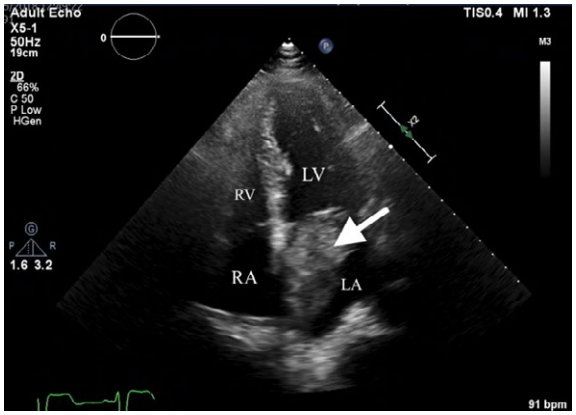

FIGURE 2. Transthoracic echocardiography, apical 4-chamber view. Cardiac mass in left atrium is attached to the interatrial septum in the region of the fossa ovalis (arrow). Histopathological characterization confirmed cardiac myxoma.

LA = left atrium, LV = left ventricle; RA = right atrium; RV = right ventricle

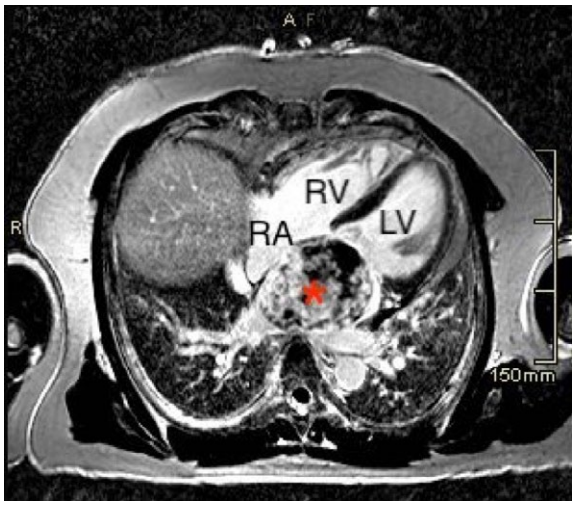

FIGURE 3. Cardiac magnetic resonance, late gadolinium enhancement, 4-chamber view. Asterix – Large mass occupying the entire left atrium with heterogeneous pattern of enhancement, consistent with cardiac myxoma.

LV = left ventricle; RA = right atrium; RV = right ventricle

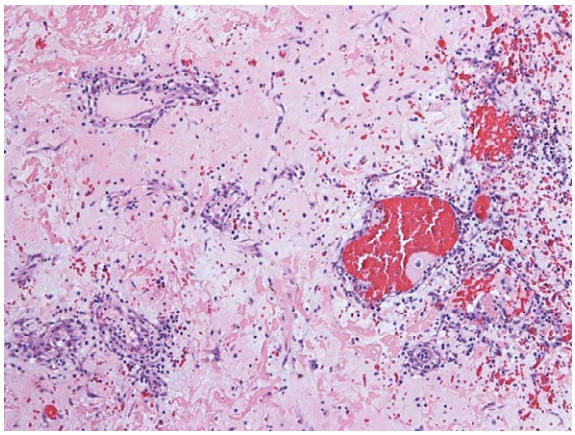

FIGURE 4. Abundant myxoid stroma with clusters of myxoma cells forming cords and ring structures (HE 100x).

85%), followed by RA (n = 6, 15%). Most CM did not cause left ventricular inflow obstruction (n = 27, 69%). Asymptomatic CM were smaller than symptomatic CM (30.2 ± 14.1 vs 41 ± 19.2 mm, p = 0.09).

Surgical treatment and follow-up

All tumours were successfully surgically resected (Figure 5). CM was most commonly located in the left atrium (n = 33, 85%) (Table 2). The diagnosis was confirmed histologically in all patients (Figure 4). The average length of hospital stay was 9 ± 4.8 days. No patient died during hospitalization. Two patients were readmitted within 30 days, one due to surgical site infection and one due to fever. Perioperative complications occurred in seven patients (18%), most commonly arrhythmias (86%), one patient had pleural effusion and one had surgical site infection.

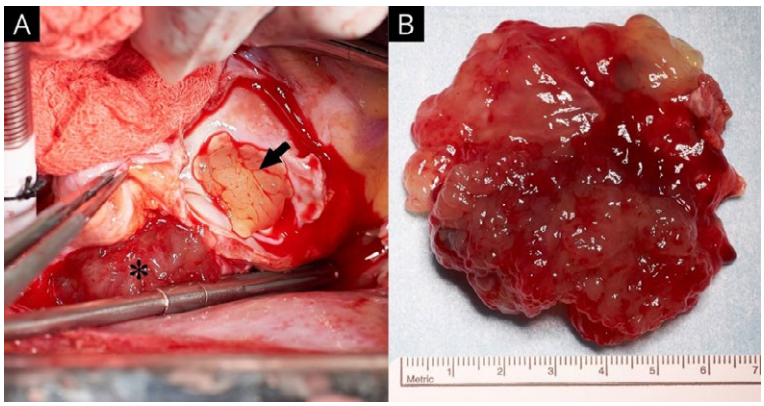

FIGURE 5. (A) Intraoperative view of myxoma protruding through fossa ovalis with its smaller part in the right atrium (arrow) and larger part in left atrium (asterisk). **(B)** The left atrial part of the myxoma.

The mean follow-up period was 7.6 years (range between 6 months and 16 years). There was no recurrence of CM on follow-up. Three patients (8%) died, but the cause of death was not related to CM.

Discussion

We present 16 years' experience in the treatment of patients with CM at the largest tertiary centre in Slovenia. CM is rare. In the study, the average annual incidence of CM was 3 per 2 million population per year, which is higher compared to other older series.[5,16-18] Some studies used earlier data, before the era of expansion of cardiac imaging, which may explain the differences in reported incidences.[5,16-18] We have diagnosed more patients in recent years, which is probably due to the increase in diagnostic procedures used for various indications. Similarly was shown in other previous studies. [5,16-18] In Slovenia, cardiovascular surgery is performed in two other institutions, where some of the patients with CM may also have been operated. Therefore, we can assume that the cumulative annual incidence of CM in Slovenia is higher than the one reported in our study.

CM is more common in women than in men, which was also confirmed in our series.[13] The mean age at diagnosis was 63.1 ± 13.6 years, which is comparable to other reports.[8,9]

The clinical presentation of CM depends on the size, location and mobility of the tumour and can be divided into three groups: obstructive cardiac (dyspnoea, arrhythmia, palpitations, syncope), embolic and constitutional symptoms.[7] In our group, dyspnoea was the most common presenting symptom (31%), followed by chest pain (15%). This is comparable to other studies that reported dyspnoea as the most common symptom.[6,8,19] None of the patients showed signs of overt heart failure. Similar to other studies, we observed embolic events in 18% of patients, which were either cerebrovascular or acute coronary syndrome. CM are gelatinous and friable, therefore such a manifestation is not surprising.[6,7,19] Smaller tumours and those with villous surface are more prone to embolic manifestations than those with smooth surface.[7,19] Frequent embolic events emphasize the need for timely diagnosis and prompt surgical treatment of CM. Constitutional symptoms occurred in only 5% of patients, which is lower than in other studies, however they may be underreported due to the retrospective design of our study or disregarded by patients themselves.[6,13] Incidental finding of CM on

different imaging modalities is not uncommon, as was the case in nearly one-third of patients (28%) in our series. Similar findings have been reported in other studies.[20] Asymptomatic CM are usually smaller than symptomatic CM, which was also observed in our study.[19]

Due to the nonspecific clinical presentation, cardiac imaging is crucial in the evaluation of patients with suspected CM. Although all our patients underwent TTE, additional imaging was performed in 56%, most commonly CMR (68%). TTE is the most common first diagnostic method of choice with 90–96% accuracy in diagnosing CM.[5,7,10] With TTE we can determine tumour size, location, morphology, mobility, and association with neighbouring structures. In patients with poor acoustic windows or atypical presentation, multimodality imaging is recommended.[10] TEE provides superior image resolution and better visualization of CM.[10,11] CT and CMR provide additional information on tissue characteristics and topographic relationships.[21,22] This information is important in deciding on the mode and extent of treatment.

Surgical resection of CM is the treatment of choice. It is associated with a low rate of postoperative complications. The 30-day mortality rate after CM excision ranges from 0% to 10%.[23] The most common postoperative complications are arrhythmias.[5] All patients in our study underwent surgical resection of CM. It has been a longstanding practice at our institution to operate on patients promptly after diagnosis to prevent possible life-threatening complications such as cerebral and coronary embolisms or valve obstruction. In the study, no patient died and only seven patients (18%) suffered from mild postoperative complications. The recurrence rate after CM resection has been reported to be less than 10%.[19,24,25] Follow-up in our study showed an excellent outcome after surgery without recurrence of CM. None of the reported deaths were related to the diagnosis or treatment of CM.

The study shows that the outcomes in our patients are comparable to those reported in other studies. We therefore conclude that the management of patients with CM in Slovenia is comparable to that in established international centres.

The retrospective nature of this study and a relatively small study population are the main limitations of this study. However, the population size is comparable to other studies on CM, reflecting the paucity of cases. This limitation could only be overcome by large multicentre studies, which could provide a larger study population.

Conclusions

CM are rare but the most common primary cardiac tumours. An average of three patients are diagnosed yearly at our tertiary institution, indicating a higher average annual incidence than reported in previous studies. Although benign, CM can lead to life-threatening complications. Therefore, correct and timely diagnosis, which often requires multimodality imaging, is crucial. Surgical resection of CM with pathohistological confirmation is the treatment of choice and should be performed promptly. Surgical and follow-up outcomes at our tertiary centre are excellent, without CM related short- or long-term mortality and a low rate of postoperative complications.

Acknowledgments

The study was financially supported by the Slovenian Research Agency - research core funding No. P3-0429, Slovenian research programme for comprehensive cancer control SLORApro.

References

1. Butany J, Leong SW, Carmichael K, Komeda M. A 30-year analysis of cardiac neoplasms at autopsy. *Can J Cardiol* 2005; **21:** 675-80. PMID: 16003450
2. Cresti A, Chiavarelli M, Glauber M, Tanganelli P, Scalese M, Cesareo F, et al. Incidence rate of primary cardiac tumors: a 14-year population study. *J Cardiovasc Med* 2016; **17:** 37-43. doi: 10.2459/JCM.0000000000000059
3. Tyebally S, Chen D, Bhattacharyya S, Mughrabi A, Hussain Z, Manisty C, et al. Cardiac tumors JACC cardiooncology state-of-the-art review. *Jacc Cardiooncology* 2020; **2:** 1-19. doi: 10.1016/j.jaccao.2020.05.009
4. Poterucha TJ, Kochav J, O'Connor DS, Rosner GF. Cardiac tumors: clinical presentation, diagnosis, and management. *Curr Treat Options Oncol* 2019; **20:** 1-15. doi: 10.1007/s11864-019-0662-1
5. Samanidis G, Khoury M, Balanika M, Perrea DN. Current challenges in the diagnosis and treatment of cardiac myxoma. *Kardiol Pol* 2020; **78:** 269-77. doi: 10.33963/KP.15254
6. Pinede L, Duhaut P, Loire R. Clinical presentation of left atrial cardiac myxoma: a series of 112 consecutive cases. *Medicine (Baltimore)* 2001; **80:** 159-72. doi: 10.1097/00005792-200105000-00002
7. Griborio-Guzman AG, Aseyev OI, Shah H, Sadreddini M. Cardiac myxomas: clinical presentation, diagnosis and management. *Heart* 2022; **108:** 827-33. doi: 10.1136/heartjnl-2021-319479
8. Lee SH, Park JS, Park JH, Chin JY, Yoon WS, Kim HY, et al. Comparison of clinical and echocardiographic characteristics between cardiac myxomas and masses mimicking myxoma. *Korean Circ J* 2020; **50:** 822-32. doi: 10.4070/KCJ.2020.0024
9. Karabinis A, Samanidis G, Khoury M, Stavridis G, Perreas K. Clinical presentation and treatment of cardiac myxoma in 153 patients. *Medicine (Baltimore)* 2018; **97:** e12397. doi: 10.1097/MD.0000000000012397
10. Colin GC, Gerber BL, Amzulescu M, Bogaert J. Cardiac myxoma: a contemporary multimodality imaging review. *Int J Cardiovasc Imaging* 2018; **34:** 1789-808. doi: 10.1007/s10554-018-1396-z
11. Engberding R, Daniel WG, Erbel R, Kasper W, Lestuzzi C, Curtius JM, et al. Diagnosis of heart tumours by transoesophageal echocardiography: a multicentre study in 154 patients. *Eur Heart J* 1993; **14:** 1223-8. doi: 10.1093/eurheartj/14.9.1223

12. Bjessmo S, Ivert T. Cardiac myxoma: 40 years' experience in 63 patients. *Ann Thorac Surg* 1997; **63:** 697-700. doi: 10.1016/S0003-4975(97)00003-9

13. Centofanti P, Di Rosa E, Deorsola L, Actis Dato GM, Patanè F, La Torre M, et al. Primary cardiac tumors: early and late results of surgical treatment in 91 patients. *Ann Thorac Surg* 1999; **68:** 1236-41. doi: 10.1016/S0003-4975(99)00700-6

14. Hill M, Cherry C, Maloney M, Midyette P. Surgical resection of atrial myxomas. *AORN J* 2010; **92:** 393-409. doi: 10.1016/j.aorn.2010.06.012

15. Garatti A, Nano G, Canziani A, Gagliardotto P, Mossuto E, Frigiola A, et al. Surgical excision of cardiac myxomas: twenty years experience at a single institution. *Ann Thorac Surg* 2012; **93:** 825-31. doi: 10.1016/j.athoracsur.2011.11.009

16. NiDhonnchu T, Daly A, Ogbo S, Keita L, Mulligan N, McCarthy J. 31 Cardiac myxoma in the Republic of Ireland: a national incidence study. [abstract]. *Heart* 2016; **102:** A16-7. doi: 10.1136/heartjnl-2016-310523.31

17. Sigurjonsson H, Andersen K, Gardarsdottir M, Petursdottir V, Klemenzson G, Gunnarsson G, et al. Cardiac myxoma in Iceland: a case series with an estimation of population incidence. *Apmis* 2011; **119:** 611-7. doi: 10.1111/j.1600-0463.2011.02777.x

18. Pérez-Andreu J, Arribas Leal JM, Gervase G, Rivera-Caravaca JM, Cánovas López S, Marín F. Epidemiology of cardiac myxoma in a Spanish population. A 30-year surgical series. *Rev Española Cardiol English Ed* 2019; **72:** 685-6. doi: 10.1016/j.rec.2018.08.021

19. Cianciulli TF, Cozzarin A, Soumoulou JB, Saccheri MC, Méndez RJ, Beck MA, et al. Twenty years of clinical experience with cardiac myxomas: diagnosis, treatment, and follow up. *J Cardiovasc Imaging* 2019; **27:** 37-47. doi: 10.4250/jcvi.2019.27.e7

20. Gui J, Maqsood A, Khadka S, Rodriguez K, Everett G. New trend of cardiac myxoma - case series and systematic review. *Clin Cardiol Cardiovasc Med* 2016; **1:** 1-5. doi: 10.33805/2639.6807.101

21. Wintersperger BJ, Becker CR, Gulbins H, Knez A, Bruening R, Heuck A, et al. Tumors of the cardiac valves: imaging findings in magnetic resonance imaging, electron beam computed tomography, and echocardiography. *Eur Radiol* 2000; **10:** 443-9. doi: 10.1007/s003300050073

22. Mendes GS, Abecasis J, Ferreira A, Ribeiras R, Abecasis M, Gouveia R, et al. Cardiac tumors: three decades of experience from a tertiary center: are we changing diagnostic work-up with new imaging tools? *Cardiovasc Pathol* 2020; **49:** 107242. doi: 10.1016/j.carpath.2020.107242

23. Jones DR, Warden HE, Murray GF, Hill RC, Graeber GM, Cruzzavala JL, et al. Biatrial approach to cardiac myxomas: a 30-year clinical experience. *Ann Thorac Surg* 1995; **59:** 851-6. doi: 10.1016/0003-4975(95)00064-R

24. Wu X, Yang D, Yang Z, Li J, Zhao Y, Wang K, et al. Clinical characteristics and long term post-operative outcome of cardiac myxoma. *EXCLI J* 2012; **11:** 240-9. PMID: 27418902

25. Obrenović-Kirćanski B, Mikić A, Parapid B, Djukić P, Kanjuh V, Milić N, et al. A 30-year-single-center experience in atrial myxomas: from presentation to treatment and prognosis. *Thorac Cardiovasc Surg* 2013; **61:** 530-6. doi: 10.1055/s-0032-1322545

research article

Development of a computational pregnant female phantom and calculation of fetal dose during a photon breast radiotherapy

Vjekoslav Kopacin[1,2], Mladen Kasabasic[1,3], Dario Faj[1,4], Marijke de Saint Hubert[5], Stipe Galic[6], Ana Ivkovic[1,3], Marija Majer[7], Hrvoje Brkic[1,4]

[1] Department of Biophysics and Radiology, Faculty of Medicine Osijek, Osijek, Croatia
[2] Department of Diagnostic and Interventional Radiology, Osijek Clinical Hospital Centre, Osijek, Croatia
[3] Department of Medical Physics, Osijek Clinical Hospital Centre, Osijek, Croatia
[4] Department of Biophysics, Biology and Chemistry, Faculty of Dental Medicine and Health in Osijek, Osijek, Croatia
[5] Unit Research in Dosimetric Applications, Belgian Nuclear Research Centre
[6] Department of Medical Physics, University Clinical Hospital Mostar, Mostar, Bosnia and Herzegovina
[7] Division of Materials Chemistry, Ruđer Bošković Institute, Zagreb, Croatia

Vjekoslav Kopacin and Mladen Kasabasic contributed equally.

Radiol Oncol 2022; 56(4): 541-551.

Received 28 July 2022
Accepted DD August 2022

Correspondence to: Assist. Prof. Hrvoje Brkić, Ph.D., Department of Biophysics, Biology and Chemistry, Faculty of Dental Medicine and Health in Osijek, Osijek, Croatia, E-mail: hbrkic@mefos.hr

Disclosure: No potential conflicts of interest were disclosed.

Background. The incidence of carcinoma during pregnancy is reported to be 1:1000–1:1500 pregnancies with the breast carcinoma being the most commonly diagnosed. Since the fetus is most sensitive to ionizing radiation during the first two trimesters, there are mixed clinical opinions and no uniform guidelines on the use of radiotherapy during pregnancy. Within this study the pregnant female phantom in the second trimester, that can be used for radiotherapy treatment planning (as DICOM data), Monte Carlo simulations (as voxelized geometry) and experimental dosimetry utilizing 3D printing of the molds (as .STL files), was developed.

Materials and methods. The developed phantom is based on MRI images of a female patient in her 18th week of pregnancy and CT images after childbirth. Phantom was developed in such a manner that a pregnant female was scanned "*in vivo*" using MRI during pregnancy and CT after childbirth. For the treatment of left breast carcinoma, 3D conformal radiotherapy was used. The voxelized geometry of the phantom was used for Monte Carlo (MC) simulations using Monte Carlo N-Particle transport code™ 6.2 (MCNP).

Conclusions. The modeled photon breast radiotherapy plan, applied to the phantom, indicated that the fetus dose is 59 mGy for 50 Gy prescribed to the breast. The results clearly indicate that only 9.5% of the fetal dose is caused by photons that are generated in the accelerator head through scattering and leakage, but the dominant component is scattered radiation from the patient's body.

Key words: Monte Carlo simulation; phantom; pregnancy; breast neoplasms; radiotherapy; fetal dose

Introduction

The incidence of carcinoma during pregnancy is reported to be 1:1000–1:1500 pregnancies, and according to FIGO 2018 report, the incidence has increased over the last 30 years.[1,2] With an incidence of 1:3000–1:10000, breast carcinoma is the most common malignant tumor during pregnancy.[3-6]

Since the fetus is sensitive to ionizing radiation, mostly during the first two trimesters due

to organogenesis (extendable until the end of the 15th week when the development of the central nervous system ends)[4,7-11], there are mixed clinical opinions and no uniform guidelines on the use of radiotherapy during pregnancy.

According to the National Comprehensive Cancer Network (NCCN) 5.2021 guidelines, radiotherapy is not an option for the treatment of breast carcinoma during pregnancy, yet mastectomy in the first trimester or neoadjuvant chemotherapy and mastectomy in the second trimester.[12] Some authors even suggest abortion in the first trimester, before the treatment has started[8], or in the cases of advanced inoperable cancer stages.[13] Moreover, the Royal College of Obstetricians and Gynecologists Guideline No. 12 considers the use of radiotherapy during pregnancy to be contraindicated.[14] Other authors consider radical mastectomy to be the treatment of choice for the cases in the first trimester or sparing breast surgery during the pregnancy and apply radiotherapy after the childbirth for the cases in the second or third trimester.[1]

According to ICRP 84[9] and ICRP 90 publications[15], as well as in NCRP report 54 and 174[7,16,17], the threshold for the fetus is 50 mGy below which there is no evidence (the risk is considered negligible) for possible congenital malformations, mental retardation, and reduced IQ. Above 50 mGy, and especially for doses above 100 mGy, the risk of stochastic effects increases. Interestingly the ICRP 84 publication states that radiotherapy of malignant diseases outside the pelvis region is possible, which was later also stated in the FIGO 2018 report. Nevertheless, careful planning and accurate dosimetry are strongly advised not to achieve fetal doses above the limit.[2,9,13,18]

Today no consensus exists on how to perform fetal dosimetry which is in practice mostly estimated or measured using computational or modified physical phantoms of pregnant women. For example, a number of groups have performed breast radiotherapy during pregnancy[18-20], but only Antypas *et al*. measured the dose experimentally *in vivo* using TLDs. They have determined that the dose at the fetal position was 36.4 ± 8.6 mGy or 0.079% of the breast dose.[18]

Since the 1960s, dosimetry phantoms have allowed measuring radiation doses in the human body, and since then 121 computer phantoms and 27 physical phantoms of the human body have been developed.[21] Initially, mathematical models[22] were used to calculate the radiation dose, but with advances in computer technology, computational phantoms became a standard in calculating the dose of ionizing radiation in the 1980s. Computer phantoms are categorized into three categories: (1) stylized phantoms, (2) voxelized phantoms, and (3) "boundary representation" (BREP) phantoms.[21] Stylized phantoms were early phantoms, where simple geometric objects that represented the human body were combined. Advances in computer technology, as well as in medical imaging technologies such as computed tomography (CT) and magnetic resonance imaging (MRI), and their wide availability have enabled voxelized phantoms, and BREP phantoms to become the standard for dosimetry studies.

According to the Handbook of Anatomical Models for Radiation Dosimetry[21], among the 121 phantoms, only a few of them are representing pregnant women. First mathematical and stylized models of pregnant females were developed while later RPI-P3, RPI-P6, RPI-P9 Pregnant Women were developed by Oak Ridge National Laboratory (ORNL).[23] Furthermore, KATJA was developed by the National Research Center for Environment and Health in Germany[24] followed by the pregnant female phantom of the Japan Atomic Energy Agency (JAEA) and the UF Family pregnant female library developed by the University of Florida.[25,26] Except for early mathematical and stylized phantoms of ORNL, all the mentioned phantoms were created by separately generating a three-dimensional model of a fetus, obtained from MRI or accidental CT examinations of pregnant women, which were subsequently inserted into an adult women phantom. Due to the huge efforts to build such phantoms and associated costs, these phantoms are often not available to research organizations performing essential research for optimized fetus dosimetry[27] as well as to clinics, requiring such models for fetus dose verification.

All mentioned pregnant phantoms are available only in the digital form, yet their physical representations are still missing. Experimental measurement in dosimetry (using active or passive detectors) can be very complex and they depend on the irradiation set-up, so it is important to have both computational and experimental representations of the phantom. Nevertheless, experimental measurements are required to validate Monte Carlo (MC) simulations, and results from both approaches are complementary. MC simulations can provide information about contributions from different field components, particle types, particle energy spectra, etc. This is useful information when choosing or combining appropriate detectors for experiments and optimization of their calibra-

tions. Our newly developed phantom offers the possibility to obtain the physical representation of the phantom, and calculate the dose on identical geometry, which is novel in dosimetry of pregnant patients.

In this study, a computational anthropomorphic phantom of a woman, in her second trimester of the pregnancy was developed. Woman was imaged during the pregnancy by MRI and after childbirth by CT. Then the feasibility study, to use the phantom for fetal dose calculations using MC simulations, was shown for a photon breast radiotherapy plan. The phantom is made available for treatment planning, in DICOM format as well as a voxelized and mesh format, to be used in Monte Carlo simulations. Finally, the phantom is available in .STL file format, suitable and prepared for 3D printing of the molds, for generation of the physical phantom to be used in further experimental dosimetry.

Materials and methods

Tena phantom creation

Clinical parameters and imaging data

After the faculty's Ethical committee's approval (IRB number: 2158-61-07-21-152, approval date: 14.7.2021.), a pregnant female phantom was developed, named Tena, based on a female patient, of central European descent, in the 18th week of pregnancy, with age 37, body mass of 72 kg (60 kg prior to pregnancy) and body height of 166 cm (BMI 26.1 kg/m^2). The patient signed a written consent authorizing the use of her diagnostic imaging materials to generate this phantom (MR examination of the chest, abdomen, and pelvis obtained during pregnancy and CT examination of the neck, chest, abdomen, and pelvis performed 4 months after delivery). The fetus's gestational age at the moment of performed MRI scan was 17 weeks and 2 days. The estimated fetal mass was calculated as the product of the segmented fetus volume (123.04 cm^3) and the average soft tissue density (1.05 g/cm^3, ICRP 89)[28], and equals 129.2 g. The crown-rump length equals 111.8 mm.

DICOM data from *in vivo* MR scanning of the pregnant female chest, abdomen and pelvis, performed on Siemens Avanto 1,5 T MR scanner as well as DICOM data from performed contrast CT study of the neck, chest, abdomen, and pelvis obtained with Siemens Sensation 40 CT scanner with the slice thickness of 1.5 mm were imported into the open-source software for segmentation "3D Slicer".[29]

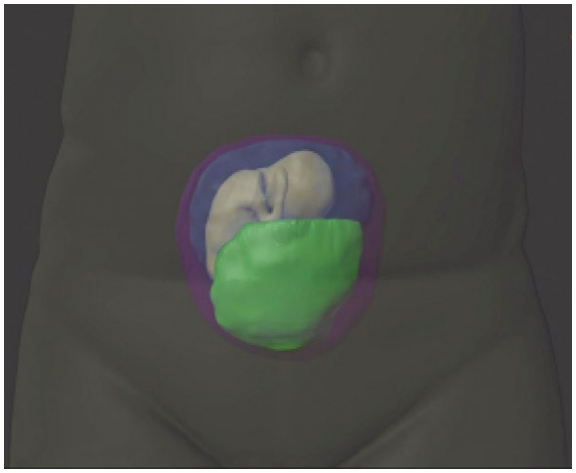

FIGURE 1. Magnified view of the computational phantom's lower abdomen and pelvis viewed as rendered polygon mesh in the computer 3D modeling software, showing the position of the 18-week-old fetus (in RST position) and placenta in relation to the uterus and the body of the mother. The fetus is shown in light gray colour, the amniotic fluid in transparent blue, the placenta in green, the uterus in transparent purple, and the body of the mother in olive green color.

Structure and organ segmentation and computer 3D modelling

In order to make the process of phantom development more understandable a schematic diagram was made and it is available in the manuscript supplement (Supplemental Figure 1). A combination of semi-automated and manual segmentation of the desired structures was performed in the aforementioned software for the generation of the polygon mesh of the organs. Later, three-dimensional (3D) CAD models of the same structures were exported as .STL files ("stereolithography", "standard tessellation language", a type of file used in CAD software and for 3D printing). Right paratracheal mediastinal lymphadenopathy and nodal mass in the right "rectus abdominis" muscle were omitted, as they were part of the patient's underlying disease, Hodgkin lymphoma.

Since the mother's head was not entirely captured by CT scanning, but up to the base of the skull, a CT scan of the whole head was taken from another patient with a similar physiognomy available in the open online DICOM data library (embodi3D, The biomedical 3D printing community, https://www.embodi3d.com/files/category/40-skull-head-and-neck-cts/). Then, polygon meshes and 3D models of the organs located in the head region were generated.

TABLE 1. List of the tissues and organs in our developed mesh pregnant female phantom in 2nd trimester (Tena), including volume, mass (calculated as the product of tissue density according to ICRP 89 and segmented organ volume) and surface area

Tissue/organ	Volume (cm^3)	Mass (g)	Surface area (cm^2)
Adrenal glands	5.1	5.2	40.2
Amniotic fluid	423.4	423.4	381.7
Blood vessels/blood	806.4	854.8	1739.3
Bones, cortex (including proximal humerus and femoral heads)	2443.4	4691.4	10667.3
Bone marrow (including proximal humerus and femoral heads)	723.4	724.4	2365.7
Central nervous system (brain and spinal cord)	1156.3	1214.1	752.4
Colon, content	454.2	472.4	825.5
Colon, wall	287.2	298.7	1914.3
Esophagus, content	4.4	0	42.0
Esophagus, wall	12.2	12.5	123.3
Eyeballs	12.4	13.1	32.9
Fetus, 17 week old	123.0	129.2	200.6
Gall bladder, content	15.5	15.9	42.3
Gall bladder, wall	15.6	16.1	104.1
Kidneys	312.3	327.9	340.4
Liver	1780.4	1869.5	1133.2
Lungs	3937.1	1515.8	2385.4
Myocardium	221.6	232.7	804.1
Pancreas	85.2	89.4	161.3
Parotid glands	24.1	24.9	64.8
Placenta	142.7	145.5	216.8
Soft tissues (muscles, adipose tissue and skin)	36080.4[1]	36802.0[2]	39186.9
Spleen	391.2	406.9	345.0
Stomach, duodenum and small intestine, content	570.3	593.1	1176.1
Stomach, duodenum and small intestine, wall	425.2	442.2	2717.9
Submandibular glands	5.3	5.5	22.0
Thyroid gland	10.0	10.4	3990.0
Upper airways (nasal cavity, pharynx and larynx) and trachea/air	136.9	0.1	426.7
Urinary bladder, content	11.1	11.6	38.6
Urinary bladder, wall	21.5	22.2	104.7
Uterus (myometrium)	552.5	580.1	917.6

[1] obtained by subtracting the sum of the volumes of all segmented organs and the total volume of the body;
[2] product of volume and 1.02 g/cm^3 which is the average value of muscle tissue density (1.050 g/cm^3), adipose tissue density (0.950 g/cm3) and skin density (1.060 g/cm^3)

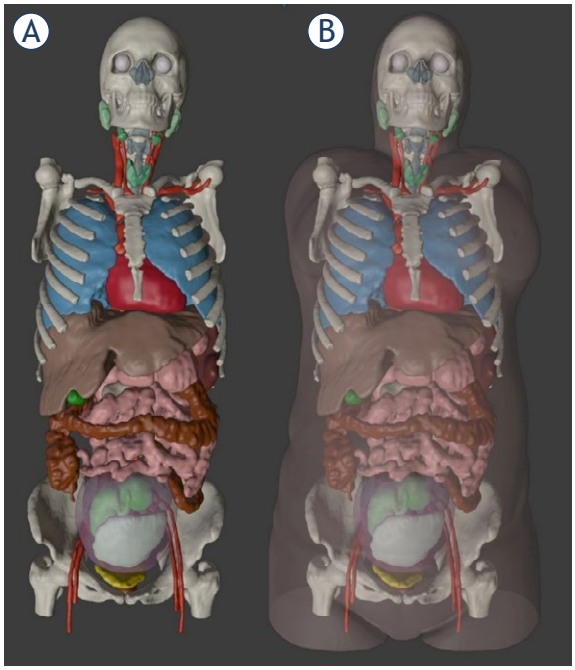

FIGURE 2. The mesh version of the Tena phantom without skin and soft tissues **(A)** and with the skin and soft tissues that are shown in transparent light brown color **(B)**. The uterus is shown in transparent purple for a better view of the fetus and its position in space and in relation to other organs.

The 17-week-old fetus, uterus, placenta, amniotic fluid, bladder, and small and large intestine were then segmented from the same patient's DICOM data obtained by MR scanning. The fetal head was positioned upwards, faced to the mother's left side of the body (right sacrum transverse (RST) position) as seen in Figure 1.

Certain bone structures such as the pelvis and both femoral heads were segmented from the MR examination as well, which then served as reference points for the registration of the organs in space (i.e. abdominal cavity). As the fetus, uterus, placenta and amniotic fluid were segmented from several different sequences of MR examination and the rest of the organs from the CT study, we could not perform a fusion of the several different studies and organ segmentation in the fused images using the "3D Slicer". Registration and correct positioning in space was performed manually by rotating and translating the objects using an open-source software Blender (Blender Foundation, Amsterdam, the Netherlands). The CAD models of the whole head including a skull, its associated organs and soft tissues were positioned according to the predefined bony structures of the pregnant female. The skull was merged with the rest of the skeleton and the upper airways were merged

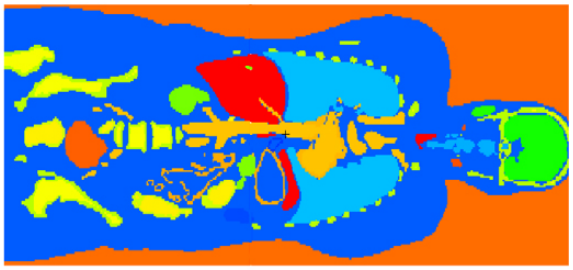

FIGURE 3. Voxelized phantom displayed using MCNP plotter.

with the pregnant female patient's trachea using the Blender CAD program and "Boolean Union" operation. The spatial resolution of the MR examination images has lower quality (thick slices and non-isovoxel) and the position of the bowels differs during pregnancy. For this reason, "Meshmixer" (Autodesk, Inc., California, U.S.A) CAM software was used for manual positioning and adjusting of the lower gastrointestinal tract (small and large intestine) according to the location of intestines obtained from MR examinations. The same actions were performed with the urinary bladder being slightly pushed towards the caudal.

After correct positioning of the bowels and the urinary bladder, using the "Meshmixer" and the "Offset" function, wall thickness was added to the esophagus, stomach, duodenum, small and large bowel, gall bladder and urinary bladder according to Proko.[30] In this way the lumen of the listed structures was created as follows: 2 mm for the esophagus, 6 mm for the stomach, 3 mm for the small bowel, 2 mm for the large bowel, 3 mm for the gall bladder and 4 mm for the urinary bladder.

Using the same CAM software, the head region was anonymized in such a manner that the facial features were altered beyond recognition (smoothing of the periorbital area, erasing of the mouth and ears).

Since our intention was to develop the phantom that is going to be suitable for various dosimetry studies, it was decided to remove both arms that were originally placed above the head during the CT scanning. The proximal part of both humerus as far as the surgical neck and both femurs down to the femoral neck were left in place since the proximal medulla of the humerus and femurs belongs to hematopoietic tissues in adults.

Development of the mesh phantom

Our phantom of a pregnant woman at the beginning of the second trimester has 31 structures, tissues and organs, seen in Figure 2 and listed in Table 1. This number is lower than in other similar phantoms (35 in RPI[23], 174 in UF[26] and 153 in Katja[24]) but we did not segment fetal structures separately due to the early stage of the fetus in our phantom. Also, we count all cortical bone and medullar bone as two structures and not separately by region as it is counted in other phantoms.

Conversion to imaging format

Exporting this dataset to DICOM presents more of a challenge. Firstly, a dataset is used as input to a multidimensional interpolation on a regular grid using scipy.[31] This allows the rescale structure set at an arbitrary resolution, so we use interpolation to derive a structure set on a sparser resolution typical for CT images in radiotherapy. Since the NRRD format contains only geometric information, without physical characteristics such as radiopacity, this information is determined from look-up tables and available curves relating to radiopacity and electron densities.[32] This allows for the reconstruction of a realistic CT image appropriate for input to a modern treatment planning system (TPS).

A separate problem is the definition of structure set in DICOM format since modern TPS typically do not support NRRD format. This is done through a workaround where another CT image set is defined, with geometry exactly like the previous but each structure is assigned with an unphysical, but distinct radiopacity. Such a spurious CT image set is imported into TPS just for the purpose to use ranger tools in order to locate each structure separately and save them to DICOM format. After the structure set is available in DICOM format, this spurious CT image set is discarded, and the structure set is used along with the realistically reconstructed CT image set for the purpose of treatment planning.

Conversion to the format for the computational dosimetry

The structure set has been exported from Slicer 3D[29] in NRRD format and imported into an in-house made software written in Python.[33] The structure set is defined as a set of overlapping bitwise masks defined on a dense cubic lattice, with approximately 1.8 mm per node. Such bitwise masks assign to each voxel a combination of covering structures and this dataset is appropriate for further processing. Exporting such a dataset to

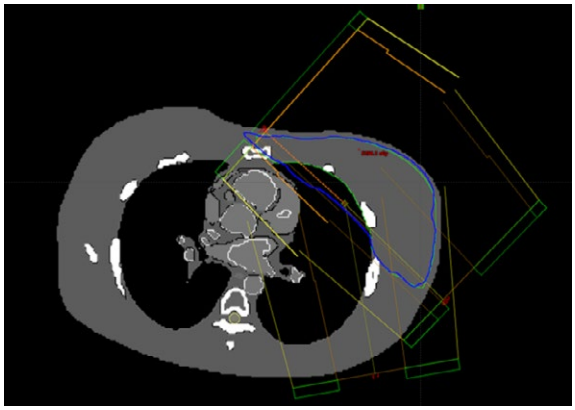

FIGURE 4. Beam arrangements in Eclipse.

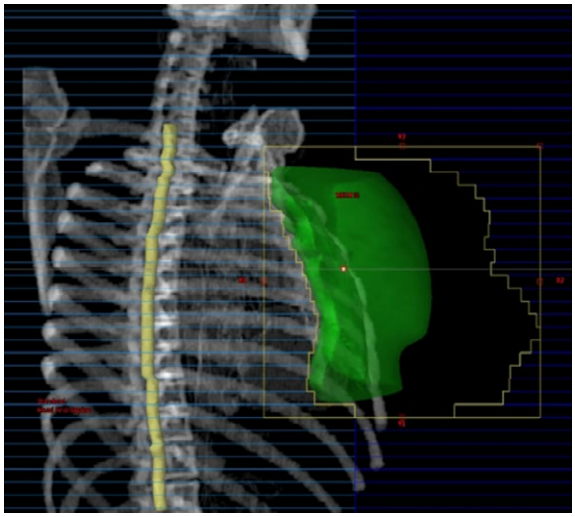

FIGURE 5. Beam Eye View of Field F1, where leafs are represented as transparent rectangles with blue edges. And PTV is colored in green.

the MCNP can be handled relatively easily, taking precautions regarding patient orientation and structure overlap which is not allowed since every voxel must have a uniquely defined chemical composition (Figure 3).

Generation of the physical phantom

As mentioned earlier in the text, phantom Tena could be obtained in its physical form for experimental dosimetry and is available for everyone to download. 3D modeling software "Blender" was used for the generation of the molds (available in Supplemental material as .STL files) for pouring the substitute tissue, thus generating a physical phantom as seen in the picture. Further description is beyond the scope of this article and will be explained in the upcoming research.

Radiotherapy plan

3D conformational radiotherapy treatment plan for the left breast irradiation was generated using Varian Eclipse 15.6 (Varian Medical Systems Inc., Palo Alto, USA) planning software. The plan was made for Siemens Oncor Expression machine using 6 MV beams. The plan consists of two main opposite fields in which beams are tangential to the chest wall. To guarantee a homogeneous dose in the breast (Planning Target Volume; PTV) three small (patch) fields are added to the main fields (Figure 4). The prescribed dose is 50 Gy in 25 fractions. The mean dose to the breast (PTV, 1688 cm^3) is 50.3 Gy and the maximum dose in the breast (PTV) is 53.5 Gy. The plan was achieved with five fields, denoted ad F1 to F5 in the text below (Figure 5). Minimal distance from the largest field (F1) used in radiotherapy plan is 22.5 cm, while the largest distance for the same field is 33 cm. For other fields these distances are even higher.

Monte Carlo simulations

Monte Carlo simulations were performed using Monte Carlo N-Particle transport code™ 6.2 (MCNP).[34] Siemens Oncor accelerator was modeled as it was described and extensively validated in our previous publications.[35-39] Parts included in the accelerator model are target, flattening filter, primary collimator, jaws, head shielding and monitor chamber. Each leaf in the multi leaf collimator is modeled independently and set up in the position that matches position in the accelerator head for corresponding field. Accelerator was modeled from electrons impinging the target with the energy of 6 MeV with a Gaussian spread of 3%. Each of the 80 leafs in the multi-leaf collimator was modeled separately and positioned to fit the field in the original radiotherapy plan. The phantom was placed in a separate universe, so the rotation of the phantom was achieved using the TR (transformation) card in the MCNP. In this way, it is relatively easy to achieve both rotation and translation of the phantom according to the accelerator head position at the same time. Phantom consisted of 219 x 148 x 479 voxels, and each of $1.55*10^7$ voxels have the dimensions of 0.186 x 0.186 x 0.186 cm^3 (Figure 3).

Materials for the phantom were used from ICRP 110 female phantom[40], and Compendium of Material Composition Data for Radiation Transport

TABLE 2. Tena phantom formats and their characteristics

Mesh format	DICOM	Voxelized
N° vertices[1]: 2889437 N° faces[1]: 5777800	Slice thickness: 0.625 mm Distance between slices: 1.867 mm Matrix: 512 x 512 Pixel dimensions: 0.82 mm	Grid size: 219 x 148 x 479 N° voxels: $1.55*10^{-7}$ Isovoxel size: 0.186 cm

[1] variable, could be decimated and adjusted to the computing power of the used computer

Modeling.[41] Since the breast is not segmented separately, TMESH tally was used to assess the breast dose for each applied field. Absorbed dose in the fetus was recorded using +F6 tally, while for obtaining the spectra in the fetus F4 tally was used. Each radiotherapy field is simulated independently with 10^{10} particles (electron impinging on target). DXTRAN sphere was set up around the fetus to speed up the calculations and to obtain each spectra bin with the minimum uncertainty possible. Spectra was collected in 200 energy bins ranging from 1 keV to 6 MeV. The results were accepted if the R-value fell below 0.1 and all 10 statistical checks were satisfied, meaning that out-of-field doses uncertainties in the fetal positions were below 10%.

MCNP provides results normalized per source particle (electron impinging on target) and both fetus and breast dose are normalized to the source particle. Each field contribution is taken from the TPS and multiplied with the dose calculated by MCNP. All 5 fields together have prescribed dose of 50 Gy (that is taken from TPS). In this way it is also possible to determine the field contribution to the fetus dose. To assess which field contributes the most to the fetal dose fetus/breast dose was calculated and expressed in mGy/Gy.

Results

Tena phantom

Within this study, three different formats of pregnant woman phantom in her 18th week of pregnancy were developed. All formats are available in the supplementary material of this paper. Characteristics of each format are given in Table 2.

Volumes of Tena organs compared with other available computational phantoms are shown in Supplemental Table 1. It can be seen, that the volumes of some structures differ, such as bones (cortex and bone marrow), upper airways, lungs, etc. This is possibly due to differences in the segmentation, counting of the structures in the phantoms, modeling of the other phantoms and phases of the CT scanning (during inspiration in our case). Structures like fetus, placenta, amniotic fluid and uterus (myometrium) also differ, but that is due to the different fetal gestational ages of the compared phantoms.

Characterization of fetus dose during photon breast radiotherapy

A radiotherapy plan with 5 RT fields gave beam contributions as shown in Table 3. Results of the

TABLE 3. Contribution of each field to the fetal dose. Fetus and breast doses are normalized per source particle, field contribution to the breast dose is obtained from treatment planning system (TPS), and the breast/fetus ratio is calculated from normalized breast and fetus doses

Field	Fetus dose per source particle [Gy/SP] 10^{-19}	Breast dose per source particle [Gy/SP] 10^{-19}	Field contribution to breast dose[1]	Fetus dose normalized to field contribution [Gy/SP] 10^{-19}	Breast dose normalized to field contribution [Gy/SP] 10^{-19}	Ratio fetus / breast dose [mGy/Gy]
F1	1.45 ± 0.12	1000 ± 90	0.437	0.634 ± 0.054	437 ± 37	1.44
F2	1.05 ± 0.09	1070 ± 90	0.378	0.399 ± 0,035	404 ± 36	0.99
F3	1.03 ± 0.08	993 ± 80	0.064	0.066 ± 0,005	63.5 ± 5	1.03
F4	0.270 ± 0.02	1010 ± 80	0.057	0.015 ± 0.001	57.3 ± 4	0.27
F5	0.854 ± 0.07	449 ± 40	0.064	0.055 ± 0,005	28.7 ± 2	1.91
Total				1.169 ± 0.064	992.5 ± 52	
Total normalized to prescribed dose				58.9 ± 3.7 mGy	50 Gy*	

[1] obtained from TPS

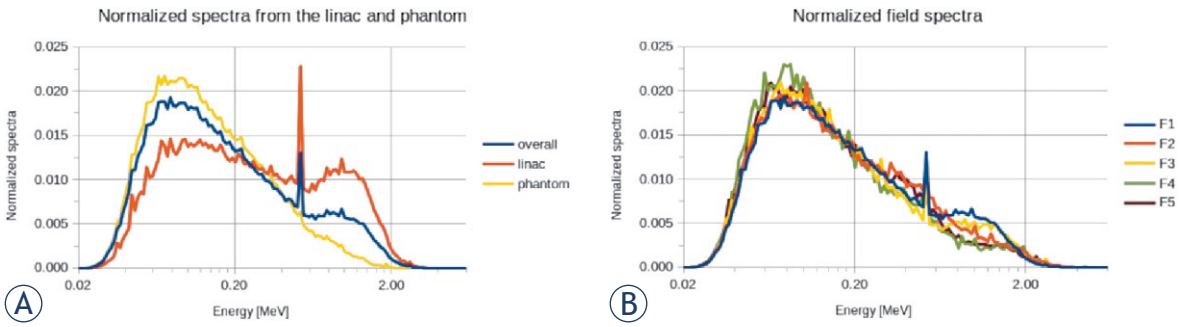

FIGURE 6. Spectra for F1 of the photons coming from the accelerator head and all the photons reaching the fetus **(A)**; Photon spectra in fetus for each field **(B)**.

fetus and breast dose, normalized per source particle were determined using MC simulations (Table 3).

Since the prescribed dose to the breast was 50 Gy, according to the data shown in Table 3 it is easy to calculate that the whole fetus will receive 58.9 mGy (with uncerintaity of 3.7 mGy).

As it can be seen from Figure 4 and Table 3, field F1 is a medial field with the major contribution to the breast dose while F2 is a lateral field. The other three patch fields with significantly lower breast dose contribution are F3 (medial), F4 (lateral) and F5 (posterior). From the fetus/breast dose ratio it is obvious that medial fields have a higher contribution to the fetal dose, while the most dominant contribution comes from the posterior F5 field.

Monte Carlo simulations enabled us to determine the place of the origin of all the photons reaching the fetus during breast radiotherapy. These data are shown in Table 4 and display the amount of the photons that are reaching the fetus and are caused by the accelerator's head leakage, or they are created within the mother. It is interesting to see that 90.5% of all the photons in the fetus are created within the mother, while only 9.5% of them are created in the accelerator's head.

Our final intention is to develop a physical phantom and perform experimental measurements using this phantom. We also evaluated the energy spectra reaching the fetus as some of the passive dosimeters can be energy-dependent. Figure 6 shows these spectra and separately display photons coming from the linac head and the mother body. It can be seen that photons that reach the fetus and are coming from the linac head have higher energies (average energy 0.43 MeV) while photons that are coming from the mother mainly originate from secondary interactions and have an average energy of 0.2 MeV.

TABLE 4. Relative contribution to the absorbed dose in the fetus (%) originating in the linac or the phantom. The ratio for each field of photons originating in linac or phantom is given in the last row

	F1	F2	F3	F4	F5	Overall
Linac (%)	6.0	2.1	0.8	0.3	0.3	9.5
Phantom (%)	37.7	35.7	5.6	5.4	6.1	90.5
Contribution ratio	16.12	5.8	14.3	5.5	4.9	

Discussion

Within this paper computational phantom of 37-year old woman in her 18th week of pregnancy was created based on CT and MRI images of the pregnant patient. To the best of our knowledge, this is the first pregnant phantom made directly from the MRI images of the pregnant patient and not done by inserting the fetus into the non-pregnant patient. To make the implementation of the phantom in the TPS possible, the DICOM format was prepared. Voxelized format, that is suitable for MC simulations, and STL format, suitable for 3D printing of molds, is also provided as a supplement to this paper. In this way, we are making possible usage of the same phantom in TPS, MC simulations and experiments once the physical representation of the phantom is going to be available.

As a proof of feasibility, a typical breast cancer plan was prepared in order to assess the dose received by the fetus during the breast cancer radiotherapy as well as to characterize the field (determine its spectra) reaching the detector. This information is important to set up experiments in the future as detectors, such as thermoluminescent detectors (TLDs), are characterized by a varying response as a function of photon energy,

which has been characterized experimentally and through modeling.[42] Input from simulations will be important for an optimal selection of detector type(s) and/or correction of this energy response may be required.

In clinical practice TPS is not able to estimate the dose to the fetus since its cutoff line for dose calculations is mostly positioned above the uterus. However, our results indicate that the fetus is going to receive only a small fraction of the dose delivered to the breast. As was mentioned earlier fetus receives the dose of 59 mGy (with the simulations uncertainty of 8%), which is close to the threshold of 50 mGy prescribed by the ICRP[15] and well below 100 mGy. It is also worth mentioning that no shielding to the fetus was applied. In the study published by Bednarz *et al*. dose of 120 mGy to the fetus was determined when the mantle was irradiated with 39 Gy with only one gantry field.[43] This is two times higher when compared to our results although no leafs are simulated in the mentioned study. Antypas *et al*. experimentally determined the dose of 39 mGy to the fetus, when 49 Gy to the breast, using two fields, was applied, which is in line with our results.[18] Several experimental studies have also determined the dose to the fetus, namely van der Giessen *et al*. reported 280 mGy to the fetus when 50 Gy to the breast was applied[20] and Ngu *et al*. reported 210 mGy with similar conditions only without shielding.[19] Mazonakis *et al*. computationally determined the dose of 131 mGy when 50 Gy to the breast of the pregnant phantom was applied without shielding.[44] These doses are all significantly higher than the dose that we determined. The cause for the large range of published fetal doses during breast radiotherapy could come due to different phantom anatomy, fetal position or gestation period, breast size and position as well as different optimization of the radiotherapy treatment plans. We will further investigate this in the future.

Our study has limitations such as Monte Carlo simulations are normalized per source particle (electron impinging on accelerator target). Besides validation experiment is not performed yet since it is planned in our future work to make a physical representation of the phantom. The phantom is made according to the anatomical data found. Nevertheless, the fetal dose during photon breast radiotherapy will differ if the patient change or if fetal position within the patient change.

Knowing each field contribution to the fetal dose, that dose can be further optimized. From the relative dose contribution to the fetus, it can be easily concluded that F5 has the largest fetus/breast ratio, followed by field F1. This result is important since the new radiotherapy plan can be tailored according to the information obtained by MC and additional reduction to the dose can be achieved by avoiding fields F5 and F1 and giving more significance to the lateral fields.

In our simulated case 9.5% of the absorbed dose in the fetus is caused by the accelerator head leakage, while 90.5% of the absorbed dose comes through the patient's body. In the literature, those values differ significantly i.e. van der Giessen in the case report states that 35% of the fetal dose comes as scattered radiation using 10 MeV X-ray beams.[20] According to Stovall *et al*., collimator scatter is the dominant component of the fetal dose at larger distances (70–90 cm) from the primary radiation field.[45] Chofor *et al*. and Mazonakis *et al*. also state that the head leakage and head scatter radiation are dominant components in fetal dose at the larger distances from the primary beam edge.[46,47] Our data correlate to Ngu *et al*. report who states that most of the secondary photons come as scattered radiation, while a smaller portion comes as leakage radiation from the linear accelerator head.[19] The data on accelerator head leakage, that reaches the fetus, depend on the accelerator type and the shielding application.[48] As already mentioned shielding is one important topic when RT is applied to pregnant women. Lead is the most commonly used apron for covering the patient during radiotherapy has an HVL (half-value layer) of 7.9 mm at the energy of 1 MeV that is comparable to our results (Figure 6B). It means that an apron of 30 x 30 cm^2 dimensions would have approximately 80 kg, and it is probably inappropriate to be positioned on the pregnant woman's belly, but rather lead shield on the rigged frame could be used as proposed by some authors.[13,19,45]

In the near future, our intention is to produce a low -cost physical phantom using a three-dimensional (3D) printer for mold making and pouring substitute tissues into 3D printed molds. Our estimation is that all the components for molding and casting such phantom is in order of 1000 €. It is our intention to validate our model experimentally and complete both experimental and computational results. Once a completed physical representation of the phantom can be further used in other fields such as interventional and diagnostic radiology and determination of dose for both patients and staff. Proton therapy of pregnant patients is also a topic of interest[49], our newly developed phantom can provide new insights into this field too.

Conclusions

Developed phantom offers the possibility to perform treatment planning and Monte Carlo on the same pregnant female phantom. There is also a possibility for 3D printing the same phantom which would enable experimental measurements on the identical geometry. This is important for the improvement of current dosimetry practices in clinics enabling more consensus on such treatments and ultimately for the optimization of such treatments. Our feasibility study demonstrated that the dose received by the fetus, during photon breast radiotherapy was just above the recommended level (59 mGy for the 50 Gy prescribed to the breast) which demonstrates the need to have good dosimetry tools in place for dose assessment and optimization. Within this study, the spectra of photon reaching the fetus are also determined, which will simplify the selection of appropriate detectors once when the physical representation of the phantom is going to be available.

Acknowledgments

This research is made as a part of the EURADOS WG9 and WG6 activities. It is financed by the Institutional projects IP3-2022 of the Faculty of Medicine in Osijek and IP4-2021 in the Faculty of Dental Medicine and Health in Osijek.

Special thanks to the pregnant woman T. Š. who allowed us to use her diagnostic images for research purposes and the development of this phantom.

References

1. Basta P, Bak A, Roszkowski K. Cancer treatment in pregnant women. *Contemp Oncol* 2015; **19:** 354-60. doi: 10.5114/wo.2014.46236
2. Botha MH, Rajaram S, Karunaratne K. Cancer in pregnancy. *Int J Gynecol Obstet* 2018; **143:** 137-42. doi: 10.1002/ijgo.12621
3. Kal HB, Struikmans H. Radiotherapy during pregnancy: fact and fiction. *Lancet Oncol* 2005; **6:** 328-33. doi: 10.1016/S1470-2045(05)70169-8
4. Fenig E, Mishaeli M, Kalish Y, Lishner M. Pregnancy and radiation. *Cancer Treat Rev* 2001; **27:** 1-7. doi: 10.1053/ctrv.2000.0193
5. Leonardi M, Cecconi A, Luraschi R, Rondi E, Cattani F, Lazzari R, et al. Electron beam intraoperative radiotherapy (ELIOT) in pregnant women with breast cancer: from in vivo dosimetry to clinical practice. *Breast Care* 2017; **12:** 396-400. doi: 10.1159/000479862
6. Shlensky V, Hallmeyer S, Juarez L, Parilla B V. Management of breast cancer during pregnancy: are we compliant with current guidelines? *Am J Perinatol Reports* 2017; **7:** e39-43. doi: 10.1055/s-0037-1599133
7. De Santis M, Di Gianantonio E, Straface G, Cavaliere AF, Caruso A, Schiavon F, et al. Ionizing radiations in pregnancy and teratogenesis: a review of literature. *Reprod Toxicol* 2005; **20:** 323-9. doi: 10.1016/j.reprotox.2005.04.004
8. Burdorf A, Figà-Talamanca I, Jensen TK, Thulstrup AM. Effects of occupational exposure on the reproductive system: core evidence and practical implications. *Occup Med* 2006; **56:** 516-20. doi: 10.1093/occmed/kql113
9. International Commission on Radiological Protection. Protection IC on R. ICRP publication 84 – pregnancy and medical radiation. *Ann ICRP*. 2000; **30(1):** 43.
10. Smith H, International Commission on Radiological Protection. *1990 recommendations of the International Commission on Radiological Protection*. ICRP Publication 60. Oxford: Pergamon press; 1991. [cited 2022 Jun 15]. Available at: https://www.icrp.org/publication.asp?id=icrp%20publication%2060
11. Organization for Occupational Radiation Safety in Interventional Fluoroscopy. *Occupational exposure to ionizing radiation in interventional fluoroscopy: severity of adverse effects of a growing health problem*. Washington D.C.: ORSIF; 2015.
12. Amant F, Han SN, Gziri MM, Vandenbroucke T, Verheecke M, Van Calsteren K. Management of cancer in pregnancy. *Best Pract Res Clin Obstet Gynaecol* 2015; **29:** 741-53. doi: 10.1016/j.bpobgyn.2015.02.006
13. Wallack MK, Wolf Jr JA, Bedwinek J, Denes AE, Glasgow G, Kumar B, et al. Gestational carcinoma of the female breast. *Curr Probl Cancer* 1983; **7:** 1-58. doi: 10.1016/s0147-0272(83)80006-3
14. Royal College of Obstetricians and Gynaecologists. Pregnancy and breast cancer. *RCOG Green-top Guidel No 12;* 2011.
15. Streffer C, Shore R, Konermann G, Meadows A, Holm LE, Stather J, et al. Biological effects after prenatal irradiation (embryo and fetus). A report of the International Commission on Radiological Protection. *Ann ICRP* 2003; **33(1-2):** 5-206. PMID: 12963090
16. Gorson RO, Brent RL, Moseley RD. Medical radiation exposure of pregnant and potentially pregnant women. *Natl Counc Radiat Prot Meas Rep* 1977; **54:** 70-100.
17. Brent RL, Frush DP, Harms RW, Linet MS. Preconception and prenatal radiation exposure: health effects and protective guidance. NCRP No. 174. *Sel Work Robert Brent* 2013; **39**.
18. Antypas C, Sandilos P, Kouvaris J, Balafouta E, Karinou E, Kollaros N, et al. Fetal dose evaluation during breast cancer radiotherapy. *Int J Radiat Oncol Biol Phys* 1998; **40:** 995-9. doi: 10.1016/s0360-3016(97)00909-7
19. Ngu SLC, DuvalL P, Collins C. Foetal radiation dose in radiotherapy for breast cancer. *Australas Radiol* 1992; **36:** 321-2. doi: 10.1111/j.1440-1673.1992.tb03209.x
20. Van der Giessen P-H. Measurement of the peripheral dose for the tangential breast treatment technique with Co-60 gamma radiation and high energy X-rays. *Radiother Oncol* 1997; **42:** 257-64. doi: 10.1016/s0167-8140(96)01884-1
21. *Handbook of anatomical models for radiation dosimetry*. Xu XG, Eckerman KF, editors. Boca Raton: CRC Press; 2009. doi: 10.1201/EBK1420059793
22. Anderson CA, Kelley KC, Goorley JT. *Mesh human phantoms with MCNP*. Los Alamos, NM (United States): Los Alamos National Lab.(LANL); 2012.
23. Xu XG, Taranenko V, Zhang J, Shi C. A boundary-representation method for designing whole-body radiation dosimetry models: pregnant females at the ends of three gestational periods – RPI-P3,-P6 and-P9. *Phys Med Biol* 2007; **52:** 7023-44. doi: 10.1088/0031-9155/52/23/017
24. Becker J, Zankl M, Fill U, Hoeschen C. Katja – the 24th week of virtual pregnancy for dosimetric calculations. *Polish J Med Phys Eng* 2008; **14:** 13-20. doi: 10.2478/v10013-008-0002-4
25. Maynard MR, Long NS, Moawad NS, Shifrin RY, Geyer AM, Fong G, et al. The UF Family of hybrid phantoms of the pregnant female for computational radiation dosimetry. *Phys Med Biol* 2014; **59:** 4325-43. doi: 10.1088/0031-9155/59/15/4325
26. Paulbeck C, Griffin K, Lee C, Cullings H, Egbert SD, Funamoto S, et al. Dosimetric impact of a new computational voxel phantom series for the Japanese atomic bomb survivors: pregnant females. *Radiat Res* 2019; **192:** 538-61. doi: 10.1667/RR15394.1
27. Xu XG. An exponential growth of computational phantom research in radiation protection, imaging, and radiotherapy: a review of the fifty-year history. *Phys Med Biol* 2014; **59:** R233-302. doi: 10.1088/0031-9155/59/18/R233

28. International Commission on Radiological Protection. Basic anatomical and physiological data for use in radiological protection: reference values. ICRP Publication 89. *Ann ICRP* 2002; **32(3-4):** 1-277.

29. Kikinis R, Pieper SD, Vosburgh KG. 3D Slicer: a platform for subject-specific image analysis, visualization, and clinical support. In: *Intraoperative imaging and image-guided therapy*. Springer; 2014. p. 277-89. doi: 10.1007/978-1-4614-7657-3_19

30. Prokop M. *Spiral and multislice computed tomography of the body*. Thieme Medical Publishers; 2003.

31. Virtanen P, Gommers R, Oliphant TE, Haberland M, Reddy T, Cournapeau D, et al. SciPy 1.0: fundamental algorithms for scientific computing in Python. *Nat Methods* 2020; **17:** 261-72. doi: 10.1038/s41592-019-0686-2

32. White DR, Griffith RV, Wilson IN. ICRU Report 46. Photon, electron, proton and neutron interaction data for body tissues. *J Int Comm Radiat Units Meas* 1992; **1:** NP.

33. Van Rossum G, Drake FL. *Python reference manual.* iUniverse Indiana; 2000.

34. Werner CJ, Bull JS, Solomon CJ, Brown FB, McKinney GW, Rising ME, et al. *MCNP version 6.2 Release notes*. Report LA-UR-18-20808. Los Alamos Natl Lab; 2018.

35. Brkić H, Ivković A, Kasabašić M, Poje Sovilj M, Jurković S, Štimac D, et al. The influence of field size and off-axis distance on photoneutron spectra of the 18 MV Siemens Oncor linear accelerator beam. *Radiat Meas* 2016; **93:** 28-34. doi: 10.1016/j.radmeas.2016.07.002

36. Ivković A, Faj D, Galić S, Karimi AH, Kasabašić M, Brkić H. Accuracy of empirical formulas in evaluation of neutron dose equivalent inside the ^{60}Co vaults reconstructed for medical linear accelerators. *Int J Radiat Res* 2020;**18:** 99-107. doi: 10.18869/acadpub.ijrr.18.1.99

37. Kolacio MŠ, Brkić H, Faj D, Radojčić ĐS, Rajlić D, Obajdin N, et al. Validation of two calculation options built in Elekta Monaco Monte Carlo based algorithm using MCNP code. *Radiat Phys Chem* 2021; **179:** 109237. doi: 10.1016/j.radphyschem.2020.109237

38. Vukovic B, Faj D, Poje M, Varga M, Radolic V, Miklavcic I, et al. A neutron track etch detector for electron linear accelerators in radiotherapy. *Radiol Oncol* 2010; **44:** 62-6. 10.2478/v10019-010-0003-2

39. Brkić H, Kasabašić M, Ivković A, Agić D, Krpan I, Faj D. Influence of head cover on the neutron dose equivalent in Monte Carlo simulations of high energy medical linear accelerator. *Nucl Technol Radiat Prot* 2018; **33:** 217-22. doi: 10.2298/NTRP1802217B

40. Zankl M. Adult male and female reference computational phantoms (ICRP Publication 110). *Japanese J Heal Phys* 2010; **45:** 357-69. 10.5453/JHPS.45.357

41. Detwiler R, McConn R, Grimes T, Upton S, Engel E. Compendium of material composition data for radiation transport modeling [Internet]. Richland, WA (United States): Pacific Northwest National Lab. (PNNL); [cited 2022 May 15]. doi: 10.2172/1782721. Available from: https://www.osti.gov/servlets/purl/1782721/

42. Parisi A, Dabin J, Schoonjans W, Van Hoey O, Mégret P, Vanhavere F. Photon energy response of LiF: Mg, Ti (MTS) and LiF: Mg, Cu, P (MCP) thermoluminescent detectors: experimental measurements and microdosimetric modeling. *Radiat Phys Chem* 2019; **163:** 67-73. doi: 10.1016/j.radphyschem.2019.05.021

43. Bednarz B, Xu XG. A feasibility study to calculate unshielded fetal doses to pregnant patients in 6-MV photon treatments using Monte Carlo methods and anatomically realistic phantoms. *Med Phys* 2008; **35:** 3054-61. doi: 10.1118/1.2938519

44. Mazonakis M, Tzedakis A, Damilakis J. Monte Carlo simulation of radiotherapy for breast cancer in pregnant patients: how to reduce the radiation dose and risks to fetus? *Radiat Prot Dosimetry* 2017; **175:** 10-6. doi: 10.1093/rpd/ncw260

45. Stovall M, Blackwell CR, Cundiff J, Novack DH, Palta JR, Wagner LK, et al. Fetal dose from radiotherapy with photon beams: report of AAPM Radiation Therapy Committee Task Group No. 36. *Med Phys* 1995; **22:** 63-82. doi: 10.1118/1.597525

46. Chofor N, Harder D, Willborn KC, Poppe B. Internal scatter, the unavoidable major component of the peripheral dose in photon-beam radiotherapy. *Phys Med Biol* 2012; **57:** 1733-43. doi: 10.1088/0031-9155/57/6/1733

47. Mazonakis M, Damilakis J. Estimation and reduction of the radiation dose to the fetus from external-beam radiotherapy. *Phys Medica* 2017; **43:** 148-52. doi: 10.1016/j.ejmp.2017.09.130

48. Schneider T, Stoll E. Molecular-dynamics study of a three-dimensional one-component model for distortive phase transitions. *Phys Rev B* 1978; **17:** 1302. doi: 10.1103/PhysRevB.17.1302

49. De Saint-Hubert M, Tymińska K, Stolarczyk L, Brkić H. Fetus dose calculation during proton therapy of pregnant phantoms using MCNPX and MCNP6. 2 codes. *Radiat Meas* 2021; **149:** 1-7. 106665. doi: 10.1016/j.radmeas.2021.106665

erratum

Trends in treatment of childhood cancer and subsequent primary neoplasm risk

Maja Cesen Mazic[1], Raoul C. Reulen[2], Janez Jazbec[1], Lorna Zadravec Zaletel[3]

[1] University Children's Hospital Ljubljana, Ljubljana, Slovenia
[2] Centre for Childhood Cancer Survivor Studies, Institute of Applied Health Research, Robert Aikten Building, University of Birmingham, Birmingham, United Kingdom
[3] Institute of Oncology Ljubljana, Ljubljana, Slovenia

Radiol Oncol 2022; 56(4): 552.; 56(3): 380-389.

Received 27 Feb 2022
Accepted 10 May 2022

Correspondence to: Maja Česen Mazić, M.D., University Children's Hospital Ljubljana, Bohoričeva ulica 20, SI-1000 Ljubljana, Slovenia.
E-mail: maja.cesenmazic@kclj.si

Disclosure: No potential conflicts of interest were disclosed.

doi: 10.2478/raon-2022-0027

The affiliation for Janez Jazbec and Maja Cesen Mazic should be added to current affiliation as Faculty of Medicine, University of Ljubljana, Ljubljana, Slovenia. For the reader's convenience, the corrected author line appears below.

Maja Cesen Mazic[1,2], Raoul C. Reulen[3], Janez Jazbec[1,2], Lorna Zadravec Zaletel[2,4]

[1] University Children's Hospital Ljubljana, Ljubljana, Slovenia
[2] University of Ljubljana, Faculty of Medicine, Ljubljana, Slovenia
[3] Centre for Childhood Cancer Survivor Studies, Institute of Applied Health Research, Robert Aikten Building, University of Birmingham, Birmingham, United Kingdom
[4] Institute of Oncology Ljubljana, Ljubljana, Slovenia

---

erratum

Dosimetric study for spine stereotactic body radiation therapy: magnetic resonance guided linear accelerator versus volumetric modulated arc therapy

Poonam Yadav, Hima B. Musunuru, Jacob S. Witt, Michael Bassetti, John Bayouth, Andrew M. Baschnagel

Department of Human Oncology, University of Wisconsin School of Medicine and Public Health, Madison, WI, USA

Radiol Oncol 2019; 53(3): 362-368.

Received 24 March 2019
Accepted 22 July 2019

Correspondence to: Poonam Yadav, Ph.D., Department of Human Oncology, University of Wisconsin School of Medicine and Public Health, 600 Highland Avenue, K4/B74, Madison, WI, USA 53792-0600. Phone: 001 608-235-2594; Fax: 001 608-263-0990; E-mail: yadav@humonc.wisc.edu

Disclosure: No potential conflicts of interest were disclosed.

doi: 10.2478/raon-2019-0042

The authors regret that the following financial relationship was not previously disclosed upon publication of this article. Please note that Dr. John E. Bayouth has reported being a member of the Advisory Board of ViewRay Inc, dating from April 4, 2018, and became a corporate manager of MR Guidance LLC dating from May 19, 2019, which provides consulting services for MRI-guided radiation therapy, and has business activity with a company that utilizes deformable image registration and motion management technology (ViewRay, Inc.).

The authors would like to apologise for any inconvenience caused.

Radiol Oncol 2022; 56(4): 409-419.
doi: 10.2478/raon-2022-0049

Imunoterapija raka s celicami CAR T. Uhojene poti in potovanje po manj znanih stezah

Smole A

Izhodišča. Celična terapija T s himernim antigenskim receptorjem (*angl. chimeric antigen receptor*, CAR) je klinično potrjena imunoterapija raka z uporabo gensko spremenjenih celic T. Uspeh takšnega zdravljenja omejujejo izzivi povezani z učinkovitostjo in varnostjo. Razvijajo širok spekter različic in aplikacij celic CAR T, v tem prispevku pa se osredotočamo na celice CAR T za zdravljenje raka. V prvem delu predstavljamo splošna načela celične imunoterapije ter strukturo in vpliv zasnove molekule CAR na njeno delovanje. V drugem delu predstavljamo pet konceptualnih izzivov, ki omejujejo uspeh zdravljenja s celicami CAR T: imunosupresivno tumorsko mikrookolje, intrinzične lastnosti celic T, usmerjanje celic T na tumor, pripravo celičnega produkta in neželene stranske učinke povezane z imunoterapijo. Prikažemo tudi sodobne pristope za reševanje teh izzivov.

Zaključki. Imunoterapija raka s celicami CAR T predstavlja spremembo paradigme zdravljenja nekaterih krvnih rakov, ki se ne odzivajo na druge razpoložljive možnosti zdravljenja. Uhojene poti, ki so jih ubrali pionirji, so pripeljale do odobritve klinične uporabe celic CAR T, zdaj se pot nadaljuje po manj znanih stezah, ki vodijo v zdravljenje različnih vrst raka in drugih resnih bolezni s celicami CAR T.

Radiol Oncol 2022; 56(4): 420-429.
doi: 10.2478/raon-2022-0051

Ugotavljanje slikovnih perfuzijskih sprememb v onkologiji s pomočjo hiperspektralnega slikanja. Pregled literature

Hren R, Serša G, Simončič U, Milanič M

Izhodišča. Hiperspektralno slikanje je obetavna slikovnodiagnostična metoda, pri kateri uporabljamo vidno svetlobo za pridobivanje informacij o pretoku krvi. Ima izrazito prednost, ker je brezstična, neionizirajoča, neinvazivna in ni potrebno, da bi pri njej aplicirali kontrastno sredstvo. V medicini lahko hiperspektralno slikanje uporabljamo za raznovrstne namene, kot so odkrivanje različnih vrst tumorjev, vrednotenje njihovega pretoka krvi, kot tudi ocenjevanje celjenja presadkov in ran. Perfuzija tumorja je eden od pomembnejših dejavnikov v onkologiji, zato smo s sistematičnim pregledom literature ovrednotili pomen hiperspektralnega slikanja pri kvantificiranju perfuzijskih sprememb med posegi v klinični onkologiji.

Materiali in metode. V elektronskih zbirkah podatkov *PubMed* in *Web of Science* smo iskali izraza „hiperspektralno slikanje perfuzije raka“ (*angl. "hyperspectral imaging perfusion cancer"*) in „hiperspektralno slikanje pri resekciji raka“ (*angl. "hyperspectral imaging resection cancer"*). Kriterij vključitve je bila uporaba hiperspektralnega slikanja v klinični onkologiji, kar pomeni, da smo izključili vse raziskave na živalih, fantomih in *ex vivo ter* eksperimentalne, raziskovalne-razvojne in povsem metodološke raziskave.

Rezultati. Kriterijem za vključitev je ustrezalo dvajset člankov. Anatomska področja novotvorb v izbranih člankih so bile naslednja: ledvice (1 članek), dojke (2 članka), oko (1 članek), možgani (4 članki), celotna prebavila (1 članek), zgornji prebavni trakt (5 člankov) in spodnji prebavni trakt (6 člankov).

Zaključki. Hiperspektralno slikanje je obetavna slikovna metoda v klinični onkologiji, zlasti pri ocenjevanju perfuzije kožnega režnja ob rekonstruktivni operaciji po mastektomiji in pri ocenjevanju perfuzije anastomoze ob rekonstrukciji gastrointestinalnega trakta.

Radiol Oncol 2022; 56(4): 430-439.
doi: 10.2478/raon-2022-0038

Napredek v diagnostiki in obvladovanju gestacijske trofoblastne bolezni

Lukinovič N, Malovrh EP, Takač I, Sobočan M, Knez J

Izhodišča. Gestacijska trofoblastna bolezen je heterogena skupina redkih tumorjev, za katere je značilna nenormalna proliferacija trofoblastnega tkiva. Sestavljajo jo benigna ali premaligna stanja, kot so popolna in delna molarna nosečnost ter različice malignih bolezni. Maligne tumorje imenujemo gestacijska trofoblastna neoplazija. Sestavljajo jo invazivna mola, horiokarcinom, trofoblastni tumor ležišča posteljice in epiteloidni trofoblastni tumor.

Zaključki. Najpogostejši simptom gestacijske trofoblastne bolezni je krvavitev iz nožnice. Z uvajanjem ultrazvočne preiskave v obdobje zgodnje nosečnosti diagnozo molarne nosečnosti najpogosteje postavimo v prvem trimesečju nosečnosti. Mestoma lahko dodatna diagnostične preiskave, kot so rentgensko slikanje prsnega koša, CT ali MRI pomagajo odkriti metastatsko bolezen. Večino bolnic je moč pozdraviti in ohraniti njihovo reproduktivno sposobnost. V tem preglednem prispevku se osredotočamo na napredek pri obravnavi gestacijske trofoblastne bolezni ter navajamo možne prihodnje usmeritve raziskav.

Radiol Oncol 2022; 56(4): 440-452.
doi: 10.2478/raon-2022-0037

Odkrivanje in lokalizacija hiperfunkcionalnih obščitničnih žlez s PET/CT z [^{18}F]fluoroholinom in z uporabo globokega učenja. Učinkovitost modela in primerjava s človeškimi odčitovalci

Jarabek L, Jamšek J, Cuderman A, Rep S, Hočevar M, Kocjan T, Jensterle M, Špiclin Ž, Maček Ležaić Ž, Cvetko F, Ležaić L

Izhodišča. PET/CT z [^{18}F]fluoroholinom ima odlično diagnostično zmogljivost za opredeljevanje primarnega hiperparatoroidizma, kjer izkušeni odčitovalci dosegajo 97,7 % občutljivost pri odkrivanju hiperaktivnega obščitničnega tkiva. Zaradi sorazmerne enostavnosti odčitavanja smo raziskali možnost, da bi uporabili metodo globokega učenja pri odkrivanju in lokalizaciji hiperaktivnega obščitničnega tkiva na slikah PET/CT z [^{18}F]fluoroholinom pri sumu na primarni hiperparatoroidizem.

Bolniki in metode. Uporabili smo podatke 93 bolnikov s primarnim hiperparatoroidizmom, ki smo jih slikali s PET/CT z [^{18}F]fluoroholinom. Med njimi je imelo 74 bolnikov vidno prekomerno aktivno obščitnično tkivo, odkrito s PET/CT z [^{18}F]fluoroholinom v nasprotju z 19 bolniki iz kontrolne skupine. Za globoko učenje smo uporabili ustaljeni model *Resnet10* in dodatno razvili nov model *mPETResnet10* za globoko učenje, ki smo ga prilagodili naši nalogi. Oba modela sta bila naučena zaznave (prisotno/odsotno) ter lociranja kvadranta (levo zgoraj, levo spodaj, desno zgoraj, desno spodaj) prekomerno aktivnega obščitničnega tkiva. Model *mPETResnet10 je v času zaznave in lokalizacije ustvaril še masko v velikosti vhodne slike, ki smo jo poskusili kvalitativno opisati.*

Rezultati. Z modeli smo zaznali prisotnost prekomerno aktivnega obščitničnega tkiva z 83 % občutljivostjo in določili kvadrant s 74 % občutljivostjo. Modeli globokega učenja so bili statistično značilno manj občutljivi ($p < 0,001$) pri obeh nalogah v primerjavi s človeškimi odčitovalci. Kljub nejasni dodani vrednosti dobljene maske pri interpretaciji [PET/CT z [^{18}F]fluoroholinom, le-ta smiselno obriše področje zanimanja signala PET.

Zaključki. Raziskava je po našem vedenju prvi poskus analize PET/CT z [^{18}F]fluoroholinom z globokim učenjem. Pokazali smo, da je možno uporabiti modele globokega učenja pri PET/CT z [^{18}F]fluoroholinom za odkrivanje in lociranje prekomerno aktivnega obščitničnega tkiva. Glede na majhen nabor podatkov so rezultati obetavni za nadaljnje raziskovanje.

RadiolOncol 2022; 56(4): 453-460.
doi: 10.2478/raon-2022-0042

FDG PET/CT kot pomembno diagnostično orodje in napovedni označevalec pri sumu na ponavljajoči se rak materničnega vratu po obsevanju. Primerjava z MR

Stojiljković M, Sobić Šaranović D, Odalović S, Popović M, Petrović J, Ranković N, Veljković M, Artiko V

Izhodišča. Ponavljajoči se rak materničnega vratu po obsevanju pogosto težko prepoznamo na slikanju z magnetno resonanco (MR). Spremembe po zdravljenju imajo namreč podoben videz in jih moramo pogosto bolj podrobno analizirati. Cilji raziskave so bili oceniti diagnostično vrednost pozitronske emisijske tomografije / računalniške tomografije z 18F-fluorodeoksiglukozo (FDG PET-CT) pri sumu na ponovitev raka materničnega vratu po obsevanju in jo primerjati z MRI ter oceniti pomembnost FDG PET-CT kot napovednega dejavnika za potek bolezni.

Pacienti in metode. V retrospektivno raziskavo smo vključili bolnice, ki smo jih predhodno zdravili z obsevanjem zaradi raka materničnega vratu in smo sumili na ponovitev bolezni. Pri vseh bolnicah smo naredili MR trebuha in medenice ter nato stanje ovrednotili s FDG PET/CT. Spremljali smo jih najmanj 12 mesecev.

Rezultati. Pri 84 bolnicah, ki smo jih vključili v raziskavo, je MR pokazala občutljivost, specifičnost in natančnost 80,1 %, 52,4 % in 66,7 %; FDG PET/CT pa 97,6 %, 61,9 % in 79,8 %. Bolnice s pozitivnimi izvidi MR (test *log rank*, p = 0,003) in PET/CT (test *log rank*, p < 0,001) so imele krajše preživetje brez napredovanja bolezni kot tiste z negativnim izvidom. V univariatnih Coxovih regresijskih modelih smo ugotovili, da so rezultati MR in FDG PET/CT povezani s preživetjem brez napredovanja bolezni (p = 0,005 oziroma p < 0,001). V multivariatni analizi pa smo dokazali, da je le FDG PET/CT neodvisen napovedni dejavnik, saj so imele bolnice s pozitivnimi rezultati FDG PET/CT skoraj devetkrat večje tveganje za napredovanje bolezni (p < 0,001).

Zaključki. Raziskava je pokazala, da je FDG PET-CT uporabno diagnostično orodje pri sumu na ponovitev raka materničnega vratu po obsevanju in kaže visoko občutljivost pri njegovem odkrivanju. Poleg tega predstavlja neodvisen napovedni dejavnik preživetja brez napredovanja bolezni pri bolnicah s ponovitvijo raka materničnega vratu.

Radiol Oncol 2022; 56(4): 461-470.
doi: 10.2478/raon-2022-0036

Diagnostična učinkovitost tomosinteze, digitalne mamografije in namenskega digitalnega sistema radiografije v primerjavi s patomorfološko oceno izrezanih lezij v dojki

Almasarweh S, Sudah M, Okuma H, Joukainen S, Kärjä V, Vanninen R, Masarwah A

Izhodišča. Namen raziskave je bil ocena uspešnosti intraoperativne digitalne mamografije z obsegom celotnega polja, digitalne tomosinteze dojke in namenskega digitalnega sistema radiografije pri zaporedno izbranih bolnicah glede na patomorfolopške ocene reseciranih lezij.

Bolnice in medtode. Resecirane tkivne vzorce zaporednih bolnic, pri katerih smo naredili široko lokalno ekscizijo lezije ali onkološko plastično konzervativno operacijo dojke, smo intraoperativno ocenili z digitalno mamografijo z obsegom celotnega polja, tomosintezo in z namenskim digitalnim sistemom radiografije. Dva neodvisna ocenjevalca sta retrospektivno ocenila vidnost lezije, njeno velikost, robove, spikulacije, kalcifikacije in diagnostično vrednost ter izbrala najboljšo izvajalsko metodo na slep način, brez vednosti kliničnih in patomorfoloških podatkov.

Rezultati. Ovrednotili smo 216 vzorcev pri 204 bolnicah. Pri maligne lezijah nismo odkrili robov, ki bi segali v zdravo tkivo. En papilom je imel pozitivne mikroskopske robove in eno bolnico smo reoperirali zaradi obsežne komponente *in situ*. Med tremi metodami ni bilo pomembnih razlik v izmerjeni velikosti lezije. Glede na preostale slikovnodiagnostične pokazatelje pa se je tomosinteza pokazala kot najbolj natančna uporabljena metoda ob upoštevanju patomorfološkega izvida. Oba ocenjevalca sta poročala, da tomositeza omogoča bistveno boljšo vidljivost lezije kot obe drugi metodi, kar je pomenilo bistveno večjo diagnostično vrednost. Prav tako je omogočila večjo prepoznavanje spikulacij in kalcifikacij. Oba ocenjevalca sta poročala, da je bila tomosinteza najboljša metoda v 76,9 % primerov. Ponovljivost ocene vidljivosti lezije glede na ocenjevalca je bila zelo visoka pri vseh treh diagnostičnih metodah.

Zaključki. Tomosinteza se je v raziskavi pokazala bolj učinkovita intraoperativna metoda kot sta digitalna mamografija z obsegom celotnega polja in namenski digitalni sistem radiografije pri odkrivanju in ocenjevanju tumorskih lezij, spikulacij in kalcifikacij ter je bila zato bolj zanesljiva za oceno popolne ekscizije lezije v dojki.

Radiol Oncol 2022; 56(4): 471-478.
doi: 10.2478/raon-2022-0040

Ocena zanesljivosti standardizirane ultrazvočne metode za zaznavo zgodnje hemofilne artropatije (HEAD-US) pri otrocih. Primerjava z magnetno resonančnim slikanjem

Plut D, Faganel Kotnik B, Pušnik L, Slak P, Snoj Ž, Salapura V

Izhodišča. Ultrazvok (UZ) se je v zadnjih letih uveljavil kot zanesljiva diagnostična metoda za prepoznavo zgodnje hemofilne artropatije pri odraslih bolnikih s hemofilijo, o njegovi uporabi pri otrocih s hemofilijo pa je malo podatkov. Zanimalo nas je, ali spreminjajoč ultrazvočni videz kosti v obdobju rasti pri otrocih ovira zmožnost UZ za oceno prisotnosti in stopnje izraženosti hemofilne artropatije. Cilj raziskave je bil oceniti zanesljivost UZ za oceno hemofilne artropatije pri otrocih s hemofilijo v primerjavi s slikanjem z magnetno resonanco (MR).

Bolniki in metode. V raziskavo smo vključili vse otroke s hudo obliko hemofilije v Sloveniji, ki so starejši od 6 let (n = 10). Pri bolnikih smo z UZ ocenili komolce, kolena in gležnje ter rezultate primerjali z MR. Korelacijo med UZ in MR oceno smo izračunali s pomočjo Pearsonovega korelacijskega koeficienta (r).

Rezultati. Korelacija med UZ in MR ocenami je bila visoka pri ocenah vseh treh sklepov (r = 0.849 za komolce, r = 1 za kolena, r = 0.842 za gležnje). Korelacija pri ocenah posameznih komponent sklepov (sinovija, sklepni hrustanec, kostnina) je bila srednja, visoka ali zelo visoka za vse komponente vseh sklepov. Najnižjo korelacijo smo opazili pri oceni hrustanca in kostnine gležnja (r = 0.546 in r = 0.478) ter pri oceni kostnine komolca (r = 0.499).

Zaključki. Rezultati raziskave kažejo, da je ocena sklepov z UZ po metodi HEAD-US pri otrocih s hemofilijo zanesljiva za oceno hemofilne artropatije in visoko korelira z izsledki MR slikanja.

Radiol Oncol 2022; 56(4): 479-487.
doi: 10.2478/raon-2022-0047

Z MRI ugotovljene večdimenzionalne značilnosti bezgavk, ki napovedujejo preživetje in dobrobit sočasne kemoterapije pri raku nazofarinksa II. stadija

Liu Y, Zhang J, Wang J, Wu J, Huang X, Wang K, Qu Y, Chen X, Li Y, Zhang Y, Yi J

Izhodišča. Neizogibno potrebujemo zanesljive napovedne kazalce za prepoznavanje bolnikov z nazofaringealnim rakom II. stadija, ki bi jim lahko koristila sočasna kemoradioterapija. Cilj raziskave je bil razviti nomogram, ki bi vključeval večdimenzionalne značilnosti bezgavk, zaznanih z MRI, za napoved preživetja in za pomoč pri odločanju za sočasno kemoradioterapijo pri nazofaringealnem raku II. stadija.

Bolniki in metode. V retrospektivno raziskavo smo vključili 242 bolnikov z nazofaringealnim rakom II. stadija, ki smo jih zdravili od januarja 2007 do decembra 2017. Primarni opazovani dogodek je bilo celokupno preživetje. Natančnost nomograma smo ovrednotili z uporabo umeritvenih krivulj, Harrellovega indeksa skladnosti (C-indeks), površine pod krivuljo (*angl. area under the curve*, AUC) in analize krivulj odločitve (*angl. decision curves analysis*, DCA) ter primerjanjem s stadijem TNM. V skladu z individualizirano oceno nomograma smo bolnike razvrstili v dve kohorti tveganja in v vsaki kohorti ovrednotili terapevtsko učinkovitost sočasne kemoradioterapije.

Rezultati. V končni nomogram smo vključili tri neodvisne napovedne kazalce za celokupno preživetje: starost ter število in lokacija pozitivnih bezgavk. Stadij T smo tudi vključili zaradi njegovega pomena pri kliničnem odločanju. Umeritvene krivulje so pokazale dobro ujemanje med napovednimi in opazovanimi stopnjami celokupnega preživetja. C-indeks za nomogram je bil 0,726, za stadij TNM pa 0,537 ($p < 0,001$). DCA je potrjevala večjo klinično uporabnost nomogramov v primerjavi s stadijem TNM. V skupini z visokim tveganjem je bilo celokupno preživetje boljše po sočasni kemoradioterapije kot po intenzivno modulirajoči radioterapiji (IMRT) (po 5-letih: 89,9 % v primerjavi s 72,1 %; po 10-letih: 72,5 % v primerjavi s 34,2 %, $p = 0,011$); te dobrobiti pa ni bilo v skupini z nizkim tveganjem.

Zaključki. Opisani nomogram, ki je temeljil na značilnostih bezgavk, je pokazal odlično razločitveno zmožnost in napovedno natančnost pri bolnikih z II. stadije bolezni in je prepoznal tiste, ki jim lahko koristi sočasna kemoradioterapija.

Radiol Oncol 2022; 56(4): 488-500.
doi: 10.2478/raon-2022-0050

Vpliv epidemije COVID-19 na breme raka in njegovo obravnavo v Sloveniji. Nadaljevanje raziskave

Žagar T, Tomšič S, Zadnik V, Bric N, Birk M, Vurzer B, Mihor A, Lokar K, Oblak I

Izhodišča. V Sloveniji so bile v odlokih vlade, namenjenim obvladovanju epidemije COVID-19, onkološke dejavnosti navedene kot izjema. Obvladovanje raka pa je odvisno tudi od drugih zdravstvenih storitev in spremenjeno vedenje ljudi dodatno vplivajo na breme raka. V pričujoči raziskavi smo analizirali spremembe v bremenu raka in njegovi obravnavi po prvem valu epidemije.

Materiali in metode. Analizirali smo tri vire rutinsko zbranih podatkov za obdobje od januarja 2019 do julija 2022: (1) patohistološke izvide in klinične obravnave iz dveh večjih onkoloških centrov v Ljubljani in Mariboru (vir: Register raka Republike Slovenije); (2) napotnice izdane za onkološke storitve (vir: sistem e-Napotnica); in (3) ambulantne obiske in diagnostične slikovne preiskave (vir: administrativni podatki Onkološkega inštituta Ljubljana, OIL). Dodatno smo na podlagi podatkov Bolnišničnega registra raka OIL analizirali spremembe nekaterih značilnosti pri onkoloških bolnikih, diagnosticiranih in zdravljenih med epidemijo (obdobje 2015–2021).

Rezultati. V juniju, juliju in avgustu 2020 se je povečalo število napotitev na kontrolne onkološke preglede, ki pa niso nadoknadili padca v prvem valu epidemije; številke pa so bile v letih 2021 in 2022 manjše kot v letu 2020. Povpraševanje po prvih onkoloških pregledih ter genetskem testiranju in svetovanju se je v letu 2021 povečalo v primerjavi z letom 2019, v letu 2022 pa še dodatno za več kot četrtino. Prvi in kontrolni ambulantni obiski ter diagnostične slikovne preiskave na OIL so se ob začetku epidemije marca 2020 zmanjšali, vendar so bile številke primerljive z obdobjem pred epidemijo že v letu 2021. Nekateri primanjkljaji ostajajo pri kontrolnih ambulantnih obiskih na kirurških in radioterapevtskih oddelkih. V obdobju COVID-19 je bilo opravljenih več pregledov CT, MRI in PET-CT kot prej. Število novih diagnoz raka se je v vseh opazovanih letih 2020, 2021 in do julija 2022 zmanjšalo za 6 %, 3 % oziroma 8 %, odvisno od vrste raka. Največji padec je bil opažen v starostni skupini 50–64 let (skoraj 14 % v 2020 in 16 % v 2021), pri bolnikih, starejših od 80 let, pa so bile številke nad pričakovanji (4 % več primerov v 2020 in 8 % v 2021).

Zaključki. Rezultati kažejo na različen učinek epidemije COVID-19 v Sloveniji za različne vrste raka in na različnih ravneh poti oskrbe pacienta – verjetno gre za preplet vedenjskih sprememb posameznikov in sistemskih sprememb v organizaciji zdravstvenega varstva. Splošno zmanjšanje števila novih primerov raka odseva omejitve v diagnostiki in bi lahko imelo resne dolgoročne posledice na kazalnike bremena raka.

Radiol Oncol 2022; 56(4): 501-507.
doi: 10.2478/raon-2022-0043

Plazemske koncentracije sICAM-1 korelirajo z volumnom ploščatoceličnih tumorjev glave in vratu pred zdravljenjem z radiokemoterapijo

Clasen K, Welz S, Faltin H, Zips D, Eckert F

Izhodišča. Biološki označevalci so zelo pomembni za optimizacijo diagnoze, napovedi poteka bolezni in usmerjanja zdravljenja pri bolnikih z rakom glave in vratu. Zlasti krvni označevalci se zdijo obetavni, saj jih je mogoče enostavno pridobiti in večkrat analizirati med radiokemoterapijo.

Bolniki in metode. Najprej smo zaradi širšega vpogleda odvzeli šest vzorcev plazme pri treh bolnikih na začetku in koncu radiokemoterapije ter ocenili več imunskih označevalcev. Pri tem predizboru se je kot najbolj obetaven pokazal topen medcelični adhezijski označevalec 1 (sICAM-1). Zato smo ga izmerili v več vzorcih (n = 86) med zdravljenjem in nadaljnjim spremljanjem kohorte enajstih bolnikov ter ga primerjali z značilnostmi tumorja in kliničnimi podatki.

Rezultati. Ugotovili smo močno povezanost med začetnimi ravnmi sICAM-1 v plazmi ter makroskopskim tumorskim volumnom (*angl. gross tumor volume,* GTV) in prizadetimi bezgavkami. Med zdravljenjem pa ni bilo mogoče ugotoviti skladne dinamike. Nismo ugotovili, da bi toksičnost ali okužbe vplivali na koncentracije sICAM-1.

Zaključki. V raziskavi se je sICAM-1 pokazal povezan s celotnim tumorskim bremenom pred zdravljenjem (primarnim tumorjem in prizadetimi bezgavkami) pri bolnikih s tumorji glave in vratu. Ni pa se pokazal kot označevalec stopnje odgovora na zdravljenje med radiokemoterapijo. Če se bodo ugotovitve raziskave v prihodnosti potrdile, bi lahko sICAM-1 uporabljali pri določanju stadija bolezni. Ob visoki vrednosti sICAM-1, vendar majhnem tumorskem bremenu, bi bilo smiselno razširiti preiskave za določanje stadija, da bi odkrili morebitna dodatna, še neodkrita mesta tumorja.

Radiol Oncol 2022; 56(4): 508-514.
doi: 10.2478/raon-2022-0035

Tekočinska optimizacija s kristaloidi ali koloidi pri bolnikih, operiranih zaradi možganskega tumorja

Markovič-Božič J, Visočnik B, Mušič P, Potočnik I, Spindler Vesel A

Izhodišča. V dvojno slepi, randomizirani raziskavi, ki smo jo naredili v Univerzitetnem kliničnem centru Ljubljana, smo proučevali vpliv tekočinske optimizacije s kristaloidi ali koloidi na pojav perioperativnih zapletov pri bolnikih, operiranih zaradi možganskega tumorja. Namen raziskave je bil ugotoviti vpliv vrste tekočine na pojav perioperativnih zapletov.

Bolniki in metode. 80 bolnikov, vključenih v raziskavo, smo razdelili v dve skupini. V prvi smo za tekočinsko optimizacijo uporabili kristaloide (n = 40), v drugi pa koloide (n = 40). Srednji arterijski tlak in možgansko oksigenacijo smo vzdrževali na izhodiščnih vrednostih ± 20 %, nihanje utripnega volumna pa ≤ 10 % z invazivnim hemodinamskim nadzorom. Pojav perioperativnih zapletov smo opazovali prvih petnajst dni po operaciji. Beležili smo tudi čas hospitalizacije.

Rezultati. Skupina, ki je dobila kristaloide, je prejela signifikantno več tekočin (p = 0,003) in fenilefrina (p = 0,02) kot skupina, ki je prejela koloide. Kljub temu med skupinama nismo opazili statistično pomembnih razlik v pojavu perioperativnih zapletov in času hospitalizacije.

Zaključki. Pri operacijah možganskih tumorjev lahko za medoperativno tekočinsko optimizacijo uporabimo tako kristaloide kot koloide. Z uporabo protokola za vzdrževanje perioperativnih hemodinamskih vrednosti vrsta tekočine ne vpliva na izid zdravljenja.

Radiol Oncol 2022; 56(4): 515-524.
doi: 10.2478/raon-2022-0053

Radioterapija s stopnjevanjem doze in hkratnim integriranim dodatnim obsevanjem kostnih metastaz pri izbranih bolnikih s predvidenim ugodnim potekom bolezni

Potkrajčič V, Mueller AC, Frey B, Gani C, Zips D, Hoffmann R, Frantz S, Warm V, Paulsen F, Eckert F

Izhodišča. Pri bolnikih s kostnimi metastazami, kjer je bolezen oligometastatska ali oligoprogresivna, vse pogosteje uporabljamo stereotaktično telesno radioterapijo (*angl. stereotactic body radiotherapy*, SBRT) s stopnjevano dozo obsevanja. Metastaze, ki niso primerne za SBRT, lahko zdravimo s 30/40 Gy v 10 frakcijah in uporabimo hkratno integrirano obsevanje (*angl. simultaneous integrated boost*, SIB). Namen raziskave je bil oceniti izvedljivost takšnega zdravljenja ter akutno in subakutno toksičnost.

Bolniki in metode. Retrospektivno smo pregledali klinične zapise zaporednih bolnikov, ki smo jih zdravili s stopnjevano radioterapevtsko dozo (24 bolnikov z 28 tarčnimi volumni za oceno onkološkega učinka in 25 bolnikov z 29 tarčnimi volumni za oceno izvedljivosti zdravljenja in analizo doznih parametrov). Analiza radioterapevtskih načrtov je vključevala velikost tarčnih volumnov ter dozimetrične parametre za tarčne volumne in ogrožene organe (*angl. organs at risk*, OAR). Akutna in subakutna toksičnost je bila ocenjena po mednarodni lestvici za neželene dogodke CTCAE V4.0.

Rezultati. Najpogostejša lokalizacija bolezni je bila hrbtenica (71,4 %); najpogostejša histološka vrsta pa rak prostate (45,8 %). Oligometastitična ali oligoprogresivna bolezen je bila indikacija za radioterapija s stopnjevano dozo pri 19/24 bolnikih (79.2 %). Zdravljenje je bilo za bolnike sprejemljivo, saj so vsi zaključili obsevanje. Akutno toksičnost 1. stopnje smo zabeležili pri 36 % bolnikov. V času sledenja bolezni smo enega bolnika napotili na operacijo zaradi kostne nestabilnosti. Lokalna kontrola in preživetje brez napredovanja bolezni po enem letu sta bila 90,0 ± 6,7 % in 33,3 ± 11,6 %.

Zaključki. Hipofrakcionirana radioterapija s stopnjevanjem doze in hkratnim integriranim obsevanjem pri kostnih metastazah omogoči dobro lokalno kontrolo bolezni ob omejeni akutni toksičnosti. Samo en bolnik je potreboval kirurški poseg. Pri izbranih bolnikih tak način obsevanja predstavlja alternativo SBRT.

Radiol Oncol 2022; 56(4): 525-534.
doi: 10.2478/raon-2022-0046

Kvantifikacija sprememb v tumorskem žilnem mikrookolju pri zasevkih v hrbtenici, zdravljenih s stereotaktično radioterapijo. Enotirna prospektivna raziskava

Vellayappan B, Cheong D, Singbal S, Tey J, Soon YY, Leong CN, Wong A, Lwin S, Lee CH, Periasamy P, Lo S, Kumar N

Izhodišča. Primarni cilj raziskave je bil količinsko opredeliti spremembe v žilnem mikrookolju pri bolnikih z metastazami v hrbtenici, ki smo jih zdravili s stereotaktičnim obsevanjem (*angl. stereotactic body radiotherapy*, SBRT) in kjer smo uporabili večparametrično magnetnoresonančno slikanje (MRI) z dinamičnim kontrastom (*angl. dynamic contrast enhanced*, DCE). Sekundarni cilj je bil preučiti plazemska biološka označevalca, povezane z endotelijsko apoptozo.

Bolniki in metode. Bolnike smo slikali z DCE-MRI pred zdravljenjem, 1 teden po- in 12 tednov po SBRT. Merili smo normalizirano časovno odvisno puščanje (*angl. normalised time-dependent leakage*, Ktrans), produkt površine prepustnosti (*angl. permeability surface product*, PS), frakcijski volumen plazme (*angl. fractional plasma volume*, Vp), zunajceličnim volumen *(angl. extracellular volume,* Ve) in perfuzijo (F). Uporabili smo model porazdeljenih parametrov. Serumsko kislo sfingomielinazo (ASM) in sfingozin-1-fosfat (S1P) smo kvantificirali z metodo ELISA. Beležili smo klinični potek bolezni, vključno s toksičnostjo, ki jo je ocenil zdravnik, in toksičnostjo, o kateri je poročal bolnik.

Rezultati. V raziskavo smo vključili 12 bolnikov (z različno primarno histologijo), deset od njih smo zdravili s SBRT. Pri devetih bolnikih (z desetimi lezijami) smo opravili vsa tri načrtovana slikanja. En bolnik je umrl zaradi pljučnice (ni bilo povezano z zdravljenjem), preden smo naredili vsa slikanja. Srednja vrednost obsevalne doze SBRT je bila 27 Gy (razpon 24–27 Gy) v treh frakcijah (razpon 2–3 frakcije). Srednja vrednost spremljanja bolnikov je bila 42 mesecev (razpon 22,3–54,3 mesecev), zabeležili smo 90-odstotno lokalno kontrolo in eno toksičnost stopnje 2 ali višjo (kompresijski zlom vretenc). Pri vseh parametrih (Ktrans/PS/Vp/Ve/F) smo ugotovili težnjo zmanjševanja vrednosti po 12 tednih. Ktrans in PS sta se zmanjšala že v enem tednu. Ve/Vp/F so se en teden po SBRT rahlo povečali, nato pa se zmanjšali pod izhodiščno vrednost. Biološka označevalca v plazmi (ASM/S1P) se po SBRT nista bistveno spremenila.

Zaključki. Tumorsko žilno mikrookolje je pokazalo težnjo zmanjševanja merjenih parametrov po SBRT. Menimo, da z žilami posredovano uničevanje celic prispeva k odlični stopnji lokalne kontrole pri SBRT. V prihodnjih raziskavah bo potrebno oceniti učinek SBRT na metastaze v hrbtenici določenih rakov (npr. pri ledvičnem raku).

Radiol Oncol 2022; 56(4): 535-540.
doi: 10.2478/raon-2022-0041

Miksomi srca. Izkušnje največjega slovenskega terciarnega centra

Kačar P, Pavšič N, Bervar M, Dolenc Stražar Z, Zadnik V, Jelenc M, Prokšelj K

Izhodišča. Miksomi so najpogostejši primarni tumorji srca. Čeprav so redki in benigni, lahko povzročajo življenje ogrožajoče zaplete kot so embolizacija ali obstrukcija mitralnega ustja. Kirurška odstranitev tumorja je metoda izbora zdravljenja. Z raziskavi smo želeli oceniti epidemiološke značilnosti, klinično sliko, slikovne značilnosti in uspeh kirurškega zdravljenja bolnikov z miksomom srca, ki so bili obravnavani v največjem slovenskem terciarnem centru.

Bolniki in metode. V retrospektivno analizo smo vključili 39 bolnikov s patohistološko potrjenim miksomom, ki so bili napoteni v naš center med januarjem 2005 in decembrom 2020.

Rezultati. Povprečna letna incidenca miksomov je bila 3 na 2 milijona prebivalcev. Več je bilo žensk (n = 25; 64 %). Povprečna starost ob diagnozi je bila 63,1 ± 13,6 let. Najpogostejši simptom je bila dispneja (n = 12; 31 %). V enajstih primerih (28 %) je bil miksom naključna najdba. Sedem bolnikov je utrpelo embolične zaplete (18 %). Dvaindvajset bolnikov (56 %) je imelo poleg transtorakalne ultrazvočne preiskave opravljeno še dodatno slikovno diagnostiko. Vsi bolniki so bili zdravljeni kirurško, peri-operativnih smrti nismo beležili. V času sledenja (od 6 mesecev do 16 let) nismo ugotovili ponovitve miksoma. Umrli so trije bolniki (8 %), vendar smrti niso bile posledica miksoma.

Zaključki. Miksom je redek srčni tumor, ki povzroča raznoliko klinično sliko. Naši podatki kažejo nekoliko višjo prevalenco miksoma v populaciji v primerjavi z do sedaj objavljenimi rezultati. Kirurška odstranitev miksoma je varen način zdravljenja z odličnimi kratkoročnimi in dolgoročnimi izidi.

Radiol Oncol 2022; 56(4): 541-551.
doi: 10.2478/raon-2022-0039

Razvoj računalniškega modela fantoma noseče ženske in izračun doze na zarodek pri fotonski radioterapiji dojke

Kopačin V, Kasabašić M, Faj D, de Saint Hubert M, Galić S, Ivković A, Majer M, Brkić H

Izhodišča. Incidenca rakov med nosečnostjo je 1:1000 – 1:1500, med njimi je najpogostejši rak dojk. Zarodek je najbolj občutljiv na ionizirajoče sevanje v prvih šestih mesecih nosečnosti, vendar pa ob različnih kliničnih pogledih še ni sprejetih enotnih smernic o uporabi radioterapije med nosečnostjo. V pričujoči raziskavi smo razvili fantom noseče ženske v drugem trimestru nosečnosti, ki ga lahko uporabljamo za načrtovanje obsevanja (kot podatke DICOM), za simulacije Monte Carlo (vokselizirana geometrija fantoma) in za eksperimentalno dozimetrijo z uporabo tiska 3D.

Materiali in metode. Fantom, ki smo ga razvili, temelji na MR slikah ženske v 18. tednu nosečnosti in na CT slikah po rojstvu otroka. Za zdravljenje raka leve dojke smo uporabili 3D konformno radioterapijo, za Monte Carlo simulacije s kodo MCNP (*angl. Monte Carlo N-Particle transport code*™ 6.2) pa vokselizirano geometrijo fantoma.

Zaključki. Izdelan obsevalni načrt za zdravljenje raka dojke, ki smo ga uporabili na fantomu, je pokazal, da ob skupni predpisani dozi 50 Gy prejme zarodek 59 mGy. Rezultati tudi jasno kažejo, da je prispevek fotonov, ki so ustvarjeni v glavi pospeševalnika (sipanje in puščanje), zgolj 9,5 % celotne doze na zarodek; prevladujoč je prispevek sipanega sevanja, ki nastane v telesu bolnice.

Fundacija "Docent dr. J. Cholewa"
je neprofitno, neinstitucionalno in nestrankarsko
združenje posameznikov, ustanov in organizacij, ki želijo
materialno spodbujati in poglabljati raziskovalno
dejavnost v onkologiji.

Dunajska 106
1000 Ljubljana
IBAN: SI56 0203 3001 7879 431

Zdravilo LUMYKRAS®▼ - prvo tarčno zdravljenje za bolnike z mutacijo KRAS G12C[1]

Peroralni zaviralec je kot monoterapija indiciran za zdravljenje bolnikov z napredovalim nedrobnoceličnim rakom pljuč (NDRP) z mutacijo KRAS G12C, pri katerih je bolezen napredovala po vsaj eni predhodni liniji sistemskega zdravljenja.[2]

80,6 %

UČINKOVITO:
stopnja nadzora nad boleznijo je 80,6 %[3]

1,4 meseca

DELUJE HITRO:
deluje že v 1,4 meseca[3]

12,5 meseca

NUDI DOLGOTRAJEN ODGOVOR:
mediana celokupnega preživetja je 12,5 meseca[3]

TARČNO ZDRAVILO:
1x dnevno jemanje in dobro prenašanje zdravila[3]

Literatura: 1. Mullard A, et al. Nat Rev Drug Discov 2021;20:496. 2. Povzetek glavnih značilnosti zdravila LUMYKRAS®, Amgen. 3. Skoulidis F, et al. N Engl J Med 2021;384:2371–81.

LUMYKRAS® 120 mg filmsko obložene tablete (sotorasib)
SKRAJŠAN POVZETEK GLAVNIH ZNAČILNOSTI ZDRAVILA
Samo za strokovno javnost. Pred predpisovanjem si preberite celoten Povzetek glavnih značilnosti zdravila.
▼Za to zdravilo se izvaja dodatno spremljanje varnosti. Poročati je potrebno o vseh domnevnih neželenih učinkih zdravila.

SESTAVA ZDRAVILA: Ena filmsko obložena tableta vsebuje 120 mg sotorasiba. **TERAPEVTSKE INDIKACIJE:** Kot monoterapija za zdravljenje odraslih z napredovalim nedrobnoceličnim rakom pljuč (NDRP) z mutacijo *KRAS G12C*, pri katerih je bolezen napredovala po vsaj eni predhodni liniji sistemskega zdravljenja. **ODMERJANJE IN NAČIN UPORABE:** Zdravljenje mora uvesti zdravnik, ki ima izkušnje z uporabo zdravil za zdravljenje raka. Pred uvedbo zdravljenja je treba z validiranim testom potrditi prisotnost mutacije *KRAS G12C*. Odmerjanje: Priporočeni odmerek je 960 mg sotorasiba (osem 120mg tablet) enkrat dnevno, vsak dan ob istem času. Zdravljenje se priporoča do napredovanja bolezni ali pojava nesprejemljive toksičnosti. *Izpuščeni odmerki ali bruhanje:* Če je od načrtovanega odmerka preteklo manj kot 6 ur, mora bolnik vzeti odmerek kot običajno. Če je od načrtovanega odmerka preteklo več kot 6 ur, bolnik ne sme vzeti odmerka. Zdravljenje mora nadaljevati naslednji dan, kot je prepisano. Če bolnik po zaužitju zdravila LUMYKRAS bruha, tisti dan ne sme vzeti dodatnega odmerka in mora zdravljenje nadaljevati naslednji dan, kot je predpisano. *Prilagajanje odmerka:* Odmerjanje je treba prilagajati glede na toksičnost zdravila LUMYKRAS. Za stopnje zmanjšanja odmerka in prilagoditve odmerka zaradi neželenih učinkov med zdravljenjem glejte celoten Povzetek glavnih značilnosti zdravila. Če se pojavijo toksični učinki, je odmerek dovoljeno zmanjšati največ dvakrat. Če bolniki ne prenašajo najmanjšega odmerka, tj. 240 mg enkrat dnevno, je treba zdravljenje z zdravilom LUMYKRAS prekiniti. Sočasna uporaba zdravila LUMYKRAS z zdravili za zmanjševanje kisline: Sočasna uporaba zaviralcev protonske črpalke (PPI) ali antagonistov receptorjev H2 z zdravilom LUMYKRAS ni priporočena. Če je potrebno zdravljenje z zdravilom za zmanjševanje kisline, se lahko uporabi nesistemski antacid, zdravilo LUMYKRAS pa je treba vzeti bodisi 4 ure pred uporabo nesistemskega antacida bodisi 10 ur po njem. Posebne populacije: Pri bolnikih, starih 75 let in več, prilagajanje odmerka ni potrebno. Prilagajanje odmerka pri bolnikih z blago okvaro jeter ni priporočeno. Uporaba sotorasiba pri bolnikih z zmerno in hudo okvaro jeter ni priporočena. Prilagajanje odmerka pri bolnikih z blago okvaro ledvic (CrCl ≥ 60 ml/min) ni priporočeno. Zdravila LUMYKRAS pri bolnikih z zmerno ali hudo okvaro ledvic (CrCl < 60 ml/min) niso preučevali. Pri zdravljenju bolnikov z zmerno ali hudo okvaro in končno odpovedjo ledvic je zato potrebna previdnost. Zdravilo LUMYKRAS ni namenjeno za uporabo pri pediatrični populaciji za zdravljenje nedrobnoceličnega raka pljuč. Način uporabe: Zdravilo LUMYKRAS je namenjeno za peroralno uporabo. Tablete je treba pogoltniti cele. Ni podatkov, ki bi podpirali jemanje zdravila LUMYKRAS tako, da se tablete zveči, zdrobi ali razpolovi, vendar je tablete mogoče raztopiti v vodi. Tablete se lahko jemljejo s hrano ali brez nje. Za uporabo pri bolnikih, ki težko pogoltnejo zdravila v trdni obliki glejte celoten Povzetek glavnih značilnosti zdravila. **KONTRAINDIKACIJE:** Preobčutljivost na učinkovino ali katero koli pomožno snov. **POSEBNA OPOZORILA IN PREVIDNOSTNI UKREPI:** Hepatotoksičnost: Sotorasib lahko povzroči hepatotoksičnost, ki lahko privede do z zdravilom povzročene poškodbe jeter in hepatitisa. Sotorasib je bil povezan s prehodnimi zvišanji ravni transaminaz (ALT in AST) v serumu. Zvišane ravni so se izboljšale ali izvenele po prilagoditvi odmerka ali trajni prekinitvi zdravljenja in v kliničnih študijah niso privedle do primerov odpovedi jeter ali smrtnih primerov. Pri bolnikih je treba spremljati delovanje jeter (ALT, AST in celokupni bilirubin), in sicer pred začetkom zdravljenja z zdravilom LUMYKRAS, nato v prvih 3 mesecih zdravljenja vsake 3 tedne, nato pa enkrat mesečno ali kot je klinično indicirano, preiskave pa je treba opravljati pogosteje pri bolnikih, pri katerih se pojavijo zvišanja ravni transaminaz in/ali bilirubina. Glede na stopnjo resnosti nenormalnih izvidov laboratorijskih preiskav je treba zdravljenje z zdravilom LUMYKRAS prekiniti do izboljšanja na stopnjo ≤ 1 ali na izhodiščno stopnjo ter v skladu s priporočili bodisi prilagoditi odmerek bodisi trajno prekiniti zdravljenje. Intersticijska pljučna bolezen (ILD)/pnevmonitis: Bolnike spremljajte za pojav novih ali poslabšanje obstoječih pljučnih simptomov, ki bi kazali na ILD/pnevmonitis (npr. dispneja, kašelj, vročina). Nemudoma prekinite zdravljenje z zdravilom LUMYKRAS pri bolnikih z domnevno ILD/pnevmonitisom in trajno prekinite zdravljenje z zdravilom LUMYKRAS, če ne odkrijete nobenih drugih morebitnih vzrokov za ILD/pnevmonitis. Intoleranca za laktozo: Zdravilo LUMYKRAS vsebuje laktozo. Bolniki z redko dedno intoleranco za galaktozo, odsotnostjo encima laktaze ali malabsorpcijo glukoze/galaktoze ne smejo jemati tega zdravila. Natrij: To zdravilo vsebuje manj kot 1 mmol (23 mg) natrija na tableto, kar v bistvu pomeni „brez natrija". **INTERAKCIJE:** Vpliv drugih zdravil na sotorasib: Sočasna uporaba sotorasiba s PPI (omeprazolom) ali antagonistom receptorjev H2 (famotidinom) je privedla do zmanjšanja koncentracij sotorasiba. Sočasna uporaba PPI in antagonistov receptorjev H2 z zdravilom LUMYKRAS ni priporočena, saj ni znano, kakšen bi bil vpliv na učinkovitost sotorasiba. Če je potrebno zdravljenje z zdravilom za zmanjševanje kisline, je zdravilo LUMYKRAS treba vzeti 4 ure pred uporabo nesistemskega antacida ali 10 ur po njem. Sočasna uporaba večkratnih odmerkov itrakonazola (močnega zaviralca CYP3A4 in Pgp) ni povečala izpostavljenosti sotorasibu v klinično pomembnem obsegu. Prilagoditev odmerka zdravila LUMYKRAS pri sočasni uporabi z zaviralci CYP3A4 ni priporočena. Sočasna uporaba močnih induktorjev CYP3A4 (npr. rifampicina, karbamazepina, enzalutamida, mitotana, fenitoina in šentjanževke) z zdravilom LUMYKRAS ni priporočena, saj lahko ta zdravila zmanjšajo izpostavljenost sotorasibu. Vpliv sotorasiba na druga zdravila: Sotorasib je zmeren induktor CYP3A4. Sočasna uporaba sotorasiba s substrati CYP3A4 je privedla do zmanjšanja njihovih plazemskih koncentracij, kar bi lahko zmanjšalo učinkovitost teh substratov. Izogibajte se sočasni uporabi zdravila LUMYKRAS s substrati CYP3A4 z ozkimi terapevtskimi indeksi, ki med drugim vključujejo alfentanil, ciklosporin, dihidroergotamin, ergotamin, fentanil, hormonske kontraceptive, pimozid, kinidin, sirolimus in takrolimus. Če se sočasni uporabi ni mogoče izogniti, prilagodite odmerek substrata CYP3A4 v skladu s trenutnim Povzetkom glavnih značilnosti zdravila. Podatki *in vitro* so pokazali, da bi sotorasib morda lahko inducíral CYP2B6, CYP2C8, CYP2C9 in CYP2C19; klinični pomen teh ugotovitev ni znan. Pri sočasni uporabi sotorasiba z drugimi zdravili, ki se presnavljajo s pomočjo teh encimov, se priporoča ustrezno spremljanje. Podatki *in vitro* so pokazali, da bi sotorasib morda lahko zaviral CYP2D6; klinični pomen teh ugotovitev ni znan. Pri sočasni uporabi zdravila LUMYKRAS s substrati CYP2D6 (npr. flekainidom, propafenonom, metoprololom), se priporoča ustrezno spremljanje. Zdravilo LUMYKRAS je šibek zaviralec BCRP. Sočasna uporaba zdravila LUMYKRAS s substratom BCRP je privedla do zvišanja koncentracije substrata BCRP, kar bi lahko povečalo vpliv tega substrata. Pri sočasni uporabi zdravila LUMYKRAS s substratom BCRP, kot so med drugim lapatinib, metotreksat, mitoksantron, rosuvastatin in topotekan, spremljajte neželene učinke substrata BCRP in zmanjšajte odmerek substrata BCRP v skladu z njegovim trenutnim povzetkom glavnih značilnosti zdravila. Sočasna uporaba zdravila LUMYKRAS s substrati Pgp z ozkimi terapevtskimi indeksi ni priporočena. Če se sočasni uporabi ni mogoče izogniti, prilagodite odmerek substrata Pgp v skladu s trenutnim Povzetkom glavnih značilnosti zdravila. **PLODNOST, NOSEČNOST IN DOJENJE:** Ženskam v rodni dobi je treba svetovati, naj se med zdravljenjem z zdravilom LUMYKRAS izogibajo zanositvi. Bolnice v rodni dobi, ki prejemajo zdravilo LUMYKRAS, morajo med zdravljenjem in še najmanj 7 dni po zadnjem odmerku zdravila LUMYKRAS uporabljati visokoučinkovite metode kontracepcije. Zdravilo LUMYKRAS lahko zmanjša učinkovitost hormonskih kontraceptivov, zato morajo ženske, ki uporabljajo hormonske kontraceptive, uporabljati tudi dodatno pregradno metodo. Zdravila LUMYKRAS ne uporabljajte pri nosečnicah in pri ženskah v rodni dobi, ki ne uporabljajo učinkovite kontracepcije. Bolnice je treba seznaniti z morebitnimi tveganji za plod, če se zdravilo LUMYKRAS uporablja med nosečnostjo ali če bolnica zanosi med jemanjem zdravila LUMYKRAS. **NEŽELENI UČINKI:** Zelo pogosti: anemija, glavobol, kašelj, dispneja, driska, navzea, bruhanje, zaprtje, bolečine v trebuhu, artralgija, bolečine v hrbtu, utrujenost, pireksija, zvišane ravni AST, zvišane ravni ALT. Pogosti: z zdravilom povzročena poškodba jeter, zvišane ravni alkalne fosfataze v krvi, zvišane ravni bilirubina v krvi, zvišane ravni gama glutamiltransferaze. Občasni: ILD/pnevmonitis. **REŽIM IZDAJE:** Rp/Spec. **IMETNIK DOVOLJENJA ZA PROMET:** Amgen Europe B.V., Minervum 7061, 4817 ZK Breda, Nizozemska. **Dodatne informacije:** Amgen zdravila d.o.o., Ameriška ulica 2, 1000 Ljubljana. **DATUM ZADNJE REVIZIJE BESEDILA:** September 2022. **DATUM PRIPRAVE INFORMACIJE:** Oktober 2022.

SVN-511-1022-80004

TANTUM VERDE®

benzidaminijev klorid

Za lajšanje bolečine in oteklin v ustni in žrelu, ki so posledica radiomukozitisa

Bistvene informacije iz Povzetka glavnih značilnosti zdravila

Tantum Verde 1,5 mg/ml oralno pršilo, raztopina
Tantum Verde 3 mg/ml oralno pršilo, raztopina

Sestava: 1,5 mg/ml: 1 ml raztopine vsebuje 1,5 mg benzidaminijevega klorida, kar ustreza 1,34 mg benzidamina. V enem razpršku je 0,17 ml raztopine. En razpršek vsebuje 0,255 mg benzidaminijevega klorida, kar ustreza 0,2278 mg benzidamina. **Sestava 3 mg/ml:** 1 ml raztopine vsebuje 3 mg benzidaminijevega klorida, kar ustreza 2,68 mg benzidamina. V enem razpršku je 0,17 ml raztopine. En razpršek vsebuje 0,51 mg benzidaminijevega klorida, kar ustreza 0,4556 mg benzidamina. **Terapevtske indikacije:** Samozdravljenje: Lajšanje bolečine in oteklin pri vnetju v ustni votlini in žrelu, ki so lahko posledica okužb in stanj po operaciji. Po nasvetu in navodilu zdravnika: Lajšanje bolečine in oteklin v ustni votlini in žrelu, ki so posledica radiomukozitisa. **Odmerjanje in način uporabe:** Uporaba: 2- do 6-krat na dan (vsake 1,5 do 3 ure). Odmerjanje 1,5 mg/ml: Odrasli: 4 do 8 razprškov 2- do 6-krat na dan. Pediatrična populacija: Mladostniki, stari od 12 do 18 let: 4-8 razprškov 2- do 6-krat na dan. Otroci od 6 do 12 let: 4 razprški 2- do 6-krat na dan. Otroci, mlajši od 6 let: 1 razpršek na 4 kg telesne mase; do največ 4 razprške 2- do 6-krat na dan. Odmerjanje 3 mg/ml: Odrasli: 2 do 4 razprški 2- do 6-krat na dan. Pediatrična populacija: Mladostniki, stari od 12 do 18 let: 2 do 4 razprški 2- do 6-krat na dan. Otroci od 6 do 12 let: 2 razprška 2- do 6-krat na dan. Otroci, mlajši od 6 let: 1 razpršek na 8 kg telesne mase; do največ 2 razprška 2- do 6-krat na dan. Starejši bolniki, bolniki z jetrno okvaro in bolniki z ledvično okvaro: niso potrebni posebni previdnostni ukrepi. Trajanje zdravljenja ne sme biti daljše od 7 dni. Način uporabe: Za orofaringealno uporabo. Zdravilo se razprši v usta in žrelo. **Kontraindikacije:** Preobčutljivost na učinkovino ali katero koli pomožno snov. **Posebna opozorila in previdnostni ukrepi:** Pri nekaterih bolnikih lahko resne bolezni povzročijo ustne/žrelne ulceracije. Če se simptomi v treh dneh ne izboljšajo, se mora bolnik posvetovati z zdravnikom ali zobozdravnikom, kot je primerno. Uporaba benzidamina ni priporočljiva za bolnike s preobčutljivostjo na salicilno kislino ali druga nesteroidna protivnetna zdravila. Pri bolnikih, ki imajo ali so imeli bronhialno astmo, lahko pride do bronhospazma. Pri takih bolnikih je potrebna previdnost. To zdravilo vsebuje 13,6 mg alkohola (etanola) v enem razpršku (0,17 ml), kar ustreza manj kot 0,34 ml piva oziroma 0,14 ml vina. Majhna količina alkohola v zdravilu ne bo imela nobenih opaznih učinkov. To zdravilo vsebuje metilparahidroksibenzoat (E218). Lahko povzroči alergijske reakcije (lahko zapoznele). To zdravilo vsebuje manj kot 1 mmol (23 mg) natrija v enem razpršku (0,17 ml), kar v bistvu pomeni 'brez natrija'. Zdravilo vsebuje aromo poprove mete z benzilalkoholom, cinamilalkoholom, citralom, citronelolom, geraniolom, izoevgenolom, linalolom, evgenolom in D-limonen, ki lahko povzročijo alergijske reakcije. Zdravilo z jakostjo 3 mg/ml vsebuje makrogolglicerol hidroksistearat 40. Lahko povzroči želodčne težave in drisko. **Medsebojno delovanje z drugimi zdravili in druge oblike interakcij:** Študij medsebojnega delovanja niso izvedli. **Nosečnost in dojenje:** O uporabi benzidamina pri nosečnicah in doječih ženskah ni zadostnih podatkov. Uporaba zdravila med nosečnostjo in dojenjem ni priporočljiva. **Vpliv na sposobnost vožnje in upravljanja strojev:** Zdravilo v priporočenem odmerku nima vpliva na sposobnost vožnje in upravljanja strojev. **Neželeni učinki:** Neznana pogostnost (ni mogoče oceniti iz razpoložljivih podatkov): anafilaktične reakcije, preobčutljivostne reakcije, odrevenelost, laringospazem, suha usta, navzea in bruhanje, oralna hipestezija, angioedem, fotosenzitivnost, pekoč občutek v ustih. Neposredno po uporabi se lahko pojavi občutek odrevenelosti v ustih in v žrelu. Ta učinek se pojavi zaradi načina delovanja zdravila in po kratkem času izgine. **Način in režim izdaje zdravila:** BRp-Izdaja zdravila je brez recepta v lekarnah in specializiranih prodajalnah. **Imetnik dovoljenja za promet:** Aziende Chimiche Riunite Angelini Francesco – A.C.R.A.F. S.p.A., Viale Amelia 70, 00181 Rim, Italija **Datum zadnje revizije besedila:** 05. 04. 2022

Pred svetovanjem ali izdajo preberite celoten Povzetek glavnih značilnosti zdravila.

Samo za strokovno javnost.

Datum priprave informacije: april 2022

ANGELINI

Odgovoren za trženje: Bonifar d.o.o.

AKTIVIRA IMUNSKI SISTEM.
PREPOZNA. **REAGIRA.**

IMFINZI™
durvalumab
50 mg/ml koncentrat za raztopino za infundiranje

IMFINZI podaljša preživetje in obenem ohranja kvaliteto življenja bolnikov z razsejanim drobnoceličnim rakom pljuč [1,2]

Po treh letih je bilo živih 3x več bolnikov zdravljenih z zdravilom Imfinzi v kombinaciji z EP kot bolnikov zdravljenih samo z EP[1]

POSODOBLJENA ANALIZA CELOKUPNEGA PREŽIVETJA (srednji čas spremljanja 39,4 mesecev)

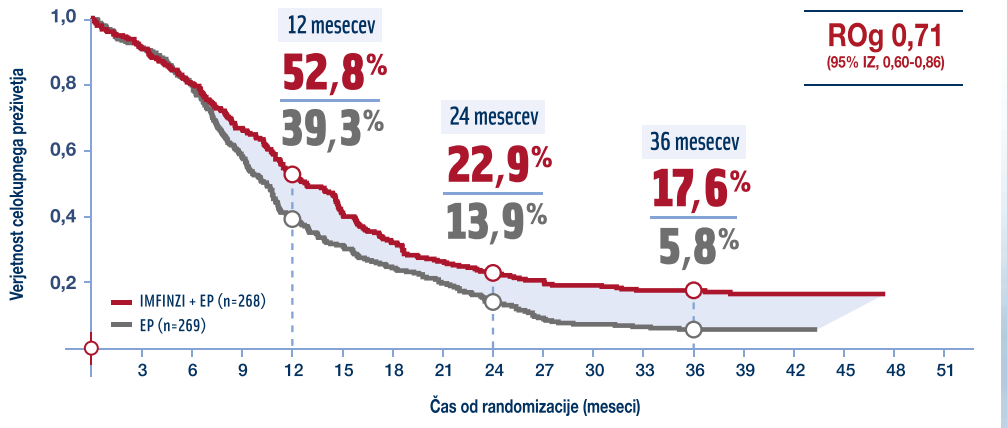

Število bolnikov izpostavljenih tveganju

IMFINZI + EP	268	244	214	177	140	109	85	70	60	54	50	46	39	25	13	3	0	0
EP	269	243	212	156	104	82	64	51	36	24	19	17	13	10	3	0	0	0

- 3-letna analiza celokupnega preživetje je bila izvedena po 469 dogodkih, ki so se zgodili v obeh skupinah bolnikov zdravljenih s kombinacijo IMFINZI + EP ali samo z EP (86% zrelost podatkov)[1]

SKRAJŠAN POVZETEK GLAVNIH ZNAČILNOSTI ZDRAVILA

▼ Za to zdravilo se izvaja dodatno spremljanje varnosti. Tako bodo hitreje na voljo nove informacije o njegovi varnosti. Zdravstvene delavce naprošamo, da poročajo o katerem koli domnevnem neželenem učinku zdravila.

Imfinzi 50 mg/ml koncentrat za raztopino za infundiranje

SESTAVA: 1 ml koncentrata za raztopino za infundiranje vsebuje 50 mg durvalumaba. Ena viala z 2,4 ml koncentrata vsebuje 120 mg durvalumaba. Ena viala z 10 ml koncentrata vsebuje 500 mg durvalumaba. **INDIKACIJE:** Zdravilo Imfinzi je kot samostojno zdravljenje indicirano za zdravljenje lokalno napredovalega, neoperabilnega nedrobnoceličnega raka pljuč (NSCLC – "non small cell lung cancer") pri odraslih, ki imajo tumorje z ≥ 1 % izraženostjo PD-L1 na tumorskih celicah in pri katerih bolezen ni napredovala po kemoradioterapiji na osnovi platine. Zdravilo Imfinzi je v kombinaciji z etopozidom in bodisi karboplatinom bodisi cisplatinom indicirano za prvo linijo zdravljenja odraslih z razsejanim drobnoceličnim rakom pljuč (ES SCLC – "extensive stage small cell lung cancer"). **ODMERJANJE IN NAČIN UPORABE:** Zdravljenje mora uvesti in nadzorovati zdravnik, ki ima izkušnje na področju zdravljenja raka. Bolnike z lokalno napredovalim nedrobnoceličnim rakom pljuč je treba za zdravljenje izbrati na podlagi izraženosti PD-L1, ugotovljene z validirano testno metodo. Odmerjanje: Priporočeni odmerek zdravila Imfinzi pri samostojnem zdravljenju je 10 mg/kg na 2 tedna ali 1500 mg na 4 tedne do napredovanja bolezni, nesprejemljivih toksičnih učinkov ali največ 12 mesecev . Bolniki s telesno maso 30 kg ali manj morajo prejemati odmerke na podlagi telesne mase, in sicer 10 mg/kg na 2 tedna ali 20 mg/kg na 4 tedne kot samostojno zdravljenje, dokler se telesna masa ne poveča na več kot 30 kg. V kombinaciji s kemoterapijo je priporočeni odmerek zdravila Imfinzi 1500 mg v kombinaciji s kemoterapijo na 3 tedne (21 dni) 4 cikluse in nato 1500 mg na 4 tedne kot samostojno zdravljenje. Zdravilo Imfinzi se uporablja v intravenski infuziji, ki traja 1 uro. Povečevanje ali zmanjševanje odmerka ni priporočljivo. Glede na individualno varnost in prenašanje je lahko potrebna odložitev odmerka ali prenehanje uporabe zdravila. V primeru domnevnih imunsko pogojenih neželenih učinkov je treba opraviti ustrezno ovrednotenje za potrditev etiologije oziroma izključitev druge etiologije. Glede na resnost neželenega učinka je treba prenehati uporabljati zdravilo IMFINZI in pričeti z dajanjem kortikosteroidov. Če se stanje ne izboljša ali se poslabša, pride v poštev povečanje odmerka kortikosteroidov in/ali dodatna uporaba sistemskih imunosupresivov. Po izboljšanju na ≤ 1. stopnjo je treba začeti s postopnim zmanjševanjem kortikosteroida in ga zmanjševati v obdobju vsaj 1 meseca. Po odložitvi uporabe je mogoče zdravilo Imfinzi znova začeti uporabljati v času 12 tednov, če se neželeni učinki izboljšajo na ≤ 1. stopnjo in je odmerek kortikosteroida zmanjšan na ≤ 10 mg prednizona ali ekvivalenta na dan. Zdravilo IMFINZI je treba dokončno ukiniti, če se imunsko pogojeni neželeni učinki 3. stopnje (močno izraženi) ponavljajo in pri katerih koli imunsko pogojenih neželenih učinkih 4. stopnje (življenjsko nevarni), razen pri endokrinopatijah, ki jih nadziramo z nadomestnimi hormoni. Pri ne imunsko pogojenih neželenih učinkih, v primeru 2. ali 3. stopnje izraženosti, odložite uporabo zdravila IMFINZI do izboljšanja neželenih učinkov na ≤ 1. stopnjo ali na izhodiščno raven. Z uporabo zdravila Imfinzi je treba prenehati v primeru neželenih učinkov 4. stopnje (razen v primeru laboratorijskih nepravilnosti 4. stopnje, pri katerih naj odločitev o prekinitvi uporabe zdravila temelji na spremljajočih kliničnih znakih oziroma simptomih in na klinični presoji zdravnika). Zdravilo Imfinzi je namenjeno za intravensko uporabo. Dati ga je treba kot raztopino za intravensko infundiranje v obdobju 1 ure. **KONTRAINDIKACIJE:** Preobčutljivost na učinkovino (učinkovine) ali katero koli pomožno snov. **OPOZORILA IN PREVIDNOSTNI UKREPI:** Za izboljšanje sledljivosti bioloških zdravil je treba jasno zabeležiti lastniško ime in številko serije uporabljenega zdravila. Imunsko pogojeni pnevmonitis: Pri bolnikih, ki so prejemali zdravilo Imfinzi, sta se pojavila imunsko pogojeni pnevmonitis ali intersticijska bolezen pljuč, opredeljeno kot potreba po uporabi sistemskih kortikosteroidov in brez jasne druge etiologije. Pnevmonitis in radiacijski pnevmonitis: Pri bolnikih, zdravljenih z radioterapijo pljuč, je pogost radiacijski pnevmonitis in klinična slika pnevmonitisa je zelo podobna. V študiji PACIFIC sta se pri bolnikih, ki so opravili zdravljenje z najmanj 2 cikloma sočasne kemoradioterapije od 1 do 42 dni pred začetkom preizkušanja, pnevmonitis ali radiacijski pnevmonitis pojavila pri 161 (33,9 %) bolnikih v skupini z zdravilom Imfinzi in pri 58 (24,8 %) bolnikih v skupini s placebom, vključno s 3. stopnjo (3,4 % in 3,0 %) in 5. stopnjo (1,1 % in 1,7 %). Bolnike je treba spremljati glede znakov in simptomov pnevmonitisa ali radiacijskega pnevmonitisa. Imunsko pogojeni hepatitis: Pri bolnikih, ki so prejemali zdravilo Imfinzi, se je pojavil imunsko pogojeni hepatitis, opredeljen kot potreba po sistemskih kortikosteroidih in brez jasne druge etiologije. Imunsko pogojeni kolitis: Pri bolnikih, ki so prejemali zdravilo Imfinzi, sta se pojavila imunsko pogojeni kolitis ali driska, opredeljeno kot potreba po sistemskih kortikosteroidih in brez jasne druge etiologije. Imunsko pogojene endokrinopatije: Imunsko pogojeni hipotiroidizem, hipertiroidizem in tiroiditis: Pri bolnikih, ki so prejemali zdravilo Imfinzi, so se pojavili imunsko pogojeni hipotiroidizem, hipertiroidizem in tiroiditis; hipertiroidizmu lahko sledi hipotiroidizem. Bolnike je treba spremljati glede nenormalnih izvidov delovanje ščitnice pred zdravljenjem in redno med zdravljenjem ter kot je potrebno glede na klinično oceno. Imunsko pogojeni hipotiroidizem, hipertiroidizem in tiroiditis je treba obravnavati in ukrepati, kot je priporočeno v povzetku glavnih značilnosti zdravila. Imunsko pogojena adrenalna insuficienca: Pri bolnikih, ki so prejemali zdravilo Imfinzi, se je pojavila imunsko pogojena adrenalna insuficienca. Bolnike je treba spremljati glede kliničnih znakov in simptomov adrenalne insuficience. Imunsko pogojena sladkorna bolezen tipa 1: Pri bolnikih, ki so prejemali zdravilo Imfinzi, se je pojavila imunsko pogojena sladkorna bolezen tipa 1, ki se lahko najprej kaže kot diabetična ketoacidoza, ki je lahko smrtno nevarna, če je dovolj zgodaj ne odkrijemo. Bolnike je treba spremljati glede kliničnih znakov in simptomov sladkorne bolezni tipa 1. Imunsko pogojeni hipofizitis/hipopituitarizem: Pri bolnikih, ki so prejemali zdravilo Imfinzi, sta se pojavila imunsko pogojena hipofizitis ali hipopituitarizem. Bolnike je treba spremljati glede kliničnih znakov in simptomov hipofizitisa ali hipopituitarizma. Imunsko pogojeni nefritis: Pri bolnikih, ki so prejemali zdravilo Imfinzi, se je pojavil imunsko pogojeni nefritis, opredeljen kot potreba po sistemskih kortikosteroidih in brez jasne druge etiologije. Imunsko pogojeni izpuščaj: Pri bolnikih, ki so prejemali zdravilo Imfinzi, se je pojavil imunsko pogojeni izpuščaj ali dermatitis (vključno s pemfigoidom), opredeljen kot potreba po sistemskih kortikosteroidih in brez jasne druge etiologije. Pri bolnikih, ki so bili zdravljeni z zaviralci PD-1, so poročali o pojavljanju Stevens-Johnsonovega sindroma ali toksične epidermalne nekrolize. Imunsko pogojeni miokarditis: Pri bolnikih, ki so prejemali zdravilo IMFINZI, se je pojavil imunsko pogojeni miokarditis, ki je lahko usoden. Drugi imunsko pogojeni neželeni učinki: Glede na mehanizem delovanja zdravila Imfinzi se lahko pojavijo še drugi potencialno imunsko pogojeni učinki. Naslednji imunsko pogojeni neželeni učinki so bili opaženi pri bolnikih, ki so prejemali samostojno zdravljenje z zdravilom Imfinzi: miastenija gravis, miozitis, polimiozitis, meningitis, encefalitis, Guillain Barréjev sindrom, imunska trombocitopenija, neinfektivni cistitis in pankreatitis. Bolnike je treba spremljati glede znakov in simptomov in ukrepati, kot je priporočeno za druge imunsko pogojene neželene učinke. Z infundiranjem povezane reakcije: Bolnike je treba spremljati glede znakov in simptomov z infundiranjem povezanih reakcij. Pri bolnikih, ki so prejemali zdravilo Imfinzi, so bile opisane hude z infundiranjem povezane reakcije. Bolniki, ki niso bili vključeni v klinična preizkušanja: V klinična preskušanja niso bili vključeni bolniki z naslednjimi značilnostmi: izhodiščno oceno zmogljivosti ECOG ≥ 2; aktivno ali predhodno dokumentirano avtoimunsko boleznijo v 2 letih pred začetkom študije; anamnezo imunske pomanjkljivosti; anamnezo hudih imunsko pogojenih neželenih učinkov; boleznimi, ki so zahtevale sistemsko imunosupresijo, razen fiziološkega odmerka sistemskih kortikosteroidov (≤ 10 mg na dan prednizona ali ekvivalenta); neobvladanimi sočasnimi boleznimi; aktivno tuberkulozo ali okužbo s hepatitisom B ali C ali HIV; bolniki, ki so prejeli živo oslabljeno cepivo v 30 dneh pred začetkom zdravljenja z zdravilom Imfinzi ali v 30 dneh po začetku. Dokler takšnih podatkov ni, je treba durvalumab v teh skupinah bolnikov uporabljati previdno ter po skrbnem individualnem pretehtanju možnih koristi in tveganj za posameznega bolnika. Varnost sočasnega profilaktičnega kranialnega obsevanja obenem z zdravilom Imfinzi pri bolnikih z ES SCLC ni znana. **MEDSEBOJNO DELOVANJE Z DRUGIMI ZDRAVILI:** Razen fiziološkim odmerkov sistemskih kortikosteroidov (≤ 10 mg na dan prednizona ali ekvivalenta) pred uvedbo durvalumaba ni priporočljivo uporabljati sistemskih kortikosteroidov ali imunosupresivov, ker lahko vplivajo na farmakodinamično aktivnost in učinkovitost durvalumaba. Vendar pa je mogoče kortikosteroide ali druge imunosupresivne uporabiti po začetku zdravljenja z durvalumabom za zdravljenje imunsko pogojenih neželenih učinkov. Z durvalumabom niso izvedli formalnih farmakokinetičnih (PK) študij medsebojnega delovanja zdravil. Primarni poti odstranjevanja durvalumaba sta katabolizem beljakovin preko retikuloendoteljskega sistema oziroma tarčno posredovano odstranjevanje, zato ni pričakovati presnovnih medsebojnih delovanj med zdravili. Farmakokinetična medsebojna delovanja med durvalumabom in kemoterapijo so ocenjevali v študiji CASPIAN; izkazalo se je, da sočasno zdravljenje z durvalumabom ne vpliva na farmakokinetiko etopozida, karboplatina ali cisplatina. Poleg tega populacijska farmakokinetična analiza kaže, da sočasno zdravljenje s kemoterapijo ne vpliva pomembno na farmakokinetiko durvalumaba. **PLODNOST, NOSEČNOST IN DOJENJE:** Ženske v rodni dobi morajo med zdravljenjem z durvalumabom in vsaj še 3 mesece po zadnjem odmerku durvalumaba uporabljati učinkovito kontracepcijo. Podatkov o uporabi durvalumaba pri nosečnicah ni. Glede na mehanizem delovanja durvalumab lahko vpliva na vzdrževanje nosečnosti; v alogenskem modelu nosečnosti pri miših je bilo ugotovljeno, da moteno signaliziranje PD-L1 poveča izgubo plodov. Pri nosečnici uporabljeni durvalumab lahko škoduje plodu in ga ni priporočljivo uporabljati med nosečnostjo in pri ženskah v rodni dobi, ki ne uporabljajo učinkovite kontracepcije med zdravljenjem in vsaj še 3 mesece po zadnjem odmerku. Ni znano, ali se durvalumab pri človeku izloča v materinem mleku. Pri človeku protitelesa lahko prehajajo v materino mleko, a možnost absorpcije in škode za novorojenčka ni znana. Toda možnega tveganja za dojenega otroka ni mogoče izključiti. Odločiti se je treba, ali naj ženska prekine z dojenjem ali naj prekine zdravljenje z durvalumabom oziroma sploh ne začne zdravljenja z njim, pri čemer je treba upoštevati koristi dojenja za otroka in koristi zdravljenja za žensko. Podatkov o možnih vplivih durvalumaba na plodnost pri človeku ali živalih ni. **NEŽELENI UČINKI:** Ugotovitve o varnosti zdravila Imfinzi pri samostojnem zdravljenju temeljijo na kumulativnih podatkih 3006 bolnikov z več vrstami tumorjev. Zdravilo Imfinzi so uporabljali v odmerku 10 mg/kg na 2 tedna ali v odmerku 20 mg/kg na 4 tedne. Najpogostejši neželeni učinki (> 10 %) so bili kašelj/produktiven kašelj (21,5 %), driska (16,3 %), izpuščaj (16,0 %), zvišana telesna temperatura (13,8 %), okužbe zgornjih dihal (13,5 %), bolečine v trebuhu (12,7 %), srbenje (10,8 %) in hipotiroidizem (10,1 %). Ugotovitve o varnosti zdravila Imfinzi v kombinaciji s kemoterapijo temeljijo na podatkih 265 bolnikov z SCLC. Zdravilo Imfinzi so uporabljali v odmerku 1500 mg na 3 tedne v kombinaciji s kemoterapijo in nato pri samostojnem zdravljenju na 4 tedne. Najpogostejši neželeni učinki (> 20 %) so bili nevtropenija (48,7 %), anemija (38,5 %), navzea (33,6 %), utrujenost (32,1 %), alopecija (31,3 %), trombocitopenija (21,1 %) in levkopenija (20,0 %). Zdravilo Imfinzi pri samostojnem zdravljenju: Zelo pogosti neželeni učinki: okužbe zgornjih dihal, hipotiroidizem, kašelj/produktiven kašelj, driska, bolečine v trebuhu, izpuščaj, srbenje, zvišana telesna temperatura, artralgija. Pogosti neželeni učinki: pljučnica, zobne okužbe in okužbe ustnih mehkih tkiv, oralna kandidoza, gripa, hipertiroidizem, pnevmonitis, disfonija, zvišanje vrednosti aspartat aminotransferaze ali zvišanje vrednosti alanin aminotransferaze, nočno znojenje, dermatitis, mialgija, zvišanje vrednosti kreatinina v krvi, disurija, periferni edemi, z infundiranjem povezane reakcije. Občasni neželeni učinki: tiroiditis, adrenalna insuficienca, intersticijska bolezen pljuč, kolitis, hepatitis, dermatitis, miozitis, nefritis, pankreatitis, psoriaza. Redki neželeni učinki: sladkorna bolezen tipa 1, hipofizitis / hipopituitarizem, diabetes insipidus, miastenija gravis, meningitis, miokarditis, pemfigois, polimiozitis, imunska trombocitopenija. Zdravilo Imfinzi v kombinaciji s kemoterapijo: Zelo pogosti neželeni učinki: nevtropenija, anemija, trombocitopenija, levkopenija, zmanjšan apetit, kašelj/produktiven kašelj, navzea, zaprtost, bruhanje, izpadanje las, utrujenost. Pogosti neželeni učinki: okužbe zgornjih dihal, pljučnica, zobne okužbe in okužbe ustnih mehkih tkiv, febrilna nevtropenija, pancitopenija, hipotiroidizem, hipertiroidizem, tiroiditis, adrenalna insuficienca, pnevmonitis, driska, bolečine v trebuhu, stomatitis, zvišanje vrednosti aspartat aminotransferaze ali zvišanje vrednosti alanin aminotransferaze, hepatitis, izpuščaj, srbenje, dermatitis, mialgija, zvišanje vrednosti kreatinina v krvi, disurija, zvišana telesna temperatura, artralgija. Občasni neželeni učinki: gripa, sladkorna bolezen tipa 1, disfonija, intersticijska bolezen pljuč.**VRSTA IN VSEBINA OVOJNINE:** 2,4 ml koncentrata v stekleni viali iz stekla tipa 1 z elastomernim zamaškom in sivo snemno aluminijsko zaporo; viala vsebuje 120 mg durvalumaba. Pakiranje vsebuje 1 vialo. 10 ml koncentrata v stekleni viali iz stekla tipa 1 z elastomernim zamaškom in belo snemno aluminijsko zaporo; viala vsebuje 500 mg durvalumaba. Pakiranje vsebuje 1 vialo. **NAČIN IZDAJANJA ZDRAVILA:** H - Predpisovanje in izdaja zdravila je le na recept. **DATUM REVIZIJA BESEDILA:** 22.8.2022 (SI-2384). **IMETNIK DOVOLJENJA ZA PROMET:** AstraZeneca AB, S-151 85, Sodertalje, Švedska

Pred predpisovanjem, prosimo, preberite celoten povzetek glavnih značilnosti zdravila. Dodatne informacije so na voljo pri družbi AstraZeneca UK Limited, Podružnica v Sloveniji, Verovškova 55, Ljubljana, telefon +386 1 51 35 600.
Samo za strokovno javnost. Informacija pripravljena oktobra 2022.

1. Paz-Ares L, Chen Y, Reinmuth N, et al. Durvalumab ± tremelimumab + platinum-etoposide in first-line extensive-stage SCLC (ES-SCLC): 3-year overall survival update from the phase 3 CASPIAN study; ESMO Open. 2022 Apr;7(2):100408. 2. Goldman JW, Garassino MC, Chen Y, et al. Patient-reported outcomes with first-line durvalumab plus platinum-etoposide versus platinum-etoposide in extensive-stage small-cell lung cancer (CASPIAN): a randomized, controlled, open-label, phase III study. Lung Cancer. 2020;149:46-52.

AstraZeneca

SI-2415

KLJUČ ZA VEČ PRILOŽNOSTI PRI ZDRAVLJENJU VAŠIH BOLNIKOV

KEYTRUDA®
(pembrolizumab, MSD)

KEYTRUDA je odobrena za zdravljenje 21 indikacij rakavih obolenj[1]

Referenca: 1. Keytruda EU SmPC

Ime zdravila: KEYTRUDA 25 mg/ml koncentrat za raztopino za infundiranje vsebuje pembrolizumab. Terapevtske indikacije: Zdravilo KEYTRUDA je kot samostojno zdravljenje indicirano za zdravljenje: odraslih in mladostnikov, starih 12 let ali več, z napredovalim (neoperabilnim ali metastatskim) melanomom; za adjuvantno zdravljenje odraslih in mladostnikov, starih 12 let ali več, z melanomom v stadiju IIB, IIC ali III, in sicer po popolni kirurški odstranitvi; metastatskega nedrobnoceličnega pljučnega raka (NSCLC) v prvi liniji zdravljenja pri odraslih, ki imajo tumorje z ≥ 50 % izraženostjo PD-L1 (TPS) in brez pozitivnih tumorskih mutacij EGFR ali ALK; lokalno napredovalega ali metastatskega NSCLC pri odraslih, ki imajo tumorje z ≥ 1 % izraženostjo PD-L1 (TPS) in so bili predhodno zdravljeni z vsaj eno shemo kemoterapije, bolniki s pozitivnimi tumorskimi mutacijami EGFR ali ALK so pred prejemom zdravila KEYTRUDA morali prejeti tudi tarčno zdravljenje; odraslih in pediatričnih bolnikov, starih 3 leta ali več, s ponovljenim ali neodzivnim klasičnim Hodgkinovim limfomom (cHL), pri katerih avtologna presaditev matičnih celic (ASCT) ni bila uspešna, ali po najmanj dveh predhodnih zdravljenjih kadar ASCT ne pride v poštev kot možnost zdravljenja; lokalno napredovalega ali metastatskega urotelijskega raka pri odraslih, predhodno zdravljenih s kemoterapijo, ki je vključevala platino; lokalno napredovalega ali metastatskega urotelijskega raka pri odraslih, ki niso primerni za zdravljenje s kemoterapijo, ki vsebuje cisplatin in imajo tumorje z izraženostjo PD-L1 ≥ 10, ocenjeno s kombinirano pozitivno oceno (CPS); ponovljenega ali metastatskega ploščatoceličnega raka glave in vratu (HNSCC) pri odraslih, ki imajo tumorje z ≥ 50 % izraženostjo PD-L1 (TPS), in pri katerih je bolezen napredovala med zdravljenjem ali po zdravljenju s kemoterapijo, ki je vključevala platino; za adjuvantno zdravljenje odraslih z rakom ledvičnih celic s povišanim tveganjem za ponovitev bolezni po nefrektomiji, ali po nefrektomiji in kirurški odstranitvi metastatskih lezij, za zdravljenje odraslih z MSI-H (microsatellite instability-high) ali dMMR (mismatch repair deficient) kolorektalnim rakom v naslednjih terapevtskih okoliščinah: prva linija zdravljenja metastatskega kolorektalnega raka; zdravljenje neoperabilnega ali metastatskega kolorektalnega raka po predhodnem kombiniranem zdravljenju, ki je temeljilo na fluoropirimidinu; in za zdravljenje MSI-H ali dMMR tumorjev pri odraslih z: napredovalim ali ponovljenim rakom endometrija, pri katerih je bolezen napredovala med ali po predhodnem zdravljenju, ki je vključevalo platino, v katerih koli terapevtskih okoliščinah, in ki niso kandidati za kurativno operacijo ali obsevanje; neoperabilnim ali metastatskim rakom želodca, tankega črevesa ali žolčnika in žolčnih vodov, pri katerih je bolezen napredovala med ali po vsaj enem predhodnem zdravljenju. Zdravilo KEYTRUDA je kot samostojno zdravljenje ali v kombinaciji s kemoterapijo s platino in 5-fluorouracilom (5-FU) indicirano za prvo linijo zdravljenja metastatskega ali neoperabilnega ponovljenega ploščatoceličnega raka glave in vratu pri odraslih, ki imajo tumorje z izraženostjo PD-L1 s CPS ≥ 1. Zdravilo KEYTRUDA je v kombinaciji s pemetreksedom in kemoterapijo na osnovi platine indicirano za prvo linijo zdravljenja metastatskega neploščatoceličnega NSCLC pri odraslih, pri katerih tumorji nimajo pozitivnih mutacij EGFR ali ALK; v kombinaciji s karboplatinom in bodisi paklitakselom bodisi nab-paklitakselom je indicirano za prvo linijo zdravljenja metastatskega ploščatoceličnega NSCLC pri odraslih; v kombinaciji z aksitinibom ali v kombinaciji z lenvatinibom je indicirano za prvo linijo zdravljenja napredovalega raka ledvičnih celic (RCC) pri odraslih; v kombinaciji s kemoterapijo s platino in fluoropirimidinom je indicirano za prvo linijo zdravljenja lokalno napredovalega neoperabilnega ali metastatskega raka požiralnika ali HER-2 negativnega adenokarcinoma gastroezofagealnega prehoda pri odraslih, ki imajo tumorje z izraženostjo PD-L1 s CPS ≥ 10; v kombinaciji s kemoterapijo za neoadjuvantno zdravljenje, in v nadaljevanju kot samostojno adjuvantno zdravljenje po kirurškem posegu, je indicirano za zdravljenje odraslih z lokalno napredovalim trojno negativnim rakom dojk ali trojno negativnim rakom dojk v zgodnjem stadiju z visokim tveganjem za ponovitev bolezni; v kombinaciji s kemoterapijo je indicirano za zdravljenje lokalno ponovljenega neoperabilnega ali metastatskega trojno negativnega raka dojk pri odraslih, ki imajo tumorje z izraženostjo PD-L1 s CPS ≥ 10 in predhodno niso prejeli kemoterapije za metastatsko bolezen; v kombinaciji z lenvatinibom je indicirano za zdravljenje napredovalega ali ponovljenega raka endometrija (EC) pri odraslih z napredovalo boleznijo med ali po predhodnem zdravljenju s kemoterapijo, ki je vključevala platino, v katerih koli terapevtskih okoliščinah, in ki niso kandidati za kurativno operacijo ali obsevanje; v kombinaciji s kemoterapijo, z bevacizumabom ali brez njega, je indicirano za zdravljenje persistentnega, ponovljenega ali metastatskega raka materničnega vratu pri odraslih bolnicah, ki imajo tumorje z izraženostjo PD-L1 s CPS ≥ 1. **Odmerjanje in način uporabe:** Testiranje PD-L1: Če je navedeno v indikaciji, je treba izbiro bolnika za zdravljenje z zdravilom KEYTRUDA na podlagi izraženosti PD-L1 tumorja potrditi z validirano preiskavo. Testiranje MSI/MMR: Če je navedeno v indikaciji, je treba izbiro bolnika za zdravljenje z zdravilom KEYTRUDA na podlagi MSI-H/dMMR statusa tumorja potrditi z validirano preiskavo. Odmerjanje: Priporočeni odmerek zdravila KEYTRUDA pri odraslih je bodisi 200 mg na 3 tedne ali 400 mg na 6 tednov, apliciran z intravensko infuzijo v 30 minutah. Priporočeni odmerek zdravila KEYTRUDA za samostojno zdravljenje pri pediatričnih bolnikih s cHL, starih 3 leta ali več, ali bolnikih z melanomom, starih 12 let ali več, je 2 mg/kg telesne mase (do največ 200 mg) na 3 tedne, apliciran z intravensko infuzijo v 30 minutah. Za uporabo v kombinaciji glejte povzetke glavnih značilnosti zdravil sočasno uporabljenih zdravil. Če se uporablja kot del kombiniranega zdravljenja skupaj z intravensko kemoterapijo, je treba zdravilo KEYTRUDA aplicirati prvo. Bolnike je treba zdraviti do napredovanja bolezni ali nesprejemljivih toksičnih učinkov (in do maksimalnega trajanja zdravljenja, če je le to določeno za indikacijo). Pri adjuvantnem zdravljenju melanoma ali RCC je treba zdravilo uporabljati do ponovitve bolezni, pojava nesprejemljivih toksičnih učinkov oziroma mora zdravljenje trajati do enega leta. Za neoadjuvantno in adjuvantno zdravljenje TNBC morajo bolniki neoadjuvantno prejeti zdravilo KEYTRUDA v kombinaciji s kemoterapijo, in sicer 8 odmerkov po 200 mg na 3 tedne ali 4 odmerke po 400 mg na 6 tednov, ali do napredovanja bolezni, ki izključuje definitivni kirurški poseg, ali do pojava nesprejemljivih toksičnih učinkov, čemur sledi adjuvantno zdravljenje z zdravilom KEYTRUDA kot samostojnim zdravljenjem, in sicer 9 odmerkov po 200 mg na 3 tedne ali 5 odmerkov po 400 mg na 6 tednov ali do ponovitve bolezni ali pojava nesprejemljivih toksičnih učinkov. Bolniki, pri katerih pride do napredovanja bolezni, ki izključuje definitivni kirurški poseg, ali do nesprejemljivih toksičnih učinkov povezanih z zdravilom KEYTRUDA kot neoadjuvantnim zdravljenjem v kombinaciji s kemoterapijo, ne smejo prejeti zdravila KEYTRUDA kot samostojnega zdravljenja za adjuvantno zdravljenje. Če je aksitinib uporabljen v kombinaciji s pembrolizumabom, se lahko razmisli o povečanju odmerka aksitiniba nad začetnih 5 mg v presledkih šest tednov ali več. V primeru uporabe v kombinaciji z lenvatinibom je treba zdravljenje z enim ali obema zdraviloma prekiniti, kot je primerno. Uporabo lenvatiniba je treba zadržati, odmerek zmanjšati ali prenehati z uporabo, v skladu z navodili v povzetku glavnih značilnosti zdravila za lenvatinib, in sicer za kombinacijo s pembrolizumabom. Pri bolnikih starih ≥ 65 let, bolnikih z blago do zmerno okvaro ledvic, bolnikih z blago ali zmerno okvaro jeter prilagoditev odmerka ni potrebna. Odložitev odmerka ali ukinitev zdravljenja: Zmanjšanje odmerka zdravila KEYTRUDA ni priporočljivo. Za obvladovanje neželenih učinkov je treba uporabo zdravila KEYTRUDA zadržati ali ukiniti, prosimo, glejte celoten Povzetek glavnih značilnosti zdravila. **Kontraindikacije:** Preobčutljivost na učinkovino ali katero koli pomožno snov. **Povzetek posebnih opozoril, previdnostnih ukrepov, interakcij in neželenih učinkov:** Imunsko pogojeni neželeni učinki (pnevmonitis, kolitis, hepatitis, nefritis, endokrinopatije, neželeni učinki na kožo in drugi): Pri bolnikih, ki so prejemali pembrolizumab, so se pojavili imunsko pogojeni neželeni učinki, vključno s hudimi in smrtnimi primeri. Večina imunsko pogojenih neželenih učinkov, ki so se pojavili med zdravljenjem s pembrolizumabom, je bila reverzibilnih in so jih obvladali s prekinitvami uporabe pembrolizumaba, uporabo kortikosteroidov in/ali podporno oskrbo. Pojavijo se lahko tudi po zadnjem odmerku pembrolizumaba in hkrati prizadanejo več organskih sistemov. V primeru suma na imunsko pogojene neželene učinke je treba poskrbeti za ustrezno oceno za potrditev etiologije oziroma izključitev drugih vzrokov. Glede na izrazitost neželenega učinka je treba zadržati uporabo pembrolizumaba in uporabiti kortikosteroide – za natančna navodila, prosimo, glejte Povzetek glavnih značilnosti zdravila Keytruda. Zdravljenje s pembrolizumabom lahko poveča tveganje za zavrnitev pri prejemnikih presadkov čvrstih organov. Pri bolnikih, ki so prejemali pembrolizumab, so poročali o hudih z infuzijo povezanih reakcijah, vključno s preobčutljivostjo in anafilaksijo. Pembrolizumab se iz obtoka odstrani s katabolizmom, zato presnovnih medsebojnih delovanj zdravil ni pričakovati. Uporabi sistemskih kortikosteroidov ali imunosupresivov pred uvedbo pembrolizumaba se je treba izogibati, ker lahko vplivajo na farmakodinamično aktivnost in učinkovitost pembrolizumaba. Vendar pa je kortikosteroide ali druge imunosupresive mogoče uporabiti za zdravljenje imunsko pogojenih neželenih učinkov. Kortikosteroide je mogoče uporabiti tudi kot premedikacijo, če je pembrolizumab uporabljen v kombinaciji s kemoterapijo, kot antiemetično profilakso in/ali za ublažitev neželenih učinkov, povezanih s kemoterapijo. Ženske v rodni dobi morajo med zdravljenjem s pembrolizumabom in vsaj še 4 mesece po zadnjem odmerku pembrolizumaba uporabljati učinkovito kontracepcijo, med nosečnostjo in dojenjem se ga ne sme uporabljati. Varnost pembrolizumaba pri samostojnem zdravljenju so v kliničnih študijah ocenili pri 7.631 bolnikih, ki so imeli različne vrste raka, s štirimi odmerki (2 mg/kg telesne mase na 3 tedne, 200 mg na 3 tedne in 10 mg/kg telesne mase na 2 ali 3 tedne). V tej populaciji bolnikov je mediani čas opazovanja znašal 8,5 meseca (v razponu od 1 dneva do 39 mesecev), najpogostejši neželeni učinki zdravljenja s pembrolizumabom pa so bili utrujenost (31 %), diareja (22 %) in navzea (20 %). Večina poročanih neželenih učinkov pri samostojnem zdravljenju je bila po izrazitosti 1. ali 2. stopnje. Najresnejši neželeni učinki so bili imunsko pogojeni neželeni učinki in hude z infuzijo povezane reakcije. Pojavnost imunsko pogojenih neželenih učinkov pri uporabi pembrolizumaba samega za adjuvantno zdravljenje (n = 1.480) je znašala 36,1 % za vse stopnje in 8,9 % od 3. do 5. stopnje, pri metastatski bolezni (n = 5.375) pa 24,2 % za vse stopnje in 6,4 % od 3. do 5. stopnje. Pri adjuvantnem zdravljenju niso zaznali nobenih novih imunsko pogojenih neželenih učinkov. Varnost pembrolizumaba pri kombiniranem zdravljenju s kemoterapijo so ocenili pri 3.123 bolnikih z različnimi vrstami raka, ki so v kliničnih študijah prejemali pembrolizumab v odmerkih 200 mg, 2 mg/kg telesne mase ali 10 mg/kg telesne mase na vsake 3 tedne. V tej populaciji bolnikov so bili najpogostejši neželeni učinki naslednji: anemija (55 %), navzea (54 %), utrujenost (38 %), nevtropenija (36 %), zaprtost (35 %), alopecija (35 %), diareja (34 %), bruhanje (28 %) in zmanjšanje apetita (27 %). Pojavnost neželenih učinkov 3. do 5. stopnje je pri bolnikih z NSCLC pri kombiniranem zdravljenju s pembrolizumabom znašala 67 % in pri zdravljenju samo s kemoterapijo 66 %, pri bolnikih s HNSCC pri kombiniranem zdravljenju s pembrolizumabom 85 % in pri zdravljenju s kemoterapijo v kombinaciji s cetuksimabom 84 %, pri bolnikih z rakom požiralnika pri kombiniranem zdravljenju s pembrolizumabom 86 % in pri zdravljenju samo s kemoterapijo 83 %, pri bolnikih s TNBC pri kombiniranem zdravljenju s pembrolizumabom 80 % in pri zdravljenju samo s kemoterapijo 77 % in pri bolnicah z rakom materničnega vratu pri kombiniranem zdravljenju s pembrolizumabom 82 % in pri zdravljenju samo s kemoterapijo 75 %. Varnost pembrolizumaba v kombinaciji z aksitinibom ali lenvatinibom pri napredovalem RCC in v kombinaciji z lenvatinibom pri napredovalem EC so ocenili pri skupno 1.456 bolnikih z napredovalim RCC ali napredovalim EC, ki so v kliničnih študijah prejemali 200 mg pembrolizumaba na 3 tedne skupaj s 5 mg aksitiniba dvakrat na dan ali z 20 mg lenvatiniba enkrat na dan, kot je bilo ustrezno. V teh populacijah bolnikov so bili najpogostejši neželeni učinki diareja (58 %), hipertenzija (54 %), hipotiroidizem (46 %), utrujenost (41 %), zmanjšan apetit (40 %), navzea (40 %), artralgija (30 %), bruhanje (28 %), zmanjšanje telesne mase (28 %), disfonija (28 %), bolečine v trebuhu (28 %), proteinurija (27 %), sindrom palmarno-plantarne eritrodizestezije (26 %), izpuščaj (26 %), stomatitis (25 %), zaprtost (25 %), mišično-skeletna bolečina (23 %), glavobol (23 %) in kašelj (21 %). Neželenih učinkov od 3. do 5. stopnje je bilo pri bolnikih z RCC med uporabo pembrolizumaba v kombinaciji z aksitinibom ali lenvatinibom 80 % in med uporabo sunitiniba samega 71 %. Pri bolnicah z EC je bilo neželenih učinkov od 3. do 5. stopnje med uporabo pembrolizumaba v kombinaciji z lenvatinibom 89 % in med uporabo kemoterapije same 73 %. Za celoten seznam neželenih učinkov, prosimo, glejte celoten Povzetek glavnih značilnosti zdravila. Za dodatne informacije o varnosti v primeru uporabe pembrolizumaba v kombinaciji glejte povzetke glavnih značilnosti zdravila za posamezne komponente kombiniranega zdravljenja. **Način in režim izdaje zdravila:** H – Predpisovanje in izdaja zdravila je le na recept, zdravilo se uporablja samo v bolnišnicah. **Imetnik dovoljenja za promet z zdravilom:** Merck Sharp & Dohme B.V. , Waarderweg 39, 2031 BN Haarlem, Nizozems

MSD
Merck Sharp & Dohme inovativna zdravila d.o.o.,
Ameriška ulica 2, 1000 Ljubljana,
tel: +386 1/ 520 42 01, fax: +386 1/ 520 43 50;
Pripravljeno v Sloveniji, 11/2022; SI-KEY-00492 EXP: 11/2024

Samo za strokovno javnost.

H - Predpisovanje in izdaja zdravila je le na recept, zdravilo pa se uporablja samo v bolnišnicah. Pred predpisovanjem, prosimo, preberite celoten Povzetek glavnih značilnosti zdravila Keytruda, ki je na voljo pri naših strokovnih sodelavcih ali na lokalnem sedežu družbe.

SEDAJ ODOBRENO PO VSAJ ENI PREDHODNI TERAPIJI NA PODLAGI ANTI-HER2[1]

ENHERTU®
trastuzumab derukstekan

NEPRIMERLJIVO PREŽIVETJE*
POSTAVLJA NOVE STANDARDE ZDRAVLJENJA HER2+ METASTATSKEGA RAKA DOJK[2]

Zdravilo ENHERTU se uporablja v monoterapiji in je v raziskavi DESTINY-Breast03 dokazalo neprimerljivo podaljšanje PFS v primerjavi s trenutnim standardom zdravljenja (T-DM1). V študiji so poročali o primerih intersticijske pljučne bolezni (ILD) in pnevmonitisa. Za diagnozo je ključno prepoznavanje simptomov, zato je bolnike treba spremljati in pričeti z zdravljenjem ob prvih znakih ILD.[1,2]

SKRAJŠAN POVZETEK GLAVNIH ZNAČILNOSTI ZDRAVILA

▼ Za to zdravilo se izvaja dodatno spremljanje varnosti. Tako bodo hitreje na voljo nove informacije o njegovi varnosti. Zdravstvene delavce naprošamo, da poročajo o katerem koli domnevnem neželenem učinku zdravila.

ENHERTU 100 mg prašek za koncentrat za raztopino za infundiranje

SESTAVA: Ena viala praška za koncentrat za raztopino za infundiranje vsebuje 100 mg trastuzumab derukstekana. Po rekonstituciji ena viala s 5 ml raztopine vsebuje 20 mg/ml trastuzumab derukstekana. Trastuzumab derukstekan je konjugat protitelesa in zdravila, ki vsebuje humanizirano monoklonsko protitelo IgG1 proti HER2 z istim zaporedjem aminokislin, kot ga ima trastuzumab. Proizvajajo ga sesalske celice (ovarij kitajskega hrčka) in je prek razcepljivega veznika na tetrapeptidni bazi kovalentno vezan na DXd, ki je derivat eksatekana in zaviralec topoizomeraze I. Na vsako molekulo protitelesa je vezanih približno 8 molekul derukstekana. *Pomožne snovi:* L-histidin, -Lhistidinijev klorid monohidrat, saharoza, polisorbat 80. **TERAPEVTSKE INDIKACIJE:** Zdravilo Enhertu kot monoterapija je indicirano za zdravljenje odraslih bolnikov z neresektabilnim ali metastatskim HER2-pozitivnim rakom dojk, ki so pred tem že prejeli eno ali več shem zdravljenja na podlagi anti-HER2. **ODMERJANJE IN NAČIN UPORABE:** Zdravilo Enhertu mora predpisati zdravnik in njegovo dajanje nadzorovati zdravstveni delavec, ki sta izkušena v uporabi zdravil proti raku. Za preprečitev napak, povezanih z zdravili, je pomembno, da preverite nalepke na vialah in se prepričate, da je zdravilo, ki se pripravlja in daje, res zdravilo Enhertu (trastuzumab derukstekan), in ne trastuzumab ali trastuzumab emtanzin. Zdravilo Enhertu se ne sme zamenjati s trastuzumabom ali trastuzumab emtanzinom. Bolniki, ki se zdravijo s trastuzumab derukstekanom, morajo imeti dokumentiran HER2-pozitiven status tumorja, ki je opredeljen kot ocena 3 + na podlagi imunohistokemije (IHC) ali razmerje ≥ 2,0 na podlagi *in situ* hibridizacije (ISH) ali fluorescenčne *in situ* hibridizacije (FISH), ocenjeno z *in vitro* diagnostičnim (IVD) medicinskim pripomočkom z oznako CE. Če IVD z oznako CE ni na voljo, je treba status HER2 oceniti z drugim potrjenim testom. Odmerjanje: Priporočeni odmerek zdravila Enhertu je 5,4 mg/kg, ki se daje z intravensko infuzijo enkrat vsake 3 tedne (21-dnevni cikel) do napredovanja bolezni ali nesprejemljive toksičnosti. Začetni odmerek je treba dati z 90-minutno intravensko infuzijo. Če bolnik prejšnjo infuzijo dobro prenaša, se lahko naslednji odmerki zdravila Enhertu dajejo kot 30-minutne infuzije. Hitrost infundiranja zdravila Enhertu je treba zmanjšati ali infundiranje prekiniti, če se pri bolniku razvijejo simptomi, povezani z infuzijo. V primeru hudih reakcij na infuzijo je treba zdravilo Enhertu trajno ukiniti. Premedikacija: Zdravilo Enhertu je emetogeno, kar vključuje zapoznelo navzeo in/ali bruhanje. Pred vsakim odmerkom zdravila Enhertu je treba bolnike premedicirati s kombiniranim režimom dveh ali treh zdravil (npr. deksametazon z antagonistom receptorjev 5-HT3 in/ali antagonistom receptorjev NK1 ter drugimi zdravili, kot je indicirano) za preprečevanje navzee in bruhanja zaradi kemoterapije. Prilagajanje odmerka: Obvladovanje neželenih učinkov lahko zajema začasno prekinitev uporabe, zmanjšanje odmerka ali ukinitev zdravljenja z zdravilom Enhertu, skladno s smernicami, podanimi v povzetku glavnih značilnosti zdravila (preglednici 1 in 2). Po zmanjšanju odmerka zdravila Enhertu se odmerek ne sme več ponovno povečati. Načrt zmanjševanja odmerka: Začetni odmerek je 5,4 mg/kg, prvo zmanjšanje odmerka (4,4 mg/kg), drugo zmanjšanje odmerka (3,2 mg/kg), pri potrebi po nadaljnjem zmanjšanju odmerka ukinite zdravljenje. *Prosimo, glejte celoten povzetek glavnih značilnosti zdravila Enhertu za prilagajanje odmerka zaradi neželenih učinkov: intersticijska pljučna bolezen (ILD)/pnevmonitis* (asimptomatska ILD/asimptomatski pnevmonitis (stopnja 1), simptomatska ILD/simptomatski pnevmonitis (stopnja 2 ali višja)), *nevtropenija* (stopnja 3 (manj kot 1,0-0,5 × 10^9/l), stopnja 4 (manj kot 0,5 × 10^9/l)), *febrilna nevtropenija* (absolutno število nevtrofilcev manj kot 1,0 × 10^9/l in telesna temperatura, višja od 38,3 °C, ali telesna temperatura 38 °C ali višja, ki vztraja več kot eno uro), *zmanjšan iztisni delež levega prekata* (LVEF) (LVEF več kot 45 % in absolutno zmanjšanje glede na izhodiščno vrednost za 10 % do 20 %; LVEF 40 % do 45 %; LVEF manj kot 40 % ali absolutno zmanjšanje glede na izhodiščno vrednost za več kot 20 %; simptomatično kongestivno srčno popuščanje). Zakasnjen ali izpuščen odmerek: Če se načrtovani odmerek zakasni ali izpusti, ga je treba dati takoj, ko je mogoče, brez čakanja na naslednji načrtovani cikel. Časovni načrt dajanja je treba prilagoditi, da se ohrani 3-tedenski razmik med odmerki. Infuzijo je treba dati s hitrostjo in odmerkom, ki ga je bolnik prenašal pri zadnji infuziji. Posebne populacije: *Starejši:* Pri bolnikih, starih 65 let ali starejših, prilagajanje odmerka zdravila Enhertu ni potrebno. Podatki pri bolnikih, starih ≥ 75 let, so omejeni. *Okvara ledvic:* Prilagajanje odmerka pri bolnikih z blago (očistek kreatinina [CLcr] ≥ 60 in < 90 ml/min) ali zmerno (CLcr ≥ 30 in < 60 ml/min) okvaro ledvic ni potrebno. Morebitne potrebe po prilagajanju odmerka pri bolnikih s hudo okvaro ledvic ni mogoče opredeliti zaradi pomanjkanja podatkov. Pri bolnikih z zmerno okvaro ledvic so opazili višjo incidenco ILD stopnje 1 in 2/pnevmonitisa, ki sta vodila do zvečanja števila prekinitev zdravljenja. Bolnike z zmerno ali hudo okvaro ledvic je treba natančno spremljati glede neželenih učinkov, vključno z ILD/pnevmonitisom. *Okvara jeter:* Pri bolnikih, ki imajo celokupni bilirubin ≤ 1,5-kratnik zgornje meje normalnih vrednosti (ZMN), ne glede na vrednost aspartat transaminaze (AST), odmerka ni treba prilagajati. Morebitne potrebe po prilagajanju odmerka pri bolnikih, ki imajo celokupni bilirubin > 1,5-kratnik ZMN, ne glede na vrednost AST, ni mogoče opredeliti zaradi pomanjkanja podatkov. Zato je treba te bolnike natančno spremljati. Način uporabe: Zdravilo Enhertu je za intravensko uporabo. Zdravstveni delavec ga mora rekonstituirati in razredčiti. Treba ga je dati z intravenskim infundiranjem. Zdravilo Enhertu se ne sme dati kot hitro intravensko injekcijo ali bolus. **KONTRAINDIKACIJE:** Preobčutljivost na učinkovino ali katero koli pomožno snov. **POSEBNA OPOZORILA IN PREVIDNOSTNI UKREPI:** Intersticijska pljučna bolezen/pnevmonitis: Pri zdravilu Enhertu so poročali o primerih intersticijske pljučne bolezni (ILD) in/ali pnevmonitisa. Nekateri primeri so bili smrtni. Bolnikom je treba naročiti, naj takoj poročajo o kašlju, dispneji, zvišani telesni temperaturi in/ali katerih koli novih dihalnih simptomih ali poslabšanju obstoječih. Bolnike je treba spremljati glede znakov in simptomov ILD/pnevmonitisa. Dokaze za ILD/pnevmonitis je treba takoj proučiti. Bolnike s sumom na ILD/pnevmonitis je treba oceniti z radiografskimi posnetki, najbolje z računalniško tomografijo (CT). Treba je razmisliti o posvetu s pulmologom. Nevtropenija: V kliničnih študijah z zdravilom Enhertu so poročali o primerih nevtropenije, vključno s primeri febrilne nevtropenije. Pred uvedbo zdravila Enhertu in pred vsakim odmerkom ter vsakič, ko je klinično indicirano, je treba preveriti celotno krvno sliko. Morda bo treba začasno prekiniti dajanje zdravila Enhertu ali zmanjšati odmerek, odvisno od tega, kako huda je nevtropenija. Zmanjšanje iztisnega deleža levega prekata: Pri zdravljenjih anti-HER2 so poročali o zmanjšanem iztisnem deležu levega prekata (LVEF). Pred uvedbo zdravljenja z zdravilom Enhertu in v rednih intervalih med njim (v skladu s kliničnimi indikacijami) je treba izvesti standardne preiskave delovanja srca (ehokardiografija ali slikanje MUGA) za oceno LVEF. Zmanjšanje LVEF je treba obvladovati s prekinitvami zdravljenja. Zdravljenje z zdravilom Enhertu je treba trajno ukiniti, če se potrdi LVEF manj kot 40 % ali absolutno zmanjšanje glede na izhodiščno vrednost za več kot 20 %. Zdravilo Enhertu je treba trajno ukiniti pri bolnikih s simptomatskim kongestivnim srčnim popuščanjem. Embrio-fetalna toksičnost: Zdravilo Enhertu lahko ima škodljiv vpliv na plod, če se da nosečnici. Pri ženskah v rodni dobi je treba pred uvedbo zdravljenja z zdravilom Enhertu preveriti status nosečnosti. Bolnice je treba seznaniti z možnimi tveganji za plod. Ženskam v rodni dobi je treba svetovati, da uporabljajo učinkovito kontracepcijo med zdravljenjem in še vsaj 7 mesecev po zadnjem odmerku zdravila Enhertu. Moškim bolnikom s partnerkami v rodni dobi je treba svetovati, da uporabljajo učinkovito kontracepcijo med zdravljenjem z zdravilom Enhertu in še vsaj 4 mesece po zadnjem odmerku zdravila Enhertu. Bolniki z zmerno ali hudo okvaro jeter: Zdravilo Enhertu je treba pri bolnikih z zmerno in hudo okvaro jeter dajati previdno. **MEDSEBOJNO DELOVANJE Z DRUGIMI ZDRAVILI IN DRUGE OBLIKE INTERAKCIJ:** Pri sočasnem dajanju trastuzumab derukstekana z zdravili, ki so zaviralci CYP3A ali OATP1B ali prenašalcev P-gp, odmerka ni treba prilagajati. **PLODNOST, NOSEČNOST IN DOJENJE:** Nosečnost: Dajanje zdravila Enhertu nosečnicam se ne priporoča. Bolnice je treba seznaniti z možnimi tveganji za plod, preden zanosijo. Ženske, ki zanosijo, se morajo takoj obrniti na zdravnika. Če ženska zanosi med zdravljenjem z zdravilom Enhertu ali v obdobju 7 mesecev po zadnjem odmerku zdravila Enhertu, se priporoča natančno spremljanje. Dojenje: Ni znano, ali se trastuzumab derukstekan izloča v materino mleko. Humani IgG se izloča v materino mleko in potencial za absorpcijo in resne neželene učinke na dojenčka ni znan. Zato ženske ne smejo dojiti med zdravljenjem z zdravilom Enhertu in še 7 mesecev po zadnjem odmerku. Odločiti se je treba med prenehanjem dojenja in prenehanjem zdravljenja z zdravilom Enhertu, pri čemer je treba pretehtati prednosti dojenja za otroka in prednosti zdravljenja za mater. Plodnost: Namenskih študij plodnosti s trastuzumab derukstekanom niso izvedli. Ni znano, ali so trastuzumab derukstekan ali njegovi presnovki prisotni v semenski tekočini. Pred začetkom zdravljenja je treba moškim bolnikom svetovati, da se posvetujejo o možnosti shranjevanja semena. Moški bolniki v celotnem obdobju zdravljenja in še najmanj 4 mesece po zadnjem odmerku zdravila Enhertu ne smejo zamrzniti ali darovati semena. **NEŽELENI UČINKI:** Združeno varnostno populacijo so ocenili pri bolnikih, ki so v kliničnih študijah dobili vsaj en odmerek 5,4 mg/kg zdravila Enhertu (n = 573) zaradi različnih vrst tumorjev. Mediani čas trajanja zdravljenja v tej združeni populaciji je bil 11,3 meseca (razpon: 0,7-37,9 meseca). *Zelo pogosti:* okužba zgornjih dihal, nevtropenija, anemija, levkopenija, trombocitopenija, limfopenija, hipokaliemija, zmanjšan apetit, glavobol, omotica, intersticijska pljučna bolezen, dispneja, kašelj, epistaksa, navzea, bruhanje, driska, bolečina v trebuhu, zaprtje, stomatitis, dispepsija, zvišane transaminaze, alopecija, mišično-skeletna bolečina, utrujenost, pireksija, zmanjšan iztisni delež, izguba telesne mase. *Pogosti:* pljučnica, febrilna nevtropenija, dehidracija, disgevzija, zameglјen vid, izpuščaj, hiperpigmentacija kože, pruritus, periferni edem, zvišana alkalna fosfataza v krvi, zvišan bilirubin v krvi, zvišan kreatinin v krvi, reakcije povezane z infuzijo. **IMETNIK DOVOLJENJA ZA PROMET Z ZDRAVILOM:** Daiichi Sankyo Europe GmbH, Zielstattstrasse 48, 81379 München, Nemčija **DATUM ZADNJE REVIZIJE BESEDILA:** 25.08.2022 (SI-2430) **REŽIM PREDPISOVANJA IN IZDAJE:** H **Prosimo, da pred predpisovanjem preberete celoten povzetek glavnih značilnosti zdravila.** Dodatne informacije so na voljo pri podjetju AstraZeneca UK Limited, Podružnica v Sloveniji, Verovškova 55, 1000 Ljubljana, telefon: 01/51 35 600.

* zmanjšanje tveganja za napredovanje bolezni ali smrti (PFS)

** tveganje za napredovanje bolezni ob zdravljenju z zdravilom ENHERTU v primerjavi s T-DM1 (HR: 0,28; 95 % IZ: 0,22-0,37; p<0,000001, ključni opazovani dogodek raziskave: PFS glede na BICR;)[1,2]

***po oceni raziskovalca je mediani PFS znašal **25,1 mesecev** pri bolnikih, ki so prejemali ENHERTU, v primerjavi s **7,2 mesecev** pri bolnikih zdravljenih s T-DM1 (HR: 0,26; 95 % IZ: 0,20, 0,35; sekundarni opazovani dogodek;)[2]

PFS - preživetje brez napredovanja bolezni, **mPFS** - mediano preživetje brez napredovanja bolezni, **T-DM1** - trastuzumab emtazin, **BICR** - ocena slepega neodvisnega centralnega pregleda, **IZ** - interval zaupanja, **HR** - razmerje ogroženosti

Literatura: 1. Povzetek glavnih značilnosti zdravila ENHERTU, dostopano 19.10.2022 **2.** J.Cortes et al; Trastuzumab Deruxtecan versus Trastuzumab Emtasine for Breast Cancer; NEJM 2022;386(12):1143-1154

Zdravilo Enhertu v Sloveniji še ni razvrščeno na listo zdravil.

Daiichi-Sankyo | AstraZeneca

Datum priprave materiala: oktober 2022. Samo za strokovno javnost. SI-2524

ROZLYTREK®▼
entrektinib

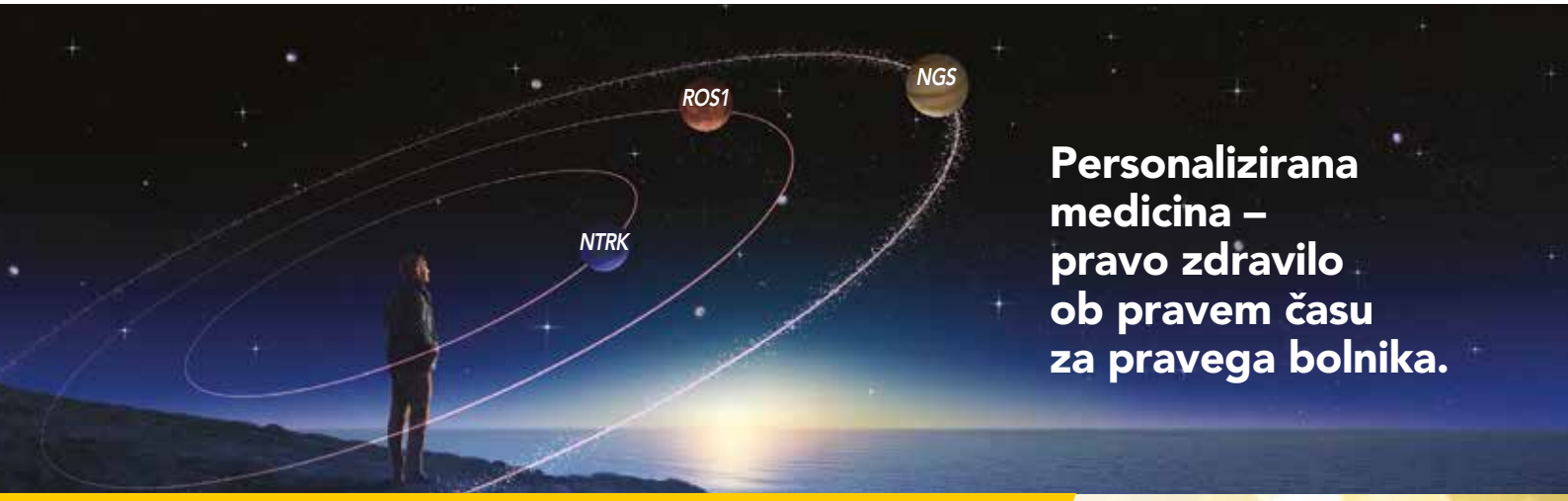

Personalizirana medicina – pravo zdravilo ob pravem času za pravega bolnika.

ROZLYTREK® (entrektinib) je prvo odobreno tumor agnostično zdravilo podjetja Roche za zdravljenje odraslih in pediatričnih bolnikov, starih 12 let ali več, s solidnimi tumorji s prisotno fuzijo gena NTRK ter za zdravljenje odraslih bolnikov z ROS1-pozitivnim napredovalim NDRP.[1]

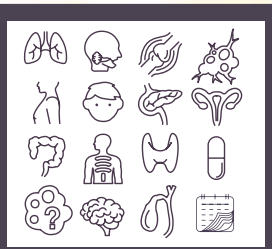

NGS = next-generation sequencing, sekvenciranje naslednje generacije

Skrajšan povzetek glavnih značilnosti zdravila Rozlytrek

▼ **Za to zdravilo se izvaja dodatno spremljanje varnosti. Tako bodo hitreje na voljo nove informacije o njegovi varnosti. Zdravstvene delavce naprošamo, da poročajo o katerem koli domnevnem neželenem učinku zdravila. Kako poročati o neželenih učinkih, si poglejte skrajšani povzetek glavnih značilnosti zdravila pod ˝Poročanje o domnevnih neželenih učinkih".**

Ime zdravila: Rozlytrek 100 mg/200 mg trde kapsule **Kakovostna in količinska sestava:** Rozlytrek 100 mg trde kapsule: Ena trda kapsula vsebuje 100 mg entrektiniba. Rozlytrek 200 mg trde kapsule: Ena trda kapsula vsebuje 200 mg entrektiniba. **Terapevtske indikacije:** Zdravilo Rozlytrek je kot monoterapija indicirano za zdravljenje odraslih in pediatričnih bolnikov, starih 12 let ali več, s solidnimi tumorji s prisotno fuzijo gena nevrotropne receptorske tirozin kinaze (***NTRK***), pri katerih je bolezen lokalno napredovala, je razsejana ali kjer bi kirurška odstranitev povzročila hudo obolevnost in ki predhodno niso prejeli zaviralca ***NTRK*** in nimajo drugih zadovoljivih možnosti zdravljenja. Zdravilo Rozlytrek je kot monoterapija indicirano za zdravljenje odraslih bolnikov z ***ROS1***-pozitivnim napredovalim nedrobnoceličnim rakom pljuč (NDRP), ki predhodno niso bili zdravljeni z zaviralci ***ROS-1***. **Odmerjanje in način uporabe:** Priporočeni odmerek za odrasle je 600 mg entrektiniba enkrat na dan. Priporočeni odmerek za pediatrične bolnike, stare 12 let ali več, je 300 mg/m² telesne površine entrektiniba enkrat na dan. Zdravilo Rozlytrek je za peroralno uporabo. Trde kapsule je treba pogoltniti cele in se jih ne sme odpirati ali raztapljati, ker je vsebina kapsule zelo grenka. Zdravilo Rozlytrek se lahko jemlje s hrano ali brez nje, ne sme pa se ga jemati z grenivko ali grenivkinim sokom. **Kontraindikacije:** Preobčutljivost na učinkovino ali katero koli pomožno snov. **Posebna opozorila in previdnostni ukrepi:** Učinkovitost med tumorskimi tipi: Korist zdravila Rozlytrek so ugotovili v študijah z eno skupino, ki so vključevale relativno majhen vzorec bolnikov, katerih tumorji izražajo fuzijo gena ***NTRK***. Pozitivni učinki zdravila Rozlytrek so se pokazali preko celokupnega odgovora in trajanja odgovora pri omejenem številu tumorskih tipov. Učinek je lahko pri različnih tumorskih tipih kvantitativno različen, vplivajo pa tudi sočasne genomske spremembe. Zato se sme zdravilo Rozlytrek uporabljati le v primerih, če ni na voljo drugega zadovoljivega zdravljenja. Kognitivne motnje: V kliničnih preskušanjih zdravila Rozlytrek so poročali o kognitivnih motnjah. Pri bolnikih je treba biti pozoren na znake kognitivnih sprememb. Glede na resnost kognitivnih motenj, je zdravljenje z zdravilom Rozlytrek treba prilagoditi. Bolnike je treba seznaniti z možnimi kognitivnimi spremembami med zdravljenjem z zdravilom Rozlytrek. Bolnikom je treba naročiti, naj v primeru simptomov kognitivnih motenj ne vozijo in ne upravljajo strojev, dokler simptomi ne minejo. Zlomi: O zlomih kosti so poročali pri bolnikih, mlajših od 12 let, zlomi so bili lokalizirani v spodnjih okončinah. Zlomi kosti so se pri pediatričnih bolnikih večinoma pojavili brez ali z majhno poškodbo. Vsi bolniki so nadaljevali zdravljenje z zdravilom Rozlytrek, pri vseh razen v enem primeru so se zlomi zacelili. Bolnike z znaki ali simptomi zloma je treba nemudoma oceniti. Hiperurikemija: Pri zdravljenju bolnikov z entrektinibom so opazili hiperurikemijo. Koncentracijo sečne kisline v serumu je treba preveriti pred začetkom zdravljenja z zdravilom Rozlytrek in periodično med samim zdravljenjem. Bolnike je treba spremljati glede znakov in simptomov hiperurikemije. Pri znakih in simptomih hiperurikemije je treba uvesti zdravljenje z zdravili, ki znižajo koncentracijo sečne kisline, če je klinično indicirano, in zdravljenje z zdravilom Rozlytrek odložiti. Odmerek zdravila Rozlytrek je treba prilagoditi glede na izrazitost. Kongestivno srčno popuščanje: V kliničnih preskušanjih zdravila Rozlytrek so pri manj kot 5 % bolnikov poročali o kongestivnem srčnem popuščanju. Opažali so ga tako pri bolnikih z anamnezo srčne bolezni kot pri bolnikih brez nje. Pri 70 % bolnikov je po uvedbi ustrezne klinične obravnave in/ali zmanjšanju odmerka oziroma prekinitvi uporabe zdravila Rozlytrek kongestivno srčno popuščanje izzvenelo. Bolnikom s simptomi ali znanimi dejavniki tveganja za kongestivno srčno popuščanje je pred začetkom zdravljenja z zdravilom Rozlytrek treba preveriti iztisni delež levega prekata. Bolnike, ki prejemajo zdravilo Rozlytrek, je treba skrbno nadzorovati. Bolnike, pri katerih se pojavijo klinični znaki in simptomi kongestivnega srčnega popuščanja, je treba ovrednotiti in zdraviti, kot je klinično ustrezno. Glede na izrazitost kongestivnega srčnega popuščanja je treba zdravljenje z zdravilom Rozlytrek prilagoditi. Podaljšanje intervala QTc: V kliničnih preskušanjih so pri bolnikih, zdravljenih z zdravilom Rozlytrek, opažali podaljšanje intervala QTc. Uporabi zdravila Rozlytrek se je treba izogibati pri bolnikih, ki imajo pred začetkom zdravljenja QTc interval daljši od 450 ms, pri bolnikih s sindromom prirojenega dolgega QTc in pri bolnikih, ki jemljejo zdravila, za katera je znano, da podaljšajo interval QTc. Zdravilu Rozlytrek se je treba izogibati pri bolnikih z motenim ravnovesjem elektrolitov ali hujšo srčno boleznijo. Če lečeči zdravnik meni, da možne koristi zdravila Rozlytrek pri bolniku s katerikolim od teh stanj pretehtajo možna tveganja, je potrebno dodatno spremljanje in razmislek o posvetu s specialistom. Priporoča se ocena EKG in elektrolitov pred začetkom zdravljenja in po 1 mesecu zdravljenja z zdravilom Rozlytrek. Periodično spremljanje EKG in elektrolitov med zdravljenjem je priporočljivo, če je klinično indicirano. Glede na izrazitost podaljšanja intervala QTc je treba zdravljenje z zdravilom Rozlytrek prilagoditi. Ženske v rodni dobi: Zdravilo Rozlytrek lahko škoduje plodu, če je uporabljeno med nosečnostjo. Ženske v rodni dobi morajo med zdravljenjem in še do 5 tednov po zadnjem odmerku zdravila Rozlytrek uporabljati visokoučinkovito kontracepcijsko zaščito. Moški bolniki, ki imajo partnerke v rodni dobi, morajo med zdravljenjem z zdravilom Rozlytrek in 3 mesece po zadnjem odmerku zdravila uporabljati visokoučinkovite kontracepcijske metode. Intoleranca za laktozo: Zdravilo Rozlytrek vsebuje laktozo. Bolniki z redko dedno intoleranco za galaktozo, odsotnostjo encima laktaze ali malabsorbcijo glukoze/galaktoze ne smejo jemati tega zdravila. Oranžno FCF (E110): Rozlytrek 200 mg trde kapsule vsebujejo oranžno FCF, ki lahko povzroči alergijske reakcije. **Medsebojno delovanje z drugimi zdravili in druge oblike interakcij:** Interakcije med zdravili: Sočasno jemanje zdravila Rozlytrek z močnimi ali zmernimi zaviralci CYP3A zviša koncentracije entrektiniba v plazmi, to pa lahko poveča pogostnost ali resnost neželenih učinkov. Pri odraslih in pediatričnih bolnikih, starih 12 let ali več, se je sočasnemu jemanju zdravila Rozlytrek z močnimi ali zmernimi zaviralci CYP3A treba izogibati. Če je pri odraslih bolnikih sočasno jemanje s temi zdravili nujno potrebno, je treba odmerek zdravila Rozlytrek znižati. Med zdravljenjem z zdravilom Rozlytrek se je treba izogibati jemanju grenivke in izdelkov, ki vsebujejo grenivko. Sočasno jemanje zdravila Rozlytrek z močnimi ali zmernimi spodbujevalci CYP3A ali P-gp zniža koncentracije entrektiniba v plazmi, kar lahko zmanjša učinkovitost zdravila Rozlytrek in temu se je treba izogibati. ***Peroralni kontraceptivi:*** Trenutno ni znano, če lahko entrektinib zmanjša učinkovitost hormonskih sistemskih kontraceptivov. Zato ženskam, ki uporabljajo hormonske sistemske kontraceptive, priporočamo, da dodatno uporabijo še pregradno metodo. **Neželeni učinki**: Najpogostejši neželeni učinki (≥ 20 %) so bili utrujenost, zaprtost, disgevzija, edem, omotica, diareja, navzea, disestezija, dispneja, anemija, povečana telesna masa, povišana vrednost kreatinina v krvi, bolečina, kognitivne motnje, bruhanje, kašelj in zvišana telesna temperatura. Najpogostejši resni neželeni učinki (≥ 2 %) so bili okužba pljuč (5,2 %), dispneja (4,6 %), kognitivne motnje (3,8 %), plevralni izliv (3,0 %) in zlomi (2,4 %). Ukinitev zdravljenja zaradi neželenega učinka je bila prisotna pri 4,6 % bolnikov. Poročanje o domnevnih neželenih učinkih: Poročanje o domnevnih neželenih učinkih zdravila po izdaji dovoljenja za promet je pomembno. Omogoča namreč stalno spremljanje razmerja med koristmi in tveganji zdravila. Od zdravstvenih delavcev se zahteva, da poročajo o katerem koli domnevnem neželenem učinku zdravila na: Javna agencija Republike Slovenije za zdravila in medicinske pripomočke, Sektor za farmakovigilanco, Nacionalni center za farmakovigilanco, Slovenčeva ulica 22, SI-1000 Ljubljana, Tel: +386 (0)8 2000 500, Faks: +386 (0)8 2000 510, e-pošta: h-farmakovigilanca@jazmp.si, spletna stran: www.jazmp.si. **Režim izdaje zdravila:** Rp/Spec **Imetnik dovoljenja za promet:** Roche Registration GmbH, Emil-Barell-Strasse 1, 79639 Grenzach-Wyhlen, Nemčija **Verzija:** 1.0/22

M-SI-00000652(v1.0)

1. Glavni povzetek značilnosti zdravila Rozlytrek, dostopano na https://ec.europa.eu/health/documents/community-register/2020/20200731148534/anx_148534_sl.pdf dne 25.10.2022.

Samo za strokovno javnost. Datum priprave informacije: oktober 2022

DODATNE INFORMACIJE SO NA VOLJO PRI: Roche farmacevtska družba d.o.o., Stegne 13G, 1000 Ljubljana

Roche

Zdravilo Lonsurf je indicirano v monoterapiji za zdravljenje odraslih bolnikov z metastatskim kolorektalnim rakom (KRR), ki so bili predhodno že zdravljeni ali niso primerni za zdravljenja, ki so na voljo. Ta vključujejo kemoterapijo na osnovi fluoropirimidina, oksaliplatina in irinotekana, zdravljenje z zaviralci žilnega endotelijskega rastnega dejavnika (VEGF – Vascular Endothelial Growth Factor) in zaviralci receptorjev za epidermalni rastni dejavnik (EGFR – Epidermal Growth Factor Receptor).[1]

Zdravilo Lonsurf je indicirano v monoterapiji za zdravljenje odraslih bolnikov z metastatskim rakom želodca vključno z adenokarcinomom gastro-ezofagealnega prehoda, ki so bili predhodno že zdravljeni z najmanj dvema sistemskima režimoma zdravljenja za napredovalo bolezen.[1]

VEČ ČASA

za več trenutkov, ki štejejo

Podaljša celokupno preživetje
v 3. liniji zdravljenja bolnikov z mCRC in mGC[2,3]

Literatura: 1. Povzetek glavnih značilnosti zdravila Lonsurf, december 2020. 2. Mayer R et al. N Engl J Med. 2015;372:1909-19. 3. Shitara K et al. Lancet Oncol. 2018;19:1437-1448.
Družba Servier ima licenco družbe Taiho za zdravilo Lonsurf®.
Pri globalnem razvoju zdravila sodelujeta obe družbi in ga tržita na svojih določenih področjih.

Lonsurf®
trifluridin/tipiracil

Skrajšan povzetek glavnih značilnosti zdravila: Lonsurf 15 mg/6,14 mg filmsko obložene tablete in Lonsurf 20 mg/8,19 mg filmsko obložene tablete
SESTAVA*: Lonsurf 15 mg/6,14 mg: Ena filmsko obložena tableta vsebuje 15 mg trifluridina in 6,14 mg tipiracila (v obliki klorida). **Lonsurf 20 mg/8,19 mg**: Ena filmsko obložena tableta vsebuje 20 mg trifluridina in 8,19 mg tipiracila (v obliki klorida). **TERAPEVTSKE INDIKACIJE*:** Kolorektalni rak - v monoterapiji za zdravljenje odraslih bolnikov z metastatskim kolorektalnim rakom, ki so bili predhodno že zdravljeni ali niso primerni za zdravljenja, ki so na voljo. Ta vključujejo kemoterapijo na osnovi fluoropirimidina, oksaliplatina in irinotekana, zdravljenje z zaviralci žilnega endotelijskega rastnega dejavnika (VEGF - Vascular Endothelial Growth Factor) in zaviralci receptorjev za epidermalni rastni dejavnik (EGFR - Epidermal Growth Factor Receptor). Rak želodca - v monoterapiji za zdravljenje odraslih bolnikov z metastatskim rakom želodca vključno z adenokarcinomom gastro-ezofagealnega prehoda, ki so bili predhodno že zdravljeni z najmanj dvema sistemskima režimoma zdravljenja za napredovalo bolezen. **ODMERJANJE IN NAČIN UPORABE*:** Priporočeni začetni odmerek zdravila Lonsurf pri odraslih je 35 mg/m^2/odmerek peroralno dvakrat dnevno na 1. do 5. dan in 8. do 12. dan vsakega 28-dnevnega cikla zdravljenja, najpozneje 1 uro po zaključku jutranjega in večernega obroka (20 mg/m^2/odmerek dvakrat dnevno pri bolnikih s hudo ledvično okvaro). Odmerek, izračunan glede na telesno površino, ne sme preseči 80 mg/odmerek. Možne prilagoditve odmerka glede na varnost in prenašanje zdravila: dovoljena so zmanjšanja odmerka na najmanjši odmerek 20 mg/m^2 dvakrat dnevno (oz. 15 mg/m^2 dvakrat dnevno pri bolnikih s hudo ledvično okvaro). Potem ko je bil odmerek zmanjšan, povečanje ni dovoljeno. **KONTRAINDIKACIJE*:** Preobčutljivost na učinkovini ali katero koli pomožno snov. **OPOZORILA IN PREVIDNOSTNI UKREPI*:** Supresija kostnega mozga: Pred uvedbo zdravljenja in po potrebi za spremljanje toksičnosti zdravila, najmanj pred vsakim ciklom zdravljenja, je treba pregledati celotno krvno sliko. Zdravljenja ne smete začeti, če je absolutno število nevtrofilcev < 1,5 x 10^9/l, če je število trombocitov < 75 x 10^9/l ali če se je pri bolniku zaradi predhodnih zdravljenj pojavila klinično pomembna nehematološka toksičnost 3. ali 4. stopnje, ki še traja. Bolnike je treba skrbno spremljati zaradi morebitnih okužb, uvesti je treba ustrezne ukrepe, kot je klinično indicirano. Toksičnost za prebavila: Potrebna je uporaba antiemetikov, antidiaroikov ter drugih ukrepov, kot je klinično indicirano. Če je potrebno, prilagodite odmerke. Ledvična okvara: Uporaba zdravila ni priporočljiva pri bolnikih s končno stopnjo ledvične okvare. Bolnike z ledvično okvaro je potrebno med zdravljenjem skrbno spremljati; bolnike z zmerno ali hudo ledvično okvaro je treba zaradi hematološke toksičnosti bolj pogosto spremljati. Jetrna okvara: Uporaba zdravila Lonsurf pri bolnikih z obstoječo zmerno ali hudo jetrno okvaro ni priporočljiva. Proteinurija: Pred začetkom zdravljenja in med njim je priporočljivo spremljanje proteinurije z urinskimi testnimi lističi. Pomožne snovi: Zdravilo vsebuje laktozo. **INTERAKCIJE*:** Previdnost: Zdravila, ki medsebojno delujejo z nukleozidnimi prenašalci CNT1, ENT1 in ENT2, zaviralci OCT2 ali MATE1, substrati humane timidin-kinaze (npr. zidovudin), hormonski kontraceptivi. **PLODNOST*. NOSEČNOST IN DOJENJE*:** Ni priporočljivo. **KONTRACEPCIJA*:** Ženske in moški morajo uporabljati zelo učinkovite metode kontracepcije med zdravljenjem in do 6 mesecev po zaključku zdravljenja. **VPLIV NA SPOSOBNOST VOŽNJE IN UPRAVLJANJA STROJEV*:** Med zdravljenjem se lahko pojavijo utrujenost, omotica ali splošno slabo počutje. **NEŽELENI UČINKI*:** Zelo pogosti: nevtropenija, levkopenija, anemija, trombocitopenija, zmanjšan apetit, diareja, navzea, bruhanje, utrujenost. Pogosti: okužba spodnjih dihal, febrilna nevtropenija, limfopenija, hipoalbuminemija, disgevzija, periferna nevropatija, dispneja, bolečina v trebuhu, zaprtje, stomatitis, bolezni ustne votline, hiperbilirubinemija, sindrom palmarne plantarne eritrodisestezije, izpuščaj, alopecija, pruritus, suha koža, proteinurija, pireksija, edem, vnetje sluznice, splošno slabo počutje, zvišanje jetrnih encimov, zvišanje alkalne fosfataze v krvi, zmanjšanje telesne mase. Občasni: septični šok, infekcijski enteritis, pljučnica, okužba žolčevoda, gripa, okužba sečil, gingivitis, herpes zoster, tinea pedis, okužba s kandido, bakterijska okužba, okužba, nevtropenična sepsa, okužba zgornjih dihal, konjunktivitis, bolečina zaradi raka, pancitopenija, granulocitopenija, monocitopenija, eritropenija, levkocitoza, monocitoza, dehidracija, hiperglikemija, hiperkaliemija, hipokaliemija, hipofosfatemija, hipernatriemija, hiponatriemija, hipokalciemija, protin, anksioznost, nespečnost, nevrotoksičnost, disestezija, hiperestezija, hipoestezija, sinkopa, parestezija, pekoč občutek, letargija, omotica, glavobol, zmanjšana ostrina vida, zamegljen vid, diplopija, katarakta, suho oko, vrtoglavica, neugodje v ušesu, angina pektoris, aritmija, palpitacije, embolija, hipertenzija, hipotenzija, vročinski oblivi, pljučna embolija, plevralni izliv, izcedek iz nosu, disfonija, orofaringealna bolečina, epistaksa, kašelj, hemoragični enterokolitis, krvavitev v prebavilih, akutni pankreatitis, ascites, ileus, subileus, kolitis, gastritis, refluksni gastritis, ezofagitis, moteno praznjenje želodca, abdominalna distenzija, analno vnetje, razjede v ustih, dispepsija, gastroezofagealna refluksna bolezen, proktalgija, bukalni polip, krvavitev dlesni, glositis, parodontalna bolezen, bolezen zob, siljenje na bruhanje, flatulenca, slab zadah, hepatotoksičnost, razširitev žolčnih vodov, luščenje kože, urtikarija, preobčutljivostne reakcije na svetlobo, eritem, akne, hiperhidroza, žulj, bolezni nohtov, otekanje sklepov, artralgija, bolečina v kosteh, mialgija, mišično-skeletna bolečina, mišična oslabelost, mišični krči, bolečina v okončinah, ledvična odpoved, neinfektivni cistitis, motnje mikcije, hematurija, levkociturija, motnje menstruacije, poslabšanje splošnega zdravstvenega stanja, bolečina, občutek spremembe telesne temperature, kseroza, nelagodje, zvišanje kreatinina v krvi, podaljšanje intervala QT na elektrokardiogramu, povečanje mednarodnega umerjenega razmerja (INR), podaljšanje aktiviranega parcialnega tromboplastinskega časa (aPTČ), zvišanje sečnine v krvi, zvišanje laktatne dehidrogenaze v krvi, znižanje celokupnih proteinov, zvišanje C-reaktivnega proteina, zmanjšan hematokrit. Post-marketinške izkušnje: intersticijska bolezen pljuč. **PREVELIKO ODMERJANJE*:** Neželeni učinki, o katerih so poročali v povezavi s prevelikim odmerjanjem, so bili v skladu z uveljavljenim varnostnim profilom. Glavni pričakovani zaplet prevelikega odmerjanja je supresija kostnega mozga. **FARMAKODINAMIČNE LASTNOSTI*:** *Farmakoterapevtska skupina:* zdravila z delovanjem na novotvorbe, antimetaboliti, oznaka ATC: L01BC59. Zdravilo Lonsurf sestavljata antineoplastični timidinski nukleozidni analog, trifluridin, in zaviralec timidin-fosforilaze (TPaze), tipiracilijev klorid. Po privzemu v rakave celice timidin-kinaza fosforilira trifluridin. Ta se v celicah nato presnovi v substrat deoksiribonukleinske kisline (DNA), ki se vgradi neposredno v DNA ter tako preprečuje celično proliferacijo. TPaza hitro razgradi trifluridin in njegova presnova po peroralni uporabi je hitra zaradi učinka prvega prehoda, zato je v zdravilo vključen zaviralec TPaze, tipiracilijev klorid. **PAKIRANJE*:** 20 filmsko obloženih tablet. **NAČIN PREDPISOVANJA IN IZDAJE ZDRAVILA:** Rp/Spec. **Imetnik dovoljenja za promet:** Les Laboratoires Servier, 50, rue Carnot, 92284 Suresnes cedex, Francija. Številka dovoljenja za promet z zdravilom: EU/1/16/1096/001 (Lonsurf 15 mg/6,14 mg), EU/1/16/1096/004 (Lonsurf 20 mg/8,19 mg). **Datum zadnje revizije besedila: december 2020. *Pred predpisovanjem preberite celoten povzetek glavnih značilnosti zdravila. Celoten povzetek glavnih značilnosti zdravila in podrobnejše informacije so na voljo pri: Servier Pharma d.o.o., Podmilščakova ulica 24, 1000 Ljubljana, tel: 01 563 48 11, www.servier.si.**

LON AD1 C1 2022-23. Samo za strokovno javnost.
Datum priprave informacije: oktober 2022.

SERVIER
moved by you

Instructions for authors

The editorial policy

Radiology and Oncology is a multidisciplinary journal devoted to the publishing original and high-quality scientific papers and review articles, pertinent to oncologic imaging, interventional radiology, nuclear medicine, radiotherapy, clinical and experimental oncology, radiobiology, medical physics, and radiation protection. Papers on more general aspects of interest to the radiologists and oncologists are also published (no case reports).

The Editorial Board requires that the paper has not been published or submitted for publication elsewhere; the authors are responsible for all statements in their papers. Accepted cannot be published elsewhere without the written permission of the editors.

Submission of the manuscript

The manuscript written in English should be submitted to the journal via online submission system Editorial Manager available for this journal at: **www.radioloncol.com**.

In case of problems, please contact Sašo Trupej at **saso.trupej@computing.si** or the Editor of this journal at **gsersa@onko-i.si**

All articles are subjected to the editorial review and when the articles are appropriated they are reviewed by independent referees. In the cover letter, which must accompany the article, the authors are requested to suggest 3-4 researchers, competent to review their manuscript. However, please note that this will be treated only as a suggestion; the final selection of reviewers is exclusively the Editor's decision. The authors' names are revealed to the referees, but not vice versa.

Manuscripts which do not comply with the technical requirements stated herein will be returned to the authors for the correction before peer-review. The editorial board reserves the right to ask authors to make appropriate changes of the contents as well as grammatical and stylistic corrections when necessary. Page charges will be charged for manuscripts exceeding the recommended length, as well as additional editorial work and requests for printed reprints.

Articles are published printed and on-line as the open access: (**https://content.sciendo.com/raon**).

All articles are subject to 1200 EUR + VAT publication fee. Exceptionally, waiver of payment may be negotiated with editorial office, at the time of article submission.

Manuscripts submitted under multiple authorship are reviewed on the assumption that all listed authors concur in the submission and are responsible for its content; they must have agreed to its publication and have given the corresponding author the authority to act on their behalf in all matters pertaining to publication. The corresponding author is responsible for informing the coauthors of the manuscript status throughout the submission, review, and production process.

Preparation of manuscripts

Radiology and Oncology will consider manuscripts prepared according to the Uniform Requirements for Manuscripts Submitted to Biomedical Journals by International Committee of Medical Journal Editors (www.icmje.org). The manuscript should be written in grammatically and stylistically correct language. Abbreviations should be avoided. If their use is necessary, they should be explained at the first time mentioned. The technical data should conform to the SI system. The manuscript, excluding the references, tables, figures and figure legends, must not exceed 5000 words, and the number of figures and tables is limited to 8. Organize the text so that it includes: Introduction, Materials and methods, Results and Discussion. Exceptionally, the results and discussion can be combined in a single section. Start each section on a new page, and number each page consecutively with Arabic numerals. For ease of review, manuscripts should be submitted as a single column, double-spaced text.

The Title page should include a concise and informative title, followed by the full name(s) of the author(s); the institutional affiliation of each author; the name and address of the corresponding author (including telephone, fax and E-mail), and an abbreviated title (not exceeding 60 characters). This should be followed by the abstract page, summarizing in less than 250 words the reasons for the study, experimental approach, the major findings (with specific data if possible), and the principal conclusions, and providing 3-6 key words for indexing purposes. Structured abstracts are required. Slovene authors are requested to provide title and the abstract in Slovene language in a separate file. The text of the research article should then proceed as follows:

Introduction should summarize the rationale for the study or observation, citing only the essential references and stating the aim of the study.

Materials and methods should provide enough information to enable experiments to be repeated. New methods should be described in details.

Results should be presented clearly and concisely without repeating the data in the figures and tables. Emphasis should be on clear and precise presentation of results and their significance in relation to the aim of the investigation.

Discussion should explain the results rather than simply repeating them and interpret their significance and draw conclusions. It should discuss the results of the study in the light of previously published work.

Charts, Illustrations, Images and Tables

Charts, Illustrations, Images and Tables must be numbered and referred to in the text, with the appropriate location indicated. Charts, Illustrations and Images, provided electronically, should be of appropriate quality for good reproduction. Illustrations and charts must be vector image, created in CMYK color space, preferred font "Century Gothic", and saved as .AI, .EPS or .PDF format. Color charts, illustrations and Images are encouraged, and are published without additional charge. Image size must be 2.000 pixels on the longer side and saved as .JPG (maximum quality) format. In Images, mask the identities of the patients. Tables should be typed double-spaced, with a descriptive title and, if appropriate, units of numerical measurements included in the column heading. The files with the figures and tables can be uploaded as separate files.

References

References must be numbered in the order in which they appear in the text and their corresponding numbers quoted in the text. Authors are responsible for the accuracy of their references. References to the Abstracts and Letters to the Editor must be identified as such. Citation of papers in preparation or submitted for publication, unpublished observations, and personal communications should not be included in the reference list. If essential, such material may be incorporated in the appropriate place in the text. References follow the style of Index Medicus, DOI number (if exists) should be included.

All authors should be listed when their number does not exceed six; when there are seven or more authors, the first six listed are followed by "et al.". The following are some examples of references from articles, books and book chapters:

Dent RAG, Cole P. In vitro maturation of monocytes in squamous carcinoma of the lung. *Br J Cancer* 1981; **43:** 486-95. doi: 10.1038/bjc.1981.71

Chapman S, Nakielny R. *A guide to radiological procedures*. London: Bailliere Tindall; 1986.

Evans R, Alexander P. Mechanisms of extracellular killing of nucleated mammalian cells by macrophages. In: Nelson DS, editor. *Immunobiology of macrophage.* New York: Academic Press; 1976. p. 45-74.

Authorization for the use of human subjects or experimental animals

When reporting experiments on human subjects, authors should state whether the procedures followed the Helsinki Declaration. Patients have the right to privacy; therefore, the identifying information (patient's names, hospital unit numbers) should not be published unless it is essential. In such cases the patient's informed consent for publication is needed, and should appear as an appropriate statement in the article. Institutional approval and Clinical Trial registration number is required. Retrospective clinical studies must be approved by the accredited Institutional Review Board/Committee for Medical Ethics or other equivalent body. These statements should appear in the Materials and methods section.

The research using animal subjects should be conducted according to the EU Directive 2010/63/EU and following the Guidelines for the welfare and use of animals in cancer research (Br J Cancer 2010; 102: 1555 – 77). Authors must state the committee approving the experiments, and must confirm that all experiments were performed in accordance with relevant regulations.

These statements should appear in the Materials and methods section (or for contributions without this section, within the main text or in the captions of relevant figures or tables).

Transfer of copyright agreement

For the publication of accepted articles, authors are required to send the License to Publish to the publisher on the address of the editorial office. A properly completed License to Publish, signed by the Corresponding Author on behalf of all the authors, must be provided for each submitted manuscript.

Conflict of interest

When the manuscript is submitted for publication, the authors are expected to disclose any relationship that might pose real, apparent or potential conflict of interest with respect to the results reported in that manuscript. Potential conflicts of interest include not only financial relationships but also other, non-financial relationships. In the Acknowledgement section the source of funding support should be mentioned. The Editors will make effort to ensure that conflicts of interest will not compromise the evaluation process of the submitted manuscripts; potential editors and reviewers will exempt themselves from review process when such conflict of interest exists. The statement of disclosure must be in the Cover letter accompanying the manuscript or submitted on the form available on **www.icmje.org/coi_disclosure.pdf**

Page proofs

Page proofs will be sent by E-mail to the corresponding author. It is their responsibility to check the proofs carefully and return a list of essential corrections to the editorial office within three days of receipt. Only grammatical corrections are acceptable at that time.

Open access

Papers are published electronically as open access on **https://content.sciendo.com/raon**, also papers accepted for publication as E-ahead of print.

LORVIQUA®
LORLATINIB

Pri bolnikih z metastazami v CŽS ali brez njih

SOOČITE

ALK+ mNSCLC Z ZDRAVILOM LORVIQUA

Zdravilo **LORVIQUA** v monoterapiji je indicirano za zdravljenje odraslih bolnikov z napredovalim nedrobnoceličnim rakom pljuč (NSCLC), ki je ALK pozitiven, in se predhodno niso zdravili z zaviralcem ALK.[1]

Zdravilo **LORVIQUA** v monoterapiji je indicirano za zdravljenje odraslih bolnikov z napredovalim NSCLC, ki je ALK-pozitiven, pri katerih je bolezen napredovala po:

- zdravljenju z alektinibom ali ceritinibom kot prvim ALK zaviralcem tirozin kinaze (TKI); ali
- zdravljenju s krizotinibom in vsaj še 1 drugim ALK TKI.[1]

BISTVENI PODATKI IZ POVZETKA GLAVNIH ZNAČILNOSTI ZDRAVILA

Lorviqua 25 mg, 100 mg filmsko obložene tablete
▼Za to zdravilo se izvaja dodatno spremljanje varnosti. Tako bodo hitreje na voljo nove informacije o njegovi varnosti. Zdravstvene delavce naprošamo, da poročajo o kateremkoli domnevnem neželenem učinku zdravila. Glejte poglavje 4.8 povzetka glavnih značilnosti zdravila, kako poročati o neželenih učinkih. **Sestava in oblika zdravila:** Ena filmsko obložena tableta vsebuje 25 mg ali 100 mg lorlatiniba in 1,58 mg oz. 4,20 mg laktoze monohidrata. **Indikacije:** Zdravljenje odraslih bolnikov z napredovalim nedrobnoceličnim rakom pljuč (NSCLC – *Non-Small Cell Lung Cancer*), ki je ALK (anaplastična limfomska kinaza) pozitiven in se predhodno niso zdravili z zaviralcem ALK, ter pri bolnikih, pri katerih je bolezen napredovala po: zdravljenju z alektinibom ali ceritinibom kot prvim ALK zaviralcem tirozin kinaze (TKI – *Tyrosine Kinase Inhibitor*) ali zdravljenju s krizotinibom in vsaj še 1 drugim ALK TKI. **Odmerjanje in način uporabe:** Zdravljenje mora uvesti in nadzorovati zdravnik, ki ima izkušnje z uporabo zdravil za zdravljenje rakavih bolezni. Odkrivanje ALK-pozitivnega NSCLC je potrebno pri izbiri bolnikov, saj so to edini bolniki, pri katerih so dokazali korist. Priporočeni odmerek je 100 mg peroralno enkrat na dan. Zdravljenje je treba nadaljevati do napredovanja bolezni ali nesprejemljive toksičnosti. Če bolnik izpusti odmerek, ga mora vzeti takoj, ko se spomni, razen če do naslednjega odmerka manjka manj kot 4 ure. Bolniki ne smejo vzeti 2 odmerkov hkrati, da bi nadomestili izpuščeni odmerek. Prilagajanje odmerkov: Ravni zmanjšanja odmerka: *prvo zmanjšanje odmerka*: 75 mg peroralno enkrat na dan; *drugo zmanjšanje odmerka*: 50 mg peroralno enkrat na dan. Zdravljenje je treba trajno prekiniti, če bolnik ne prenaša odmerka 50 mg peroralno enkrat na dan. Za prilagajanje odmerkov zaradi neželenih učinkov glejte preglednico 1 v SmPC-ju. Posebne populacije: *Starejši bolniki (≥ 65 let):* Zaradi omejenih podatkov priporočil o odmerjanju ni mogoče dati. *Okvara ledvic*: Prilagajanje odmerkov pri bolnikih z normalnim delovanjem in blago ali zmerno okvaro [absolutna ocena hitrosti glomerulne filtracije (eGFR – estimated Glomerular Filtration Rate): ≥ 30 ml/min] ni potrebno. Pri bolnikih s hudo okvaro ledvic (absolutna vrednost eGFR < 30 ml/min) je priporočljiv zmanjšan odmerek lorlatiniba, npr. začetni odmerek 75 mg peroralno enkrat na dan. Podatkov pri bolnikih na ledvični dializi ni na voljo. *Okvara jeter*: Pri bolnikih z blago okvaro ni potrebno prilagajanje odmerkov. Podatkov o uporabi pri zmerni ali hudi okvari ni, zato uporaba ni priporočljiva. *Pediatrična populacija*: Varnost in učinkovitost pri otrocih in mladostnikih, starih < 18 let, nista bili dokazani. Način uporabe: Peroralna uporaba, vsak dan ob približno istem času, s hrano ali brez nje. Tablete je treba pogoltniti cele. **Kontraindikacije:** Preobčutljivost na učinkovino ali katerokoli pomožno snov. Uporaba močnih induktorjev CYP3A4/5. **Posebna opozorila in previdnostni ukrepi:** Hiperlipidemija: Uporaba je povezana z zvečanji vrednosti holesterola in trigliceridov v serumu – morda bo treba uvesti ali povečati odmerek zdravil za zniževanje ravni lipidov. Učinki na osrednje živčevje: Opazili so učinke na osrednje živčevje, vključno s psihotičnimi učinki in spremembami v kognitivni funkciji, razpoloženju, duševnem stanju ali govoru – morda bo treba prilagoditi odmerek ali prekiniti zdravljenje. Atrioventrikularni blok: Pri bolnikih, ki so prejemali lorlatinib, so poročali o podaljšanju intervala PR in AV-bloku. Potrebno je spremljanje EKG in morda bo treba prilagoditi odmerek. Zmanjšanje iztisnega deleža levega prekata: Pri bolnikih, ki so prejemali lorlatinib in pri katerih so opravili izhodiščno in še vsaj eno nadaljnjo oceno iztisnega deleža levega prekata (LVEF – *Left Ventricular Ejection Fraction*), so poročali o zmanjšanju LVEF. Če imajo bolniki dejavnike tveganja za srce ali stanja, ki vplivajo na LVEF, ali se jim med zdravljenjem pojavijo pomembni srčni znaki/simptomi, je treba razmisliti o spremljanju srca, vključno z oceno LVEF. Zvečanje vrednosti lipaze in amilaze: Pri bolnikih, ki so prejemali lorlatinib, se je pojavilo zvečanje vrednosti lipaze in/ali amilaze. Zaradi sočasne hipertrigliceridemije in/ali morebitnega intrinzičnega mehanizma je treba upoštevati tveganje za pankreatitis. Bolnike je treba spremljati glede zvečanja vrednosti lipaze in amilaze. Intersticijska bolezen pljuč (ILD – *Interstitial Lung Disease*)/pnevmonitis: Pri uporabi lorlatiniba so se pojavili hudi ali življenjsko ogrožajoči pljučni neželeni učinki, skladni z ILD/pnevmonitisom. Vse bolnike, pri katerih pride do poslabšanja respiratornih simptomov, ki kažejo na ILD/pnevmonitis, je treba takoj pregledati glede ILD/pnevmonitisa. Hipertenzija: Pri bolnikih, ki so prejemali loratinib, so poročali o hipertenziji. Pred uvedbo lorlatiniba mora biti krvni tlak pod nadzorom. Med zdravljenjem je treba krvni tlak preveriti po 2 tednih in nato najmanj enkrat na mesec ter glede na stopnjo resnosti zdravljenje prekiniti in nato nadaljevati z zmanjšanim odmerkom ali trajno prekiniti. Hiperglikemija: Pri bolnikih, ki so prejemali loratinib, se je pojavila hiperglikemija. Pred uvedbo je treba oceniti koncentracijo glukoze v serumu na tešče in jo nato redno spremljati v skladu z nacionalnimi smernicami ter glede na stopnjo resnosti zdravljenje prekiniti in nato nadaljevati z zmanjšanim odmerkom ali trajno prekiniti. Laktoza: Vsebuje laktozo. Bolniki z redko dedno intoleranco za galaktozo, odsotnostjo encima laktaze ali malabsorpcijo glukoze/galaktoze ne smejo jemati tega zdravila. **Medsebojno delovanje z drugimi zdravili in druge oblike interakcij:** Učinek zdravil na lorlatinib: *Induktorji CYP3A4/5:* Sočasna uporaba močnih induktorjev CYP3A4/5 (npr. rifampicin, karbamazepin, enzalutamid, mitotan, fenitoin in šentjanževka) je kontraindicirana. *Zaviralci CYP3A4/5:* Sočasni uporabi močnih zaviralcev CYP3A4/5 (npr. boceprevir, kobicistat, itrakonazol, ketokonazol, posakonazol, troleandomicin, vorikonazol, ritonavir, paritaprevir v kombinaciji z ritonavirom in ombitasvirom in/ali dasabuvirom ter ritonavir v kombinaciji z elvitegravirom, indinavirom, lopinavirom ali tipranavirom in grenivka ali grenivkin sok), se je treba izogibati, saj lahko pride do zvečanja koncentracij lorlatiniba v plazmi (če je sočasna uporaba nujna, je priporočljivo zmanjšati odmerek lorlatiniba). Učinek lorlatiniba na druga zdravila: *Substrati CYP3A4/5:* Izogibati se je treba sočasnemu dajanju lorlatiniba in substratov CYP3A4/5 z ozkimi terapevtskimi indeksi (npr. alfentanil, ciklosporin, dihidroergotamin, ergotamin, fentanil, hormonski kontraceptivi, pimozid, kinidin, sirolimus in takrolimus), saj lahko lorlatinib zmanjša koncentracije teh zdravil. *Substrati P-glikoproteina:* Substrate P-gp, ki imajo ozke terapevtske indekse (npr. digoksin, dabigatraneteksilat), je treba v kombinaciji z lorlatinibom uporabljati previdno, saj obstaja verjetnost, da se koncentracija teh substratov v plazmi zmanjša. *Študije in vitro s prenašalci zdravil, ki niso P-gp:* Lorlatinib je treba v kombinaciji s substrati BCRP, OATP1B1, OATP1B3, OCT1, MATE1 in OAT3 uporabljati previdno, saj klinično pomembnih sprememb v plazemski izpostavljenosti teh substratov ni mogoče izključiti. **Plodnost, nosečnost in dojenje:** Ženskam v rodni dobi je treba svetovati, naj se med zdravljenjem z lorlatinibom izogibajo zanositvi in naj med zdravljenjem uporabljajo visoko učinkovito nehormonsko metodo kontracepcije, saj lahko lorlatinib povzroči, da hormonski kontraceptivi postanejo neučinkoviti. Učinkovito kontracepcijo je treba uporabljati še vsaj 35 dni po zaključku zdravljenja. Med zdravljenjem in še vsaj 14 tednov po zadnjem odmerku morajo bolniki, ki imajo partnerice v rodni dobi, uporabljati učinkovito kontracepcijo. Nosečnost: Študije na živalih so pokazale embriofetalno toksičnost, zato uporaba med nosečnostjo ali pri ženskah v rodni dobi, ki ne uporabljajo kontracepcije, ni priporočljiva. Dojenje: Med zdravljenjem in še 7 dni po zadnjem odmerku je treba prenehati z dojenjem. Plodnost: Zdravljenje lahko ogrozi plodnost pri moških. **Vpliv na sposobnost vožnje in upravljanja strojev:** Ima zmeren vpliv na sposobnost vožnje in upravljanja strojev. Potrebna je previdnost, saj se pri bolnikih lahko pojavijo učinki na osrednje živčevje. **Neželeni učinki:** Zelo pogosti: anemija, hiperholesterolemija, hipertrigliceridemija, učinki na razpoloženje, učinki na kognitivne funkcije, periferna nevropatija, glavobol, motnja vida, hipertenzija, diareja, navzea, zaprtje, izpuščaj, artralgija, mialgija, edem, utrujenost, zvečanje telesne mase, zvečanje vrednosti lipaze, zvečanje vrednosti amilaze. **Način in režim izdaje:** Rp/Spec - Predpisovanje in izdaja zdravila je le na recept zdravnika specialista ustreznega področja medicine ali od njega pooblaščenega zdravnika. **Imetnik dovoljenja za promet:** Pfizer Europe MA EEIG, Boulevard de la Plaine 17, 1050 Bruxelles, Belgija. **Datum zadnje revizije besedila:** 04.04.2022

Pred predpisovanjem se seznanite s celotnim povzetkom glavnih značilnosti zdravila.

Literatura: 1. Povzetek glavnih značilnosti zdravila Lorviqua, 4.4.2022.

ALK = anaplastična limfomska kinaza, **CŽS** = centralni živčni sistem, **mNSCLC** = (Metastatic Non-Small Cell Lung Cancer) metastatski nedrobnocelični rak pljuč, **NSCLC** = (Non-Small Cell Lung Cancer) nedrobnocelični rak pljuč, **TKI** = (Tyrosine Kinase Inhibitor) zaviralec tirozin kinaze.

Pfizer Luxembourg SARL, GRAND DUCHY OF LUXEMBOURG, 51, Avenue J.F. Kennedy, L – 1855,
Pfizer, podružnica Ljubljana, Letališka cesta 29a, 1000 Ljubljana

PP-LOR-SVN-0005
Datum priprave: april 2022.
Samo za strokovno javnost.

Radiology and Oncology | Ljubljana | Slovenia | https://sciendo.com/journal/RAON

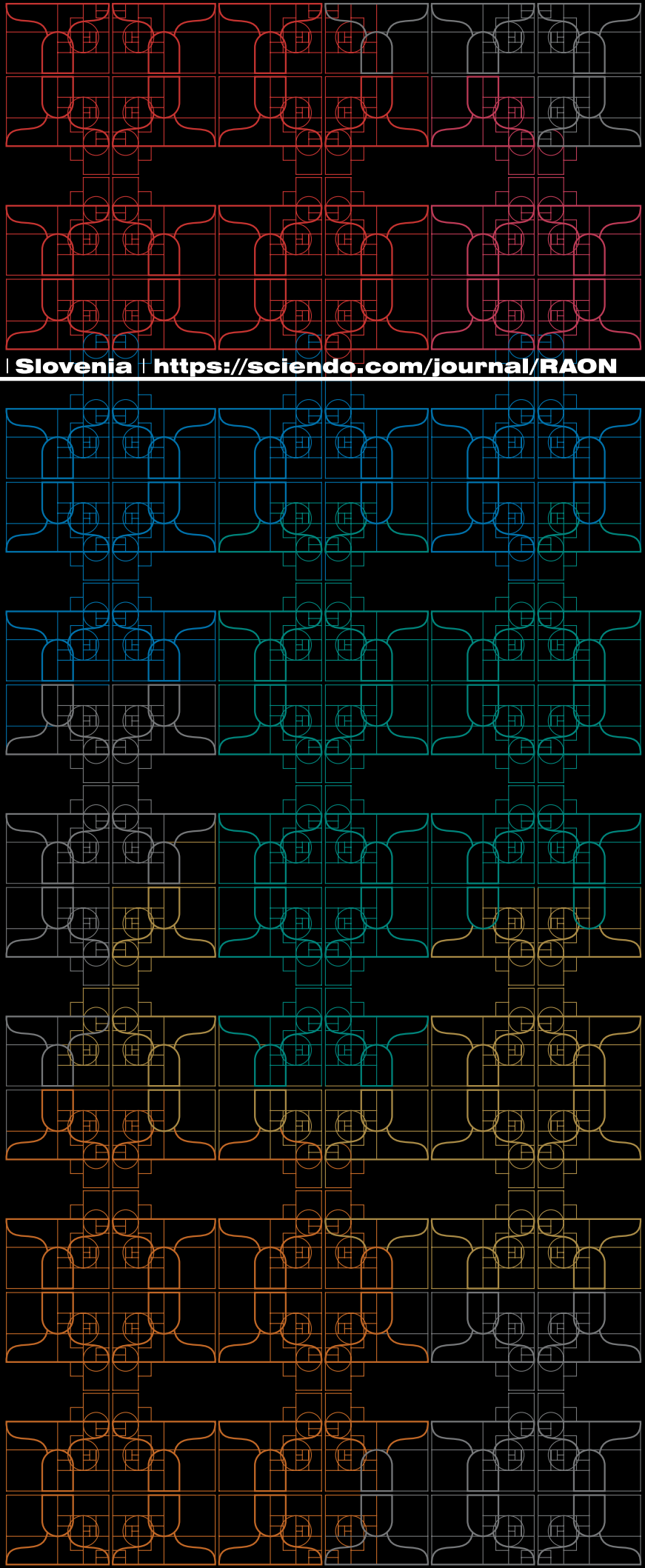

ISSN 1318 - 2099